Three-dimensional slope stability effects in the failure at the Mount Polley Tailings Storage Facility

by

Elena Zabolotnii

A thesis submitted in partial fulfillment of the requirements for the degree of

Doctor of Philosophy

in

GEOTECHNICAL ENGINEERING

Department of Civil and Environmental Engineering
University of Alberta

ABSTRACT

On 4 August 2014, a breach occurred in the perimeter embankment at the Mount Polley Tailings Storage Facility in British Columbia, Canada, causing a spill of mining waste into the environment. The Government of British Columbia retained an Independent Review Panel (2015) to determine the cause of failure.

The breach was sudden and without observable precursors. During the collapse, the mass of soil underwent a rotational-translational movement involving large horizontal displacements in a foundation unit ~10m below original ground level. The slippage at the base took place in a thin (≤2m) deposit designated as the "Upper Glaciolacustrine Unit", or the Upper GLU. The IRP determined that undrained strengths controlled this unit's mechanical behaviour during failure. Furthermore, the clay's strain-weakening properties made it susceptible to progressive failure. The IRP found that the breach occurred when the peak undrained shear strength of this material was exceeded. These findings were supported by two-dimensional analyses.

A detailed three-dimensional static analysis demonstrated that, due to large amounts of shearing resistance developed along the sides of the slide, the entire Upper GLU area involved in the failure would have to fully weaken in order to bring the soil mass to a limiting equilibrium. Such a result posed two additional questions, one related to pre-failure deformation levels and another pertaining to the failure modes in the Upper GLU.

Laboratory tests indicate that shear strains ≥60% would be required for the unit to fully weaken; in a 2m deposit, this may mean lateral deformations ≥1.2m prior to collapse. From the brittle nature of this failure we know that no such deformations had taken place. Additionally, deformation analyses have shown that a portion of Upper GLU in the failure zone, about ⅓ by area, would have remained overconsolidated during collapse and thus much stronger.

To reconcile the apparent incongruity of conclusions suggested by static and deformation analyses, it has been hypothesized that (a) the Upper GLU strained non-linearly, weakening considerably prior to collapse, but without significant shear displacements; and (b) some other material was weaker at failure than originally thought. The rockfill material in the shell area was a suspect due to poor compaction during placement. A proposition was put forward that the rockfill's deformation modulus was significantly lower than that of other materials involved in this failure. In the absence of substantial deformations prior to collapse, this material was thought to have only partially mobilized its shear strength.

The failure at Mount Polley was investigated using three-dimensional deformation analysis. The mechanical behaviours of soils involved in the failure were captured through customized constitutive models that were developed on the basis of, and calibrated against, laboratory testing results and published data. The embankment construction sequence was simulated in nine loading stages.

The simulation results indicate that the progressive failure at Mount Polley started as early as 2011, advancing as the embankment construction proceeded, but remaining contained until the summer of 2014. By the fall of 2013, in addition to the contained failure, three specific material conditions developed in the foundation materials that brought the structure to the verge of instability. These are (a) the substantial depletion of reserve shear strengths in the materials surrounding the plastic yield zones; (b) the emergence of a large area close to the precipice of weakening; and (c) the extension of some brittle soil units in the failure zone.

In the final construction stage, the addition of 2.5-4m of embankment materials in the shell, crest and beach areas triggered collapse under undrained conditions. The collapse unfolded in two distinct phases. In phase one, the failure processes were largely contained to a thin shear band in the Upper GLU where ongoing strain-weakening processes resulted in a decrease of shear resistance and an accumulation of shear displacements. In phase two, the shear zone propagated into other soils, and multiple local failures developed in the upstream region of the slide. In this phase, a sustained drop of mobilized shear resistance levels was observed at the base and in the upstream regions of the slide. In the shell zone, the shear strength of the rockfill was not fully mobilized even in the advanced stages of collapse.

To my mentors over the years

Paul D. Hunt

Emmanuel K. Quaye

Augusto Lucarelli

ACKNOWLEDGMENTS

First and foremost, I would like to recognize that this research project builds on the foundation of knowledge laid by two exemplary investigation teams that studied the failure at the Mount Polley Tailings Storage Facility. These are:

- The Independent Engineering Expert Investigation and Review Panel established by the Government of British Columbia in conjunction with the Williams Lake Indian Band and the Soda Creek Indian Band, that evaluated the events at Mount Polley in the aftermath of the collapse.
- The investigation team assembled by the engineering consultancy Klohn Crippen Berger to carry out an independent review of the collapse on behest of the Chief Inspector of Mines with British Columbia's Ministry of Energy and Mines.

In addition, I would like to acknowledge the many agencies that have supported this research through funding as well as educational and work partnerships:

- The Government of Canada and its Vanier Canada Graduate Scholarships program.
- The Government of Alberta and its Alberta Innovates Scholarship program.
- The Itasca Consulting Group and its Educational Partnership program. A special thanks goes to Augusto Lucarelli, Principal Engineer with Itasca, for his mentorship through the more challenging modelling aspects in this project.
- Soilvision® by Bentley Systems Incorporated for the strong working relationship we enjoyed throughout this project and beyond. A special thanks goes to Murray Fredlund, HaiHua Lu and Rob Thode.
- The Canadian Dam Association and its Gary Salmon Scholarship Fund.
- Klohn Crippen Berger and its Earle Klohn Scholarship program.

TABLE OF CONTENTS

LIST OF TABLES

LIST OF APPENDIX TABLES

LIST OF FIGURES

LIST OF APPENDIX FIGURES

GLOSSARY

anisotropy	variation of properties as a function of direction
artesian conditions	pore water pressure that is above hydrostatic and is associated with an upward flow of groundwater
aspect ratio	the ratio of the depth of the width of a slide
average force ratio	as defined by Itasca (2018), the sum of all out-of-balance force components at every gridpoint divided by the sum of all total forces applied at gridpoint
back-analysis	a slope stability analysis of a failed slope with the objective of determining the mechanics of failure; in such analysis, the safety factor is generally assumed to be equal to unity or reasonably close to it
crest of embankment	top of embankment, usually around the core
deformation analysis	the evaluation of slope performance using the principles of mechanics of deformable solids in combination with numerical techniques; commonly referred to as "numerical analysis"
dilatancy	a soil's tendency to increase in volume on shearing
discretization error	the difference between the exact and approximate solutions in the context of deformation analysis
dry density	the contribution to density by the solid phase only, i.e. the ratio of the mass of solids to total volume
end effects	three-dimensional slope stability effects
foundation failure	a slide with a base located in a soil unit below original ground elevation

glaciofluvial soil	a soil deposited in flowing glacial water
glaciolacustrine soil	a fine-grained soil deposited in a glacial lake
headscarp	the top edge of the slide on the upstream; often distinguished from downward soil movements
lateral stress	in the context of triaxial tests, the confining stress $\sigma_2 = \sigma_3$
limit equilibrium analysis	a type of analysis intended to evaluate the stability of a slope by calculating the ratio of available shear strengths to working shear stresses along the critical slip surface, also known as the slope's safety factor
limiting equilibrium	a condition where the mobilized shear resistance along the critical slip surface equals the available shear strength, resulting in a safety factor of unity
local safety factor	the ratio of available shear strength to the mobilized shear resistance in a single element (zone) of a discrete model
normally consolidated soil	a soil whose present effective overburden pressure is also the highest effective overburden pressure that it has experienced in the past
overconsolidated soil	a soil that has been subjected to effective overburden pressures that are higher than the current ones
overconsolidation ratio	the ratio of preconsolidation pressure to the present effective overburden stress
overtopping	water flowing over the crest of an embankment or other structure
peak undrained shear strength	the maximum undrained shear resistance of a soil, typically at low strain levels

pore pressure	pore water pressure
pore water pressure	the pressure of water in the pores of a soil
porosity	the ratio of volume of voids to the total volume
post-peak shear strengths	undrained shear strengths below peak values
preconsolidation pressure	the maximum effective overburden stress experienced by a soil
pre-sheared plane	a polished plane formed by prior shearing of the soil
quick clays	clays deposited in a marine environment where the seawater in the pores was gradually replaced with fresh groundwater; and exhibiting high sensitivities as a result of this
residual undrained shear strength	the minimum undrained shear resistance of a soil, typically at large shear strains or due to significant disturbance
scale effects	the variation of a simulation response resulting from a variation of discretization levels
sensitivity	the ratio of peak to residual undrained shear strengths
shell	the downstream portion of the earthen embankment whose function is to buttress the core; at Mount Polley, comprised largely of weak-to-medium strength rockfill material
side wall effects	three-dimensional slope stability effects; also sidewall resistance
soil crust	the weathered portion of soil located at ground surface
static analysis	limit equilibrium analysis
strain-softening material	strain-weakening material; see §1.3.1.3

strain-weakening material	a material that experiences a loss of shear strength due to an accumulation of plastic strain
three-dimensional slope stability effects	the difference between the two- and three-dimensional safety factor calculated using Eq. 1.1 in §1.1.2
toe of slide	the region at the base of the slide on the downstream side; often distinguished from upward soil movements
undisturbed strength	peak undrained shear strength
undrained analysis	a slope stability analysis using undrained shear strengths
undrained strength	strength that accounts for the effects of pore pressures that develop in the shear zone on rapid and/or constant volume shearing
undrained strength ratio	ratio of undrained shear strength to overburden effective stresses, s_u/σ'_{ov}
unsaturated soil	a soil with a saturation below 100%, where some air or other gas is present in the pores
varved clay	a clay deposit with a laminated macro-structure formed as a result of seasonal or other variations of flow velocity
void ratio	the ratio of volume of voids to the volume of solids
weakening	loss of shear strength

LIST OF ABBREVIATIONS

CPT	Cone Penetration Test
DSS	Direct Simple Shear Test
FOS	Safety Factor or Factor of Safety
GLU	Glaciolacustrine Unit
IRP	The Independent Engineering Expert Investigation Panel
KCB	Klohn Crippen Berger
LGF	Lower Glaciofluvial Unit
LGLU	Lower Glaciolacustrine Unit
MEM	British Columbia's Ministry of Energy and Mines
MGT	Middle Glacial Till
OCR	Overconsolidation Ratio
SSR	The shear strength reduction method for calculating the safety factor
TSF	Tailings Storage Facility
UGF	Upper Glaciofluvial Unit
UGLU	Upper Glaciolacustrine Unit
UGT	Upper Glacial Till, also Upper Till

LIST OF SYMBOLS

c'	cohesion parameter, in units of pressure
I_1	first invariant of the stress tensor
s_u	undrained shear strength, in units of pressure
$s_{u,peak}$	peak undrained shear strength, in units of pressure
$s_{u,residual}$	residual undrained shear strength, in units of pressure
s_u/σ'_{ov}	undrained strength ratio; used to describe the depth-dependent increase in undrained strength, which is often linear
s_u/σ'_{vc}	ratio of undrained strength to vertical consolidation pressures, used to describe the gain in undrained shear strength due to consolidation in the vertical direction
γ_{bulk}	bulk unit weight, in units of force per volume
γ^p_s	plastic shear strain, in percent or unit-free
σ'_{cv}	vertical consolidation pressure, same as preconsolidation pressure
σ'_n	the effective stress acting normal to a plane
σ'_{ov}	effective overburden pressure
σ_p	preconsolidation pressure
τ_{cr}	mobilized shear stress along the critical plane
τ_f	shear strength, in units of pressure
τ_{xz}	in the context of this thesis, the mobilized shear stress along the plane normal to the vertical axis in the downstream direction, i.e. along the direction of soil movement
ϕ'	effective friction angle, in degrees or radians

ϕ'_{peak} peak effective friction angle, in degrees or radians

$\phi'_{residual}$ residual effective friction angle, in degrees or radians

THESIS ORGANIZATION

This Thesis contains six chapters organized as follows.

Chapter One sets out to clarify the meaning and origin of three-dimensional slope stability effects. In this chapter, seven classic case histories of slope stability are revisited and their two- and three-dimensional limit equilibrium back-analyses are compared. The findings are then reviewed as a whole in order to determine how the omission of three-dimensional stability effects from analysis may affect the conclusions.

Chapter Two introduces the hypothesis at the foundation of this thesis. In this chapter, prior investigations of the failure at the Mount Polley Tailings Storage Facility are evaluated to highlight the outstanding questions. Two- and three-dimensional back-analyses of this failure are evaluated side-by-side in order to quantify the magnitude of three-dimensional slope stability effects. Finally, two propositions are put forward that may help explain the apparent inconsistencies between the three-dimensional static analyses, laboratory data and field observations.

Chapter Three documents the development of a three-dimensional deformation model intended to evaluate the propositions formulated in Chapter Two.

Chapter Four introduces the results of the three-dimensional deformation analysis of the failure at Mount Polley obtained under the large strain calculation scheme.

Chapter Five introduces the results of the three-dimensional deformation analysis of the failure at Mount Polley obtained under the small strain calculation scheme.

In Chapter Six, the results of the deformation analyses in Chapters Four and Five are examined to evaluate the hypothesis put forward in Chapter Two and to propose an interpretation of the unfolding of progressive failure at the Mount Polley Tailings Storage Facility.

INTRODUCTION

Background

On 4 August 2014, a breach occurred in the perimeter embankment at the Mount Polley Tailings Storage Facility (TSF) in British Columbia, Canada, causing a spill of mining waste into the environment. This event received extensive news coverage and triggered an unprecedented level of industry reviews and evaluations. The Government of British Columbia, together with the Williams Lake Indian Band and the Soda Creek Indian Band, established an Independent Expert Engineering Investigation and Review Panel (IRP) to determine the cause of failure and to make recommendations regarding best practices that would prevent the occurrence of such events in the future.

The IRP determined that the breach of the embankment at the Mount Polley TSF took place by shear failure in the foundation when the loads imposed onto the structure exceeded the capacity of dam and foundation materials to sustain it (IRP 2015, p. 135). During the embankment collapse, the mass of soil underwent a rotational-translational movement involving large horizontal displacements in a foundation unit ~10m below the original ground level. The slippage at the base took place in a thin varved clay deposit designated as the "Upper Glaciolacustrine Unit", or the Upper GLU. The IRP found that the breach occurred when the peak undrained shear strength of this material was exceeded and was of the view that *progressive failure was involved in the initiation of the collapse* (IRP 2015, p.103). The IRP findings were supported by two-dimensional static and deformation analyses that suggested that average strengths slightly below peak values were acting at failure in the Upper GLU.

The IRP also completed a cursory three-dimensional static analysis of the breach and determined that *substantial three-dimensional stability effects were present at the failure location*. This finding suggests that the two-dimensional back-analyses of the breach are in some error. The IRP stated that these findings merit an explanation and hypothesized that the weakening in the Upper GLU at the start of collapse may have been more extensive than indicated by the two-dimensional analyses, possibly full.

Outline of the research opportunity

Dr. N.R. Morgenstern, Chair of the IRP, championed the research undertaking at the centre of this thesis, seeking comprehensive answers regarding the unfolding of the progressive failure at Mount Polley in the context of considerable three-dimensional stability effects present at the site.

To the geotechnical researcher, the Mount Polley case study offers a rare opportunity to expand our understanding of progressive failure. The site conditions at Mount Polley, including the soil profile, the history of embankment construction, the material properties of the structure and foundations, the water balance and more, have been recorded in detail. Such level of data resolution would enable one to create fairly comprehensive simulations of the events, calibrate and verify the response against observation, and closely examine the failure processes within. Furthermore, neither the structure nor the foundation soils are unordinary in any way. The embankment was built using a modified centreline design much in the same way many other tailings dams are built around the world. The materials used in its construction were from nearby borrows and their material properties are fairly well understood. The glaciolacustrine unit at the base of the slide that triggered the embankment failure is a type of deposit that is rather common in areas subjected to glaciations in the past, and its strain-weakening properties that made it susceptible to progressive failure are typical for such soils. Therefore, lessons learnt from this event would serve us well in our pursuit of zero failures.

Questions central to this thesis

Detailed static three-dimensional analyses of the breach at Mount Polley indicate that, to overcome the shear resistance along the three-dimensional slip surface, the shear resistance in the Upper GLU would have to be reduced to the lowest estimates of residual values. Such a result raised two additional questions, one regarding the pre-failure deformation levels that would be associated with such severe weakening, and another related to the failure modes in the Upper GLU.

Pre-failure deformation levels: Laboratory tests indicate that shear strains ≥60% would be required to reduce the shear resistance in the Upper GLU to its residual value; in a deposit with a thickness of ~2m, this suggests deformations in the order of 1.2m. From the brittle nature of this failure it is clear that no such deformations could have taken place prior to the initiation of the collapse. To reconcile this apparent inconsistency, a hypothesis was put forward that the Upper GLU acted not as a uniform block but as a layered system whereby a thin layer of this material strained more than others, weakening in the process. Under this proposition, it is conceivable that the entire Upper GLU area in the failure zone could have strained sufficiently but without observable shear deformations.

Failure modes in the Upper GLU: The IRP found that it was the transition of the Upper GLU from a state of overconsolidation to a state of normal consolidation that made this material susceptible to undrained failure. However, preliminary deformation analyses indicated that at least ⅓ of the Upper GLU in the failure zone was still overconsolidated at the time of collapse. This material remained dilative on shearing and stronger than the normally consolidated portion of the unit. If its shearing resistance could not be reduced to its undrained residual value, then it would be impossible to bring the failed soil mass to a limiting equilibrium unless some other soil or soils in the failure zone were also weaker than indicated by the two-dimensional back-analyses. Following an extensive examination of site data and a literature review, a second hypothesis was formulated that the deformation modulus of the rockfill material in the shell was lower than that of other materials in the failure zone, resulting in an incomplete mobilization of shear strength in this material during collapse.

Research methodology

The two hypotheses formulated to explain the embankment collapse at Mount Polley in the context of pronounced three-dimensional slope stability effects present at the location were tested using three-dimensional deformation analysis produced in Itasca's FLAC3D software. The simulation was conducted using uncoupled flow and mechanical calculations and was completed under the large strain calculation scheme. Scale effects were evaluated through the use of three models with varying mesh discretization levels and by completing analyses of the upper and a lower limit state. To simulate the mechanical response in the Upper GLU during the construction of the embankment up to its collapse, the existing constitutive model *strain-softening* was augmented with custom functions and calibrated against laboratory data. The deformation modulus of the rockfill was modelled after data in Leps (1970) as a function of confining stresses.

Findings

The results of the three-dimensional deformation analysis of the breach at Mount Polley validate the two hypotheses formulated in the previous section, and provide many insights into its mechanism of progressive failure.

Non-linear straining in the Upper GLU: The analysis of the breach at Mount Polley demonstrates that the non-linear straining of the Upper GLU is critical to the initiation of collapse. The simulation predicted the initiation of strain localization and the start of shear band formation in the Upper GLU as early as three years prior to the collapse of the embankment. The analysis of scale effects suggests that a shear band with a thickness above zero but no greater than 12.5cm formed in the Upper GLU and ultimately controlled this unit's mechanical response to shearing.

Asynchronous mobilization of shear resistance: The results of the simulation of the breach at Mount Polley indicate that the mobilization of shear resistance in the failing materials was distinctly asynchronous whereby, in the early stages of collapse, the upper till and core units in the upstream region failed locally due to growing shear displacements in the Upper GLU, whereas the mobilization of shear strength in the rockfill remained incomplete throughout.

Material preconditions for progressive failure: Preliminary static three-dimensional analyses suggested that a considerable, possibly full, weakening of the Upper GLU was pre-requisite to the initiation of collapse. Contrary to this finding, the results of the three-dimensional deformation analysis suggest that the drop in the resistance of the Upper GLU prior to collapse was not significant. Instead, the analysis reveals the emergence of three other material conditions in the foundation soils that appear to be instrumental to the initiation and unfolding of collapse.

The simulation results indicate that progressive failure at the Mount Polley TSF started as early as 2011, advancing as the construction of embankment proceeded but remaining contained until the summer of 2014. Prior to collapse, the extent of progressive failure was minor and had a nearly imperceptible effect on the immediate stability of the embankment. By the fall of 2013, in addition to the contained failure, three distinct material conditions developed in the foundation soils that brought the structure to the verge of instability. These are (a) the substantial depletion of reserve shear strengths in the materials surrounding the plastic yield zones; (b) the emergence of a large area close to the precipice of weakening; and (c) the extension of some brittle soil units in the failure zone. These changes rendered the embankment and foundation susceptible to failure under a variety of loading conditions.

CHAPTER ONE

A RE-EVALUATION OF HISTORIC CASE STUDIES IN THREE DIMENSIONS

1.1. OVERVIEW

Case studies of slope failures form the foundation of the knowledge base in geotechnical engineering. Slope failure events are treated as learning opportunities, with insights to be gained about the strength behaviour of soils.

The bulk of to-date historic case studies of slope instability were back-analyzed in two dimensions. The reduction of slope stability problems to two dimensions was done out of necessity at a time when the state of research and technology had not yet progressed to handle three-dimensional solutions. Such simplification was done under the assumption that the error it introduces into the solution is not large and does not affect the outcome substantively. Consequently, the findings from the two-dimensional analyses of case studies were accepted as accurate.

As research on the matter advanced, it became increasingly clear that the two- and three-dimensional solutions can differ a great deal. Therefore, the necessity arose to re-evaluate the lessons learned on the basis of two-dimensional analysis.

In this chapter, a number of historic case studies of slope stability were revisited in order to evaluate the magnitude of three-dimensional effects and to gain insights into the impact of these on the outcome. The collection of classic case studies of slope stability was reviewed in order to identify suitable candidates for re-evaluation. A number of historic papers on two-dimensional limit equilibrium analysis were selected based on two attributes:

- Sufficient original data was reported by the original investigators to re-create the model of the case study in three dimensions; and
- A three-dimensional analysis of the case study was judged to have the potential to offer insight into the nature and/or impact on outcome of three-dimensional slope stability effects.

1.1.1 CHAPTER ORGANIZATION

Seven classic case studies of slope stability are re-evaluated in this chapter. Each of the sections §1.2.1 to §1.2.7 introduces a case study by first reviewing the original findings and then presents the results of the three-dimensional analyses along with a brief discussion. In the interest of keeping the chapter concise and focused on its main objective, the description of modelling approach, including method, strength models, pore pressures, slip surfaces and more, is provided in Appendix 1A.

The results and their interpretation are discussed in §1.3 and §1.4. The discussion and conclusions focus largely on issues that were deemed pertinent to the advancement of the subject of this thesis.

1.1.2 DEFINITIONS

For clarity, two quantities that are useful in the context of this chapter are defined: three-dimensional slope stability effects and the ratio of three- to two-dimensional safety factors.

In this thesis, three-dimensional slope stability effects are defined using Eq. 1.1:

$$\frac{FOS_{3D} - FOS_{2D}}{FOS_{2D}} \qquad \textit{Eq. 1.1}$$

The ratio of three- to two-dimensional factors of safety are defined using Eq. 1.2:

$$\frac{FOS_{3D}}{FOS_{2D}} \qquad \text{Eq. 1.2}$$

1.1.3 REVIEW OF THE HISTORIC APPROACH TO EVALUATE SLOPE STABILITY USING LIMIT EQUILIBRIUM METHODS

Roughly at the midpoint of the 20th Century, the geotechnical research community initiated a broad effort to validate the existing and emergent tools to assess slope stability.

Those tools could be seen as belonging to two broad categories: (i) limit equilibrium calculation methods and (ii) shear strength models. The former category included the ordinary method (Fellenius 1936); Bishop's (1955) simplified method; and later on, the Morgenstern-Price (1965) method; the Spencer (1967) method etc. The latter category included the drained strength model (also referred to as "the effective stress method" or "the c, ϕ method," and known today as the Mohr-Coulomb strength envelope model) and the undrained strength model (also referred to as "the total stress analysis" or "the $\phi = 0$ method").

The validation process generally involved the back-analysis of a known slope failure using one or more of the limit equilibrium methods and one or both shear strength models. The strength models were developed using field and laboratory tests. A search for the slip surface with the minimum safety factor ensued. The analysis was deemed valid if the back-analysis of failure produced a safety factor reasonably close to unity; such analysis then became evidence to support the validity of calculation methods and/or the strength model. Factors of safety well above or well below unity cast doubt on the validity of either the calculation methods or strength models.

Occasionally, analyses of stable slopes were also conducted to evaluate the shear strength models, with the expectation that a valid strength model will result in a safety factor above unity. One such case study is revisited here (§1.2.2).

1.1.4 SOURCE OF THREE-DIMENSIONAL SLOPE STABILITY EFFECTS

The two-dimensional limit equilibrium methods used for the analysis of the historic case studies were developed at a time when knowledge about soil strength behaviour was emergent, and computations were done mostly by hand. The reduction of slope stability problems to two dimensions was necessary to render the solution feasible. Such simplification was done with the assumption that any three-dimensional slope stability effects, also called “end effects” or “side wall effects,” are negligible. Since no three-dimensional slope stability methods were available at the time, the accuracy of this assumption could not be evaluated to any significant degree, in spite of the problem being recognized by the practitioners.

Sevaldson (1955), Bjerrum and Kjaernsli (1957) and Kjaernsli and Simons (1962) are some of the researchers discussing, and attempting to address, the question of three-dimensional slope stability effects and their impact on two-dimensional solutions. In time, theoretical models to estimate such effects were developed (Skempton 1985; Gens et al. 1989). As the state of knowledge and technology progressed over time, three-dimensional analyses of increasing sophistication became feasible. Beginning with the 1970s, studies have been routinely published on the comparison of two- and three-dimensional stability analyses of both actual and fictitious case studies. Fredlund and Krahn (1977), Hungr et al. (1989), Seed et al. (1990), Zhang et al. (2014) and Stark (2017) are just a few examples of such studies. Researchers have consistently shown that (i) three-dimensional factors of safety are larger than their two-dimensional equivalents and that (ii) the difference between the two- and three-dimensional factors of safety is not negligible.

The conclusion is, the reduction of slope stability problems to two dimensions comes at the cost of introducing a considerable error into the solution. Three-dimensional slope stability effects represent the magnitude of error introduced into a slope stability analysis due to its reduction to two dimensions.

1.1.5 MODELLING SOFTWARE

The accurate evaluation of three-dimensional slope stability effects involves a side-by-side comparison of two- and three-dimensional stability analyses. In the interest of eliminating sources of discrepancy of outcome other than the problem dimensionality, all modelling parameters in such two- and three-dimensional models, including soil properties and limit equilibrium methods, should be kept constant whenever possible.

The original papers evaluating the classic case studies revisited here generally provide thorough evaluations in two dimensions that establish a basis for comparison against the three-dimensional case. However, some of the strength models used in these historic papers – such as the depth-dependent undrained shear strength plots commonly used by the Norwegian Geotechnical Institute – have been replaced with newer alternatives and cannot be directly reproduced by modern limit equilibrium software. For this reason, it is desirable to replicate the two-dimensional slope stability analyses in the original papers prior to proceeding with the three-dimensional analyses, as this approach provides for the most accurate comparison.

The above considerations impose a number of requisite capabilities on the limit equilibrium software to be chosen for the task, such as:

- A capability for both two- and three-dimensional limit equilibrium analysis;
- The capability for seepage analysis in both two and three dimensions;
- The ability to replicate complex subsurface geometry in thee dimensions;

- The inclusion of a broad variety of limit equilibrium methods, including historic approaches such as The Ordinary Method of Slices, Bishop's Simplified Method etc., and
- A broad selection of strength envelopes that could be adapted to emulate historic strength models.

SoilVision®'s SVOffice™ software package was identified as the limit equilibrium software of choice for this task. SVOffice™ consists of a number of modules designed for different types of analyses of soils. Three of its modules, SVSolid™, SVFlux™ and SVSlope™, were used to complete the objectives of this chapter. Below is a brief review of each of these modules and their functions.

SVSolid™ is a module that enables the creation of complex three-dimensional soil models, including layered stratigraphy, discontinuous soil deposits, surface ponds and more. Soil models developed in SVSolid™ can be readily imported into the other SVOffice™ modules where seepage, slope stability and other analyses can be performed using them. Additionally, SVSolid™'s ability to output files in the *.stf format proved to be exceptionally useful for the development of the Mount Polley TSF deformation model, detailed in Chapter Three.

SVFlux™ has the capability to perform two- and three-dimensional seepage analysis, and the results can be imported into SVSlope™ for use in limit equilibrium calculations. The module has basic tools for developing a model's geometry in two dimensions, and to extrude it into three if desired. The module includes the isotropic and anisotropic permeability models, and a broad variety of unsaturated flow models. The anisotropic permeability and the unsaturated flow models were not used in the analyses presented in this chapter.

SVSlope™ offers the ability to perform limit equilibrium analysis using a number of methods, including the Ordinary Method of Slices, Bishop's Simplified Method, Janbu's Method, Spencer's Method, the Morgenstern-Price Method and the Fredlund Method. In two dimensions, the slip line can be specified using circles, wedges or other geometric shapes. Analogously, in three dimensions, the slip surface can be described using ellipses with varying aspect ratios, wedges and weak planes, or be defined by the user. Finally, the module includes a broad range of strength models, both modern and historic.

The SoilVision® software is continually validated by the developer in accordance with the procedures outlined in its verification manuals (SoilVision 2018; SoilVision 2019). For slope stability problems, the verification methodology includes the replication of benchmark problems, comparisons with solutions by equivalent software, manual calculations etc. (SoilVision 2019, p. 6). In addition, full information on calculations, including free body diagrams, the magnitude of forces and stresses, and pore pressures acting at the base of each slice, is accessible to the user for each solution obtained in SVSlope™. In the analyses introduced in this chapter, this information was used to perform spot-checks.

1.2. RE-EVALUATION OF CASE STUDIES

1.2.1 THE SLIDE AT LODALEN, 6 OCTOBER 1954

1.2.1.1. REVIEW OF THE ORIGINAL STUDY

The analysis of the Lodalen slide by Sevaldson (1956) is viewed in the practice of géotechnique as a seminal case study. In this study, the drained strength model was used in conjunction with Bishop's Simplified Method to accurately predict the onset of failure by producing a safety factor near unity. Additionally, the location of the slip surface predicted by the analysis was in good agreement with that observed in the field. Sevaldson found that while the use of undrained strengths yields similar factors of safety, the location of the slip surface is not accurately predicted by this strength model. The original back-analysis of the slide was conducted in two dimensions along three cross-sections oriented in the direction of the slip (seen in Figure 1.1). In doing that, Sevaldson recognized the aggregate effect of shear strengths and stresses acting along various, including non-critical, portions of the slip surface, on stability.

1.2.1.2. A RE-EVALUATION OF THE LODALEN SLIDE IN THREE DIMENSIONS

A rotational slide such as at Lodalen, with a width-to-depth ratio of about 2.6, would mobilize some "sidewall" resistance which is only partially considered in the original analysis by Sevaldson. Therefore, it is of interest to explore the extent of three-dimensional stability effects that may have been present at the site.

A three-dimensional limit equilibrium model of the slope was built in SoilVision® software using data in the original paper. The drained and undrained models were both tested. In the drained analysis, the numeric effect on stability of artesian pore water pressures at the site (modelled by

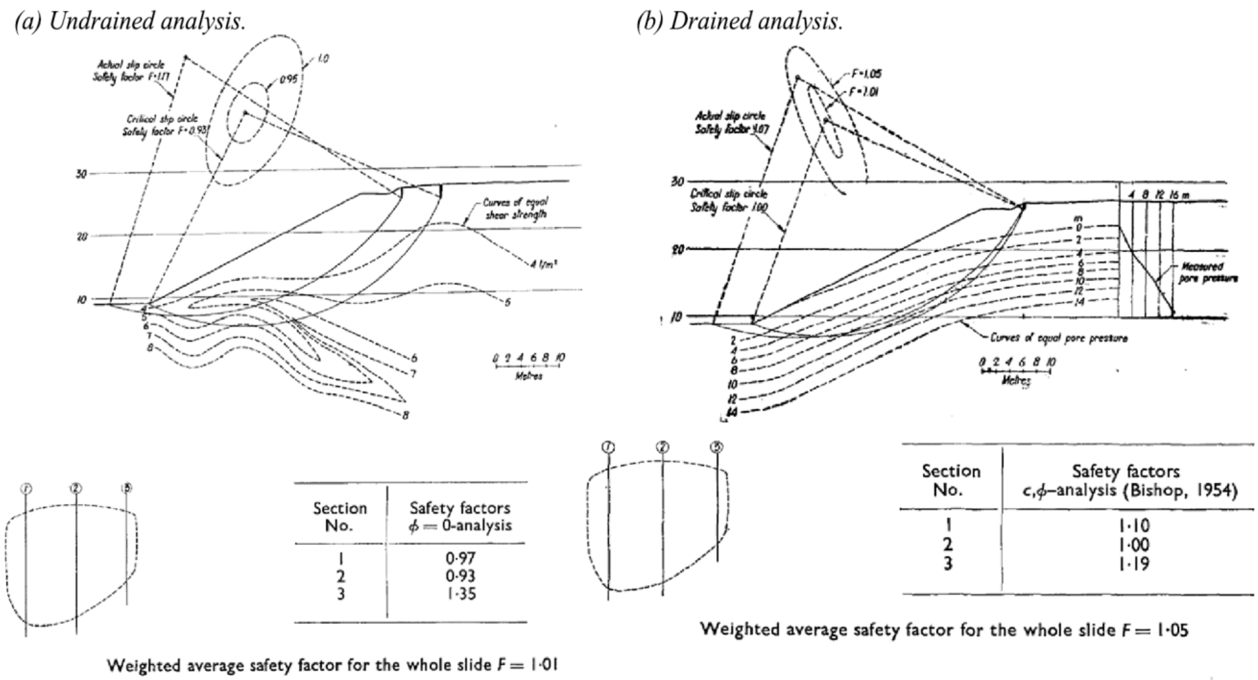

Section No.	Safety factors $\phi = 0$-analysis
1	0·97
2	0·93
3	1·35

Section No.	Safety factors c,ϕ–analysis (Bishop, 1954)
1	1·10
2	1·00
3	1·19

Figure 1.1 The slope stability analyses of the slide at Lodalen by Sevaldson (1956, Figs. 17 & 19) (reproduced with permission from ICE Publishing).

Sevaldson as a gradient of about 12kPa/m below the phreatic surface) was emulated by setting the water density value at ~1.2g/cm^3. The results are illustrated in Figure 1.2.

The three-dimensional limit equilibrium analysis using the drained soil strength model produced a safety factor ranging between 1.08 and 1.19 depending on the interpretation of the position of the phreatic surface; this represents a 3 to 13% increase in the safety factor compared to the original analysis. The location and size of the failure agrees well with the field observations. It can be concluded that minor three-dimensional effects are present in the slide at Lodalen which are not captured by the original analysis.

The three-dimensional results identified by this study are somewhat lower than those published by Gitirana et al. (2008), who reported a three-dimensional safety factor of the Lodalen slide that was 18-29% higher than the one calculated by Sevaldson. This discrepancy is owed in part to the different pore pressure models and possibly to different interpretations of the three-dimensional *(a) Drained analysis using a high estimation of groundwater table.*

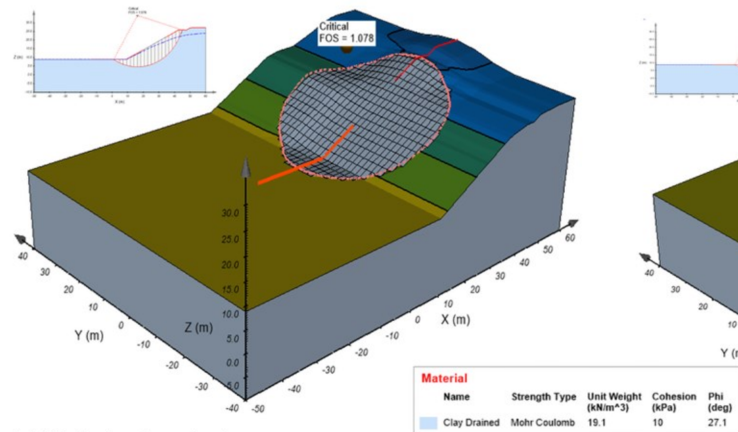

(b) Drained analysis using a low estimation of groundwater table.

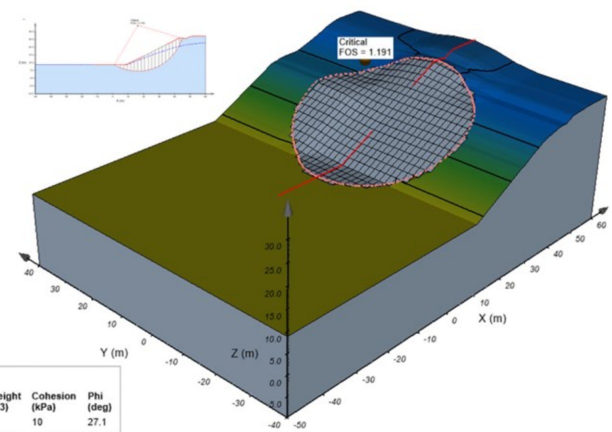

(c) Undrained analysis.

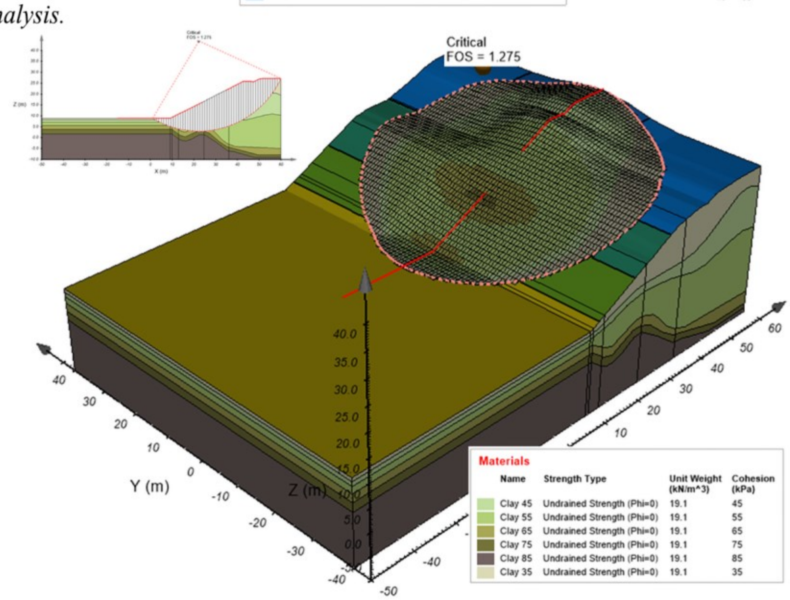

Figure 1.2 A three-dimensional limit equilibrium analysis of the Lodalen slide.

shape of the ground surface using the scant topographic data in the original paper. Gitirana et al. (2008) uses pore pressure values produced by a three-dimensional steady-state flow analysis and then multiplied by a correction factor of 1.34 to simulate artesian conditions, whereas Sevaldson (as well as this study) uses a simplified approach where artesian pore pressure distributions are represented by a groundwater surface with a pressure gradient uniformly applied below it. A sensitivity analysis confirmed that the pore pressure parameter played an important role in the stability of the Lodalen slope, as even minor pore pressure changes produced dramatic variations of the safety factor.

The undrained three-dimensional analysis yields a safety factor of 1.28, and the slip surface is located significantly deeper into the slope than actually observed. In addition, it appears that lower safety factor surfaces could be found by expanding the boundaries of the model; due to a lack of original topographic data, this possibility was not investigated.

The undrained analysis confirms findings by Golder and Palmer (1955), Sevaldson (1956) and Bjerrum and Kjaernsli (1957) that undrained analysis does not reliably predict the location of the slip surface. Skempton (1945) indicates that undrained analyses tend to predict slip surfaces deeper than actual due to the model's interpretation of soils as purely cohesive materials. An undrained model interprets soil strength as a "wholesale" quantity whereas a c', ϕ' model derives it from two sources: cohesion and friction. The latter depends on the effective weight acting at the base of a slice or column and is lower for shallow surfaces. Therefore, the undrained model over-predicts the strength of a shallow slide and consequently overestimates its safety factor.

1.2.1.3. DISCUSSION

The results of the three-dimensional limit equilibrium analysis of the slide at Lodalen indicate the presence of modest three-dimensional slope stability effects (of about 3 to 13%) not captured by the original study by Sevaldson (1956). Sevaldson's analysis attempts to mitigate the error introduced by the simplifying assumptions of the two-dimensional methods by evaluating the slide's stability across three cross-sections rather than considering the critical section only, as would be the case with a conventional two-dimensional analysis. Consequently, the discrepancy between his analysis and a three-dimensional one is attenuated. The critical section analyzed by Sevaldson (1956), passing through the middle of the slide, has a safety factor of 1.00 using the drained strength model and of 0.93 using the undrained strength model. If these results are taken in isolation as representing the outcomes of true two-dimensional analyses, the three-dimensional stability effects increase to 8-19% for the drained model and to 37% for the undrained model.

The question is, does the two-dimensional limit equilibrium analysis by Sevaldson (1956) provide adequate answers regarding the failure mechanism in spite of ignoring three-dimensional slope stability effects? The findings here demonstrate relatively small three-dimensional effects as well as high sensitivity to pore water pressures. Therefore, the failure mechanism proposed by Sevaldson remains credible even when three-dimensional slope stability effects are considered.

1.2.2 THE STABLE SLOPES AT BAKKLANDET, TRONDHEIM

1.2.2.1. REVIEW OF THE ORIGINAL STUDY

The natural soft silty clay slopes around Upper Bakklandet in Trondheim, Norway were the subject of a slope stability evaluation in the context of a broader study published by Bjerrum and Kjaernsli (1957). The study concluded that undrained analysis significantly underestimates the long-term stability of normally consolidated clay slopes.

The natural slopes around the Nidelva River in Upper Bakklandet, were made of normally consolidated marine clays that were described as either “very sensitive” or “quick” and were known to be stable. The undrained strengths, measured by vane and laboratory tests, were mapped as a function of depth below surface. Three cross-sections, identified in the study as Profiles A, B and C (Bjerrum and Kjaernsli 1957, Figure 5), were subjected to two-dimensional slope stability analyses using the undrained method, producing safety factors between 0.65 and 0.74. Such low safety factor values in stable slopes were interpreted as evidence that the undrained strength model is unsuitable for evaluating the stability of such slopes. In the paper, the authors explore the possibility that three-dimensional slope stability effects (referred to as “end effect”) may explain such low two-dimensional factors of safety but conclude that such “deviation between theory and practice cannot be explained by <these>” (Bjerrum and Kjaernsli 1957, p. 5).

1.2.2.2. A RE-EVALUATION OF THE STABLE SLOPES IN BAKKLANDET IN THREE DIMENSIONS

The original study of the stable clay slopes in Bakklandet includes a map of topographic elevations in the area and records of the undrained strength distributions throughout it. These data offer an opportunity to re-evaluate the stability of slopes along Profiles A and B in three dimensions in order to assess whether the conclusions by the original investigators remain valid when three-dimensional stability effects are taken into consideration. The map of topographic elevations does not provide sufficient information to replicate the surface and subsurface around Profile C.

Table 1.1 Comparison of two- and three-dimensional safety factors for the stable slopes at Bakklandet.

Location	FOS^{2D}_{Bishop}	$FOS_{along\ same\ profile}$		$\frac{FOS_{3D}-FOS_{2D}}{FOS_{2D}}(\%)$	FOS_{min}		notes
		FOS^{3D}_{Bishop}	FOS^{3D}_{M-P}		FOS^{3D}_{Bishop}	FOS^{3D}_{M-P}	
Profile A	0.74	1.05	1.03	39-42%	0.99	0.99	convex; O/C crust thickness est.4 m
Profile B	0.67	1.08	1.08	61%	1.01	1.01	concave; O/C crust thickness est. 3 m
Profile B rotated 10° CCW*	-	-	-	-	0.94	0.94	concave; O/C crust thickness est. 3 m

*The original study by Bjerrum and Kjaernsli (1957) did not investigate rotated profiles; the 3D:2D % safety factor increase is calculated based on two-dimensional calculations along Profile B.

Effect of topography on stability: A three-dimensional analysis of the stable slopes at Bakklandet may offer some insight into the effects of surface topography on three-dimensional stability effects. The local topography includes a number concavities and convexities; Profile A is convex and Profile B is concave. Such surficial features were previously found to have a discernible effect on the three-dimensional safety factor: all other things being equal, convex slopes appear less stable, and concave slopes appear more stable than uniform, flat slopes (Zhang et al. 2014; Chaudhary et al. 2016). This effect can be explained in terms of the ratio of soil volume to slip area in a slide: in a convex slope, this ratio is greater, and in a concave slope, it is lower than in a uniform slope.

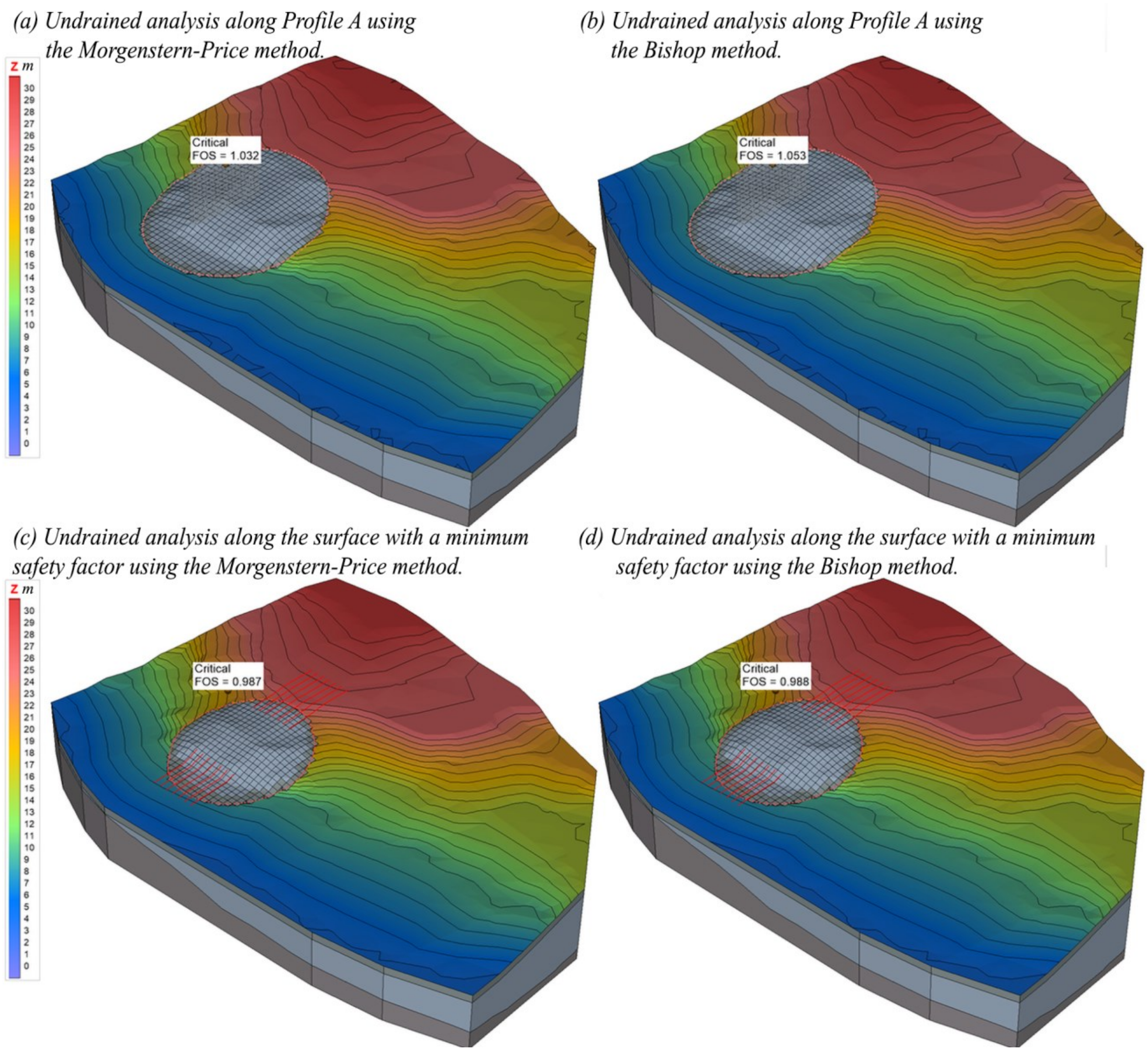

Figure 1.3 A three-dimensional stability analysis of the Bakklandet slopes.

Effects of surface shape on soil crust: It is generally understood that convex slopes, with a greater surface area exposed to atmospheric boundary conditions, can form thicker crusts; in concave slopes, the opposite happens. This effect has been noted by geotechnical engineers working in cold climate, where the depth of frost penetration and weathering is of great practical importance. The detailed vane shear and undrained triaxial testing results published in the original study by the

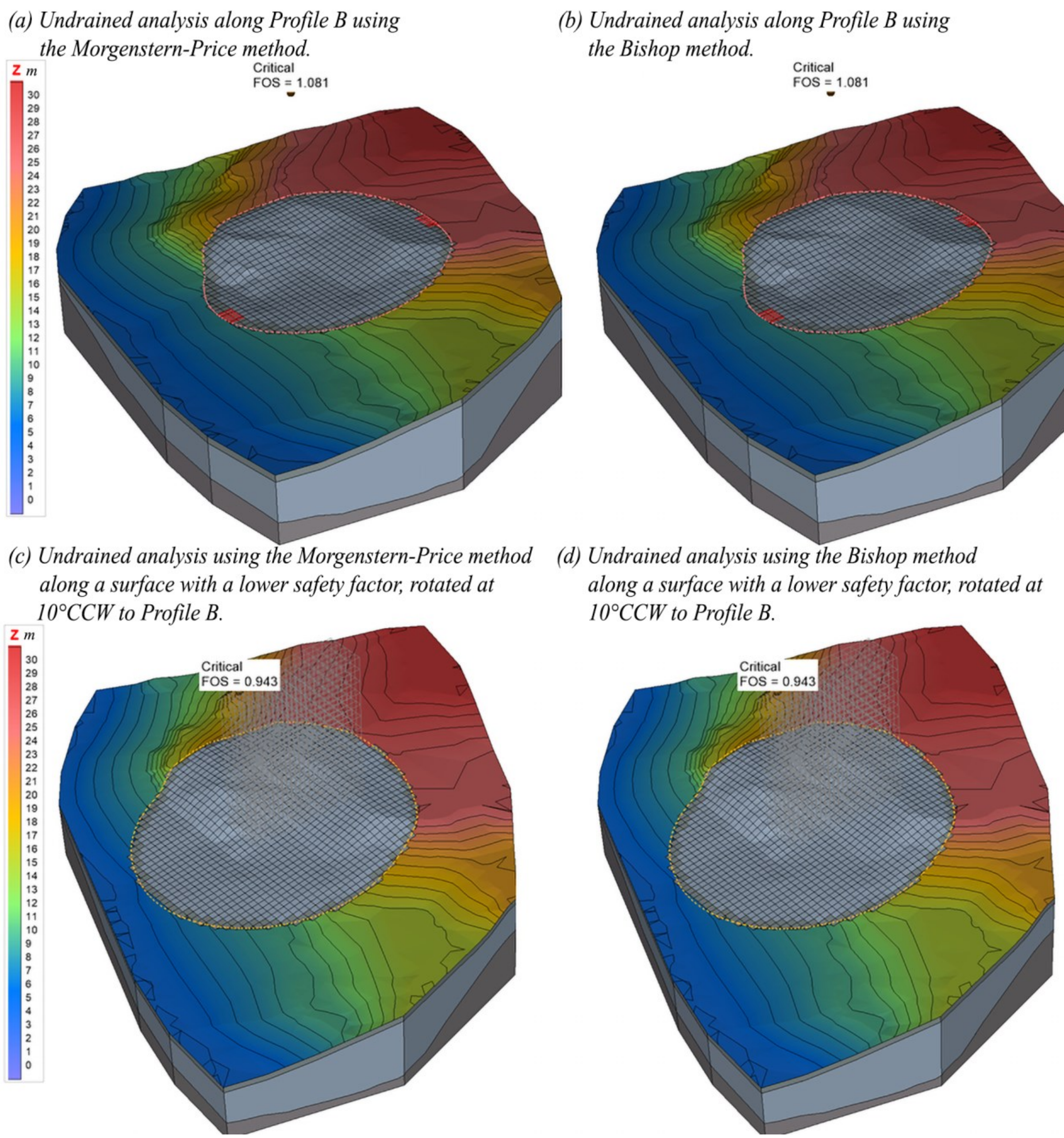

Figure 1.4 A three-dimensional stability analysis of the Bakklandet slopes along Profile B.

Norwegian Geotechnical Institute shed some light on the consequences of this effect. The plots of undrained strength along Profiles A and B (Bjerrum and Kjaernsli 1957, Figures 6a and 6b) show that the soil crust is 1m or so thicker along Profile A. Consequently, a three-dimensional analysis of Profiles A and B may offer some insight into the impact of such effects on slope stability.

Considerations for slip surface selection: When conducting three-dimensional analyses of stable slopes, a decision must be made regarding the aspect ratio of the potential slip surfaces. Generally, slip surfaces with greater aspect ratios produce lower safety factors, with infinitely wide slides yielding, in theory, values approaching those obtained by two-dimensional analysis (Skempton 1985; Gens et al. 1988). As a consequence, an unconstrained search for any arbitrary surface with the minimum safety factor can lead to irrelevant results. Recognizing that the purpose of replicating the analysis of the stable slopes at Bakklandet in three dimensions is to quantify the slope stability effects that may be ignored in a two-dimensional analysis, slip surfaces were selected that produced similar slide aspect ratios (e.g. values of about 2 to 3) to those observed in like soils (such as at Lodalen, §1.2.1; and Drammen, §1.2.3). Such slide ratios are generated by ellipsoids with an aspect ratio of about unity.

Modelling approach and results: The three-dimensional limit equilibrium models of the Bakklandet stable slopes were developed on the basis of the data reported by the original investigators. The shear strength distributions reported in the original study were simulated using depth-dependent undrained shear strength functions, and the surficial crust was simulated as a separate soil layer with its own distinct strength. Stability calculations were performed along three-dimensional surfaces extrapolated from the original cross-sections used by Bjerrum and Kjaernsli (1957) using an ellipsoid aspect ratio of one. In addition, a search for slip surfaces with lower factors of safety was conducted in the neighbourhood of the original profiles.

The results are illustrated in Figure 1.3 (Profile A) and Figure 1.4 (Profile B) and summarized in Table 1.1.

1.2.2.3. DISCUSSION

The results point out to considerable three-dimensional slope stability effects. Analyses of three-dimensional slip surfaces corresponding to cross-sections along Profiles A (Figure 1.3*(a)* and *(b)*) and B (Figure 1.4*(a)* and *(b)*) produce factors of safety considerably larger than their two-dimensional equivalents and marginally above unity. This supports the proposition that three-dimensional effects have a considerable bearing on these slopes' stability. However, the presence nearby of potential slip surfaces with factors of safety below unity in these stable slopes (Figure 1.3*(c)* and *(d)*; Figure 1.4*(c)* and *(d)*) casts doubt on the validity of the analysis and supports the case made by Bjerrum and Kjaernsli (1957) that the undrained strength model is unsuitable for assessing the long-term stability of clays, underestimating the stability of slopes made of such soils.

The extent of three-dimensional slope stability effects noted here can be explained by the contribution to resistance of the high-strength soil crust layer: in these relatively shallow slides, the fraction of the slip surface passing through the crust is significant. In a two-dimensional analysis, this contribution is largely ignored, whereas a three-dimensional analysis captures it in full.

The three-dimensional slope stability effects are more pronounced in the concave slope corresponding to Profile B. This observation is in agreement with findings by Zhang et al. (2014). The thinner soil crust at this location does not appear to offset this effect to any discernible extent.

Finally, a cursory analysis was performed to evaluate the sensitivity of stability calculations to changes in the soil crust strength estimates. The results demonstrate that the soil crust strength is a highly sensitive parameter, and even small errors in its evaluation can lead to considerable over- and underestimations of three-dimensional safety factors.

1.2.3 THE 1955 SLIDE ON THE BANK OF DRAMMEN RIVER

1.2.3.1. REVIEW OF THE ORIGINAL STUDY

The original investigators of the slide on the bank of Drammen River (Bjerrum and Kjaernsli, 1957; Kjaernsli and Simons, 1962) used this event to test the reliability of then emergent slope stability methods. Their study served as evidence to validate the drained strength model (referred to in the studies as “the effective stress analysis”) as well as Bishop’s simplified method for stability calculations.

The soil conditions around Drammen River were historically known to be challenging from a geotechnical perspective, with record of bank failures going back to the 18th Century. The investigators note that in the area “slips have occurred at intervals of approximately 30 years” (Kjaernsli and Simons 1962, p. 148).

On 6 January 1955, a slide occurred in the pile-enforced north bank of the Drammen River. The failure took place in a period of low water and after some fill had been placed on the edge of the bank. Erosion at the bank toe was considered a factor. The clay soil involved in the 1955 failure was normally consolidated away from the bank and lightly overconsolidated near water due to erosion-related unloading (Kjaernsli and Simons 1962, p. 151). The clay strength was meticulously tested to determine its undrained strengths and effective strength envelope, and the results were considered highly reliable due to good agreement between different testing methods. Kjaernsli and Simons (1962) conducted total and effective stress analyses of the failure itself as well as of two stable slopes nearby.

The two-dimensional total stress analysis produced a safety factor of 0.47 for the failure (identified in the paper as Profile B) and safety factors of 0.58 to 0.71 for the stable slopes immediately downstream (Profile C) and upstream (Profile A) of it, respectively. Such low safety factor values were interpreted by the investigators as evidence confirming that total stress analysis is wholly unsuitable for assessing the stability of natural clay slopes at Drammen River. The authors assert that three-dimensional slope stability effects (referred to in the paper as “forces at the ends of the cylinder”) would be of minor importance, amounting to 10% or less of the safety factor (Kjaernsli and Simons 1962, p. 162).

A two-dimensional effective stress analysis of the slide using the Bishop method produced a safety factor value of 1.01. Safety factors of 1.14 to 1.26 were calculated for the stable slopes upstream and downstream of the failure location. The investigators concluded that the effective stress analysis using the Bishop method produces satisfactory safety factor values for such slopes.

1.2.3.2. A RE-EVALUATION OF THE SLIDE AT DRAMMEN IN THREE DIMENSIONS

The original paper by Kjaernsli and Simons (1962) offers a reasonable amount of information regarding local topography, bathymetry, the slide's approximate position and extent, and cross-sectional views of several soil profiles. These data were integrated to create, to the best ability, a three-dimensional model of the area that encompasses Profiles A (upstream of failure), B (at the failure location) and C (downstream of the failure).

The original study features two types of analysis, using the drained and undrained strength models. The undrained strength model proposed by the researchers represents a complicated map of strength distributions throughout the three profiles. A replication of this model in three dimensions would necessitate considerable guesswork and would be rather inexact. For this reason, only a drained analysis was conducted in three dimensions. The drained strength model employed the same strength parameters c' and ϕ' as those used by Kjaernsli and Simons (1962, Figure 13). As with the original study, the pore pressure conditions were modelled using a groundwater table ~2m below ground surface and a river water level of -1m.

The extent, position and depth of the slip surface are not precisely known due to subsequent retrogressive slides and partially submerged conditions; therefore, the three-dimensional slip surface was determined by searching the immediate area around the profiles for surfaces with the lowest safety factor. The Bishop and Morgenstern-Price stability methods were used to calculate safety factors across a wide range of ellipsoid surfaces with varying aspect ratios.

Results: The results of the three-dimensional analyses of Profiles A to C are summarized in Table 1.2 and illustrated in Figure 1.5.

The back-analysis of the failure (Profile B) produce a three-dimensional safety factor of about 1.09; this value represents an 8% increase over the two-dimensional safety factor at this location. The slip surfaces determined using both the Morgenstern-Price and Bishop methods are in good agreement with the reported shape, size and position of the slide, and their critical cross-sections closely resemble the one produced by the original investigators.

Table 1.2 Comparison of two- and three-dimensional factors of safety for the 1955 Drammen River failure and stable slopes nearby.

Location	FOS^{2D}_{Bishop}	FOS^{3D}_{Bishop}	FOS^{3D}_{M-P}	$\frac{FOS_{3D}-FOS_{2D}}{FOS_{2D}}(\%)$
Profile B (failure location)	1.01	1.09	1.09	8
Profile A (upstream of failure)	1.14	1.37	1.31	15 - 20
Profile C (downstream of failure)	1.26	1.89	1.79	42 - 50

As discussed in §1.2.1.2, three-dimensional analyses of the stable slopes on the upstream and downstream of failure are more open-ended because there are no actual slip surfaces to match. Three-dimensional analyses using larger slide aspect ratios will generally produce lower factors of safety, so an unconstrained search for the surface with the minimum safety factor can produce unrealistic results. The purpose of investigating these sections is to get a sense of how much more stable these sections are compared to the failure location. Therefore, slip surfaces with an aspect ratio similar to the critical one passing through Profile B were specified.

Three-dimensional slip surfaces corresponding to Profile A upstream of the failure produce safety factor values equal to or greater than 1.31; this represents an increase of 15% or more over the two-dimensional safety factor. Three-dimensional slip surfaces corresponding to Profile C downstream of the failure produce safety factors equal to or greater than 1.79; this represents an increase of 42% or more over the two-dimensional safety factor. The agreement between the critical three-dimensional slip surface and its two-dimensional equivalent is poor. The configuration of ground

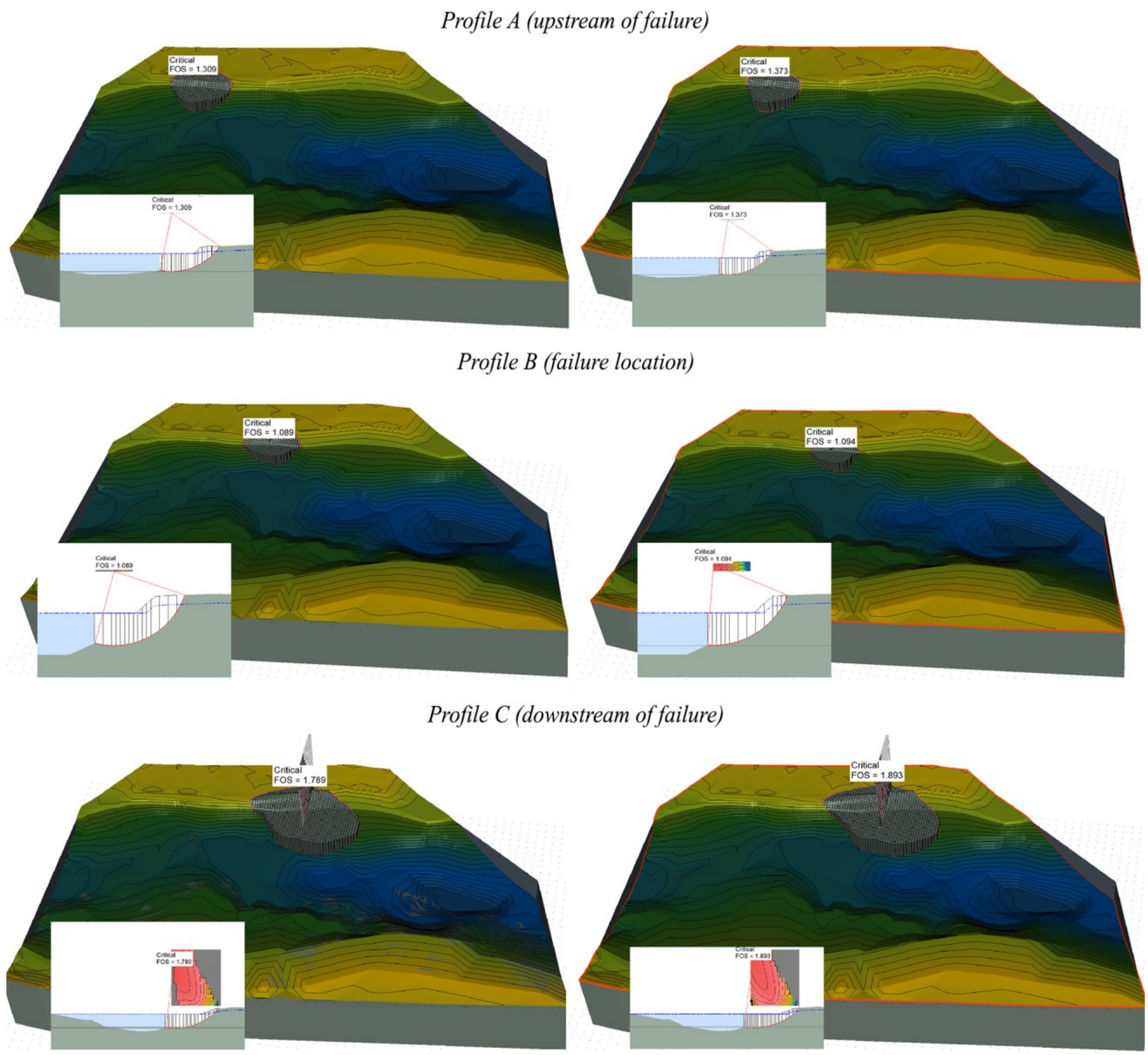

Figure 1.5 A three-dimensional limit equilibrium analysis of the Drammen slopes. Left column: Results obtained using the Morgenstern-Price method. Right column: Results obtained using the Bishop method.

surface at this location is very complex, and the distinct possibility exists that arbitrary slip surfaces (i.e. non-ellipsoid slip surfaces or surfaces oriented in a different direction) with lower factors of safety may exist. The complicated configuration of the ground surface around Profile C may also be the reason behind uncharacteristically high three-dimensional slope stability effects at this location.

Effect of wooden piles: The Drammen River bank at the failure location was enforced with timber piles placed 1m on-centre to a depth of about 7m below regular water level. The analysis by Kjaernsli and Simons (1962, p. 162) ignores their effect on stability: the investigators reason that "circles can be found deeper than the critical one with a safety factor only slightly higher than the critical one." The critical slip line produced by the two-dimensional stability analysis passes immediately below the piles (Kjaernsli and Simons 1962, Figure 13).

In a three-dimensional model, the effect of piles on bank stability is more complex. Any potential elliptical slip surface, even if located sufficiently deep to pass below the piles in the middle of the slide, would traverse through some of the piles located closer to the edges. Using the lowest safety factor surface found, it is estimated that 10 to 15 piles would be sheared in this model of failure, increasing the three-dimensional safety factor value from 1.09 to 1.3-1.4 (based on published shear strength values for timber piles). With only sparse original data on pile dimensions or strengths, as well as on the exact location and shape of the slip surface, detailed three-dimensional models of failure involving pile effects (including pile failure modes other than shearing, or deeper and/or irregular slip surface shapes) would be highly speculative and were not considered. It suffices to state here that the timber piles create additional stabilizing effects not considered by the two-dimensional back-analysis in the original study.

1.2.4 THE 1953 SCRAPSGATE EMBANKMENT FAILURES

1.2.4.1. REVIEW OF THE ORIGINAL STUDY

In January 1953, a series of floods on the east coast of England were followed by thirty or so failures of earth embankments used as sea defences. Golder and Palmer (1955) carried out an investigation of the failures. Drained and undrained analyses of the failure were conducted. The study's drained analysis produced a safety factor of 1.3. With this analysis, in conjunction with the knowledge that the bank failed three days after it was raised to its maximum height of 14 ft, the authors concluded that the failure mode was undrained.

To establish the undrained strength models, the investigators evaluated the vane shear testing data used in the design of the embankments against undrained triaxial and compression tests conducted after the failure. The former produced higher values than the latter. Noting the sensitivity of local soils ranging between 3.7 and 7.9, the investigators proposed that vane tests were conducted on low disturbance samples and thus produced readings closer to peak shear strengths, whereas compression and triaxial tests were conducted on somewhat disturbed samples that experienced a partial loss of strength due to sensitivity.

This proposition was corroborated by field observations. The design, based on vane shear readings, called for an embankment height of 16ft. However, the actual height of embankment at failure ranged between 12 and14ft. The investigators concluded that the shear strengths used in the design must have been higher than the actual strengths at failure.

To test this proposition, the investigators conducted two undrained stability analyses, one using vane shear test results, and another using values from undrained triaxial tests. The analysis using vane shear test strengths produced a safety factor equal to 1.3. The analysis using undrained triaxial tests produced a safety factor of unity.

The authors concluded that in sensitive soils such as the alluvial clays under the failed embankments, progressive failure may take place, where some remoulding and associated loss of peak strength gradually reduces the bank stability. In the authors' estimation, the average undrained strength of the alluvium clay dropped from its undisturbed value of 350psf (~17kPa) to 205psf (~10kPa) at failure, i.e. the clays were thought to experience a reduction in strength of about 40%.

The important conclusion that field vane readings may be overestimating, in sensitive soils, undrained shear strengths at failure was later expounded by Bjerrum (1973) through the introduction of a correction factor that relates the degree of strength overestimation by way of vane measurements with the soil's plasticity.

1.2.4.2. A RE-EVALUATION OF THE SCRAPSGATE FAILURE IN THREE DIMENSIONS

A three-dimensional limit equilibrium stability analysis of the Scrapsgate embankment failure was carried out using the two undrained strength models proposed by Golder and Palmer (1955). The three-dimensional geometry and soil profile were produced by extruding the two-dimensional cross-section used by the original investigators (Golder and Palmer 1955, Figure 32).

The three-dimensional stability analysis using undrained shear strengths that were established by undrained triaxial tests produced a three-dimensional safety factor of 1.22, a value 22% greater than the two-dimensional equivalent in the original study. The analysis using the undrained shear strength models that were based on vane tests produced a three-dimensional safety factor of 1.58, a value 22% greater than the two-dimensional equivalent in the original study.

Expanding on the authors' original conclusion that the soil strength at failure was lower than its vane-tested values performed on undisturbed samples, a failure of the Scrapsgate embankment was modelled in three dimensions by decreasing the undrained shear strength of the alluvial clay to attain a safety factor equal to unity. The results (seen in Figure 1.6*(c)*) indicate that the clay's undrained strength would have to drop, on average, by more than 2.3 times from its undisturbed value in order for failure to take place.

1.2.4.3. DISCUSSION

The mechanism of failure proposed by Golder and Palmer (1955) is that of a progressive loss of strength starting in a zone of overstress owing to soil sensitivity. This mechanism appears to be plausible in principle if not numerically even when three-dimensional effects are considered.

(a) Shear strengths s_u based on triaxial tests.

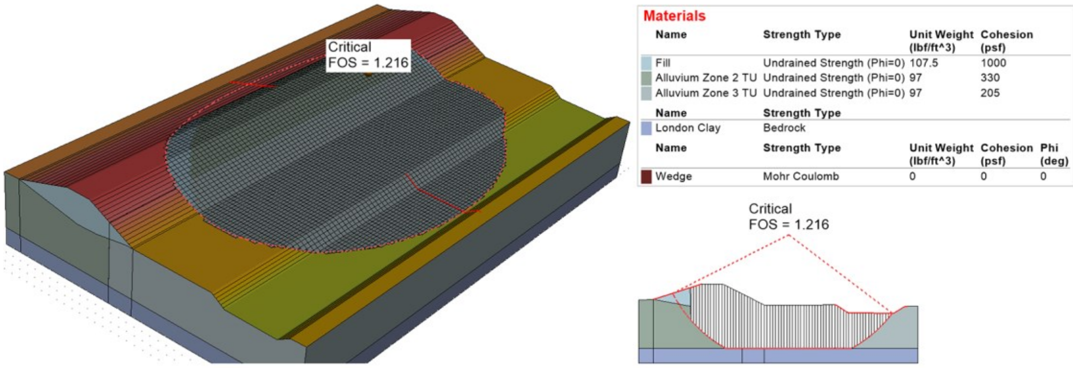

Name	Strength Type	Unit Weight (lbf/ft^3)	Cohesion (psf)	Phi (deg)
Fill	Undrained Strength (Phi=0)	107.5	1000	
Alluvium Zone 2 TU	Undrained Strength (Phi=0)	97	330	
Alluvium Zone 3 TU	Undrained Strength (Phi=0)	97	205	
London Clay	Bedrock			
Wedge	Mohr Coulomb	0	0	0

(b) Shear strengths s_u based on shear vane tests.

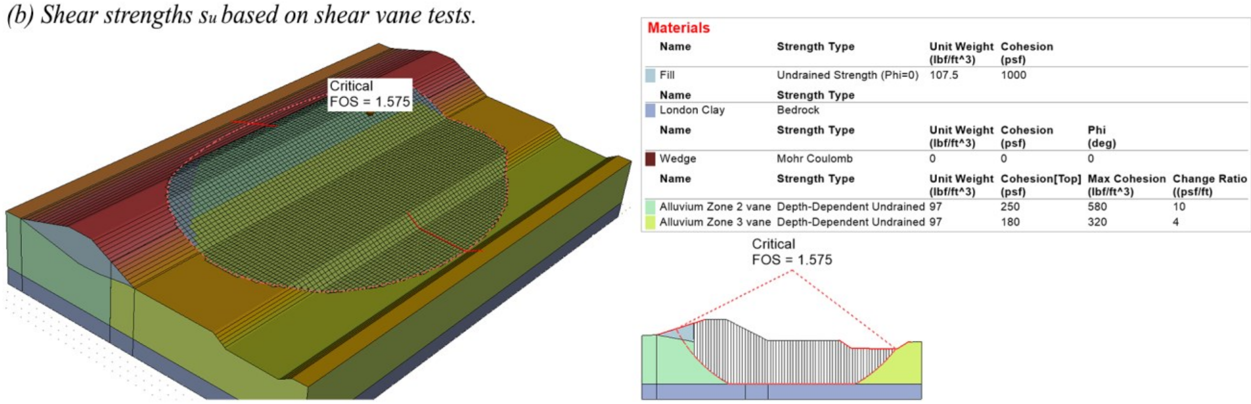

Name	Strength Type	Unit Weight (lbf/ft^3)	Cohesion (psf)	Phi (deg)
Fill	Undrained Strength (Phi=0)	107.5	1000	
London Clay	Bedrock			
Wedge	Mohr Coulomb	0	0	0

Name	Strength Type	Unit Weight (lbf/ft^3)	Cohesion[Top] (psf)	Max Cohesion (lbf/ft^3)	Change Ratio ((psf/ft)
Alluvium Zone 2 vane	Depth-Dependent Undrained	97	250	580	10
Alluvium Zone 3 vane	Depth-Dependent Undrained	97	180	320	4

(c) Shear strengths $s_u = s_{u,peak}/2.3$ based on shear vane tests.

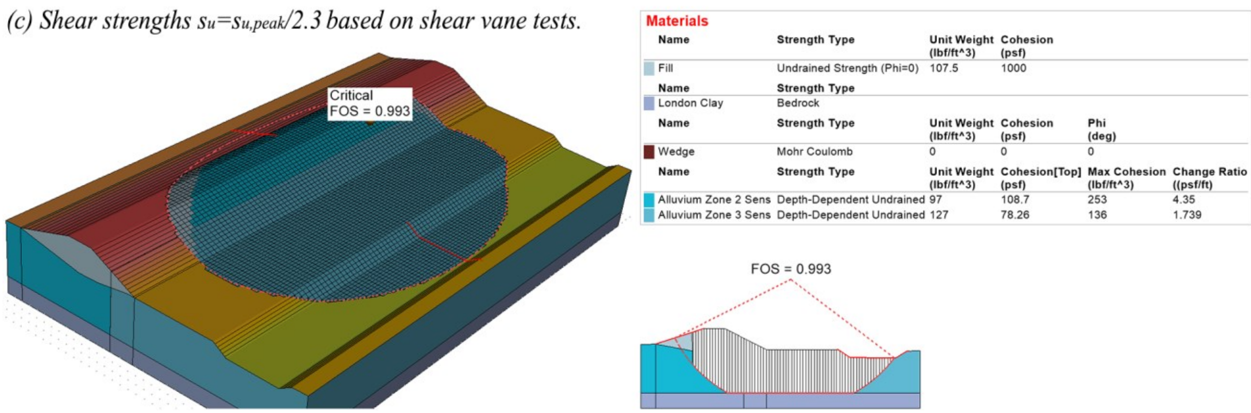

Name	Strength Type	Unit Weight (lbf/ft^3)	Cohesion (psf)	Phi (deg)
Fill	Undrained Strength (Phi=0)	107.5	1000	
London Clay	Bedrock			
Wedge	Mohr Coulomb	0	0	0

Name	Strength Type	Unit Weight (lbf/ft^3)	Cohesion[Top] (psf)	Max Cohesion (lbf/ft^3)	Change Ratio ((psf/ft)
Alluvium Zone 2 Sens	Depth-Dependent Undrained	97	108.7	253	4.35
Alluvium Zone 3 Sens	Depth-Dependent Undrained	127	78.26	136	1.739

Figure 1.6 A three-dimensional analysis of the Scrapsgate embankment failure.

However, neither vane shear tests nor undrained triaxial tests appear to provide a good average estimation of strengths at failure. The results of the three-dimensional stability analysis indicate that the average strengths at failure would have had to drop by 57% from their peak values (as measured by vane shear tests) in order for failure to take place; such average strength is substantially below that measured by undrained triaxial tests.

The implications of the findings produced by the three-dimensional analysis of the failure of the Scrapsgate embankment are further discussed in §1.3.3.

1.2.5 THE 1952 CONGRESS STREET OPEN CUT FAILURE

1.2.5.1. REVIEW OF THE ORIGINAL STUDY

The original study by Ireland (1954) evaluates the failure in an excavation made during the construction of the Congress Street “superhighway” in Chicago, IL. The failure took place during excavation works of saturated glacial clays; a portion of slope failed suddenly over a length of 200 feet when the depth of the cut reached 47 feet. The investigator concluded that “there was not time for any appreciable dissipation of porewater pressure” (Ireland 1952, p.163) and hence undrained conditions were in effect at failure.

The undrained shear strengths of the clay layers were determined by way of conducting unconfined compressive tests on soil samples from 2” Shelby tubes; these samples were described as “rather disturbed” (Ireland 1954, p. 163). The author relies on a comprehensive study of engineering properties of Chicago soils published by Peck and Reed (1954) to assert that the disturbed clays of Chicago area, including the failure site, exhibit undrained shear strengths that are significantly lower than those measured in relatively undisturbed samples. Ireland uses a correction coefficient of 1.35 reported by Peck and Reed (1954) to estimate the in-situ undrained shear strengths of clays used in his two-dimensional limit equilibrium model of failure.

A two-dimensional limit equilibrium analysis of the Congress Street failure conducted in SoilVision® SVSlope produces a minimum safety factor of 1.04 and a safety factor of 1.41 along the actual failure surface. These results, along with the original two-dimensional model of failure by Ireland (1954) are seen in Figure 1.7.

(a) *The two-dimensional analysis results by Ireland (1954, Figure 4)*
(reproduced with permission from ICE Publishing)

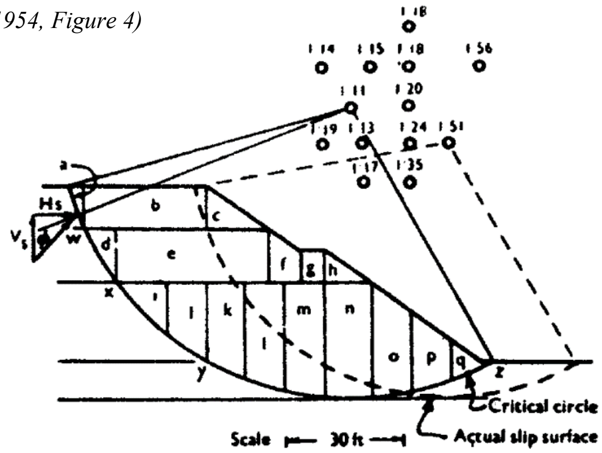

(b) The minimum two-dimensional factor of safety

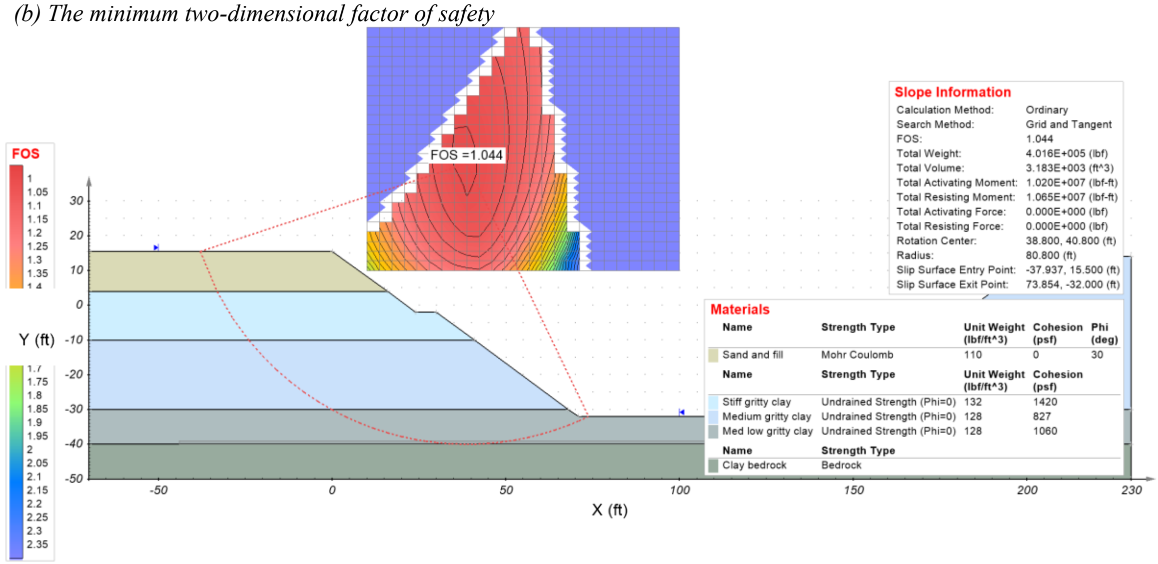

(c) The two-dimensional factor of safety along the actual slip surface

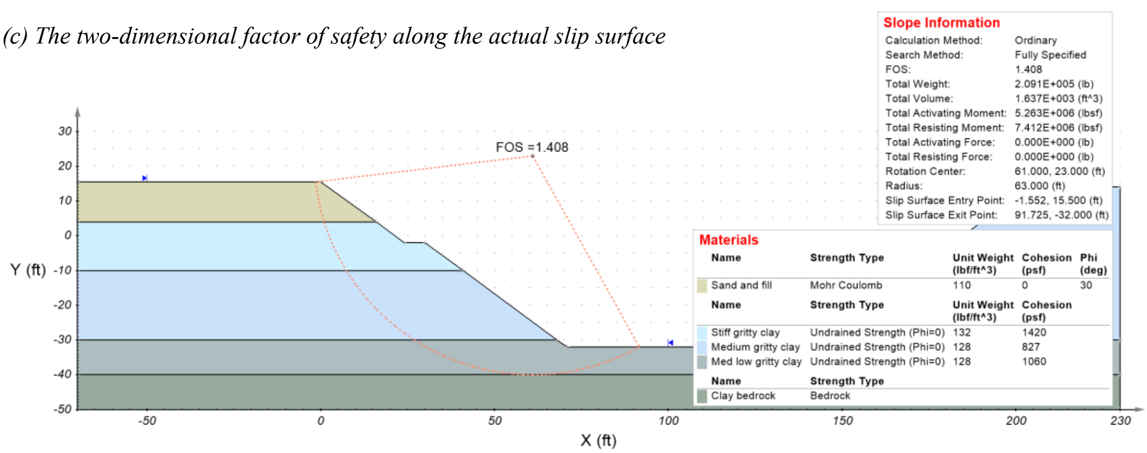

Figure 1.7 A two-dimensional limit equilibrium analysis of the embankment failure at Congress Street, Chicago.

1.2.5.2. A RE-EVALUATION OF THE CONGRESS STREET EMBANKMENT FAILURE IN THREE DIMENSIONS

A three-dimensional limit equilibrium analysis of the embankment failure at Congress Street in Chicago was conducted using original data on geometry and undrained soil strength values applied by Ireland (1954) in his stability analysis. The results are presented in Figure 1.8.

Recall that the undrained shear strengths used in the original analysis were obtained from disturbed 2” Shelby tube samples and were adjusted by multiplying the measured values by a correction factor of 1.35. The three-dimensional limit equilibrium analyses of the failure using these strength yield a minimum safety factor of 1.20 and a safety factor of 1.46 across the actual slip surface (Figure 1.8*(a)* and *(b)*). This represents an increase of, respectively, 15% and 4% over the two-dimensional equivalents.

The failure of the embankment was simulated in a three-dimensional limit equilibrium analysis by applying a correction factor of 1.15 to the undrained shear strength values measured from disturbed Shelby tube samples. This represents a 15% decrease from the estimated undisturbed strengths used by Ireland (1954). The results of this analysis are illustrated in Figure 1.8*(c)*.

1.2.5.3. DISCUSSION

The mechanism of embankment failure at Congress Street in Chicago proposed by Ireland (1954) whereby peak undrained shear strengths acted along the slip surface does not appear plausible when three-dimensional slope stability effects are taken into consideration. The simulation of failure shown in Figure 1.8*(c)* demonstrates that undrained strengths would have to drop, on average, by at least 15% in order for failure to take place. This average strength at failure matches neither the “disturbed” strengths measured from Shelby tubes nor the estimated undisturbed shear strength.

(a) The three-dimensional analysis of the failure at Congress Street producing the minimum safety factor.

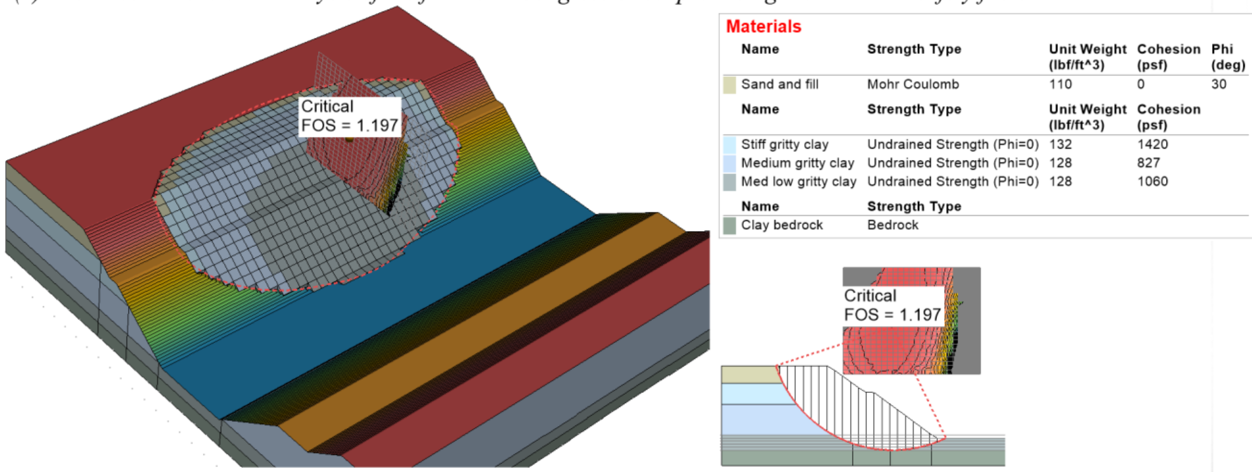

(b) The three-dimensional analysis of the failure at Congress Street along the actual slip surface.

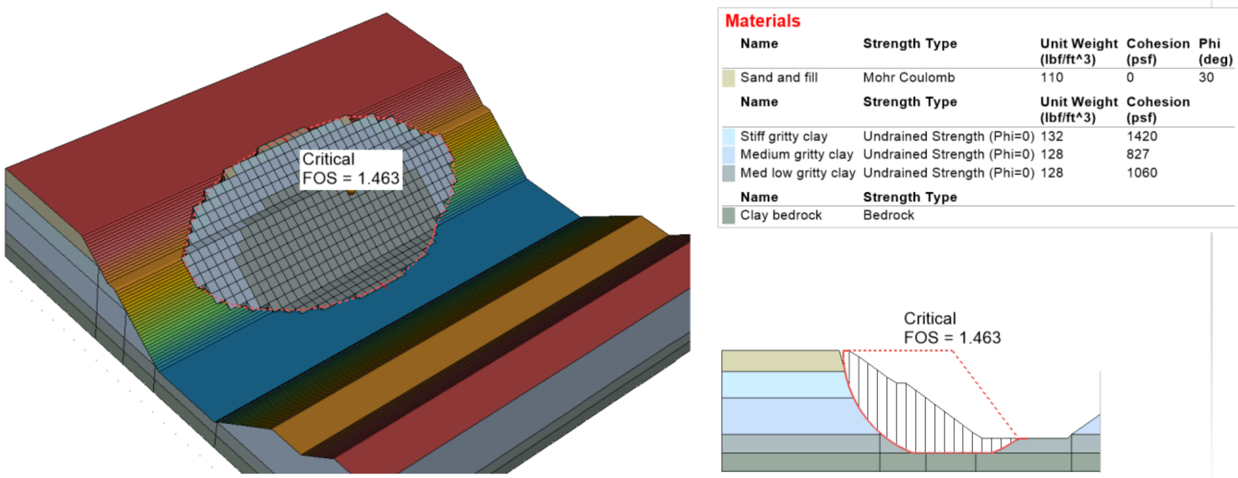

(c) The soil mass is brought to a limiting equilibrium in three dimensions by means of a 15% reduction in peak shear strengths.

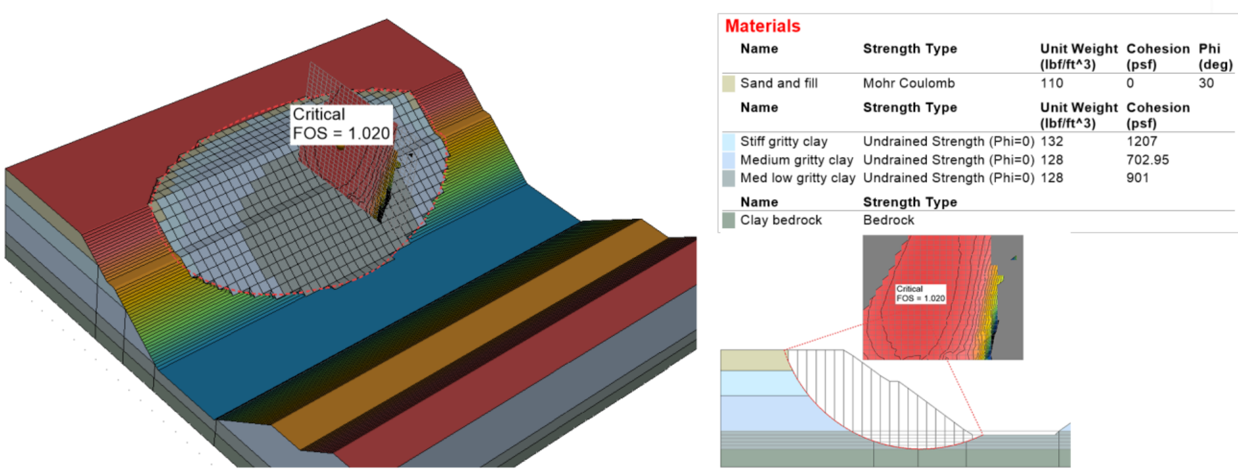

Figure 1.8 A three-dimensional limit equilibrium analysis of the embankment failure at Congress Street, Chicago.

The implications of the findings produced by a three-dimensional analysis of the embankment failure at Congress Street in Chicago are discussed in §1.3.3.

1.2.6 THE 1951-53 JACKFIELD SLIDE IN SHROPSHIRE

1.2.6.1. REVIEW OF THE ORIGINAL STUDY

The Jackfield slide is a historically significant case study in géotechnique. Its original investigators found evidence of soil strength behaviours that were not entirely understood at the time; these findings (along with other observations) triggered research efforts that ultimately led to the identification of some of the strain-weakening mechanisms in soils.

The failure took place in the valley of River Severn in England. The valley is thought to have been formed in recent geological history when glacial lake water overflowed the area and eroded the ground (Henkel and Skempton 1955). Possibly as a consequence of erosion, the surficial soils, made of low plastic clays, were heavily overconsolidated. The slide began in 1950, initially manifesting itself as a slow movement over an extended area. By 1951, the movement accelerated considerably, possibly triggered by heavy rains. At that time, the slide was about 400 ft wide, and downstream displacements reached in places 60ft. The slide was wholly contained within the weathered zone that extended about 25ft below ground surface; a slip surface was identified 17 or 18ft below ground level and had markedly lower strengths than the surrounding soils in spite of being part of the same geologic unit (Henkel and Skempton 1955; Skempton 1964).

The initial slope stability evaluation by Henkel and Skempton (1955) considered two soil strength models. The possibility that full undrained shear strengths (measured at 1,600 lb/ft^2) were acting along the slip surface at failure was ruled out, as those would produce very high factors of safety. The investigators considered an undrained failure whereby much lower undrained shear strengths measured in the slip zone (of about 450 lb/ft^2) were acting along the slip surface; a stability analysis using this strength model produced a safety factor equal to 1.12, a value considered “a satisfactory check” (Henkel and Skempton 1955, p. 135). A drained strength model was also evaluated, with the strength parameters c' = 150 lb/ft^2 and ϕ' = 21° determined by direct shear tests; a stability analysis using this strength model produced a safety factor value of 1.45, prompting the investigators to conclude that full drained strengths were not acting at failure. Henkel and Skempton (1955) speculated that a combination of factors acting at the slip surface, such as cyclical stress changes, local movements and weathering processes, may have weakened the soil in that zone, eventually reducing its cohesion value c' to zero. A stability analysis using strength parameters c' = 0 and ϕ' = 21° produced a safety factor of 1.07.

The case study was revisited by Skempton in his Terzaghi Lecture (1964) in the context of a discussion on strength reduction in soils. Skempton re-evaluated the direct shear tests of intact clay samples from outside the slide that were initially used to determine the effective strength parameters c' and ϕ'. He noted that a peak shear stress response was followed by a drop in shear resistance as strains accrued and defined two distinct strength envelopes, one for peak and another for residual strengths: $\tau_{peak} = 220 + \sigma_n' \ tan\ 25°$ lb/ft^2; $\tau_{res} = \sigma_n' \ tan\ 19°$ lb/ft^2 (Skempton 1964, Figure 12). A stability analysis using the residual strength envelope produced a safety factor equal to 1.12, a value considered sufficiently close to unity “when the approximate nature of $\phi'_{residual}$ is taken into account” (Skempton 1964, p. 90). Skempton ultimately concluded that the presence of fissures and joints at Jackfield has led to a reduction of strengths to residual, causing a progressive failure of the slope.

The loss of strength in an overconsolidated soil such as that at Jackfield was thought to be caused by two mechanisms: dilation on undrained shearing at small strains and by particle realignment in the direction of shearing at large strains (Skempton 1964). Loss of strength due to sensitivity was not likely a factor here as the soil at Jackfield did not exhibit a drop in strength on remoulding (Henkel and Skempton 1955).

1.2.6.2. A RE-EVALUATION OF THE JACKFIELD SLIDE IN THREE DIMENSIONS

The Jackfield slide was relatively shallow, with a slip surface found at a uniform depth of 17-18ft below ground surface. The slide covered a very large area, eventually reaching a width of ~400ft (120m) and a length of ~600ft (180m). Such slide has a very high aspect ratio, so much so that its two-dimensional stability analyses by Henkel and Skempton (1955) and Skempton (1964) were carried out using the "infinite slope" method that only considers resistance at the bottom of a slide while disregarding any contribution to stability anywhere along the entry to or exit from the slip surface.

A slide with such configuration is not normally expected to exhibit any appreciable three-dimensional effects because the "side wall" resistance would presumably act only along a small fraction of the slip surface. However, based on the dimensions and configuration of this slide, it is roughly estimated that the surface of the "side wall" contributes 12-15% of area to the overall slip surface. Additionally, the soil above the slip was described as having a much greater shear strength than the two-inch slip zone and could potentially contribute a considerable portion of resistance. Such resistance would manifest itself as three-dimensional slope stability effects.

A three-dimensional limit equilibrium analysis of the Jackfield slide was conducted to see what can be learnt from such exercise and whether it is of value to apply such method of evaluation to this type of slips. To model the slip surface in three dimensions, an assumption about the shape and inclination of the side walls had to be made. From the original descriptions of the slide, it is clear that it was shaped as a slab with a relatively even thickness; one could assume vertical walls at the ends of the slip surface. However, three-dimensional limit equilibrium analysis does not consider resistance along vertical sections of a slip surface, as it is formulated to consider only the surface area at the base of a column (Chen and Chameau 1982; Hungr 1987; Lam and Fredlund 1993). This shortcoming of limit the equilibrium analysis is highlighted by Stark and Eid (1998). As a

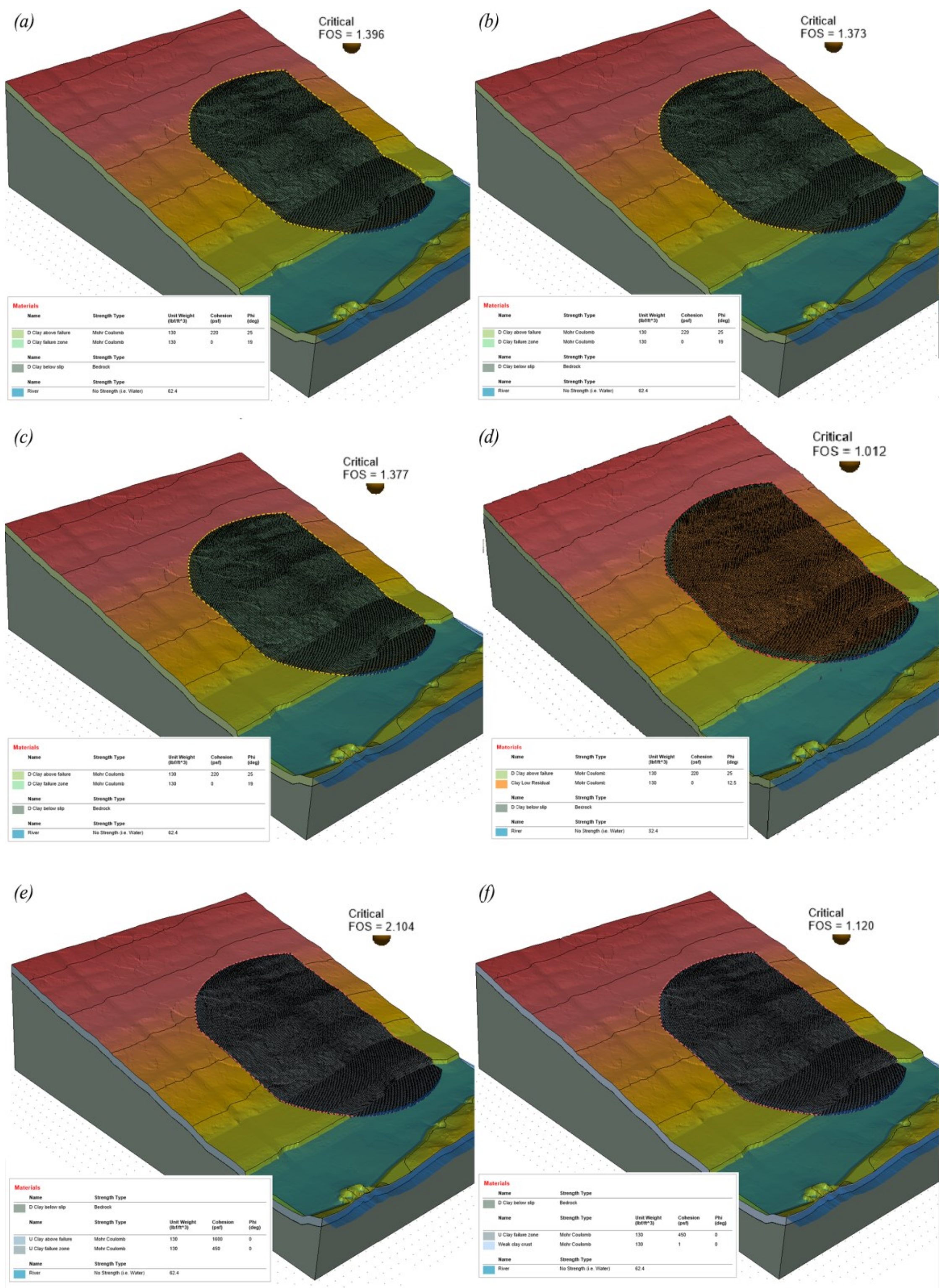

Figure 1.9 A three-dimensional limit equilibrium analysis of the Jackfield slide. (a), (b) and (c): Drained analyses with side walls inclined, respectively, at 45, 30 and 15° to vertical. (d): A drained analysis using near-null strengths above the slip zone. (e) and (f): Undrained analyses using, respectively, full shear strengths and near-null shear strengths above the slip zone.

next best alternative under the constraints of a limit equilibrium analysis, inclined side walls were assumed and three different analyses were conducted using wall inclinations of 45, 30 and 15° to the vertical. The safety factors produced by these analyses are, respectively, 1.40, 1.37 and 1.38 (seen in Figure 1.9 *(a)*, *(b)* and *(c)*). It appears that the safety factor calculation is not particularly sensitive to the inclination of side walls.

To estimate the contribution of side wall resistance, a three-dimensional analysis was done with null strength assigned to the soil above the slip zone. This analysis returned a safety factor of 1.04 (seen in Figure 1.9*(d)*). This safety factor would be equivalent to a two-dimensional limit equilibrium analysis of this slide, as it ignores side resistance. This means that the estimated three-dimensional slope stability effects in this slide are substantial at about 33%.

A separate analysis with undrained strengths was also carried out using the model with side wall inclination of 15° to vertical. The results are illustrated in Figure 1.9 *(e)* and *(f)*. The safety factor produced by the undrained analysis using full shear strengths in the crust is 2.10. The safety factor produced by the same using null strengths in the crust is 1.12, a value identical to that produced by Skempton (1964) using two-dimensional analysis. This means that the three-dimensional slope stability effects estimated by a limit equilibrium analysis of this slip using undrained strengths are excessively high at about 90%.

Lastly, the magnitude of three-dimensional slope stability effects at Jackfield was roughly estimated using the method by Akhtar and Stark (2017) combined with the drained strength model by Skempton (1964). An average estimation of side resistance along the vertical side walls using a coefficient of lateral pressure $K_\tau = 0.5$ (i.e. higher than the coefficient of active pressure and lower than the at-rest coefficient of lateral pressure) yields three-dimensional stability effects in the order of 15% or more. A conservative estimation of the same using the assumption of active failure along the sides of the slide and zero resistance along the headscarp and toe places the three-dimensional stability effects at around 2%; this is largely due to small active stresses acting at low depths in soils with high cohesion.

1.2.6.3. DISCUSSION

The three-dimensional limit equilibrium analyses of the Jackfield slide generate safety factor values well above unity. This result is an indication that one or more of the modelling parameters is incorrect. Skempton (1964) discusses the possibility that his residual strength model errs on the high side, and suggests, based on two-dimensional safety factor calculations, that the residual angle of friction ϕ'_{res} at failure may have been as low as 17.1°, generating, along the base of the slide, an estimated shear resistance s of about 400psf (19kPa). A three-dimensional back-analysis of the same demonstrates that, if full crust strengths are applied, the residual angle of failure would have to drop by about 35% to a value of 12.5° in order to attain limiting equilibrium (Figure 1A.1 in Appendix 1A). While there is a possibility that there is *some* error with the residual strength model proposed by Skempton (1964), the likelihood that the error is this large is remote.

Instead, the possibility must be considered that the error in the three-dimensional analysis lies at least in part with the crust strength model. The soil profile containing the slide was described as weathered, fissured, cracked and with substantial bulging (Henkel and Skempton 1955; Skempton 1964). It would not be unusual for such soil to have a lower strength on the macroscopic scale of a slide than it was shown by tests of relatively intact specimens retrieved from that zone. The original investigators were aware of this effect; for example, Skempton equivocates his determination of crust strength by stating the following: "the weathered clay, though quite firm and still retaining the characteristics of an over-consolidated clay is nevertheless far less strong than the hard, almost rocklike, unweathered strata" (Skempton 1964, p. 89). This may be one reason why three-dimensional slope stability effects were not considered by the original investigators (the high aspect ratio of this slide being the other reason). One can speculate that, on a macroscopic scale, the resistance developed the soil crust may have varied from zero in zones with tensile cracks to low in areas where a variety of weathering processes reduced the cohesion to null values but some frictional strength remained (as argued by Henkel and Skempton in their 1955 paper).

The other possibility is that an error is introduced into the three-dimensional analysis due to inaccurate assumptions about horizontal forces acting on the vertical or near-vertical side walls. The method by Akhtar and Stark (2017), aimed at mitigating this particular type of error, appears to produce lower three-dimensional effects. In the context of this case study, lower three-dimensional stability effects are more in line with expectation.

From the above, the conclusion can be reached that three-dimensional limit equilibrium methods are not well-suited to analyze translational slides with vertical side walls, such as the one at Jackfield; the method by Akhtar and Stark (2017) or deformation analysis may be more befitting for this purpose. Broadly speaking, three-dimensional analyses are considered to be better and more accurate than two-dimensional equivalents. The three-dimensional analysis of the Jackfield slide presented here offers an object lesson as to why this may not always be the case.

Lastly, it is possible that scale effects apply to the strength behaviour of the soil crust due to its macro-structure such as cracks and fissures; if such effects cannot be adequately replicated in a three-dimensional modelling exercise, its results are of little value.

1.2.7 THE LANDSLIDE AT SELSET, YORKSHIRE

1.2.7.1. REVIEW OF THE ORIGINAL STUDIES

A slow-moving landslide on the bank of River Lune in Selset, Yorkshire, was studied by Skempton and Brown (1961). The 180ft wide slip was discovered in 1955 and monitored until 1960. The relatively deep movement occurred in overconsolidated boulder clays; well-defined tension cracks pinpointed the headscarp location. The boulder clay was described as uniform and without fissures or joints in the zone of seasonal variations (Skempton and Brown 1961). Sandstone, limestone and shale strata were discovered at a depth of approximately 30ft below the valley floor; appreciable flows of water and artesian pressures were encountered in the bedrock during the drilling operations.

The soil strength parameters were determined from consolidated-drained triaxial tests; the clay was found not to be sensitive to disturbance or remoulding. Because of the slow-developing nature of the slide, long-term conditions were assumed and a drained strength model was adopted with strength parameters c' = 180 psf and ϕ' = 32°.

An initial analysis of the slide was conducted using the Bishop and Morgenstern (1960) stability coefficients for earth slopes and two different flow condition: horizontal flow (corresponding to a pore pressure ratio r_u = 0.45) and flow parallel to the surface (corresponding to a pore pressure ratio r_u = 0.35). The resulting factors of safety were, respectively, 0.99 and 1.14.

A more complex slope stability calculation was also performed using the Bishop method. In this analysis, pore pressure conditions were modelled by flownets simulating two conditions: (a) a large contrast between the clay and bedrock permeabilities coupled with artesian pressures; and (b) no contrast in the clay and bedrock permeabilities (Skempton and Brown 1961, Figure 5). This analysis produced safety factors of 1.00 to 1.01, the lower value corresponding to the condition of low permeability of the bedrock. The authors concluded that, in a marked contrast with results found from other long-term slips in overconsolidated clays (such as the Jackfield slide), full cohesion values must have been acting at failure and that the slope stability conditions were not very sensitive to changes in pore water pressure conditions.

This case study was revisited by Skempton in his 1964 Terzaghi lecture. The original drained triaxial tests conducted on boulder clay were re-evaluated to determine the peak and residual envelopes: $\tau_{peak} = 180 + \sigma_n' \tan 32°$ lb/ft^2; $\tau_{res} = \sigma_n' \tan 30°$ lb/ft^2 (Skempton 1964, Figure 16). Skempton notes that even though the residual envelope is only marginally lower than the peak strength envelope, this difference has a marked effect on stability. A two-dimensional analysis of the slide using peak strengths produces safety factors close to unity, whereas the same analysis using residual strengths results in a safety factor of 0.69; this represents an error of about 30% (Skempton 1964, p. 91). Skempton ultimately concludes that full peak strengths must have been acting at failure, having been almost simultaneously mobilized across the entire slip surface. Skempton remarks that "even in this intact, non-fissured clay one might perhaps expect to find a rather more pronounced indication of progressive failure" than suggested by the results of his stability analysis (Skempton 1964, p. 93).

1.2.7.2. A RE-EVALUATION OF THE SELSET SLIDE IN THREE DIMENSIONS

The Selset slide is an especially interesting case study from the perspective of three-dimensional slope stability effects. This is a case where the potential for progressive failure has been clearly identified. Yet the conclusion based on two-dimensional stability calculations is that no drop in strength below peak values took place. It is of interest to see whether the inclusion of three-dimensional stability effects into the analysis would affect this conclusion. The three-dimensional slope stability effects are expected to be pronounced at this site due to the concave

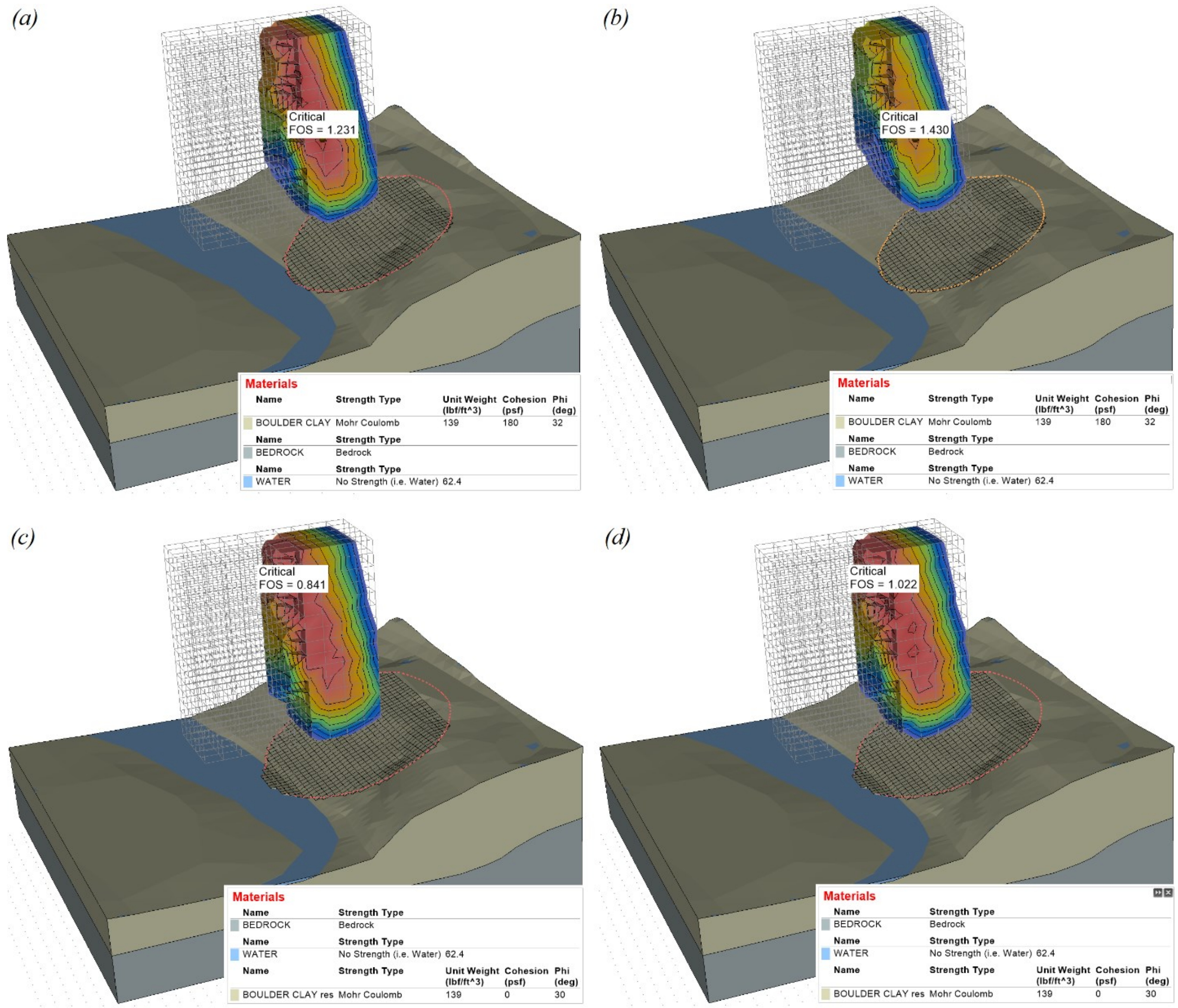

Figure 1.10 A three-dimensional limit equilibrium analysis of the Selset slide. Top: results produced using peak strength envelopes, with pore pressure conditions simulating (a) horizontal flow; and (b) flow parallel to surface. Bottom: results produced using residual strength envelopes, with pore pressure conditions simulating (c) horizontal flow; and (d) flow parallel to surface.

aspect of the slide surface as documented by the topographic map of the area provided by Skempton and Brown (1961, Figure 1).

Four three-dimensional limit equilibrium analyses of the Selset slide were conducted. The first two analyses used the boulder clay's peak strength envelope under two separate pore pressure conditions simulating horizontal flow; and flow parallel to the surface.

The results of these analyses are seen in Figure 1.10*(a)* and *(b)*. The analysis using pore pressure distributions resulting from horizontal flow produced a safety factor equal to 1.23; this represents a 24% increase over the equivalent two-dimensional safety factor. The analysis conducted under the assumption of flow parallel to the surface produced a safety factor of 1.43; this represents a 25% increase over the equivalent two-dimensional safety factor.

Two additional stability analyses were conducted using the residual strength envelope in combination with the two pore pressure conditions described in the previous paragraph. The results of these analyses are seen in Figure 1.10*(c)* and *(d)*. The analysis using pore pressure distributions resulting from horizontal flow produced a safety factor equal to 0.84. The analysis conducted under the assumption of flow parallel to the surface produced a safety factor of 1.02.

The pore pressure conditions specified by flownets (Skempton and Brown 1961, Figure 5) could not be replicated in three dimensions due to the complex configuration of the area and a general lack of knowledge about the groundwater conditions at the site.

1.2.7.3. DISCUSSION

The results of the three-dimensional analysis of the Selset slide indicate that the average strengths at failure would have been below peak values and perhaps equal to or close to residual values depending on the actual pore pressure conditions. These conclusions are opposite to those reached based on two-dimensional stability calculations. It is possible that, had three-dimensional analysis been available to the original investigators, they would have reached entirely different conclusions.

1.3. DISCUSSION OF FINDINGS

1.3.1 MAGNITUDE OF THREE-DIMENSIONAL SLOPE STABILITY EFFECTS

The side-by-side examination of two- and three-dimensional limit equilibrium solutions introduced in this chapter invites the conclusion that three-dimensional safety factors are generally greater than their two-dimensional equivalents. Table 1.3 lists the two- and three-dimensional safety factors for the case studies reviewed here; in this sample, the three-dimensional slope stability effects range from 3 to 61%.

Table 1.3 Comparison of select two- and three-dimensional limit equilibrium analyses of historic case studies.

Case Study	2D analysis		3D analysis		$\frac{FOS_{3D}-FOS_{2D}}{FOS_{2D}}(\%)$	Aspect Ratio	Soil Sensitivity
	FOS	Method	FOS	Method			
Lodalen	1.05	Bishop	1.08-1.19	Morgenstern-Price	~8 (3-13)	2.6 (2-3)	2-5
Bakklandet A	0.74	Bishop	1.03-1.05	Morgenstern-Price, Bishop	~41 (39-42)	2.5	n/a
Bakklandet B	0.67	Bishop	1.08	Morgenstern-Price	61	2.5	n/a
Drammen B	1.01	Bishop	1.09	Morgenstern-Price	8	3.5 (3-4)	n/a
Drammen A	1.14	Bishop	1.31-1.37	Morgenstern-Price, Bishop	17 (15-20)	3.5	n/a
Drammen C	1.26	Bishop	1.79-1.89	Morgenstern-Price, Bishop	46 (42-50)	3.5	n/a
Scrapsgate	1.00	Ordinary	1.22	Morgenstern-Price	22	5.5 (5-6)	3.7-7.9
Congress Street	1.04	Ordinary	1.20	Morgenstern-Price	15	4	~4
Jackfield	1.07	Infinite slope	1.39	Morgenstern-Price	33	22	n/a
Selset	0.99-1.14	Stability coefficients	1.23-1.43	Morgenstern-Price	24 (24-25)	3	0

This conclusion is supported by prior research. Over the years, the argument has been made by many that, as a rule, a slope's three-dimensional safety factor is greater than its two-dimensional equivalent. Hoek and Bray (1977) ascertain that the ratio of three- to two-dimensional safety factors for wedge solutions can vary between 1 and 3. Cavounidis (1987) put forward an algebraic argument demonstrating that the minimum safety factor of a slope is always higher in three dimensions than it is in two, provided that the two-dimensional slip line is a subset of the three-dimensional slip surface. Hungr (1987) uses a parametric study to demonstrate that three-dimensional safety factors are always greater than their two-dimensional equivalents, approaching the latter asymptotically as the slide's width approaches infinity. Stark and Eid (1998) conclude, based on parametric studies and on back-analyses of a number of wedge slides, that three-dimensional safety factors are greater than their two-dimensional equivalents.

The range of three-dimensional slope stability effects reported in Table 1.3 is comparable to figures reported by others. For example, Gens et al. (1989) estimate the range of error associated with the reduction of stability problems from three to two dimensions between 3 and 31%, with an average of 13.9%.

Several exceptions to the above have been noted. Hovland (1977) demonstrates that, theoretically, specific situations exist where the three-dimensional safety factor is lower than its two-dimensional equivalent. Seed et al. (1990) report the case study of the Kettleman Hills landfill failure, where a complex layering of liners and geotextiles described by Mitchell et al. (1990) has created conditions where shallow cross-sections had lower two-dimensional safety factors than the deepest cross-section of the slide, and the three-dimensional safety factor was 10-15% below it.

Exceptions such as the case of the Kettleman Hills failure in fact promote a better understanding of three-dimensional stability effects. Two-dimensional stability calculations traditionally focus on the deepest cross-section of a slip, which is usually also the critical one, with the lowest ratio of strength to driving stresses (i.e. the minimum safety factor). Studies by Hungr et al. (1989) and Sevaldson (1956) demonstrate that shallow cross-sections closer to the edges produce higher safety factors. These studies offer evidence to support the proposition that three-dimensional stability effects are generated at least in part in shallow areas at the ends of a slide due to their relatively high contributions to the available resistance and relatively low contributions to the driving stresses. However, the Lodalen slide as well as the hypothetical examples used by Hungr et al. (1989) all evaluate uniform soil profiles. It is conceivable that in a composite soil profile made of a variety of materials with contrasting shear strength properties the deepest cross-section passing through stronger soils may not produce the minimum two-dimensional safety factor. The

Kettleman Hills case study is a real life example of such a profile. One lesson learned from this case study is that landslides that take place in slopes made of multiple materials may display three-dimensional slope stability effects that are manifestly different from the established pattern.

The conclusion can be reached that, with some exceptions, the three-dimensional factors of safety are larger than their two-dimensional equivalents.

In the following sections, factors that may influence the magnitude of three-dimensional slope stability effects are examined.

1.3.1.1. ASPECT RATIO

The three-dimensional slope stability effects are thought to be largely related to "end effects" that are ignored in two-dimensional analyses. Consequently, the relative width-to-depth ratio of a slide, known as the slide's aspect ratio, is thought to have an impact on the magnitude of end effects. Generally speaking, the wider the slide is, the more it approaches the theoretical model of an infinitely wide body where the contribution to available resistance along the curved ends and/or "sidewalls" is negligible compared to that mobilized at its base. Likewise, the deeper the slide is, the more "sidewall" resistance there is that is unaccounted for in a model only considering the resistance in the middle. All other things being equal, a slide with a greater aspect ratio has lower three-dimensional effects on slope stability than a slide with a lower one.

The relationship between a slide's aspect ratio and the magnitude of its three-dimensional stability effects has been extensively explored by researchers. Arellano and Stark (2000), Gens et al. (1988), Hungr (1987), Chen and Chameau (1982) and others demonstrate in a series of theoretical models that such effects are more pronounced in slide configurations with lower aspect ratios. Skempton (1985) advocates decreasing shear strength values obtained from two-dimensional back-analyses of slides by applying a reduction factor f_{red} to allow for the strength developed on the sides of the actual three-dimensional slide:

$$\mathrm{f_{red}} = \frac{1}{1 + \frac{K}{R_a}} \qquad \textit{Eq. 1.3}$$

where K is the coefficient of lateral earth pressure and R_a is the aspect ratio of the slide. Stark and Ruffing (2017) propose a procedure for an upward correction of the three-dimensional safety factor which accommodates scale effects as well as uncertainties associated with input parameters.

A number of correlations between the magnitude of a slide's three-dimensional stability effects and its aspect ratio were proposed by Akhtar and Stark (2017, Figs. 1-4), Arellano and Stark (2000, Figure 4), Gens et al. (1989, Figs. 18-20), Hungr (1987, Figure 3), Chen and Chameau (1982, Figure 9) and many others. These correlations take the general form of an inverse relationship between three-dimensional stability effects and the aspect ratio, with the former asymptotically approaching zero as the latter nears infinity[1].

We will now explore whether such a correlation can be observed in the dataset of case studies evaluated in this chapter. Table 1.3 summarizes the aspect ratios of the historic case studies reviewed here along with their three-dimensional stability effects; Figure 1.12 illustrates the relationship between the two graphically. Additional materials are included in Appendix 1B-I.

The data in in Figure 1.12 appear to cluster with no obvious trend, suggesting that the correlation between a slide's three-dimensional slope stability effects and its aspect ratio is rather weak in this

[1] In some early work, assertions were made that at large aspect ratios, the three-dimensional factors of safety may become lower than their two-dimensional equivalents (Chen and Chameau 1982), resulting in inverse correlations of three-dimensional stability effects vs. aspect ratio dipping below zero at high aspect ratio values, and inverse correlations of ratios of three- to two-dimensional factors of safety vs. aspect ratio dipping below unity at high aspect ratio values. These assertions were later disputed (Hutchinson and Sarma 1985) and are probably erroneous.

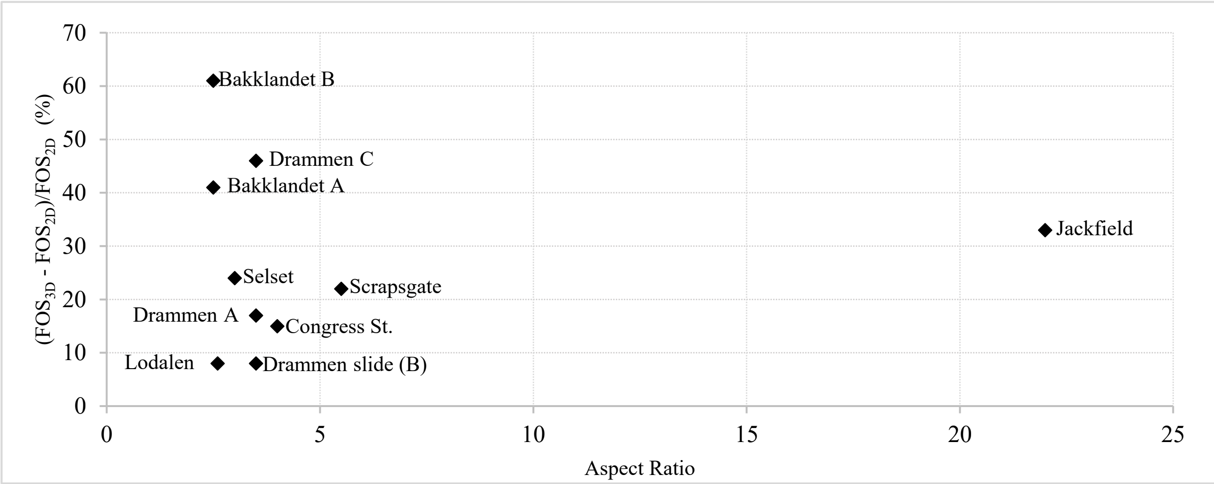

Figure 1.11 A plot of three-dimensional slope stability effects vs. slide aspect ratios for case studies reviewed in Chapter One.

particular sample. The relationship between three-dimensional stability effects and aspect ratio can be expanded to factor in the inclination of the face in order to determine whether a clearer pattern can be established. Figure 1.12 presents the same data in a different form by plotting the ratios of three- to two-dimensional factors of safety against the slides' aspect ratios; this allows for a direct comparison with the relationships reported by Gens et al. (1988, Figure 18*(e)*) that correlate the magnitude of three-dimensional stability effects in a slide with two quantities, its aspect ratio and its slope inclination. From this figure, the correlation between predicted and calculated values appears rather weak; the relationships by Gens et al. (1988) appear to over-predict the magnitude of three-dimensional slope stability effects for nearly all cases. It is conceivable that other slope features, such as surface topology and/or complex soil profile, affect the magnitude of three-dimensional slope stability effects, obscuring the relationship explored here.

Based on the data from Chapter One alone, any conclusive and/or quantitative assessments to the nature of relationship between a slide's aspect ratio and its three-dimensional effects cannot be made. The following sections explore whether other slide characteristics can provide clues about the magnitude of three-dimensional slope stability effects.

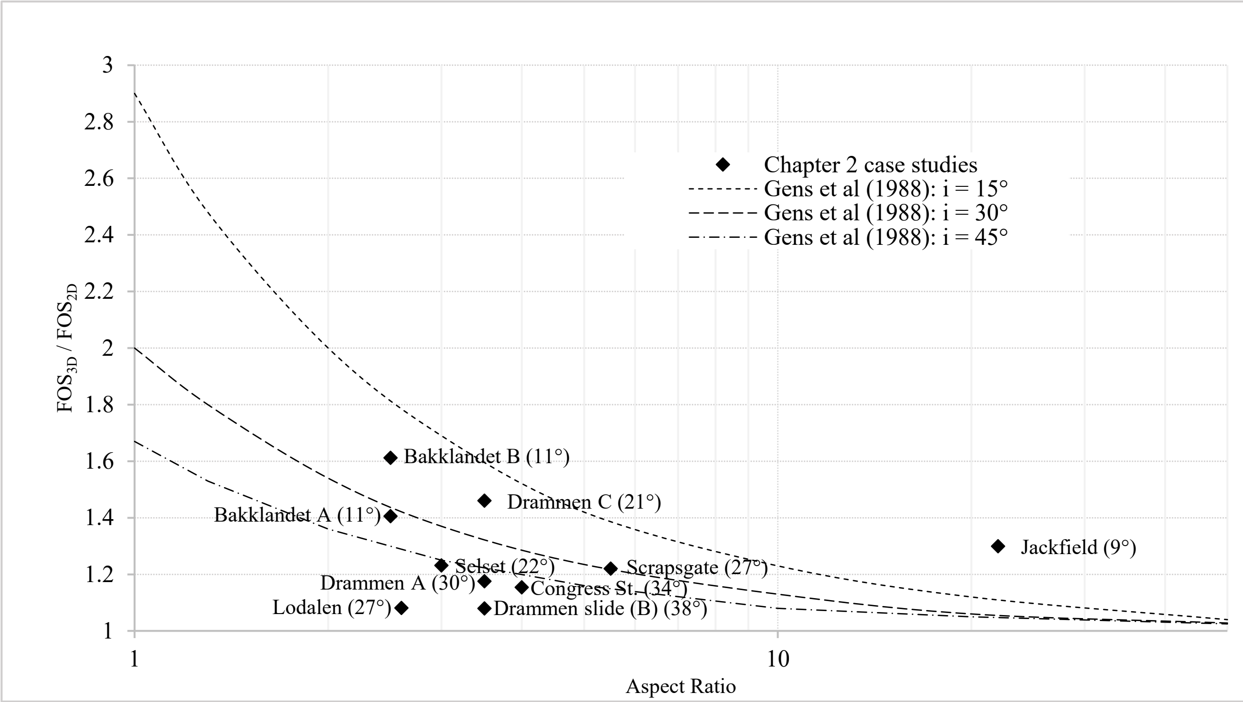

Figure 1.12 Ratios of three- to two-dimensional safety factors for case studies in this chapter plotted against relationships reported by Gens et al (1988) correlating a slide's aspect ratio and face angle i with its three-dimensional stability effects for power curve ends and critical depth

1.3.1.2. SURFACE TOPOLOGY

The effect of surface topology on three-dimensional stability effects has been explored by Fredlund et al. (2017), Chaudhary et al. (2016) and Zhang et al. (2014) using a combination of parametric studies and case histories. These studies consistently show that concave and convex slopes have more pronounced three-dimensional slope stability effects than planar slopes. Chaudhary et al. (2016) assert that in convex slopes, the increase in the three-dimensional stability effects ranges between 10 and 25%, whereas in concave slope, they can reach 32 to 38%.

Among the case studies revisited here, the Bakklandet A and Drammen C stable slopes feature distinctly convex surfaces. They both demonstrate an increase of, respectively, 7 and 28% in three-dimensional stability effects over the values predicted for planar slopes. Such differences are more or less in line with those reported by Chaudhary et al. (2016).

The Bakklandet B and Drammen A stable slopes and the Selset slide have convex surface topology. The stable slopes demonstrate an increase of, respectively, 27 and 8% in three-dimensional stability effects over the predicted values for planar slopes. Such increases are lower than those predicted by Chaudhary et al. (2016). However, contrary to reported trends, the Selset slide demonstrates three-dimensional stability effects that are 27% lower than the predicted value.

It is worth noting that the Bakklandet A and B as well as the Drammen A and C profiles are stable slopes and not actual slips; therefore, all results and conclusions stemming from the analyses of these should be given about the same level of credence as parametric studies.

1.3.1.3. NON-UNIFORM SOIL PROFILE

The relationships between a slide's aspect ratio and its three-dimensional slope stability effects reported by researchers such as Gens et al. (1988), Hungr (1987), Chen and Chameau (1982) and others were developed using parametric models with uniform soil profiles. In non-uniform slopes made of two or more materials with different strengths, a departure from these is expected, as a three-dimensional slip surface with side walls passing through a stronger material would mobilize more resistance at limiting equilibrium than a slip surface passing through a weak one. Akhtar and Stark (2017) and Arellano and Stark (2000) conducted parametric studies on models[2] comprised of two Mohr-Coulomb type materials with contrasting strength parameters to explore, among other things, the effect that non-uniform soil profiles have on the magnitude of three-dimensional stability effects.

In actuality, the vast variability of soil profiles and strength behaviours makes the exercise of determining, via parametric studies, the relationship between a slide's aspect ratio and its three-

[2]The models used by Akhtar and Stark (2017) and Arellano and Stark (2000) were developed for wedge slides and do not apply to most case studies revisited here, with perhaps the exception of Jackfield.

dimensional stability effects rather complicated and possibly of minor practical value. In today's technological environment, it may be easier and better to conduct a three-dimensional analysis of a specific embankment rather than speculate about its three-dimensional stability effects on the basis of parametric studies. Therefore, the mere realization that a slide with a weak base material and stronger soils above[3] should be expected to produce higher three-dimensional safety factors than one with uniformly weak material throughout (all other things being the same) may be sufficient by itself.

Among the case studies reviewed in this chapter, all of them except Lodalen, Drammen and Selset are slopes made of non-uniform soils, i.e. soils with strengths behaviours that cannot be captured by a single strength model. If the theoretical reasoning above holds true, three-dimensional slope stability effects would be expected to be more pronounced in such slopes. The plot in Figure 1.12 demonstrates that a clear distinction cannot be made between three-dimensional slope stability effects in uniform and non-uniform slopes.

Crust strength

Soil crusts commonly exhibit strength properties that are drastically different from underlying materials. A variety of complex processes in the weathering zone create soil peds and blocks that are overconsolidated as well as unsaturated and therfore very strong, but also promote fissures, cracks and other macroscopic structure. Tests to determine the shearing strength of this material are typically run on intact specimen obtained from blocks without obvious macroscopic features and commonly yield high strength values. As a consequence, strength models developed on the

[3] Only slopes where stronger materials are underlain by weaker ones should be considered, since in a slope with weaker materials at the top, the slip surface with the lowest safety factor is not likely to pass through the stronger foundation materials.

basis of such tests do not include the effects of macroscopic structure and likely overestimate the soil's strength on a macroscopic scale.

Consider the soil strength measurements at Bakklandet, Drammen (Bjerrum and Kjaernsli 1957, Figs. 2 and 6) and Jackfield (Henkel and Skempton 1955). The weathered profiles display undrained shear strength values that are 3 to 4 times higher than the unweathered soils below. The incorporation of crust strength models developed on the basis of such tests into three-dimensional stability calculations would obviously result in substantial three-dimensional stability effects. The important question is, are these effects real?

The results of three-dimensional limit equilibrium analyses of the Jackfield slide provide a good indication that the application of intact strength values to a heavily overconsolidated yet heavily weathered crust produces safety factors well above actual. It appears that a soil crust's strength on the scale of a slide can be substantially lower than on the scale of an intact sample.

These findings invite the conclusion that three-dimensional safety factor calculations that use crust strength models derived from tests on intact samples may overestimate the magnitude of three-dimensional stability effects. In the example of the Jackfield slide, the error introduced into the analysis due to the use of intact crust strength is around 30% when using the drained strength model and over 100% when using the undrained strength model.

Scale of slide vs. magnitude of three-dimensional effects

The majority of historic case studies used to validate the various strength models and limit equilibrium methods are rather small in scale, as far as landslides go (see

Table 1.4). This section explores some of the consequences of their modest scale on the accuracy of the calculation results.

Table 1.4 Landslide physical dimensions and volumes.

	Case Study	Est. Area, m^2*10^3	Est. Volume, m^3*10^3	Depth, m
Case studies revisited in Ch. 1	The Lodalen slide, 1954	2.6	11	22
	The Drammen river bank failure, 1955	0.5	<2	11
	The Scrapsgate failure, 1953	2.7	16	13
	The Congress Street open cut failure,1952	1.7	11	17
	The 1951-53 Jackfield slide in Shropshire	17	70	5
	The landslide at Selset, Yorkshire, 1955	1.5	40	15
Other Landslides	The 1974 Rio Mantaro slide, Peru (after Lee and Duncan, 1975)	not reported	1,500,000	unknown
	The 1977 landslide at Tuve, Sweden (after Duncan et al. 1980)	150	est. >2,000	~30
	The 1988 Kettleman Hills failure, California (after Mitchell et al. 1990; Seed et al. 1990)	not reported	440	~30
	The Mount Polley TSF failure	30	450	50

The previous section demonstrated that the use of crust strength models derived from intact samples not representative of the weathered profile leads to an over-prediction of three-dimensional stability effects. At Jackfield, where, in a three-dimensional analysis, strengths are overestimated across 12-15% of the total slip area, the three-dimensional safety factors are in error by as much as 30-100%.

In a much larger slide, all other things being equal, the fraction of area passing through the soil crust would be lower; this would attenuate the error in three-dimensional stability effects associated with an overestimated crust strength.

Consider the stable slopes at Bakklandet, where a crust with a thickness of 3-4m was documented. Profiles A and B investigated by Bjerrum and Kjaernsli (1957) are relatively shallow at 10-20m. This means that a considerable portion of the three-dimensional slip surface, possibly as much as 30-40%, would pass through the crust. Consequently, any error in the strength estimation of this material on the scale of the slide would lead to substantial over- or underestimations of three-dimensional slope stability effects.

One could argue that in large slides, the crust constitutes a relatively small fraction of the slip area and its contribution to three-dimensional stability effects is less significant than in small slides, where it represents a substantial fraction of the slip surface. Consequently, an error in the crust strength model would be exacerbated in small slides and diminished in large ones.

1.3.2 THE IMPACT OF THREE-DIMENSIONAL SLOPE STABILITY EFFECTS ON THE INTERPRETATION OF RESULTS

All limit equilibrium solutions for slope stability aim to satisfy the equations of force and moment equilibria along a slide's slip surface. However, due to limitations inherent to each method as well as to this approach as a whole, some of the equilibrium conditions remain unsatisfied. For example, all limit equilibrium methods up to but not including solutions by Morgenstern-Price (1965) and Spenser (1967) do not satisfy the equations for moment equilibrium. Furthermore, limit equilibrium methods ignore stress-strain relationships and rely instead on various assumptions regarding lateral forces along with the weight of the soil column to determine stress states. Finally, two-dimensional limit equilibrium methods may satisfy the equations of equilibria along the slip line along the bottom of a selected cross-section but not along the entire slip surface.

The recognition that the equations of stress and moment equilibria shall be satisfied across the entire slip surface rather than along one or more of its cross-sections invites the conclusion that three-dimensional stability solutions produce safety factors that are closer to the true ones than those obtained by two-dimensional methods. This conclusion holds true whether the three-dimensional safety factors are greater than their two-dimensional equivalents (as shown by most research on this subject including the re-evaluations presented in this chapter) or lower than them (such as in the case of the Kettleman Hills failure investigated by Seed et al. 1990). Accordingly, the three-dimensional stability effects can be thought of as a measure of error introduced into a stability analysis due to its reduction to two dimensions.

Going forward, for the sake of simplicity, exceptions such as the Kettleman Hills case study will be ignored and three-dimensional safety factors will be assumed to be greater than their two-dimensional equivalents, as it has been shown by most research.

The findings from the re-evaluations of the slope stability case studies in three dimensions introduced in this chapter can be summarized to conclude the following:

Assuming that representative shear strengths and driving stresses are assigned along the failure surface, the limit equilibrium back-analysis of a failure should yield a safety factor of unity in three dimensions and below unity in two.

There are two implications stemming from the above conclusion.

Implication #1: Two-dimensional limit equilibrium back-analyses of slope failures that produce safety factors equal to unity are probably in error. Such results indicate that the model parameters and/or calculations may be incorrect, i.e. either the strength models or stress states used in the calculation of the safety factor are in some error. The extent of this error is reflected in the magnitude of the three-dimensional slope stability effects: if the difference between the two- and three-dimensional safety factors is substantial, so is the error (and vice versa).

Two substantial sources of error have been explored so far: (i) strength models and (ii) stress states. Because we are somewhat better at calculating stresses than we are at evaluating shear strengths, and because we know of the three-dimensional resistance effects acting at the ends of a slide, it can be reasoned that the former is a greater contributor to the error.

Geotechnical researchers have long recognized that two-dimensional back-analyses of failures likely overestimate soil strengths. Eide and Bjerrum (1955) and Sevaldson (1956) recognize the potential three-dimensional stability effects and compensate for these, to a degree, by calculating average safety factors across multiple cross-sections. Skempton (1985) advocates the use of a strength reduction factor to apply a downward correction to strengths obtained in two-dimensional back-analyses of failures; he suggests that corrected rather than back-calculated strength values should be matched against laboratory data.

In this context, the findings by Bjerrum and Kjaernsli (1957) regarding the slopes of Bakklandet and Drammen, along with various other studies of the time that produced two-dimensional factors of safety below unity (Cadling and Odenstad 1950; Bjerrum 1954), are not as problematic as they appeared at the time of their publication. Back then, these findings triggered a re-examination of the undrained strength model and its applicability to slope stability problems. Had the three-dimensional stability effects been better understood at the time of publication of these studies, it is possible that the undrained strength model would have not scrutinized to the extent that it has. In hindsight, this re-evaluation was a most useful undertaking that significantly advanced our understanding of undrained strengths, including, but not limited to, strain-weakening processes (summarized by Skempton 1964), consolidation-driven changes (Ladd 1990) as well as strength anisotropy and its impact on three-dimensional stability effects (discussed by Toyota et al. 2014).

Implication #2: Three-dimensional back-analyses of failures that do not yield safety factors near unity are also likely in error.

Based on the above findings, one may wonder if the entire body of knowledge amassed from two-dimensional limit equilibrium analyses should be questioned. However, the case-by-case review of the historic investigations of slope failures in this chapter offers ample evidence that correct conclusions about the mechanism of failure can in fact be reached even when the assessment tools, such as the safety factor calculation methods, are in some error. In these investigations, safety factor calculations were treated as mere checks to evaluate a hypothesis that has been formulated about the failure mechanism. The hypothesis itself was developed by integrating field observations, laboratory data and general knowledge of soil behaviours. Provided that the limitations of the analysis are understood and appreciated, correct conclusions can still be reached in the absence of error-free tools; studies such as those of the Lodalen, Jackfield and Scrapsgate slides demonstrate that.

However, it has also become clear that in the absence of a good way to estimate three-dimensional effects, two-dimensional limit equilibrium analyses can be and have been used to reach and/or justify incorrect conclusions. For example, where a two-dimensional safety factor of unity was used to back-calculate shear strengths at failure, the latter may have been overestimated.

How could such over-estimation go unnoticed? The historic cases reviewed in this chapter have been most thoroughly examined by the original investigators, and a good match was often attained between laboratory-tested and back-calculated strength values. The original papers also attest to the significant efforts made to ensure that soil sampling and testing were done in a responsible and consistent manner using the best practices of the time. Therefore, merely asserting that the technicians and engineers of the time erred in estimating the soil strengths by as much as 30 or even 50% will not do. Another explanation, or explanations, must exist. In the next section, two important sources of error in the soil strength models used to assess slope stability are explored in the context of the reviewed historic case studies.

Finally, while a review of historic back-analyses of slides may provide valuable insights into the possible reasons for the suspected errors in their strength models, a definitive pronouncement on the matter would not be possible without access to sites and samples, a condition that cannot be fulfilled decades after the occurrence of these events. However, this theoretical exercise will assist in formulating new hypotheses regarding true soil strengths at failure as well as soil strength behaviour. These hypotheses then may be tested using more current case studies such as the 2014 failure at the Mount Polley TSF.

1.3.3 SOME REASONS FOR ERRONEOUS INTERPRETATIONS OF SOIL STRENGTHS

The probable reason for the errors associated with the soil strength models used in stability assessments is that soil strength behaviour is complicated and can vary a great deal depending on numerous factors such as the manner in which the soil is sheared, the degree of disturbance, loading history and more.

Geotechnical researchers have long drawn a distinction between undrained and drained strengths, differentiated by the manner in which the samples are sheared. Of equal importance is the recognition that disturbance or remoulding can decrease the undrained shear strength of a clayey soil. This effect was initially studied in quick clays (Rosenqvist 1953) as these exhibit a rather extreme form of such behaviour; however, researchers realized fairly soon that most clayey soils display some degree of sensitivity (Skempton and Northey 1952). Lastly, the propensity of some soils to develop residual strengths after attaining a peak value was noted by Skempton (1985; 1964) who used this new understanding about soil strengths to re-evaluate a number of case histories that were, in his view, inadequately explained by the original investigations.

This section focuses on residual strength and soil sensitivity.

1.3.3.1. RESIDUAL STRENGTH

In evaluating potential reasons as to why the actual soil strengths at failure may be lower than the values estimated by two-dimensional limit equilibrium back-analyses, the propensity of clayey soils to weaken upon disturbance and/or shearing should be considered.

The clayey soils' propensity to weaken upon an accumulation of shear displacements has been initially noted in direct shear tests at large shear strains. Skempton (1985, 1964) attributes this behaviour to two soil phenomena: (i) dilatancy on shearing and (ii) re-orientation of platy minerals.

A distinct peak in a soil's strength is observed in overconsolidated soils at relatively small strains as the soil dilates and its water content increases; this peak takes place at relatively small strains and is followed by a drop in resistance as the shear strains accumulate. A reorientation of platy minerals happens at much larger displacements and results in the creation of preferential slip planes in the direction of shearing (i.e. pre-sheared planes); the surface resistance along these planes defines the residual angle of friction. A loss of strength due to particle reorientation can be observed in both overconsolidated and normally consolidated soils with a clay weight fraction in excess of 20-25% (Skempton 1985).

The post-peak decrease of a soil's strength upon straining, known as "strain-weakening," [4] is associated with soil sensitivity and related to the breakdown of the soil structure. The transition from peak to residual strengths is not instant but takes place gradually over a range of plastic shear strains. The function that correlates accumulated plastic shear stresses with resistance to shearing is known as the strain-weakening curve. This curve defines a variety of intermediate strength values that act in the soil after its peak resistance is exceeded and before its residual strength is reached. A safety factor may differ considerably depending on whether it is calculated using peak, residual or intermediate strength values. Furthermore, if the straining is not uniform, the mobilized shear resistance may also vary, meaning that the same soil element can have vastly varying strengths as a function of accrued plastic shear strains.

---

[4] Two terms, "strain-softening" and "strain-weakening," are used interchangeably in geotechnical literature to describe the stress response to shear straining. However, the term "strain-weakening" describes a strength response to straining whereas "strain-softening" is better suited to describe a response in stiffness (per conversations with Dr. C.D. Martin and Dr. N.R. Morgenstern). Therefore, the term "strain-weakening" is adopted throughout this thesis to describe such mechanical behaviour while the term "strain-softening" is used exclusively in reference to its namesake constitutive model in FLAC3D.

Limit equilibrium solutions do not consider the effect of shear straining on strength; instead, an equivalent “average” strength value is most commonly applied to the entire slip surface. The selection of the appropriate strength value in modeling a slope’s stability becomes then a matter of judgement based on what is known of the soil’s state in the field rather than a mere matching of laboratory-tested values.

Two of the historic cases revisited in this chapter, the Selset and Jackfield slides, are discussed in Skempton’s 1964 Rankine Lecture in view of the possibility that post-peak strengths, rather than full resistance, were acting at failure.

The Selset slide

At Selset, the boulder clay in which failure occurred was heavily overconsolidated but contained only 17% of clay particles. Consequently, the difference between the peak and residual angles of friction is insignificant at 2°, and the cohesion intercept of the peak strength envelope is “not large.” Even so, Skempton estimated that the factors of safety obtained using peak and residual strength models would differ by over 30%. The analysis of the slide introduced here, conducted using three-dimensional limit equilibrium methods and simplified assumptions about pore pressures, shows that, when three-dimensional effects are factored in, there is a 40-50% difference between safety factors calculated using peak and residual strength values.

The two-dimensional back-analysis of the slide by Skempton (1964) using peak strengths produced a safety factor near unity, prompting the conclusion that even though a potential exists in this soil to develop post-peak and residual strengths, the operational strengths at failure were more or less equal to peak values along the slip line. When three-dimensional effects are factored in, it becomes clear that post-peak rather than peak strengths were acting along the slip surface at failure.

The Jackfield slide

The 1952 slide at Jackfield was initially investigated by Henkel and Skempton (1955) at a time when residual strengths were not well understood; he subsequently reassessed the original analysis and concluded that in the long term, operational strengths along the slip surface were reduced to post-peak values (Skempton 1964). Skempton re-evaluated the testing data to determine a peak friction angle of 25° and a peak cohesion value of 220psf; the residual envelope was described by a friction angle of 19° and a zero cohesion value. Skempton concluded that average strength values close to residual were acting on the slip surface at the time of failure.

The three-dimensional limit equilibrium analysis of the failure does not contribute in any significant way to Skempton's (1964) ultimate assessment of the slide mechanism.

Summary

The post-peak drop of strength known to occur in some soils may constitute a valid explanation for a number of slides where the back-analysis of failure based on peak strengths is unsatisfactory. The potential for post-peak strengths acting along the slip surface at failure shall be considered where the following additional attributes are present:

- The soil in the slip zone is overconsolidated and field evidence indicates a localized increase of water content in the failure zone; and/or
- The soil in the slip zone contains a clay fraction greater than 20-25% and field evidence exists of particle realignment in the direction of movement in the slip zone. Such evidence could include historic landslides or movement documented at the same location, pre-sheared planes and/or evidence of clay particles' realignment at a microscopic level.

Of the historic cases reviewed in this chapter, aside from the Jackfield and Selset slides, the following slope failures possess some of these attributes:

- The slide at Lodalen: The soil at the failure location had a clay fraction of 30-50% and was lightly overconsolidated. Evidence of dilation and of a slip surface were found in two of three boreholes in the slide area. The conclusions can be reached that a post-peak strength behaviour may have been a factor in the failure.
- The Congress Street open cut failure in Chicago: The study by Peck and Reed (1954) of the engineering properties of soil in the Chicago area reports that local clayey depositions contain a clay mineral fraction roughly between 40 and 60%; the same study describes both strain-weakening behaviour and loss of strength on remoulding (sensitivity). Ireland (1954) references this study in justifying his soil strength model. However, no evidence of dilation and/or clay particle realignment is mentioned in the original study of the failure. Additionally, there is no evidence to suggest prior or long-term movement along the same slip surface. Therefore, there is no documented evidence to suggest that post-peak strength behaviour was a factor.

1.3.3.2. SOIL SENSITIVITY

Sensitivity is a property defined as the ratio of undisturbed to remoulded undrained shear strengths of a soil at its natural water content (Terzaghi 1944). This property, which describes a decrease in the soil's shear strength due to disturbance, is commonly reported in clayey soils.

While Norwegian and Quebecois quick clays, with sensitivities often reaching 150, are perhaps the most famous as well as extreme examples of such soils, they are not the focus of this section. These types of clays been studied by geotechnical researchers such as Rosenqvist (1953), Bjerrum (1967, 1954) and Penner (1963), and their mechanisms of strength reduction are understood reasonably well. Instead, this section is focusing on ordinary clayey soils which can also be sensitive, albeit to a much smaller degree.

As a matter of fact, Skempton and Northey (1952) note that there are very few examples of non-sensitive clays whereas sensitivities of 2 to 4 are rather common among normally consolidated clays. Recognizing the same, Rosenqvist (1953) designates normal clays as having sensitivities between 1.5 and 5. These soils are distinct from quick clays in that they exhibit thixotropic behaviour, i.e. over time, they regain some or all of their undisturbed strength; in contrast, quick clays do not show any appreciable gain in strength overtime after remoulding (Skempton and Northey 1952; Rosenqvist 1953).

A sensitivity of 2 to 4 is an indication that the soil has the potential to lose 50 to 75% of its undrained strength if disturbed. In the context of slope stability, such loss of strength can be substantial and merits evaluation.

While in the laboratory, the disturbance of a soil is realized by remoulding or fatiguing, in-situ disturbance and associated loss of strength occur via other mechanisms. Skempton and Northey (1952) indicate that disturbance can be induced by pile-driving; and Troncone et al. (2016) describes the Senise landslide, where loss of strength in soils with sensitivities of about 1.3 and 2.7 was induced by excavation. It is therefore conceivable that failure may be triggered by nearby disturbance in slopes made of slightly sensitive soils.

Direct simple shear test

The direct simple shear test was developed at the Norwegian Geotechnical Institute to study the strength behaviour of sensitive clays in translational slides such as at Furre (Bjerrum and Landva 1966). In these slides, the soil elements along the base of the slip surface are thought to be strained in “simple shear,” and the test is designed to replicate this condition. The direct simple shear test has been standardized under ASTM 6528. It is conducted in two steps: consolidation and shearing. The first step is a one-dimensional incremental consolidation process where the soil is brought to a desired effective overburden stress while being constrained laterally in a manner equivalent to that in an oedometer test. In the second step, constant-volume, uniform lateral straining of the soil is conducted while measuring lateral displacements and stresses. The lateral straining of the soil is conducted in a single direction to strains of about 20%. At this point, the course of straining can be reversed and the soil is deformed in the opposite direction until strains of about -20%; such cyclic reversals can be repeated a number of times to evaluate the soil's shearing resistance at large strains.

The strain-stress response recorded in the second phase of a direct simple shear test is similar to the strain-weakening curve of soils transitioning from peak to residual resistance in that it exhibits a peak at low strains followed by a gradual drop in resistance until the soil is fully weakened at large strain levels.

The loss of strength in sensitive soils is different from that observed in soils that have reached residual strength in that the weakening process is triggered by particle disturbance and rearrangement rather than realignment along a distinct plane that produces an ordered micro-structure. In sensitive soils, remoulding or kneading by hand produces the same weakening effect as straining; therefore, despite similarities among the two behaviours, the mechanisms triggering a loss of strength are fundamentally different.

Case studies involving sensitive soils

Table 1.3 lists the sensitivities of the soils in the historic case studies evaluated in this chapter. In all reported cases with the exception of Selset, the soils have some sensitivity (the boulder clay at Selset was heavily overconsolidated and not sensitive for that reason, as discussed by Skempton and Northey, (1952)).

Of the case histories evaluated in this chapter, two failures warrant a closer examination in the context of sensitivity effects on slope stability; these are the 1952 Congress Street open cut failure and the Scrapsgate embankment failure.

The Scrapsgate embankment failure

The Scrapsgate failure occurred in soils with sensitivities between 3.7 and 7.9 which were subjected to ground loading exerted by the newly built 14ft embankment. The failure took place three days after the embankment was raised to its final height. The deep-seated slide with a tension crack developed without evidence of prior long-term movement (which may have otherwise caused a post-peak drop in strengths due to a realignment of clay particles). Golder and Palmer (1955) postulated that progressive failure had taken place whereby the clay strength dropped from an undisturbed to a remoulded value first in the zone of overstress, then across the broader failure surface. While this proposition initially generated some debate in the geotechnical community, it was shown in time to be fundamentally correct conceptually, if not numerically. As it is shown by the three-dimensional limit equilibrium back-analysis of this failure (Figure 1.6), the average strength across the slip surface at Scrapsgate would have to drop by almost 60% to satisfy the limiting equilibrium condition. Such a drop in strength from its undisturbed value, although very significant, is plausible considering the sensitivity of the failed soil. It follows that the post-peak average resistance values were acting along the slip surface at failure.

In closing, it will be noted that a limit equilibrium analysis of the failure provides a measure of the average soil strength across the slip surface but offers no insight about the deformation-dependent progression of failure which was non-uniform in the slide as pointed out by Golder and Palmer (1955) and probably resulted in varying degrees of soil weakening throughout.

The Congress Street open cut failure

The Congress Street open cut failure in Chicago occurred during excavation works related to the construction of a local superhighway. Ireland (1953) does not report the sensitivity of the clay involved in the slip but relies on the findings by Peck and Reed (1953) who evaluated the clays of the area, including in the vicinity of failure, to conclude that the strength of the disturbed Shelby tube samples taken from the failure location were lower than the undisturbed values and required an upward adjustment by 35%. The adjusted undrained strength values produce a reasonable safety factor value of 1.1 when the failure is back-analyzed in two dimensions.

In his investigation, Ireland (1953) does not entertain the idea of lower than undisturbed in-situ strengths at failure nor does he consider progressive failure. In accordance with the state of knowledge of the time, Ireland's model of soil strength relies on the implicit assumption that the in-situ soil strengths at failure are equal to their full undisturbed values.

However, the diminished strength of the Shelby tube samples due to disturbance is indicative of a sensitive soil. The study by Peck and Reed (1953, Figure 43) on which Ireland relies to determine his strength model does report sensitivity values of about 4 for the glacial clays in the area.

In view of the reported soil sensitivity along with disturbance due to ongoing excavation and other construction activities, some sensitivity effects on the Congress Street open cut are conceivable. The three-dimensional limit equilibrium back-analysis of the failure (Figure 1.8) demonstrates that the average strength along the entire slip surface was not as low as that from the disturbed Shelby tube samples but also not as high as the undisturbed in-situ values estimated using Peck and Reed (1953). Therefore, the proposition whereby in-situ soils underwent a loss of strength due to disturbance, thus triggering failure, has some merit.

Summary

The reduction of shear strengths in sensitive soils due to in-situ disturbance may be a causal factor in some failures. When assessing whether sensitivity contributed to a failure, the following slide attributes shall be considered:

- The presence of a sensitive soil in the failure zone.
- Ground disturbance shortly prior to failure. Such disturbance may include to pile driving, excavation or other construction works, static or dynamic loading and more.

In addition to the Scrapsgate and Congress Street embankment failures, the slide at Lodalen has the attributes described above: the slope was excavated a relatively short time prior to failure, and the soil involved in the slip had a sensitivity of 2 to 5. Therefore, a modern investigation of a slide such as Lodalen should probably include a review of the potential for strain-weakening due to sensitivity or residual strength development, either of which, if present at the site, could help explain the minor three-dimensional effects. The artesian pressures present at the Lodalen site could also help explain the three-dimensional effects as the analysis was shown to be highly sensitive to the pore pressure values.

1.4. CONCLUSIONS

The general conclusions arising from the re-evaluations of historical case studies of slope stability in three dimensions presented in this chapter are listed below.

1. The reduction of a slope stability analysis from three to two dimensions results in the introduction into the solution of an error, with resulting factors of safety being generally lower than those produced by three-dimensional analyses. Accordingly, the three-dimensional effects can be thought of as a measure of error introduced into a stability analysis due to its reduction to two dimensions.
2. The magnitude of error introduced into the solution due to its reduction from three to two dimensions, calculated as a percentage difference between three- and two-dimensional factors of safety, ranges from negligible at 3-4%, to substantial at 40-50% or more.
   - Based on findings in this chapter and elsewhere in geotechnical literature, a practitioner should generally expect three-dimensional slope stability effects in the order of 20-30% for slides with an aspect ratio of 2-3.
3. On the basis of the case studies revisited here, the extent of three-dimensional stability effects cannot be reliably quantified as a function of a slide's aspect ratio and face inclination.
   - There is some weak indication that the surface topology of a slide may affect the magnitude of three-dimensional slope stability effects, with concave and convex slopes both exhibiting increased three-dimensional safety factors over the base case of planar slopes.
4. Scale effects may apply to the strength of overconsolidated soil crust in the weathered zone, where the strengh of intact soil blocks may be significantly higher than the overall strength of the weathered soil mass on the scale of a slide.

- The extent of three-dimensional slope stability effects may be artificially exaggerated when excessive strengths, such as soil crust models developed from tests on intact specimens, are applied in calculations. This effect may be substantial in small slides and diminished in large slides.
- In slides where three-dimensional slope stability effects are present, two-dimensional limit equilibrium back-analyses of failed slopes resulting in a safety factor of unity are in error. Two significant sources of error have been identified: (i) the soil strength models and (ii) the assumed stress states, especially along the sections of slip surface with inclinations close to vertical.
- The errors of two-dimensional safety factors seem to be partially mitigated by calculations of weighted safety factors across multiple cross-sections. The analysis of the Lodalen slide is an example of such correction.

5. A three-dimensional analysis of a failed slope resulting in a safety factor that is significantly different from unity signifies that the model is incorrect. Three-dimensional analyses that employ correct shear strengths at failure and make accurate determinations of shear stresses along the shear planes are expected to produce safety factors near unity.
6. Two reasons for erroneous interpretations of strength at failure have been identified:
   (i) A reduction in shearing strength from peak to residual values due to clay particle realignment is known to take place in soils with a clay fraction above 20-25%. Where such processes are at play, field evidence exists of some of the following processes:
      - Long-term displacements at the slide location.
      - Particle realignment in the direction of movement. Such realignment can be evidenced by the formation of pre-sheared planes and/or ordered micro-structure.
      - Presence of soils that are dilatant on shearing, such as overconsolidated soils.

(ii) A drop in shear strength owing to disturbance or deformation may take place in sensitive soils.

In closing, a small matter of terminology will be addressed. In this thesis and elsewhere in research, the term "three-dimensional slope stability effects"[5] is used to describe the difference between two- and three-dimensional safety factors. While the term offers a convenient way to denote this particular aspect of slope stability methods, it should be recognized that such effects only exist in the context of a two-dimensional analysis. Historically, two-dimensional analyses often represented baselines for all other analyses; three-dimensional slope stability effects are distinguished only in comparison to these.

[5] A number of similar terms are used in the literature, of which "3D effects" (Stark et al. 2017), "end effects" (Zhang et al. 2014; Kjaernsli and Simons 1962; Bjerrum and Kjaernsli 1957), "three-dimensional effects" (Gens et al. 1988) and, in older references, "sidewall effects" or "end-cylinder effects" appear most commonly.

CHAPTER TWO

PROPOSED INTERPRETATION OF THREE-DIMENSIONAL STABILITY EFFECTS IN THE FAILURE AT THE MOUNT POLLEY TSF

2.1. OVERVIEW

On August 4, 2014, a breach occurred in the perimeter embankment at the Mount Polley TSF in British Columbia, Canada, resulting in a spill of an estimated 25 million m^3 of wastewater, tailings and construction materials into the nearby Hazeltine Creek, as well as into the Mount Polley and Quesnel Lakes (Golder Associates 2016; SNC Lavalin et al. 2014). This event produced significant damage to the environment and triggered a number of reviews of mining industry practices. Two independent investigations of this failure were conducted. The first one was commissioned by the Government of British Columbia and completed by an Independent Expert Engineering and Review Panel (IRP) in 2015. The second one was ordered by British Columbia's Ministry of Energy and Mines and completed by Klohn Crippen Berger (KCB) also in 2015.

The breach was sudden and without observable precursors. During the embankment collapse, the mass of soil underwent a rotational-translational movement involving large horizontal displacements in a foundation unit ~10m below original ground level. The slippage at the base took place in a thin (≤2m) varved clay deposit designated as the Upper Glaciolacustrine Unit, or the Upper GLU. The IRP (2015) made a determination that undrained strengths controlled this unit's mechanical behaviour during failure. Furthermore, the clay's strain-weakening properties made it susceptible to progressive failure. The IRP found that the breach occurred when the peak undrained shear strength of this material was exceeded. These findings were supported by the results of two-dimensional static and deformation analyses suggesting that average strengths slightly below peak values were acting at failure in the Upper GLU. A cursory three-dimensional static analysis found that substantial three-dimensional stability effects were present in the failure which merit an explanation.

This chapter seeks to establish the extent of three-dimensional effects present in the failure at Mount Polley and proposes an interpretation of the failure mechanism that would account for these. These objectives are attained through a series of undertakings described below.

- First, the fundamental mechanisms of failure proposed by the two investigators were revisited (§2.2) and replicated using two-dimensional limit equilibrium and deformation analyses (§2.3). The replication of such analyses is necessary to accurately define the soil strength models and other relevant parameters that would simulate failure. The two-dimensional simulations of failure become, in effect, benchmarks that three-dimensional analyses can be compared to in order to establish the extent of three-dimensional slope stability effects.
- A three-dimensional limit equilibrium slope stability analysis of the failure at the Mount Polley TSF was conducted with the soil strength models and other model parameters that were used to simulate failure in two dimensions (§2.4). The two- and three-dimensional solutions were compared to quantify the extent of three-dimensional slope stability effects.
- In light of the findings presented in Chapter One, the discrepancy between the two- and three-dimensional results was interpreted as being caused mainly by an over-estimation of soil strengths. The strength behaviours of all soils involved in the failure were examined to identify potential sources of error. The Upper GLU, having been identified by both investigators as a soil with strain-weakening properties and a sensitivity of 2-3, was an obvious suspect. The three-dimensional limit equlibrium simulations of the failure were re-done using a variety of post-peak shear strengths to gauge the kind of strength loss required to take place in order to overcome the three-dimensional stability effects in the slope and generate failure (§2.4).

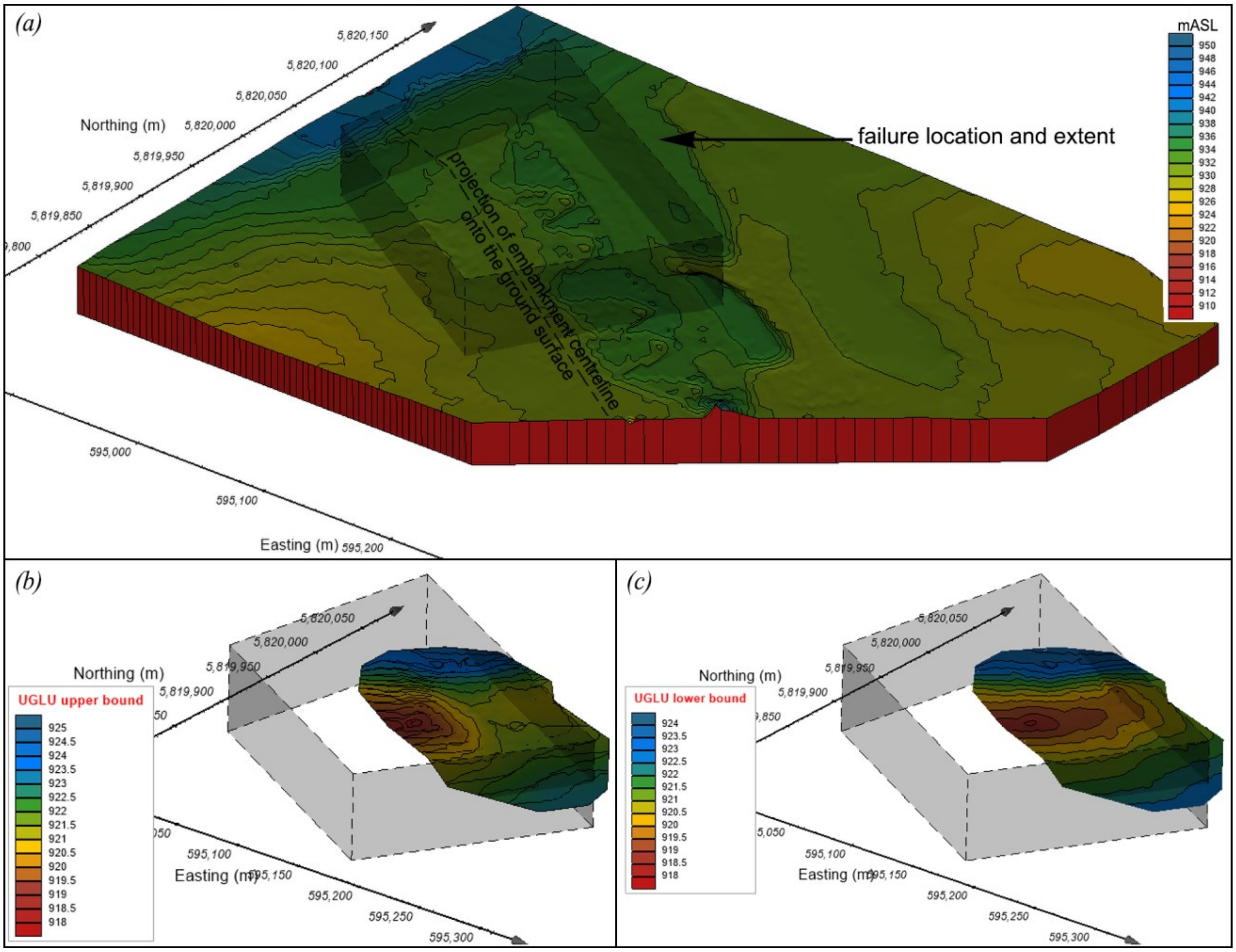

Figure 2.1(a) Original ground topography around the failure location prior to the TSF construction. (b) Extent and upper bound of the Upper GLU. (c) Extent and lower bound of the Upper GLU.

- Finally, a hypothesis was formulated regarding the evolution of the failure at the Mount Polley TSF (§3.5). This hypothesis builds on the failure models proposed by the two investigators, expanding them to explain the three-dimensional slope stability effects.

2.1.1 SITE DESCRIPTION

The Mount Polley Mine is a copper and gold mine operated by the Mount Polley Mining Corporation (MPMC). The mine is located in the interior of Central British Columbia at approximately 52°33'N 121°38'W. The mine was operated from 1997 to 2001 and from 2005 to

2014. The waste products from the mining operations were deposited as a slurry at the mine's TSF located at approximately 52°30'53"N, 121°36'6"W.

The Mount Polley TSF is a U-shaped earthen structure with a modified centerline design. The total length of the structure is approximately 4.9km. The dam is located to take advantage of both a natural topographic low it encompasses to serve as the tailings storage reservoir, as well as the topographic high immediately to the north of it, used as a natural embankment to shorten the length of the manmade earthen structure. The original ground elevation in the vicinity of the failure is illustrated by a three-dimensional rendition in Figure 2.1*(a)*.

The in-situ stratigraphy was defined by glaciation processes in the area, and consists of glacial tills containing a number of discontinuous interstitial glaciofluvial and glaciolacustrine soil strata. A representative cross-section of the dam and underlying soils at the failure location developed using surface and subsurface investigations by IRP (2015) and KCB (2015) is seen in Figure 2.2*(b)*.

At the location of failure, two distinct glaciolacustrine layers were identified, the Upper Glaciolacustrine Unit (Upper GLU) at elevations of 921 to 924mASL, and a Lower Glaciolacustrine Unit (Lower GLU) 6-8m below it. Laboratory tests by IRP (2015) and KCB (2015) differentiate the two units based on their overconsolidation ratios and dry densities, with the upper unit being, prior to the dam construction, less overconsolidated and less dense. The spatial extent and position of the Upper GLU was established using field testing data from both investigation reports (IRP 2015; KCB 2015); its three-dimensional rendition is shown in Figure 2.1*(b)* and *(c)*.

At the failure location, the Perimeter Embankment of the TSF reached a height at crest of 40m with a 1.3:1 slope on the downstream side. A 2m deep excavation was made at the toe of the dam in Stage 9A, about a year before failure, with the intent of replacing the local soil with a better material. The pre-failure surface topography of the site and a representative cross-sectional view of the perimeter dam and underlying soil depositions are shown in Figure 2.2.

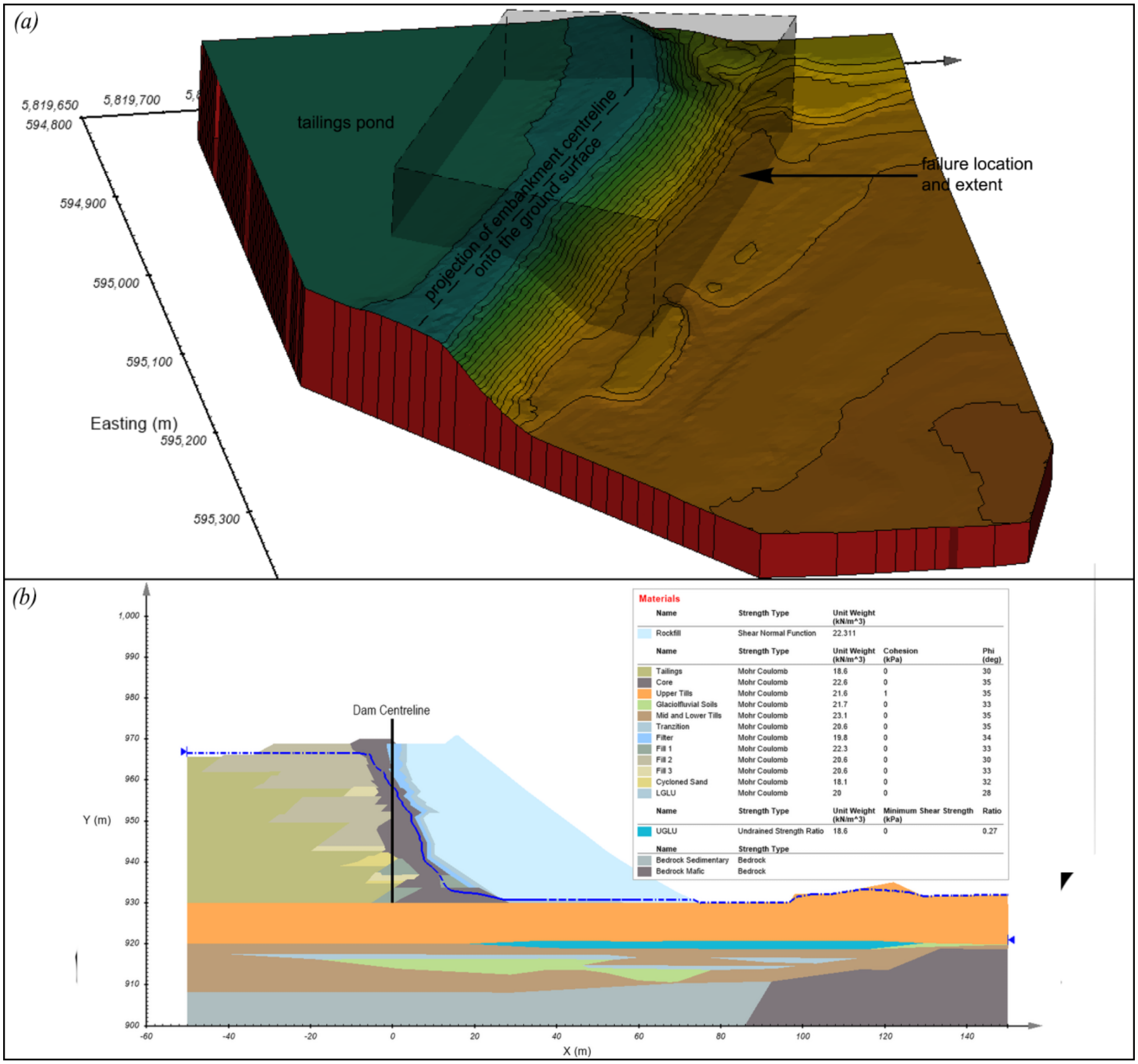

Figure 2.2 Top: A 3D rendition of pre-failure surface elevations at the breach location. Bottom: A representative cross-section of the dam and underlying stratigraphy at the failure location, developed based on drawings and data by KCB (2015) and the IRP (2015).

2.2. PRIOR INVESTIGATIONS

2.2.1 INVESTIGATION BY THE INDEPENDENT REVIEW PANEL (IRP 2015)

Subsequent to the 4 August 2014 breach at the Mount Polley TSF, the Government of British Columbia in conjunction with the Williams Lake Indian Band and the Soda Creek Indian Band established an Independent Expert Engineering Investigation and Review Panel to study the failure. The IRP conducted a field investigation supplemented by an in-situ and laboratory testing programme. The design, construction and operational records were also reviewed. On the basis of these data, the IRP made a determination on the cause of failure, provided comments on what actions could have been taken to prevent it and commented on mitigation measures that may avert similar events in the future.

2.2.1.1. SOIL TESTING

The investigation team oversaw extensive in-situ and laboratory works.

The in-situ works included sonic coring and logging of the subsurface, cone penetration testing, electronic vane shear testing and pressuremeter testing. These data were supplemented by boring data, cone penetration testing and vane shear testing conducted concurrently by KCB; and by seismic refraction and resistivity surveys completed by Frontier Geosciences.

The laboratory testing programme included computed tomography scanning of foundation materials, oedometer testing of foundation materials, as well as direct shear tests and consolidated undrained triaxial tests of the foundation materials including the upper glaciolacustrine unit.

The investigation report includes full data records for these works.

2.2.1.2. KEY FINDINGS

Key findings made by the IRP that lay at the foundation of its determinations are summarized below.

(1) The Perimeter Embankment where the failure took place had a lower height than the Main Embankment. This is an indication that the failure was caused by local site conditions rather than by dam design.

(2) The breach was sudden, with no documented prior movement.

(3) No evidence of overtopping prior to failure was found.

(4) No evidence of piping or core cracking resulting in uncontrolled internal erosion was found.

(5) The field investigation provided ample evidence of soil failure and large translational movements in the foundation below the embankment, coupled with a translational-rotational movement of the soil mass above it.

(6) The foundation profile at the failure location consisted of three primary soil types: (a) glacial tills deposited over a number of separate glaciation periods, (b) glaciofluvial soils deposited in running water during periods of glacier retreat, and (c) interstitial glaciolacustrine deposits deposited in standing water after periods of glacier retreat.

(7) The two distinct glaciolacustrine deposits, the Upper GLU and the Lower GLU, were differentiated by their moisture content and overconsolidation ratio; the upper unit had a substantially higher moisture content (of about 32%) than the lower unit (of about 24%). Additionally, the Upper GLU pre-construction overconsolidation pressure was lower at ~430kPa, compared to 750kPa for the Lower GLU.

(8) The Upper GLU's undisturbed undrained strength was determined to range between $0.22\sigma'_{ov}$ and $0.27\sigma'_{ov}$. The soil exhibited a sensitivity ranging between 1 and 3.

(9) Soil samples from outside the slide zone showed minimal disturbance. Soil samples from within the slide zone showed significant disturbance. The thinly laminar, varved structure of the Upper GLU was folded and contorted in the slide zone.

(10) No continuous pre-sheared plane was found in the Upper GLU outside the failure area.

2.2.1.3. THE FAILURE MODEL

The IRP identified the Upper GLU as the critical soil unit involved in the failure. Initially overconsolidated to a preconsolidation pressure of ~430kPa, this deposit became normally consolidated under the new loading imposed by the embankment.

Overconsolidated and normally consolidated soils respond differently to shearing. The former are dilative on shearing; if shearing is rapid or under constant volume conditions (i.e. undrained), negative pore pressures develop in the shear band. In such materials, undrained strengths are substantial and drained strengths control failure. In contrast, normally consolidated materials are contractive on shearing and excess pore pressures develop in the shear band under undrained conditions. In such materials, undrained strengths govern.

It follows from the above that the transition of the Upper GLU from a state of overconsolidation to a state of normal consolidation under new loading made it susceptible to undrained failure.

The IRP determined that failure in the foundation took place when the shear stresses in the foundation exceeded the Upper GLU's undrained shear strength.

Noting the strain-weakening properties of the Upper GLU, the IRP evaluated the potential for progressive failure at the site. Two-dimensional limit equilibrium and deformation back-analyses of the failure demonstrated that failure occurs when peak undrained shear strengths are acting in the Upper GLU.

A cursory three-dimensional limit equilibrium back-analysis of the failure was conducted using an extrusion of the two-dimensional cross-section at the centre of the slide. This analysis produced a safety factor of about 1.3, indicating the presence of substantial three-dimensional stability effects at the failure site. On the basis of this finding, the IRP reached the conclusion that progressive failure was involved in the initiation of collapse (IRP 2015, p. 103). The IRP briefly explored the extent of strength reduction in the Upper GLU that would be required to initiate collapse, and found that the unit would have to be fully weakened.

2.2.2 INVESTIGATION BY KLOHN CRIPPEN BERGER (2015)

Following the 4 August 2014 failure at the Mount Polley TSF, the Chief Inspector of Mines completed an independent investigation of the event. KCB was commissioned to conduct the investigation and presented its findings in a report released in August 2015 (KCB 2015).

2.2.2.1. SOIL TESTING

The KCB investigation team oversaw an extensive field and laboratory testing programme. Field works included eight electric resistivity survey lines, seven seismic refraction lines, thirty-two sonic boreholes, think-walled tube and block sampling, trench and pit excavations, standard penetration tests, seismic cone penetration tests and vane shear tests (KCB 2015, pp. 17-18). The laboratory testing programme included water content measurements, specific gravity tests, Atterberg limits, diffraction tests, particle size and hydrometer tests of all fine-grained soils, Standard Proctor tests on till core samples, triaxial permeability and compression tests on the upper glacial tills and core, direct shear and direct simple shear tests on glaciolacustrine deposits and oedometer tests on glaciolacustrine on intact and reconstituted soil samples (KCB 2015, pp. 18-19).

The testing data results are included in the appendices of the investigation report and formed the basis for the determination of relevant properties of all soils involved in the failure.

2.2.2.2. KEY FINDINGS

KCB completed an extensive investigation of the failure involving field reconnaissance, an in-situ drilling and testing programme, a laboratory testing programme and a review of prior documentation. These data were integrated to create a geotechnical profile of the failure site. The main findings are listed below.

(1) The native soil profile in the area consists of glacial tills with interstitial glaciofluvial and glaciolacustrine deposits. Figure 2.2 shows a characteristic cross-sectional view of the soil profile at the failure location developed based on KCB's (2015) findings.

(2) Prior to embankment construction, the Upper GLU had a preconsolidation pressure ranging between 380 and 420kPa and an overconsolidation ratio of 4. The hydralic conductivities of the unit ranged between 10^{-8} and 10^{-9}m/s.

(3) The Upper GLU drained strength parameters were determined as c'=0, $\phi'_{peak}=22°$, $\phi'_{residual}=12…14°$.

(4) The Upper GLU's undrained shear strength behaviour was established from a series of direct simple shear tests. The peak undrained shear strength was approximated as $s_{u,peak}=0.22(OCR)^{0.8}\sigma'_{cv}$. The soil exhibited a propensity for weakening on disturbance or shearing, with a sensitivity of 2-4. A post-peak reduction in undrained shear resistance was observed at shear strains in excess of 5%, and full weakening was attained at shear strains in excess of 60%.

(5) Significant disturbance was encountered in the Upper GLU in the slide zone but not below it.

(6) At the failure location, a 2m deep, 20m wide excavation at the toe of the dam was constructed in 2013 with the purpose of replacing the poor native soil with a more appropriate fill material.

(7) A block of soil displaced by 6.5m upward was documented on the downstream side of the failure location. This displaced block corresponds to the "whaleback" feature discussed by IRP (2015) and is thought to be an upthrust of foundation materials in the region of the slide toe.

(8) Vertical displacements in excess of 3m at the crest and horizontal displacements of up to 10m in the foundation were inferred from field evidence.

2.2.2.3. THE FAILURE MODEL

KCB (2015) states that the failure took place due to large horizontal displacements in the Upper GLU. Such displacements caused a substantial crest drop, triggering an overtopping event. The Upper GLU was lightly overconsolidated before the commencement of construction works and became normally consolidated under the added weight of the embankment. The failure initiated under conditions where some excess pore pressures were present in the Upper GLU due to ongoing construction. Local yielding in the Upper GLU started when "the static shear stresses (…) exceeded the available drained shear strength" of this material, initiating undrained failure (KCB 2015, p. 35).

Recognizing the unit's potential for strain-weakening, the investigators conducted a series of direct simple shear tests at a wide range of overburden consolidation stresses in order to establish the relationship between Upper GLU's undrained shearing resistance and the accrued shear strain. The tests were used to develop a conceptual model of the Upper GLU's strain-weakening behaviour (reproduced in Figure 2.3).

Deformation analyses demonstrated that, at the time of collapse, the shear stresses induced in the embankment at the Mount Polley TSF would have exceeded the drained resistance of the Upper GLU, triggering a progressive failure under undrained conditions. Using a series of two-dimensional analyses, the investigators determined that the use of peak undrained strength values in the Upper GLU in combination with loading-induced transient pore pressure conditions yields a

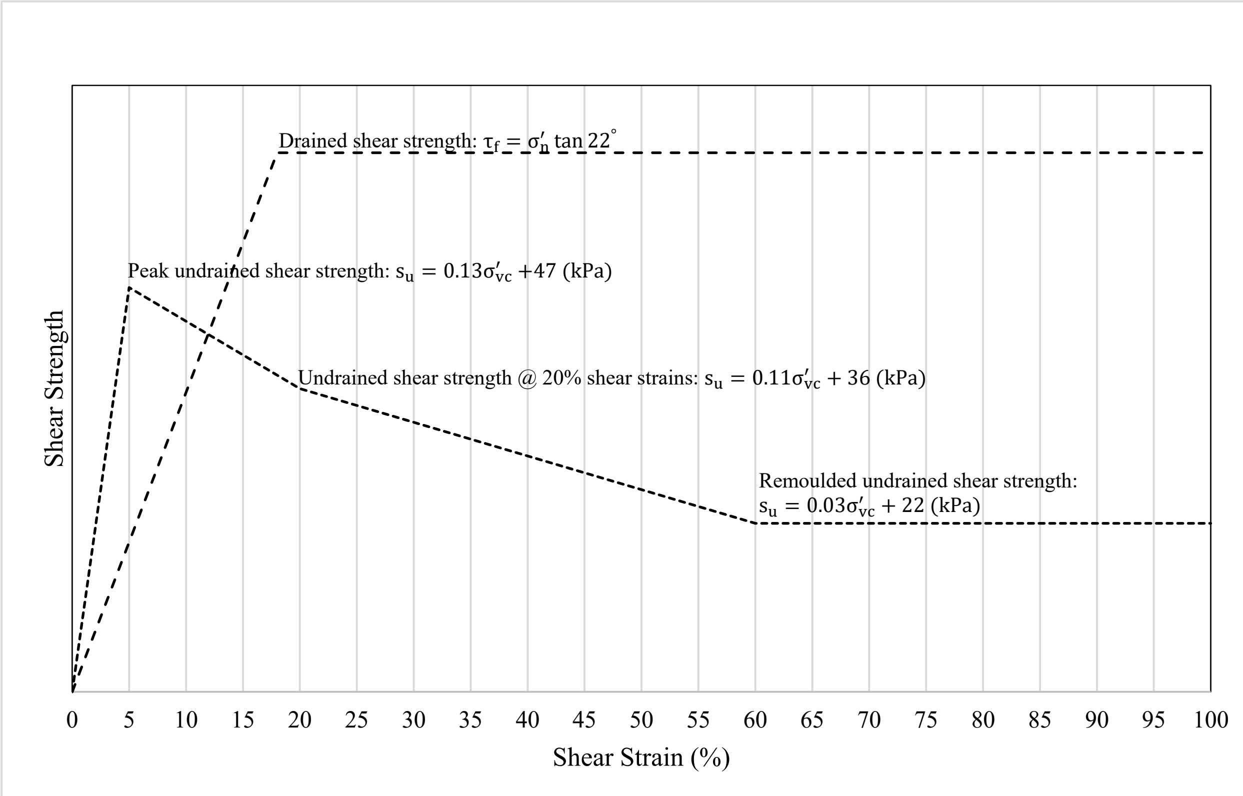

Figure 2.3 KCB's conceptual model of shear strength in the Upper GLU.

safety factor marginally below unity (0.98) and shear deformations in the Upper GLU in the order of 0.1m or less.

The investigators concluded that a progressive failure was triggered in the foundation at Mount Polley, and the embankment collapsed when the available peak drained strength was exceeded and the shear resistance in the Upper GLU was reduced to its peak undrained strength. During the collapse, the progressively larger shear strains in the Upper GLU led to a weakening of the unit, causing a further reduction of the safety factor and the acceleration of the soil mass. The Upper GLU's propensity for strain-weakening was identified as the reason for the rapid failure of the embankment.

2.2.3 AGGREGATE EVALUATION OF THE FINDINGS

The two investigators agree that the root cause of the failure at Mount Polley is the undrained mechanical response in the Upper GLU. Furthermore, both concur that this unit failed progressively, i.e. that it strain-weakened as the failure unfolded.

Their opinion somewhat differs with regard to the starting point of progressive failure in the Upper GLU. The IRP concludes that the unit began weakening prior to the collapse event and that global failure initiated when the average undrained resistance in it dropped to post-peak, possibly residual values. KCB (2015, p. 45) asserts that the collapse of the embankment initiated when peak undrained shear strengths were acting in the Upper GLU and that the weakening of this unit took place during collapse. This difference of opinion appears to be numerical in nature and originating with the results of their stability analyses.

2.2.3.1. SLIDE CONFIGURATION

The configuration of the slide at Mount Polley can be partially reconstructed from the information contained in the IRP (2015) and KCB (2015) reports.

The investigators identified the base of the slide ~10m below original ground in the Upper GLU. With a pre-collapse embankment height of ~40m, this places the depth of slide at Mount Polley at ~50m. The aerial photo and map of the slide seen in Figures 5.1.6 and 5.1.7 of the IRP (2015) report (reproduced here in Figure 4.30) show the zone of upthrust located between stations 4+100 and 4+300. This feature maps the position and extent of the slide toe and provides indication that at foundation level, the width of the slip surface was over 150m, possibly as much as 200m. This in turn suggests that the slide at Mount Polley had an aspect ratio of 3-4.

At the embankment level, the failure is more modestly sized. The width of the breach is in the order of 50m at ground level and 100-150m at crest level. The final width of the breach is likely a result of mechanical instability combined with water erosion. Evidence of water erosion is seen in Figure 4.30 and can also be inferred from the overtopping event.

The location of the slip surface on the upstream of the slide can be inferred from the multiple shear zones and cracks identified by the IRP (2015, Figure 5.1.7 and Attachment C2) and KCB (2015, pp. 19-20 and Figure 4.5) as passing through the till core. These features are also indicative of a relatively brittle response in the core and upper till units.

The aerial view of the slide seen in Figure 4.30 also illustrates the considerable deformation in the shell zone. Displacements in the order of 10-15m are seen at the toe of embankment, with the rockfill reaching the toe of the slide. Several minor failure planes can be distinguished in the rockfill from the sloughing patterns. These features are indicative of a more ductile deformation-stress response in the shell than that observed in the core and upper till units.

In all, the geometry of the slip surface appears to be composite and does not easily lend itself to being approximated with simple geometric shapes such as ellipses, wedges or combinations thereof.

2.2.3.2. THE UPPER GLU

The mechanical behaviour of the Upper GLU has been identified by both investigators as critical to the initiation and unfolding of the collapse at Mount Polley. This warrants an in-depth review of this unit’s mechanical properties.

The data assembled by the investigators (IRP 2015, Figure 5.2.6; KCB 2015, Figure 5.9) indicate that the Upper GLU was a thin interstitial deposit that was thin, with a thickness of 2-2.5m in the middle and thinner towards the edges, and spatially limited, with a length ≤300m and a width ≤200m.

The Upper GLU is a varved clay with a distinct sub-horizontal macro-structure consisting of 10-30mm layers of clay-rich soil separated by thin (~1mm) layers of silt and fine sand materials. The layered structure of this unit is owed to its deposition history. Varved clays are created by particle sedimentation in glacial lake environments; seasonal and other variabilities of water velocities such as spring runoff cause a variation in the diameter of particles deposited atop of the lake floor. The resulting laminated macro-structure of such deposits has been associated with anisotropy. The stability analysis of a tailings dam built on varved clays by Capozio et al. (1982, pp. 476-478) notes a variation of undrained shear strength possibly due to the weaker clay seams. The strength anisotropy of varved clays was noted by Lacasse et al. (1977) on the basis of their review of failure at New Liskhead; they remark the significant scatter in the measurements of undrained shear strengths and state that the clay weaker sublayers control the overall mechanical response of the unit (pp. 369-372). Tankiewicz (2015) demonstrates using the varved clay deposits near Bełchatów, Poland, that the strength of such soils is anisotropic, with the weaker direction oriented along the varves. Furthermore, the measurement of shear strengths in such materials is inconsistent and can vary as a function of stress path and testing procedure as demonstrated by Ching and Phoon (2013) or directionally as shown by Wrzesinski and Lechonowisz (2013).

The results of the tests conducted on the Upper GLU are consistent with these findings. The Upper GLU was determined to have anisotropic permeability and strength: its ratio of horizontal to vertical hydraulic conductivity was seen to vary between 10 and 30 (KCB 2015, Table 5.7 and p. 27); and its drained friction angle ϕ' was higher when the specimens were sheared across the varves than when they were sheared along them, varying between 23 and 28° for the former and 21 and 25° for the latter (KCB 2015, Figure 5.21).

The IRP (2015, p. 61) lists two potential failure modes in the Upper GLU:, one associated with slips along weak pre-sheared planes and another associated with strain-weakening in this slightly sensitive unit. The latter mechanism is credible in the context of the two- and three- back-analysis results introduced by the IRP (2015, pp. 96-98). The former mechanism was ruled to be unlikely due to a lack of physical evidence of pre-sheared planes in the failure zone; this conclusion is corroborated by the results of stability analyses suggesting that failure along pre-sheared planes would have happened at an earlier construction stage than observed (KCB 2015, p. 45).

Finally, both investigators remark on the Upper GLU's tendencies for dilation on shearing when overconsolidated and for contraction when normally consolidated (IRP 2015, p. 76; KCB 2015, p. 27). This behaviour, long noted from triaxial tests on fine-grained soils, is thought to have a marked effect on the pore water pressures in the shear band upon undrained shearing and on the resulting mechanical response of these materials. Henkel (1956) observed during tests conducted on remoulded Weald clay and London clay specimens that when sheared under constant volume conditions, pore pressures drop in overconsolidated specimens and spike in normally consolidated ones; and that these changes are associated with higher shearing resistance in the former and a lower shearing resistance in the latter. Holtz et al. (2011, pp. 564-567) elaborates that the noted spike in the shearing resistance of overconsolidated clays, referred to as the "preconsolidation hump," maps the strength envelope of such soils above the normally consolidated strength envelope; this effect vanishes once the specimens' preconsolidation pressure is reached. On the other hand, the pore pressure spike upon undrained shearing of normally consolidated soils causes a localized decrease in effective stresses and an associated drop in shear strength (Holtz et al. 2011, pp. 570-572). In the laboratory, the measured pore pressure changes have been successfully correlated with the drained strength envelope; in the field, where the pore pressure changes in the shear band are typically unknown, the drop in the shear resistance of normally consolidated clays is commonly emulated through the use of undrained strengths. It is evident from the above that the loading history of fine-grained soils plays a critical role in determining their mechanical response upon shearing.

2.2.3.3. THE ROCKFILL

The investigators did not identify the rockfill material in the shell zone as being critical in any manner to the unfolding of the collapse at Mount Polley. However, the significant deformation of the rockfill seen at the failure location indicates that this material played some kind of role in the unfolding of the collapse; common sense suggests that a substantial portion of the three-dimensional slip surface (i.e. its sidewalls) necessarily passed through this zone. Therefore, the mechanical properties of this material should be evaluated in the context of this failure.

Geotechnical research shows that rockfill materials exhibit a curved rather than a linear strength envelope. Leps (1970, p. 1162) asserts that linear strength envelopes do not accurately describe the observed strength behaviour of rockfills in that they appear to predict shallow slip surfaces with safety factors equal to or below unity in structures that have remained stable and concludes based on empirical evidence that their strength at low confining stresses is "stronger than has been indicated by triaxial tests" conducted at higher lateral stresses. This conclusion by Leps is supported by empirical data by Silvestri (1961) who reports a friction angle of 65° for crushed aggregate tested at low confining stresses. Findings by Marsal (1973; 1967), Becker (1972), and Marachi et al. (1972; 1969) indicate that rockfills such as that used in the shell zone at the Mount Polley TSF are high strength materials with curved, upward convex strength envelopes. Marsal (1967) demonstrates on the basis of triaxial tests conducted on rockfill from the El Infernillo dam that the friction angle of this material decreases as the confining stresses increase, giving the material's strength envelope a curved appearance. Rosengren and Jaeger (1969) and Jaeger (1971; 1970) also report curved envelopes for interlocked granular materials. Correlations developed by Leps (1970, Figure 1) on the basis of aggregate data from Holtz and Gibbs (1956), Hall and Gordon (1963), Marsal et al. (1965) and Marsal (1967) show that in these materials, the internal angle of friction ϕ' decreases with increasing normal stresses and, all other things being equal, is lower in poorly graded, less dense samples.

Using data reported by Leps (1970) it is estimated that, depending on its classification, gradation and in-situ dry density, the rockfill material in the shell zone of the Mount Polley TSF embankment may have had an internal friction angle ϕ' varying between 50 and 60° at the surface and 35 and 45° near the core. This means that the rockfill was the strongest of all materials involved in this failure. Therefore, its contribution to shearing resistance along the slide's side walls should not be overlooked.

The significant deformations noted in the shell zone at the failure location should also be evaluated in the context of the rockfill's mechanical response during collapse. Marachi et al. (1972) reports that the deformation characteristics of rockfill specimen are affected by confining stresses. Leps (1970) notes that the stress-strain behaviour at low confining stresses (below 70kPa) is distinct from that at higher confining stresses (in the range of 700kPa). Deformation moduli estimated on the basis of data reported by Leps increase with increasing confining stresses; this behaviour appears to be more pronounced in uncompacted or poorly compacted samples. Marsal (1973, p. 195) states that in rockfills, the mobilization of shear strength requires appreciable deformation, and that "stability analyses that do not take into account the large strains required to develop shearing resistance [in these materials] are inadequate."

The large deformations noted in the shell zone at the Mount Polley TSF could be evidence that in this material, the deformation modulus was low. This in turn may mean that large deformations would have been required for this material to fully mobilize its shear strength. This problem may have been exacerbated by the poor compaction of this material reported by KCB (2015, p. 7).

Considering that the rockfill at Mount Polley was a well-drained material with the highest shear strength of all units involved in the failure and that its deformation behaviour was markedly different than that of the core or upper till units, its role in the collapse at Mount Polley should be re-evaluated.

2.3. A TWO-DIMENSIONAL ANALYSIS OF THE MOUNT POLLEY FAILURE

The original investigators of the Mount Polley failure relied on two-dimensional limit equilibrium and deformation analyses to verify the mechanisms of failure that they had put forward.

Two-dimensional limit equilibrium and deformation analyses were completed as part of this research undertaking with the goal of replicating those original analyses. The purpose of such replication work is two-fold. First, replicating the two-dimensional analyses by the original investigators allows fine-tuning the modelling parameters that are not always fully described in the reports. Second, the safety factors produced by the two-dimensional limit equilibrium analyses are used as a baseline to estimate the magnitude of three-dimensional slope stability effects.

2.3.1 MODELLING PARAMETERS

The two-dimensional limit equilibrium and deformation models of the Mount Polley failure were developed largely on the basis of material parameters used by the original researchers in their own analyses. Where information lacked regarding the material properties used in the models, it was supplemented by the data collected from the in-situ and laboratory tests of soil from the failure site and, occasionally, appropriate literature-published values. For the rockfill strength model, a curved envelope was developed on the basis of data published by Marsal (1973, pp. 167-168, Sample 1).

The material parameters used to develop the two-dimensional limit equilibrium and deformation analyses in §2.3 and also the three-dimensional limit equilibrium analyses in §2.4 are provided in Appendix 2B and illustrated in Figure 2.4.

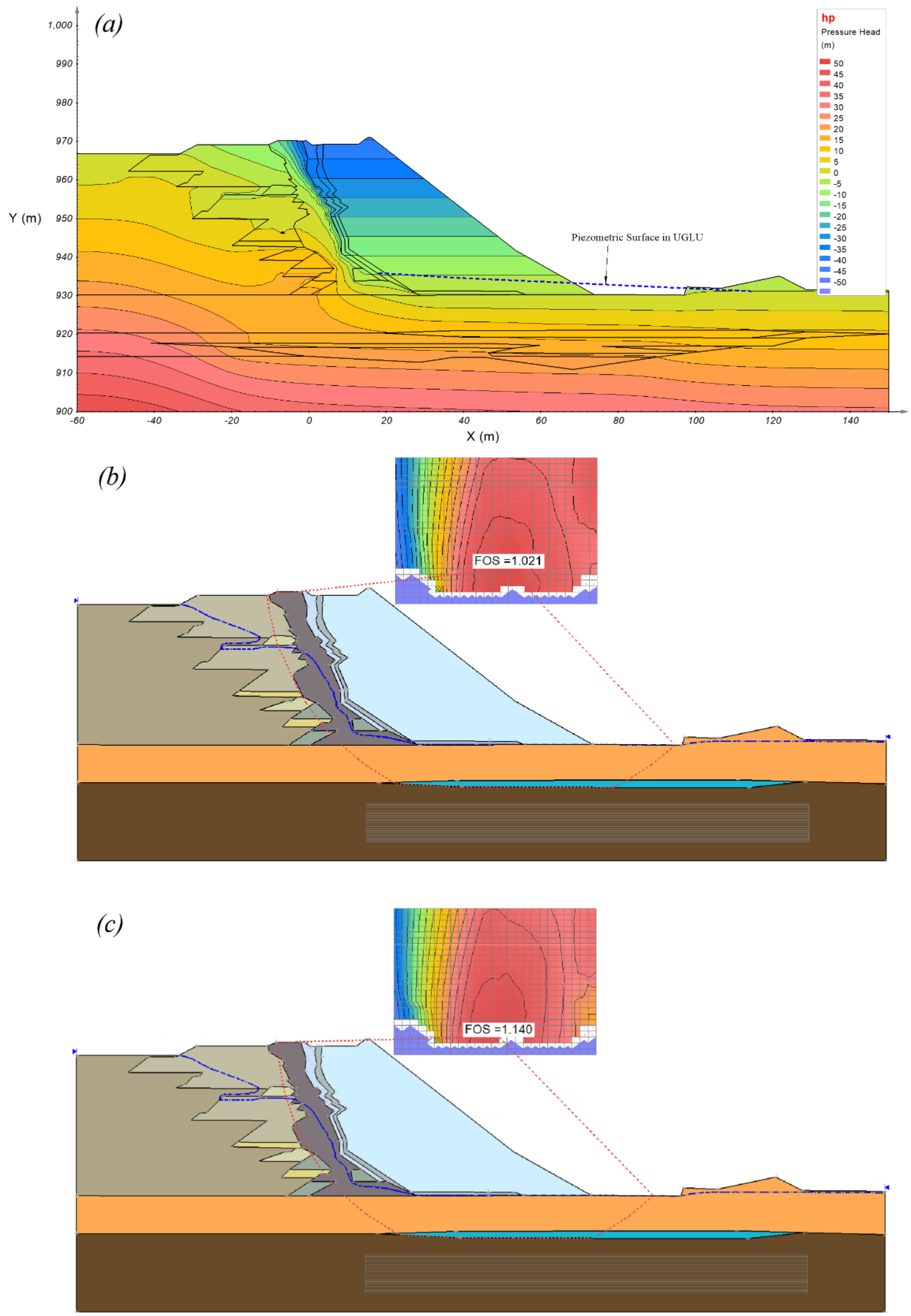

Figure 2.4 A two-dimensional limit equilibrium analysis of the Mount Polley failure using (a) steady-state pore pressures, (b) the IRP (2015) strength model; and (c) the KCB (2015) strength model.

2.3.2 A TWO-DIMENSIONAL LIMIT EQUILIBRIUM ANALYSIS OF THE MOUNT POLLEY FAILURE

Two-dimensional limit equilibrium back-analyses of the Mount Polley failure were conducted using the models put forward by the IRP (2015) and KCB (2015). The input parameters, including the cross-sectional geometry and soil properties, were developed based on data reported by the original investigators. The analyses were completed in the SoilVision® software SVOffice™. The module SVFlux was used to estimate the steady-state pore water pressure distributions at failure; these results were imported into the SVSlope module to evaluate stability. The results are illustrated in Figure 2.4.

The results of the two-dimensional limit equilibrium analysis of the Mount Polley TSF using the IRP (2015) model indicate that failure can be generated using a strength model defined by the undrained strength ratio $s_{u,avg}=0.18\sigma'_{vc}$ in the Upper GLU material, about ¼ to ⅓ below the peak undrained strength determined by testing. This finding is in agreement with the conclusion by the IRP that during collapse, the average shear resistance in the Upper GLU was reduced to a value somewhat below its peak undrained strength.

The results of the two-dimensional limit equilibrium analysis of the Mount Polley TSF using the KCB (2015) model indicate that the use of its peak undrained shear strength model $s_{u,peak}=0.134\ \sigma'_{cv}+47.5\ (kPa)$ in a back-analysis of the Mount Polley TSF does not bring the soil mass to a limiting equilibrium. This finding supports the conclusion by the IRP (2015) that some strain-weakening had already taken place in the Upper GLU prior to the collapse.

2.3.3 A TWO-DIMENSIONAL DEFORMATION ANALYSIS OF THE MOUNT POLLEY FAILURE

An exploratory two-dimensional deformation analysis of the Mount Polley TSF embankment was conducted. A representative cross-section at the failure location developed by KCB (2015, Figure 2.6) was used as the basis for the model geometry (shown in Figure 2A.1 of Appendix 2A). The analysis was conducted in four steps replicating loading conditions corresponding to pre-construction ground surface and construction stages 3, 6 and 9. The analysis was conducted to explore the evolution of stresses, deformations and strengths in the soil mass over the duration of embankment construction up to its failure.

The strength behaviour of the Upper GLU was modelled in accordance with the determination made by the IRP (2015) whereby the unit's drained strength controlled its mechanical behaviour until the preconsolidation pressure was exceeded, and its undrained strength controlled its behaviour afterward. KCB's (2015) undrained shear strength model was used to estimate the undrained shear resistance in the Upper GLU as a function of average overburden effective stresses and shear strains. The following modelling procedure was used:

- The overburden effective stresses in the Upper GLU were examined after each modelled stage to determine whether the unit's preconsolidation pressure of 400kPa was exceeded.
- When the overburden effective stresses in portions of the Upper GLU exceeded its preconsolidation pressure, the unit's strength model in that region was modified from drained ($\tau_f = \sigma'_n \tan 22°$) to peak undrained, roughly approximated by the following relationship: $s_{u,peak} = 0.134\ \sigma'_{cv} + 47.5$ (kPa).
- Following the transition to undrained strength, the mobilized shear resistance, strains and deformations in the Upper GLU were monitored to determine whether further strength adjustments were warranted to emulate strain-weakening.

- Lastly, stage 9 safety factors were calculated using the shear strength reduction method.

The deformation analysis was conducted using Itasca's FLAC software, Ver. 7. The results are included in Appendix 2A.

2.3.3.1. RESULTS

Construction stage 3

After the embankment and foundation materials adjusted to the stage 3 loading conditions and to a pond elevation increase to 941.5mASL, the overburden effective stresses in the Upper GLU ranged from about 120kPa on the downstream to just below 300kPa under the embankment (Appendix 2A, Figure 2A.2). The unit's shear stresses in the horizontal direction (i.e. the main direction of displacements observed in the Upper GLU at failure) increased under the embankment to a maximum value of 50 to 60kPa (Appendix 2A, Figure 2A.3); and the mobilized maximum shear stresses throughout it were well below the unit's drained strength. A slight rotation of the effective stress tensor was noted in this region (Appendix 2A, Figure 2A.4). Shear strains in the Upper GLU under the embankment remained well below 1% and generated predominantly horizontal displacements in the unit and materials above it (Appendix 2A, Figure 2A.5).

Such results indicate that after the completion of construction stage 3, the Upper GLU was still overconsolidated, although its overconsolidation ratio decreased in places from a value of ~4 to ~1.3. This means that after the completion of construction stage 3, the Upper GLU material under the embankment would have behaved as a lightly overconsolidated material. The magnitudes of mobilized shear stresses in the unit remained well below its shear strength. A rotation of the effective stress tensor under the embankment toe is expected in slopes and causes the realignment of the plane of critical shear stress with a position somewhat closer to horizontal. In all, these results are indicative of a stable embankment configuration; a safety factor calculation for this stage was deemed unnecessary.

Construction stage 6

After the embankment and foundation materials adjusted to the stage 6 loading conditions and to a pond elevation increase to 954mASL, the overburden effective stresses in the Upper GLU ranged from about 150kPa on the downstream to 600kPa or more under the embankment (Appendix 2A, Figure 2A.6). On the upstream, the Upper GLU's preconsolidation pressure of 400kPa was exceeded and the soil became normally consolidated. In the normally consolidated portion of the Upper GLU, the shear stresses in the horizontal direction ranged between 80 and 105kPa (Appendix 2A, Figure 2A.7), and the maximum shear stress did not exceed the estimated peak undrained shear strength. Elsewhere in the model, a continuous failure surface was observed to emerge on the upstream in the tailings and at the toe of the dam but not in the Upper GLU (Appendix 2A, Figure 2A.8). These findings suggest that no significant strain-weakening processes had yet taken place in the normally consolidated portions of this unit at this time. Based on an estimated average overburden effective (i.e. consolidation) pressure of about 500kPa, an undrained strength value $s_{u,peak}=c'=0.134\ (500) + 47.5=115$ (kPa) was assigned to this portion of the Upper GLU, and the model was re-run to obtain a new static equilibrium that reflected the changed conditions.

Under the new static equilibrium conditions, readjustments were noted as follows:

- In and around the normally consolidated portion of the Upper GLU, the shear stresses in the horizontal direction dropped below 100kPa (Appendix 2A, Figure 2A.11). A decrease of effective overburden stresses, coupled with a sligth rotation of the stress tensor, was also noted (Appendix 2A, Figure 2A.9 and Figure 2A.10), indicating a further realignment of the plane of critical stress with the horizontal plane.
- In the normally consolidated portion of the Upper GLU, shear strains of up to 4 % were noted (Appendix 2A, Figure 2A.12), and horizontal deformations reached 10cm (Appendix 2A, Figure 2A.15).

Construction stage 9

To approximate the undrained resistance in the Upper GLU during construction stages 7 through 9, the stage 9 load was added gradually and the unit's average peak undrained shear strength was adjusted in step. The addition of embankment material to its full height of 970mASL prior to failure in conjunction with a pond increase to 966.83mASL raised the maximum overburden effective stresses in the Upper GLU from ~600 to ~800kPa (Appendix 2A, Figure 2A.16). Under the new conditions, more Upper GLU material became normally consolidated. In the normally consolidated portion of the unit, the vertical consolidation pressures averaged just above 600kPa. A further rotation of the effective stress tensor was noted (Appendix 2A, Figure 2A.17) and the material reached yield (Appendix 2A, Figure 2A.21). The shear strains in portions of the normally consolidated Upper GLU material exceeded 5% (Appendix 2A, Figure 2A.19); this level of shear strain was identified by KCB (2015) as the point of onset of strain-weakening processes. Substantial horizontal displacements of up to 20-30cm were observed in the Upper GLU. Horizontal displacements in the failing soil mass above the Upper GLU ranged from 10-20cm at the crest to 40-50cm at the toe (Appendix 2A, Figure 2A.20). Under these conditions, the two-dimensional safety factor of the structure calculated using averaged peak undrained shear strengths in the Upper GLU dropped to 1.071. Such results indicate that at least some strain-weakening took place prior to the collapse; these findings confirm the conclusions by the IRP (2015).

Collapse was simulated in the model by assigning average post-peak undrained strengths (approximated by the relationship: $s_{u,post\text{-}peak}=0.122\sigma'_{cv}+36$ (kPa)) to the normally consolidated portion of the Upper GLU (Appendix 2A, Figure 2A.22 and Figure 2A.23). In KCB's (2015) strength model for this material, this undrained resistance corresponds to 20% shear strains; such level of shear strains are reasonably consistent with lateral deformations seen in the Upper GLU prior to the downward adjustment of its shear strength.

2.3.3.2. FAILURE SEQUENCE

The results of the deformation analysis were used to reconstruct the sequence of failure as follows:

a) In construction stages 1 through 3, the Upper GLU remained lightly overconsolidated and the embankment was stable. A mild rotation of the effective stress tensor took place under the embankment.

b) Portions of the Upper GLU under the embankment became normally consolidated sometime between construction stages 4 and 6. This transition was associated with a change in strength from drained to undrained. After the foundation material adjusted to the new loading conditions brought about by stage 6 works, roughly one quarter of the Upper GLU material became normally consolidated, with overburden consolidation stresses in excess of 600kPa. At this point, the mobilized shear stresses in portions of the normally consolidated Upper GLU material increased to peak undrained shear strength values. In stage 6, horizontal displacements in the foundation were around 10cm, but the shear strains were not sufficiently large to trigger strain-weakening processes.

c) Sometime during construction stages 7 through 9, a plastic yield zone emerged in the Upper GLU.

d) After the construction of stage 9, the portion of the Upper GLU located directly under the embankment and comprising about one third of its total area was normally consolidated. The portions of the Upper GLU under the embankment toe and downstream of the structure were overconsolidated. On the basis of safety factor calculations and observed horizontal displacements in the Upper GLU, some minor strain-weakening was inferred to have taken place prior to collapse. Pre-collapse displacements at the surface ranged between 10 and 40cm; it is conceivable that such levels of deformation would have gone unnoticed, especially considering that it took place cumulatively between 2008 and 2014, in stages 6 to 9.

2.4. A THREE-DIMENSIONAL LIMIT EQUILIBRIUM ANALYSIS OF THE MOUNT POLLEY FAILURE

The report by the IRP (2015) notes the substantial three-dimensional stability effects present in the Mount Polley TSF failure. These effects were estimated from a three-dimensional limit equilibrium analysis conducted on a simplified model. The analysis produced a three-dimensional safety factor of about 1.3, suggesting that appreciable amounts of shearing resistance may developed at failure along the three-dimensional slip surface that are ignored by two-dimensional analysis.

In order to accurately assess the three-dimensional slope stability effects at Mount Polley, a three-dimensional limit equilibrium analysis was conducted. A model of the Mount Polley TSF was developed in the SoilVision® SVSolid module using information reported in KCB (2015) and IRP (2015). The process of creating the geometry is largely identical to that detailed in §3.2.1 and will not be covered here. This model was imported into the SoilVision® SVSlope module that was used to calculate three-dimensional factors of safety using the Morgenstern-Price limit equilibrium method. The pore pressure conditions were specified via a phreatic surface determined using the two-dimensional steady-state seepage analysis illustrated in Figure 2.4. The soil parameters used in the two-dimensional analyses (in §2.3) were also used here with the following exceptions. The soil profile was simplified in three areas: all materials upstream of the core were represented as a single tailings material; the filter and transition materials were grouped together with the rockfill; and the materials underlying the Upper GLU were treated as a single unit designated as the Lower Glacial Till with a unit weight of 21.2 kN/m^3 and a friction angle ϕ'=35°.

The results are presented in Figure 2.5.

2.4.1 AN EVALUATION OF THE IRP (2015) FAILURE MODEL IN THREE DIMENSIONS

Recall that the IRP (2015) concluded that some minor strain-weakening had taken place in the Upper GLU prior to global collapse. The two-dimensional analysis of the failure in §2.3.2 using the IRP (2015) modelling parameters indicates that post-peak undrained shear strengths in the Upper GLU that are up to one third lower than peak values bring the slope to a limiting equilibrium. This section explores how the three-dimensional stability effects present in the slide affect these estimations.

A three-dimensional limit equilibrium analysis of the failure was conducted using Upper GLU post-peak undrained shear strengths: $s_{u,post\text{-}peak} = ⅔s_{u,peak} = 0.18\sigma'_{ov}$. The resulting safety factor of 1.18 suggests that some inputs used in the analysis are incorrect (Figure 2.5*(a)*), as failure would have not taken place under these conditions. In line with the reasoning presented in §1.3, it can be surmised that the error is largely with the strength models and that the at-failure strength of one or more soils has been overestimated.

Of the materials in the embankment and foundation, the Upper GLU is an immediate suspect due to both its strain-weakening properties and its role in the failure. Testing by the IRP (2015) pegged this soil's sensitivity between 2 and 3, meaning that, with sufficient disturbance, this material could experience a drop in its undrained shear resistance of up to 67%. Testing by KCB (2015) shows that with sufficient shear straining, this material has the potential to lose 70% or more of its undrained strength.

The Upper GLU was classified as a varved clay (CL-CH according to the Unified Soil Classification System). The high clay content of this soil means that pre-sheared surfaces in a preferential direction could have formed in this unit under certain conditions, such as long-term, slow shear movements. Had such processes taken place in the Upper GLU, they would have been

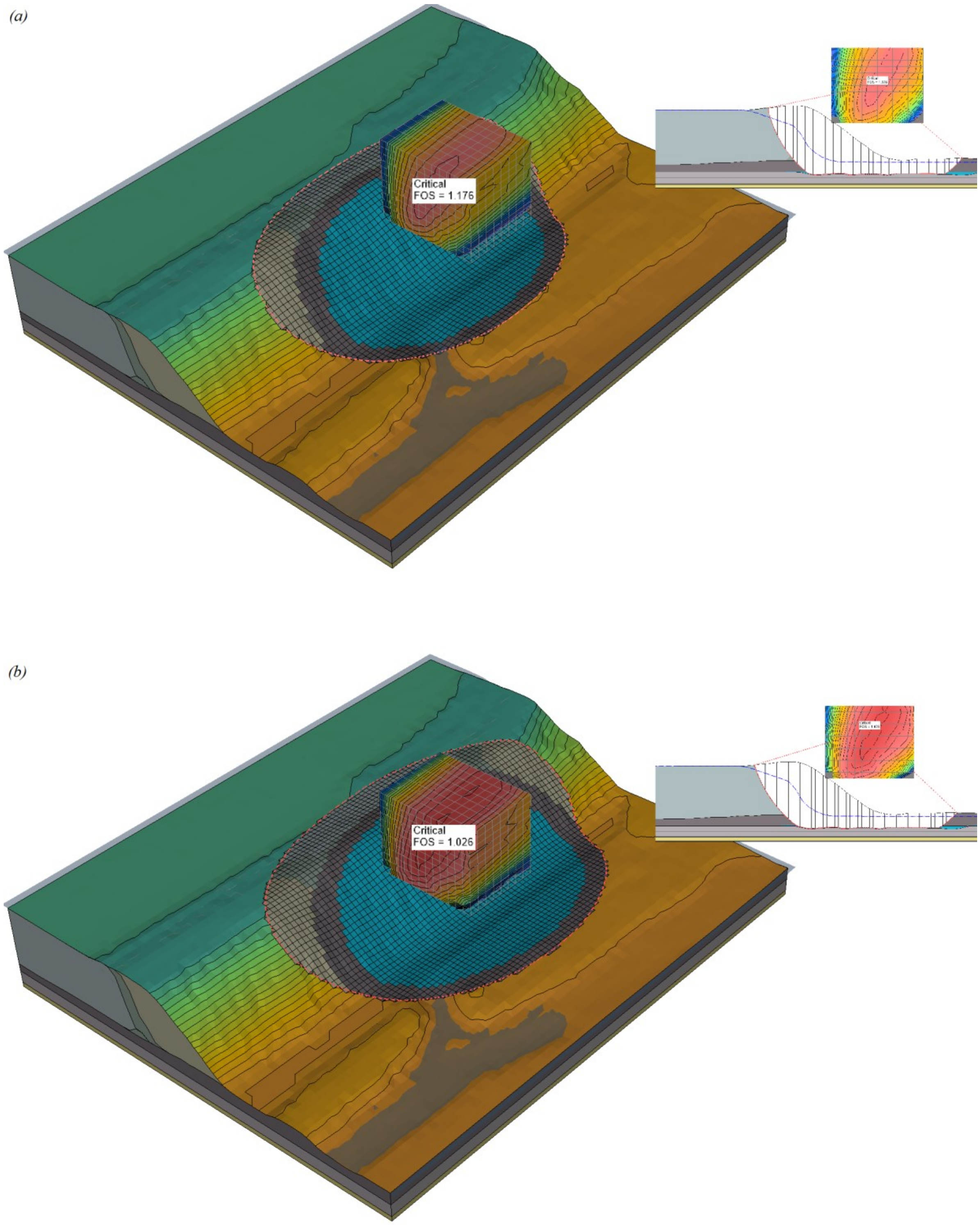

Figure 2.5 A three-dimensional limit equilibrium analysis of the failure at the Mount Polley TSF using the IRP (2015) strength model. (a) FOS = 1.18 obtained using post-peak undrained shear strengths $s_u = \frac{2}{3} s_{u,peak} = 0.18\sigma'_{ov}$ *in the Upper GLU. (b) FOS = 1.03 obtained using residual strength values* $s_u = \frac{1}{3} s_{u,peak} = 0.09\sigma'_{ov}$ *in the Upper GLU.*

evidenced by the presence of continuous pre-sheared surfaces, including outside failure. Such evidence was not found at the site (IRP 2015, p. 38; KCB 2015, p. iii), suggesting that an overtime reduction of strength to residual values due to particle realignment was probably not a mechanism at this site. However, a reduction in undrained strength from peak to residual values due to disturbance such as shear straining must be considered.

Both investigators agree that some post-peak reduction in shear strength did take place either pre- or post-collapse. Building on this conclusion, a proposition is put forward that advanced strain-weakening processes had taken place in the Upper GLU prior to collapse, eventually bringing the slope to a limiting equilibrium.

This proposition was tested in a series of three-dimensional limit equilibrium analyses. The results indicate that a reduction of undrained shear strengths in the Upper GLU to residual values across the entire surface involved in the failure brings the slope to limiting equilibrium (Figure 2.5*(b)*).

2.4.2 AN EVALUATION OF KCB'S (2015) FAILURE MODEL IN THREE DIMENSIONS

The KCB (2015) investigators concluded that at the time of failure, peak undrained strength values were acting along the Upper GLU and that post-failure strain-weakening had taken place, briefly reducing the safety factor below unity prior to the re-stabilization of the soil mass on the downstream. The two-dimensional limit equilibrium and deformation analyses in §2.3 using the KCB (2015) strength model indicate that some relatively minor strain-weakening had taken place prior to failure. Such discrepancy in results does not indicate a fundamental disagreement about the mechanism of failure but a mere difference of opinion regarding the time of onset of the strain-weakening processes.

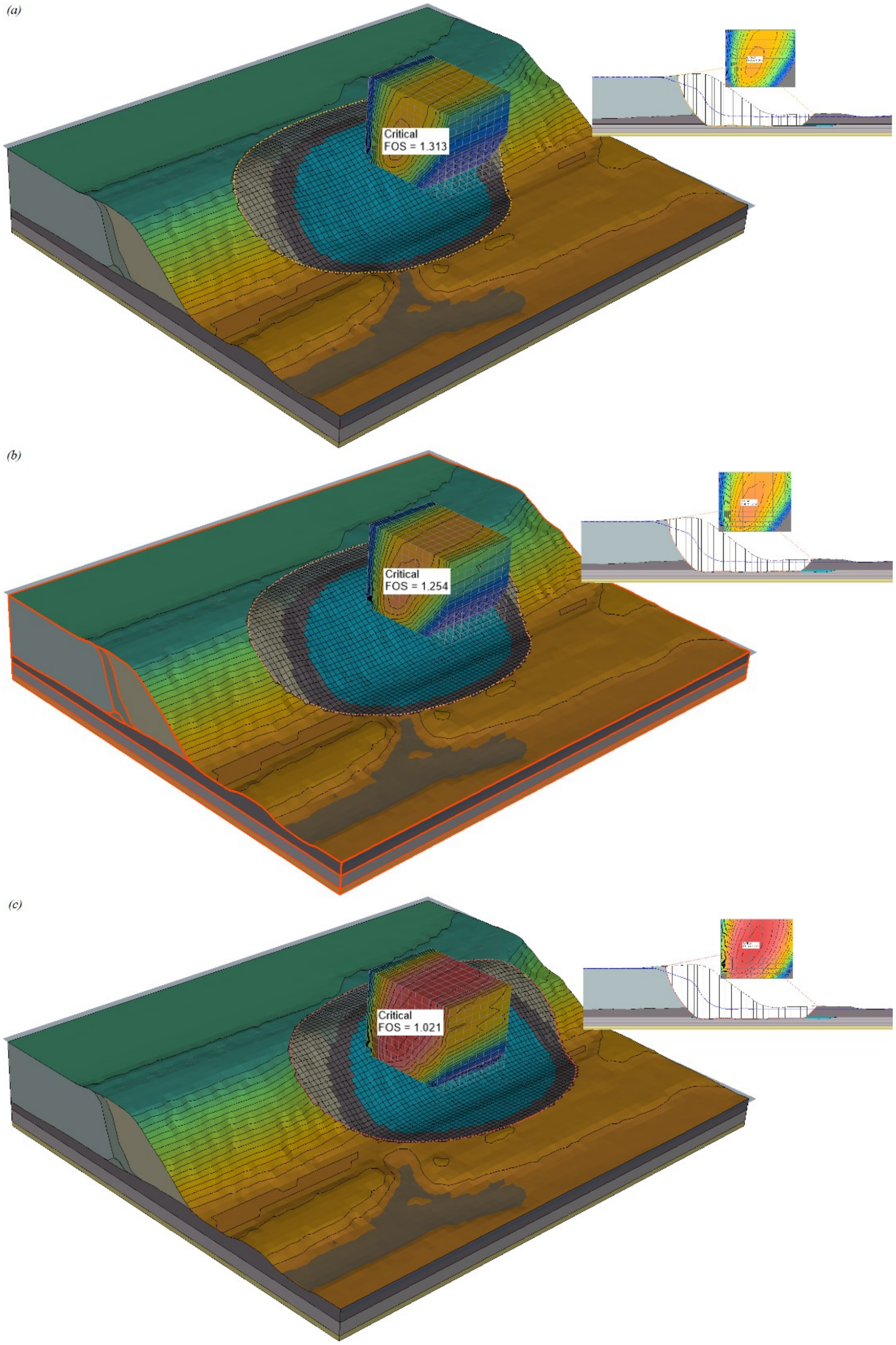

Figure 2.6 A three-dimensional limit equilibrium analysis of the failure at the Mount Polley TSF using the KCB (2015) strength models. (a) FOS = 1.31 obtained using Upper GLU peak undrained shear strengths $s_{u,peak}=0.134\sigma'_{cv}+48$ *kPa. (b) FOS = 1.25 obtained using Upper GLU post-peak undrained shear strengths* $s_{u,20\%strain}=0.122\sigma'_{cv}+38$ *kPa. (c) FOS = 1.02 obtained using Upper GLU residual strength values* $s_{u,residual}=0.029\sigma'_{cv}+21$*kPa.*

It is of interest to establish how the inclusion of three-dimensional stability effects into the stability analysis of Mount Polley would affect these conclusions. A three-dimensional limit equilibrium analysis of the failure was conducted using peak and post-peak undrained shear strength values: $s_{u,peak} = 0.134\sigma'_{cv} + 48kPa$ and $s_{u,20\%strain} = 0.122\sigma'_{cv} + 38kPa$ (recall that these were the strength models that brought about collapse in the analysis by KCB (2015) as well as the two-dimensional analyses introduced in §2.3). The resulting safety factors of 1.31 and 1.25 respectively indicate that neither strength model brings the soil mass to a limiting equilibrium (Figure 2.6*(a)* and *(b)*).

In line with the findings presented in §2.4.1, it is posited that advanced strain-weakening processes may have taken place in the Upper GLU prior to collapse, eventually bringing the slope to a limiting equilibrium. This proposition was tested by reducing the Upper GLU's undrained shear to its residual value measured by KCB (2015): $s_{u,residual} = 0.029\sigma'_{cv} + 21$ (kPa). This brought the slope near its limiting equilibrium by producing a safety factor of 1.02 (Figure 2.6*(c)*).

2.5. THE PROPOSED MODEL OF FAILURE AT THE MOUNT POLLEY TSF

2.5.1 PROBLEM STATEMENT

The static slope stability analyses introduced in §2.4 indicate that substantial three-dimensional effects were present in the Mount Polley TSF failure. Three-dimensional stability analyses of the breach using the IRP (2015) and KCB (2015) models generate safety factors of 1.18 and 1.31, respectively; this is well above the expected value of unity.

The presence of three-dimensional stability effects at Mount Polley serves as an indication that the failure model developed on the basis of two-dimensional analyses may be not entirely accurate. Three-dimensional stability effects are understood to be a measure of error introduced into the stability analysis due to its reduction to two dimensions. As it has been demonstrated in Chapter One, such an error is probably brought about by the overestimation of shear strength for at least some of the involved materials, by an erroneous determination of shear stresses acting along the slip plane or by a combination of both.

In the two-dimensional analysis of the failure at Mount Polley, the source of this error is thought to be at least in part related to an overestimation of shear resistance at failure in the Upper GLU. This material was shown to lose appreciable amounts of shear strength under specific conditions, namely a state of normal consolidation and in-situ shearing or disturbance. Both of these conditions were shown to be present at failure.

The three-dimensional limit equilibrium analyses raise, in fact, two additional questions about the failure: one regarding the extent of weakening in the Upper GLU prior to collapse and another pertaining to pre-failure deformation levels.

2.5.1.1. PRE-FAILURE EMBANKMENT DEFORMATIONS

The failure at Mount Polley was characterized as a brittle collapse that occurred without any advance warning or observable precursors (IRP 2015, p. 13). The deformation analysis in §2.3.3 predicts pre-failure horizontal displacements in the Upper GLU in the order of 0.4m, with at least some of these deformations accruing in the earlier construction stages. The soils above the Upper GLU would have experienced similar or slightly greater levels of horizontal displacements. It is conceivable that such deformations could have gone unnoticed.

On the other hand, the three-dimensional static analyses in §2.4 demonstrate that failure can only take place if the entire Upper GLU area in the slip zone is fully weakened. This level of weakening is reached at shear strains ≥60%; in a soil unit that is 2m thick, such strains translate into shear displacements ≥1.2m in the foundation soils. Such pre-failure levels of displacements would have been evident and are not likely to have taken place. It is therefore necessary to explain how the high levels of strain-weakening suspected to have taken place in the Upper GLU prior to collapse could have happened without excessive ground displacement.

2.5.1.2. AREAL EXTENT OF STRAIN-WEAKENING

Suppose that the entire portion of the Upper GLU in the slip area had fully strain-weakened prior to collapse, as it is suggested by the three-dimensional static analyses. This would imply that all of this material would have been normally consolidated at failure. The field investigators established that a substantial portion of the Upper GLU, including large areas downstream of the embankment up to the “whaleback” features, was involved in failure. Those areas had not experienced substantial increases in loading and have remained largely overconsolidated at the time of collapse. This is confirmed by the deformation analysis introduced in §2.3.3 and is illustrated in Figure 2.7.

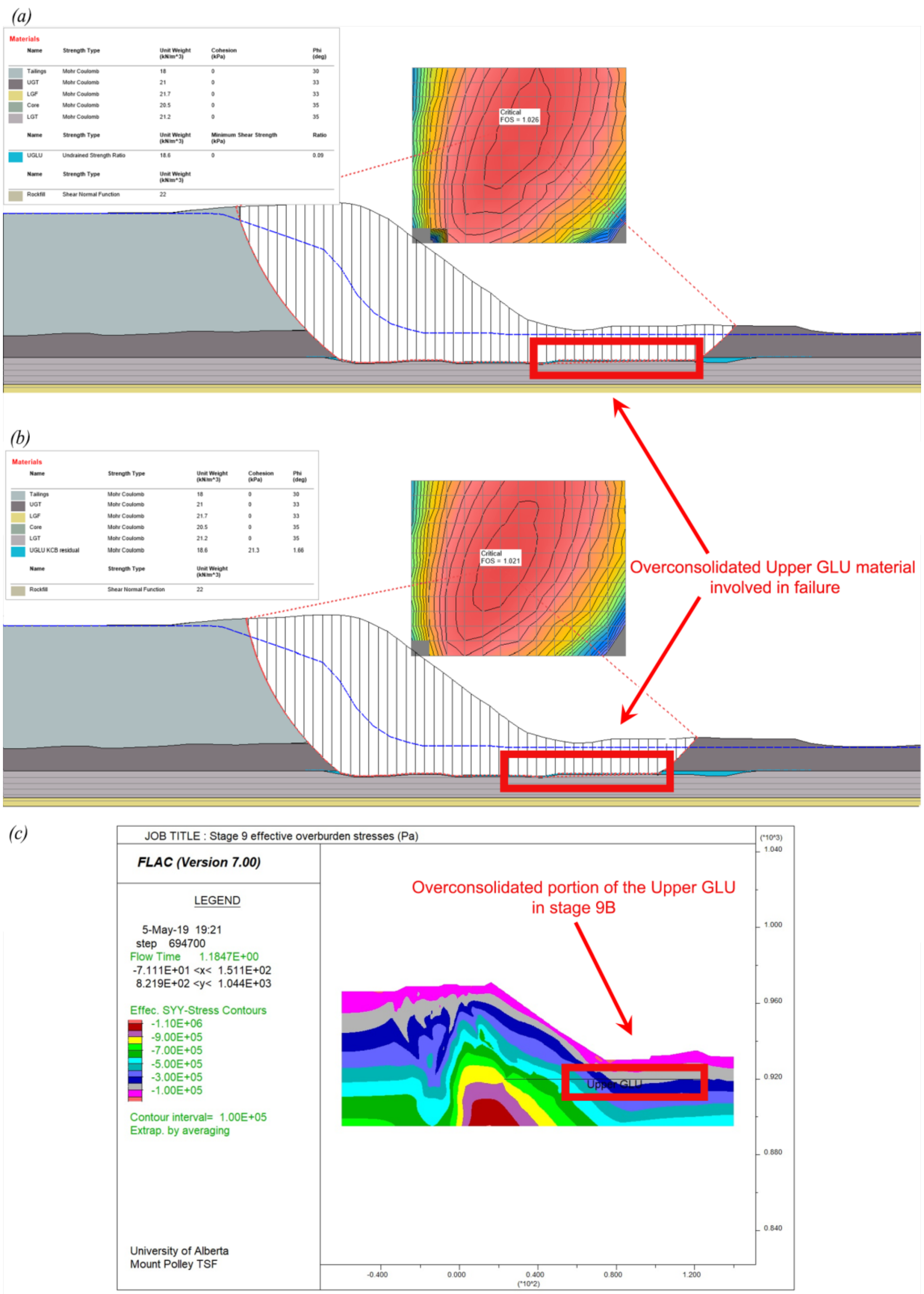

Figure 2.7 Areal extent of overconsolidated Upper GLU material involved in failure estimated from (a, b) cross-sectional views of three-dimensional limit equilibrium models of failure using the IRP (2015) and KCB (2015) strength models; and (c) the stage 9 overburden effective stresses evaluated through deformation analysis.

This means that the average resistance across the entire Upper GLU material involved in the failure could have not dropped to residual values even if all of its normally consolidated portion had fully weakened. We can therefore surmise that another material or materials had lower levels of mobilized resistance at failure than it has been assumed in the models.

2.5.1.3. THE STRENGTH BEHAVIOUR OF THE ROCKFILL

The rockfill material forming the shell of the embankment played a significant role in the collapse: a substantial portion of the three-dimensional slip surface passed through this material along the sides of the slide (see Figure 2.5 and Figure 2.6), potentially mobilizing considerable amounts of shearing resistance along it.

In the two-dimensional analyses conducted by both investigators as well as those introduced here, the rockfill's contribution to shear resistance in the slide is fully neglected, as the critical slip line does not pass through it. Therefore, the strength model assigned to this material has no bearing on the predicted levels of stability. The IRP (2015) assigned to the rockfill a curved strength envelope, and KCB (2015) chose a linear one. In the end, both produced adequate results.

In a three-dimensional slope stability analysis of the failure, an accurate determination of the rockfill's strength behaviour would be essential. Rockfills are high-strength materials, capable of mobilizing substantive amounts of shearing resistance. At Mount Polley, the rockfill had relatively uniform gradation and was composed of fine to coarse gravel with trace to some sand, some cobbles and trace of boulders, with a recorded fines content of 10% (KCB 2015, p. 7, Appendix I-D). Even though some the rockfill was deposited with little compaction, this material is relatively strong and capable of mobilizing considerable amounts of shear resistance.

In the preliminary three-dimensional analyses introduced in this chapter, a suitable strength envelope was identified from the literature. The three-dimensional limit equilibrium analyses discussed in §2.4 use a curved strength envelope for a weak-to-average rockfill material adapted from Marsal (1973). Four strength envelopes reported by Marsal for rockfill samples 1, 2, 3 and 6 (1973, pp. 167-168) were evaluated in the three-dimensional limit equilibrium analyses; the results do not appear particularly sensitive to the choice of strength envelope, as long as it fits the general description of rockfill type. It is shown in Figure 2.8 that the four strength envelopes produce near-identical safety factors.

In addition to possessing a curved strength envelope, rockfill materials have been shown to display a non-linear deformation-stress behaviour whereby their deformation moduli increase with confining pressures. Leps (1970) reports that at lateral pressures ≤10psi (≤ 70kPa), strains at failure are about a third to a half of those measured at pressures of 100psi (700kPa).

Such non-linear deformation-stress behaviour would have likely been present at Mount Polley. In an embankment with a total height at failure of only 40m, the confining stresses in the shell region were not particularly high, ranging from zero at surface to 0.5MPa or so near the core base. Additionally, the non-linear deformation-stress response in the rockfill would have been exacerbated by the poor compaction on placement. One can surmise that a full mobilization of the rockfill shearing resistance would require substantial deformations. Conversely, the shearing strength of the rockfill would remain under-utilized at low deformation levels.

In the absence of visible precursors to the embankment collapse, large deformations in the shell area prior to failure can be ruled out. Low levels of rockfill deformation and associated low levels of mobilized shear resistance in this material may help explain how the soil mass could have

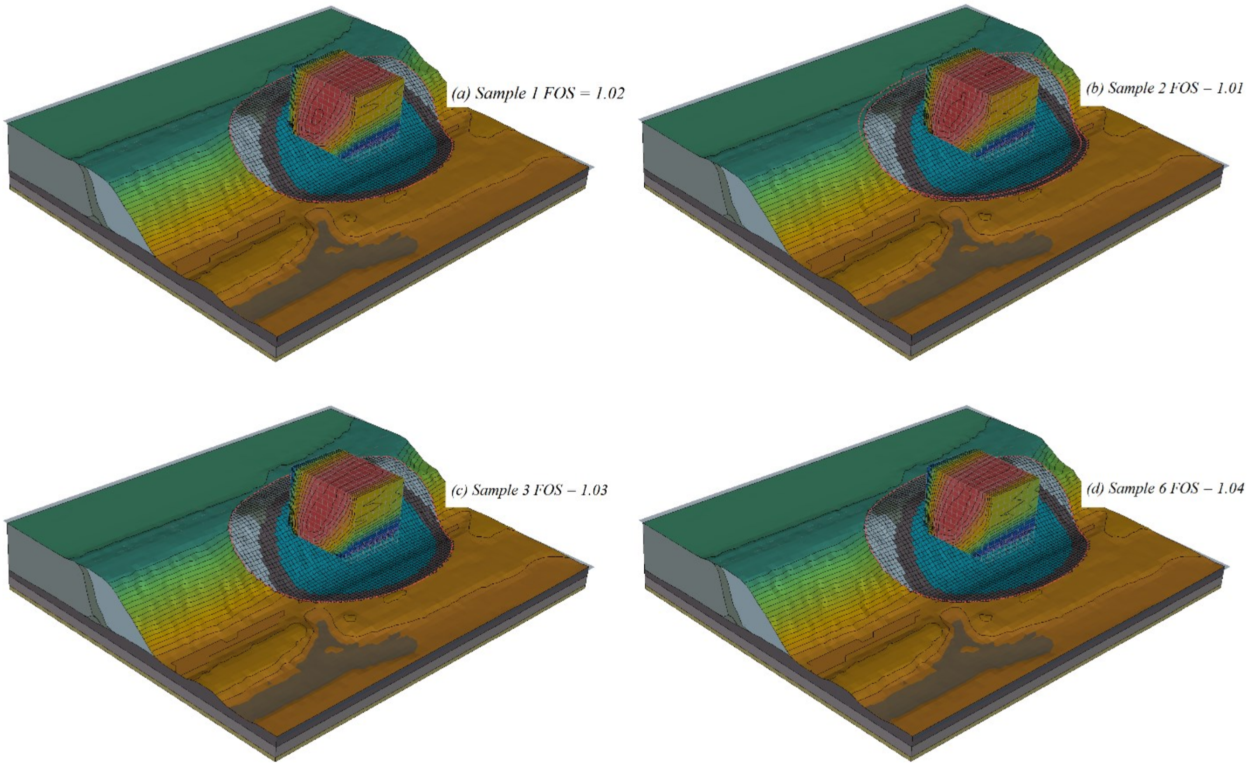

Figure 2.8 Sensitivity assessment of the rockfill strength envelope using strength models for Samples 1, 2, 3 and 6 by Marsal (1973, pp. 167-168).

reached a state of limiting equilibrium without the average shear strength in the Upper GLU dropping to residual.

2.5.2 HYPOTHESIS

The two- and three-dimensional analyses introduced in this chapter, combined with field evidence, highlight a number of outstanding questions about the failure at Mount Polley. The three-dimensional limit equilibrium analyses suggest that the Upper GLU must have fully weakened prior to failure. Laboratory data indicate that such a loss of resistance takes place at shear strains equal to or greater than 60%, inferring shear displacements in the order of 1.2m prior to failure. Field data offer no evidence of such displacement prior to collapse. Furthermore, deformation analysis results indicate that about one third of the Upper GLU material involved in the failure would have been overconsolidated and exhibit a different strength behaviour; this raises the question whether it was at all possible for the average resistance in this stratum to reach undrained residual values prior to collapse. Finally, if the average shear resistance in the Upper GLU at collapse was above residual, some other material involved in the failure must have been weaker than initially thought.

To reconcile these apparent inconsistencies, two propositions are put forward: one regarding the manner of straining in the Upper GLU and another regarding the rockfill's mobilized shear resistance at collapse.

First, it is proposed that prior to and during the collapse, the Upper GLU strained non-uniformly, acting as a layered system rather than a single block. In this scenario, a thin layer in the unit accrued substantial shear strains, weakening considerably in the process, whereas the rest of the stratum neither strained nor weakened excessively. Non-uniform shear straining of the Upper GLU would explain how significant portions (by area) of this unit can weaken substantially, even fully, in the absence of noticeable shear displacements.

Second, it is proposed that at low confining stresses, the rockfill exhibited low deformation moduli and required substantial deformations to mobilize its shear strength. If full weakening took place at low deformation levels as proposed above, at the time of collapse, the rockfill would have not fully mobilized its shear resistance.

It is proposed that the combination of non-linear straining in the Upper GLU and the insufficient mobilization of shear resistance in the rockfill at low deformation levels has brought the slope to a limiting equilibrium, triggering the collapse.

CHAPTER THREE

MODEL DEVELOPMENT

3.1. OVERVIEW

This chapter documents the formulation and development of the numerical model used to simulate the failure at the Mount Polley TSF. Along with chronicling the modelling choices, this chapter includes a discussion on the reasoning behind the more important selections.

3.1.1 METHOD

In Chapter One of this thesis, the reduction of a slope stability problem from three to two dimensions was identified as a source of error in stability evaluations. The substantial three-dimensional stability effects present in the failure at Mount Polley are a compelling reason to evaluate this particular case study in three dimensions and not in two.

There are two classes of solutions for slope stability problems that are currently available to geotechnical researchers: limit equilibrium methods and deformation methods. Both offer the capability for three-dimensional analysis. However, the former has other limitations even when it is conducted in three dimensions, one being its failure to incorporate stress-strain relationships. In the problem of the failure at Mount Polley, this limitation is expected to strongly affect the outcome as the shear strengths and stress states in at least two soils, the Upper GLU and the rockfill, are strongly dependent on the state of straining in the model. Deformation analysis addresses this source of error because it evaluates the stresses in soils as a function of their current strain levels. For these reasons, the evaluation of the failure at the Mount Polley TSF was conducted with the use of three-dimensional deformation analysis.

3.1.1.1. MODELLING SOFTWARE

The basic requirements for the deformation modelling software that would be used to complete the Chapter Three objectives are outlined below:

- The ability to conduct deformation analysis in three dimensions.
- The ability to handle substantial deformations in the modelled domain.
- The availability of constitutive models that can be used to adequately describe the mechanical behaviour of the soils involved in the Mount Polley failure. In particular, the use of constitutive models for strain-weakening soils and for soils with stress-dependent deformation moduli is a requirement.
- A calculation scheme that is suitable for simulating post-peak weakening behaviour.
- A capability for flow calculations.

The simulation of the Mount Polley failure was carried out using Itasca's FLAC3D software. FLAC3D is an explicit Lagrangian finite volume numerical modelling programme that enables the user to conduct deformation analyses in three dimensions. The software has a large strain calculation mode that accommodates domain deformations; this feature is discussed in §3.3.2. Coupled and uncoupled flow calculations can be performed in the software. FLAC3D includes a variety of built-in constitutive models that accommodate strain-weakening behaviour. These are the *strain-softening*, *bilinear strain-softening ubiquitous joint*, *double-yield*, *cap-yield* and *simplified cap-yield* models. In addition, FLAC3D allows for the customization of constitutive models through the use of its internal functions written in its proprietary coding language FISH. FLAC3D models can be augmented with the use of custom, user-defined constitutive models written in C++ (Itasca 2018). Finally, Itasca's FLAC and FLAC3D software packages have been established as an industry standard for the evaluation of major failures in tailings dams and have been used in the evaluations of a number of such recent events such as the breach at Mount Polley

TSF by KCB (2015), the failure at Feijão Dam near Brumadinho by Robertson et al. (2019) and the loss of containment at the Cadia Northern Tailings Storage Facility by Jefferies et al. (2019).

The FLAC3D software was provided by the developer under an educational partnership agreement. This particular modelling environment allows for custom constitutive models to describe complex soil behaviours.

Deformation analysis has its own sources of error stemming from assumptions and simplifications associated with its formulation. Two of these are the error associated with the assumption of domain continuity and the error associated with an insufficient level of discretization. The former is related to the fundamental assumption of continuum mechanics (that lays the foundation for this method) that the modelled matter is continuous and can be described with mathematical functions; this assumption ignores the inherently discrete nature of soil systems in particular and of the universe in general. This error is thought to be addressed by the fact that the scale of the problem is larger by many orders of magnitude than the scale of the discrete particles. The latter is associated with the discretization of the modelled continuum into finite elements and arises from the approximation of the exact solution by piecewise functions. This error gives rise to so-called "scale effects" where models with different discretization levels produce different outcomes. The errors associated with numerical modelling briefly described here are discussed extensively by Zienkiewicz and Taylor (2000, Ch. 14-15).

FLAC3D offers a mesh discretization scheme whereby the size of finite elements can be varied throughout the domain. This solution offers an improved degree of control over the magnitude of discretization error as the model mesh can be refined in the critical areas but not elsewhere, saving computational power.

3.1.2 CHAPTER ORGANIZATION

The numerical modelling of stability problems includes the standard steps of (a) specifying the geometry of the domain, (b) defining the relevant material behaviours and (c) designating appropriate boundary and initial conditions. The process of modelling these steps in the problem of the Mount Polley failure is detailed in §3.2.1 to §3.2.4.

In addition to these standard modelling components, a number of specific strategies were used in the simulation of the Mount Polley TSF to improve the model fit. Due to the dependency of a deformation solution on the stress path, the sequence of embankment construction and pond elevation changes was simulated from original ground up (see §3.3.1). The scale effects in this model were investigated by developing three separate models with a variable mesh resolution in the area of the Upper GLU (§3.2.1). Two separate solutions were obtained under the large and small calculation schemes (§3.3.2). Finally, in view of the variable discretization of the models and contrasting deformation behaviours throughout the domain, a composite approach to evaluating convergence was taken (§3.3.3).

A flowchart of the process used to model the failure at Mount Polley is illustrated in Figure 3.1.

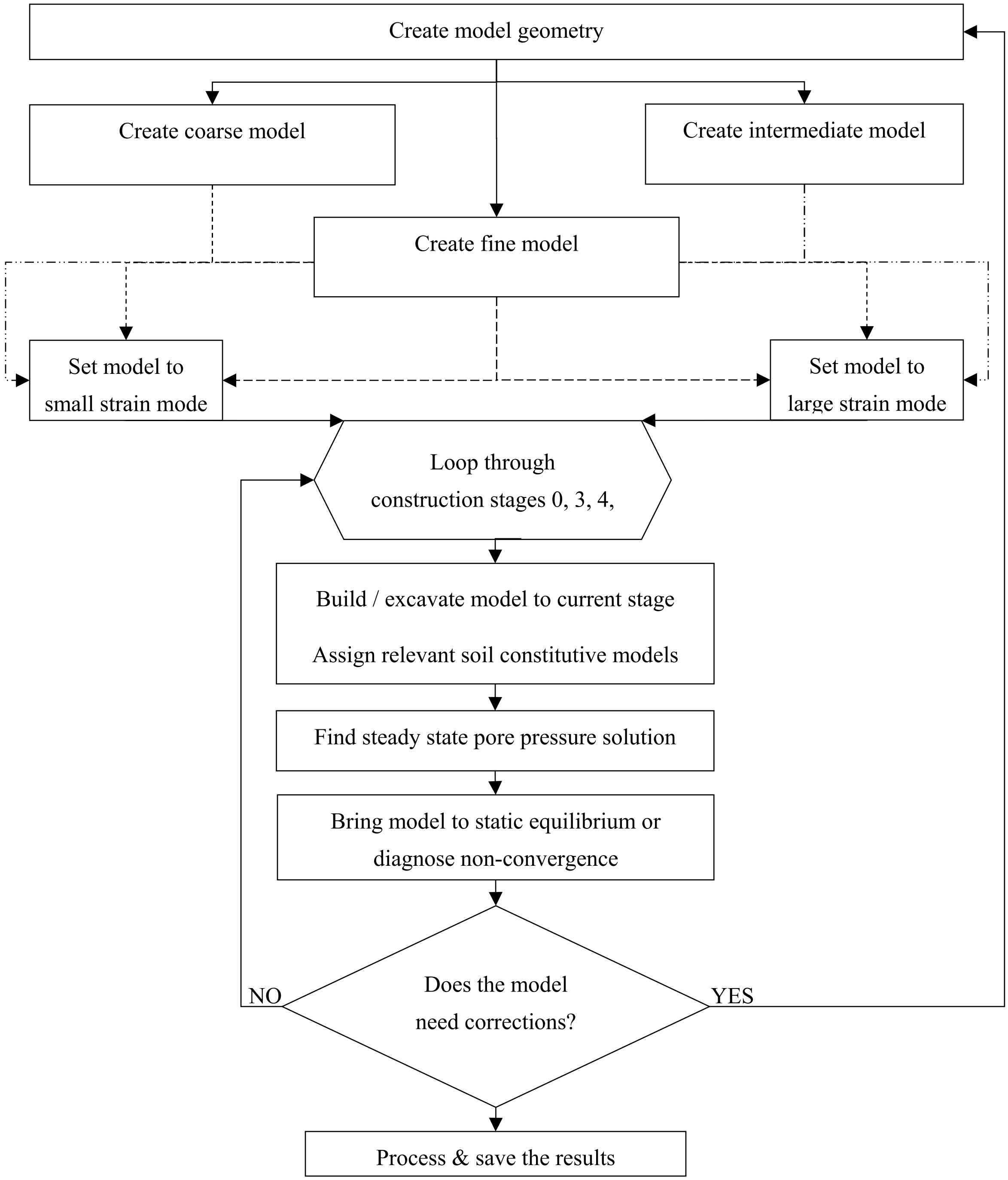

Figure 3.1 Modelling procedure used to perform a three-dimensional deformation analysis of failure at the Mount Polley TSF.

3.2. MODEL INPUTS

3.2.1 GEOMETRY

The surface and subsurface conditions at the Mount Polley TSF and surrounding area have been well-documented by the dam operator starting in the planning stages and until its failure. In the aftermath of the failure, field investigations were conducted by the IRP (2015) and KCB (2015). These data were integrated to develop a three-dimensional model of foundation soil distributions at the failure location, as well as of the embankment structure and surface elevations of each of the modelled construction stages. The main steps of this process are as follows:

- Topographic maps of the original ground (KCB 2015, Figures 5.1 and 5.2) were used to create a three-dimensional surface representing pre-construction ground elevations. This surface subsequently became the interface between foundation and embankment materials.
- A pre-failure topograhic map of the embankment and surrounding areas (KCB 2015, Figures 2.9 and 2.10), the cross-sectional views of the embankment (KCB 2015, Figure 2.6) and the material deposition records (IRP 2015, Figure H.A1-1) were combined to create a three-dimensional surface representing the embankment top elevations at construction stage 9B.
- The embankment deposition history (IRP 2015, Appendix H; KCB 2015, Figure 2.6) was used to reconstruct the top elevation surfaces in construction stages 3 and 6. Where lacking data, an assumption was made that the typical cross-section aspect was constant along the dam centreline in a direction normal to it.
- The embankment deposition history was used to estimate the extent and placement of added material in construction stages 4, 5, 7, 8 and 9A. Although the modelled surfaces in these stages appear more rough than those generated for stages 3, 6 and 9B, the added effective loads are

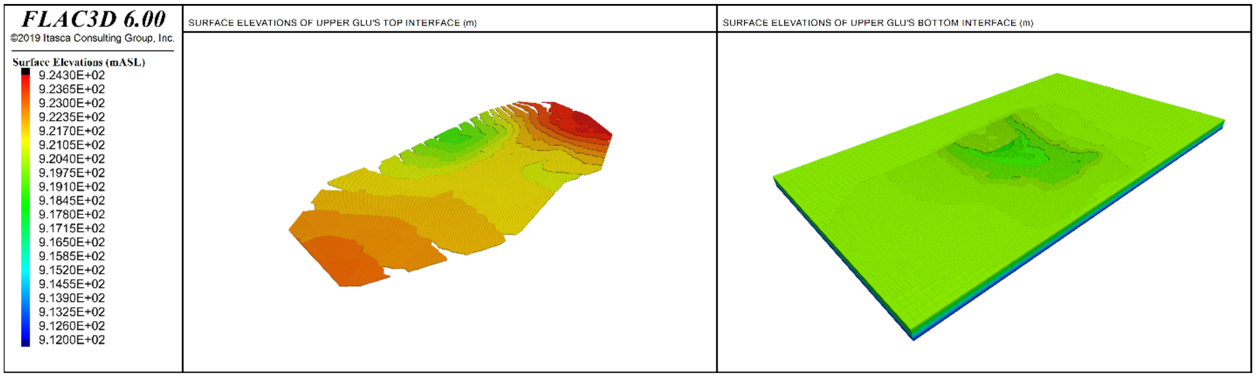

Figure 3.2 Upper GLU's spatial extent, and top and bottom surface elevations in the FLAC3D model.

replicated reasonably well. Embankment surface elevations for all modelled construction stages are seen in Figure 3.5.

- All borehole data reported by the two investigators were processed to determine the interface elevations of the foundation soils. These data were used to first estimate the spatial extents of the various units and then to generate surfaces and volumes to represent these in the three-dimensional model. Figure 3.2 illustrates the modelled extent, shape and elevation of the Upper GLU.
- The soil profile at the failure location was simplified to include six soil types: the Upper GLU, the upper and middle glacial tills (UGT and MGT, accordingly), the rockfill, the core and tailings. The full and simplified soil profiles along with the soil distributions in the three-dimensional model are seen in Figure 3.3. The Glaciofluvial Units located below the Upper GLU (shown in Figure 3.3, left, in lime green) were modelled for flow calculations only by assigning the units' hydraulic properties to the appropriate volume.

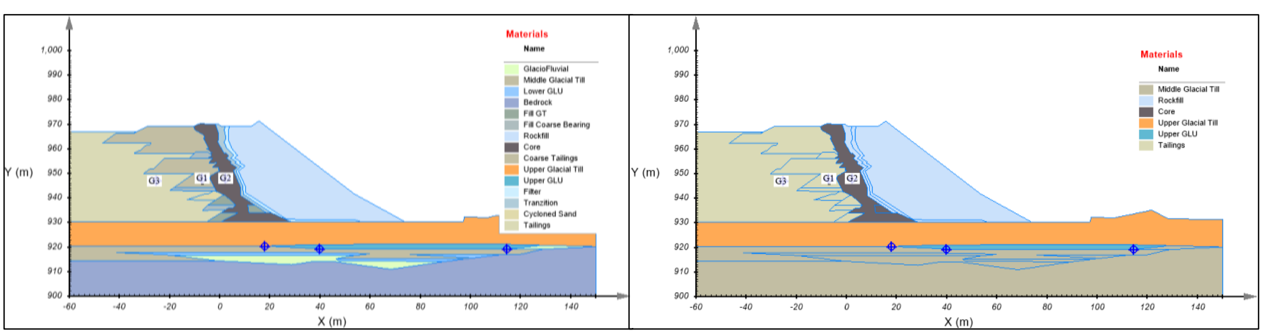

Figure 3.3 Full (left) and simplified (right) cross-sectional views of the embankment at the failure location.

All of the model's three-dimensional surfaces were created using SVSolid in SoilVision® SVOffice™. The surfaces were exported to the AutoCAD® file formats *.stl* or *.dxf* and then processed in FLAC3D. It is worth noting that the three-dimensional deformation model in FLAC3D was developed using the same geometry that was used to create the three-dimensional limit equilibrium analysis of the failure presented in Chapter 3. The close agreement between the models' geometries makes it easier to compare limit equilibrium and deformation analysis results by eliminating the error associated with such discrepancies.

3.2.1.1. MODEL RESOLUTION

Continuum mechanics takes the view that the mechanical behaviour of matter can be described by continuous functions. However, adequately describing a domain with continuous mathematical functions cannot be easily done and has not been accomplished but for a few simple cases. Therefore, in order to model the behaviour of materials, including soil and rock, engineers find it necessary to partition the model domain into smaller elements whose behaviour of interest can be mathematically described to the desired level of accuracy.

The finite element methods are numerical analysis schemes used to simplify the task of describing a continuous domain by subdividing it into basic elements whose behaviours are fully defined by mathematical models. This process, called "discretization," introduces an error into the solution.

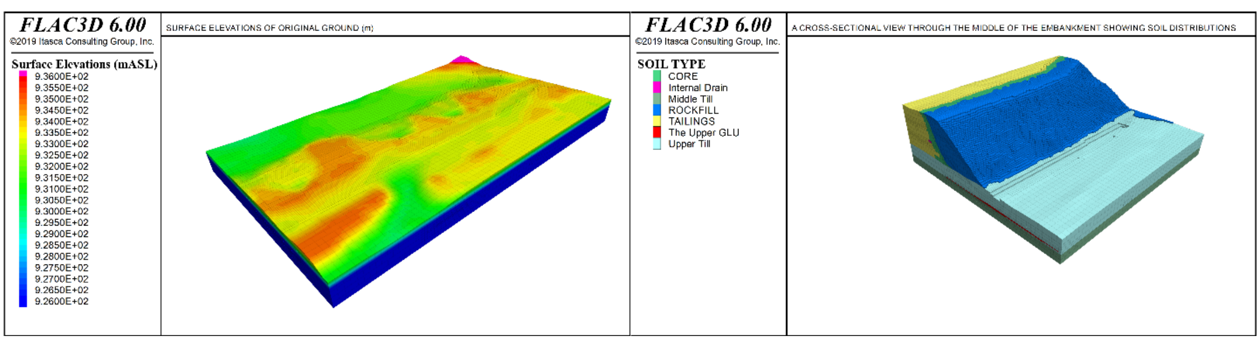

Figure 3.4 Views of the three-dimensional model of the Mount Polley TSF at the failure location. Left: pre-construction surface topography. Right: a cross-sectional view of the model showing the distribution of foundation soils and embankment materials at construction stage 9B in the summer of 2014.

Its root lies in part with the inability of a discrete element to fully capture the deformation behaviour of matter (Dow 2013; Zienkiewicz and Taylor 2000). Since a higher level of domain discretization helps better emulate the true behaviour of materials, it follows that all other things being equal, models with higher levels of discretization (i.e. models with a higher resolution) yield solutions that are more accurate than those with lower levels of discretization.

The error associated with the level of discretization leads to a modelling phenomenon known as "scale effects," where models that are identical in every way except their discretization levels yield different outcomes. Scale effects are known to be more pronounced in models with strongly non-linear behaviours. In the case of Mount Polley, strongly non-linear straining behaviours are believed to be taking place, in particular in the Upper GLU. Consequently, scale effects must be investigated in the model of this failure.

FLAC3D makes use of the finite volume method to model the behaviour of materials. The software discretizes the model domain into basic elements called "zones." FLAC3D treats a model's attributes across a zone during a single calculation step as either constant (e.g. dry density, the stress tensor or the strain increment tensor) or varying linearly between its nodes called gridpoints (e.g. soil saturation, pore water pressures).

In models with relatively large zones (i.e. low resolution models), low levels of discretization may be adequate for simulations where real behaviours are closely approximated by their linearization between adjacent elements but could be lacking if distinctly non-linear behaviours take place within spans that are comparable to the size of the zones. Decreasing the zone size (i.e. increasing the model resolution) addresses this problem at the cost of increasing the complexity of the model, which in turn can greatly affect computational requirements. In other words, simulations produced by lower resolution models are less accurate than those produced by higher resolution models but may or may not be adequate depending on the specifics of each model as well as the goals set out

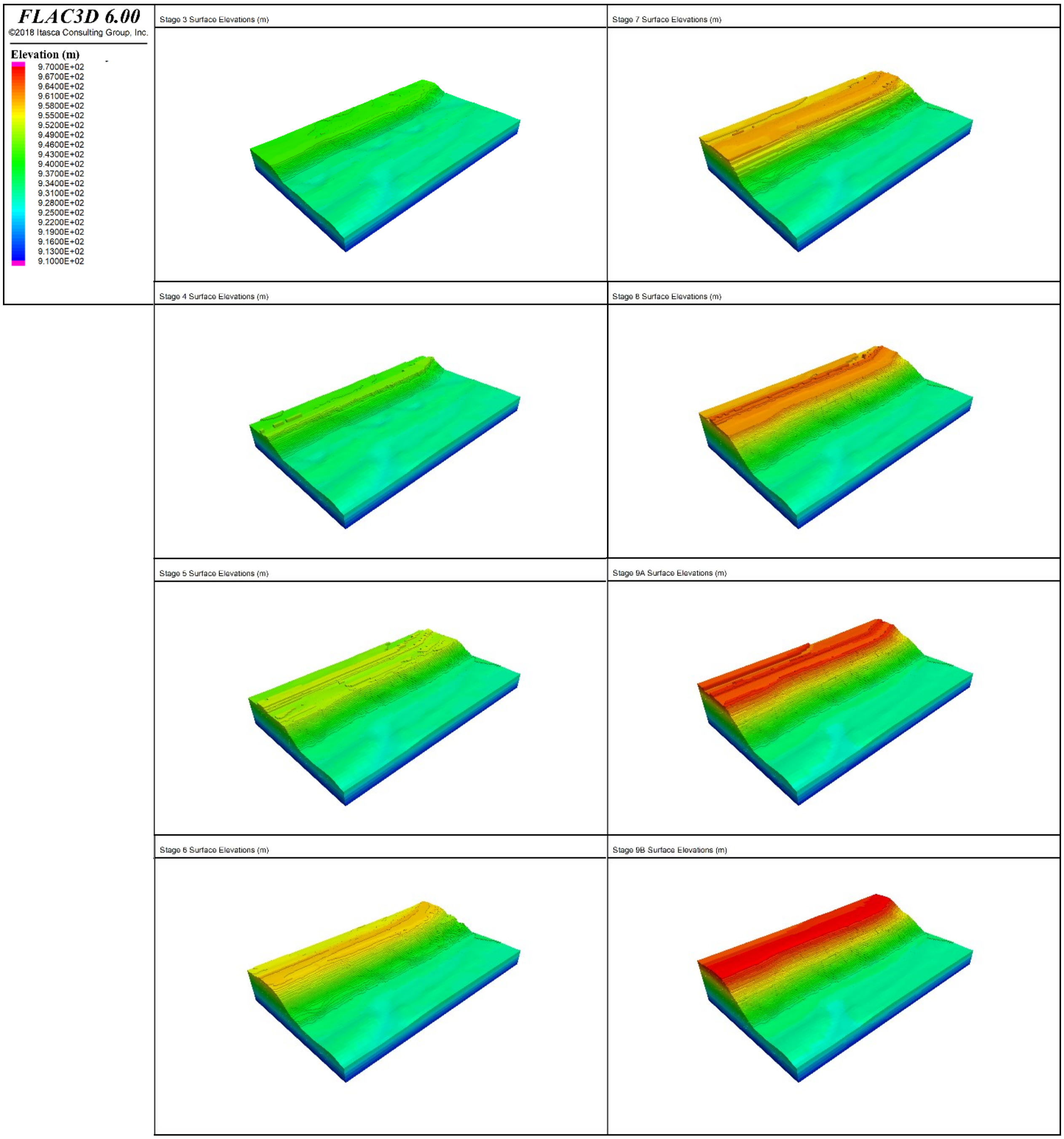

Figure 3.5 Embankment surface elevations at the Mount Polley TSF failure modelled in FLAC3D. Note: Stages 9A & 9B are shown without excavation.

by the modeller. For example, the FLAC3D manual notes that finer meshes produce better representations of high-stress gradients (Itasca 2018).

If computational capacity is no object, high levels of discretization are always preferred, assuming that the input data warrant such level of detail. When computational requirements are a potential constraint, as it is often the case, feasibility demands that model resolution is carefully balanced against computational requirements. In FLAC3D, one way to achieve this balance is to vary a model's resolution through the domain as needed. The software allows the modeller to increase the model resolution in areas of special interest (for example, in the materials governing the failure or in areas where sharp contrasts of relevant material properties exist), as well as in areas where strongly non-linear processes are being modelled.

The FLAC3D model of the Mount Polley failure was developed with a base resolution of 4x4x4m^3 zones, with these being further discretized in the areas of special interest.

Zone densification around embankment surfaces (construction stages 3, 6 and 9)

In developing the FLAC3D model of the Mount Polley failure, a design choice was made to use cube-shaped zones rather than degenerated and/or irregular zones when creating the dam volume; this choice was made to lower the risk of convergence errors brought about by poor geometry at large deformation levels under the large strain calculation scheme. However, this approach creates two problems: (a) the face of the dam is approximated by cubes which do not readily conform to its sloped shape, producing an unnatural blocky aspect; and (b) the cubic zones comprising the slope create a multitude of vertical faces that in a simulation may generate local "open cut" type failures, preventing the overall model from running its course.

To address both problems, zones were decreased to a size of about 2x2x2m^3 in the areas corresponding to the embankment surface at construction stages 3, 6 and 9. Smaller cubic zones allow a better geometric approximation of the dam face, mitigating the first problem. In addition, with the height of the vertical faces at the surface of the dam now halved, the problem of local "open cut" type failures becomes more manageable and was addressed here by either assigning nominal cohesion values at low effective normal stresses where Mohr-Coulomb strength models were used or by modelling the zones prone to this type of failure as elastic materials.

Zone densification around the Upper GLU

In models involving strain-weakening materials, solutions obtained using the finite element method can be dependent on the mesh resolution and have been shown to manifest pronounced scale effects (Zhang et al. 2013; Conte et al. 2010; Potts et al. 1990). This problem is related to the assumption of uniform strain rates across individual mesh elements.

In the analysis of the Mount Polley failure, the effect of the mesh size on the solution was explored by conducting three separate simulations using increasingly finer resolutions in the region of the Upper GLU. An initial coarse model discretized the Upper GLU material into uniform cubic zones with edges of 0.5m. Two additional models involved further mesh refinements where the edges of the cubic zones in the Upper GLU were reduced to a size of 0.25 and 0.125m, respectively. The three models are respectively referred to in this thesis as "the coarse model," the intermediate model" and "the fine model." In this context, the terms "simulation" and "model are used interchangeably.

3.2.2 BOUNDARY CONDITIONS

Boundary conditions are artificially imposed constraints applied at the model edges in order to limit the problem to the finite domain of interest. In the simulation of the Mount Polley failure, mixed boundary conditions were used:

- For mechanical calculations, a fixed boundary condition was applied upstream, downstream, bottom and lateral faces of the domain where the velocity component in the direction normal to a face is set at zero.
- For flow calculations, stress distributions were specified on the upstream and downstream faces of the model (see §3.2.4).

The physical boundaries of the model were set as follows:

- The width of the model (along the y-axis in the direction normal to the slide movement) was set at 300m wide, ~150m away from the slide centre on each side and ~100m wider than the actual width of the slide at its base. At this width, the left and right boundaries were deemed to be sufficiently far away from the simulated failure so as to not interfere with the solution; this assumption was later confirmed by examining the simulation results.
- In the coarse and intermediate models, the length of the model (along the x-axis parallel to the slide movement) was set at 182m, with the upstream face defined 42m upstream of the dam centreline and the downstream face defined 140m downstream of the dam centreline and ~65m downstream of the dam toe. At this length, the upstream and downstream boundaries were deemed to be sufficiently far away from the simulated failure as to not to interfere with the solution. This assumption was supported by preliminary analyses that show the failure surface developing in the crest region at a distance of 5-15m upstream of the dam centreline, and in the region of the toe 80-90m downstream of the dam centreline. An examination of the simulation results (specifically of the safety factors) further supported this assumption.
- In the fine model, the upstream and downstream boundaries were moved, respectively, to 34m upstream of the dam centreline and 132m downstream of the dam centreline. Such modification of the model boundaries was done to maximize mesh discretization levels while maintaining a reasonable number of zones as well as sufficiently minimizing interference with the model response.

3.2.3 SOIL PROPERTIES

3.2.3.1. GLACIAL TILLS

The foundation at the Mount Polley TSF failure location is largely formed of glacial tills sequentially deposited during at least three glaciation periods. These deposits are differentiated mostly by their void ratios, preconsolidation pressures and shear strengths (Table 3.1). A variety of interstitial deposits, including the Upper GLU, the Lower GLU and a variety of glaciofluvial materials, are found at the interfaces of these tills and serve as separation pointers for distinct glaciation events.

Of the three glacial till deposits present in the foundation at the failure location, the UGT was the only one involved in the failure. This material is dense, exhibits a high shear strength and was lightly overconsolidated prior to construction. Laboratory tests conducted on this soil by KCB (2015) suggest that consolidation processes induced by embankment loading changed this unit's strength in the later stages of construction, with the friction parameter ϕ' decreasing from 35° to 33° in extension and 34° in compression. In the three-dimensional model of the Mount Polley failure, this material was modelled using material parameters determined from IRP (2015) and KCB (2015) laboratory tests. A Mohr-Coulomb strength envelope was used with a cohesion c' = 0kPa, and a friction angle ϕ' varying from 35° in construction stages 3-7 to 33° afterward. A dry density value of 1851 kg/m^3, and a void ratio value of 0.41 were selected.

The other glacial till units are located below the Upper GLU and remained largely intact. KCB (2015) further differentiates these tills into the Middle Glacial Till and the Lower Glacial Till, while the IRP (2015) treats them as a single unit. In the three-dimensional model of the failure, these tills were treated as a single soil type using a Mohr-Coulomb strength envelope with a friction angle ϕ'=32° and a cohesion c'=0kPa, a dry density value of 1827 kg/m^3, and a void ratio of 0.5.

The deformation moduli of the tills were estimated from cone penetration tests conducted by ConeTec and pressuremeter tests conducted by In-Situ Engineering for the IRP (2015, Appendix D) and KCB (2015) using the approach documented by Rocscience (2016) and Robertson (2009). Select calculations are included in Appendix 3F. The selected values were verified against published data by Obrzud and Truty (2018), Bowles (1988), Kezdi (1974) and FLAC3D documentation (Itasca 2018). The design values are listed in Appendix 3C, Table 3C.1.

Table 3.1 Select mechanical properties of glacial tills at the Mount Polley TSF.

Void ratio (-)	Dry Density (kg/m^3)	Preconsolidation pressure (kPa)	Friction angle (°)	Undrained strength ratio (-)	Source
Upper Glacial Till Unit (UGT)					
0.41	2023	200	33…34 (under embankment) 35 (free-field)	0.38	KCB 2015
0.38-0.74	1851	76-380	35	0.43	IRP 2015
Middle Glacial Till Unit (MGT)					
0.5	1960	400	32	-	KCB 2015
Lower Glacial Till Unit (LGT)					
0.5	2021	-	35	-	KCB 2015
0.448-0.456	1827	331-355	-	-	IRP 2015

3.2.3.2. THE UPPER GLU

The Upper GLU played a pivotal role in the 2014 failure at the Mount Polley TSF. The unit's geomechanical properties, along with its location relative to the embankment, were thought to be critical to the development of a progressive yield zone, ultimately leading to the collapse of the embankment.

The position of the Upper GLU relative to the failure location (in Figure 2.1) was particularly unfavourable. The region under a slope typically experiences some of the largest shear-to-normal stress ratios. The rotation of the stress tensor under the asymmetric embankment loading causes the plane of critical stress to rotate to a position closer to horizontal, promoting shearing in the downstream direction. These factors make the presence of a strain-weakening material with a sub-horizontal macrostructure (such as the Upper GLU) under the embankment especially problematic.

In Chapter Two of this thesis, a determination has been made on the basis of three-dimensional static analyses that (a) undrained shear strengths controlled the mechanical behaviour of the Upper GLU at failure, and (b) post-peak undrained resistance, possibly at or close to residual values, was acting on average along the base of the slip surface passing through this unit. Two potential causes for such strength reduction were identified from the literature and from static three-dimensional analyses in Chapter One: (a) sensitivity and (b) post-peak strength reduction due to particle realignment. The latter was ruled as improbable due to a lack of field evidence of pre-sheared planes, and a hypothesis was adapted that the strength reduction to post-peak values in the Upper GLU was owed to the unit's sensitivity. This hypothesis forms the foundation of the constitutive model developed to simulate the mechanical behaviour of this material over the course of the embankment construction up to its collapse.

To recap, the Upper GLU is a varved clayey soil with a sensitivity of ~2-3. Prior to the embankment construction, this unit was overconsolidated. As the construction proceeded, the effective stresses in the ground gradually increased and a portion of the Upper GLU located under the embankment became normally consolidated. As a result of this change, this section of the Upper GLU became susceptible to undrained failure, opening up the potential for progressive failure in this strain-weakening material.

The extensive laboratory testing data and soil classification by the IRP (2015) and KCB (2015) were used to develop and calibrate two distinct strength models: drained and undrained. In the simulation, the appropriate model was selected on the basis of the current preconsolidation pressure that was tracked throughout.

Soil classification and general properties

The Upper GLU is a clay soil of glaciolacustrine provenance. It is a varved deposit categorized as CL-CH according to the Unified Soil Classification System (IRP 2015; KCB 2015). It has a sub-horizontal macro-structure with thin laminations (IRP 2015, Figure 5.2.8; KCB 2015, Figure 5.10). Based on reported in-situ moisture contents of 32 – 36%, a specific gravity of 2.7 – 2.77 and fully saturated conditions, a dry density of 1351kg/m^3 and a void ratio of 1.2 were adopted for modelling purposes.

Consolidation tests on undisturbed Upper GLU samples were used to determine the soil's preconsolidation pressure prior to construction. Oedometer tests by Thurber Engineering (IRP 2015, Appendix E2) show preconsolidation pressures σ_p' ranging between 300 and 535kPa, with a mean value of 433kPa. Oedometer tests show preconsolidation pressures σ_p' ranging between 380 and 420kPa, with a mean value of 400kPa (KCB 2015, Figure 5.15).

In addition to one-dimensional consolidation tests, Klohn Crippen Berger conducted a series of direct simple shear (DSS) tests on undisturbed Upper GLU samples (KCB 2015, Figure 5.22). Even though DSS tests are intended to investigate the undrained strength behaviour of a soil in a stress state of simple shear strain (ASTM D6528-17, 2017; Bjerrum and Landva 1966), they also offer an indirect way to evaluate the preconsolidation pressure of a soil using the strength ratio relationship reported by Ladd (1991):

$$\frac{s_u}{\sigma'_{ov}} = S_{fv} * \left(\frac{\sigma'_p}{\sigma'_{ov}}\right)^m \qquad \textit{Eq. 3.1}$$

where S_{fv} and m are constants evaluated from testing data, s_u is the undrained shear strength of the soil, σ'_{ov} is the in-situ overburden effective stress and σ'_p is the vertical preconsolidation pressure.

The direct shear test data available for undisturbed Upper GLU samples were used to find the best fit curve of the form shown in Eq. 3.1 by varying the preconsolidation pressure between 380 and 500kPa. A value of 430kPa was found to generate a curve that provided the best fit for the testing data (see Appendix 3B). This preconsolidation pressure value was adopted for modelling purposes.

In the model, Upper GLU zones with vertical effective pressures below this value were assigned the drained strength model and the ones that reached or exceeded it were assigned the undrained strength model.

Initial values for deformation moduli were estimated from cone penetration tests conducted by ConeTec and from pressuremeter tests conducted by In-Situ Engineering for the IRP (2015, Appendix D) and KCB (2015) using the approach documented by Rocscience (2016) and Robertson (2009). Select calculations are included in Appendix 3F. The selected values were verified against published data by Obrzud and Truty (2018), Bowles (1988), Kezdi (1974) and FLAC3D documentation (Itasca 2018) and calibrated against laboratory testing data. The in-situ tests indicate that the Upper GLU is slightly stiffer than the upper till deposit above it. The selected values of the deformation moduli are listed in Appendix 3C.

Drained strength

The drained model used in the deformation analysis of the Mount Polley failure was developed on the basis of triaxial test results reported by the IRP (2015, Appendix E4) and by KCB (2015, Appendix VI).

The IRP's (2015) consolidated undrained triaxial tests were conducted on undisturbed Upper GLU samples over a range of mean effective stresses p between 130 and 420kPa, thus capturing this soil's overconsolidated behaviour. The triaxial data, fitted to a linear regression model, produce the following linear envelope strength parameters:

$$c' = 30 \ldots 33 \text{ (kPa)}$$

$$\phi' = 21 \ldots 22°$$

These parameters are consistent with a Mohr-Coulomb envelope of an overconsolidated clayey soil such as the Upper GLU.

The KCB (2015) triaxial compression tests were conducted on thin-walled and block samples over a range of mean effective stresses p between 400 and 800kPa, capturing both overconsolidated and normally consolidated behaviours of the Upper GLU. The triaxial data, fitted to a linear regression model with a zero intercept, produce friction angle values ϕ' of 22 and 28° for block samples, and 25 and 32° for thin-walled samples.

In selecting the parameters for a Mohr-Coulomb failure envelope to best represent the drained strength behaviour in the Upper GLU, a couple of considerations discussed below were evaluated.

The state of the Upper GLU over the course of the construction, especially during the unfolding of the progressive failure: Prior to the construction of the embankment, the effective vertical stresses in the Upper GLU were estimated to be in the range of 100kPa and the unit's overconsolidation ratio was around 4. The strength behaviour of this soil would be well represented by a Mohr-Coulomb envelope with a non-zero cohesion value such as the one reported below:

$$\tau_{ff} = \sigma'_{ff} * \tan 22° + 31\ (kPa)$$

As construction proceeded, the effective stresses gradually increased in some critical portions of the Upper GLU located directly under the embankment toe and immediately downstream of it. In all, about one quarter to one third of the Upper GLU was ultimately involved in the failure, with some portions being normally consolidated and others being overconsolidated at the time of failure. Preliminary deformation modelling results indicate that in this critical portion of the Upper GLU, vertical effective stresses either came close to or exceeded the preconsolidation pressure value of 430kPa as early as construction stage 4, about eight years prior to the global failure. Consequently, those areas of the Upper GLU involved in the failure that did not exceed the unit's preconsolidation pressure had vertical consolidation stresses close to 430kPa and were only lightly overconsolidated with an overconsolidation ratio <1.2. The strength behaviour of such materials is better represented by a Mohr-Coulomb envelope with a zero or near-zero cohesion value.

Testing parameters, sample disturbance and failure modes: Of the four triaxial tests conducted by KCB (2015), three were completed on specimens consolidated to vertical effective stresses of 400kPa, and one on a specimen consolidated to a vertical effective stress of 800kPa. Two of the four samples were from thin-walled tubes and failed across the bedding planes. The other two specimens, including the one consolidated to 800kPa, were obtained from block samples and failed along the bedding planes. Block samples are arguably less susceptible to disturbance during extraction and preparation than thin-walled tubes, and failure along the bedding planes is more representative of the Upper GLU's failure mode in the field, as evidenced by significant horizontal displacements observed in situ.

With these two considerations in mind, the following strength model was selected to represent Upper GLU's drained behaviour in the deformation analysis:

$$\tau_{ff} = \sigma'_{ff} * tan\,22° \qquad \text{Eq. 3.2}$$

This model matches the drained strength model adapted by KCB (2015) for its own two-dimensional analyses of this failure.

In the three-dimensional deformation model of the Mount Polley failure, the Upper GLU was shown to fail as a drained material in the region of the slide toe, where the involved materials rotated upward to form the "whaleback" features documented by the IRP (2015) and KCB (2015). This finding is consistent with the theoretical understanding that drained failure takes place at an angle α_{cr}=45°+ϕ'/2=56° to the plane of major principal effective stress, the latter acting on a near-horizontal plane in this region.

Undrained strength

During the failure at the Mount Polley TSF, the mass of displaced material rapidly shifted in the downstream direction in a rotational-translational movement. The nature of the observed deformation in the Upper GLU suggests that in this unit, displacements were largely horizontal (with the exception of the slide toe, discussed in the previous section). A shearing of this type is thought to be approximated, to a degree, by DSS tests (Bjerrum and Landva 1966; Ladd 1991). Such tests offer a means to quantify a soil's propensity to weaken as a function of straining and/or disturbance when strained more or less in simple shear.

There are a couple of important reasons for exercising caution when interpreting DSS testing results in terms of strain-stress relationships. First of all, DSS tests, intended to evaluate the undrained shearing resistance of a soil consolidated under K_0 conditions, do not accurately replicate in-situ strengths in the latter stages of embankment construction, where a deviation from such conditions takes place due to the rotation of the stress tensor (Ladd 1991, p. 567). Researchers have demonstrated that anisotropic consolidation resulting from such deviation from K_0 conditions produce lower undrained shear strength values in cohesive high plastic soils (Wrzesinski and Lechonowisz 2013). In accepting DSS tests as being sufficiently representative of in-situ conditions, one must recognize that a degree of uncertainty about the true magnitude of in-situ strengths is introduced into the model. Second, the manner in which the soil is strained in a DSS test is different from in-situ conditions, especially in the latter testing stages. As a consequence, the rate of strain-weakening and/or the shape of the strain-weakening curve in a DSS test may not be fully representative of in-situ behaviour. Therefore, while DSS tests provide a good starting point for developing a constitutive model, the insights they generate about strength magnitudes and strain-weakening rates of in-situ soil elements should be evaluated in the context of modelling results and field observations.

Direct simple shear tests on undisturbed Upper GLU specimen conducted by KCB (2015, Figure 5.23) form the basis of the unit's initial undrained shear strength model. These were replicated in a FLAC3D DSS test model developed specifically for this purpose and calibrated for best fit by modifying the shape of strain-weakening curve.

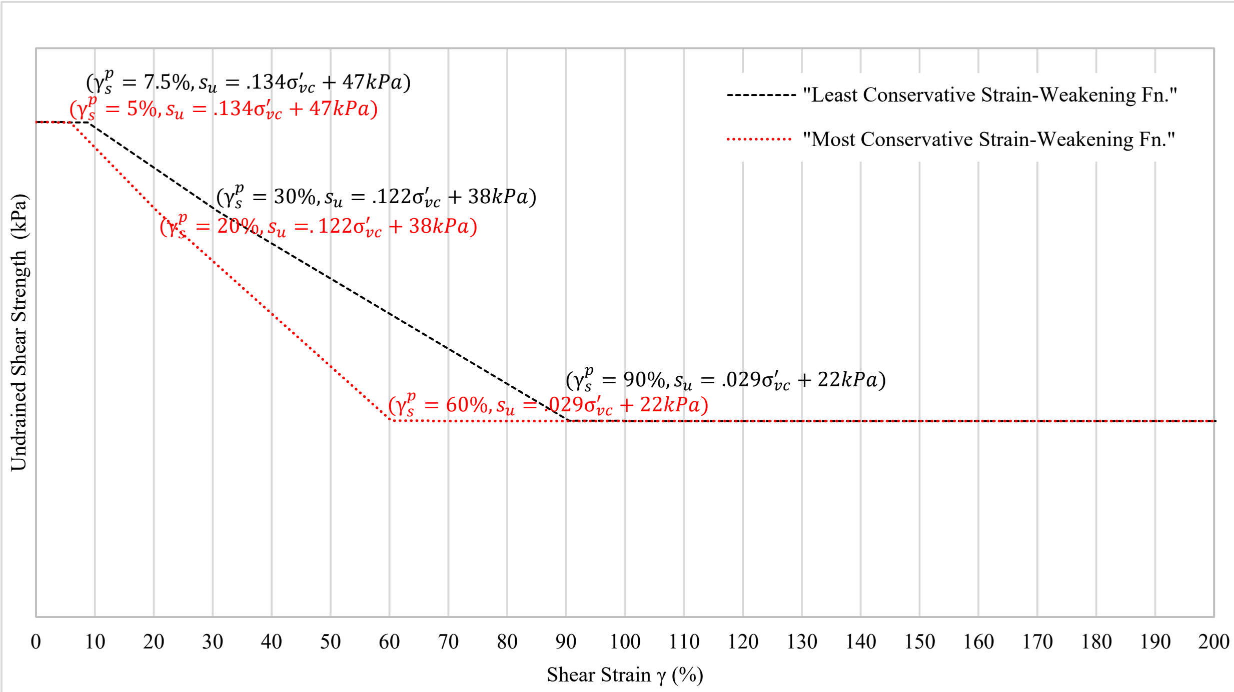

Figure 3.6 Upper GLU's least and most conservative undrained strength models.

The calibration graphs of the modelled DSS tests and their respective strain-weakening functions are found in Appendix 3B; simulations 1 and 2 were both judged to adequately fit the laboratory data. The strength model used to generate simulation 1 matches the undrained strength model proposed by Klohn Crippen Berger (2015) and represents the most conservative interpretation of the DSS data whereby the onset of weakening takes place at plastic shear strains of 5% and full weakening takes place at plastic shear strains of 60%. The strength model used for simulation 2 represents a less conservative interpretation of the DSS data whereby the onset of weakening takes place at plastic shear strains of 7.5% and full weakening occurs at plastic shear strains of 90%. The strain-weakening curves representing the undrained strength models in simulations 1 and 2 are pictured in Figure 3.6.

The strength model used to generate Simulation 1 forms the basis of the initial constitutive model used to model the Mount Polley failure. The undrained strength model was ultimately revised based on the evaluation of simulation results and modified to its final form (see §4.3.2 and §6.5).

Implementation of the Upper GLU's constitutive model

The deformation behaviour of strain-weakening soils in slopes and foundations has been successfully replicated by researchers in two- and three-dimensional finite element analyses (Potts et al. 1990; Lobbestael et al. 2013; Conte et al. 2013; Troncone et al. 2016). On reviewing literature and evaluating several strain-weakening constitutive models, an approach similar to that reported by Lobbestael et al. (2013) was deemed most appropriate whereby the weakening of strength parameters is related to the accumulation of plastic shear strains by means of a user-specified function.

FLAC3D's built-in constitutive model *strain-softening* allows the user to specify strain-weakening functions by defining the strength parameters through a series of continuous piece-wise linear functions of accumulated deviatoric plastic strain (Itasca 2018). The Upper GLU's complicated strength behaviour over the course of embankment construction was captured in the FLAC3D analysis through a combination of this constitutive model, a number of custom functions written in the software's internal language FISH and subroutine processes run in parallel with the solver. At the start of the modelling process, all Upper GLU zones are assigned the drained strength model and a preconsolidation pressure of 430kPa. As an initial step to establish custom undrained strength models for all of the Upper GLU zones that eventually become normally consolidated, a series of tables containing strain-weakening functions for the undrained shear strength are declared and defined. As FLAC3D proceeds to solve the model, a subroutine process is run at a predefined frequency with the purpose of evaluating each Upper GLU zone's current stress state and, if warranted, update its strength model based on its current preconsolidation pressure. An implementation flowchart for the Upper GLU's constitutive model is provided in Appendix 3B.

3.2.3.3. ROCKFILL

At the Mount Polley TSF, the rockfill zone had the function of buttressing the core against excessive deformation. The three-dimensional limit equilibrium analysis of the failure introduced in Chapter Two provides good indication that a significant amount of resistance against sliding was generated in this relatively high-strength material. Even so, the exact extent of mobilized resistance in the rockfill cannot be properly estimated by means of limit equilibrium analysis as this approach does not take into consideration stress-deformation relationships and is therefore unsuited for models consisting of a combination of materials with sharply contrasting deformation moduli.

In the failure at the Mount Polley TSF, the Upper GLU exhibited a mechanical response whereby upon the accumulation of low levels of shear displacements its undrained shear resistance was reduced, potentially to residual values. Such a response can be described as "brittle" in accordance with the criteria listed by Hobbs (2015, Ch. 8) including an associated loss of cohesion, the development of a localized continuous deformation zone and sensitivity to changes in pore pressure. On the other hand, during collapse, the rockfill in the shell zone at the failure location underwent large scale deformations that are suggestive of a ductile material. Rockfill materials have been shown to be ductile at low normal effective stresses, manifesting an increase in their deformation moduli as a function of σ'_3 or $⅓I_1$ (Leps 1970). For these reasons, it is conceivable that peak resistance in the Upper GLU and in the rockfill were not mobilized simultaneously.

Consequently, one must accurately evaluate both the strength and the extent of strength mobilization in the rockfill throughout the course of this progressive failure in order to map out the evolution of stress and deformation behaviour in the Upper GLU.

The most common method for determining the strength behaviour of rockfill is by conducting large scale triaxial tests on representative samples. The investigations of the Mount Polley failure by the IRP (2015) and KCB (2015) did not include such testing, as determining the exact progression of the failure and its three-dimensional effects was not essential to the completion of their stated goals. As a consequence, proxy indicators, such as the soil classification of rockfill and information about its placement and compaction, were used to compare this material to other rockfill materials in order to find identify a suitable model for its strength behaviour.

Soil classification

According to the dam construction logs evaluated in KCB's report (2015, p. 7, I-5, I-6), the rockfill was deposited in two distinct phases, the first one taking place over the course of construction stages 1 to 6 and the second one over the course of construction stages 7 to 9:

- During construction stages 1 through 6, the rockfill was deposited by means of truck dumping in lifts varying in thickness from 1 to 2m and compacted by 10-ton vibratory smooth drum rollers in four passes or more. The material was sourced from the Rock Borrow, the Wight Pit, the Springer Pit, the Southeast Zone and the Pond Zone Pits.
- In stages 7 through 9B, the rockfill was deposited in lifts of 1.2-2m by end-dumping, resulting in a slope equal to the angle of repose of about 38°. At this time, the material was comprised of run-of-the-mine waste rock from Springer Pit and compacted by haul trucks and spreading equipment.

The rockfill material had relatively uniform gradation and was composed of fine to coarse gravel with trace to some sand, some cobbles and trace of boulders, with a recorded fines content of 10% (KCB 2015, p.7, Appendix I-D). No differentiation in the particle size distribution of the rockfill as a function of its time of deposition or source was noted.

The information about the grain size distribution and placement methods summarized above suggests a classification of this material along the guidelines laid out by Leps (1970) and Marsal (1973) as a weak to medium strength rockfill.

The laboratory tests by KCB (2015) place the rockfill's in-situ dry density at around 2025 kg/m^3, with a porosity of 0.25 and a saturation of about 20%. As-built reports place the rockfill's fines content at 10%.

Strength model

The exploratory three-dimensional limit equilibrium analysis of the Mount Polley failure evaluated a variety of strength envelopes for weak and average rockfill material produced by Marsal (1973); the analysis results indicate that the shape of the strength envelope of the rockfill has a negligible impact on stability, with safety factor variations less than 2% from the average value (§2.5.1.3). Strength envelopes for samples 1 to 4 in Marsal's (1973, p. 166) were identified as suitable candidates to form the basis of a strength envelope in FLAC3D.

The selected strength envelopes were evaluated against the aggregate data assembled by Leps (1970) to ensure that they fall into the lower to medium range of tested strength values for rockfill materials, corresponding to low to medium density, poorly to fairly graded rockfill materials with weak to average particles. The plot combining Marsal's aggregate rockfill strength data with the testing results for samples 1 through 4 is seen in Figure 3.8. From the plot, it can be seen that samples 1 and 2 fall within the range of strengths corresponding to weak-to-average rockfill materials. It is worth noting that testing data is sparse for the range of effective stresses below 1MPa, which is also the range of effective stresses in the rockfill at Mount Polley.

The strength envelopes illustrated in Figure 3.7 can be approximated by a variety of strength models available in the modeling software FLAC3D. Two constitutive models were evaluated for this purpose: the Hoek-Brown model and a custom Mohr-Coulomb model with strength parameters

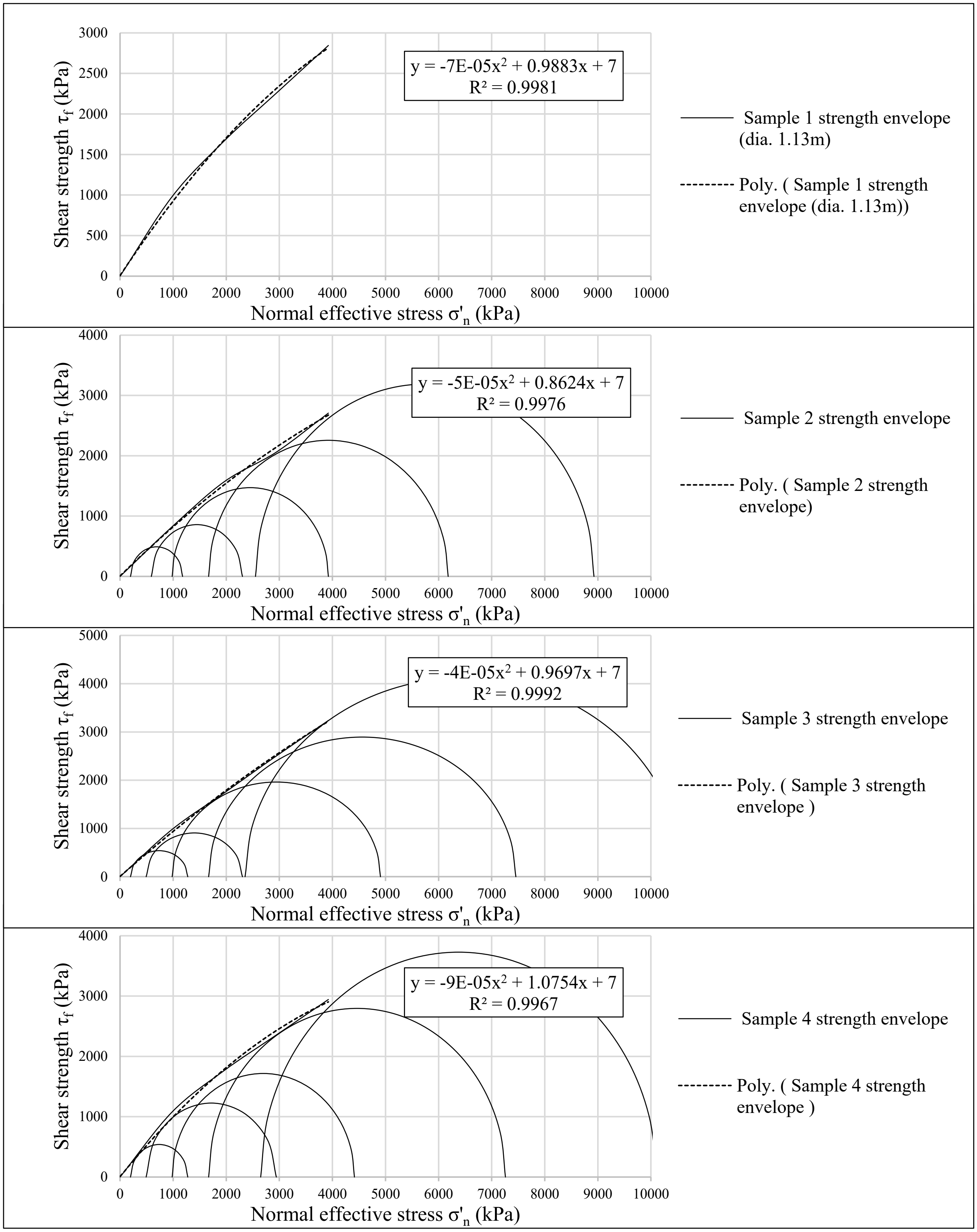

Figure 3.7 Triaxial testing results and strength envelopes for weak to average rockfill materials (from Marsal 1973, p. 166).

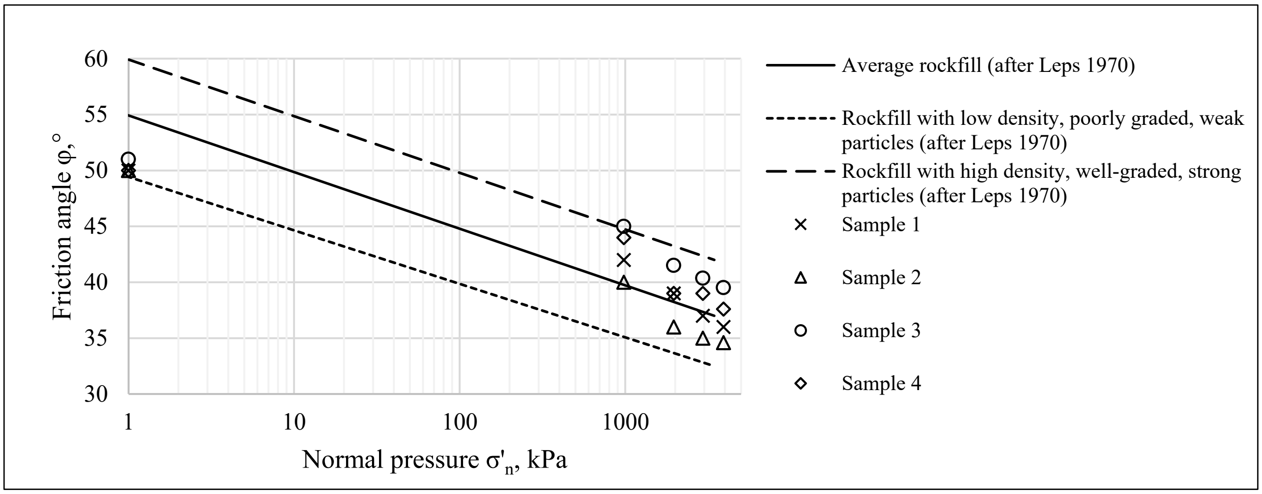

Figure 3.8 Rockfill strength envelopes for samples 1-4 from Marsal (1973, p.166) plotted against aggregate data from large scale triaxial tests on rockfill assembled by Leps (1970, Figure 1).

that vary as a function of stress. The implementation of each model and its associated advantages, disadvantages, issues and errors are discussed further.

The Hoek-Brown model

The Hoek-Brown failure criterion is a strength envelope developed using empirical data to describe the type of material whose peak stress σ'_1 increases non-linearly as a function of the confining stress σ'_3. Its curved envelope mimics the strength behaviour observed in rock materials and is approximated by a power function of the general form (Hoek 1983):

$$\sigma_1 = \sigma_3 + \sigma_{ci}(m_b \frac{\sigma_3}{\sigma_{ci}} + s)^a \qquad \textit{Eq. 3.3}$$

The input variables σ_1 and σ_3 are the effective principal stresses recorded in a sample of no less than five drained triaxial tests performed on a material; the parameters a, σ_{ci}, s and m_b are evaluated using regression analysis.

The Hoek-Brown failure criterion was thought to be suitable to represent the curved envelopes of the selected rockfill materials. Triaxial test results for samples 2, 3 and 4 published by Marsal (1973) were used to evaluate the Hoek-Brown failure envelope parameters. The evaluations, provided in full in Appendix 3A, show that no real values for the parameters σ_{ci} and m_b are generated using these particular sets of triaxial tests, inviting the conclusion that the Hoek-Brown failure criterion cannot be adapted for these materials using the available data.

A custom Mohr-Coulomb model

The Mohr-Coulomb failure envelope describes a material whose shear strength along any plane increases linearly as a function of the effective normal stress acting on that plane. The parameter controlling the rate of change in shear strength due to a change in normal stress is known as the effective friction angle ϕ'; the portion of shear strength that is constant and does not vary with normal stress is known as the cohesion parameter c'.

In FLAC3D, the Mohr-Coulomb constitutive model requires the input of two parameters, ϕ' and c', as constant values associated with a single grid element. In order to adapt this constitutive model to a material with a non-linear failure envelope, the equivalent friction angle ϕ' and cohesion c' are determined for any value of normal effective stress. If the material's failure envelope can be approximated, over the range of in-situ stresses, by one or more algebraic relationships of the form $\tau_f = f(\sigma_n') = f$, then the equivalent values of ϕ' and c' can be found as functions of normal stress using the following relationships:

$$\phi'_{eq} = \tan^{-1}\left(\frac{df}{d\sigma'_n}\right) \qquad \textit{Eq. 3.4}$$

$$c'_{eq} = \tau_f - \left[\frac{df}{d\sigma'_n}\right]\sigma'_n \qquad \textit{Eq. 3.5}$$

Figure 3.9 illustrates the above concept using a generic non-linear strength envelope.

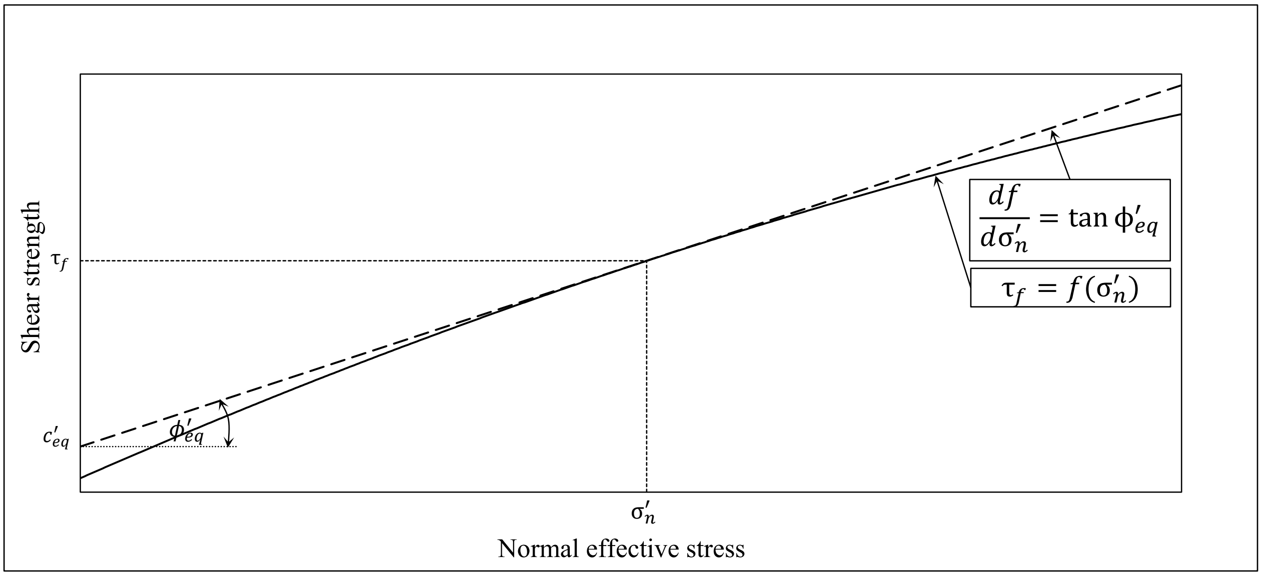

Figure 3.9 Schematic representation of a non-linear shear strength envelope and its equivalent Mohr-Coulomb strength envelope.

Algebraic approximations of failure envelopes: The non-linear strength envelopes of rockfill samples 1 to 4 were adequately approximated, over a range of effective stresses between 0 and 4MPa, by power functions of the second order (shown in Figure 3.7 and Table 3.2).

Table 3.2 Functions approximating the failure envelopes of samples 1 to 4 and equivalent Mohr-Coulomb strength parameters.

Sample No.	Strength envelope approximated by algebraic relationship (kPa):	R^2	φ'_{eq}	c'_{eq} (kPa)
1	τ_f=-0.00007$(\sigma'_n)^2$+0.9883(σ'_n)+7	0.9981	$\tan^{-1}$(-0.00014σ'_n+0.9883)	τ_f-(-0.00014σ'_n+0.9883)σ'_n
2	τ_f=-0.00005$(\sigma'_n)^2$+0.8624(σ'_n)+7	0.9976	$\tan^{-1}$(-0.0001σ'_n+0.8624)	τ_f-(-0.0001σ'_n+0.8624)σ'_n
3	τ_f=-0.00004$(\sigma'_n)^2$+0.9697(σ'_n)+7	0.9992	$\tan^{-1}$(-0.00008σ'_n+0.9697)	τ_f-(-0.00008σ'_n+0.9697)σ'_n
4	τ_f=-0.00009$(\sigma'_n)^2$+1.0754(σ'_n)+7	0.9967	$\tan^{-1}$(-0.00018σ'_n+1.0754)	τ_f-(-0.00018σ'_n+1.0754)σ'_n

Tensile cut-off and minimum cohesion value: The soil classification of rockfill at Mount Polley gives an indication that the material's tensile strength is zero and its minimum cohesion is close to zero.

For modelling purposes, assigning a nominal non-zero cohesion value to the rockfill may be useful as it enables the modeller to maintain a uniform internal geometry (i.e. composed of elements that are shaped as near-undistorted cubes) without triggering localized failures along the cubic-shaped faces. The minimum cohesion value that would not trigger local failure depends on the size of the element; practitioners commonly use values around 5kPa. The failure envelopes of rockfill samples 1 to 4 can be approximated with a high degree of accuracy using an intercept value of 7kPa.

Equivalent Mohr-Coulomb strength parameters for Samples 1 to 4: The algebraic functions approximating the strength envelopes of Samples 1 to 4 from Marsal (1973, p. 166) were used in Eq. 3.4 and Eq. 3.5 and 3 to find the equivalent friction angle ϕ'_{eq} and cohesion c'_{eq} (the results are presented in Table 3.2).

Implementation in FLAC3D: In FLAC3D, the Mohr-Coulomb constitutive model requires the assignment of a number of parameters (deformation moduli, density, friction angle, cohesion, tension and dilation) as constants over each element of the model. This means that only one value of each equivalent friction ϕ'_{eq} and equivalent cohesion c'_{eq} can be assigned to a zone regardless of the range of effective normal stresses across that element and their associated equivalent linear failure envelopes.

To address this problem, the following procedure was adapted. It was noted that, over the range of in-situ effective stresses of 0 to 1000kPa, the equivalent friction angle of the failure envelopes for samples 1 to 4 varies between 37° and 47°, with an average value of about 42°. The critical value of the effective normal stress can be then approximated as the normal stress on the plane inclined from the plane of major principal stress at an angle of $\alpha = \pi/4+\phi'_{avg}/2$:

$$\sigma'_{\mathrm{n,cr}} = \sigma'_3 + \left[\frac{(\sigma'_1 - \sigma'_3)}{2}\right](1 - sin\,\phi'_{\mathrm{avg}}) \qquad \textit{Eq. 3.6}$$

This value is close to the normal effective stress acting on the critical plane of the element, i.e. $\sigma'_{n,cr} \approx \sigma'_{ff}$ if the element is in a state of failure. This concept is illustrated in Figure 3.10 using the sample 4 failure envelope as an example. The figure demonstrates that although the approximated value of $\sigma'_{n,cr}$ does not precisely correspond to the true normal effective stress, the difference

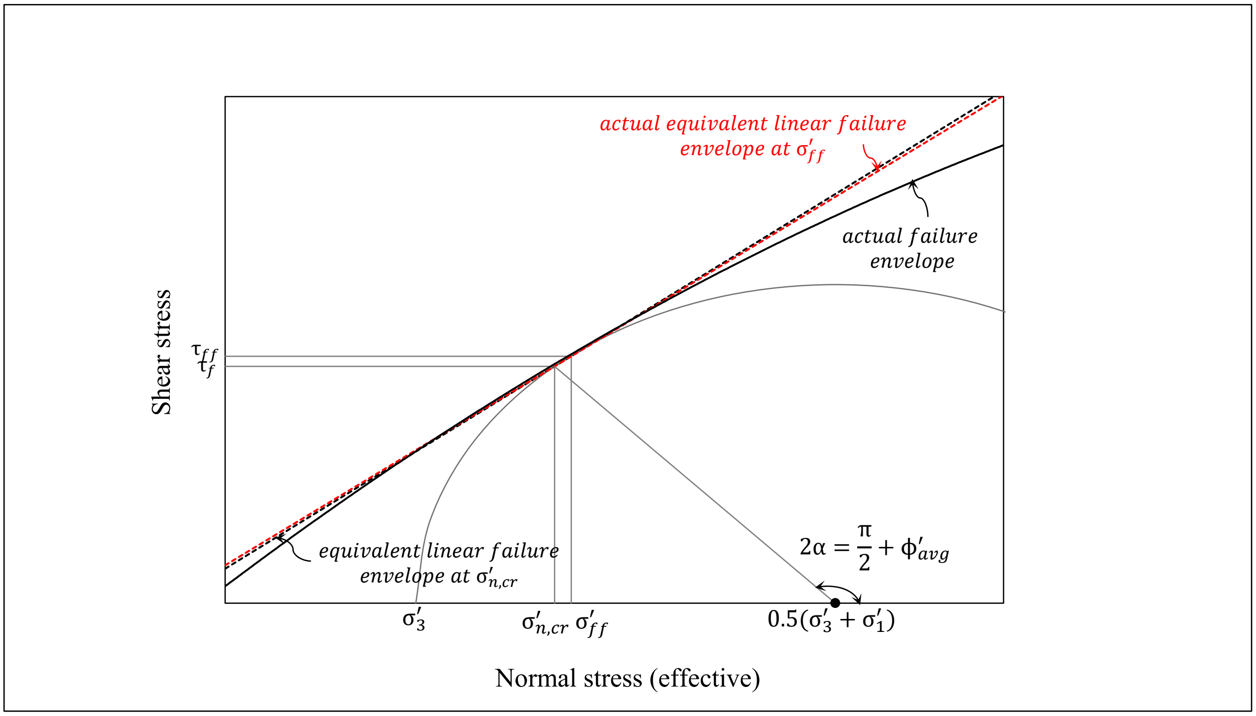

Figure 3.10 Estimated vs. actual normal effective stress on the failure plane for a zone element in a state of failure.

between the equivalent linear envelopes (and their corresponding ϕ'_{eq} and c'_{eq}) is negligible across the relevant range of stresses.

Deformation modulus

Leps (1970) documents a deformation-stress behaviour manifested by rockfill materials whereby axial strains at failure are much higher for high stresses than those for low stresses; loose, poorly graded, poorly compacted rockfills demonstrate a particular proclivity for this behaviour. Leps reports that axial strains recorded at normal pressures about or below 10 psi (≤70kPa) are significantly lower than those recorded at 100 psi (700kPa), the former being in the order of 0.3 to 0.5 of the latter.

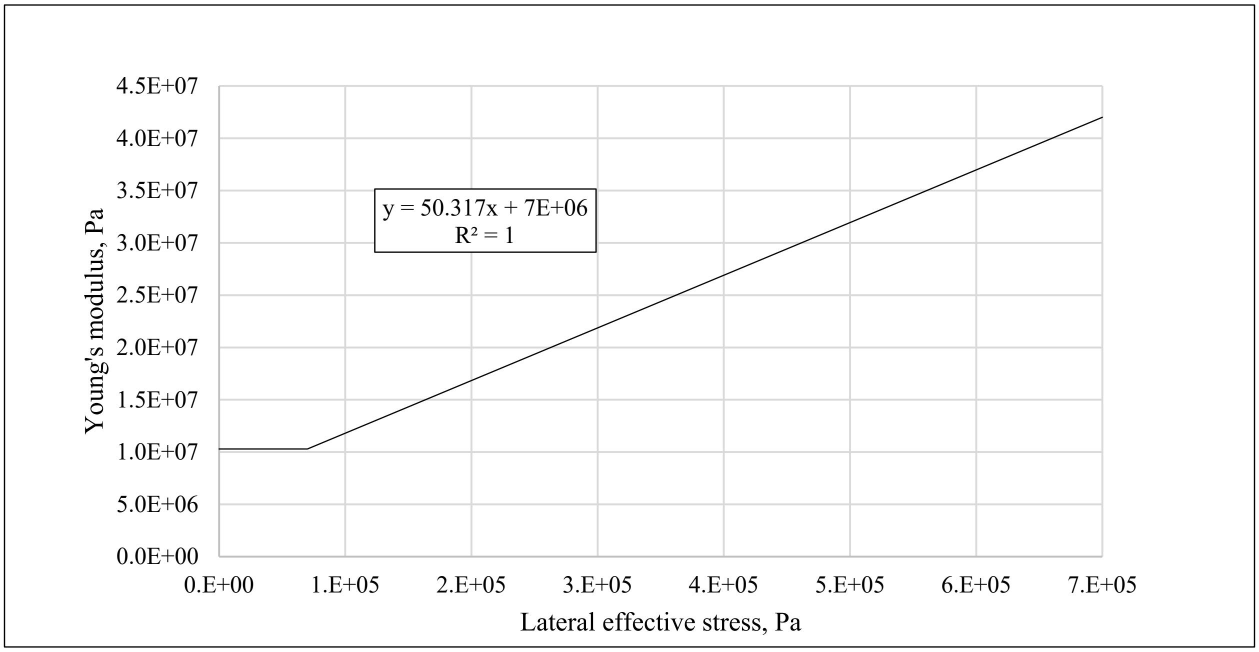

Figure 3.11 A model of the rockfill's Young's modulus as a function of minor principal effective stress.

With limited testing data, only a crude correlation can be established between lateral stresses and the deformation moduli of rockfills. A tentative relationship between a rockfill's lateral stress and its Young's modulus, developed based on triaxial data reported by Leps (1970), is presented in Figure 3.11; a lower cut-off value for Young's modulus was specified due to an absence of reported data for lateral stresses below 70kPa. This relationship was captured in the FLAC3D model of the Mount Polley failure with the use of a custom FISH function (included in Appendix 3A) that is actuated, along with the function for updating the rockfill strength, in a recurring manner during model cycling.

In developing the model of Young's modulus for the rockfill used in the analysis of the Mount Polley failure, a number of important assumptions were made.

First, the rockfill's deformation modulus and Young's modulus are assumed to be one and the same, one implication being that, in the model, a rockfill zone's current deformation is only a function of its current stress state. This assumption is generally incorrect when applied to soils and rock, but its use is acceptable in this specific case because in both circumstances, that of triaxial tests reported by Leps (1970) and that of the embankment construction at the Mount Polley TSF, the material was subjected to loading but not to unloading. As a result, any potential changes in the deformation behaviour of the rockfill due to its loading/unloading history would not be observed here. It is probably not advisable to use this same relationship for problems involving unloading as it is likely that the increase of lateral stress is associated with compaction in loose, uncompacted rockfill – a process that is largely irreversible on unloading and results in a change in the strain-stress behaviour of the material, as evidenced by the differences in deformation behaviours of compacted versus uncompacted samples reported by Leps (1970).

Second, the relationship between the rockfill's lateral stress and Young's modulus is assumed to be linear. With only two data clusters reported by Leps (1970), one on the lower side and one in the mid-range of lateral stress values, only a simple relationship, such as a linear one, is defendable. Two alternative options to this model were considered. In the first option, Young's modulus is assumed to be an averaged and constant value. In the second option, the rockfill zones are binned into either the "high lateral stress" or "low lateral stress" category and assigned, respectively, a high or low Young's modulus value. The approximation of Young's modulus by the linear relationship illustrated in Figure 3.11 offers a better error minimization strategy in the modelling of the Mount Polley failure than these two alternatives because the first ignores the distinct deformation behaviour of rockfill at low stress states, and the second one creates an unnatural split in the behaviour of an otherwise continuous mass of material.

Last, the rockfill's Young modulus was defined as a function of minor principal stress σ_3' and not as a function of spherical (i.e. confining) stress $\frac{1}{3}I_1$. In fact, both functions ($E = k_1\sigma_3'$ and $E = k_2 I_1$) were evaluated in calibration tests, and the difference was found to be inconsequential. Therefore, even though there may be a good case for defining a deformation modulus as a function of spherical stress, a decision was made in favour of the model requiring fewer guesses.

Implementation of the rockfill constitutive model

In the rockfill, the equivalent strength parameters $c'_{eq}$and ϕ'_{eq} as well as Young's modulus are functions of a zone's current stress state. Therefore, the proper implementation of its constitutive model requires that:

- An initial stress state is established in the rockfill prior to the application of the proposed model of strength envelope and Young's modulus;
- With ongoing stress state changes as the calculations proceed, the strength envelope parameters and Young's modulus must be periodically redefined in FLAC3D; and
- The application of Young's modulus values must be done in a gradual manner as to avoid abrupt transitions.

The implementation of the rockfill's constitutive model in the FLAC3D deformation analysis of the Mount Polley failure is shown in a flowchart in Appendix 3A. The strength envelopes for samples 2 and 3 were selected for implementation in the model and were both evaluated in early analyses; the difference in results was seen to be inconsequential.

3.2.4 PORE WATER PRESSURES

At the Mount Polley TSF, tailings were added to the storage pond in step with the embankment construction. Shortly after the completion of each new construction stage, completed at intervals of one year or more, pond elevations were raised to dam crest elevation minus some freeboard.

As a result, the groundwater regime at the site was complex, with transient flow conditions being triggered by all loading and pond elevation changes. An adequate model of the groundwater regime at the site need not fully replicate this complexity; instead, it must reasonably approximate those aspects of it that are relevant to the stability analysis.

This section summarizes the method used to evaluate the pore water pressure distributions in the three-dimensional model of the Mount Polley TSF that were used in the mechanical analysis to determine effective stress distributions and associated shear strengths. A detailed description of the method, including preliminary analyses, along with information on calibration and verification, is found in Appendix 3D.

3.2.4.1. SELECTION OF FLOW REGIME

Two types of groundwater flow regime are distinguished: transient and steady-state.

A steady-state groundwater flow regime is described by seepage and pore pressure conditions that remain constant over time. Under these conditions, effective stresses are also constant. Steady-state regimes are therefore associated with drained conditions.

A transient flow is triggered by any change in boundary conditions or loading, such as an increase in pond elevations or the addition of embankment material. These changes result in a readjustment of pore pressures over time, initiating soil consolidation processes and associated changes in shear strength. A transient flow is therefore associated with a transition from undrained conditions at the time a flow regime change takes place to drained conditions by the time the change-induced excess pore pressures fully dissipate. Consequently, effective stresses and shear strengths, including undrained shear strengths, vary as well.

In order to establish whether transient flow states affected the mechanical stability of the Mount Polley TSF structure over its lifecycle, a determination must be made whether there was sufficient time for transient pore water pressures to dissipate prior to the failure. Evaluations of the time rates of consolidation conducted by the IRP (2015, Figures H.A1-6 and H.A1-7) demonstrate that excess pore pressures induced by the staged addition of embankment material dissipated fully in most construction stages. In stages 5, 7 and 8, minor excess pore pressures (< 40kPa) persisted. Stage 9 was built in two phases starting in 2013; at the time of failure, the excess pore pressures were estimated at ~ 80kPa under the crest and < 40kPa under the mid-slope. In a separate investigation, Klohn Crippen Berger concludes that excess pore water pressures of about 97 to 158kPa may have persisted at failure in the Upper GLU portions located directly under the dam (KCB 2015, Appendix VI), which included the pore pressure spike induced by embankment works immediately prior to failure.

The dissipation of these remaining pore pressures would have contributed, in the Upper GLU, to a shear strength increase of 1 to 4kPa, or 3 to 10%, directly under the dam crest and considerably less elsewhere (see Section IV of Appendix 3D). Considering the minor effect of remaining excess pore pressures on shear strength, the use of fully drained conditions in the three-dimensional deformation analysis of the Mount Polley failure is warranted for the most part. The effect of undrained loading due to embankment materials added in the summer of 2014, amounting to a height increase of 3m in the shell zone, 1.4m at the core and 2m in the upstream zone, was simulated in the normally consolidated portions of Upper GLU material by halting the processes of re-evaluation of preconsolidation pressures and associated recalculations of its undrained shear strength when evaluating the stability of embankment in stage 9.

Drained conditions were evaluated in FLAC3D using uncoupled flow calculations until a steady state was reached. Separate flow analyses were conducted for construction stages 3 through 9.

3.2.4.2. BOUNDARY AND INITIAL CONDITIONS

In the three-dimensional analysis of flow at the Mount Polley TSF, the boundary and initial conditions were established using a combination of site information and the results of a series of two-dimensional seepage analyses.

Site information

Pond elevations: The construction reports from the Mount Polley TSF contain detailed information on pond elevations and embankment construction throughout the lifecycle of the structure. In a steady-state analysis, pond elevations represent an important boundary condition best described by constant head elevations at the surface of tailings. Pond elevations of about 941.5m, 944.0m, 947.5m, 954.0m, 957.0m, 960.0m and 966.83m were recorded following construction stages 3 through 9 (IRP 2015, Figure G1). Constant pore pressure values corresponding to these total heads were accordingly assigned to the top surface of tailings.

Internal drain: During the construction of stage 4, an internal drain was added in the tailings beach region upstream of the embankment core at an elevation of 946.3m. This created a drainage boundary in the tails and an associated low pore pressure zone around it. The internal drain was included as a boundary conditions for the analysis of stages 4 through 9, and was modelled as a region of constant pressure. The constant pressure values assigned to the internal drain region varied from 0kPa in stage 4 to 50kPa in stage 9 and were obtained by calibrating the two-dimensional steady-state seepage analysis against data from three piezometers installed in the area of the failure. The process used to estimate the boundary conditions in the region of drain is documented in Appendix 3D, Section II.

Two-dimensional steady-state seepage analysis

Two-dimensional steady-state seepage analyses of construction stages 3, 6 and 9 were conducted and calibrated against field data using the software package SoilVision® SVOffice™. The resulting steady-state pore pressure distributions were used to approximate upstream and downstream boundary conditions in the three-dimensional model by using pore-pressure gradient functions (listed in Figure 3D.6) and the position of phreatic surfaces after each construction stage. Additionally, the steady-state pore pressure distributions obtained in the two-dimensional seepage analyses of stages 3, 6 and 9 served as benchmarks to evaluate the quality of three-dimensional flow solutions.

A detailed description of the two-dimensional seepage analyses and their application in the three-dimensional model is found in Sections II and III of Appendix 3D.

It is worth noting that the initial distribution of pore water pressures at the start of flow calculations, approximated in the model by phreatic surfaces, has no bearing on the flow calculation results, as the steady-state seepage solution is independent of transient states and is defined solely by the model's boundary conditions and hydrological properties. However, defining initial conditions that are close to steady state speeds up the onset of steady state.

3.2.4.3. HYRDOLOGICAL PROPERTIES

The hydrological properties of the soils at the failure location were tested extensively by Klohn, Crippen and Berger (KCB 2015). The reported test results on the soils' hydraulic conductivities and porosities (or void ratios) were used as the foundation of the hydrological soil models. The selected hydraulic conductivity values were calibrated using the two-dimensional seepage analyses described in the previous section in order to verify that they result in steady-state pore pressure distributions that are reasonably close to those expected based on data from field instrumentation and consolidation analyses.

The soils' hydraulic conductivities and porosities used in the three-dimensional flow calculations are shown in Figure 3D.6.

3.2.4.4. FLUID MODEL

A number of soils involved in the failure at the Mount Polley TSF exhibit anisotropic permeability, with the ratio of horizontal to vertical hydraulic conductivities k_h/k_v ranging from 1 in uniform, homogeneous materials such as the rockfill to 10 in structured deposits such as the Upper GLU (KCB 2015, Tables 5.7, 5.8 and 6.2).

To explore the effect of this anisotropy on pore pressure distributions, two steady-state analyses of the stage 9 cross-section were conducted, one using the isotropic hydraulic conductivity model and the other using reported k_h/k_v values. The results of this analysis are illustrated in Figure 3D.3. While the two solutions are not identical, the main variations in pore pressure distributions appear to take place on the upstream, and the differences in the failure zone are not pronounced. In the Upper GLU, the anisotropic model predicts a piezometric surface only 0.2m higher than the one in the isotropic model. Additionally, the anisotropic model appears to be a poorer predictor of pressures observed in the piezometers installed in the dam materials (as seen from Table 3D.1).

The results of this analysis suggest that the use of the isotropic hydraulic conductivity model is acceptable. These conclusions are supported by findings reported by the Independent Review Panel whose two-dimensional consolidation analysis shows that anisotropy has only a minor effect on consolidation times (IRP 2015, Figure H.A1-7).

In FLAC3D, it is possible to use either the isotropic or anisotropic models, but the computational requirements for the latter are more significant. Therefore, a decision was made to use the former in the modelling of the Mount Polley failure. The results of the two-dimensional anisotropic analysis were consulted for verification.

3.2.4.5. CALIBRATION

The quality of the three-dimensional flow calculation results was evaluated using instrumentation records and prior analyses.

Instrumentation records used for calibration primarily include May to July 2014 readings from three piezometers, G1, G2 and G3, installed at Station 4+300 in the core and beach area at elevations roughly equal to that of the internal drain. The piezometers' elevations and positions relative to the dam centreline are shown in Figure 3D.1. These readings were assumed to represent steady-state seepage conditions after the completion of stage 9A works in 2013 (but not including embankment works done immediately prior to the failure). Both the two- and three-dimensional steady-state seepage analysis produce results that compare well to the actual readings (actual and modelled readings are reported in Table 3D.1).

To adequately reconstruct the history of pore pressure distributions through the lifecycle of the embankment, model calibration against the sparse instrumentation records was supplemented with a verification of results against the results of the two-dimensional seepage analysis. The cross-sectional aspects of the three-dimensional flow solutions for stages 3, 6 and 9 were compared to the two-dimensional seepage solutions. The piezometric elevations in the Upper GLU were reasonably comparable in the two- and three-dimensional flow analyses (seen respectively in Figure 3D.4 and Figure 3D.7), especially considering that the three-dimensional rendition of this soil unit has variations in elevation (from ~917m to ~924m) and shape not captured by the two-dimensional models.

3.2.4.6. RESULTS

The steady-state pore pressure distributions obtained by three-dimensional flow analysis are seen in Figure 3D.8.

3.3. MODELLING STRATEGIES

3.3.1 STAGED LOADING

In the interest of examining the progression of the failure at the Mount Polley TSF, the embankment was modelled in nine sequential steps to simulate construction stages 3 (completed in 2005), 4 (completed in 2006), 5 (completed in 2007), 6 (completed in 2010), 7 (completed in 2011), 8 (completed in 2012), 9A (completed in 2013) and 9B (ongoing at failure in August 2014). In stage 3, the embankment dry densities were gradually adjusted upward in three increments to simulate a more realistic stress path. In each step, uncoupled flow calculations were conducted to establish steady state pore water pressure distributions, followed by uncoupled mechanical calculations to establish a solution.

3.3.1.1. STRESS PATH

In each modelled construction stage, new embankment material can be added under two contrasting conditions: drained and undrained.

Under drained conditions, the added load results in an increase in both total and effective stresses and is supported by embankment and foundation materials that now have a higher shear strength than prior to its addition. Such modelling approach approximates field conditions where the new load is added very gradually, with plenty of time for the dissipation of excess pore pressures.

Under undrained conditions, the new load results in an increase in total stresses but also in a pore pressure response to those loads. As a result, the new loads are supported by the foundation and embankment materials that have not yet benefited from a gain in shear strength induced by the consolidation processes under the added load and additionally are experiencing some excess pore pressures that can affect their shearing resistance. This modelling approach simulates a field condition where the new load is added instantly and the pond level is simultaneously increased.

Transient conditions are seen in a model when a load is added under undrained conditions and coupled flow and mechanical calculations are performed in parallel to simulate a gradual transition from undrained to drained conditions. This modelling approach best reflects actual field conditions but is time-consuming and requires detailed records on water balance.

Each of the three modelling approaches impose different loading paths that may result in divergent outcomes. Therefore, it is of interest to investigate the effect of selected approach on the solution.

In §3.2.4.1, an argument was made that an uncoupled analysis under steady state pore pressure conditions is warranted for this problem. To verify the impact of the stress path on the outcome, a simulation of partially undrained conditions was also conducted whereby in each stage, the load was added under undrained conditions in the Upper GLU only, i.e. while halting the update of shear strengths in this unit. Once a static equilibrium was attained under such conditions, the strengths in the Upper GLU were updated to reflect the new loading conditions, and a new static equilibrium was attained. The outcomes obtained by the drained and partially undrained simulations were then compared to determine the magnitude of error associated with the drained assumption.

3.3.2 LARGE AND SMALL STRAIN SOLUTIONS

FLAC3D uses a Lagrangian calculation scheme to model deformation. This scheme is prone to grid distortion problems that become progressively more severe as strain accumulates. Models involving strain-weakening materials, such as the Mount Polley TSF, are especially susceptible to this problem, and their grids may distort to a point where the geometry of some zones becomes invalid.

The FLAC3D developers offer several strategies to overcome this problem:

- The calculations can be run in the “small strain mode” that is the default setting. In small strain, the strain increments for each timestep are calculated using the usual Lagrangian scheme, but the gridpoint coordinates are not updated to reflect the deformation increments. As a result, the grid remains unchanged and its shape does not reflect accumulated strains and deformations. This assumption is valid only in models where stresses are much lower in magnitude than moduli (Chambon 2002).
- When calculations are run in the “large strain mode,” the coordinates of gridpoints are updated after each timestep to reflect the deformation increments incurred over its duration; this creates a distortion of the grid that simulates the movement of material. Severe grid distortions can create geometry errors and are mitigated by either a procedure called “remeshing” or by halting the update of gridpoint coordinates in the problem zones. Currently, a number of other strategies to address the grid distortion problem are being conceptually explored and have not been yet implemented in practice; these include hybrid Lagrangian-Eulerian calculation schemes and streamlined zone repair or subdivision strategies (Russell 2018).

The Mount Polley failure was modelled using both the large and small strain modes; the results are reported in Chapters Four and Five of this thesis. Four strategies to mitigate geometry errors generated in large strain mode due to severe grid distortion were evaluated. These are: global remeshing, local remeshing, using a localized small strain mode for severely distorted zones, and zone repair. Appendix 3E documents this evaluation process.

The use of localized small strain mode in severely distorted areas was ultimately selected as most suitable option for the three-dimensional analysis of the Mount Polley TSF. The main concern with the application of this strategy is that, if enough zones are eventually switched to the small strain mode, the error associated with this mode may affect the large strain solution. Therefore, the application of this strategy was monitored by tracking the number and spatial distribution of zones that have been “switched off” during each calculation cycle. Over the course of modelling the Mount Polley TSF, the large strain mode was disabled in an insignificant fraction of zones (<0.01%). Lastly, the effect of the error associated with the small strain mode was evaluated by comparing the small strain and large strain solutions.

3.3.3 REACHING EQUILIBRIUM

In a FLAC3D deformation analysis of slope stability, a solution is considered to be found in one of the two cases: (a) when the model has reached a state of static equilibrium; or (b) when the model continues to deform indefinitely, i.e. it fails to converge. In the first case, the slope is considered stable with a safety factor above unity, and in the second case, the slope is unstable with a safety factor equal to or below unity.

FLAC3D has five different criteria for assessing convergence to static equilibrium, all of which evaluate, in a number of ways, the ratios of forces at the model’s gridpoints. One of the five criteria, termed “the average force ratio,” is defined as the ratio of the sum of all out-of-balance force components to the sum of all out of balance forces. This criterion using a default value of 10^{-5} (-) is considered to be a reliable measure of convergence. However, the FLAC3D manual advises caution in applying this criterion to non-uniform models or to models with large contrasts in stiffness, as “localized convergence problems can be lost in the average” (Itasca 2018). Both of these characteristics are present to some extent in the model of the Mount Polley TSF.

The average force ratio criterion using the default convergence value of 10^{-5} (-) was used in the Mount Polley TSF model as an initial indicator of static equilibrium. In addition to this criterion, several additional checks were put in place to ensure that all regions of the model have reached equilibrium. These include:

- Evaluating velocities at equilibrium. The Mount Polley failure was modelled in nine sequential steps to simulate the embankment loads added during construction stages 3 through 9B. The volume of material "added" in the model during each step was usually small relative to the rest of the model that was previously brought to equlibrium. As a result, the average force ratio would sometimes reach the default convergence value while local convergence in the added material was not yet attained. To ensure that convergence was reached in all regions of the model, the model was cycled past the default average force ratio value while monitoring velocities. As a rule of thumb, velocities in the order of 10^{-7} to 10^{-6} m/s throughout the system including in the newly added material are a good indicator of convergence.
- Evaluating displacements in key regions. Displacements were liberally tracked in the model regions known to be prone to deformation under new loading, such as the Upper GLU material under the embankment; the core; the rockfill; and the newly added embankment material. Convergence in these areas is reached when deformations stop accruing over time.

3.3.4 SAFETY FACTOR CALCULATIONS

3.3.4.1. THE CLASSIC DEFINITION AND INTERPRETATION

In engineering, a safety factor is generally understood to represent the ratio of maximum stress (i.e. strength) to the working stress in a structure. In lay terms, a safety factor is a measure of how many times stronger a structure is than it needs to be in order to support the current load.

Historically, factors of safety have been used as a main indicator of a slope's mechanical stability. The classic definition of the safety factor can be formulated for soils in terms of the Mohr-Coulomb failure criterion as follows:

$$\text{FOS} = \frac{shear\ strength}{shear\ stess} = \frac{1}{s}(c' + \sigma_n' \tan\phi') \qquad \text{Eq. 3.7}$$

where *FOS* denotes the safety factor, *s* represents the mobilized shear stress across a slip surface, and *c'* and *ϕ'* are the cohesion and friction coefficients in terms of effective stresses (adapted from Morgenstern and Price 1965). Based on this formulation, the safety factor is sometimes defined as the coefficient by which the shear strength of a soil must be divided to bring the slope to the verge of failure (Duncan 1996; Dawson et al. 1999).

The safety factor definition in Eq. 3.7 is straightforwardly applied in limit equilibrium analysis, where the ratio of shear strengths to stresses is calculated along the selected slip surface. Assuming that (a) the slip surface is accurately identified and (b) the stress states are correctly determined, safety factor calculations produced by limit equilibrium methods fit the general definition.

3.3.4.2. SAFETY FACTOR CALCULATIONS IN DEFORMATION ANALYSIS

Deformation analysis does not easily lend itself to safety factor calculations. There are two reasons for this: a lack of knowledge about the location of slip surface and the method used to determine the onset of global failure. Unlike limit equilibrium methods, deformation analysis does not require defining a potential slip surface location as a calculation input; rather, the deformation zone is allowed to develop naturally. As a result, the location, shape and continuity of the slip plane or planes are not known. Furthermore, the failure is not determined by computing some mathematical value such as the safety factor but rather by cycling through calculation steps to evaluate convergence. Due to these particularities, the implementation of safety factor calculations necessitates some adaptation as well as careful interpretation.

The strength reduction method (Zienkiewicz et al. 1975; Matsui and San, 1992; Griffith and Lane 1999; Dawson et al. 1999), is one such adaptation that came to be broadly accepted by the practice of géotechnique. The method consists of selecting a series of trial safety factor values that are used to adjust the strength parameters *c'* and *ϕ'* of a Mohr-Coulomb envelope using Eq. 3.8 and Eq. 3.9:

$$c'_{trial} = \frac{c'}{FOS_{trial}} \qquad \textit{Eq. 3.8}$$

$$\phi'_{trial} = tan^{-1}(\frac{\tan\phi'}{FOS_{trial}}) \qquad \textit{Eq. 3.9}$$

Following such adjustment, a simulation is run to determine whether generalized failure takes place. In FLAC3D, such failure is diagnosed if the system is unable to reach convergence, indicating that displacements continue to accrue indefinitely. The lowest FOS_{trial} value that brings the slope to the verge of collapse equals to the safety factor. Higher FOS_{trial} values will result in collapse, and lower FOS_{trial} values will leave the slope stable.

Initially developed for the Mohr-Coulomb strength model, this approach to calculating a slope's safety factor was expanded to include the Hoek-Brown failure envelope (Hammah et al. 2005). In FLAC3D, the shear strength reduction method to determine the safety factor of slopes can be currently applied to slopes made of materials with strength models *Mohr-Coulomb*, *Hoek-Brown* and *ubiquitous-joint* (Itasca 2018).

The *strain-softening* constitutive model used to simulate the Upper GLU strength behaviour is not one of the materials amenable to this type of analysis. A stain-weakening material's strength parameters are not constant but vary as a function of accumulated plastic shear strain. FLAC3D's *strain-softening* model determines each zone's current strength parameter values as a function of accumulated plastic shear strain using a series of linked piecewise linear functions specified by user-defined tables. Therefore, it is not clear which strength parameter value should be adjusted, and how to incorporate (if at all) strain-weakening processes in safety factor calculations.

One strategy would be to convert such material to a Mohr-Coulomb model using its operational strength parameters to determine c' and ϕ', then to conduct a safety factor analysis as described above. Such approach would not take into consideration any further strain-weakening processes, with unclear implications on the meaning of results.

An alternative strategy proposed by Zhang et al. (2013) consists in adjusting the height of the entire strain-weakening curve by way of multiplying it by $1/FOS_{trial}$. While such adjustment would produce operational strength parameter values that are adjusted according to Eqs. 4.8 and 4.9 at all times, it is not clear how such numeric manipulations would affect the interpretation of results.

3.3.4.3. HYBRID APPROACHES

It is evident that there are significant limitations to the classic definition of the safety factor with application to strain-weakening materials. For the purpose of this thesis and with an understanding of such limitations, the following definition of the safety factor can be adopted:

"A safety factor will be defined here as the factor that, when applied to the operational strength parameters, brings the soil mass to a limiting equilibrium."

Such definition would suffice for the purpose of evaluating the relative stability of different simulations of the same model such as that of the failure at the Mount Polley TSF. To calculate factors of safety in accordance with this definition, an approach referred to as "enhanced limit strength methods" may be considered whereby deformation analysis is used to establish the stress state throughout the model, and the resulting stress distributions are used in limit equilibrium safety factor calculations (Kulhawy 1969; Stianson 2008). In problems involving strain-weakening materials, such as the Mount Polley TSF, not only stresses but also strengths can be deformation-dependent and cannot be correctly determined by limit equilibrium analyses. Therefore, it would be necessary to expand the "enhanced limit strength methods" approach to incorporate strength values and/or parameters determined by deformation analysis. Additionally, where the three-dimensional shape and/or location of the slip surface is particularly complicated (such as it was determined for Mount Polley, see §4.5), it must be at least tentatively determined from the results of a deformation analysis.

We have been unable to identify any commercial modelling software that is currently capable of such hybrid analysis. Therefore, this approach was abandoned as unfeasible at present.

3.3.4.4. SELECTED APPROACH

Safety factor calculations using the strength reduction method were conducted in FLAC3D using the operational strength parameters established at static equilibrium to define the soils' Mohr-Coulomb strength envelopes. The strength parameters were adjusted gradually in multiple steps. In each step, in accordance with advice by Itasca (Lucarelli 2018), their magnitude was reduced by ~1% at a time as the system was brought to static equilibrium. The steps were repeated until nonconvergence was diagnosed signalling failure.

Recognizing the serious limitations of such analysis, including its stress-path dependency and its general irrelevance to strain-weakening materials, the safety factors calculated in this manner must be interpreted with extreme caution and were used for the sole purpose of comparing the responses of the coarse, intermediate and fine models.

CHAPTER FOUR

A THREE-DIMENSIONAL DEFORMATION ANALYSIS OF THE FAILURE AT THE MOUNT POLLEY TSF IN LARGE STRAIN

This chapter documents the results of a three-dimensional deformation analysis of the failure at the Mount Polley TSF completed under the large strain calculation scheme. This analysis includes three separate simulations that were conducted using a coarse, an intermediate and a fine model as detailed in §3.2.1.1.

In this chapter, the information is organized into seven sections, each describing a specific aspect of the mechanical response in the embankment soils to staged loading. In each of these sections, the relevant results from the coarse, intermediate and fine simulations are reported concurrently in order to detect and evaluate trends in the model response that are related to the scale effects. These trends are deemed to be an important component of the findings: in the concluding chapter of this thesis, these are evaluated in conjunction with other modelling data, field findings and analytical arguments to reach conclusions regarding the likeliest scenario for the unfolding of collapse, the true thickness of the shear band, pre-collapse shear deformation levels, scale effects and more.

A significant number of figures are introduced in this chapter. The vast majority of these figures are views of the coarse, intermediate and fine models of the Mount Polley TSF showing with the use of colour maps the various aspects of mechanical response in the embankment materials after the addition of stage 3 through 9B materials. Two views are predominantly used. The first one (seen, as an example, in Figure 4.1) shows half of the embankment model, with a cross-section cut through it roughly at the mid-point of the breach location; the other half is rendered invisible everywhere except the Upper GLU unit. This particular view was developed to best illustrate the mechanical responses of interest in the entire embankment. The second view (seen, as an example, in Figure 4.20) shows an isometric view of the Upper GLU, with the rest of the model rendered invisible.

4.1. STRESS DISTRIBUTIONS

4.1.1 OVERBURDEN STRESSES

The perimeter embankment at the Mount Polley TSF was constructed in stages between 1996 and 2014. At the failure location, the embankment was raised to a final height of ~40m, with pre-failure ground surface elevations reaching 970mASL in the core and shell zones, and ~967mASL at the tailings pond. The addition of material over the duration of construction induced a gradual increase in overburden stresses in the embankment and foundation.

In the simulation of the Mount Polley TSF, the distribution of total and effective vertical stresses was evaluated after each of the construction stages 3 through 9B using the coarse, intermediate and fine models. The evolution of total and effective overburden stresses is illustrated in Figure 4.1 to Figure 4.6. These figures show that the largest stress increases take place in the core and shell regions, as well as foundation materials directly beneath them. The core material, with a high dry density of around 2,100kg/m^3, and with the phreatic surface passing through it, contributes significantly to the added total and effective stresses in the soils situated below it; and the rockfill, largely drained and with a considerable dry density of over 2,000kg/m^3, generates increases in total and effective overburden stresses in the materials beneath it to a near equal extent.

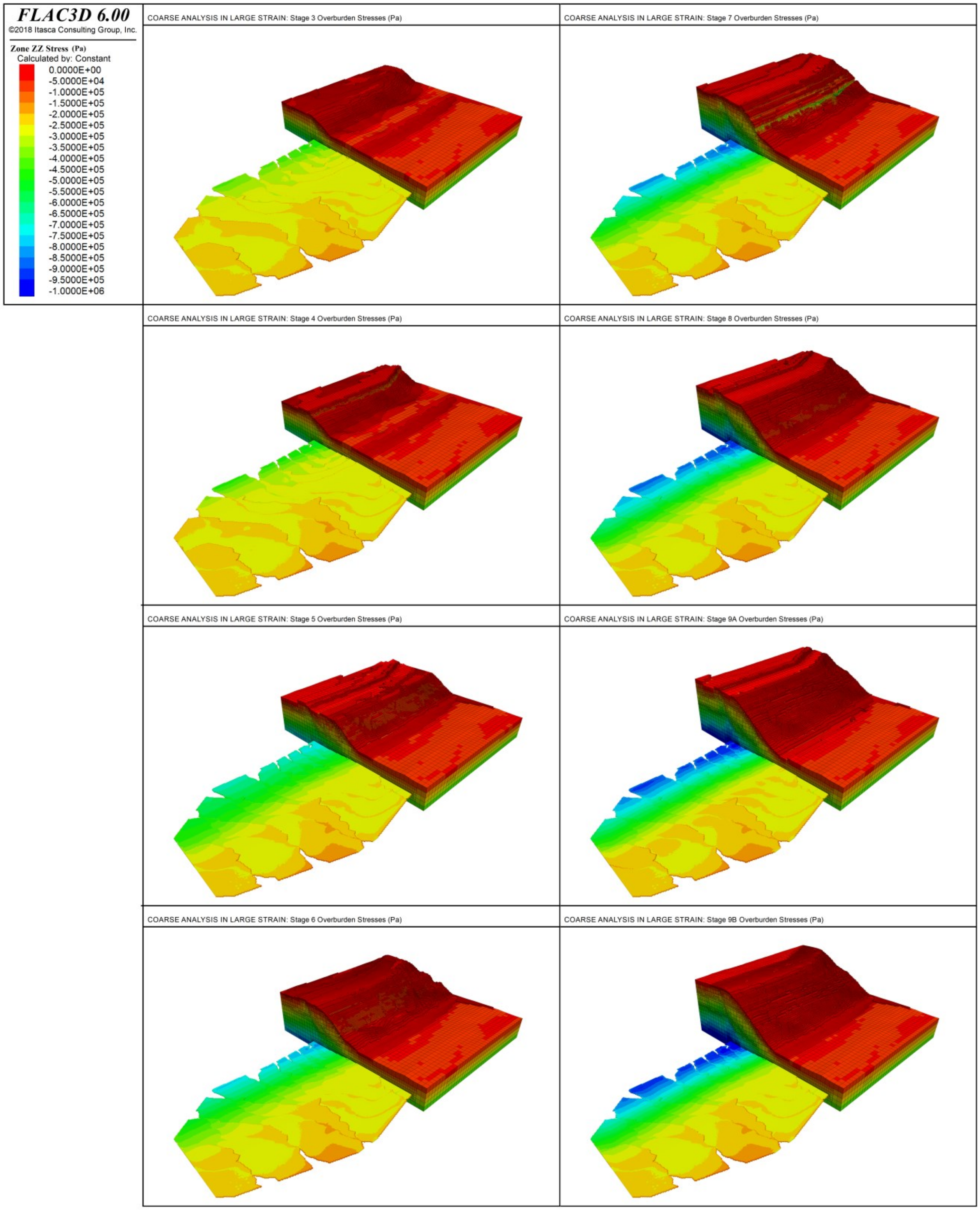

Figure 4.1 Total overburden stresses after the completion of construction stages 3 through 9B under steady-state conditions predicted by the coarse model in large strain (pictured view: full model sliced in the direction normal to the dam centreline at the centre of the failure; and the Upper GLU unit, seen in full).

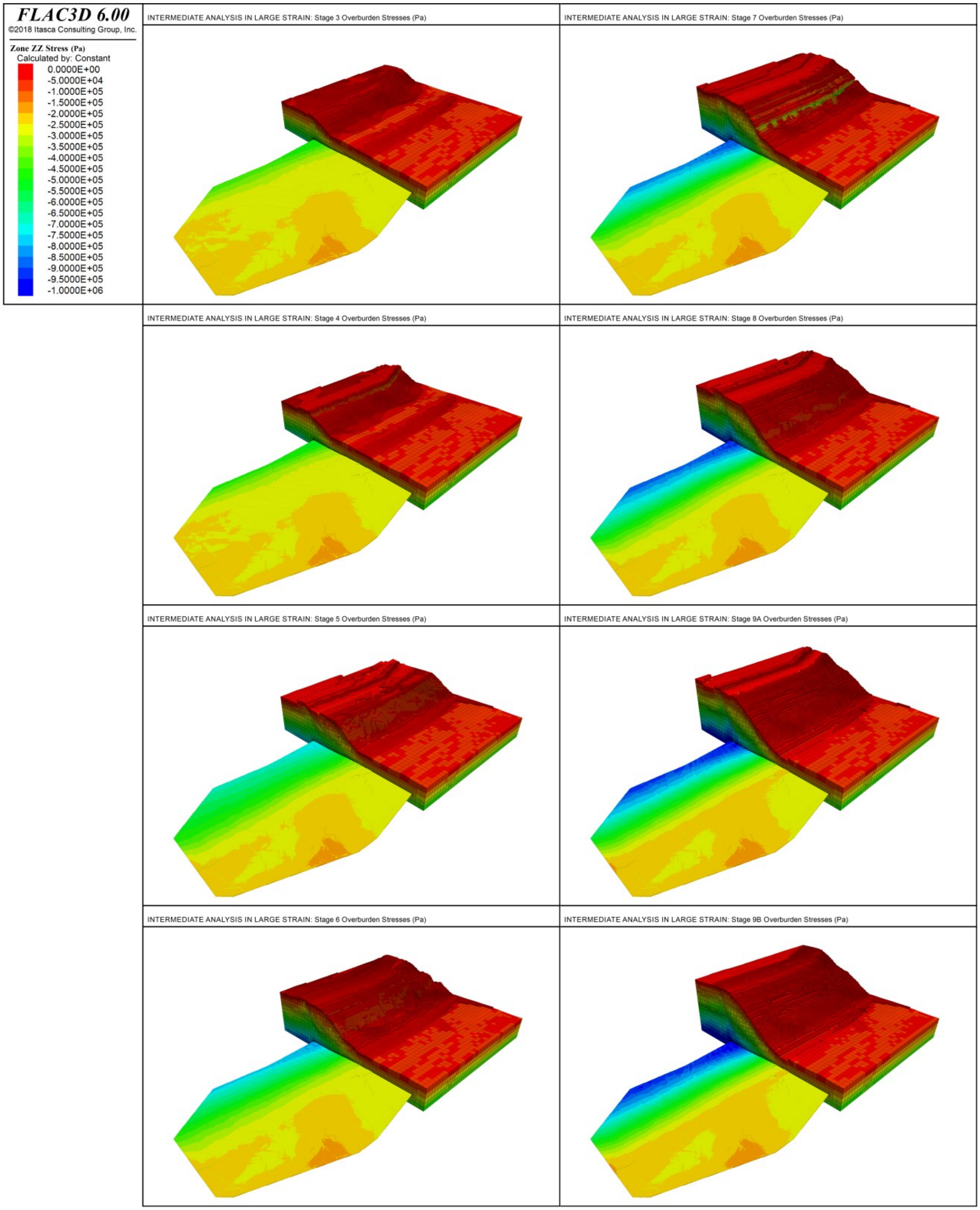

Figure 4.2 Total overburden stresses after the completion of construction stages 3 through 9B under steady-state conditions predicted by the intermediate model in large strain.

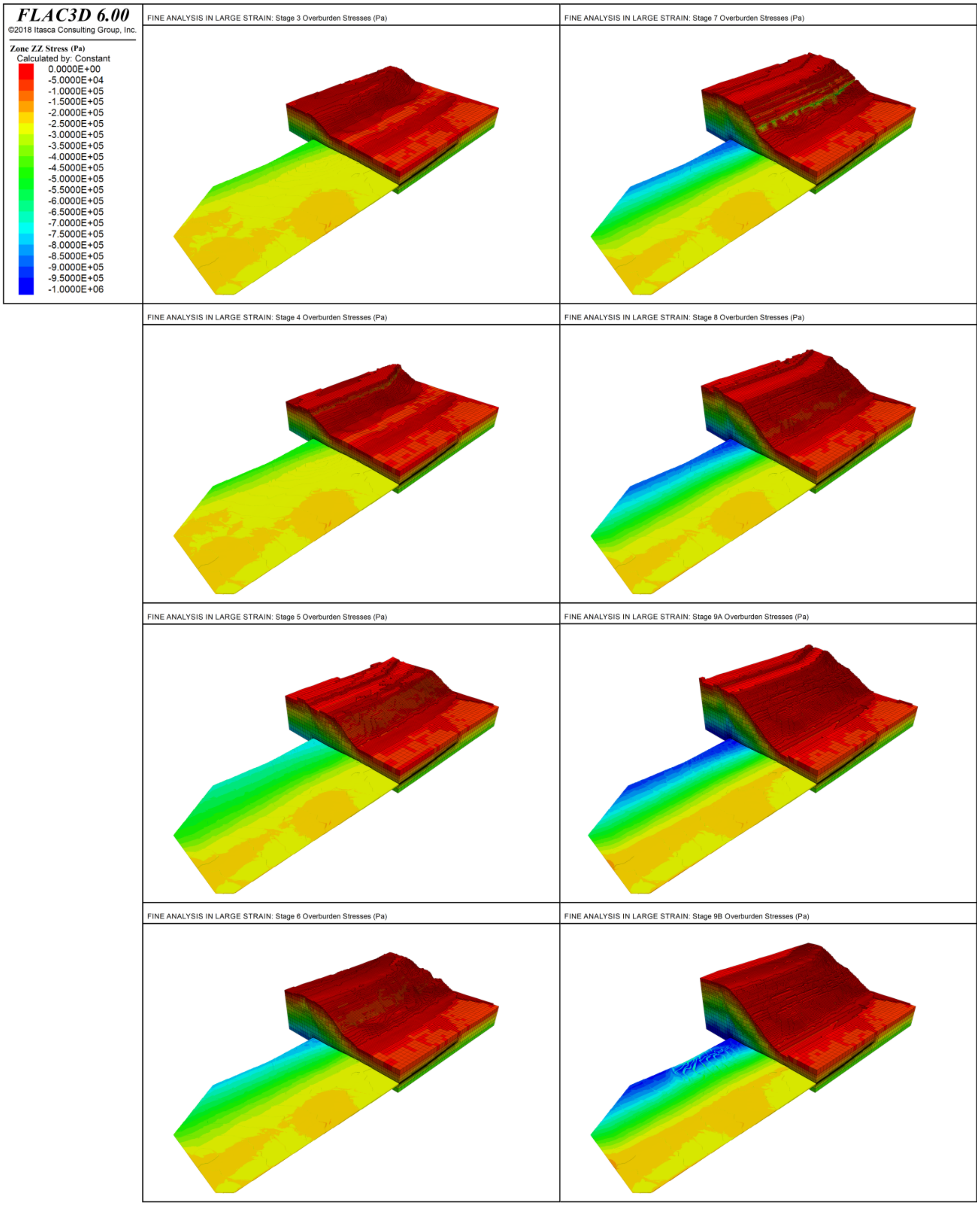

Figure 4.3 Total overburden stresses after the completion of construction stages 3 through 9B under steady-state conditions predicted by the fine model in large strain.

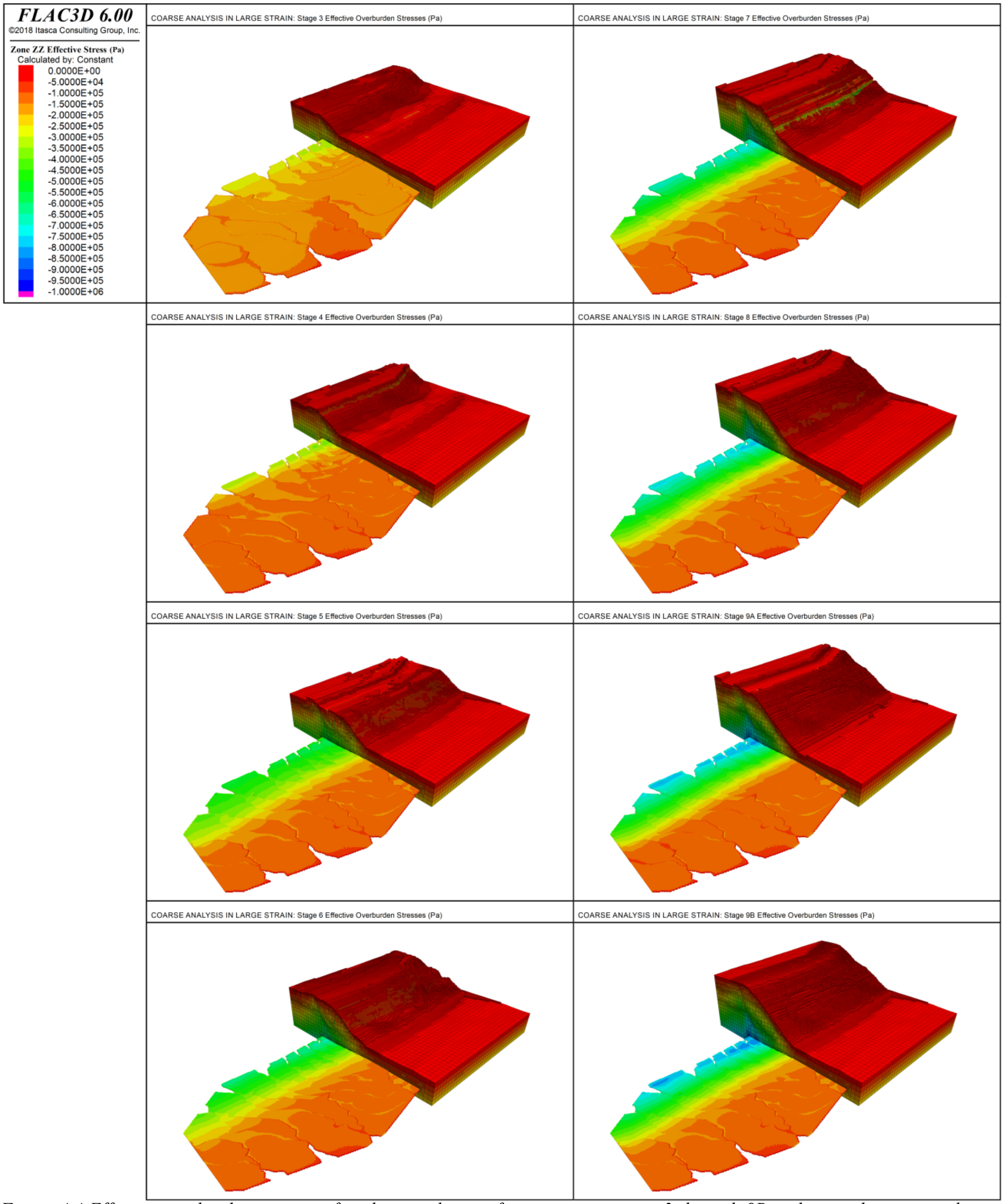

Figure 4.4 Effective overburden stresses after the completion of construction stages 3 through 9B under steady-state conditions predicted by the coarse model in large strain (pictured view: full model sliced in the direction normal to the dam centreline at about the centrepoint of failure; and the Upper GLU unit, seen in full).

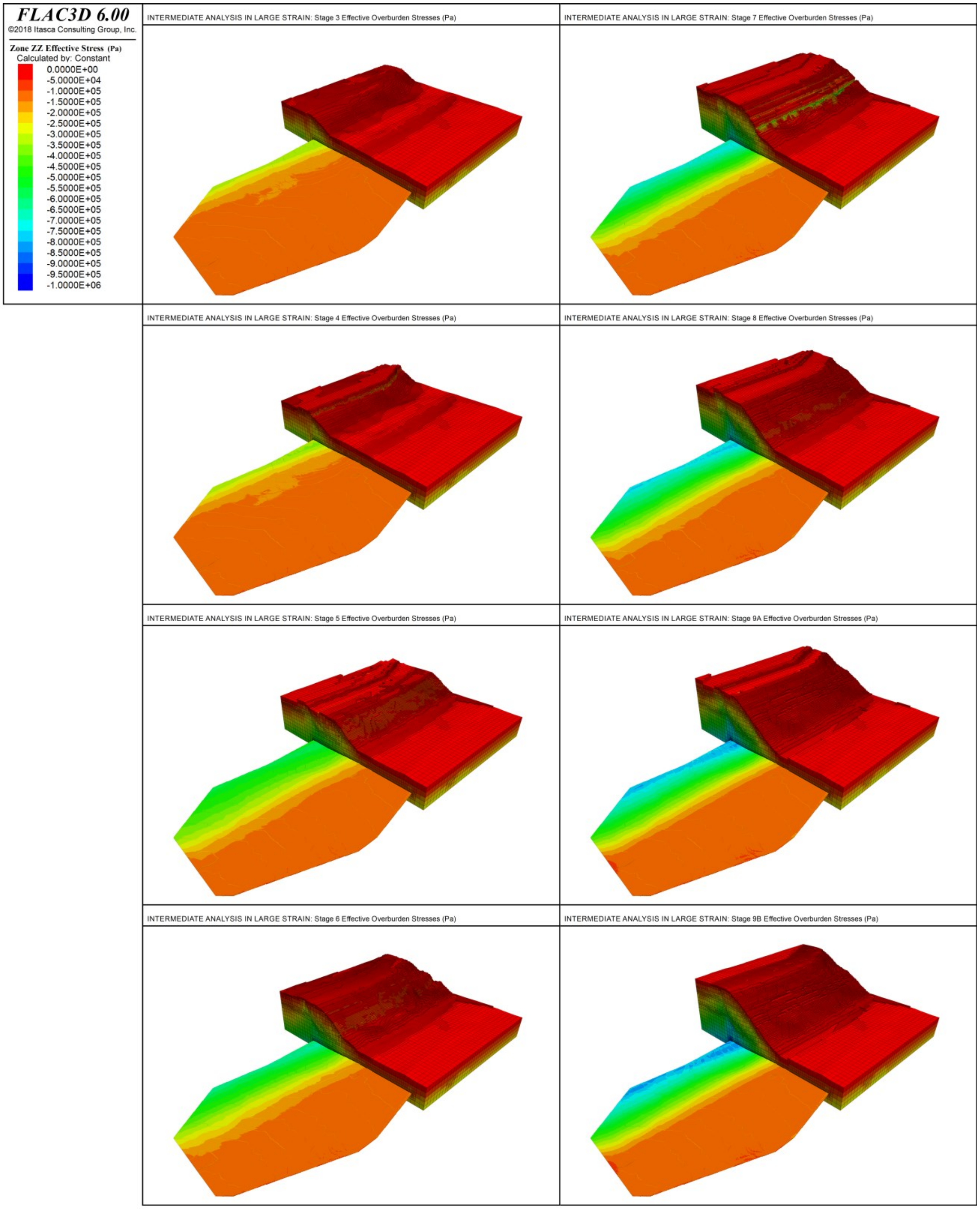

Figure 4.5 Effective overburden stresses after the completion of construction stages 3 through 9B under steady-state conditions predicted by the intermediate model in large strain.

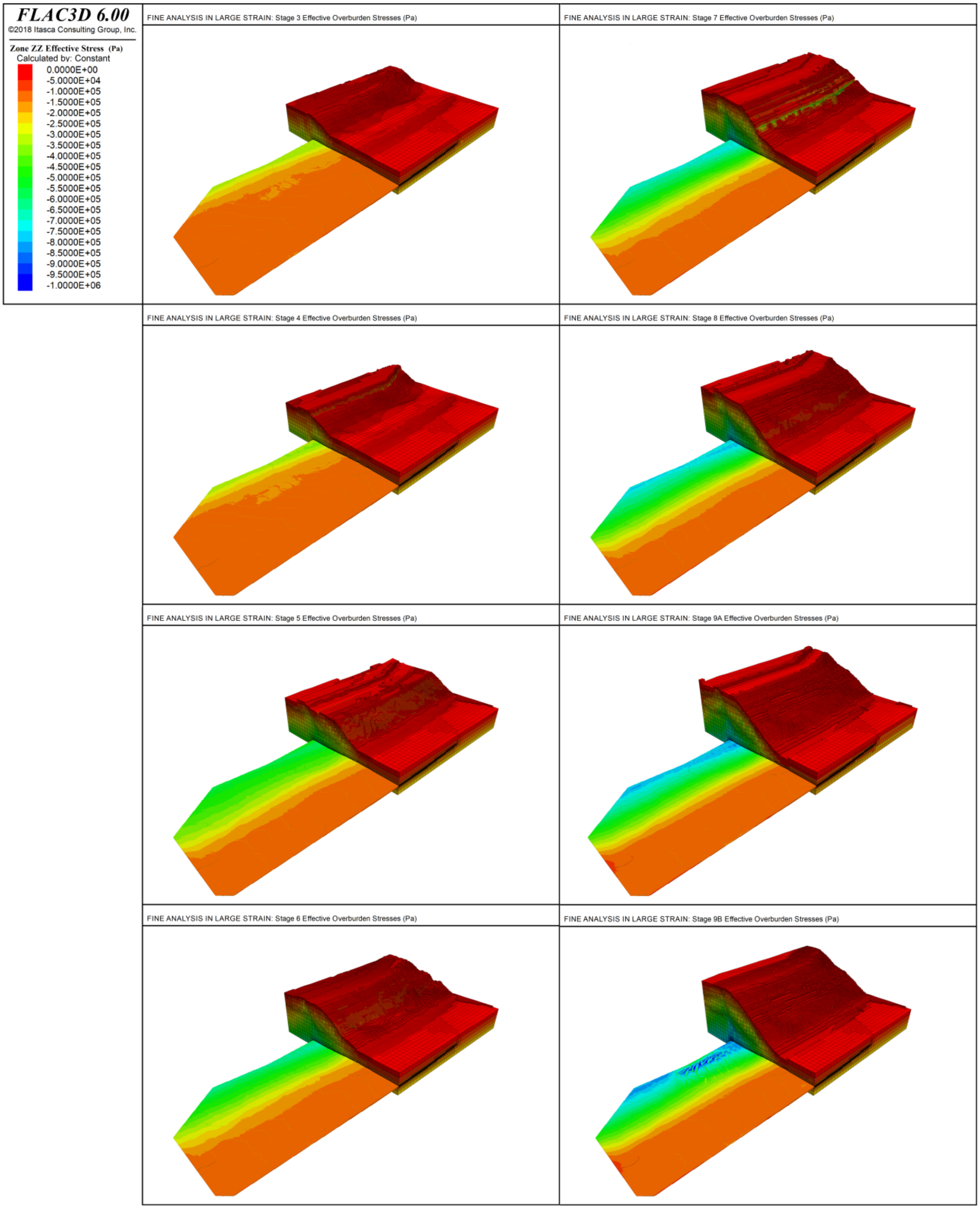

Figure 4.6 Effective overburden stresses after the completion of construction stages 3 through 9B under steady-state conditions predicted by the fine model in large strain.

Up to and including construction stage 9A, the distributions of total and effective overburden stresses predicted by the coarse, intermediate and fine models are very comparable. A divergent stress response is noted in some key areas, chiefly in and around the upstream portion of the Upper GLU. The difference in the stress responses is illustrated in Table 4.1 that lists maximum total and effective overburden stresses in this unit. The data in the table reveals that in each modelled construction stage, the maximum stresses are greater in the models with a higher mesh resolution. This disparity is owed to two modelling aspects: the discrete nature of finite element modelling and the strategy adopted to create the subsurface geometry of this model. This effect is discussed in detail in §6.4.1.

Table 4.1 Overburden stresses predicted by the coarse, intermediate and fine models in large strain.

	Maximum total overburden stresses in the Upper GLU (kPa)			Maximum effective overburden stresses in the Upper GLU (kPa)		
Mesh	coarse	intermediate	fine	coarse	intermediate	fine
Stage 3	504	570	602	350	418	456
Stage 4	531	595	627	379	445	481
Stage 5	746	816	850	605	674	722
Stage 6	830	891	930	690	756	802
Stage 7	920	981	1036	773	836	885
Stage 8	973	1037	1095	826	886	937
Stage 9A	1041	1121	1176	883	924	995
Stage 9B	1066	1161	varies*	918	967	varies*

*during active collapse.

4.1.2 ROTATION OF STRESS TENSOR UNDER EMBANKMENT

In slopes, a rotation of the stress tensor is known to take place where the principal stress moves from a vertical to an inclined position. A re-orientation of the plane of critical stress also takes place. The new inclination of this plane is often more conducive to promoting shearing in the direction of soil mass displacements during a slip. Consequently, observing the rotation of stress tensors throughout the history of the embankment structure offers an insight into the progression of the failure.

The rotation of stress tensors in the Upper GLU was tracked in stages 3 through 9B, and the results are found in Appendix 4A, Figure 4A.1. In all simulations, a rotation of the stress tensor is observed from the earliest stages of embankment construction, increasing with the embankment height. As the simulations advance, the stress tensors in the embankment and foundation continue to rotate, and by stage 7 or 8, the critical planes in the normally consolidated portions of Upper GLU (oriented at 45° to the plane of major principal stress) become somewhat close to horizontal. Also at this point into the simulation, a plastic yield zone is seen to emerge in this material.

4.1.3 SHEAR STRESSES IN THE UPPER GLU

The gradual re-orientation of the critical plane to a near-horizontal position in the Upper GLU under embankment can be indirectly observed by comparing the evolution of two variables, the magnitude of shear stresses in the horizontal plane in the downstream direction, and the magnitude of shear stresses on the critical plane.

In the Upper GLU, the evolution of shear stresses along the horizontal plane (i.e. the plane normal to the z-axis) in the direction of soil mass movement (i.e. along the x-axis that was set to be roughly perpendicular to the dam centreline) may provide some insight into the progression of the failure as this was the dominant direction of soil displacement in this unit, especially in the areas under embankment. The shear stresses τ_{xz} were tracked through each simulated construction stage using the coarse, intermediate and fine models. The results are included in Appendix 4A, Figure 4A.2 to Figure 4A.3.

Observing the evolution of shear stresses along the critical plane τ_{cr} in this unit also helps reconstruct some of the aspects of the progressive failure. The orientation of critical planes is not fixed throughout the life of the structure but changes as the stress tensors in the embankment and foundation rotate. By stage 8 or so, the critical plane become sub-horizontal in some of the more critical portions of the Upper GLU (see Figure 4A.1 in Appendix 4A). This suggests that starting in stage 8, τ_{cr} and τ_{xz} values somewhat converge in those critical areas. In the Upper GLU, the shear stresses along the planes of critical stress τ_{cr} were tracked through each simulated construction stage using the coarse, intermediate and fine models. The results are included in Appendix 4A, Figure 4A.5 to Figure 4A.7. To better compare the two variables, they have been plotted side-by-side in Figure 4.7. From the figure, it can be seen that although some convergence of these values is observed in construction stages 8 through 9B (largely in the area located under the embankment), it is not clear-cut. The convergence of these two values is, in fact, very good in some of the layers of the Upper GLU at the base of the unit where the plastic yield zone has developed but not throughout its entire thickness.

Figure 4.7 illustrates another process indicative of a progressive failure, namely the stress transfer from the weakening materials onto adjacent, stronger soils. In stages 9A and 9B, a pronounced transfer of stress onto the downstream materials is observed. The areas where a marked increase in shear stresses is apparent consist of soils that are overconsolidated, whereas the areas where the shear stresses are decreasing are normally consolidated (see §4.2.1).

Lastly, the stress transfer described above is not seen in the simulation results produced by the coarse or intermediate models. Such divergent response is related to the different straining and strain-weakening behaviours observed in the coarse, intermediate and fine models, and will be fully explained later in this chapter starting with §4.2.2. For now, it suffices to state that the coarse and intermediate models produce very stable embankment configurations up to and including construction stage 9B, whereas the fine simulation predicts the start of a progressive failure around stage 7-8 and collapse in stage 9B; this difference of simulated outcome is the cause of the noted divergence.

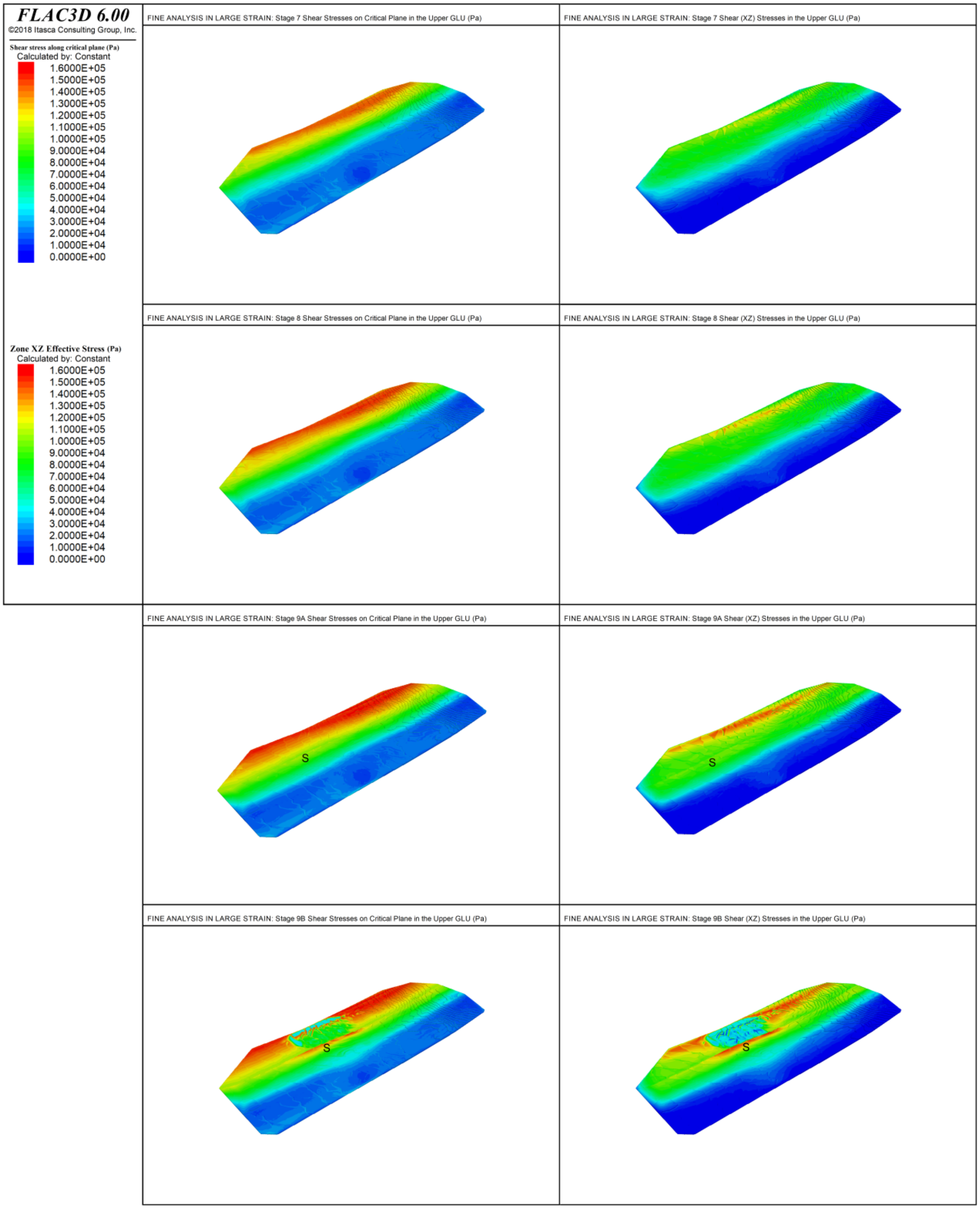

Figure 4.7 Shear stresses along the critical plane τ_{cr} (left column) and shear stresses along the horizontal plane in the direction of soil mass displacement τ_{xz} (right column) in the Upper GLU predicted by the fine model in large strain. Locations of stress transfer onto the downstream areas are labelled with "S."

4.2. THE UPPER GLU'S STRENGTH BEHAVIOUR

Over the course of embankment construction at the Mount Polley TSF, the Upper GLU material underwent fundamental changes pertaining to its mechanical behaviour. Prior to the embankment construction, this unit was lightly overconsolidated and dilative on shearing, and drained strengths controlled its mechanical stability. The addition of embankment materials atop of foundation had two distinct effects on the unit, which in turn triggered changes in its shear strength.

The first effect was to increase the vertical consolidation pressures in the foundation, including parts of the Upper GLU, to levels equal to and eventually exceeding preconsolidation pressures, causing portions of the unit to become normally consolidated. These areas became contractive on shearing, and undrained shear strengths controlled their mechanical stability.

The second effect was to induce a deformation response in the foundation and embankment materials, which included an accumulation of shear strain, especially in the materials under the slope. In time, plastic shear strains accrued in some of the Upper GLU material under the embankment; eventually, the shear strain levels became sufficiently large to trigger strain-weakening processes.

In this section, the Upper GLU's state of consolidation and the plastic shear strains are tracked through all simulated construction stages, and the impact of these variables on the unit's shear strength is evaluated.

4.2.1 TRANSITION TO A NORMALLY CONSOLIDATED STATE

Prior to the commencement of construction works, the Upper GLU was a lightly overcnsolidated deposit with preconsolidation pressures around 400-500kPa. As the embankment was raised, consolidation processes were induced in the foundation. The loading-induced increase in vertical consolidation stresses to levels equal to or exceeding the unit's preconsolidation pressure was identified as the reason for this unit's transition from a drained to an undrained mode of failure.

The transition of the Upper GLU material from a state of overconsolidation to a state of normal consolidation did not happen uniformly or simultaneously. The emergence and evolution of the normally consolidated zone was evaluated in construction stages 3 through 9B using the coarse, intermediate and fine models. The results are compiled in Figure 4.8 to Figure 4.10.

Simulation results indicate that negligible amounts of material in the Upper GLU become normally consolidated as early as construction stage 3. At this stage, the normally consolidated portions of the Upper GLU are limited to a small number of zones at the base of the unit. The finer resolution models predict a somewhat earlier emergence of a normally consolidated zone and also higher maximum vertical consolidation stresses; this difference of predicted outcome is related to the higher overburden stresses in the models with a higher resolution discussed in §6.4.1. Material amounts of the Upper GLU transition to a state of normal consolidation after addition of stage 5 materials.

The location, spatial distribution and growth of normally consolidated zone in the Upper GLU is generally comparable in the coarse, intermediate and fine models.

Finally, the normally consolidated area of the Upper GLU is identical in construction stages 9A and 9B. The reason for this is that the new load in stage 9B is applied under undrained conditions, as explained in §3.2.4.

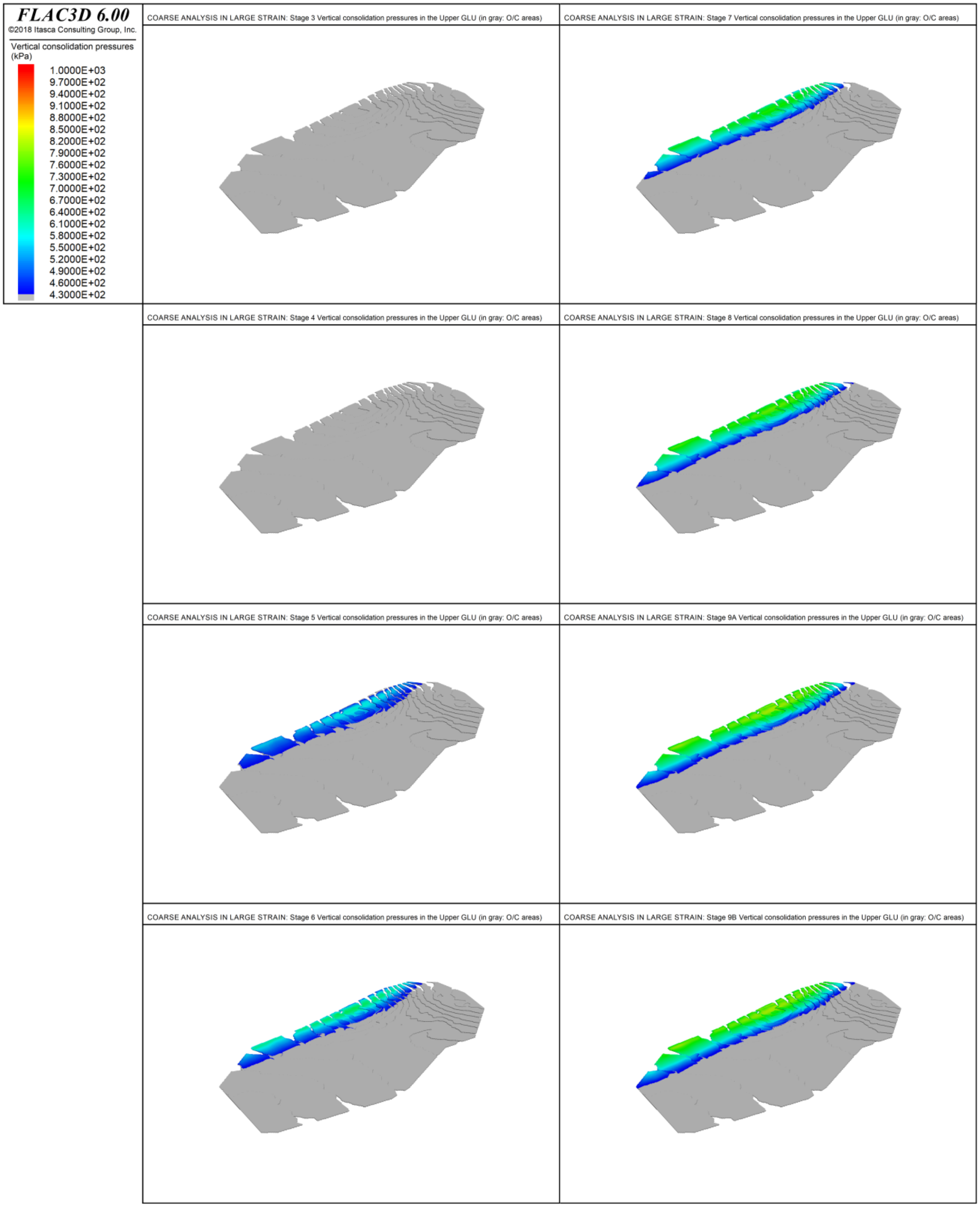

Figure 4.8 Vertical consolidation pressures in the Upper GLU after the completion of each construction stages 3 through 9B under steady-state conditions predicted by the coarse model in large strain.

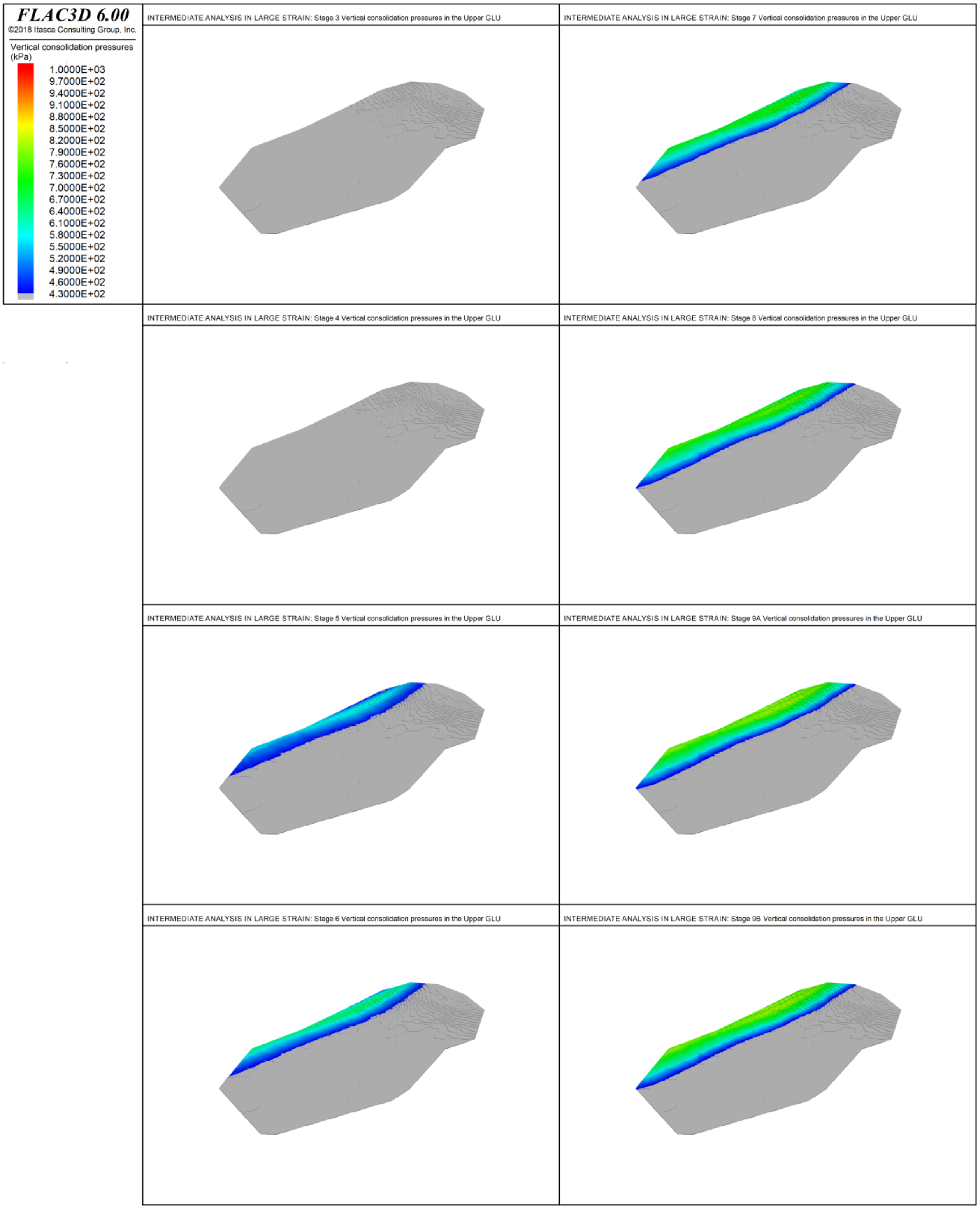

Figure 4.9 Vertical consolidation pressures in the Upper GLU after the completion of each construction stages 3 through 9B under steady-state conditions predicted by the intermediate model in large strain.

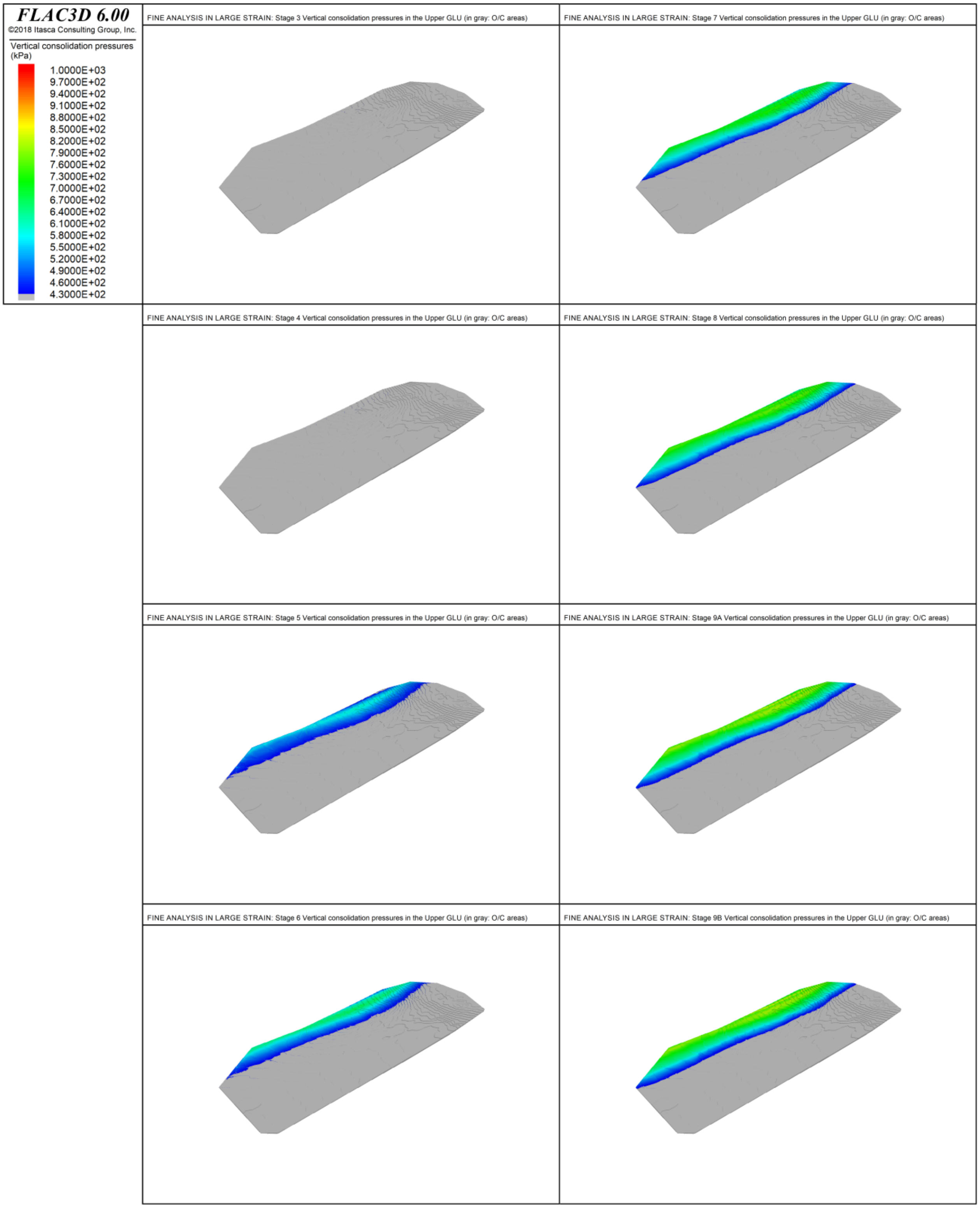

Figure 4.10 Vertical consolidation pressures in the Upper GLU after the completion of each construction stages 3 through 9B under steady-state conditions predicted by the fine model in large strain.

4.2.1.1. LOCAL SAFETY FACTORS

A transition of the Upper GLU material to a state of normal consolidation is associated with an immediate drop in shear strength. As a result, areas that may have been well below the failure envelope prior to such transition may have suddenly reached failure. To examine this phenomenon in the models, local safety factors, defined as a zone's ratio of shear strength *s* to mobilized shear stress along the critical plane τ_{cr}, are evaluated:

$$FOS_{local} = \frac{s}{\tau_{cr}} \qquad \text{Eq. 4.1}$$

In the constitutive model defining the Upper GLU's undrained behaviour, the critical plane is oriented at 45° to the plane of major principal stress, and local safety factors are calculated using the following expression:

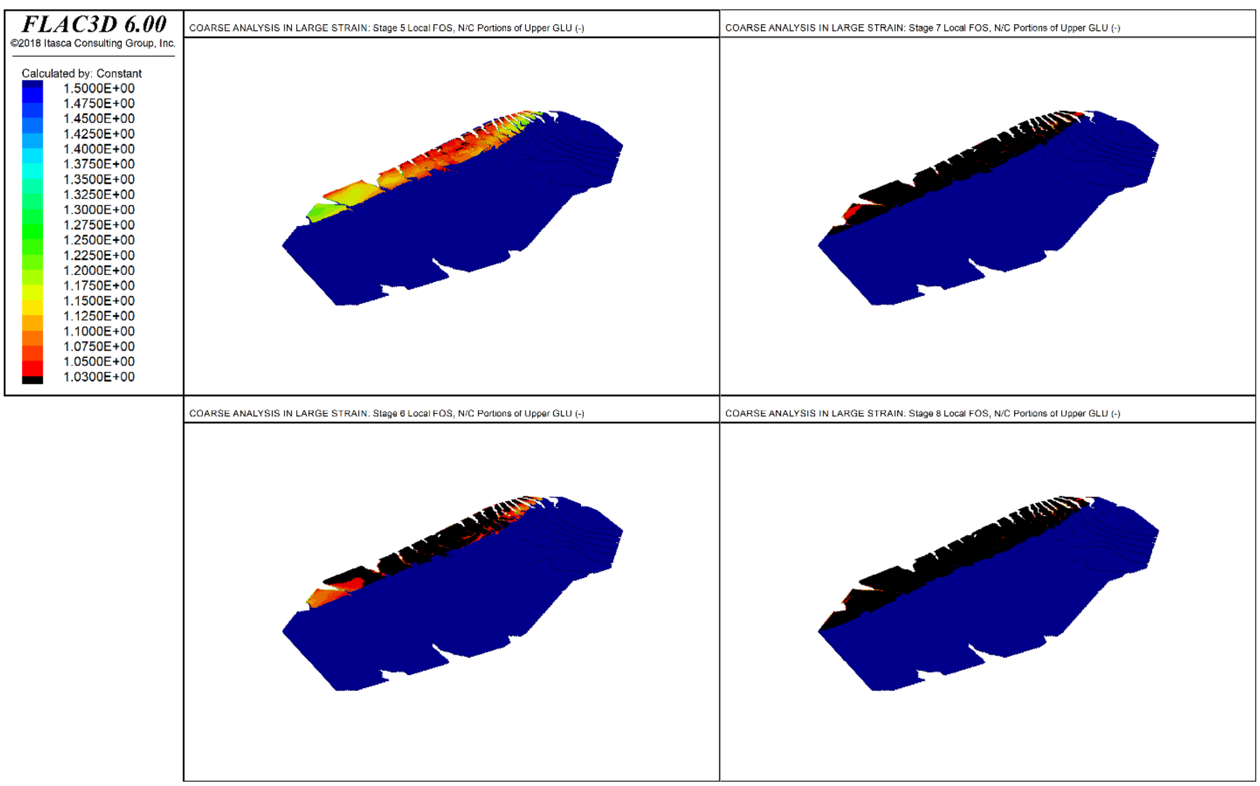

Figure 4.11 Local safety factors in the normally consolidated portions of the Upper GLU predicted by the coarse model in large strain.

$$FOS_{local} = \frac{s_u}{\frac{1}{2}(\sigma_1' - \sigma_3')} \qquad \textit{Eq. 4.2}$$

A local safety factor above unity indicates that the soil element has not yet fully mobilized its shear resistance, and a safety factor equal to unity signals that the element has reached the failure envelope and is at yield. Plots of safety factors, in addition to helping determine whether local failures developed due to a transition to a state of normal consolidation, also illustrate the process of shear strength mobilization over the duration of construction in the critical portion of the Upper GLU.

Local safety factors have been calculated in the normally consolidated portions of the Upper GLU starting with the construction stage 5; their plots are seen in Figure 4.11 to Figure 4.13. The plots demonstrate that in the early construction stages, the shear stresses along the critical planes are

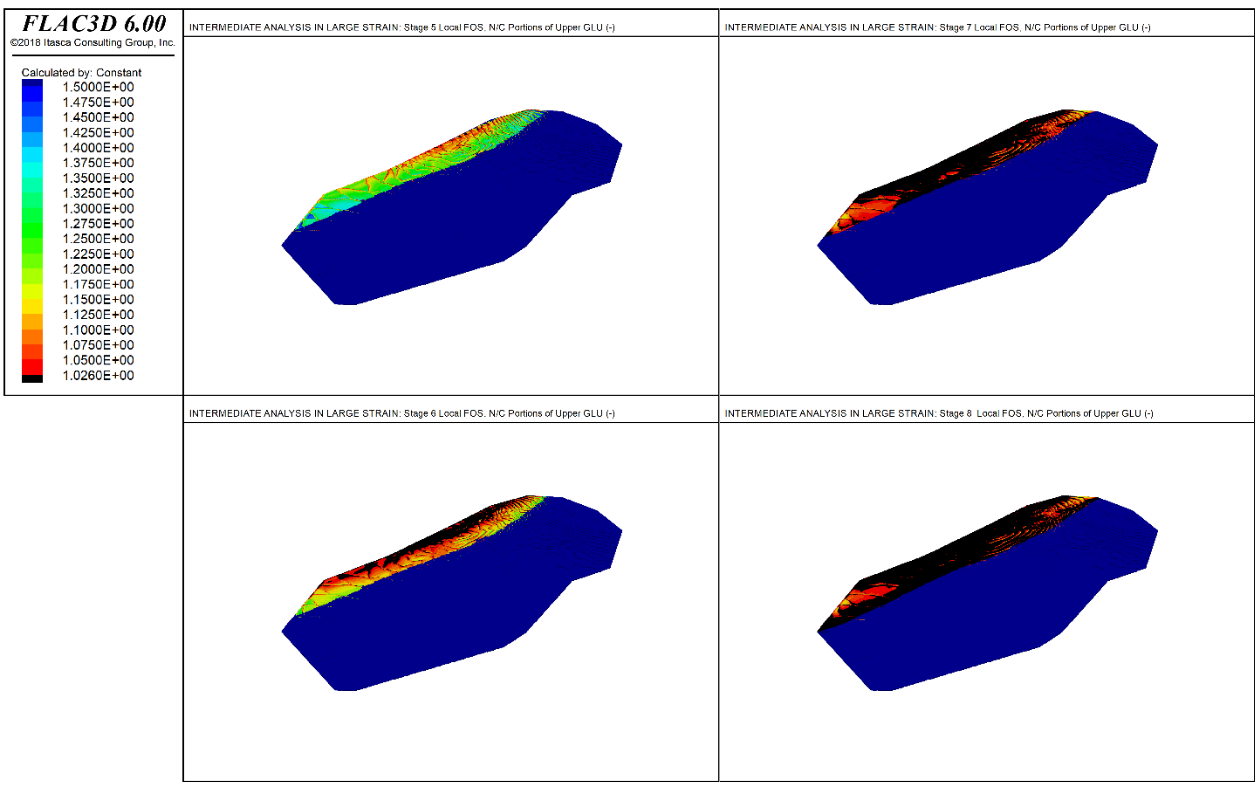

Figure 4.12 Local safety factors in the normally consolidated portions of the Upper GLU predicted by the intermediate model in large strain

largely below the deposit's undrained shear strengths. By construction stage 7, significant portions of this soil have either reach the failure envelope, or are very close to it; additionally, some of the Upper GLU material that has newly transitioned to a state of normal consolidation (at the leading edge of the normally consolidated region) would immediately reach failure as a result of such transition.

4.2.2 STRAIN-WEAKENING

The Upper GLU material was slightly sensitive and was shown by laboratory and field tests to lose up to 50-70% of its peak shearing resistance on remoulding or at large shear strains under constant volume conditions. Under an embankment, such weakening would be realized through an accumulation of plastic shear strain that would accrue in this material in response to loading. The rotation of stress tensor in this stratum described in §4.1.2 facilitated such shearing.

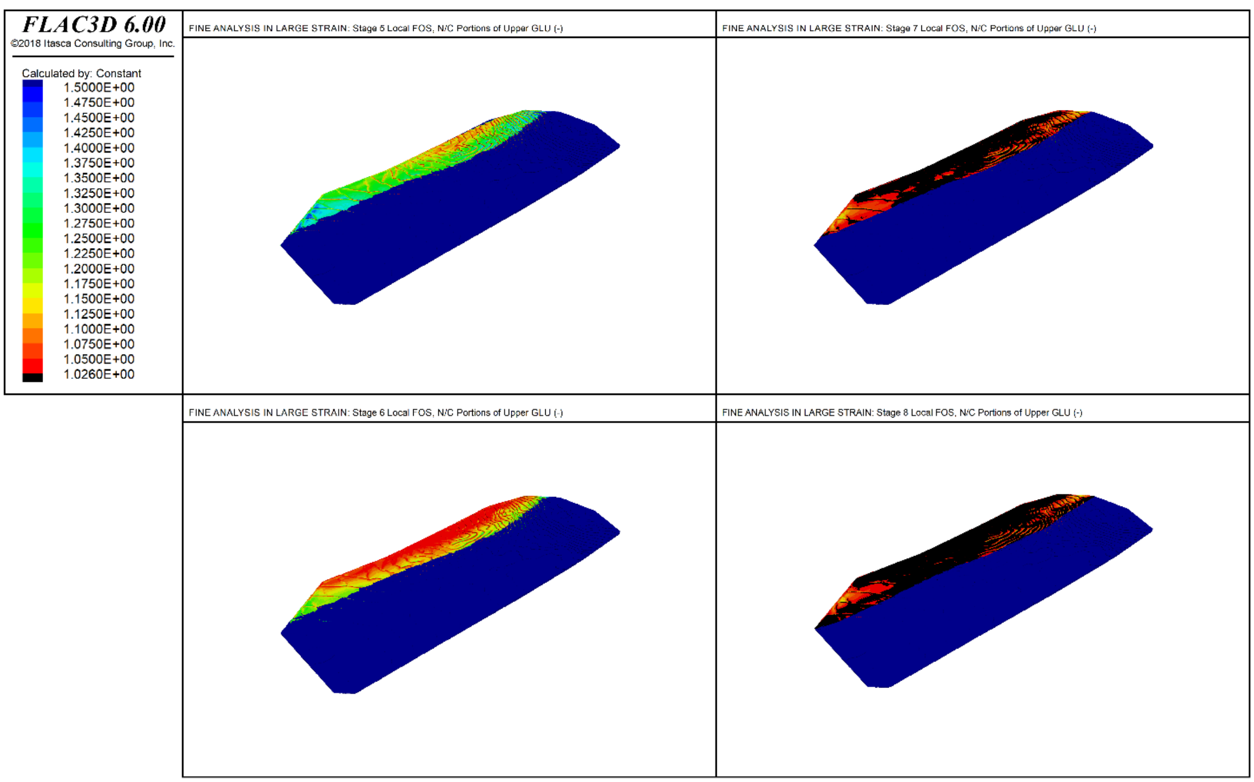

Figure 4.13 Local safety factors in the normally consolidated portions of the Upper GLU predicted by the fine model in large strain.

The shear strength model adapted in this study to represent the undrained behaviour of the Upper GLU is defined by a strain-weakening function with peak undrained shear strengths acting at up to 5% of plastic shear strains and with strain-weakening processes setting in after this level of plastic shear strains is exceeded. In the same model, the material is fully weakened at plastic shear strains in excess of 60%. This model was calibrated against direct simple shear testing data and is thought to be represent a conservative interpretation of the in-situ behaviour of the Upper GLU under the embankment.

This section documents the onset and advancement of strain-weakening processes in the normally consolidated portions of the Upper GLU that was observed in the coarse, intermediate and fine models.

4.2.2.1. PLASTIC SHEAR STRAINS

The accumulation of plastic shear strains in the Upper GLU was tracked through each simulated construction stage in the coarse, intermediate and fine models. The plots in Figure 4.14 to Figure 4.16 illustrate the distributions of plastic shear strains in the Upper GLU in the later construction stages; and Table 4.2 lists the maximum values of plastic shear strain in the unit.

Table 4.2 Maximum plastic shear strains at static equilibrium in the Upper GLU (%) predicted in large strain.

Mesh	coarse	intermediate	fine
Stage 3	-	-	-
Stage 4	-	0.4	0.8
Stage 5	1.0	1.5	2.3
Stage 6	1.3	2.1	3.0
Stage 7	1.6	3.7	5.5
Stage 8	2.1	4.5	7.8
Stage 9A	4.0	8.1	14.3
Stage 9B	6.7	14.4	indefinite

The three models produce very different predictions of the evolution of this variable over time. In the coarse model, plastic shear strains are first noted after construction stage 5, yet their accretion

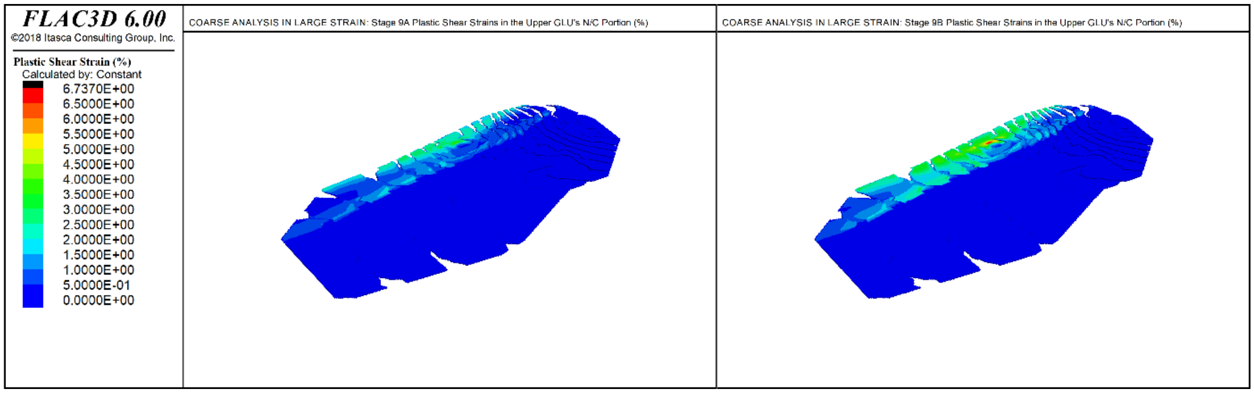

Figure 4.14 Plastic shear strains in the Upper GLU predicted by the coarse model in large strain.

in subsequent stages is slow, reaching by stage 9B a maximum value of 6.7%. In the intermediate model, plastic shear strains first appear in construction stage 4 and accumulate more rapidly in subsequent stages, reaching in stage 9B a maximum value of 14.4%. In both of these simulations, the plastic shear strains are not sufficiently large to trigger any significant weakening, and the embankment remains stable until the endpoint of simulation in stage 9B.

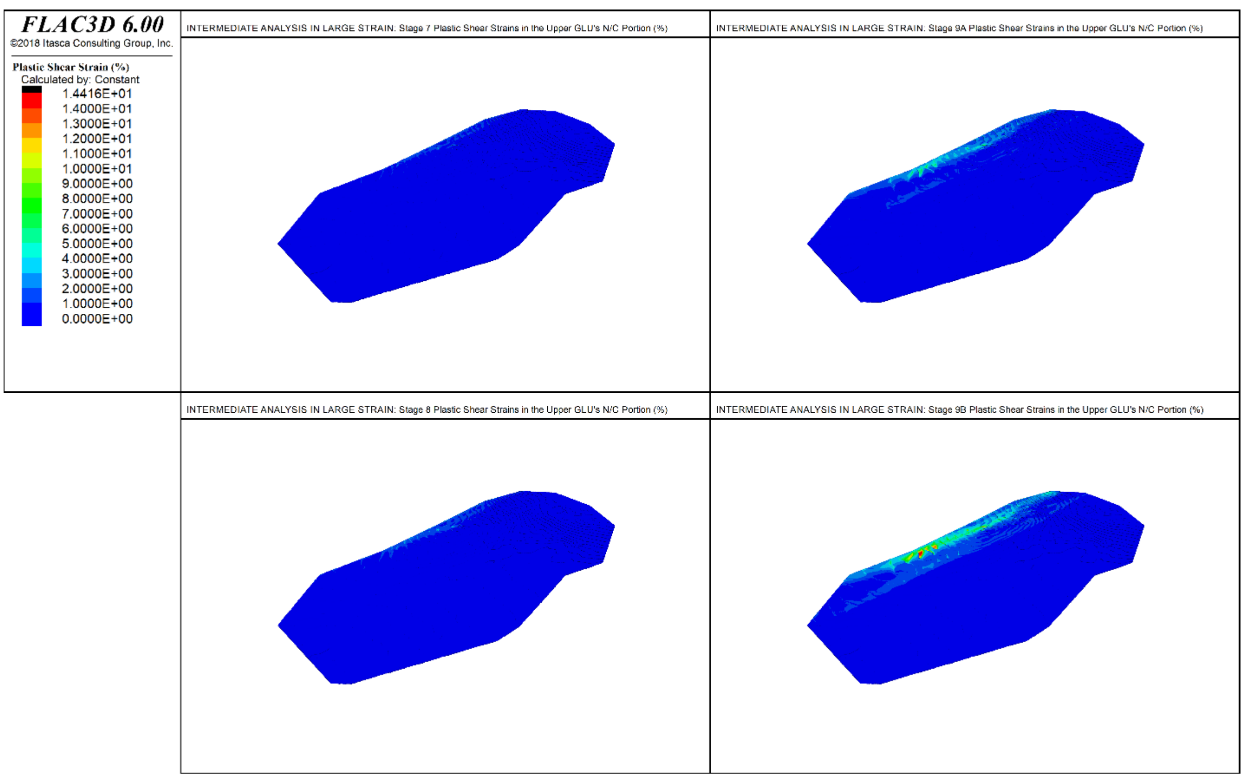

Figure 4.15 Plastic shear strains in the Upper GLU predicted by the intermediate model in large strain.

In the fine model, plastic shear strains are first noted in construction stage 4, and their accumulation in subsequent stages is more rapid than in either the coarse or intermediate models. By stage 7, a small number of zones accumulate plastic shear strains in excess of 5%, and by stage 9A, a small area under the core has accrued plastic shear strains well in excess of 10%. From stage 7 on, shear strain levels are sufficiently large to trigger weakening in some portions of the unit; by stage 9B, strain-weakening processes become uncontained and continue indefinitely as the collapse unfolds. This outcome stands in contrast with the results of the other two simulations and points to the presence of substantial scale effects.

4.2.2.2. EMERGENCE AND GROWTH OF PLASTIC SHEAR ZONE

Both original investigators (IRP 2015; KCB 2015) made a determination that a progressive failure took place at Mount Polley, concluding that a plastic yield zone had developed in the Upper GLU

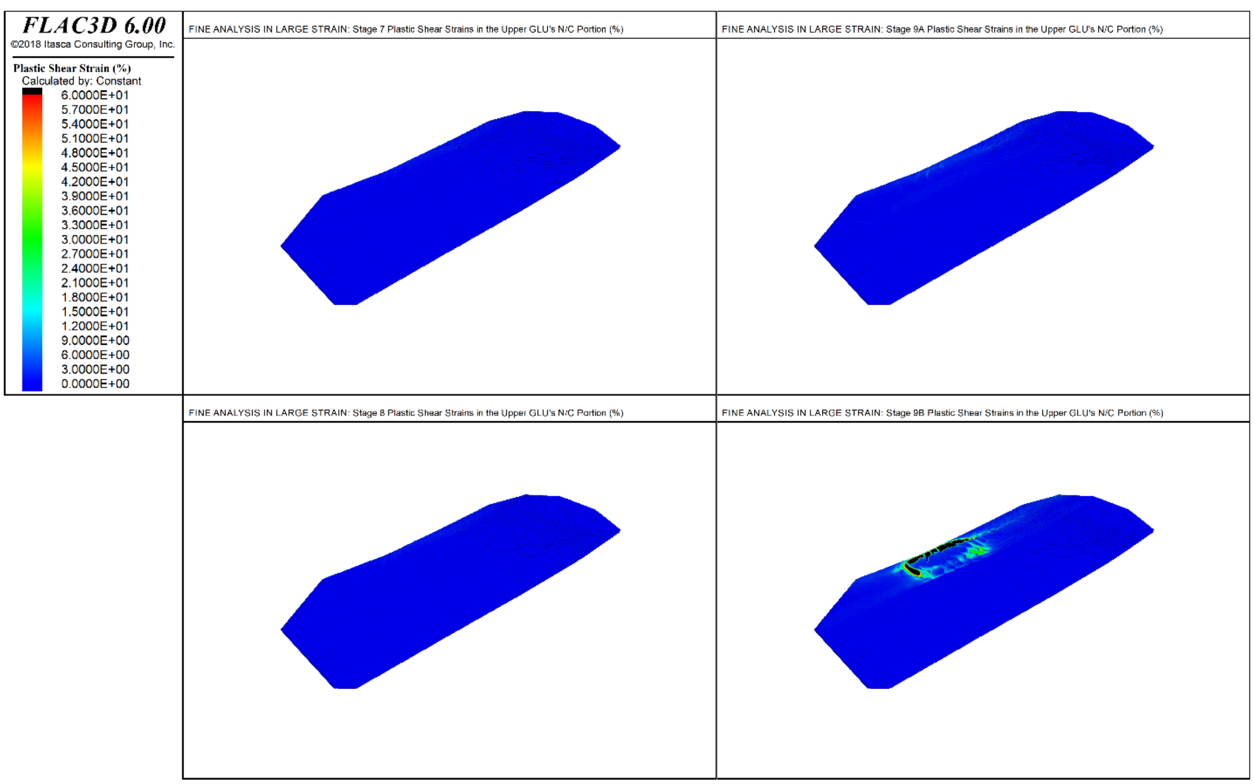

Figure 4.16 Plastic shear strains in the Upper GLU predicted by the fine model in large strain. In black: fully weakened material.

either shortly before or during the collapse and that either peak or slightly post-peak undrained shear strengths were acting along the Upper GLU surface when collapse initiated.

The three-dimensional static analysis of this failure introduced in Chapter Three suggests that, due to large amounts of shearing resistance developed in the shell along the sides of the slide (the so-called "three-dimensional stability effects"), the entire Upper GLU area involved in the failure would have had to fully weaken in order to bring the soil mass involved in the failure to a limiting equilibrium. This result indicates that the progressive failure may have developed in the foundation to a greater extent and at an earlier stage than suggested by the initial investigations.

The staged three-dimensional deformation analysis of the Mount Polley failure offers the capability to monitor the emergence and growth of the plastic yield zone from the early stages of embankment construction. In the constitutive model adapted for the Upper GLU, weakening processes begin when plastic shear strains exceed 5%. Zones with plastic shear strains equal to or in excess of this value were tracked through each simulated construction stage.

The plots of the plastic yield zones are shown in Figure 4.17 to Figure 4.19. In the figures, the zones with plastic shear strains <5% (i.e. the zones that are not strain-weakening) are rendered transparent in order to fully reveal the weakening areas, including those locater at the base and/or in the middle of this soil unit and may be otherwise concealed.

The results from the coarse simulation indicate that strain-weakening processes first emerge in construction stage 9B in a small area, about 15X8m^2, located directly below the embankment core. In this simulation, maximum plastic shear strains in this zone do not exceed 7%, and the average plastic shear strains are around 5.5%. As a consequence, the plastic flow in the yield zone remain fully contained.

The results from the intermediate simulation indicate that strain-weakening processes first emerge in construction stage 9A in a number of isolated small areas located under the core. In this stage,

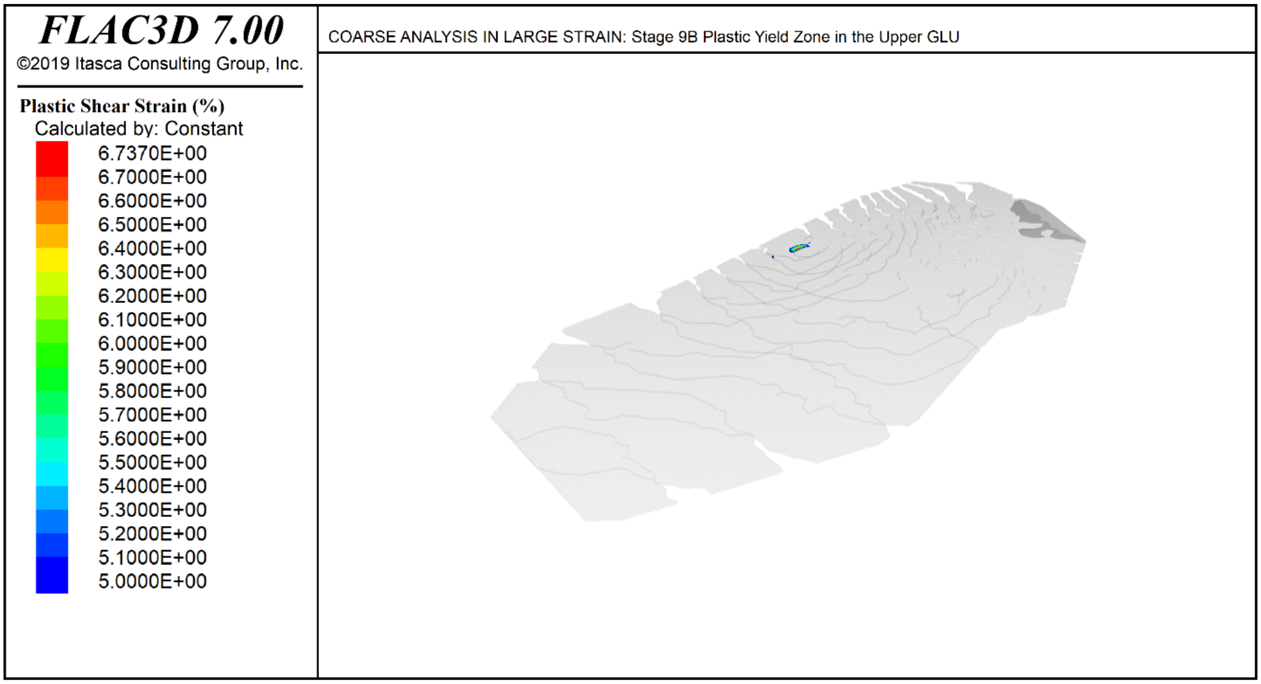

Figure 4.17 The plastic yield zone predicted by the coarse model in large strain.

maximum plastic shear strains in the Upper GLU are around 8% and average shear strains across the plastic yield zone are around 5.5%. In stage 9B, the plastic yield zone expands significantly, reaching a width of over 100m, maximum shear strains reach 14% and average shear strains are at around 8-9%. However, the area of the plastic yield zone is still relatively small, and plastic flow remains fully contained. In this simulation, some stress transfer is noted in construction stages 9A and 9B, where areas in the Upper GLU located on the downstream of the plastic yield zone experience an increase in shear stresses (see Appendix 4A, Figure 4A.4 and Figure 4A.6).

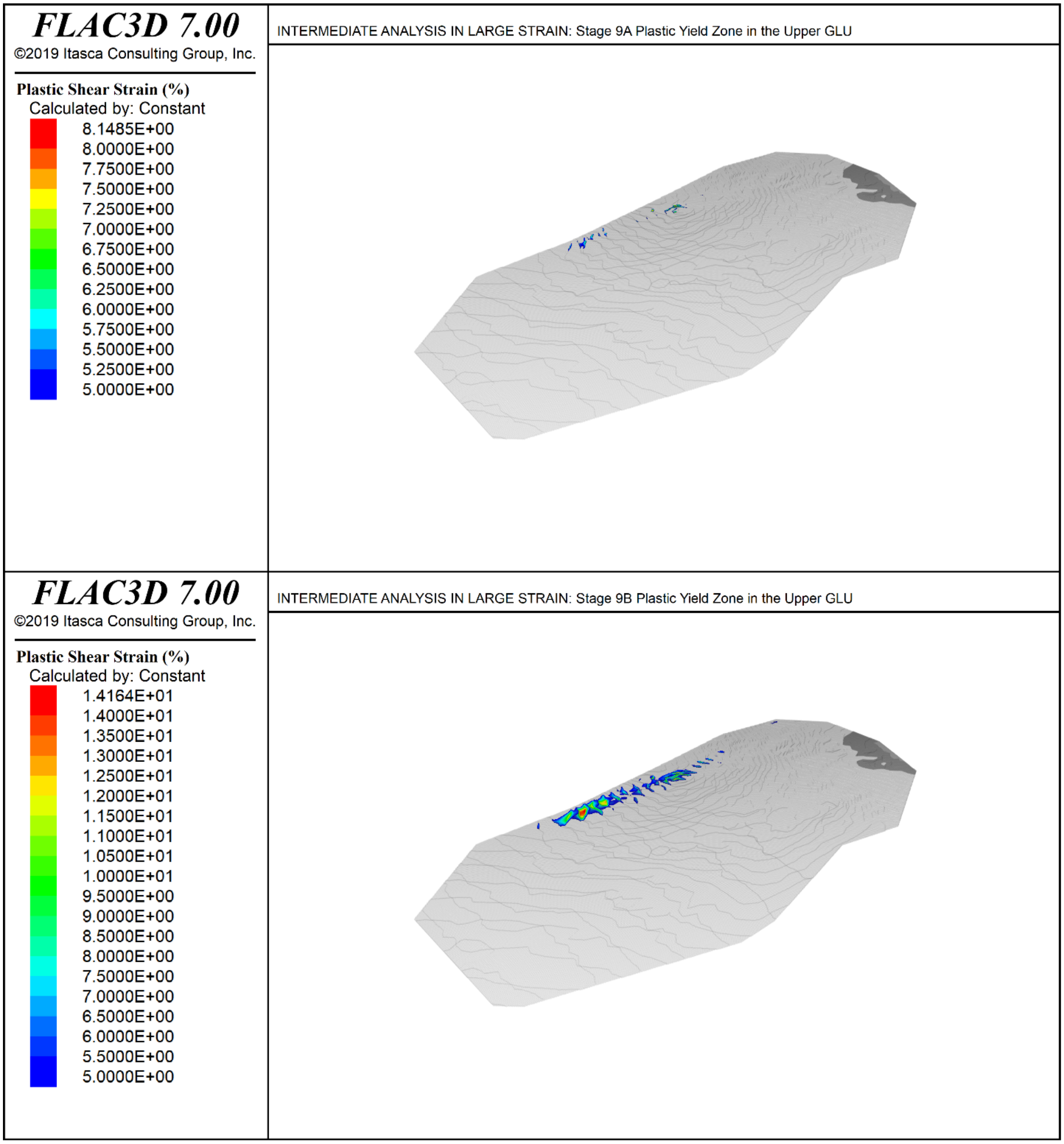

Figure 4.18 The emergence and growth of the plastic yield zone predicted by the intermediate model in large strain.

In the fine simulation of the Mount Polley failure, the plastic yield zone first emerges around construction stage 7 (completed in 2011) when small areas of the Upper GLU material under the core exceed plastic shear strain levels of 5%. In construction stages 7 and 8, the aerial extent of the plastic yield zone is negligible and the weakening within it has no material impact on the overall stability of the embankment. In construction stage 9A (completed in 2013), a large number of isolated plastic yield zones are predicted to emerge under the core, with maximum shear plastic strains reaching 14% and average plastic shear strains reaching 6-7%. In construction stage 9B, the plastic flow in the yield zone becomes uncontained, and the zone continues to propagate indefinitely. The plot of stage 9B plastic yield zone in Figure 4.19 illustrates the spatial distribution of the weakening area at a relatively advanced stage of collapse. It can be seen from this figure that the length of the strain-weakening zone in the foundation reaches 100-150m, and its width encompasses the entire normally consolidated portion of this unit. As it will be demonstrated in

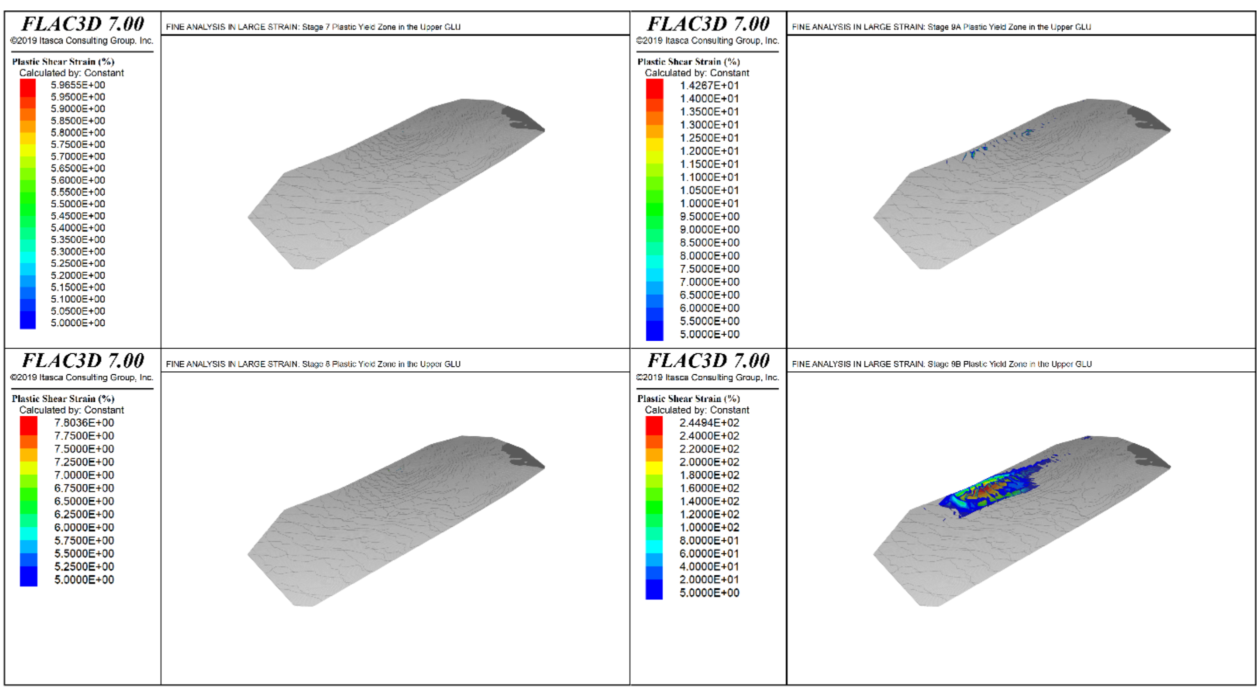

Figure 4.19 The emergence and growth of the plastic yield zone predicted by the fine model in large strain.

§4.4.3, the correspondence of the predicted and actual location and size of failure at foundation level is remarkable.

4.2.3 EVOLUTION OF SHEAR STRENGTH

The evolution of shear strengths in the Upper GLU would have taken place in step with its transition to a state of normal consolidation as well as with the accumulation of plastic shear strains.

Figure 4.20 illustrates the distributions of undrained shear strengths in the Upper GLU in construction stages 3 through 9B predicted by the coarse model. The figure shows that in construction stage 5, substantial portions of this unit transition to an undrained strength model; at this point into the simulation, the undrained shear resistance in its normally consolidated area varies from ~105 to ~130kPa, with an average value of 110kPa. In subsequent stages, undrained shear strengths are seen to gradually rise in step with the increase in vertical overburden stresses (seen in Figure 4.8). In this model, weakening due to an accumulation of plastic shear strains in excess of 5% is not observed in stages 3 through 9A. In stage 9B, some weakening is seen to take place in the region of the plastic yield zone (shown in Figure 4.17), but the average decrease in shear resistance of less than 1%, or <1.5kPa, is not noticeable in the plot.

Figure 4.21 plots the distributions of undrained shear strengths in the Upper GLU in construction stages 3 through 9B obtained using the intermediate model. The figure shows that in construction stage 5, about a quarter of this unit by area transitions to an undrained strength model; at this point into the simulation, the undrained shear resistance in its normally consolidated area varies from ~105 to ~135kPa, with an average value just over 110kPa. In subsequent stages, undrained shear strengths are seen to gradually rise in step with the increase in vertical overburden stresses (seen in Figure 4.9). In this simulation, weakening processes begin in construction stage 9A, when plastic shear strains exceed 5% in a number of small areas under the core (see §4.2.2 and Figure 4.18). In this stage, the loss of shear resistance to strain-weakening in the plastic yield zones is minor at

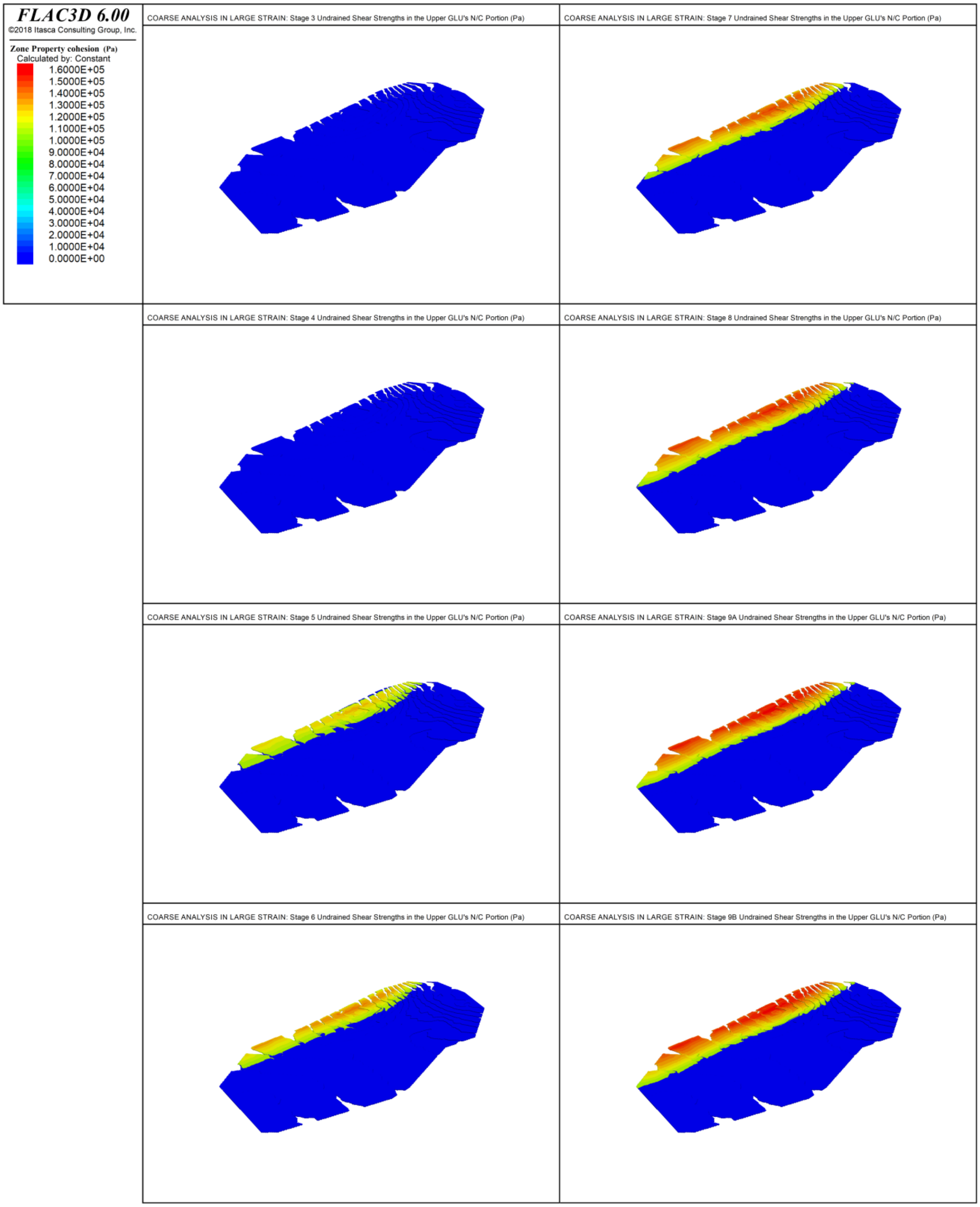

Figure 4.20 Undrained shear strengths in the normally consolidated portion of the Upper GLU predicted by the coarse model in large strain. In blue are the overconsolidated portions of the Upper GLU where drained strength model governs.

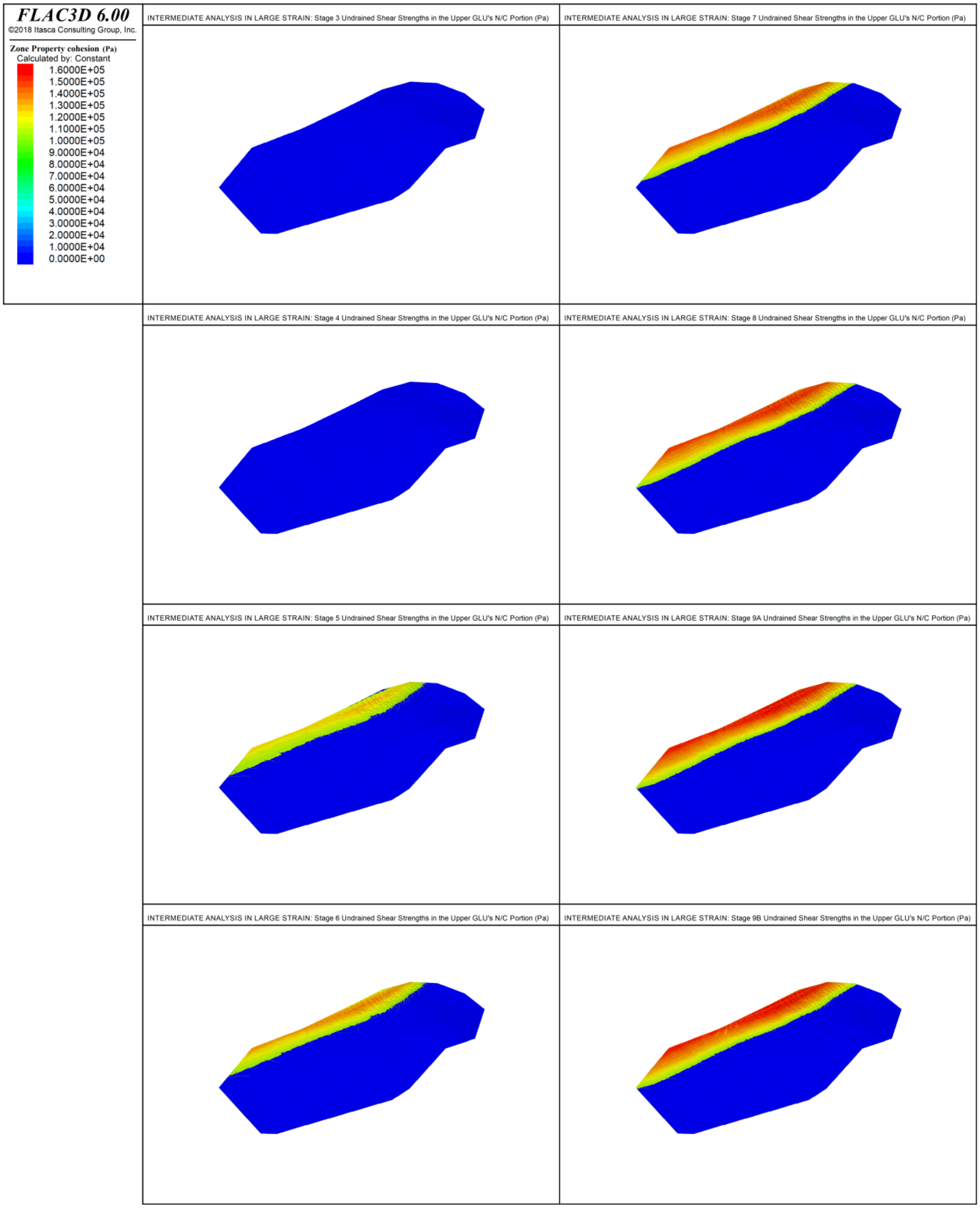

Figure 4.21 Undrained shear strengths in the normally consolidated portion of the Upper GLU predicted by the intermediate model in large strain.

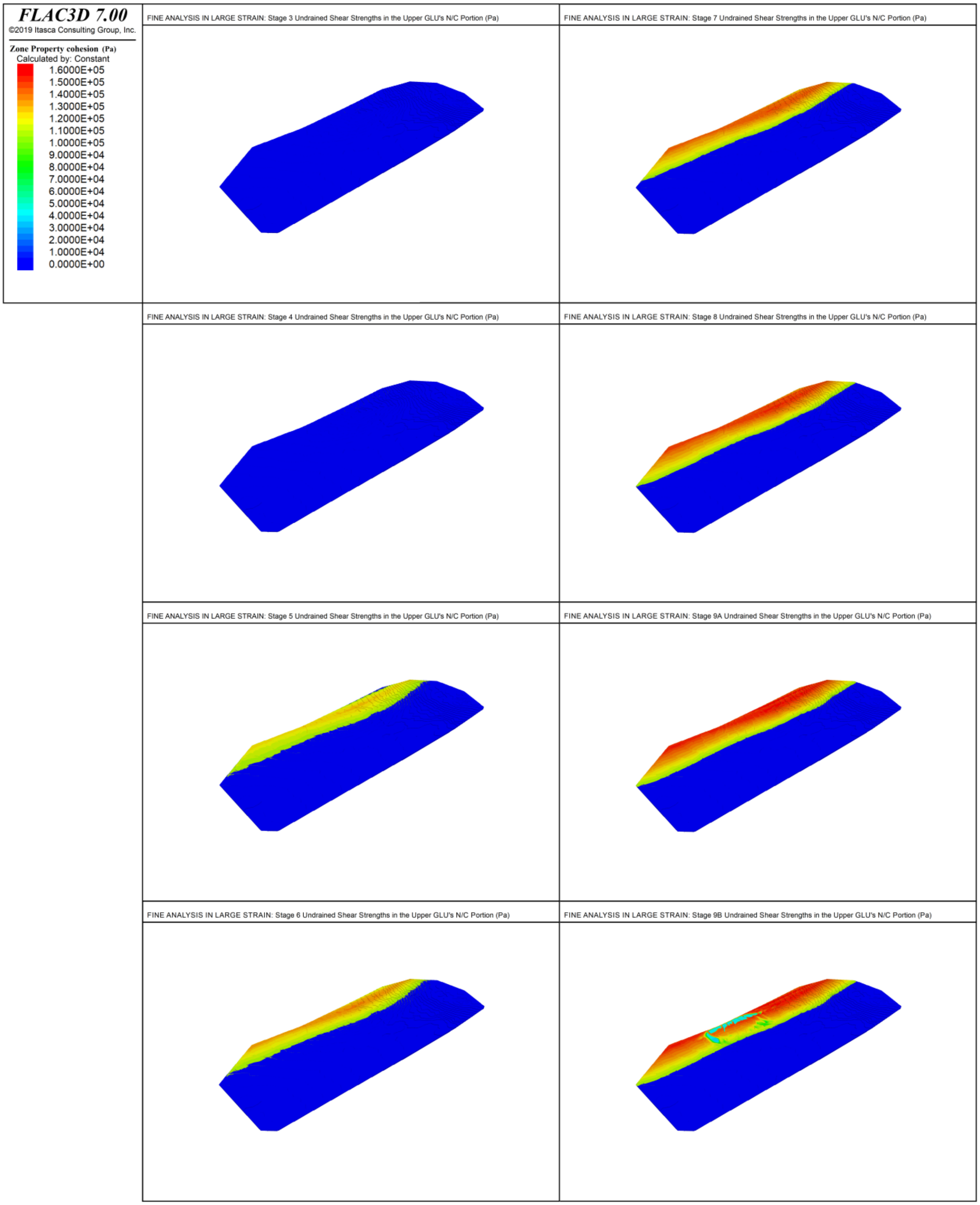

Figure 4.22 Undrained shear strengths in the normally consolidated portion of the Upper GLU predicted by the fine model in large strain.

around 1%, or ~1.5kPa, and is not noticeable in the plot. In stage 9B, a further loss of shear resistance in the plastic yield zone is observed to an average value of about 3-4%. This loss of shearing resistance is visualized on the plot as lighter patches (Figure 4.21, bottom right).

Figure 4.22 illustrates the distributions of undrained shear strengths in the Upper GLU in construction stages 3 through 9B predicted by the fine model. The figure shows that in construction stage 5, about a quarter of this unit by area transitions to an undrained strength model; at this point, the undrained shear resistance in its normally consolidated area varies from ~105 to ~135kPa, with an average value of 115kPa. In subsequent stages, undrained shear strengths are seen to gradually rise in step with the increase in vertical overburden stresses (seen in Figure 4.10). In this simulation, the onset of strain-weakening takes place in construction stage 7 when the plastic yield zone first emerges. In construction stages 7 and 8, the loss of shear resistance due to strain-weakening is negligible and cannot be detected on visual examination (Figure 4.22, right column, top two plots). In stage 9A, the drop in shear resistance due to strain-weakening in the plastic yield zones scattered in the region under the core reach, on average, about 1%, or 1.5kPa. This decrease in shear strength is not visually noticeable (Figure 4.22, right column, third plot down) because it is minor and because it takes place mostly in the soil layers located closer to the base of the unit. In construction stage 9B, the plastic flow in the yield zone becomes uncontained, and strain-weakening processes continue until the soil in this area is fully weakened. Figure 4.22 (bottom right) illustrates the plastic shear strains in the Upper GLU at an advanced stage of collapse; in the figure, some of the soil layers located at the top of the Upper GLU are fully weakened (in light blue), and their shear resistance drops to 40-50kPa. However, the bulk of strain-weakening is taking place in soil layers located at the base and in the middle of this unit and is concealed in this view.

A better view of the soil layers that have sustained appreciable strain-weakening at this stage is seen in Figure 4.23 (bottom) illustrating the undrained shear strengths in of the Upper GLU in a cross-sectional view passing approximately through the center of the slide. In this figure, a single continuous soil band is seen at or close to the base of the unit (in light blue), where the undrained shear resistance has decreased to residual strength.

4.2.3.1. BIFURCATION

The emergence of the plastic yield zone pinpoints the moment when a condition called "bifurcation" materializes in the modelled domain. "Bifurcation" is a mathematical concept used in continuum mechanics to describe the appearance of a discontinuity in the strain increment field and to denote the onset of a non-uniform response in the model (Sulem 2010). At the moment of bifurcation, the strain rates and velocities begin to diverge inside and outside this discontinuity and, in a strain-weakening material such as Upper GLU, the shear resistance also begins diverging. The plastic yield zone, is, in effect, an example of such discontinuity.

The divergence of strain rates and velocities brought about by bifurcation is referred to in literature as "strain localization" (Hill 1962; Vardoulakis and Sulem 1995; Sulem 2010). This term emphasizes the increasingly disparate strain response of the material in and outside the discontinuity over time that leads to the formation of a distinct "shear band." In the simulation of Mount Polley, the emergence and development of this shear band is observed in step with the growth of the plastic yield zone. In this zone, the higher strain rates and velocities result in an accelerated accumulation of plastic shear strains. This effect can be appreciated from Figure 4.23 showing the plots of plastic shear strains and undrained shear strengths in the Upper GLU at an advanced stage of collapse in a cross-sectional view passing through the middle of the slide. In the figure, the top plot shows that a single, continuous soil band in the unit, with a thickness of more or less a single zone, has accrued considerable amounts plastic shear strains; and Upper GLU zones located immediately above or below this band are considerably less strained. The bottom plot shows that the soil elements in the shear band have substantially lower shear strengths than the material above or below in spite of being a part of the same unit.

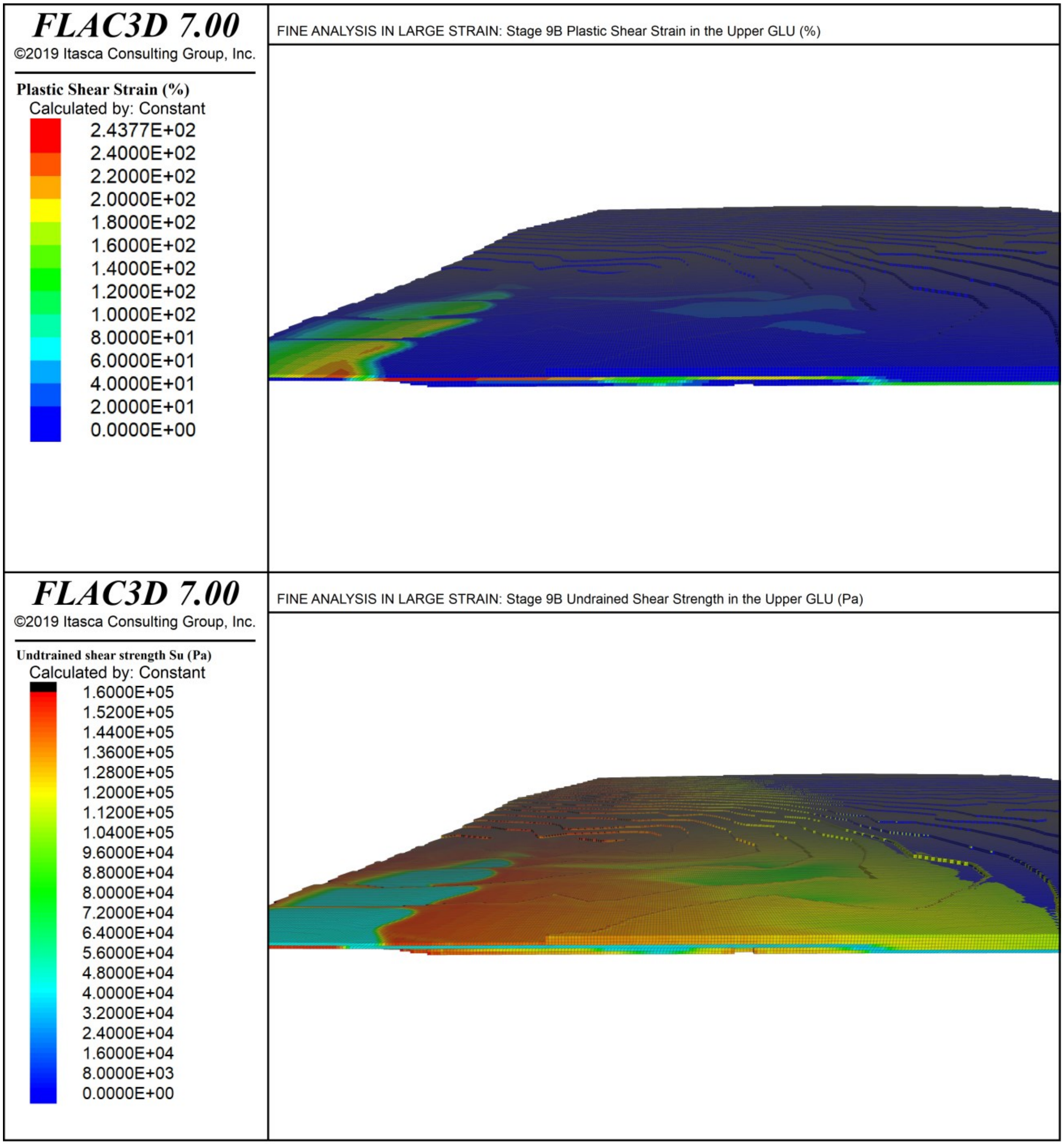

Figure 4.23 A cross-sectional view of the Upper GLU at an advanced point of collapse in construction stage 9B predicted by the fine model in large strain.

4.2.3.2. SHEAR BAND THICKNESS

In a numerical simulation such as that of Mount Polley, the thickness of a shear band discontinuity is bound by the height of a zone, i.e. 0.5m in the coarse model, 0.25m in the intermediate model, and 0.125m in the fine model. This limitation of discrete modelling is a consequence of the assumption that strain increment tensors are constant across a single zone. This characteristic of discrete modelling is one source of scale effects in the simulation of Mount Polley.

Modelling alone cannot be used to determine the true thickness of a shear band discontinuity: increasing the model resolution results in a decrease of the shear band, and vice versa. Theoretically, a model with an infinitely refined mesh will develop shear zones that are infinitely thin. This problem is rooted in the fact that constitutive models do not contain material parameters that include the dimension of length, so that the thickness of the shear band remains undefined (Sulem 2010; Vardoulakis and Sulem 1995, p.10). Therefore, in order to establish the correct thickness of a shear discontinuity, other evidence must be evaluated.

The question of the actual thickness of the shear band is revisited in §4.3 and fully addressed in §6.2.1.

4.3. ONSET OF FAILURE

The "scale effects" phenomenon is briefly discussed in Chapter Three. This phenomenon is caused by discretization errors and is encountered when models identical in every way except their resolution produce different outcomes. Scale effects were anticipated in the model of Mount Polley and were investigated using three models with varying levels of discretization: the coarse, intermediate and fine models.

Pronounced scale effects have been in fact identified in the simulations of Mount Polley; some of them have already been reported in this chapter. Of those, the most consequential one is related to the different rate of accumulation of plastic shear strains in the Upper GLU and the associated rate of weakening in this material: in the fine model, a much higher rate of plastic shear strain accumulation is observed, resulting in an earlier emergence of a plastic yield zone and a greater extent of weakening from stage 7 on.

In the fine model, the loss of shear resistance to weakening in stage 9B becomes uncontained. This response is markedly different from that of the coarse and intermediate models where the structure remains stable and a static equilibrium is reached. This effect is illustrated in Figure 4.24 showing the plots of the average force ratio during the mechanical calculation steps in construction stage 9B. The figure shows that in the coarse and intermediate models, the average force ratio eventually reaches a value of 10^{-5}, indicating convergence and the attainment of static equilibrium. In the fine model, convergence is not attained and the model continues to deform indefinitely.

Stage 9B safety factors calculated for the coarse and intermediate models using the strength reduction method as specified in §3.3.4.4 are, respectively, 1.34 and 1.04. The safety factor of the fine model in stage 9B is taken as unity due to the observed collapse; in actuality, the

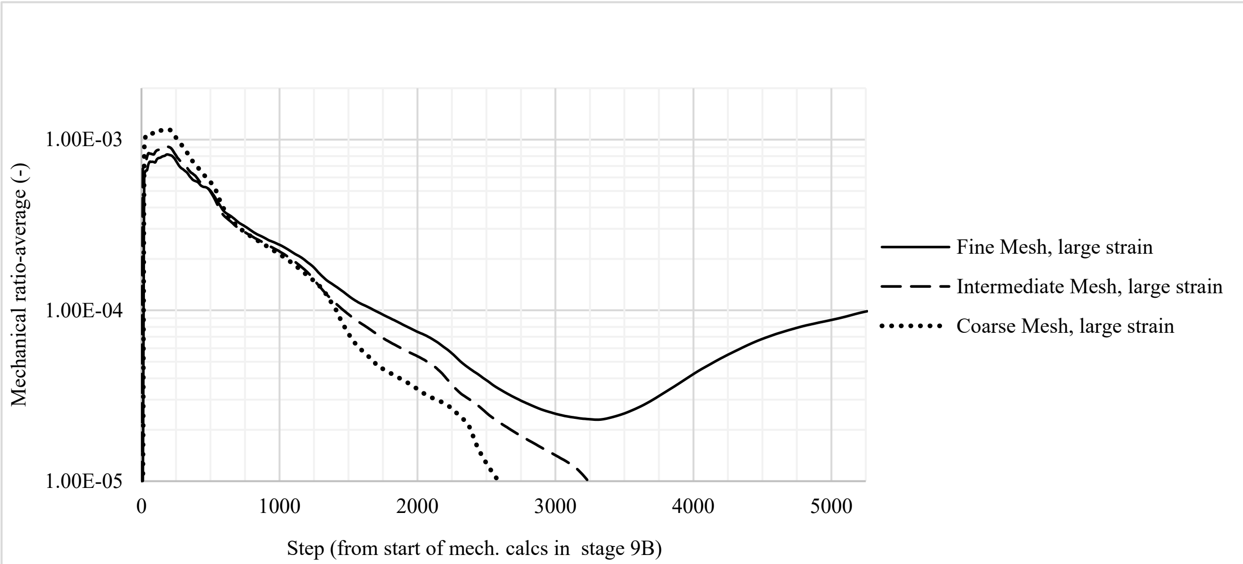

Figure 4.24 The plots of average force ratios vs. mechanical calculation steps in construction stage 9B.

safety factor (as defined in §3.3.4.3) likely varies throughout the collapse phase depending on the degree of weakening in the Upper GLU as well as the extent of mobilization of shear resistance elsewhere in the failing soil mass.

In situ, the collapse of the Mount Polley TSF embankment occurred within 2-4 weeks of the start of construction stage 9B. This means that the fine model correctly replicates the onset of failure.

The presence of the noted scale effects is an indication that the discretization levels of the coarse and intermediate models are not sufficient to minimize discretization errors. This means that these two models do not adequately replicate field conditions. The failure of these two models to correctly replicate the onset of collapse in stage 9B cements this conclusion.

4.3.1 DISCRETIZATION ERROR IN THE FINE MODEL

The correct replication of the onset of failure by the fine model could be taken as evidence that the level of discretization in this model may be sufficient to minimize discretization errors.

However, the correct replication of the onset of failure by the fine model is not definite proof that this model adequately minimizes the discretization error and thus accurately replicates all field conditions. The onset of failure in stage 9B can be potentially simulated by any number of models with a variety of parameter combinations. While the parameters used in the Mount Polley model are realistic in that they are reasonable estimates of material properties derived from testing data, the possibility of error in estimating these should be considered that may offset the error associated with discretization.

In modelling the failure at Mount Polley, a choice was made to select the most conservative estimation of the strain-weakening curve (shown in red in Figure 3.6), where strain-weakening begins at 5% of plastic shear strain, and the material is fully weakened at 60% of plastic shear strain. The calibration of Upper GLU's constitutive model against direct simple shear testing data yields a range of strain-weakening curves that reasonably fit the experimental results, with the strain-weakening processes starting at plastic shear strains somewhere between 5 and 7.5%, and full weakening taking place at plastic shear strains between 60 and 90% (see Appendix 3B).

The discretization error has the effect of delaying the onset of failure: in stage 9B, the coarse model with the largest error produces the most stable slope configuration, the intermediate model produces a slope configuration that is only marginally stable, and the fine model predicts an unstable slope.

On the other hand, a conservative error in the estimation of the strain-weakening curve has the effect of speeding up the onset of failure, i.e. causes it to take place at an earlier construction stage, or at lower embankment loading levels. This effect was evaluated by re-running the fine model using the least conservative estimate of the strain-weakening curve where the onset of strain-weakening takes place at plastic shear strains of 7.5%, and full weakening take at plastic shear strains of 90%. This simulation produces a stable slope configuration.

Figure 4.25 and Figure 4.26 illustrate the results of the fine simulation using the least conservative estimate of the strain-weakening curve. Figure 4.25 shows the plot of the average force ratio in stage 9B. From the figure, it can be seen that an average force ratio of 10^{-5} is reached after ~3,700 mechanical calculation steps, indicating convergence and attainment of static equilibrium. Figure 4.26 illustrates the distribution of plastic shear strains and the plastic yield zone in stage 9B. The magnitude of plastic shear strains and the area of the plastic yield zone predicted in stage 9B by the fine model using the least conservative strain-weakening curve is greater than that predicted in stage 9A by the fine model using the most conservative strain-weakening curve (seen in Figure 4.16, top right, and Figure 4.19, top right). The degree of weakening, the area of the yield zone, and the cumulative horizontal displacements in the Upper GLU predicted by this model in stage 9B are slightly lower than those predicted in stage 9A by the intermediate model; this suggests that the former predicts a marginally more stable configuration.

It can be argued from the above that the correct onset of failure observed in the fine model is not a result of an adequate level of discretization but a combined effect of some discretization error and an exceedingly conservative choice of the strain-weakening curve. It can be inferred that a model

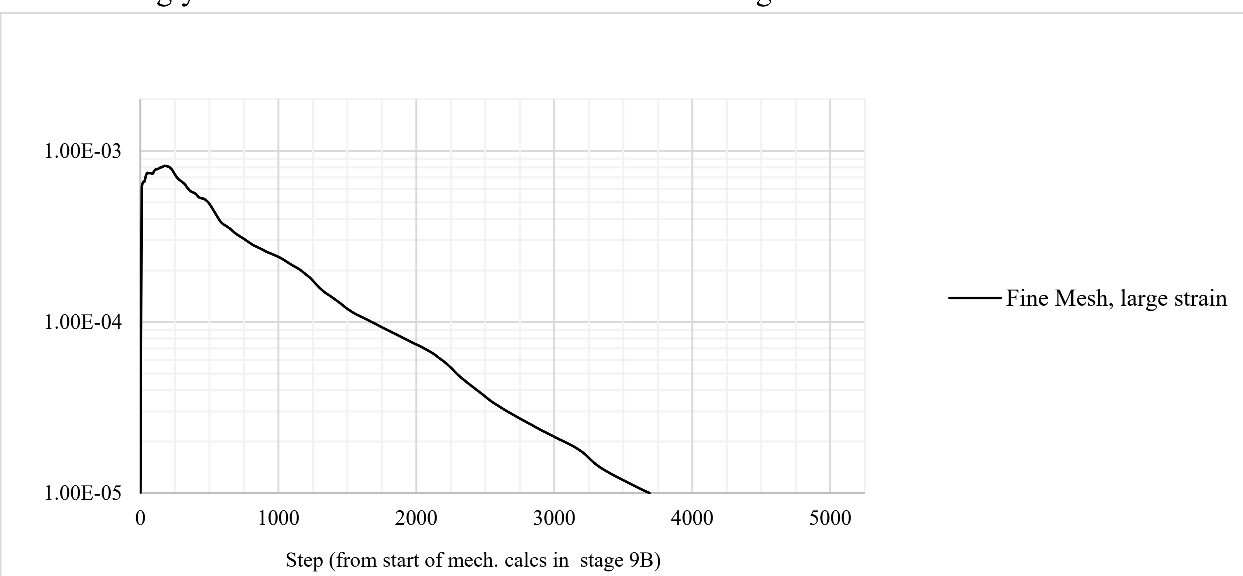

Figure 4.25 A plot of Stage 9B average force-ratio vs. calculation step predicted by the fine model in large strain using the least conservative strain-weakening curve.

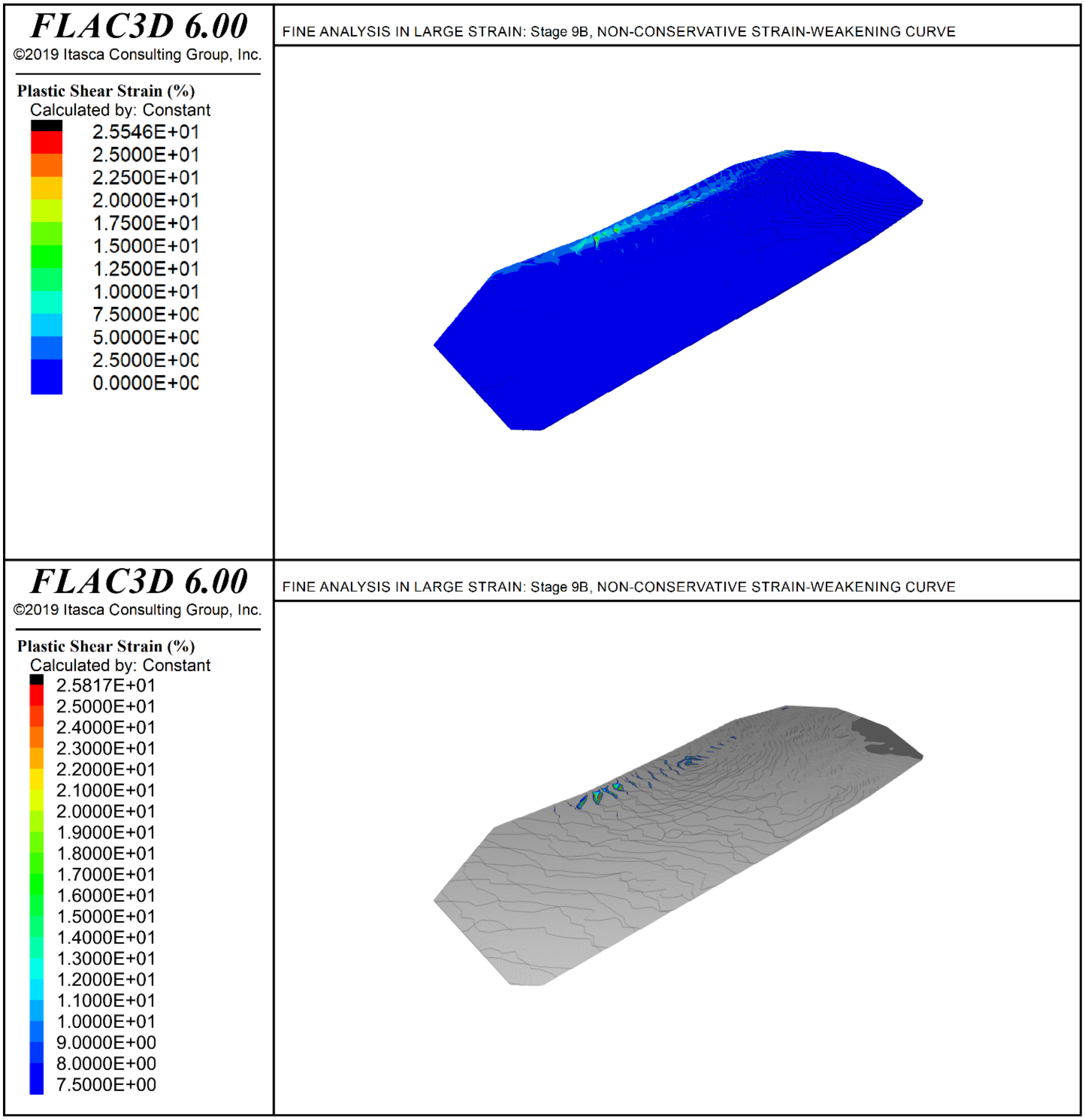

Figure 4.26 Plots of plastic shear strains (top) and yield zone (bottom) in the Upper GLU after the addition of stage 9B material predicted by the fine model in large strain using the least conservative strain-weakening curve.

with a mesh that is even more refined than the one used in the fine model would also accurately replicate the onset of failure if paired with a less conservative choice of a strain-weakening curve.

4.3.2 UPPER AND LOWER LIMIT STATES

The deformation analysis of Mount Polley described in this chapter manifests strong scale effects. Their presence is evidence that the discretization levels of all but the fine resolution model is insufficient to minimize the discretization errors. As a consequence, the coarse and intermediate simulations emulate the assigned material behaviours rather poorly.

From the analysis of the scale effects alone, it is difficult to determine whether the discretization error in the fine resolution model is sufficiently minimized to adequately replicate the mechanical behaviour of soils at the failure location. The stage 9B safety factors (FOS_{coarse}=1.34, $FOS_{interm.}$=1.04 and FOS_{fine}≈1.0) give an indirect indication that in the fine model, the discretization error is not particularly large. There is a considerable decrease in the safety factor due to a mesh refinement in the Upper GLU from 50cm in the coarse model to 25cm in the intermediate model; this suggests that a rather substantial discretization error present in the coarse model is eliminated in the intermediate one. Analogously, the minor decrease in the safety factor brought about by the mesh refinement in the Upper GLU from 25cm in the intermediate model to 12.5cm in the fine model suggests that the discretization error in the intermediate model is not particularly large. This, in turn, may mean that the discretization error in the fine model is smaller yet; however, in the absence of a super-refined mesh analysis, it is difficult to gauge its magnitude.

A further mesh refinement of the Mount Polley model was not feasible due to computational constraints. Therefore, to estimate the magnitude of discretization error in the fine model, another approach was used, referred to as “the analysis of the lower limit state.” It was reasoned that, if a mesh can be discretized ad infinitum, the size of its elements would approach zero. Such elements, should they be prone to strain-weakening, would become fully weakened at zero plastic shear deformation. Therefore, it is possible to approximate the behaviour of a strain-weakening material in a model with an infinitely refined mesh using a model with a regularly sized mesh by assigning to such material an “instant weakening” shear strength behaviour where the onset of full weakening takes place as soon as the plastic shear strains exceed a value of zero. Such analysis would mimic an infinitely thin shear band (as opposed to a shear band that is 50, 25 or 12.5cm thick) and should yield the lowest safety factor, i.e. the lower limit safety factor.

Such a lower limit analysis was conducted in the coarse model by assigning to the normally consolidated portion of the Upper GLU a strain-weakening model that attains full weakening at zero plastic shear strains. In this model, the failure is triggered after the undrained addition of stage 9A loads. This result stood in contrast with field observations, as the actual failure took place in stage 9B, a year after the placement of stage 9A material.

This result invites two conclusions.

First, the results indicate that some discretization error is present in the fine model, albeit it is not large. This finding, in conjunction with the reasoning presented in §4.3.1, invites the conclusion that the most conservative strain-weakening model used to simulate the undrained shear strength behaviour of the Upper GLU material may be too conservative.

Second, the results of the lower limit analysis are evidence that the actual thickness of the shear band is greater than zero. Had the analysis correctly replicated the failure in stage 9B, such result would have suggested a zero shear band thickness; conversely, the premature failure in stage 9A indicates that the “instant weakening” undrained model over-predicts the rate of weakening. This in turn suggests that some non-zero plastic shear deformation must have accrued prior to the failure and consequently that the shear band was thicker than zero.

Similar to the reasoning used to develop the “analysis of the lower limit state,” an argument was made for an “analysis of the upper limit state.” In the coarse model, the strain-weakening processes are minor, and the loss of shear resistance to weakening in the Upper GLU is immaterial. In this analysis, the Upper GLU shows effectively no propensity to strain-weaken, and its undrained resistance equals to its peak undrained strength. If the "lower limit stat" analysis is a simulation of an "instantly weakened" material, then the "upper limit state" analysis is a simulation of a "non-weakening," or non-sensitive, material. Such analysis is somewhat equivalent to the three-dimensional limit equilibrium analysis of the failure using peak undrained strengths introduced in §2.4 and produces a very comparable safety factor value (FOS_{SSR}=1.34 vs. FOS_{LE}=1.31).

The safety factor reduction seen in the intermediate and fine models below the value of 1.34 is owed entirely to the strain-weakening processes in the Upper GLU. Because strain-weakening is virtually absent in the coarse model, it can be argued that a yet coarser mesh model would yield the same, or a very similar, safety factor. In other words, the safety factor produced by the coarse model represents the upper limiting value for the safety factor.

4.3.3 EXCAVATION AT TOE

In construction stage 9A, a 2-m deep, 20-m wide excavation was started at the toe of the dam with the goal of replacing in-situ soils with better fill material. The addition of toe excavation was speculated to have potentially contributed to the collapse, with the investigators noting that further analysis is needed to fully evaluate its effect on stability (KCB 2015, p. 41).

To evaluate the effect of toe excavation, stages 9A and 9B were re-run without the removal of material at the toe. This simulation fails to converge as evidenced by the history chart of stage 9B average force ratio seen in Figure 4.27.

These results indicate that the collapse of the embankment at Mount Polley would have taken place with or without toe excavation.

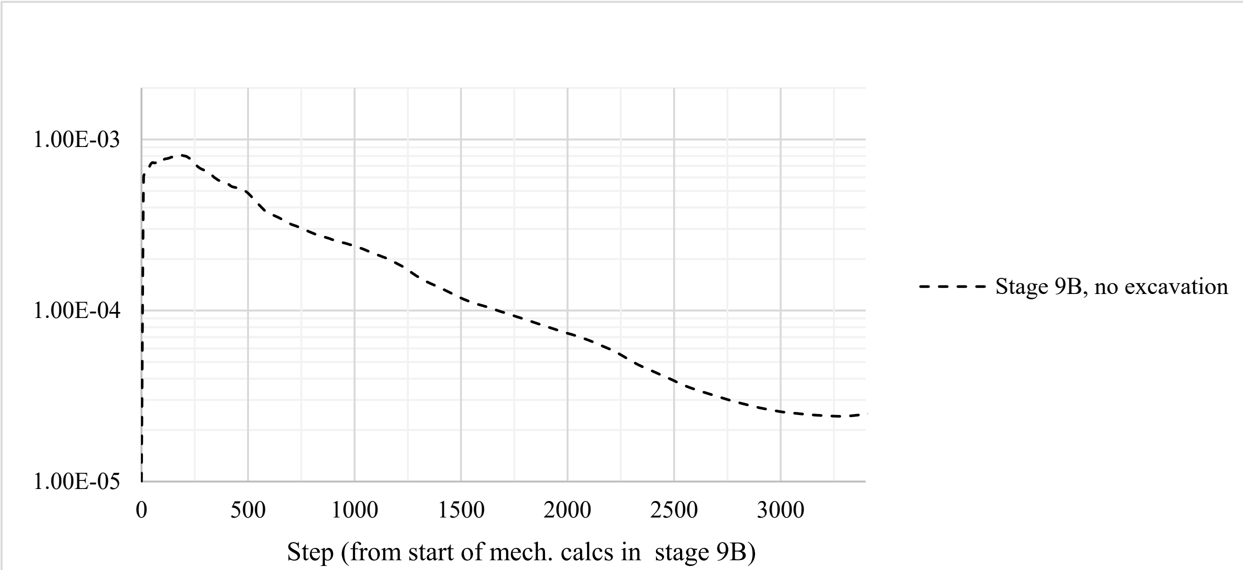

Figure 4.27 A plot of stage 9B average force ratios vs. mechanical calculation steps predicted by the fine model without toe excavation.

4.4. EMBANKMENT DEFORMATIONS

Records of embankment deformations at Mount Polley offer some of the most valuable clues about the unfolding of this failure. Pertinent field observations about embankment deformations prior to and during the embankment collapse have been compiled from the investigation reports and are summarized below. The simulated deformations were evaluated against these in order to determine whether they adequately replicate the actual events.

(1) The embankment collapse was brittle and with no observable precursors, "even on the eve of the breach" (IRP 2015, p. 138). The instrumentation at the failure location was sparse (IRP 2015, p. 13), meaning that little is known about pre-failure deformation levels in the foundation and in the thick of the embankment. However, no surficial indicators of large deformations, such as significant displacements of material at the face, crest or toe, were noted before the collapse occurred at midnight of August 4, 2014.

(2) In the aftermath of collapse, the Independent Review Panel identified field evidence of upthrust in the region of the slide toe, designated as "whaleback features" (IRP 2015, p.16 & Figures 5.1.6, 5.1.7). The upthrusted till was located ~90m downstream of the dam centreline and ~15m downstream of the dam toe, and extended along the dam over a length of 150m or so. The upthrusted region was much broader than the opening in the breached perimeter and supports the conclusion by the IRP (2015) that the breach followed the slip in the foundation.

(3) Parts of the slide headscarp were located on the right abutment in the shell and core area, and the rockfill found on the downstream of the headscarp accrued considerable deformation (IRP 2015, p. 21 & Figure 5.1.6).

(4) There was ample evidence of rotational displacement in the failed soil mass, including the "whaleback" features, tilted bedding/lift lines (IRP 2015, Figure 5.1.5; KCB215, Figure 5.40b) and post-failure overtopping (KCB 2015, p. 34).

(5) A large shear zone was identified in the core material near the foundation on the upstream edge of the slide. Multiple cracks, softening, disturbance and infilling with foreign materials including tailings, gravel and cobbles were observed in the shear zone (KCB 2015, p. 19). Block samples from the area show microscopic shear zones (IRP 2015, Appendix C).

4.4.1 EMBANKMENT SETTLEMENT

In a numerical simulation, the model domain accrues deformations in response to loading irrespective of whether the structure is stable or not. For example, in the model of Mount Polley, surface settlement and other minor deformations take place in all simulated stages, despite all but one (stage 9B in the fine model) having stable slope configurations. Further in this section, such deformations will be referred to as "settlement" for simplicity, although they also include some lateral deformations.

Similar ground deformations would have also been observed in the field, as consolidation settlement would have taken place in response to new loading after each construction stage. However, it is not possible to assess how well the predicted ground settlements match the actual ones, since settlement was not tracked throughout the construction, and no attempt was made to calibrate this aspect of modelling predictions.

Why track settlement? Deformations predicted in a stable model can be thought of as "background noise," meaning that they are not associated with failure processes and therefore they do not offer any insight about the unfolding of the failure. However, in models that do predict failure, such deformations are still present. In order to distinguish the deformations associated specifically with failure, settlement was tracked and subtracted from total deformations.

How was settlement tracked? The coarse simulation of the Mount Polley TSF predicts, in construction stage 9B, a very stable embankment configuration. In this simulation, strain-weakening processes are not observed until stage 9B; when these finally emerge, they remain restricted to a minimal area and are negligible in magnitude. This means that the deformation in stages 3 through 9B predicted by the coarse model can be taken as a baseline case, where virtually all observed deformation is adjustment in response to new loading and is not associated with failure processes. By comparing it to the deformation predicted by the fine model (that does predict failure in stage 9B, as observed in actuality), the deformation component associated specifically with the failure processes can be isolated.

The deformations predicted by the coarse, intermediate and fine models are nearly-identical up to the point where the progressive failure begins. This means that the deformations predicted by the coarse model in the later construction stages can be used to establish the deformation baseline for the other two models.

Tracking settlement proved particularly useful when evaluating the extent of crest drop and toe uplift during collapse, as it helped better identify the predicted location and extent of this type of deformation. Additionally, tracking settlement through the staged simulation of Mount Polley helped identify a source of discrepancy between simulation results obtained in large vs. small strain; this finding is discussed in §6.6.1.

Table 4.3 Embankment settlement in the area of the slide obtained from the coarse simulation in large strain.

Location	Approximate settlement of embankment surface due to the addition of material in the beach, crest and shell areas (m)		
	beach	crest	shell
Stage 3	0.12	0.13	0.13
Stage 4	0.11	0.11	0.12
Stage 5	0.18	0.19	0.32
Stage 6	0.14	0.20	0.23
Stage 7	0.14	0.21	0.18
Stage 8	0.17	0.20	0.16
Stage 9A	0.17	0.23	0.26
Stage 9B	0.14	0.23	0.26

The settlement of the embankment surface tracked in construction stages 3 through 9B with the use of the coarse model is illustrated in Appendix 4B. The approximate magnitudes of downward displacements at the embankment surface at the mid-point of the slide in the beach, crest and shell areas are listed in Table 4.3. These data indicate that in each construction stage, predicted embankment surface settlements ranged between 0.1 and 0.3m and were greater in the shell and crest areas.

4.4.2 LATERAL DISPLACEMENTS

In order to assess, in a meaningful way, deformations brought about by the progressive failure of the embankment and foundation materials, two types of deformation are distinguished: *cumulative* and *incremental*.

The embankment at the Mount Polley TSF was built in multiple stages over the course of nearly two decades. Some deformation (such as settlement discussed in §4.4.1) was accrued *incrementally* every time after a change in loading conditions (i.e. an addition of material) took place; on the basis of the one- and two-dimensional consolidation studies conducted by the Independent Review Panel (IRP 2015, Appendix H) the conclusion is reached that ground adjustments to new loading were largely complete by the time of the subsequent construction stages. In a staged construction process, deformations accrued in preceding stages are concealed, i.e. visually "reset to zero," in subsequent stages by the addition of new material to a predetermined embankment elevation and horizontal position. As a result, all embankment deformations associated with progressive failure, such as horizontal displacements or a drop at crest, as an example, would have been observed in situ along with incremental displacements associated with the ongoing construction stage, and not as a part of the total of deformations from the start of the dam construction.

In the simulation of the Mount Polley TSF, deformations in the domain accrue in each simulated construction stage. By stage 9B, domain displacements are composed of the totality of these deformations, plus the deformations brought about by the contained progressive failure (in the intermediate and fine models) as well as the embankment collapse (in the fine model only). Therefore, *cumulative* deformations are not particularly useful in evaluating the match between predicted and observed surface deformations either prior to or during collapse. For example, one should not compare the predicted cumulative surface deformations to stage 9A to in-situ deformations prior to the collapse as the former is cumulative whereas the latter are incremental. Instead, incremental deformations associated with each construction stage (especially starting with stage 7 when the plastic yield zone was first noted in the fine model) must be assessed separately against field observations over the pertinent period.

On the other hand, cumulative deformations are useful when assessing displacements in the foundation materials that remained undetected in the field until collapse due to a lack of instrumentation.

The cumulative and incremental deformations were tracked through the staged simulation of Mount Polley using the fine model; the former was used to evaluate displacements in the foundation materials, and the latter was used to assess the extent of predicted surface deformations.

4.4.2.1. CUMULATIVE SHEAR DISPLACEMENTS IN THE FOUNDATION

The accumulation of horizontal displacements in the Upper GLU was tracked in stages 3 through 9B and is documented in Appendix 4C. The maximum horizontal cumulative displacements predicted in each construction stage using the coarse, intermediate and fine models are listed in Table 4.4. The upstream-to-downstream direction of horizontal displacement is taken as sign-positive.

A number of observations were made on the examination of horizontal displacements accumulated in the Upper GLU over the duration of embankment construction; these are discussed below.

Table 4.4 Cumulative maximum horizontal displacements in the Upper GLU (m).

Mesh	coarse	intermediate	fine
Stage 3	0.049	0.043	0.044
Stage 4	0.053	0.053	0.053
Stage 5	0.061	0.060	0.061
Stage 6	0.077	0.085	0.086
Stage 7	0.095	0.104	0.105
Stage 8	0.103	0.113	0.113
Stage 9A	0.129	0.139	0.138
Stage 9B	0.145	0.156	indefinite

(1) Horizontal displacements are largely in the upstream-to-downstream direction, i.e. consistent with the movement of the soil mass during collapse. The horizontal displacements in the direction parallel to the dam centreline are smaller by one or two orders of magnitude and do not appear to offer any particular insight about the mechanical behaviour of the structure.

(2) In each simulated stage, horizontal displacements closely follow the footprint of the embankment, and the areas exhibiting the largest displacements are located under the core, where the extent of loading is the greatest. This suggests that horizontal displacements in the Upper GLU were largely driven by embankment loading.

(3) The horizontal displacements predicted by the coarse, intermediate and fine models are close[6]. The difference between the predictions by the fine and coarse models of maximum horizontal displacements is near-zero in stages 3 through 5 and in the order of 1cm in stages 6 through 9A. The differences between the predictions by the intermediate and coarse models of same are very similar.

(4) There appears to be no notable accumulation of horizontal displacements in the direction of downstream that can be attributed to plastic yielding[6]. In the intermediate model, the plastic yield zone first emerges in construction stage 9A; yet only a slight increase in deformation levels (in the order of 1cm) can be detected when the results of the coarse and intermediate

[6] With the exception of stage 9B where failure was predicted by the fine model but not by the coarse or intermediate ones.

models are compared. In the fine model, the plastic yield zone first appears in construction stage 7; a similar increase in deformation levels in the order of 1cm can be detected in this stage when the results of the coarse and fine models are compared.

Cumulative horizontal displacements in the downstream direction throughout the entire structure were also examined; some representative results are illustrated in Figure 4.28. From the figure, the following observations are made:

(1) Movements in the foundation and embankment are concentrated in the zone above the Upper GLU; no significant lateral displacements are noted below the base of this unit.

(2) The lateral displacements in the foundation materials directly above the Upper GLU are very close to those seen in the Upper GLU. This suggests that the soil mass is "riding" on top of the Upper GLU.

(3) In stage 7 and on, the slide begins to take shape: the soil mass experiencing notable lateral displacements corresponds to the soil mass that eventually fails. In the cross-sectional view at

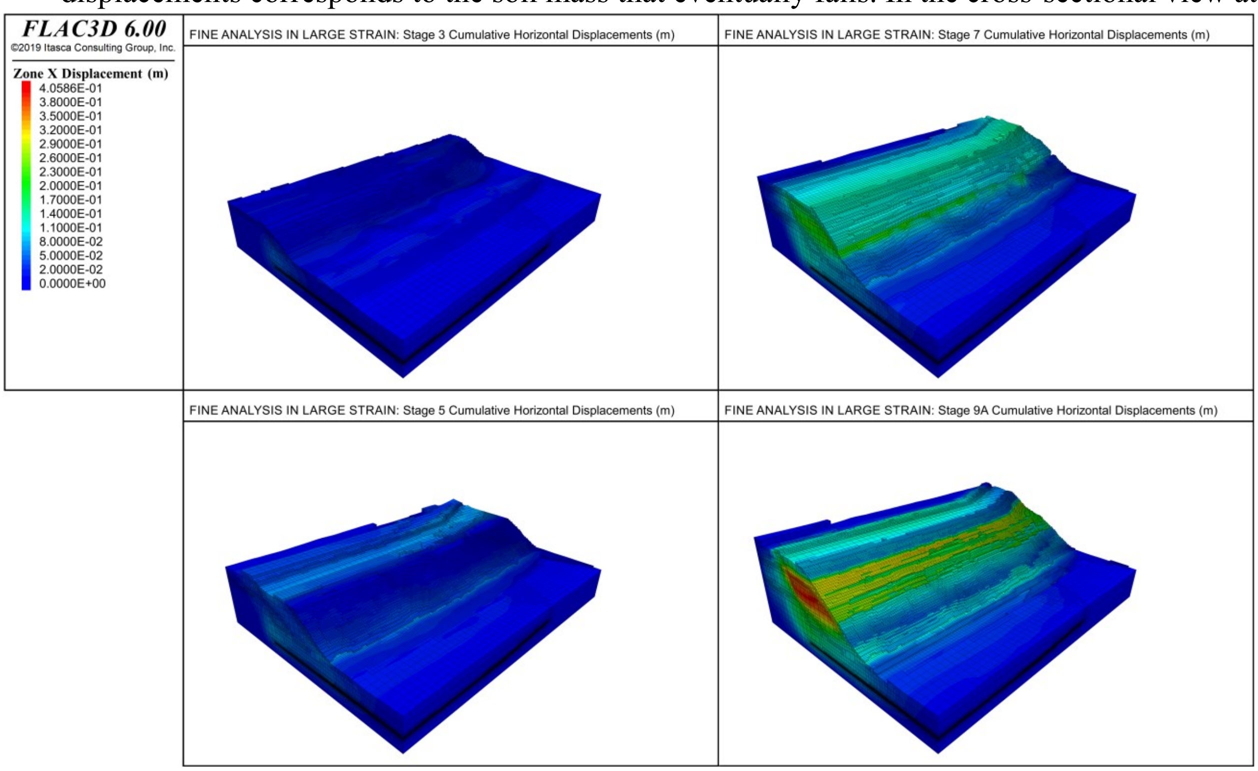

Figure 4.28 Lateral displacements accrued in the embankment and foundation materials predicted by the fine model in large strain.

the middle of the failure location, the upstream extent of slide passing through the upper till and core materials is clearly defined. Likewise, the extent of the slide on the downstream around the toe location can be identified by the presence of lateral displacement in the slide area and the absence of it on the downstream.

A number of conclusions can be drawn from the results presented in this section:

(a) The lateral displacements seem to originate in the portion of the Upper GLU located directly under the embankment.

(b) The horizontal displacements in the Upper GLU appear to largely drive the movement in the rest of the soil mass.

(c) Since the cumulative displacements predicted in the Upper GLU by the coarse, intermediate and fine simulations are nearly identical at every stage prior to collapse. As these displacements appear to be the primary driver of deformations elsewhere in the model domain, a conclusion can be drawn that the extent of shear strength mobilization through the soil mass in response to deformation is nearly identical in the three models. The marginally higher levels of lateral displacement seen in the finer models can be seen as a response to the slightly higher levels of weakening seen in these models.

(d) The almost identical levels of lateral displacements predicted by the coarse, intermediate and fine models stand in contrast with the different levels of accumulated plastic shear strains[6]. This suggests that lateral deformations are not a reliable indicator of the extent of shear strain and should not be used to judge the extent of strain-weakening.

(e) The nearly identical levels of lateral displacements in the coarse, intermediate and fine models (excluding collapse) are not as suprising as they may seem in the context of scale effects noted with regard to the different rate of accummulation of plastic shear strains. Prior to collapse, the plastic shear strains are not particularly large, and do not translate into significant lateral displacements to begin with. Second, the magnitude of predicted plastic shear strains increases with model resolution, but, with lower zone heights, such increase in strains does not translate into larger displacements. For example, the stage 9A maximum plastic shear strains predicted by the coarse model are 4.0%, translating into 2cm of lateral displacement. This amount of displacement due to plastic shearing is not particularly different from that predicted by the intermediate model (at 2.02cm representing 8.1% of maximum plastic shear strain) or by the fine model (at 1.72cm representing 14.3% of maximum plastic shear strain).

4.4.2.2. PRE-FAILURE SURFACE DEFORMATIONS

The failure at Mount Polley was characterized as brittle and with no observable precursors. This suggests that the pre-collapse deformations at the embankment surface that may been caused by the progressive failure were minor and easily overlooked. In this section, the incremental deformations predicted by the fine model at the embankment surface are examined to determine whether the predictions by the fine model match observation.

The incremental surface deformations predicted by the fine simulation in stages 6 through 9A are shown in Figure 4.29. From the figure, the following observations are made:

(1) In construction stage 9A, horizontal displacements at the face of the dam range between 2 and 8cm, and vertical displacements range between 10 and 25cm. These movements take place mostly at near the top of the face; at the toe, the deformations are negligible.
(2) In the region of the toe excavation, some minor uplift in the order of 2cm is predicted in stage 9A. This deformation cannot be seen from the figure and is identified by way of examination of gridpoint displacements in the local zones.
(3) The highest levels of deformation are observed at the crest in the core area where horizontal displacements reach 10-15cm and vertical displacements reach 30cm.
(4) The magnitude and location of incremental displacements in stage 9A are not materially different from those seen in stages 6 to 8. In each construction stage, the embankment surface

settles by 10 to 30cm; in this context, the downward displacements in stage 9A do not stand out. Similarly, stage 9A incremental horizontal displacements at the face of the dam are very comparable to those seen in stages 6 through 8. Finally, the largest deformations are consistently observed at the crest and at the top of the face.

(5) The magnitude and location of vertical displacements predicted by the fine simulation in stages 7 through 9A are comparable to settlement levels determined in §4.4.1. This suggests that deformations associated with plastic flow are insignificant.

In situ, incremental deformations after the addition of stage 9A material would have been accrued between the fall of 2013 and the early summer of 2014. The magnitude of incremental displacements predicted by the fine model in stage 9A is comparable to those seen in previous stages. This finding suggests that the levels of deformation predicted by the fine model in stage 9A would have not been visually detectable at the face of the embankment. This result matches field observations.

In stage 9B, the fine model cannot attain a static equilibrium and deformations accrue indefinitely. Consequently, pre-failure incremental deformations were not evaluated this stage, since there is no simple way to distinguish pre-collapse deformations from deformations accrued after the initiation of collapse.

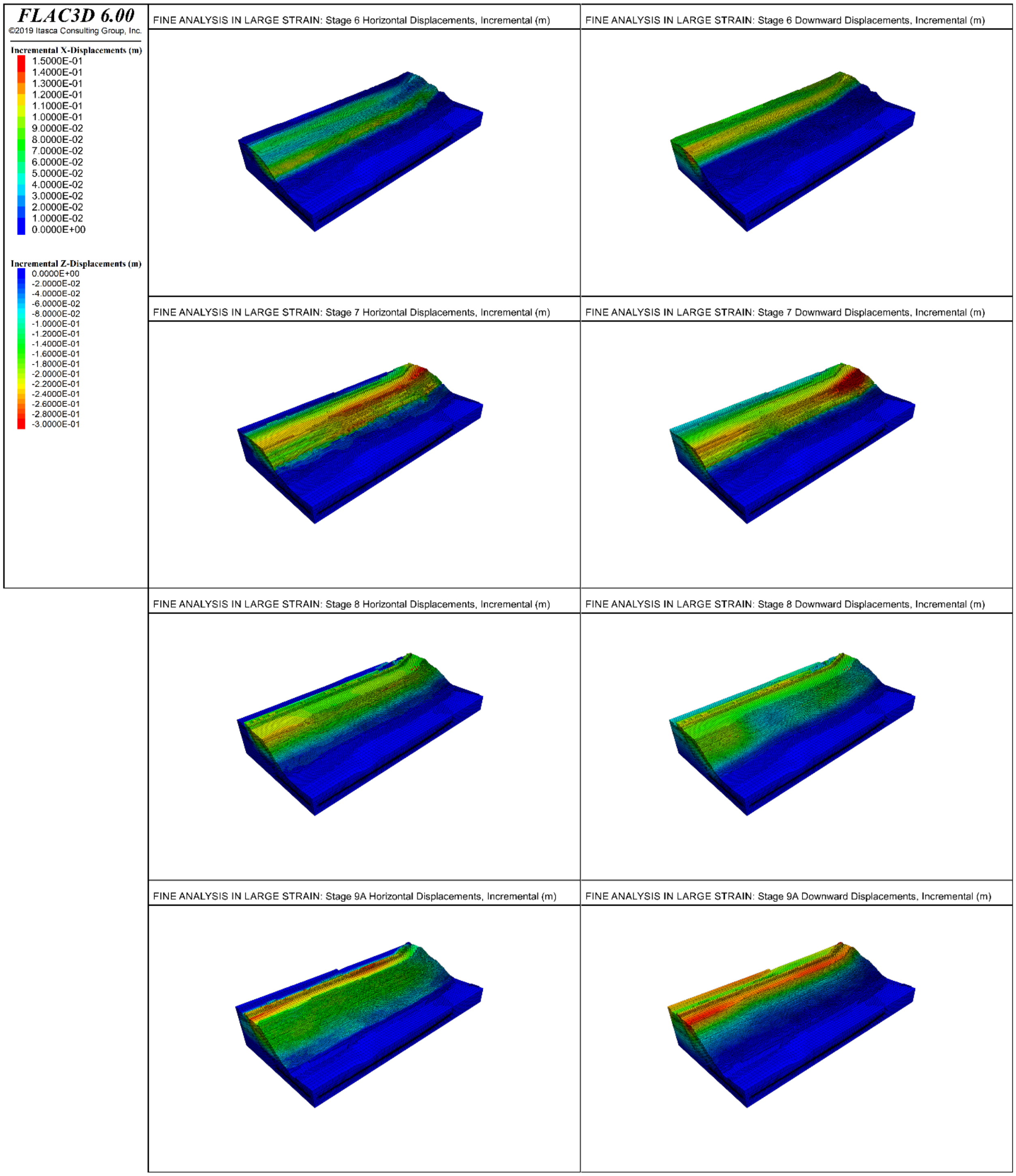

Figure 4.29 Incremental deformations of the embankment surface in construction stages 6 through 9A predicted by the fine model in large strain.

4.4.3 GEOMETRY OF FAILURE

The geometry of failure at the Mount Polley TSF was reconstructed by the Independent Review Panel from surface and subsurface investigations. Figure 4.30 (reproduced from IRP (2015)) illustrates the main features of the slide. On the left of the figure, the location of the failure is shown in plan view. The width of the slide at the foundation level extends approximately between Stn. 4+100 and Stn. 4+300. The width of the slide at the foundation level can be appreciated from the length of the uplift zone in the toe region, seen in the photo to the right.

At the ground and crest levels, the slide appears to have a much smaller footprint, spanning a width of just under 100m from Stn. 4+200 to Stn 4+290.

The toe of the slide, identified from the "whaleback" features (labelled as "W" in the photo to the right), is located approximately 85 to 95m downstream of the dam centreline. Cracks in the exposed soils demarcate the upstream extent of the slide.

The geometry of failure predicted by the fine model was determined by examining the simulation of stage 9B at an advanced point of collapse. The predicted results were then compared to field observations to evaluate the goodness of fit of the simulation.

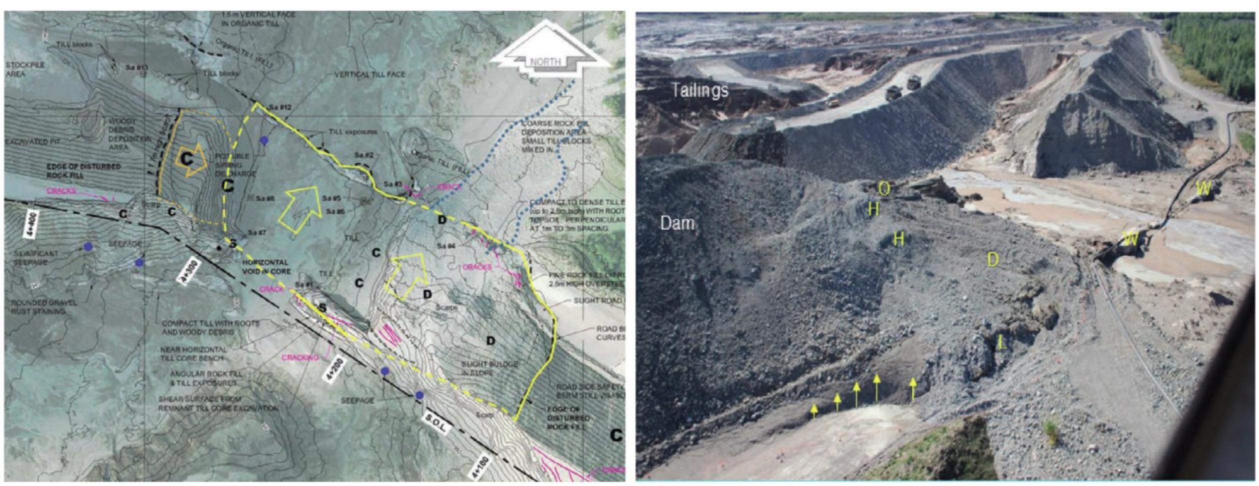

Figure 4.30 The geometry of failure at the Mount Polley TSF (reproduced, with permission from the Govt. of British Columbia, from the IRP 2015 report, Figures 5.1.6 and 5.1.7).

4.4.3.1. EXTENT AND LOCATION OF THE FAILURE

The predicted width and location of the slide base can be estimated from the size and location of the plastic yield zone in stage 9B at an advanced point of collapse. Figure 4.31, showing a view of the Upper GLU 6700 mechanical calculation steps after the addition of stage 9B material, visualizes the plastic yield zone in the Upper GLU. At this point in the simulation, the zone spans a width of ~140m from Stn. 4+145 to Stn. 4+285.

The plastic yield zone grows appreciably wider as the collapse progresses; this process can be noted by comparing Figure 4.19, bottom right, to Figure 4.31. The former shows the plastic yield zone at a point where collapse is underway, and the maximum plastic shear strains reach 250%; the latter shows the plastic yield zone at an advanced point of collapse, where maximum plastic shear strains are in excess of 400%. The width of the plastic yield zone in the latter is roughly double of that in

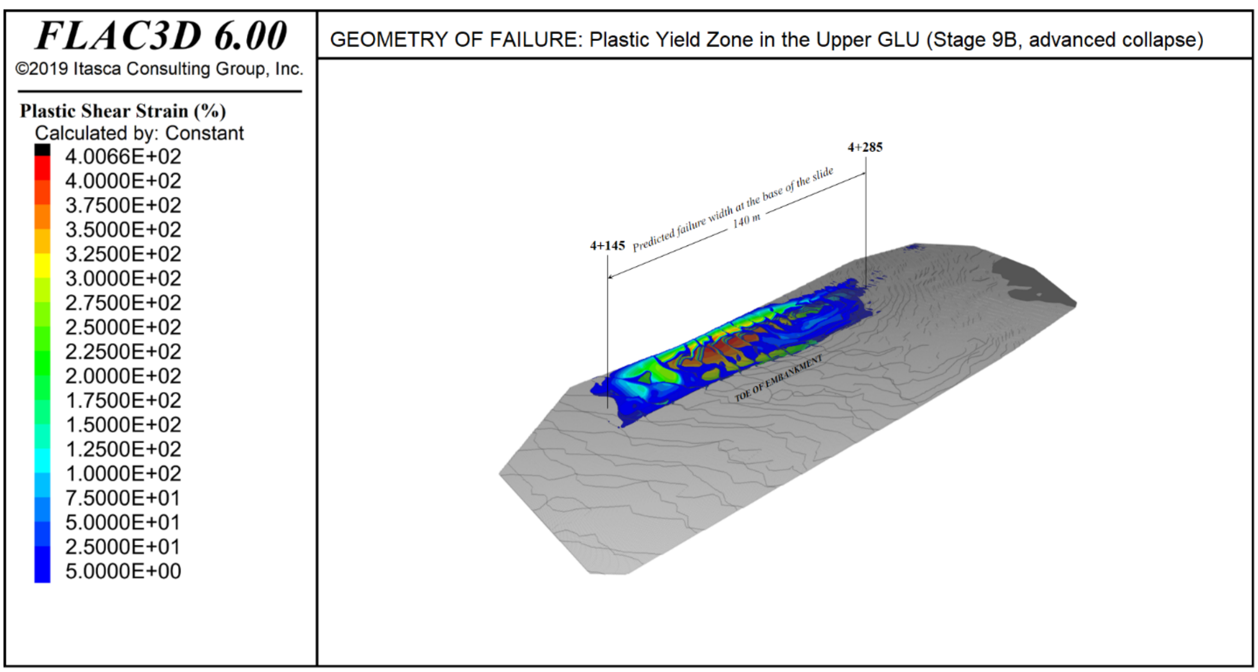

Figure 4.31 Plastic yield zone in the Upper GLU at an advanced point of collapse in stage 9B predicted by the fine model in large strain.

the former. It is conceivable that the predicted width of the slide would have grown further had the simulation of collapse continued.

Figure 4.31 also shows that in the middle of the plastic yield zone, in an area with a width of about 40-50m, the plastic shear straining and associated weakening processes are significantly more advanced than anywhere else in the unit. In this area, coloured in hues of reds, the plastic shear strains vary between 300 and 400%, the soil is fully weakened, and associated shear displacements are significant, ranging from 0.4 to 0.5m. Elsewhere in the plastic yield zone, plastic shear strains range anywhere from 200% near the “red zone” to well below 50% closer to the edges. In Figure 4.32 showing Upper GLU’s cumulative horizontal displacements in the downstream direction at the same point in the simulation, the “red zone” is the area with substantially larger shear displacements than the neighbouring regions.

The predicted extent and location of the slide in the embankment materials can be assessed from Figure 4.33 showing incremental horizontal displacements at the same point of collapse. From the

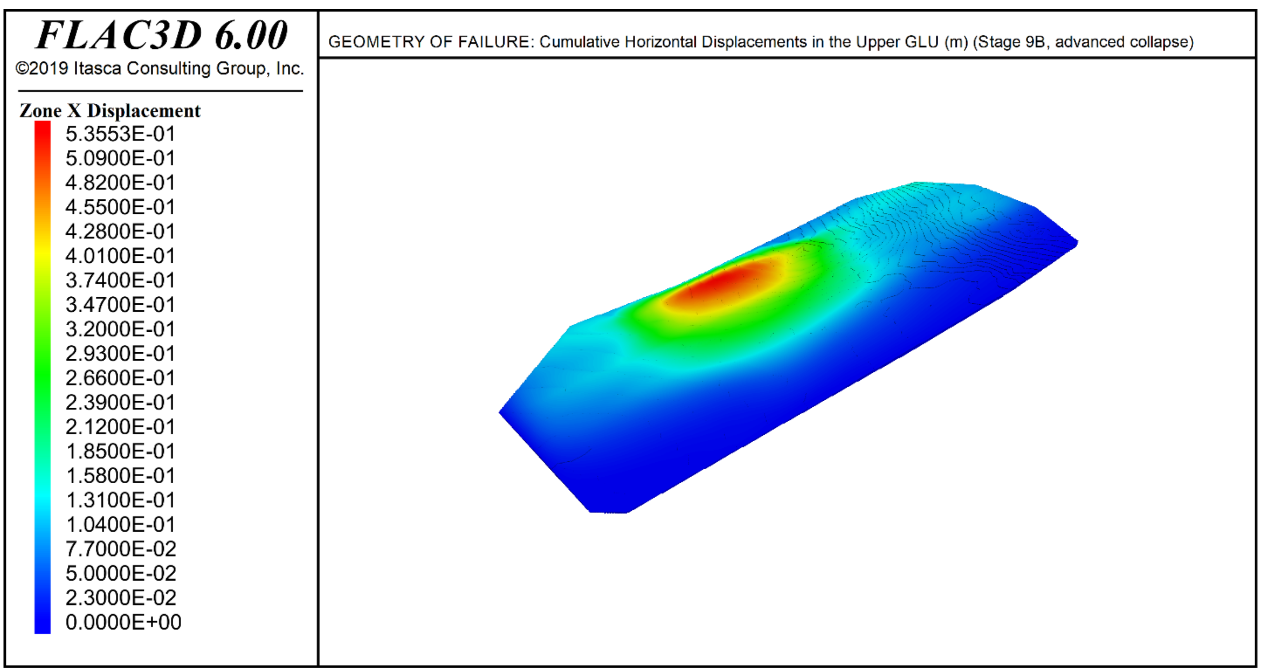

Figure 4.32 Cumulative horizontal displacements in the Upper GLU at an advanced point of collapse in stage 9B predicted by the fine model in large strain.

figure, the slide is seen to extend over a width of ~100m from Stn. 4+165 to 4+270. Also from the figure it is evident that that the “red zone” illustrated in Figure 4.31 is situated precisely below the predicted slide location in the embankment materials; this suggests that the movement in the embankment is related to the large displacements in the “red zone.”

A cross-sectional view of the embankment and foundation materials is seen in Figure 4.34 showing incremental horizontal displacements accrued 6700 mechanical calculation steps after the addition of stage 9B material. The figure illustrates the volume of the failing soil mass and the shape of the slip surface at the midpoint of the slide. On the upstream, the slip surface passes through the core and upper till materials to meet the Upper GLU at its upstream edge. In the Upper GLU, the slip surface becomes horizontal, with no significant displacements below it.

The shape and location of the slip surface that develops at this point in the simulation can also be identified from the plots of maximum shear strain rates, such as the one in Figure 4.35. In the figure, the zones that are rapidly accruing shear strains are shown in hues of reds, greens and pale

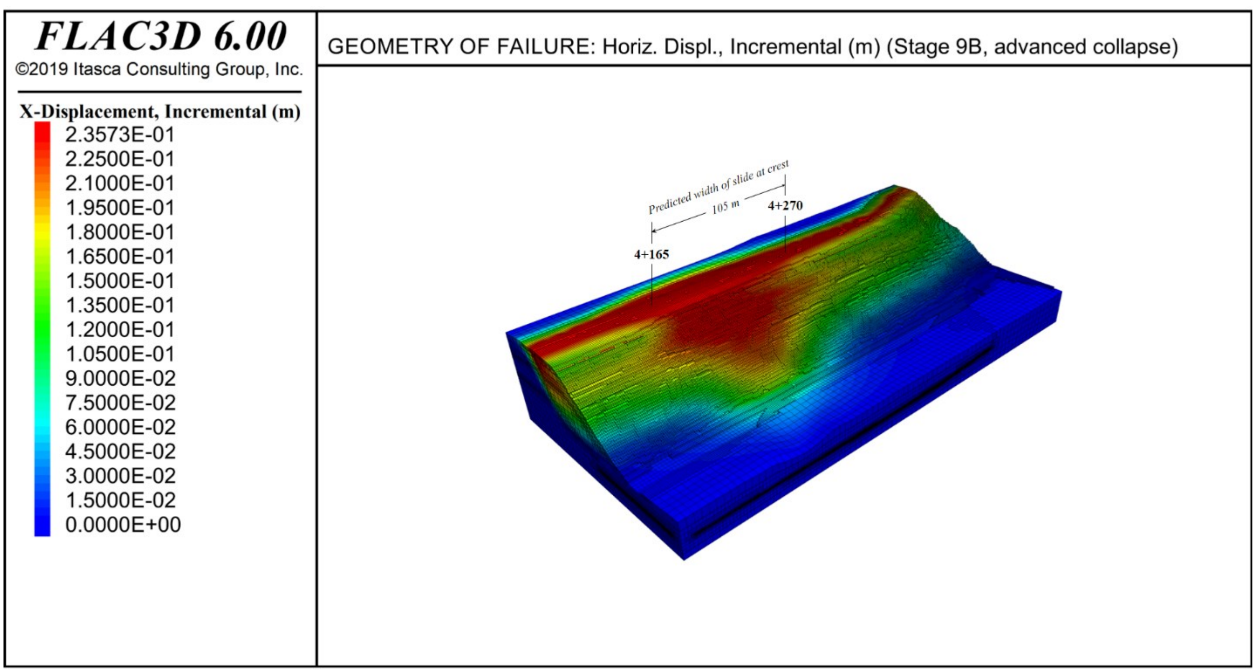

Figure 4.33 Incremental horizontal displacements in embankment at an advanced point of collapse in stage 9B predicted by the fine model in large strain.

blues; these zones stand in contrast with the other regions of the model that are not actively shearing, and are shown in dark blue. In the middle of the slide, the shear zone is seen to pass on the upstream through the core and upper till materials. At the base, the shear zone is clearly limited to the Upper GLU (the shear band, in red, is barely visible in the figure due to the small size of the zones in the region). On the upstream, the shear zone exits the foundation materials downstream of the dam toe. At the crest, the shear zone passes through the tailings beach region in the middle of the slide and is seen to begin curving into the core and shell areas closer to edges. The extent and curved aspect of the shear zone is better illustrated in Figure 4.36 showing the maximum shear strain rates in a full view of the model. From this figure, the width of the slip surface can be estimated at ~200m extending from Stn. 4+100 to Stn. 4+300. The predicted location and width of the slide at base agrees, to a reasonable extent, with field observations. The predicted width of the plastic yield zone in the Upper GLU is lower than actual by about 50m; in the context of trends observed in the collapse phase, it is conceivable that, had the simulation run longer, the predicted width of the yield zone would have increased further.

Finally, the location and shape of the slip surface predicted by the fine model and pictured in Figure 4.34 and Figure 4.35 is consistent with the location of cracks mapped by the field investigation team in the exposed core and surficial tills (Figure 4.30, left) and with the evidence of large horizontal displacements in the Upper GLU but not below it.

4.4.3.2. SLIDE CREST

In the advanced stages of collapse simulated by the fine model, a vertical drop is observed in the crest area. Figure 4.37 shows the incremental downward displacements in the embankment surface at the most advanced simulated point of collapse. From the figure, a vertical drop at crest in the order of 0.6m can be seen at the exact slide location (pictured in Figure 4.33). If downward

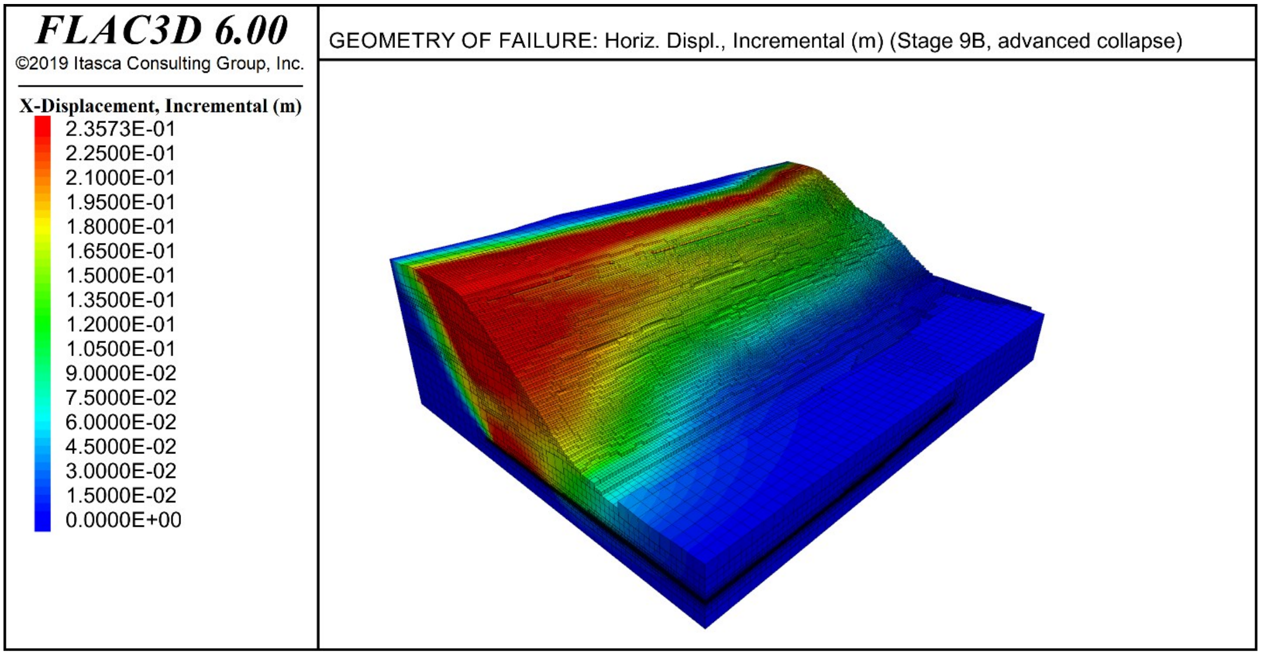

Figure 4.34 A cross-sectional view of the embankment and foundation in stage 9B showing incremental horizontal displacements predicted by the fine model in large strain.

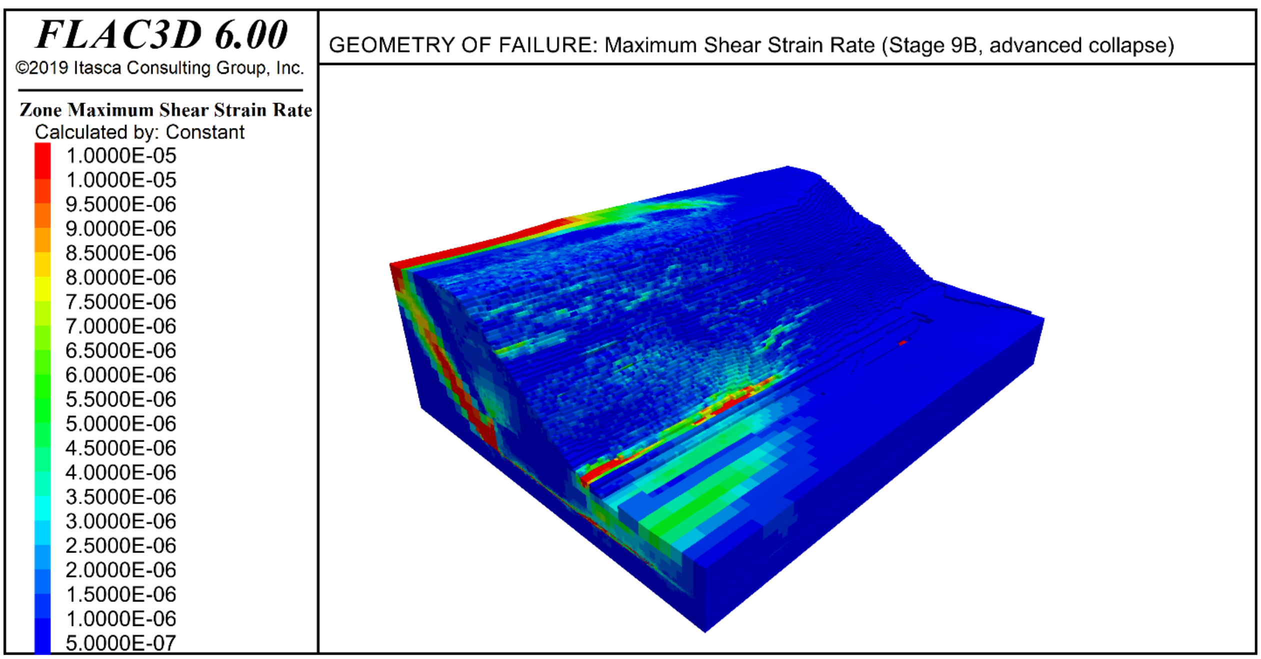

Figure 4.35 A cross-sectional view of the Mount Polley TSF embankment showing maximum shear strain rates 6800 mechanical calculation steps after the application of stage 9B material.

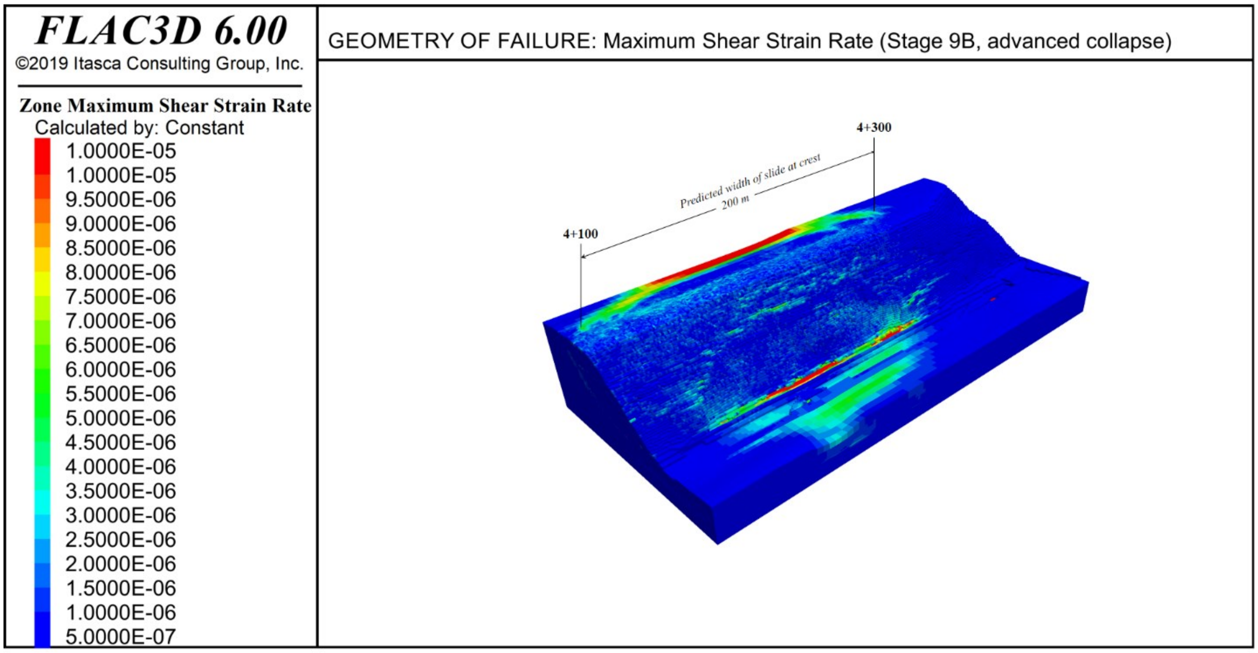

Figure 4.36 A full view of the Mount Polley TSF embankment showing maximum shear strain rates 6800 mechanical calculation steps after the application of stage 9B material.

displacements due to settlement, in the order of 0.25m, are taken into consideration, then ~0.35m of vertical drop at the crest are attributable to failure processes.

During the simulated collapse, a trend was noted where the downward displacements at crest increase overtime. It is conceivable that, had the simulation been continued, the crest would have dropped further.

The predicted downward displacement at crest level is consistent with the findings by the two investigating teams, who independently concluded that a crest drop took place and caused an overtopping event.

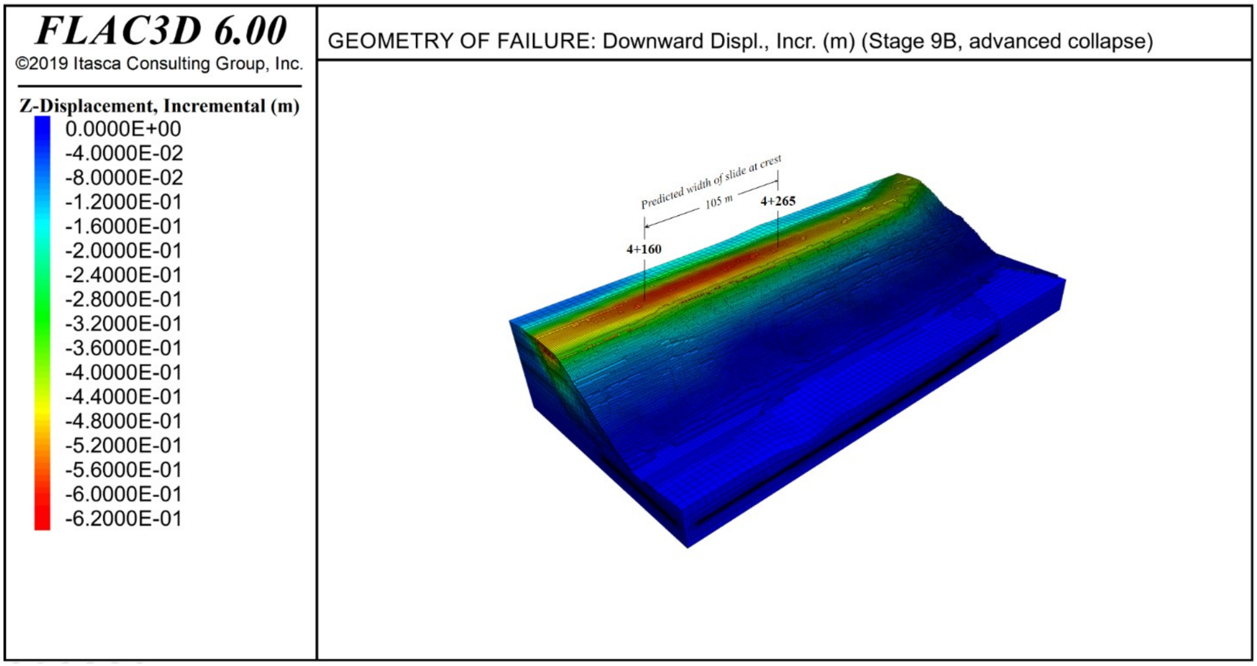

Figure 4.37 Incremental downward displacements in embankment at an advanced point of collapse in stage 9B predicted by the fine model in large strain.

4.4.3.3. SLIDE TOE

In the collapse stages simulated by the fine model, the embankment toe is seen to uplift. Figure 4.38 shows the incremental upward displacements in the embankment surface at the most advanced simulation point. From the figure, the surface at the toe of the embankment directly in front of the unfolding slide is seen to uplift. At this point in the simulation, the upward displacements range from 4cm directly at the toe of the slope to 15cm in the middle and at the downstream edge of the toe excavation, and the uplifted area spans a width of ~120m.

The location of the uplifted area at the embankment toe is reasonably consistent with the position of the "whaleback" features seen in Figure 4.30. The "whaleback" features are located at an estimated 85-95m downstream of the dam centreline, whereas the predicted location of uplift is ~85m downstream of the dam centreline.

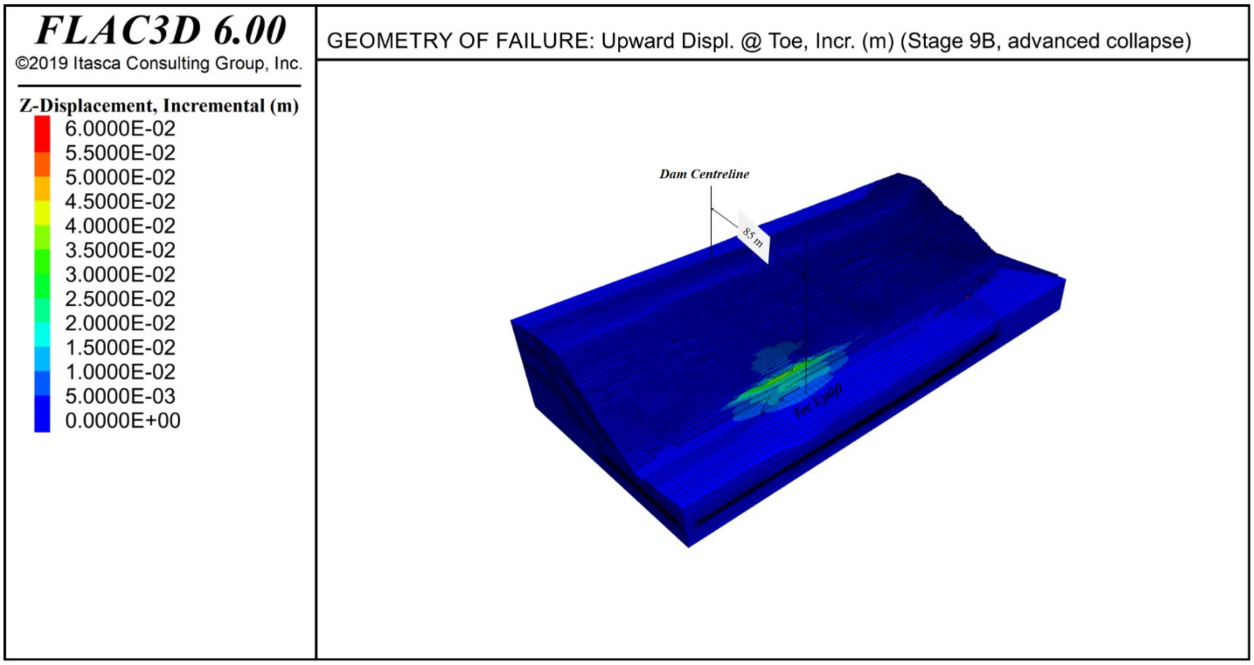

Figure 4.38 Incremental upward displacements at the embankment toe at an advanced point of collapse in stage 9B predicted by the fine model in large strain.

4.5. THE COLLAPSE PHASE

After the addition of stage 9B material under undrained conditions, the fine model predicts failure, meaning that static equilibrium is not attained and the domain continues to deform indefinitely. In large strain, the simulation of collapse in stage 9B is concluded after 6,710 mechanical calculation steps because at that point (a) the geometry errors in the model become prevalent and (b) the maximum plastic shear strains in the Upper GLU are well outside the tested range, and the simulated plastic behaviour of this material cannot not be reliably assessed. Additionally, the embankment deformation levels seen in the simulation at that point can be interpreted as sufficient to trigger overtopping, and any further simulation of collapse was judged to be meaningless.

To investigate the behaviour of the model during this phase, a series of model states were saved at seven successive points of failure. Additionally, relevant variables such as deformation and stress states were liberally tracked throughout the domain during the simulation of collapse as well as prior to it. Finally, the development of the shear zone was observed in order to to determine the location and shape of the slip surface at various points of collapse. From these data, the mechanical behaviour of the soils involved in the failure was reconstructed. The strength behaviour of each of the four soil units (the Upper GLU, upper till, core and rockfill) is examined in isolation in §4.5.2, and in conjunction in §6.1.4.

The results collected from the simulation of the collapse phase were interpreted with caution, as the plastic behaviour of soils is difficult to model reliably and verification data is sparse. For these reasons, the findings from this portion of the simulation were treated as qualitative evidence used to evaluate trends in the mechanical behaviour of the soil mass throughout the collapse rather than quantitatively to pinpoint specific events (such as the precise moment when the failure initiated, as an example).

4.5.1 EMERGENCE AND PROPAGATION OF SLIP SURFACE

The emergence and propagation of the slip surface during collapse can be reconstructed from Figure 4.39. The figure shows four successive plots of the maximum shear strain rates that are taken in stage 9B at 0, 2680, 5170 and 6710 mechanical calculation steps after the addition of embankment material. In these plots, only the zones with maximum shear strain rates in excess of $2*10^{-6}$ are shown in colour, and all other zones are rendered transparent.

From the figure, a number of observations can be made:

- The plot of maximum shear strain rates immediately after the addition of stage 9B material (top left) indicates that at the start of this stage, there are no actively shearing regions anywhere in the domain. Considering that in stage 9A immediately preceding this point in the simulation, the soil mass was in static equilibrium, this result is expected.

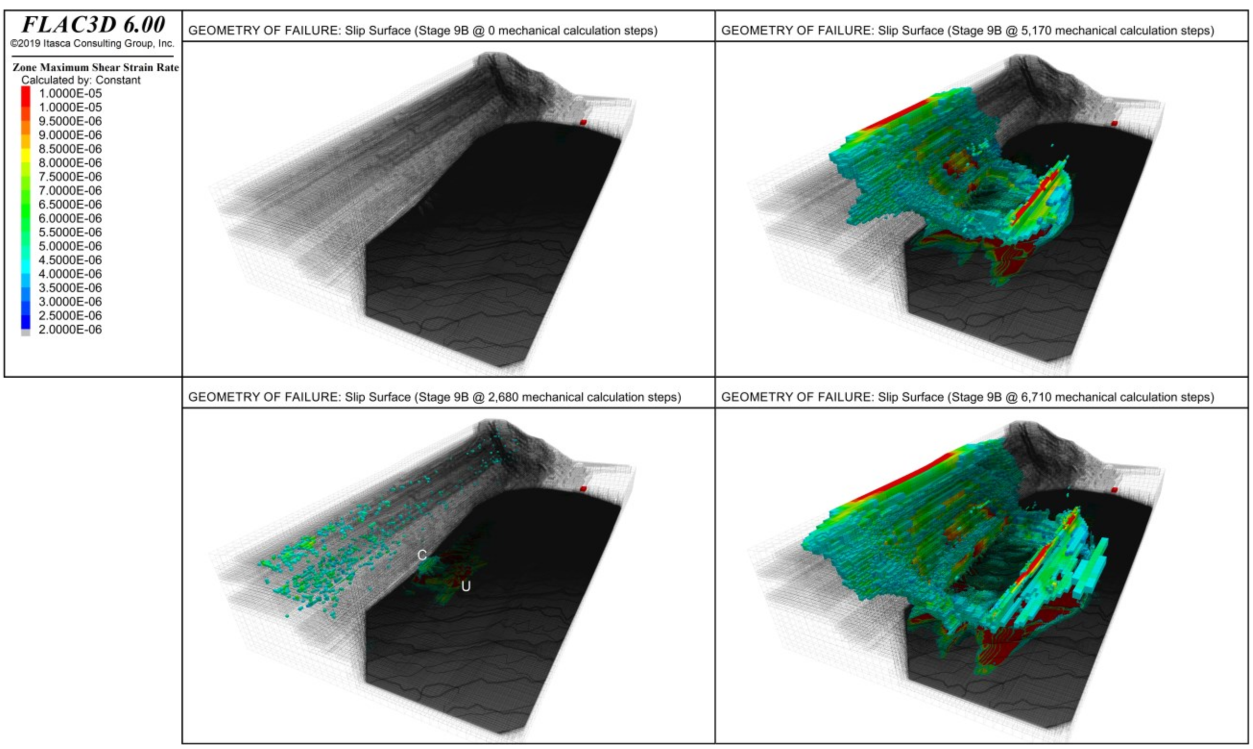

Figure 4.39 The emergence and propagation of the slip surface during stage 9B. Zones of active shearing in the core and the Upper GLU at 2680 mechanical calculation steps are labelled as "C" and "U" respectively.

- The plot of maximum shear strain rates 2680 mechanical calculation steps after the addition of stage 9B material (bottom left) indicates that sometime after the commencement of stage 9B works, an area in the Upper GLU with the approximate dimensions of 50x40m^2 begins shearing at rates several orders of magnitude greater than the rest of the domain (with the exception of the region of newly added soil where the material has not yet fully adjusted to the change in loading). The location of rapidly shearing area corresponds to the location of the plastic yield zone in stages 9A and 9B (seen in Figure 4.19 to the right). This finding supports the assertion by the original investigators that the collapse initiated in the Upper GLU. Also from this plot, a small region that is rapidly shearing can be seen in the upper till material above the upstream edge of the Upper GLU. This suggestst that the failure propagated in the foundation materials on the slide upstream before it progressed elsewhere.
- The plot of maximum shear strain rates at 5170 mechanical calculation steps after the addition of stage 9B material (top right) shows that at this point in the simulation, the slip surface is rapidly propagating on the upstream of the slide. The slip surface is seen to pass through the

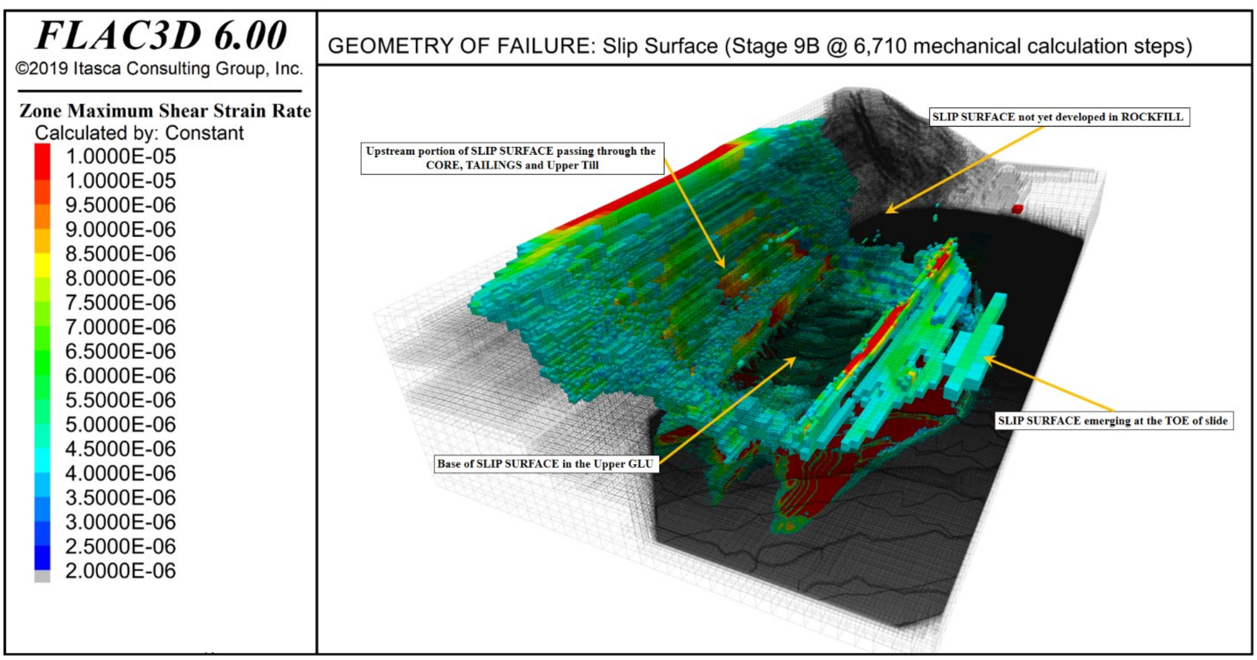

Figure 4.40 A view of the slip surface at the Mount Polley TSF, identified as the zones with high shear strain rates 6800 mechanical calculation steps after the addition of stage 9B material.

foundation till and propagate into the core. In the Upper GLU, the shear zone increases considerably, extending over a width in excess of 100m. About one third of the shear zone seen in the Upper GLU is located in the overconsolidated region of this unit. On the downstream, the slip surface is seen to pass through the foundation tills, emerging in the area corresponding to the in-situ location of the "whaleback" features.

- The plot of maximum shear strain rates at 6170 mechanical calculation steps after the addition of stage 9B material (bottom right) shows that at this point in the simulation, the slip surface has expanded considerably. This plot of the slip surface offers a number of clues that are essential for understanding the mechanical behaviour of embankment and foundation soils during collapse at Mount Polley. For this reason, the plot is reproduced at a larger scale and supplied with annotations in Figure 4.40. The figure shows that on the upstream of the slide, the slip surface expanded to a width consistent with that observed in the field, seen in Figure 4.30. The slip surface has also begun to curve at the ends and is starting to propagate out of the core and into the rockfill material. However, no sizeable shear zones are in observed the rockfill. At the base of the slide, the shear zone in the Upper GLU has now expanded to a width consistent with that observed in the field, as seen in Figure 4.30.
- Finally, it can be seen from the four plots in Figure 4.39 that a significant change in the state of the model takes place sometime between 2680 and 5170 mechanical calculation steps from the application of stage 9B loading. The history plot of the average force ratio during the mechanical calculations in stage 9B, seen in Figure 4.41, shows that at 2680 steps, the model appears to approach convergence; this suggests that despite the weakening in the shear zone of the Upper GLU at that time, the associated deformation of the foundation and embankment materials results in the mobilization of sufficient amounts of shear resistance to cause an

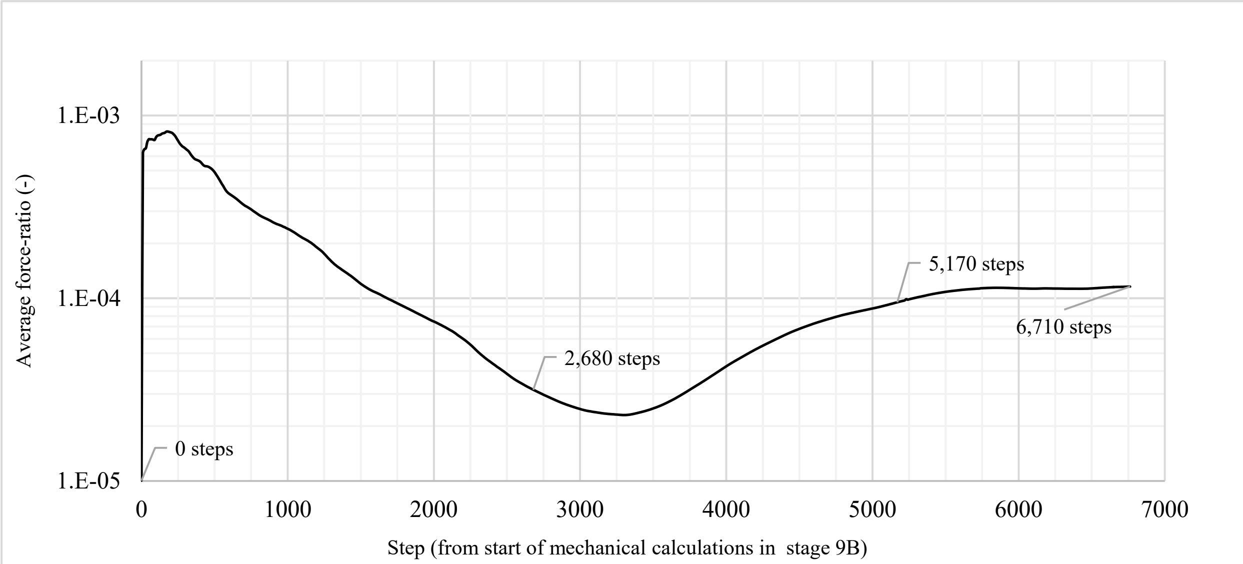

Figure 4.41 A Plot of average force ratios vs. mechanical calculation steps during collapse in stage 9B.

overall decceleration of soil mass. After ~3000 steps, the rate of loss of shear strength in the Upper GLU appears to have overtaken the rate of mobilization of shear strength elsewhere in the domain.

4.5.2 MECHANICAL BEHAVIOUR OF SOILS

4.5.2.1. THE UPPER GLU

The mechanical response of the Upper GLU during collapse can be evaluated from Figure 4.42 showing four successive plots of the cumulative shear displacements (seen at the top) and of the plastic yield zone in the Upper GLU (seen at the bottom) in stage 9B at 500, 2680, 5170 and 6710 mechanical calculation steps after the addition of embankment material. From the plots, the following observations can be made:

- 500 steps after the application of stage 9B loading, the plastic yield zone is comparable in size to that in stage 9A (pictured in Figure 4.19, top right). The loss of shearing resistance in the Upper GLU at this point is modest, with average plastic shear strain values <10% and maximum plastic shear strains <20%. Cumulative shear displacements in the horizontal direction range from 10-14cm under the core to 7cm and less under the shell and toe areas.

- 2680 steps after the application of stage 9B loading, the areal extent of the plastic yield zone has increased fivefold. The shearing resistance across the zone is estimated at 8% below peak undrained strengths, with average plastic shear strains of ~15% and maximum platic shear strains of ~50%. Under the core, the cumulative shear displacements increase to 12-16cm; under the shell and toe areas, displacements range between 5 and 8cm.
- Between 2680 and 5170 steps after the application of stage 9B loading, the areal extent of the plastic yield zone triples. At 5170 steps after the application of stage 9B loading, this region is between 15 and 20 times larger than in stage 9A at static equilibrium (the latter is seen in Figure 4.19, top right). Additionally, an area in the middle of the plastic yield zone (seen in hues of green) is now fully weakened and has accrued shear displacements in the downstream direction in the order of 30-35cm; elsewhere in the plastic yield zone outside the fully weakened area, the displacements are about half that. Outside the plastic yield zone, displacements in the downstream direction are significantly lower; there appears to be a direct correlation between the degree of weakening and that of shear displacement.
- Between 5170 and 6710 steps after the application of stage 9B loading, the areal extent of the plastic yield zone roughly doubles. At 6710 steps after the application of stage 9B loading, its area is 30-40 times larger than in stage 9A. At 5170 steps, the fully weakened area has accumulated plastic shear strains of up to 300 and 400%, and exhibits shear displacements in the order of 0.5m. In the plastic yield zone outside the fully weakened "red zone," displacements in the downstream direction remain significantly lower at <0.2m.

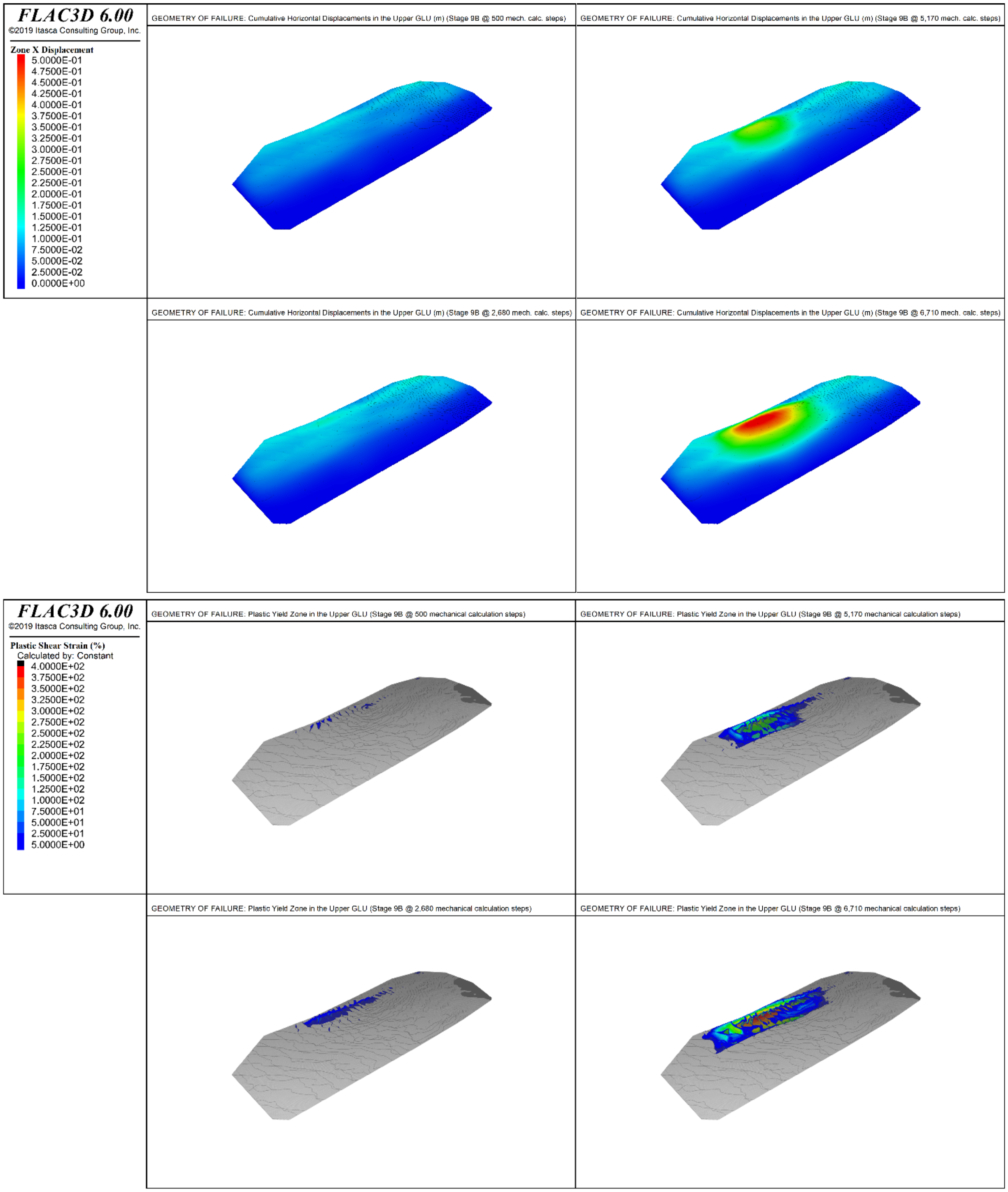

Figure 4.42 The deformation and strength responses in the Upper GLU during collapse. Top four plots: cumulative shear displacements in the downstream direction. Bottom four plots: plastic shear strains.

4.5.2.2. UPPER TILL AND CORE

Figure 4.39 indicates that sometime before 2700 steps after the application of stage 9B loading, the slip surface propagates into the upper till on the upstream edge of the Upper GLU and that sometime before 5170 steps after the application of stage 9B loading, the slip surface propagates into the core. The strength behaviour of the upper till and core materials in the upstream region of the slip zone was investigated by tracking the stress states in representative zones from an early construction phase through the collapse. The full data is included in Appendix 4D. Figure 4.43 and Figure 4.44 show the evolution of stress states on the critical plane in representative core and upper till zones situated on the shear surface close to the slide centre. In these zones, the stress state on the critical plane is seen to consistently increase in construction stages 5 through 9A. In stages 7 through 9A, the stress state on the critical plane is very close to the failure envelope, finally reaching it about 1000 mechanical calculation steps after the application of stage 9B loads. Shortly after this point in the simulation, the normal and shear stresses on the critical planes are seen to begin dropping rapidly; this behaviour continues until the endpoint of the simulation. This reversal takes place at shear displacements in the Upper GLU of 10-12cm.

4.5.2.3.ROCKFILL

The slip surface visualized in Figure 4.39 does not appear to propagate through the shell zone to any significant extent. Even in the late stages of collapse simulation, only a limited number of zones in the rockfill, located adjacent to the core and close to the base, are seen to experience rapid shearing. The strength behaviour of rockfill was investigated by tracking the stress states in a variety of zones from an early construction phase through the collapse. The full data is included in Appendix 4D. Figure 4.45 shows the evolution of stress state on the critical plane in a rockfill zone situated near the shear zone in the core, close to the foundation. In this zone, the stress state at all simulation points plots well below the strength envelope, indicating that the shear strength has not

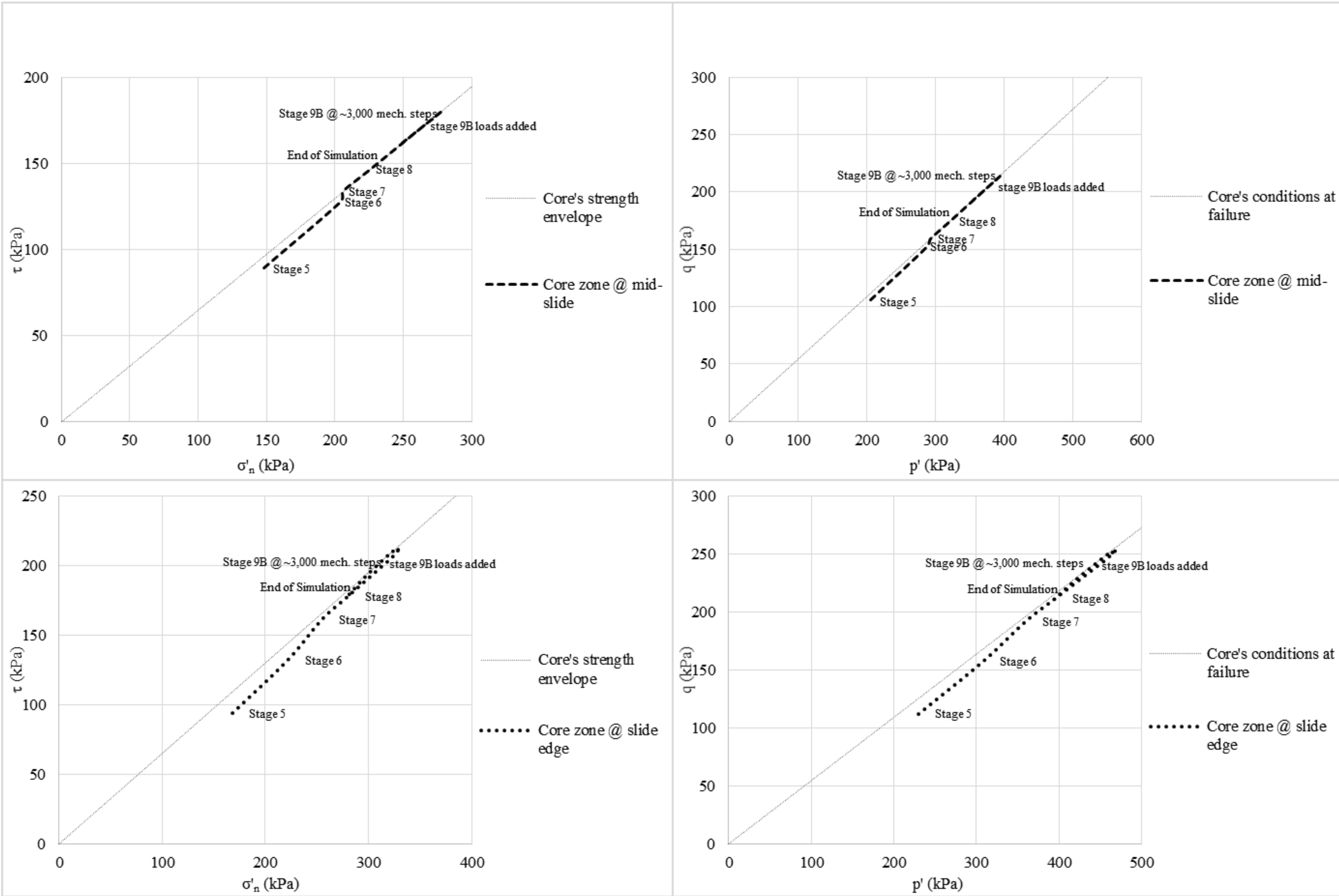

Figure 4.43 Stress state on the critical plane (left column) and stress path (right column) in representative core zones in the slip zone above the upstream edge of the Upper GLU.

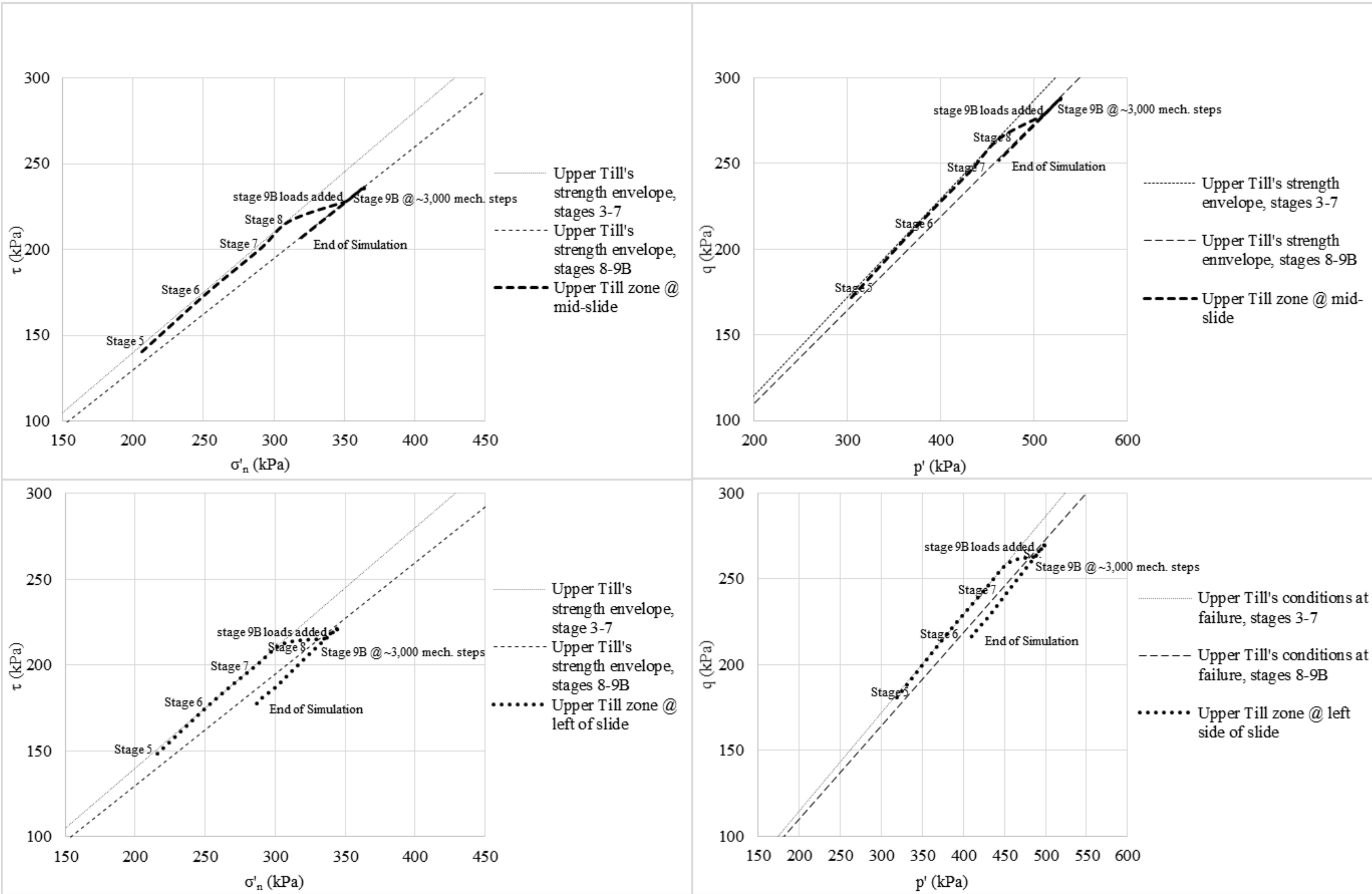

Figure 4.44 Stress state on the critical plane (left column) and stress path (right column) in representative upper till zones in the slip zone above the upstream edge of the Upper GLU.

been fully mobilized even in the latest stages of collapse simulation. After the addition of stage 9B material, only a minimal increase in the normal and shear stresses on the critical plane is observed in this zone; the increase in the mobilized shearing resistance in this zone is modest when compared to the decrease in the shear resistance of adjacent core zones over the same simulation period. This behaviour is typical of that observed in other tracked rockfill zones thought to be located along the not yet developed slip surface.

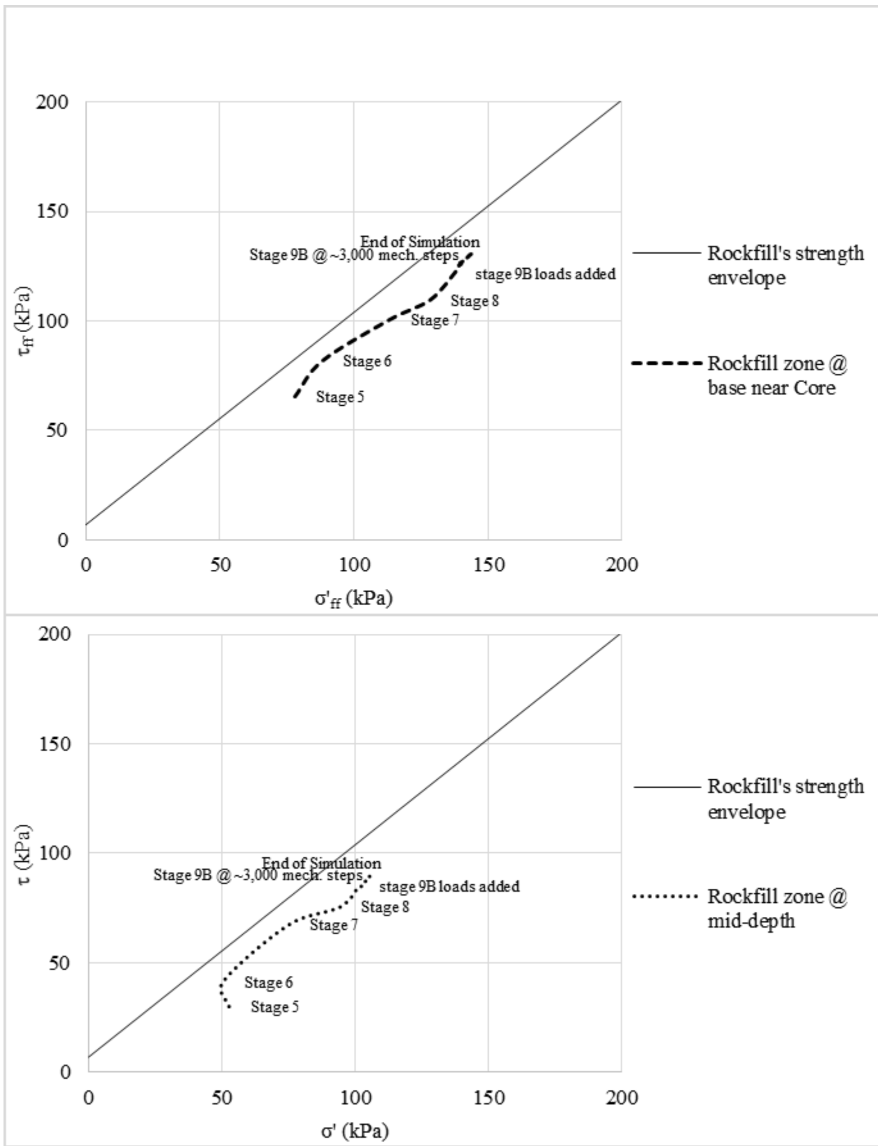

Figure 4.45 Stress state on the critical plane a rockfill zone near the slip surface in the core and close to the foundation.

4.6. STRESS PATH

The results presented in this chapter so far were generated under drained conditions with the exception of stage 9B where an undrained response was simulated in the Upper GLU only. The sensitivity of model response to the stress path was evaluated in a separate simulation that was conducted using the intermediate and coarse models where a partially undrained response was

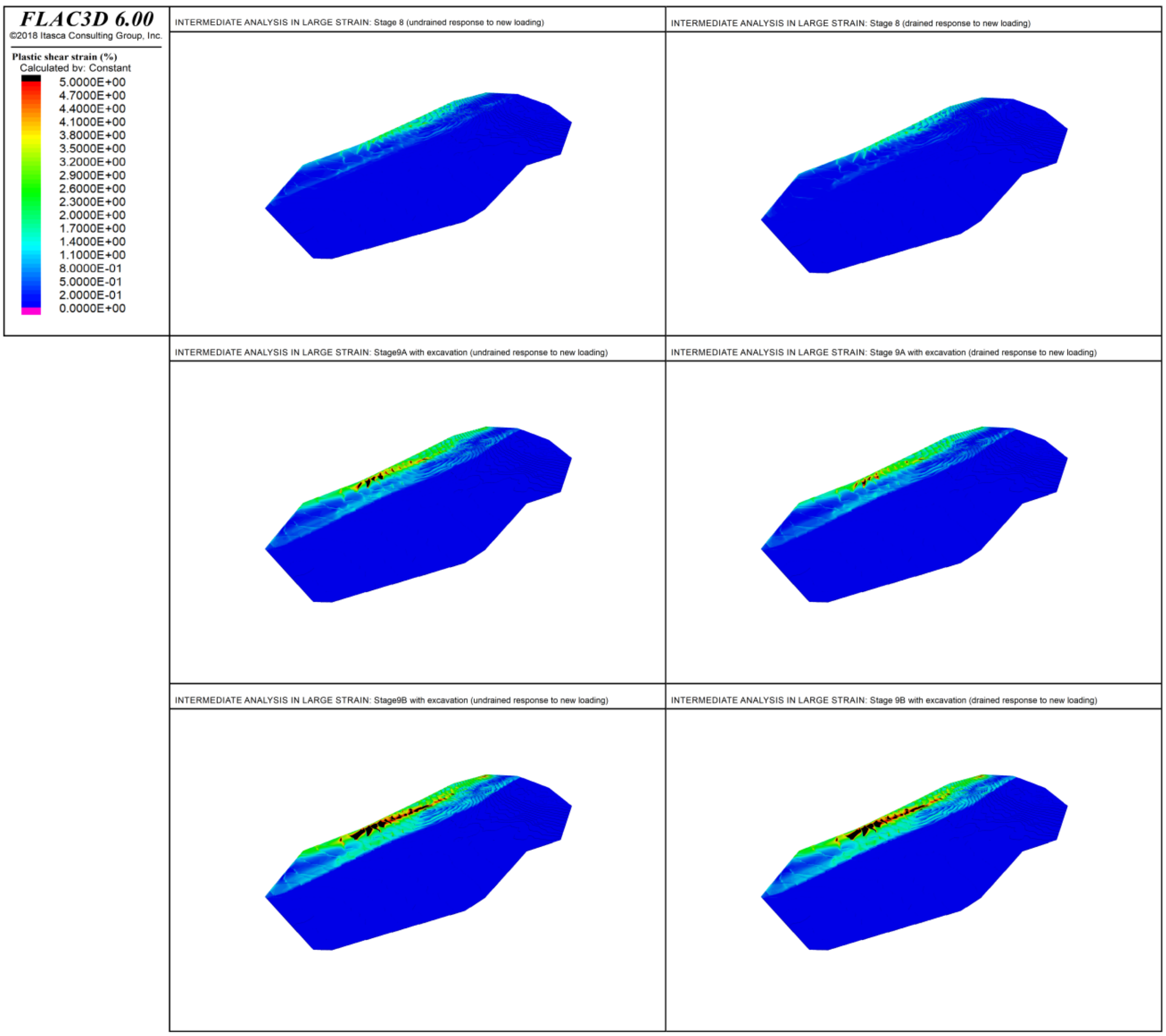

Figure 4.46 The evolution of plastic shear strains in the Upper GLU in the intermediate model under drained and undrained conditions.

emulated as discussed in §3.3.1.1. For simplicity, the former and latter analyses will be referred to as “drained” and “undrained.”

The evolution of plastic shear strains in the Upper GLU predicted by the intermediate model under drained and undrained conditions is illustrated in Figure 4.46. The results from the drained analysis are shown in the right column, and those from the undrained analysis are in the left column. The plastic shear strains predicted by the drained and undrained analysis are not identical, but the differences are minor. The undrained analysis predicts slightly greater plastic shear strains, and a marginally larger plastic yield zone. The stage 9B safety factors are equal to 1.04 under both conditions. Similar conclusions were drawn from the results produced by the coarse model. These results indicate that the effect of stress path on the outcome is largely inconsequential.

4.7. SUMMARY OF FINDINGS

(1) *The fine analysis in large strain adequately models field conditions and can be used to evaluate the failure events.* The deformation analysis of Mount Polley exhibits significant scale effects. These results suggest that the coarse and intermediate analyses are in considerable error and do not adequately replicate field conditions. Conversely, the discretization error associated with the fine model is minor. The correct replication by the fine model of key characteristics of the slide, such as the pre-failure deformation levels, the onset of collapse in stage 9B and the geometry of the slide, corroborates this conclusion.

(2) *In the fine model, the total and effective stresses in the embankment and foundation materials increase steadily over the duration of construction works.* The largest stress increases take place under the core and, to a lesser extent, under the shell. By the simulation endpoint, in the Upper GLU region under the core, the pre-failure effective stresses near 1 MPa.

(3) *In the fine model, parts of the Upper GLU become normally consolidated around construction stage 5; the normally consolidated portion of the unit continues expanding until it encompasses one quarter to one third of the unit by area prior to collapse.* The transition of this material to a state of normal consolidation marks the point of change in failure modes from drained to undrained, opening up the potential for strain-weakening.

(4) *A loss of shear resistance to strain-weakening takes place in portions of the Upper GLU starting stage 7 on.* In stages 7 through 9A, the loss of shear strength is negligible. The strain-weakening processes becomes uncontained in stage 9B.

(5) *The Upper GLU strains non-linearly.* The fine simulation predicts the development of a shear band with the thickness of a single zone, or 12.5cm. This zone strains more severely than the Upper GLU above or below it, weakening in the process. The soil outside the shear

band does not accrue plastic shear strains to any appreciable degree and retains peak undrained strengths.

(6) *The shear band thickess is greater than zero.* The analysis of the lower limit state demonstrates that a shear band with a thickness of zero would cause the embankment to fail earlier than in stage 9B.

(7) *Pre-collapse levels of deformation predicted by the fine model are negligible.* Pre-collapse deformations associated with the plastic yielding of the foundation are minor; this result matches field observations.

(8) *In the fine model, collapse initiates in response to the undrained application of stage 9B loads.* The collapse initiates in the Upper GLU when a sizeable portion of the unit that reaches the precipice of strain-weakening sometime after stage 9A begins weakening under new loading added in stage 9B. Rapid shear displacements in the Upper GLU ensue, causing the upper tills and core material above to fail in extension; after this point, the core and upper till materials located in the shear zone experience a sustained drop in mobilized shear resistance. In the shell zone, the deformation levels brought about by the unfolding failure are not sufficient to fully mobilize the shear strength of the rockfill.

(9) The predicted geometry of the failure matches well that observed in the field.

(10) *The response of the Mount Polley simulation is mesh-dependent*. Models with a higher discretization level:

- Predict slightly greater overburden effective and total stresses in the Upper GLU. This in turn results in an earlier transition to a state of normal consolidation in portions of this stratum.
- Predict a higher rate of accummulation of shear plastic strain and an earlier onset of strain-weakening processes.

- Simulate the onset of failure under lower loading conditions or at an earlier construction stage.
- Predict marginally greater shear displacements in the foundation under equivalent loading conditions (with the exception of stage 9B where, in the fine simulation, deformations accrue indefinitely).

CHAPTER FIVE

A THREE-DIMENSIONAL DEFORMATION ANALYSIS OF THE FAILURE AT THE MOUNT POLLEY TSF IN SMALL STRAIN

This chapter documents the results of a three-dimensional deformation analysis of the failure at the Mount Polley TSF completed under the small strain calculation scheme. This analysis includes three separate simulations that were conducted using a coarse, an intermediate and a fine model. In this chapter, the information is organized into seven sections, each describing a specific aspect of the mechanical response in the embankment soils to staged loading. In each of these sections, the relevant results from the coarse, intermediate and fine simulations are reported concurrently in order to establish any trends in the model response that are related to the scale effects.

Justification for the small strain assumption

Small strain is a computation scheme whereby the model mesh coordinates are not updated after a calculation cycle in spite of accrued strain and deformation. Under this scheme, subsequent calculations are done using the initial, non-deformed configuration (Chambon 2002). This calculation mode is more robust than the large strain mode, as it is not subject to mesh distortion issues discussed in §3.3.2. Nonetheless, such simplification of the calculation scheme introduces an error into the solution. Chambon (2002) demonstrates that the magnitude of this error is not related to the magnitude of strains and deformations, as it is commonly thought, but instead depends on the relative magnitude of stresses and moduli. Chambon asserts, based on the comparison of large and small strain equations, that the small strain assumption is not justified in models where a large portion of the domain is in a plastic state and should only be used where the deformation moduli are significantly higher than the stresses.

The circumstances that invalidate the use of the small strain assumption are present in the simulation of the Mount Polley failure. As the model nears collapse, considerable portions of the domain reach a plastic state, and in the strain-weakening portions of the Upper GLU, significant shear plastic deformations take place. It appears that, in this particular case, the small strain assumption could be introducing a discernible error into the solution. So why use it?

There are two sensible reasons for conducting a small strain analysis in this case. First, conducting the simulation in this mode offers the modeller the opportunity to work out all of the problems and test the constitutive models without the added complication of mesh distortion errors. In actuality, the failure at Mount Polley was first simulated in small strain before proceeding with the large strain calculations reported in Chapter Four.

Second, modelling this problem both under small and large strain assumptions presents an opportunity to evaluate the type and magnitude of errors introduced into the solution by this assumption. In this chapter, the simulations of the failure at Mount Polley obtained under the large and small calculation schemes are compared by evaluating, in each modelled construction stage, key variables side-by-side. The findings are reported and their significance is discussed in Chapter Six.

5.1. STRESS DISTRIBUTIONS

5.1.1 OVERBURDEN STRESSES

The distribution of total and effective vertical stresses at Mount Polley was evaluated after each of the construction stages 3 through 9B using the coarse, intermediate and fine models. The evolution of total and effective overburden stresses is illustrated in Figure 5.1 to Figure 5.6. It can be seen from these figures that the largest stress increases take place in the core and shell regions, as well as foundation materials beneath them. The core material, with a high dry density of around 2100kg/m^3 and the phreatic surface passing through it, contributes significantly to the added total and effective stresses in the soils situated below it; and the rockfill, largely drained and with a considerable dry density of over 2000kg/m^3, generates increases in total and effective overburden stresses in the materials beneath it to a near equal extent. In this respect, the stress distributions obtained under the small strain calculation scheme do not differ in a material way from those predicted in large strain.

Up to and including construction stage 9A, the distributions of total and effective overburden stresses predicted by the coarse, intermediate and fine models seem very comparable overall. However, as it has been the case with the results obtained in large strain, a divergent stress response is noted in some key areas, chiefly in and around the Upper GLU. The difference in the stress responses is illustrated in Table 5.1 that lists maximum total and effective overburden stresses in this unit. It can be seen from the table that in each construction stage, the maximum stresses are greater in the models with a higher mesh resolution. The noted disparity is owed to a two modelling aspects: the discrete nature of finite element modelling, and the strategy adopted to create the subsurface geometry of this model. This effect and its implications on the predicted mechanical stability of the model are discussed in §6.4.1.

The overall distributions of total and effective overburden stresses predicted by the models begin to diverge significantly during the simulation of stage 9B, with the coarse and intermediate models producing similar results, and the fine model predicting a very different distribution from these two, particularly in the Upper GLU. The stress response of the fine model at this stage is largely the result of a growing plastic yield zone in this critical soil unit and the associated stress adjustments in and around it. Such yield zone does not sufficiently develop in the coarse and intermediate models (as discussed in §5.2.2).

Table 5.1 Overburden stresses predicted by the coarse, intermediate and fine models in small strain.

	Maximum total overburden stress in the Upper GLU (kPa)			Maximum effective overburden stress in the Upper GLU (kPa)		
Mesh	coarse	intermediate	fine	coarse	intermediate	fine
Stage 3	497	563	600	333	416	455
Stage 4	520	593	623	368	443	471
Stage 5	727	804	833	588	672	699
Stage 6	815	878	918	669	746	771
Stage 7	903	963	1017	753	821	858
Stage 8	956	1020	1079	804	875	912
Stage 9A	1031	1100	1150	862	917	978
Stage 9B	1071	1139	varies*	896	947	varies*

*during active collapse.

Finally, the stress distributions predicted in small strain appear consistently lower than those predicted in large strain; this can be appreciated by comparing the data in Table 4.1 and Table 5.1, and has been confirmed by comparing the large and small strain solutions after each simulated stage. The source of this discrepancy is explained in §6.6.1.

5.1.2 ROTATION OF STRESS TENSOR UNDER EMBANKMENT

The rotation of stress tensors in the Upper GLU was tracked in stages 3 through 9B, and the results are included in Appendix 5A, Figure 5A.1.

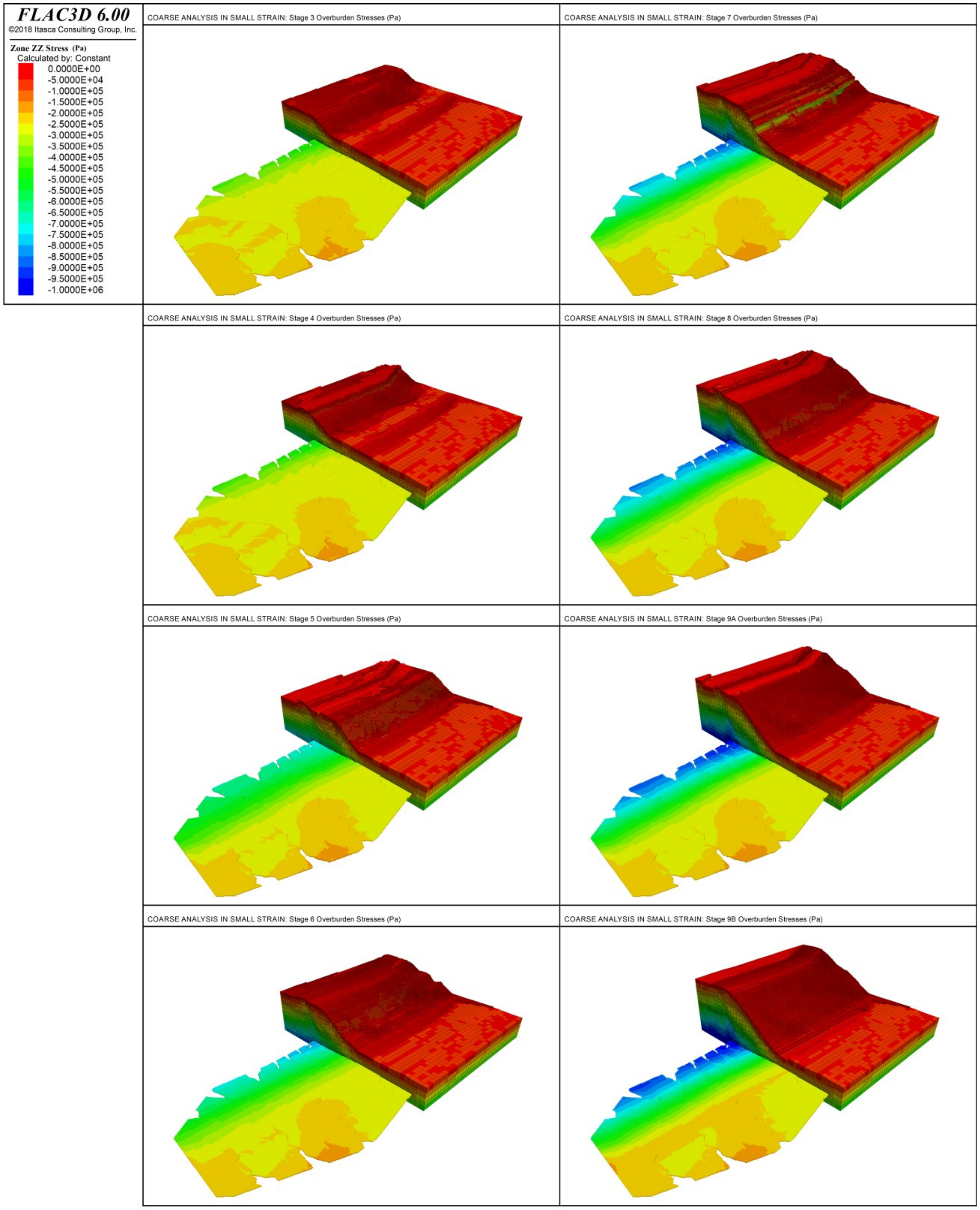

Figure 5.1 Total overburden stresses after the completion of construction stages 3 through 9B under steady-state conditions predicted by the coarse model in small strain (pictured view: full model sliced in the direction normal to the dam centreline at about the centrepoint of failure; and the Upper GLU unit, seen in full).

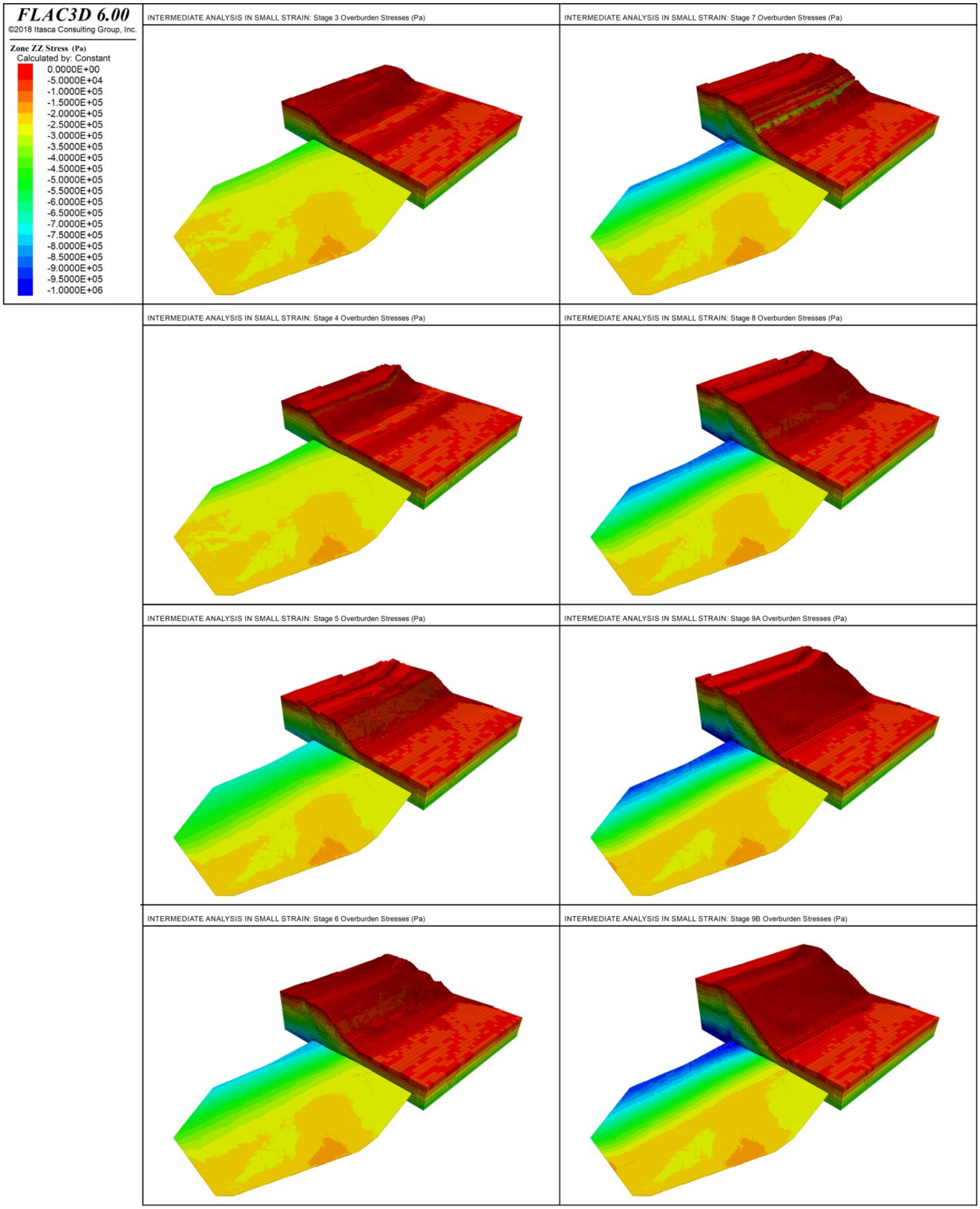

Figure 5.2 Total overburden stresses after the completion of construction stages 3 through 9B under steady-state conditions predicted by the intermediate model in small strain.

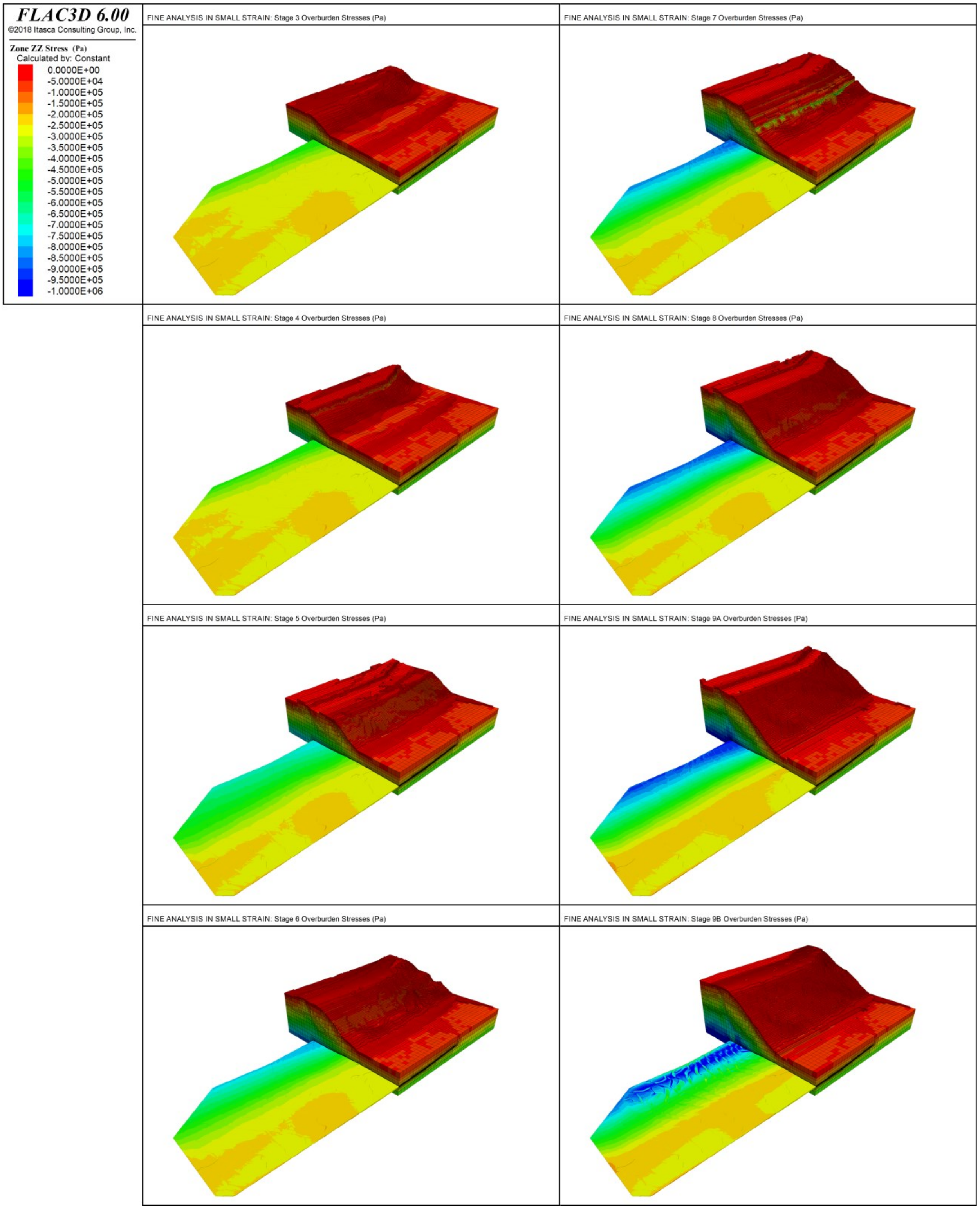

Figure 5.3 Total overburden stresses after the completion of construction stages 3 through 9B under steady-state conditions predicted by the fine model in small strain.

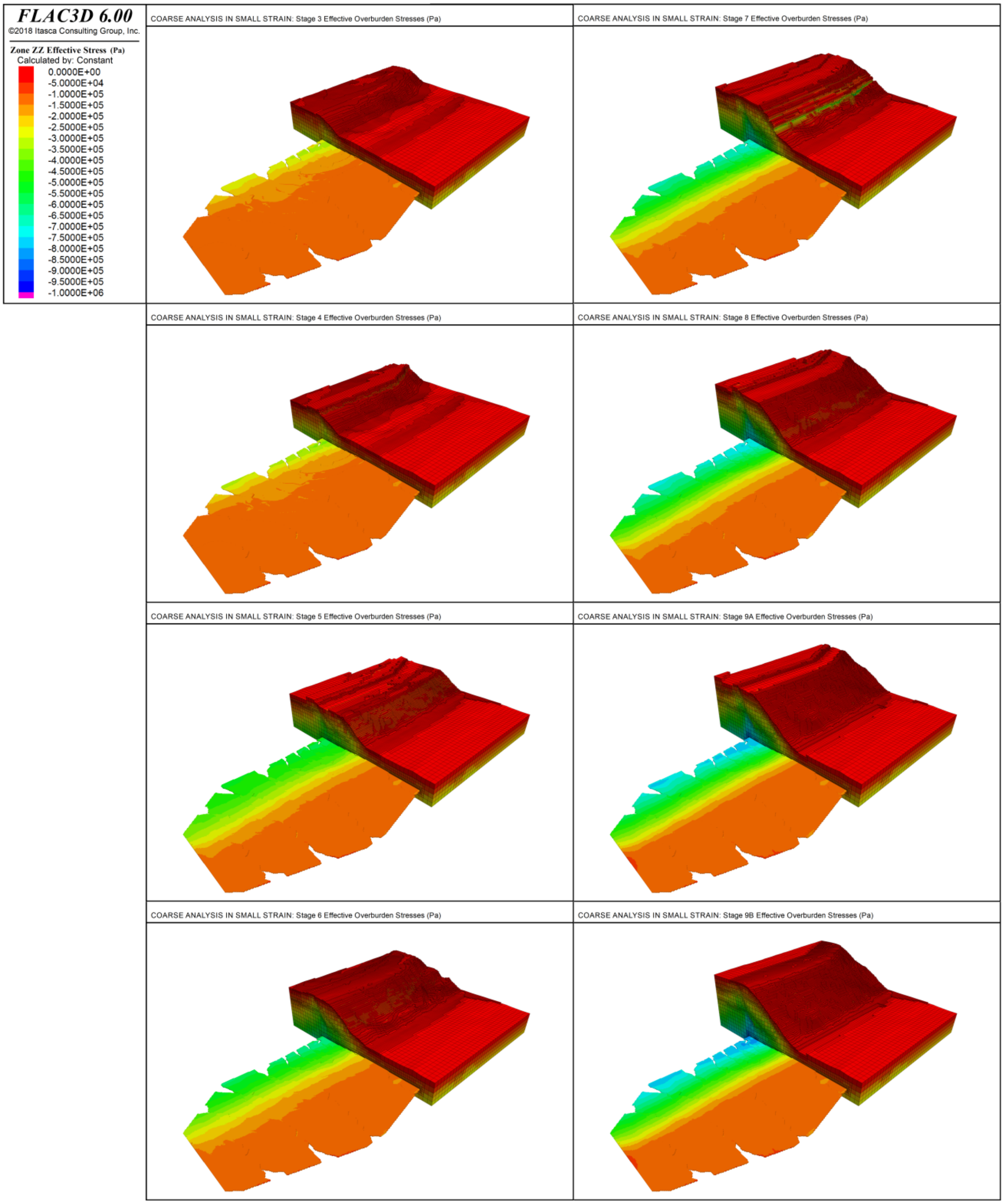

Figure 5.4 Effective overburden stresses after the completion of construction stages 3 through 9B under steady-state conditions predicted by the coarse mode in small strain (pictured view: full model sliced in the direction normal to the dam centreline at about the centrepoint of failure; and the Upper GLU unit, seen in full).

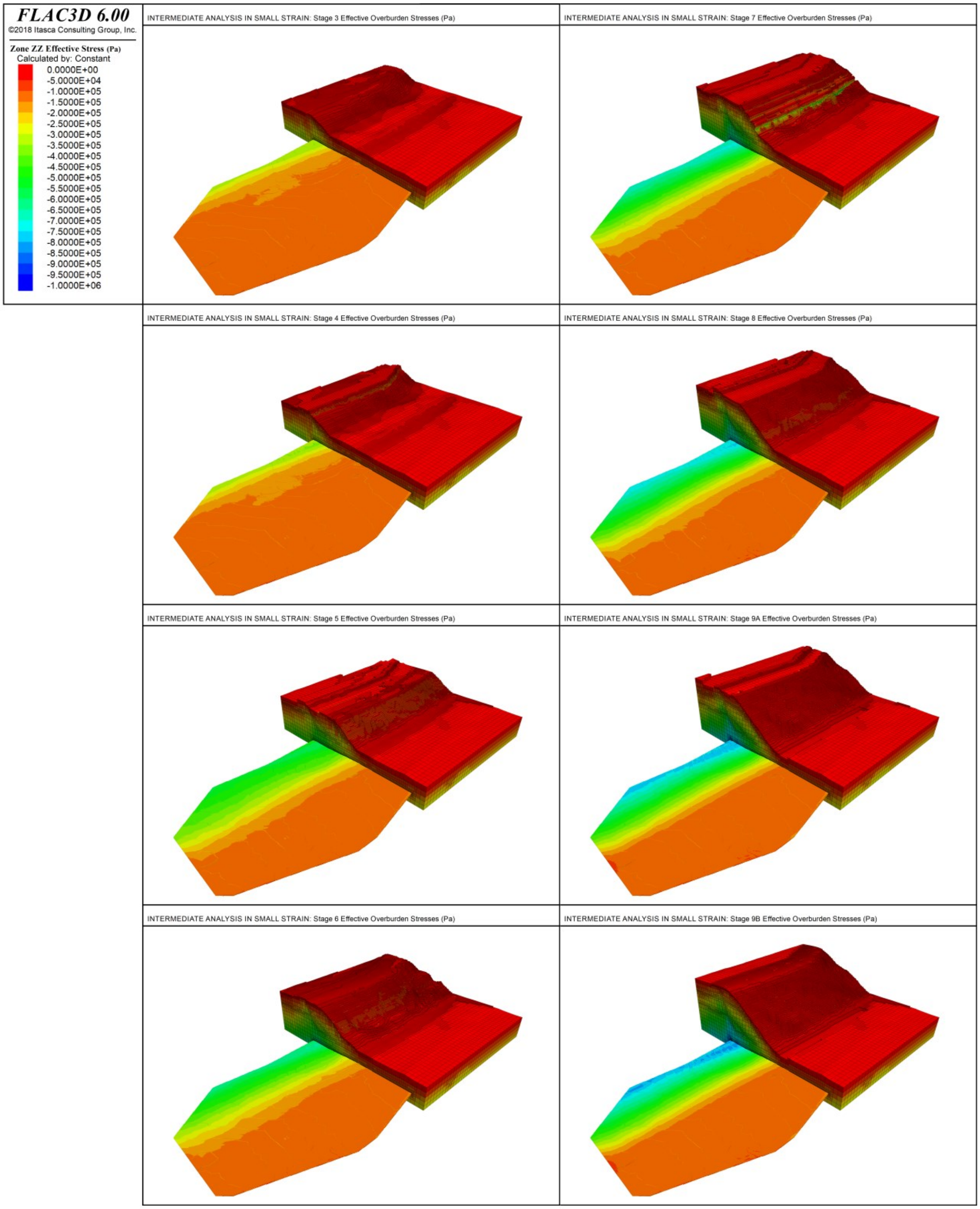

Figure 5.5 Effective overburden stresses after the completion of construction stages 3 through 9B under steady-state conditions, predicted by the intermediate model in small strain.

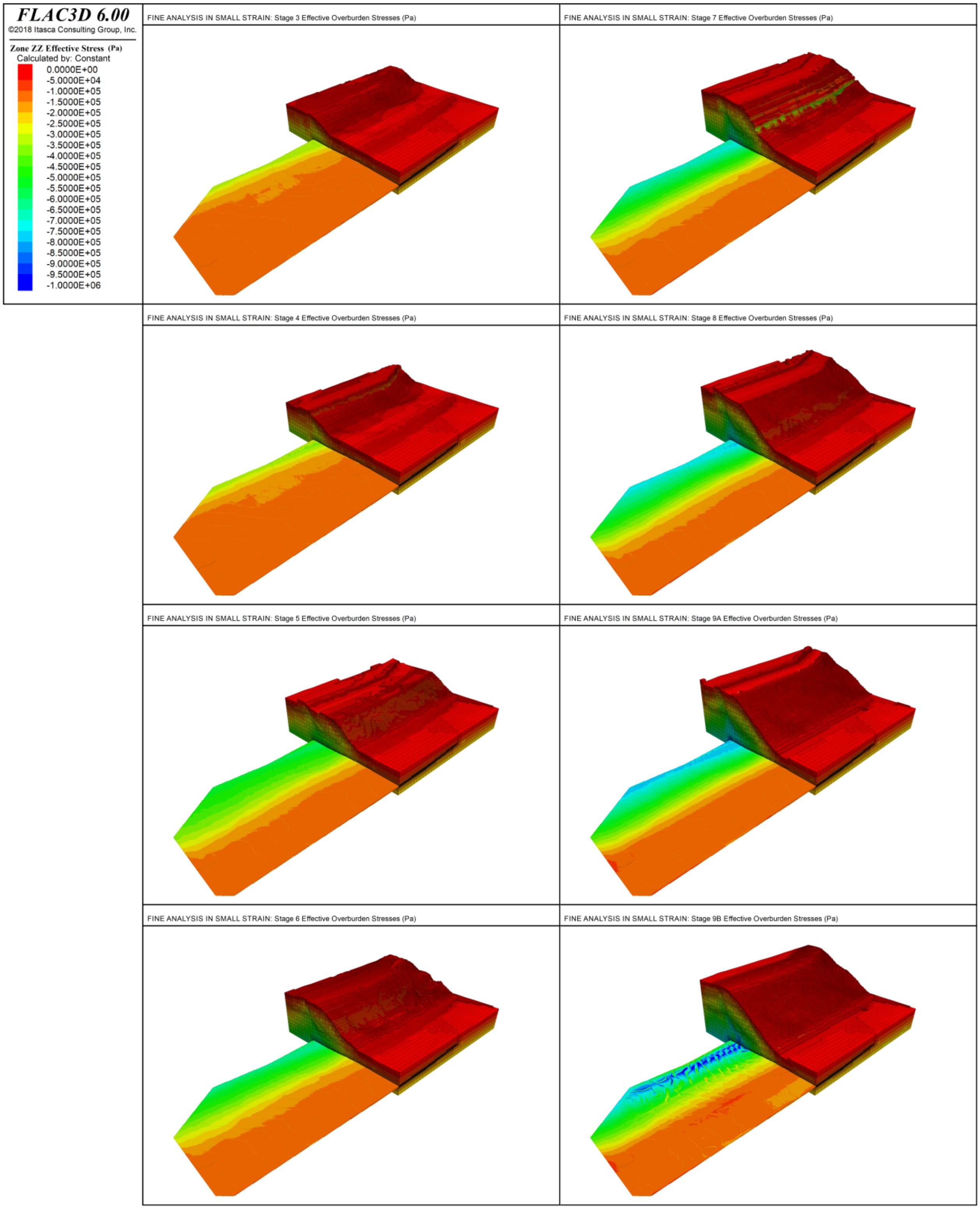

Figure 5.6 Effective overburden stresses after the completion of construction stages 3 through 9B under steady-state conditions predicted by the fine model in small strain.

In all simulations, a gradual rotation of the stress tensor is observed from the earliest stages of embankment construction, increasing as the embankment height grew. As the simulations progress, the stress tensors in the embankment and foundation rotate and by stage 7 or 8, the critical planes in the normally consolidated portions of Upper GLU (oriented at 45° to the plane of major principal stress) become sub-horizontal; this is also the time when a plastic yield zone is first observed in this material.

5.1.3 SHEAR STRESSES IN THE UPPER GLU

The shear stresses τ_{xz} were tracked in each simulated construction stage using the coarse, intermediate and fine models. The results are included in Appendix 5A, Figure 5A.2 to Figure 5A.4. The shear stresses in the Upper GLU along the critical planes τ_{cr} were also tracked; the results are found in Appendix 5A, Figure 5A.5 to Figure 5A.7.

As it has been discussed in Chapter Four, the comparison of these two variables over the duration of embankment construction offers an indirect means to observe the re-orientation of the plane of critical stress in the Upper GLU, since closer to failure the two quantities are expected to begin converging, especially in the area under the embankment.

For comparison, the two variables have been plotted side-by-side in Figure 5.7. As it is the case with the large strain results, this figure shows that although some convergence of these values is observed in construction stages 8 through 9B, especially in the area located under the embankment, it is not unequivocal. The convergence of these two values is actually very good in some of the layers of the Upper GLU at the base of the unit but not throughout. As it has been explained in Chapter Four, the critical planes become near-horizontal in stages 8 through 9B in the weaker layers of the Upper GLU at the base of the unit; these are the layers where the strain-weakening processes are most active, and where the plastic yield zone emerges. However, Figure 5.7 displays the top layers of the Upper GLU, where these processes are not as pronounced.

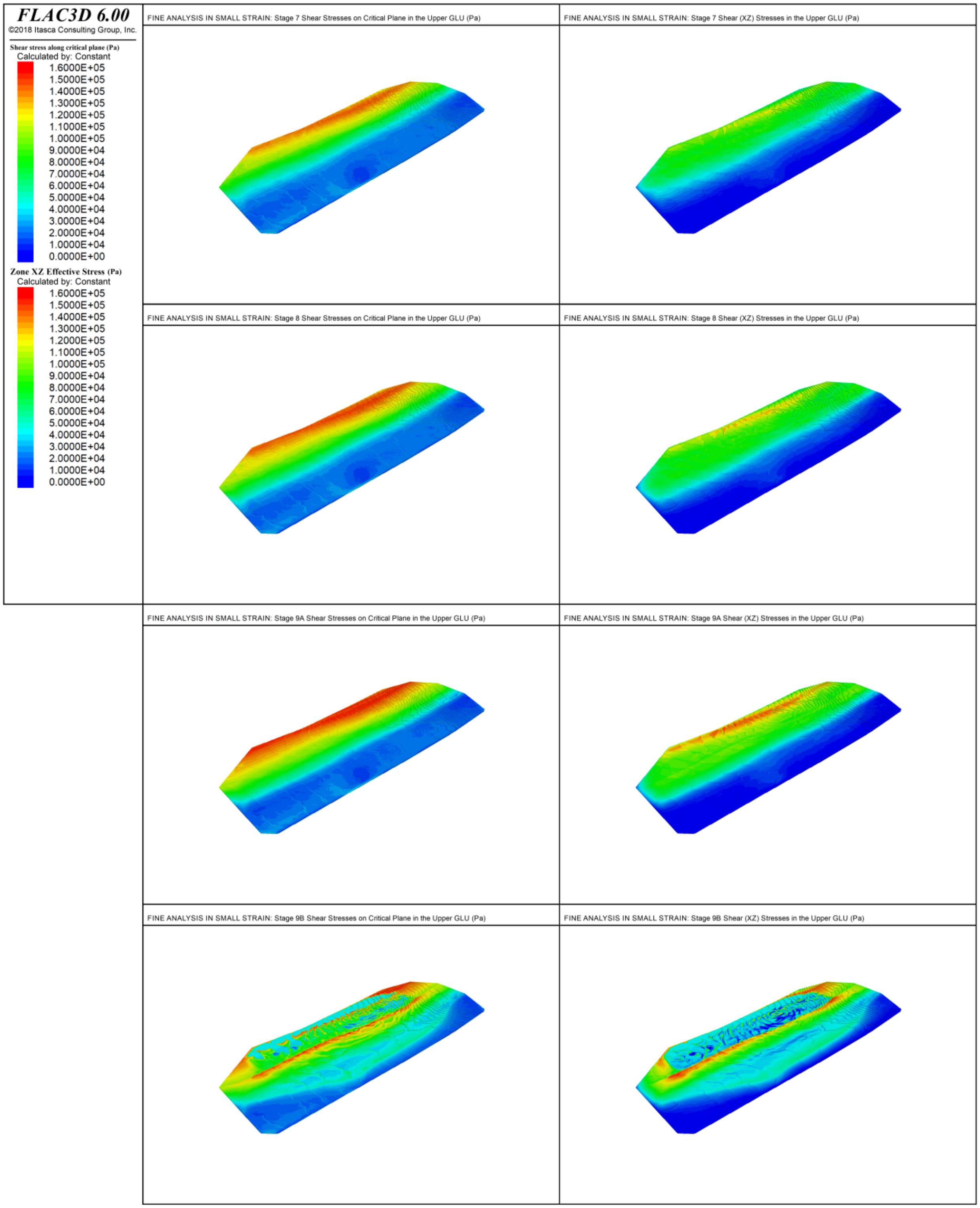

Figure 5.7 Shear stresses along the critical plane τ_{cr} (left column) and shear stresses along the horizontal plane in the direction of soil mass displacement τ_{xz} (right column) in the Upper GLU predicted by the fine model in small strain.

Figure 5.7 visualizes the stress transfer from the weakening materials onto adjacent, stronger soils in the late construction stages as a leading edge of higher stresses (in reds or yellows) immediately downstream of a section with lower shear stresses (in light green). It will be shown in §5.2.1 that the leading edge of higher stresses is also the boundary between the normally consolidated portion of the Upper GLU material on the upstream and its overconsolidated portion on the downstream.

Finally, it should be noted that the stress transfer described above is not apparent in the simulation results produced by the coarse or intermediate models. The reason is, these simulations predict stable embankment configurations in these stages, as discussed in §5.3.

5.2. THE UPPER GLU'S STRENGTH BEHAVIOUR

5.2.1 TRANSITION TO A NORMALLY CONSOLIDATED STATE

Prior to the commencement of construction works, the Upper GLU was a lightly overconsolidated deposit with preconsolidation pressures around 400-500kPa. As the embankment was raised, consolidation processes were induced in the foundation. The embankment-induced increase in vertical consolidation stresses to levels equal to or exceeding the unit's preconsolidation pressure was identified as the reason for this unit's transition from a drained to an undrained mode of failure.

The emergence and evolution of the normally consolidated zone was evaluated in construction stages 3 through 9B using the coarse, intermediate and fine simulations. The results are compiled in Figure 5.8 to Figure 5.10.

Simulation results indicate that negligible amounts of material in the Upper GLU become normally consolidated as early as a construction stage 3. At this very early stage, these areas are limited to just a few zones at the base of the unit. The finer resolution models predict a somewhat earlier emergence of the normally consolidated zone and also higher maximum vertical consolidation stresses; this difference is caused by the prediction of higher overburden stresses in models with a higher resolution, as discussed in §4.1.1 and §6.6.1. A substantive fraction of the Upper GLU becomes normally consolidated sometime around construction stage 5.

The location, spatial distribution and growth of normally consolidated zone in the Upper GLU is generally comparable in the coarse, intermediate and fine simulations.

As it has already been discussed in §4.2.1, the normally consolidated portion of the Upper GLU is identical in construction stages 9A and 9B; this is the case because the load in stage 9B is applied under partial undreained conditions whereby the update of preconsolidation pressures and shear resistance is halted as described in §3.3.1.1.

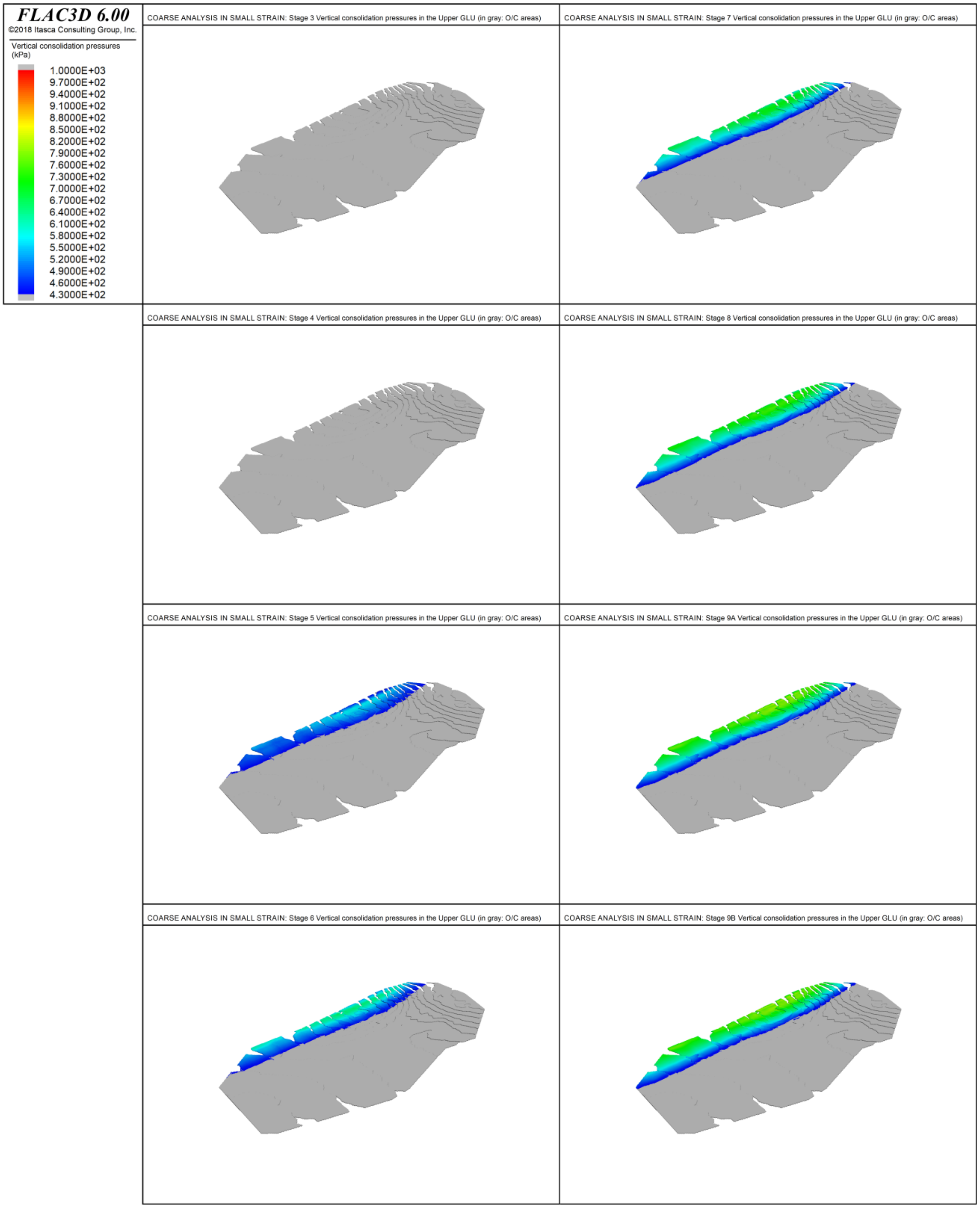

Figure 5.8 Vertical consolidation pressures in the Upper GLU after the completion of stages 3 through 9B under steady-state conditions predicted by the coarse model in small strain.

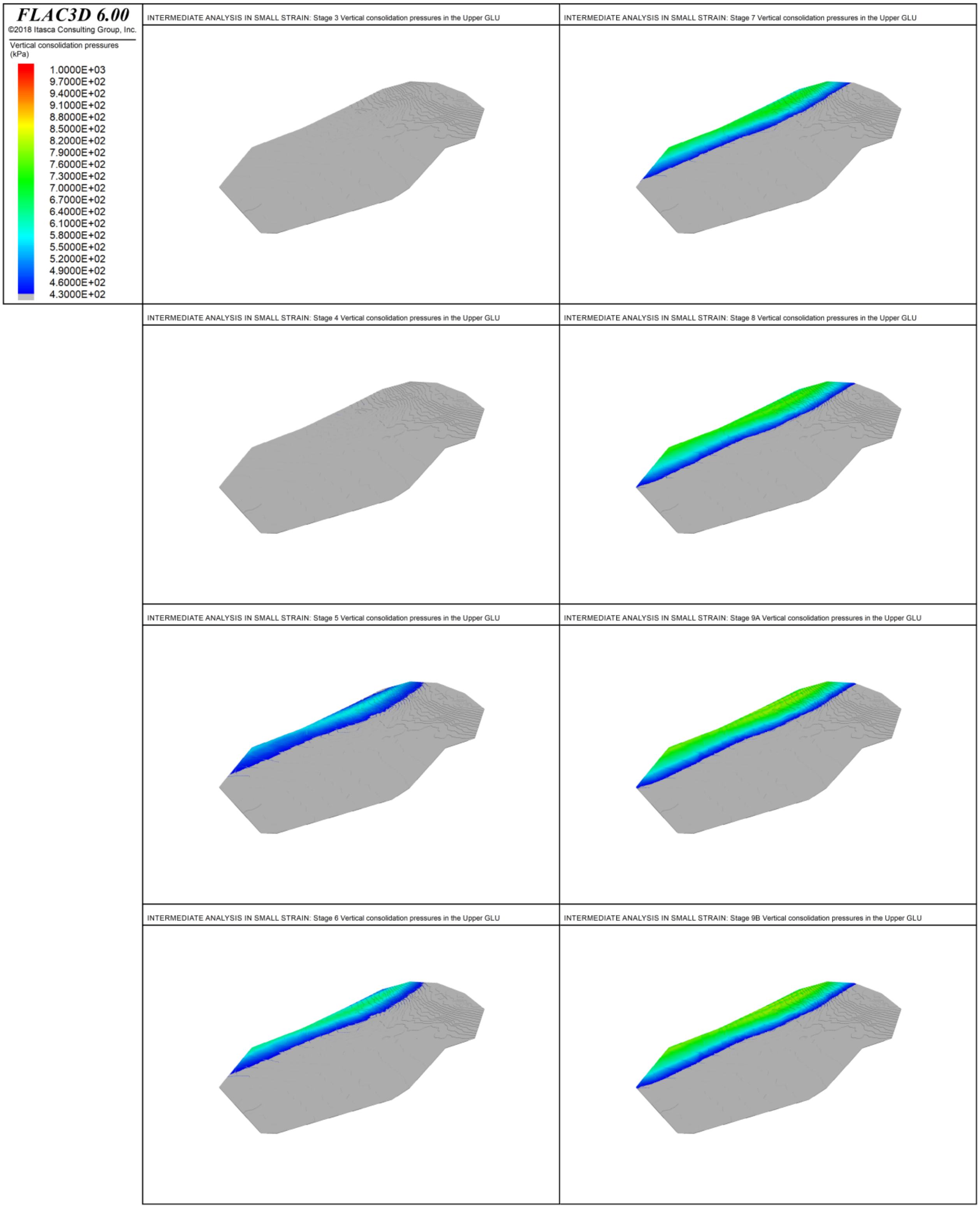

Figure 5.9 Vertical consolidation pressures in the Upper GLU after the completion of stages 3 through 9B under steady-state conditions predicted by the intermediate model in small strain.

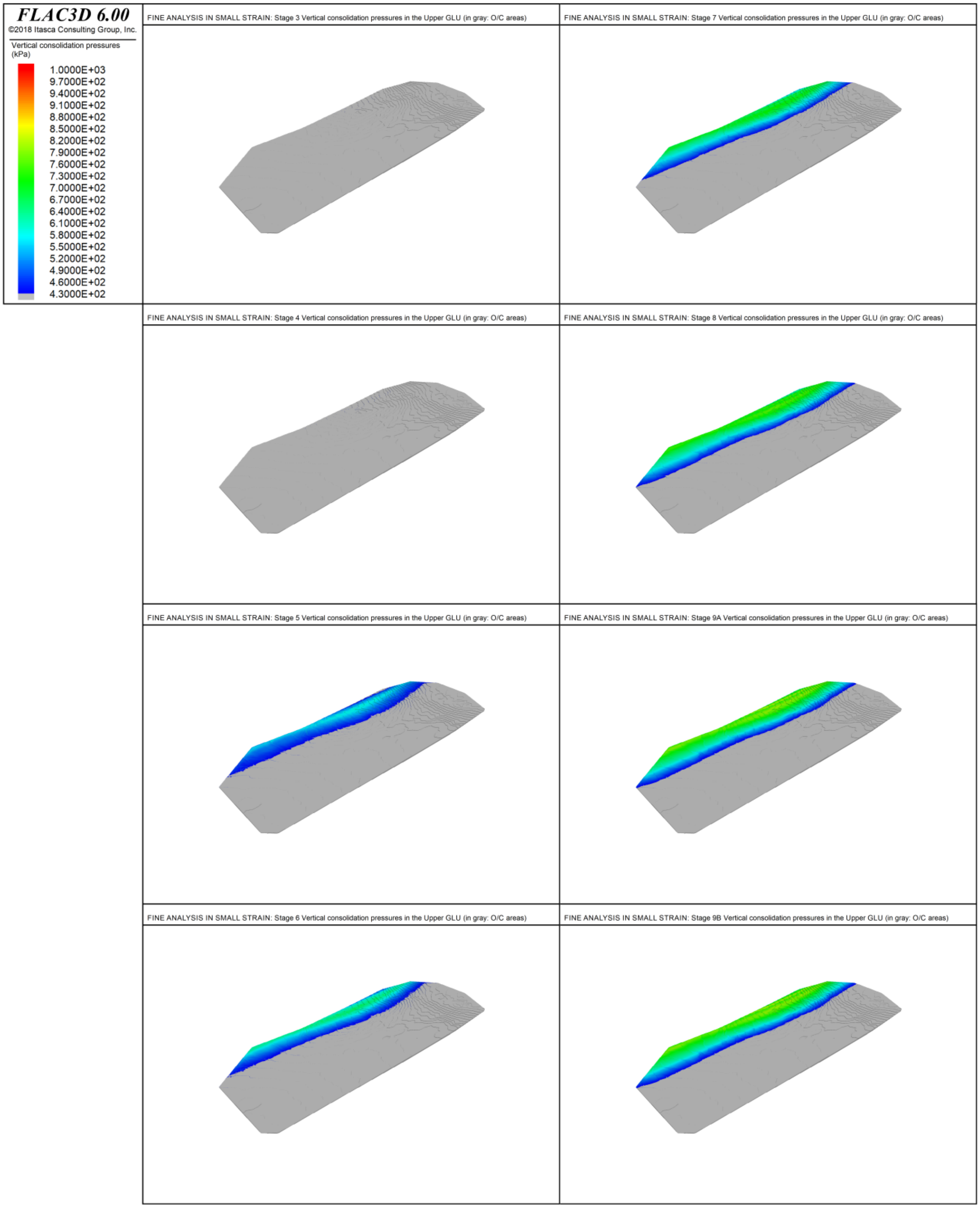

Figure 5.10 Vertical consolidation pressures in the Upper GLU after the completion of stages 3 through 9B under steady-state conditions predicted by the fine model in small strain.

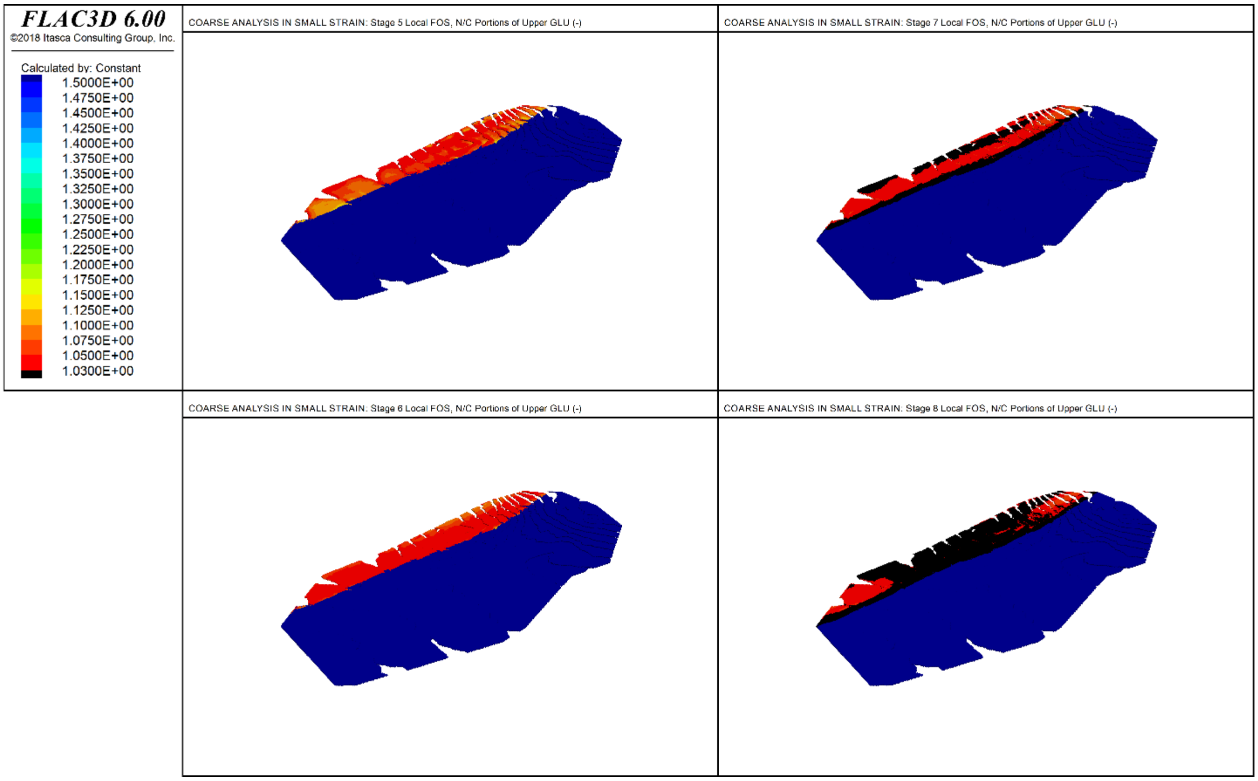

Figure 5.11 Local safety factors in the normally consolidated portions of the Upper GLU predicted by the coarse model in small strain.

5.2.1.1. LOCAL SAFETY FACTORS

Using the approach described in §4.2.1.1, local safety factors have been calculated in the normally consolidated portion of the Upper GLU starting with construction stage 5. The safety factor plots are seen in Figure 5.11 to Figure 5.13. The plots provide indication that in the early construction stages, the shear stresses along the critical planes are still somewhat below the material's undrained shear strength and that by construction stage 7, significant portions of this soil have either reached the failure envelope or are very close to it. The plots also show that starting with stage 7, the Upper GLU material that had newly became normally consolidated at the downstream edge of the normally consolidated region immediately reaches yield.

These results are not materially different from those obtained in large strain.

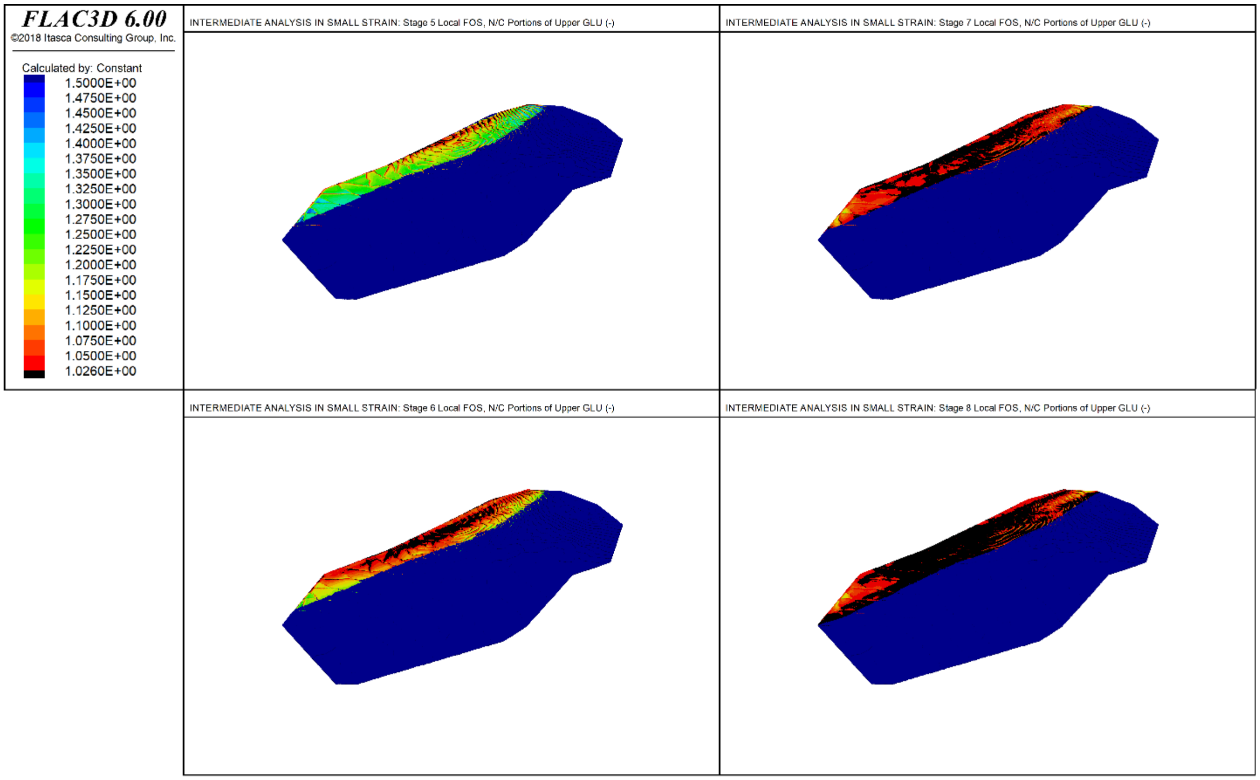

Figure 5.12 Local safety factors in the normally consolidated portions of the Upper GLU predicted by the intermediate model in small strain.

5.2.2 STRAIN-WEAKENING

5.2.2.1. PLASTIC SHEAR STRAINS

The accumulation of plastic shear strains in the Upper GLU was tracked through each simulated construction stage in the coarse, intermediate and fine models. The results are seen in Figure 5.14 to Figure 5.16 showing the plots of the plastic shear strains in the Upper GLU in the later construction stages and in Table 5.2 listing the maximum values of plastic shear strain in the stratum.

The three models produce very different predictions of the evolution of this variable over time. In the coarse model, plastic shear strains are first observed after construction stage 5 and their

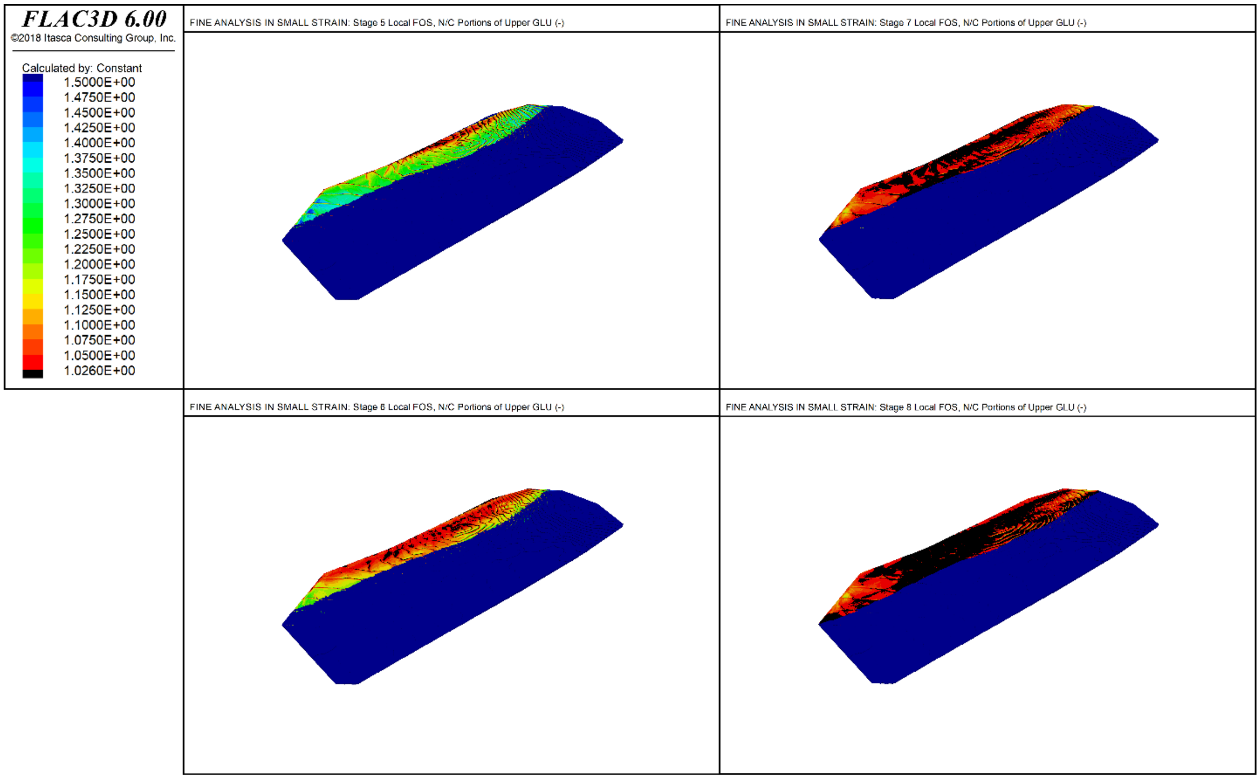

Figure 5.13 Local safety factors in the normally consolidated portions of the Upper GLU predicted by the fine model in small strain.

accumulation in subsequent stages is slow, reaching by stage 9B a maximum value of 7.2%. In the intermediate model, plastic shear strains first appear in construction stage 4 and accumulate more rapidly in subsequent stages, reaching in stage 9B a maximum value of 14.4%.

Table 5.2 Maximum plastic shear strains at static equilibrium in the Upper GLU (%) predicted in small strain.

Mesh	coarse	intermediate	fine
Stage 3	-	-	-
Stage 4	-	0.4	0.8
Stage 5	1.0	1.5	1.8
Stage 6	1.2	1.8	3.0
Stage 7	2.0	3.1	5.7
Stage 8	2.3	4.1	7.6
Stage 9A	4.4	7.0	14.4
Stage 9B	7.2	11.5	indefinite

In both of these simulations, the plastic shear strains are not sufficiently large to trigger any significant weakening and to destabilize the structure. In the fine model, plastic shear strains are

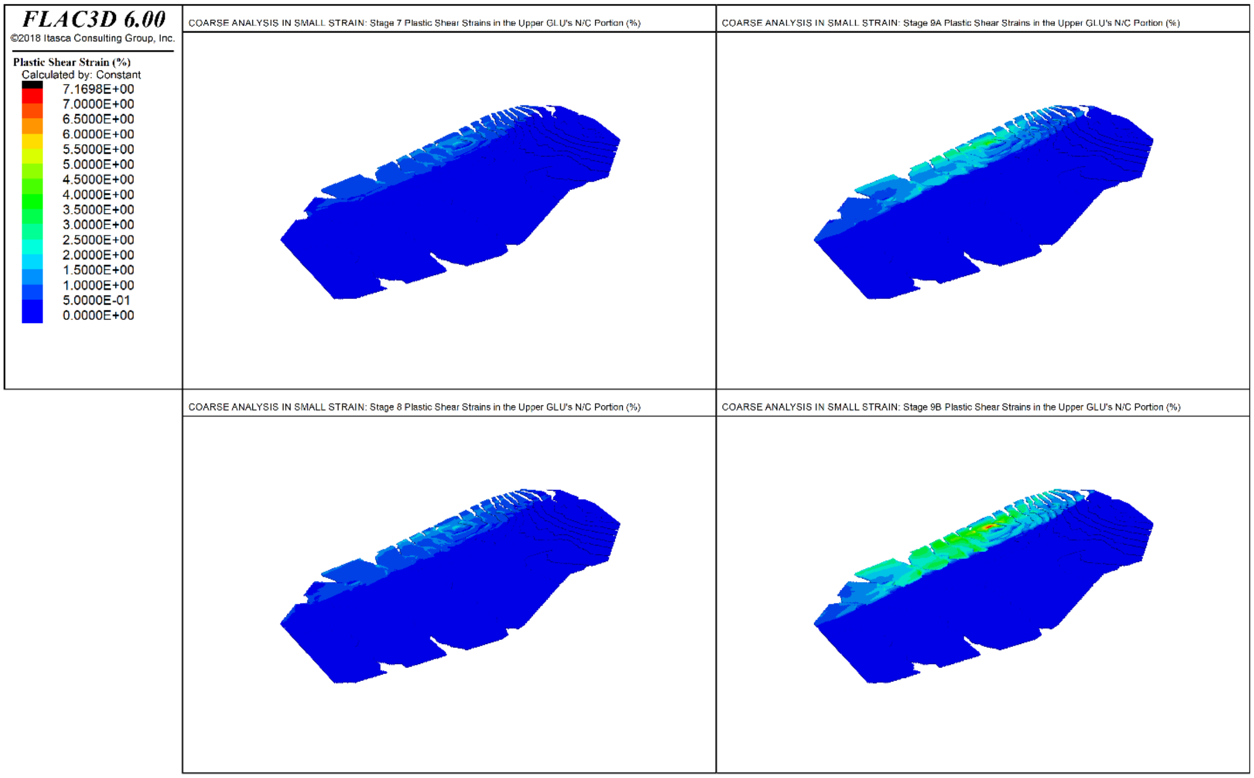

Figure 5.14 Plastic shear strains in the Upper GLU predicted by the coarse model in small strain.

first seen in construction stage 3 and their accumulation in subsequent stages is more rapid than in either the coarse or the intermediate models. In this simulation, by stage 8, a small number of zones accumulate plastic shear strains in excess of 5%, and by stage 9A, a small area under the core has accrued plastic shear strains well in excess of 10%. In stage 9B, the accumulation ofplastic shear strains continues indefinitely as global collapse unfolds. This response stands in contrast with that of the other two simulations, thus indicating the presence of consequential scale effects.

With the notable exception of the fine simulation of stage 9B, the plastic shear strain distributions predicted under the small strain calculation scheme are not materially different from those obtained in large strain.

In stage 9B, the fine model predicts collapse under both the large and small strain calculation schemes. However, the predicted plastic shear strain distributions differ greatly. In small strain, the

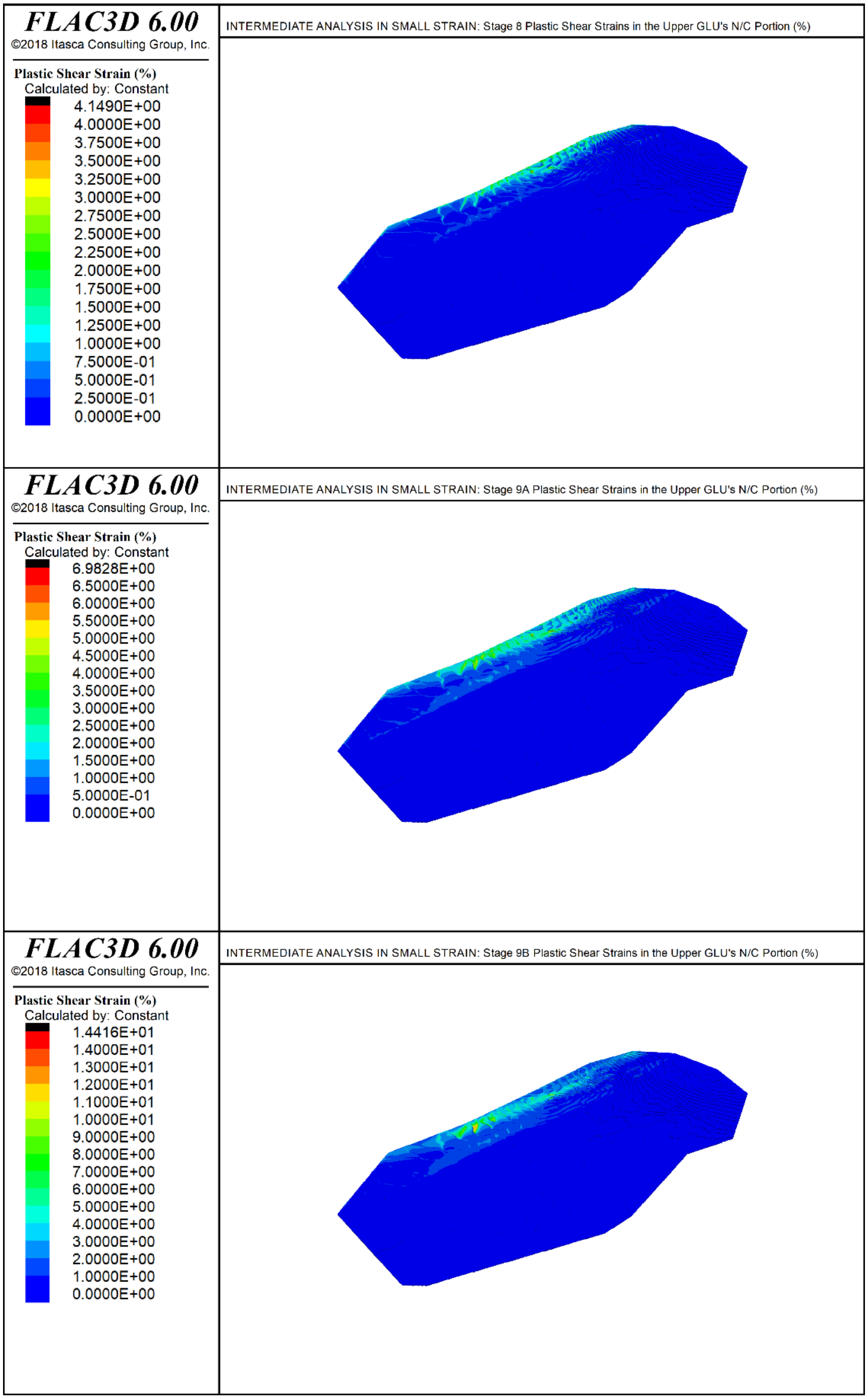

Figure 5.15 Plastic shear strains in the Upper GLU predicted by the intermediate model in small strain.

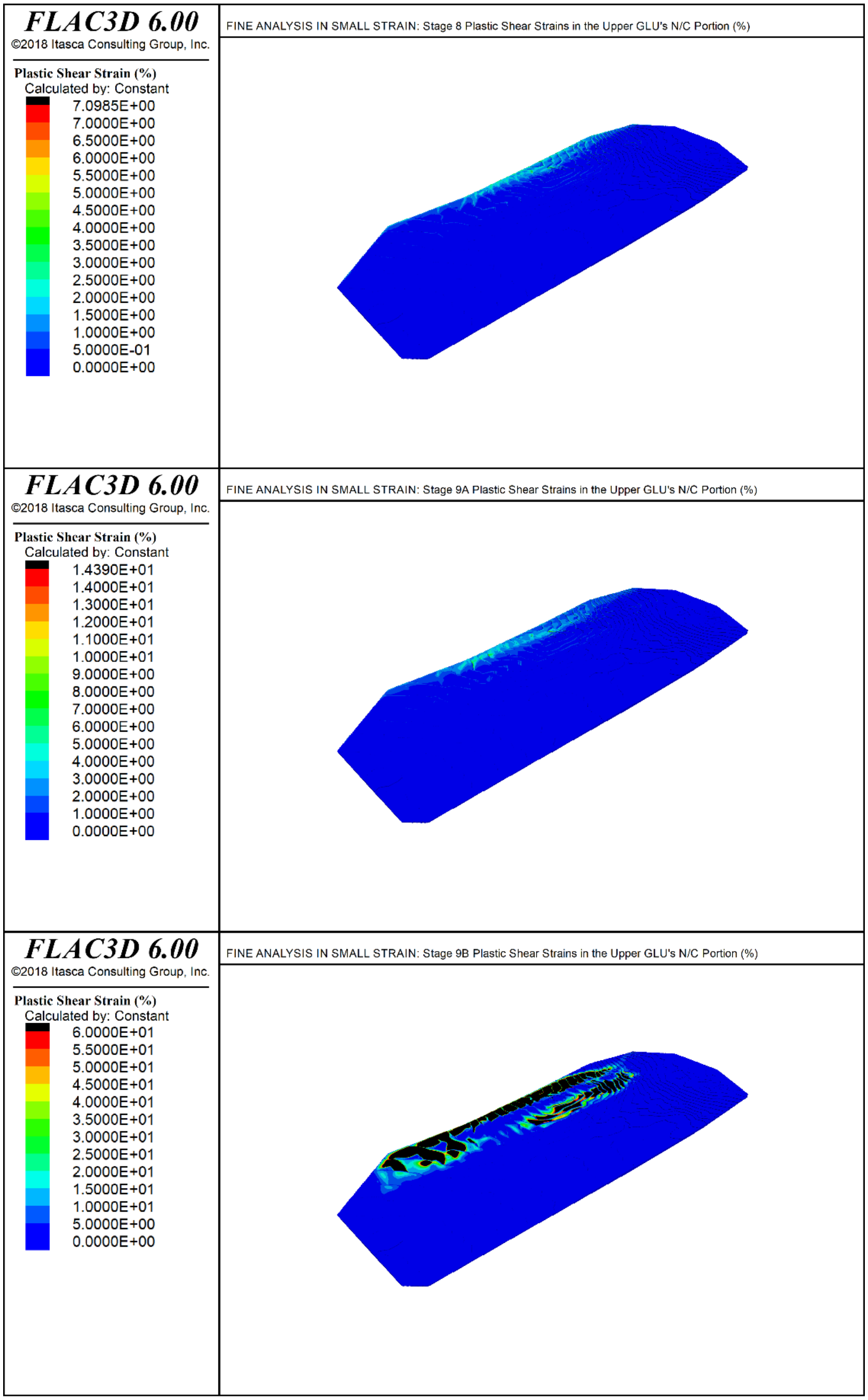

Figure 5.16 Plastic shear strains in the Upper GLU predicted by the fine model in small strain. In black: portions of Upper GLU that are fully weakened.

width of the fully weakened zone (seen in black in Figure 4.16 and Figure 5.16) is much greater in small strain, creating a slide that is considerably wider than that in large strain and than that observed in situ.

5.2.2.2. EMERGENCE AND GROWTH OF PLASTIC YIELD ZONE

The plots of the plastic yield zones are shown in Figure 5.17 to Figure 5.19. In the figures, the zones with plastic shear strains <5% (i.e. the zones that are not strain-weakening) are rendered transparent in order to fully reveal the weakening areas, including those located at the base and/or in the middle of this soil unit.

The results from the coarse simulation indicate that strain-weakening processes first emerge in construction stage 9B in a small area, about 15X8m^2, located directly below the embankment core. This simulation predicts that maximum plastic shear strains in this zone barely exceed 7%, with an average plastic shear strain value of about 5.5%. As a consequence, the plastic flow in the yield

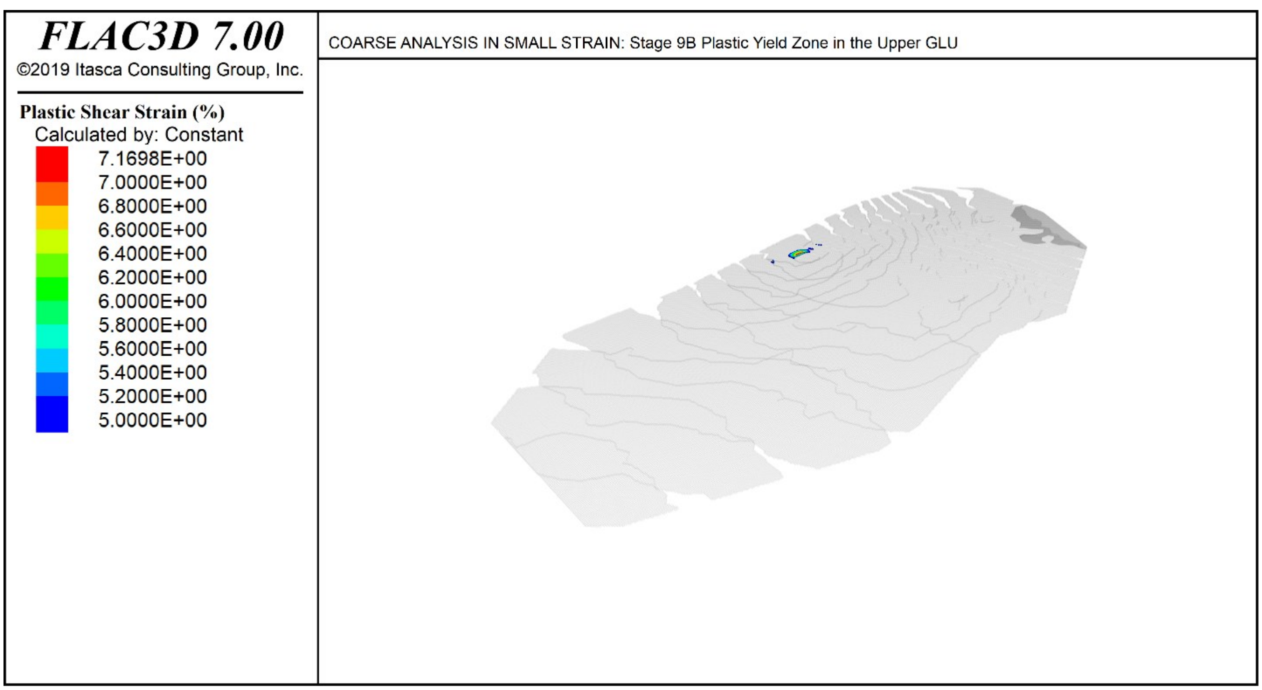

Figure 5.17 The plastic yield zone predicted by the coarse model in small strain.

zone is contained and the embankment remains stable. The results obtained by the coarse simulation under the small and large calculation schemes are very close.

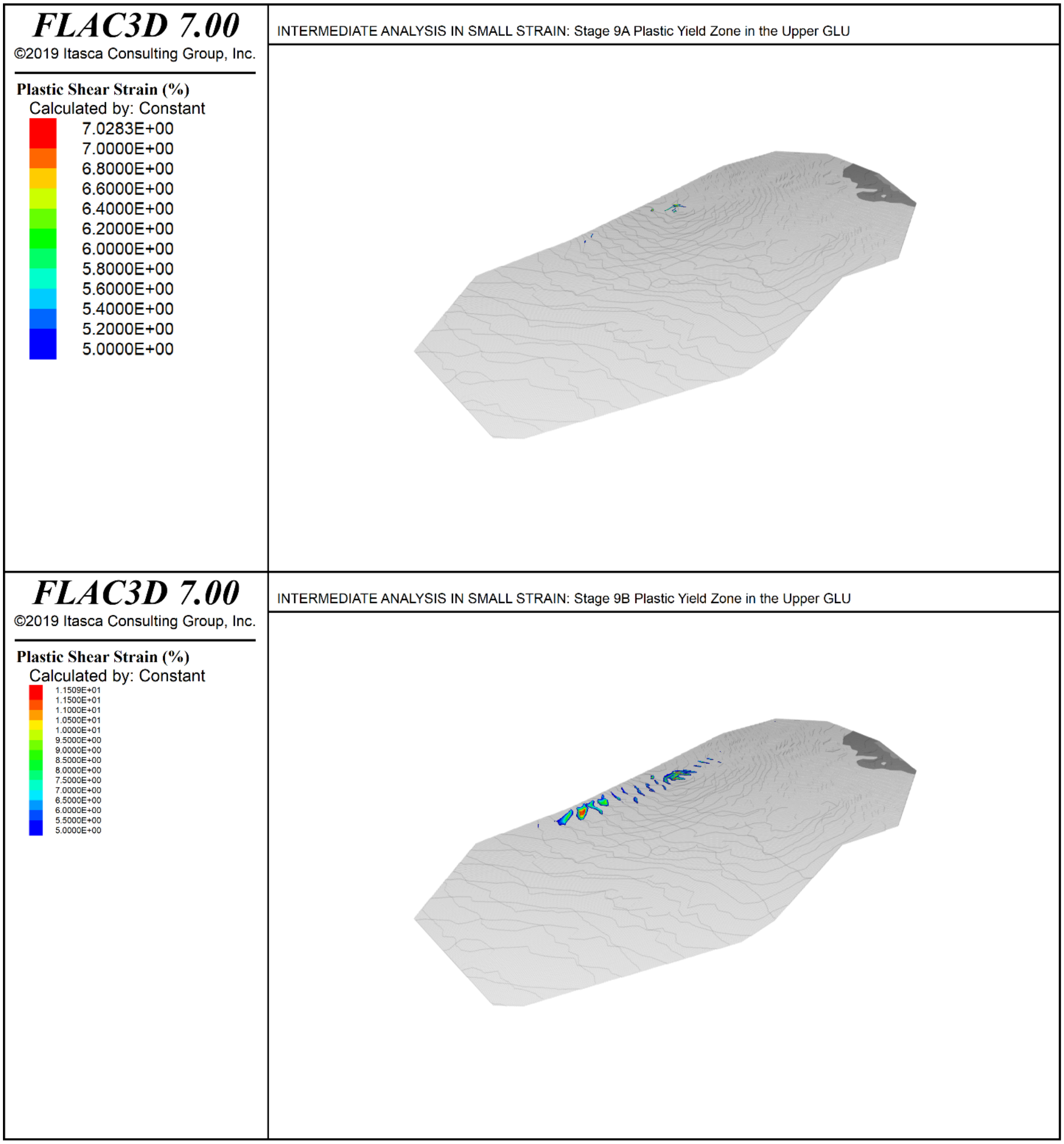

Figure 5.18 The emergence and growth of the plastic yield zone predicted by the intermediate model in small strain.

The results from the intermediate simulation indicate that a plastic yield zone first emerges in construction stage 9A in a number of isolated areas located under the core. At this stage, maximum plastic shear strains in the Upper GLU reach 7% and average shear strains across the plastic yield zones are about 5.3%. In stage 9B, the areal extent of the plastic yield zone expands considerably, reaching a width of over 100m; maximum shear strains reach ~12% and average shear strains are at ~8-9%. However, the area of the plastic yield zone was still comparatively small in comparison with the rest of the Upper GLU, and the plastic flow in it remains fully contained. In this simulation, some stress transfer is seen in construction stages 9A and 9B, where some areas in the Upper GLU located immediately downstream of the yield zone experience an increase in shear stresses (seen in Appendix 5A, Figure 5A.3 and Figure 5A.6).

There are marked differences between the plastic yield zones predicted by the intermediate model under the small and large calculation schemes, especially in stage 9B. On comparing Figure 4.18 and Figure 5.18, a determination can be made that the area of the plastic yield zone is considerably

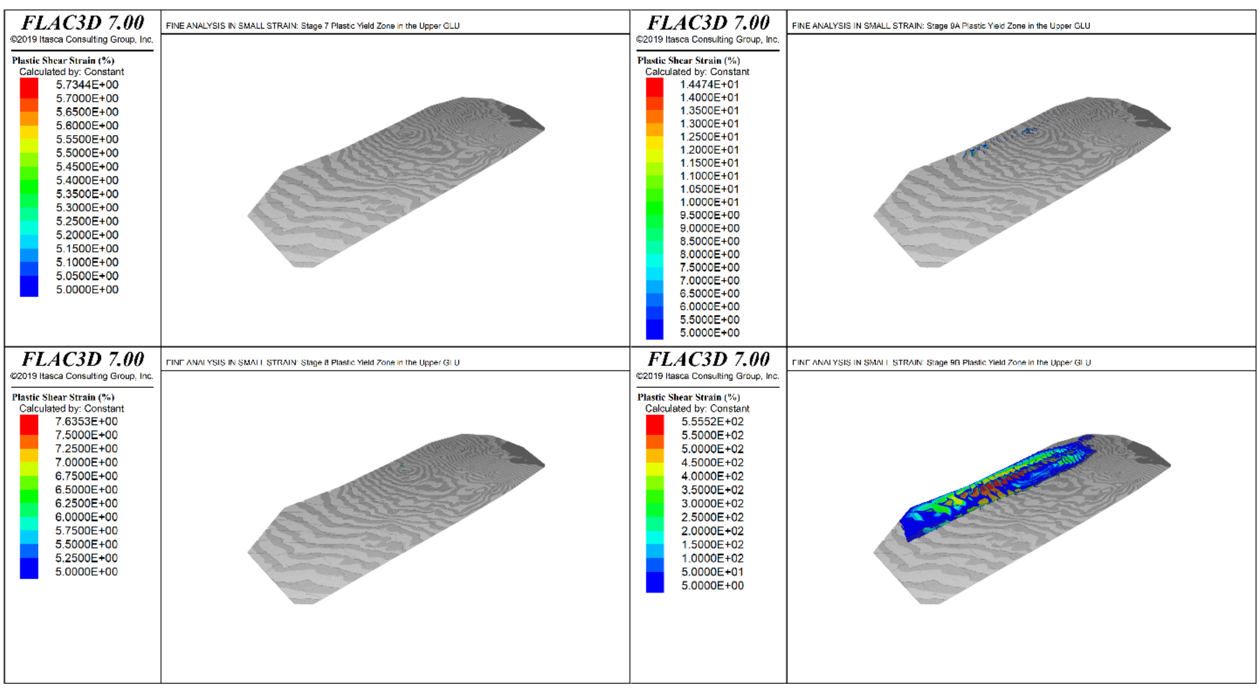

Figure 5.19 The emergence and growth of the plastic yield zone predicted by the fine model in small strain.

larger in large strain than it is in small strain at over double the area. Additionally, the maximum plastic shear strains predicted in large strain are greater than those predicted in small strain, 14.4% vs. 11.5%. These results suggest that the use of the small strain calculation scheme in problems involving substantial plastic straining and strain-weakening materials may lead to an under-prediction of plastic shear strains and an under-estimation of weakening processes. At least some of the noted differences can be attributed to the variation of loading conditions in large and small strains (explained in §6.6.1).

The fine simulation of the failure at Mount Polley predicts the emergence of the plastic yield zone in construction stage 7 (completed in 2011); in this stage, plastic shear strains in portions of the unit exceed 5% and begin weakening. In construction stages 7 and 8, the extent of the weakening areas is negligible and the plastic flow in the yield zone remains contained. In construction stage 9A (completed in 2013), numerous isolated plastic yield zones are seen to emerge under the core, with maximum shear plastic strains of 14% and average plastic shear strains of 6-7%. In construction stage 9B, the plastic flow in the yield zone becomes uncontained, and the plastic yield zone continues to grow indefinitely. The plot of stage 9B plastic yield zone in Figure 5.19 illustrates the spatial distribution of the predicted weakening area at an advanced stage of collapse. From the figure, the size and shape of the plastic yield zone can be appreciated. At this point in the simulation, this zone is excessively wide at nearly 300m, and encompasses almost the entire portion of the normally consolidated Upper GLU. Such result stands in contrast with results predicted by the fine simulation in large strain.

5.2.3 EVOLUTION OF SHEAR STRENGTH

The evolution of shear strengths in the Upper GLU, illustrated in Figure 5.20 to Figure 5.22, was observed in step with its transition to a normally consolidated state and the accumulation of plastic shear strains.

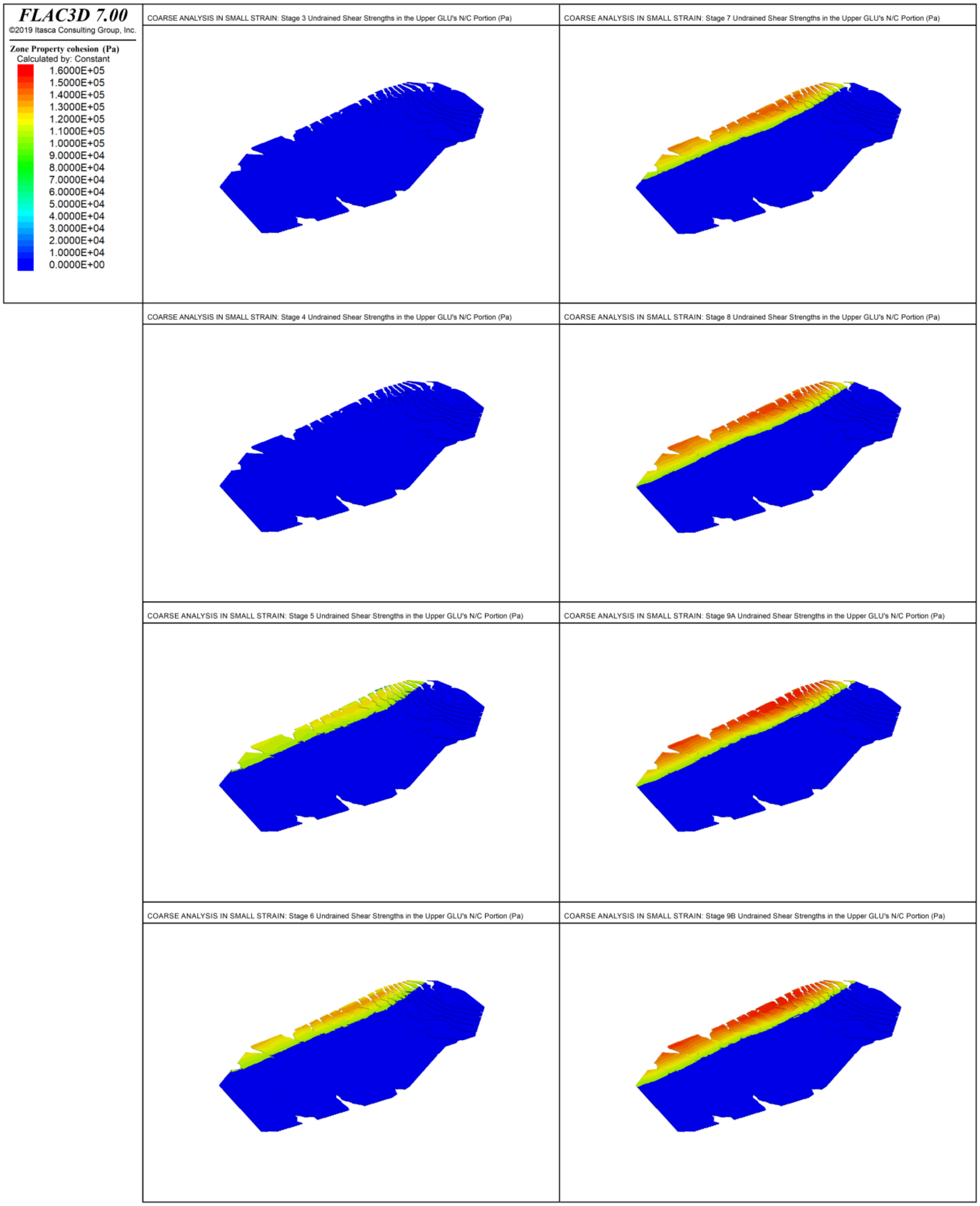

Figure 5.20 Undrained shear strengths in the normally consolidated portion of the Upper GLU predicted by the coarse model in small strain.

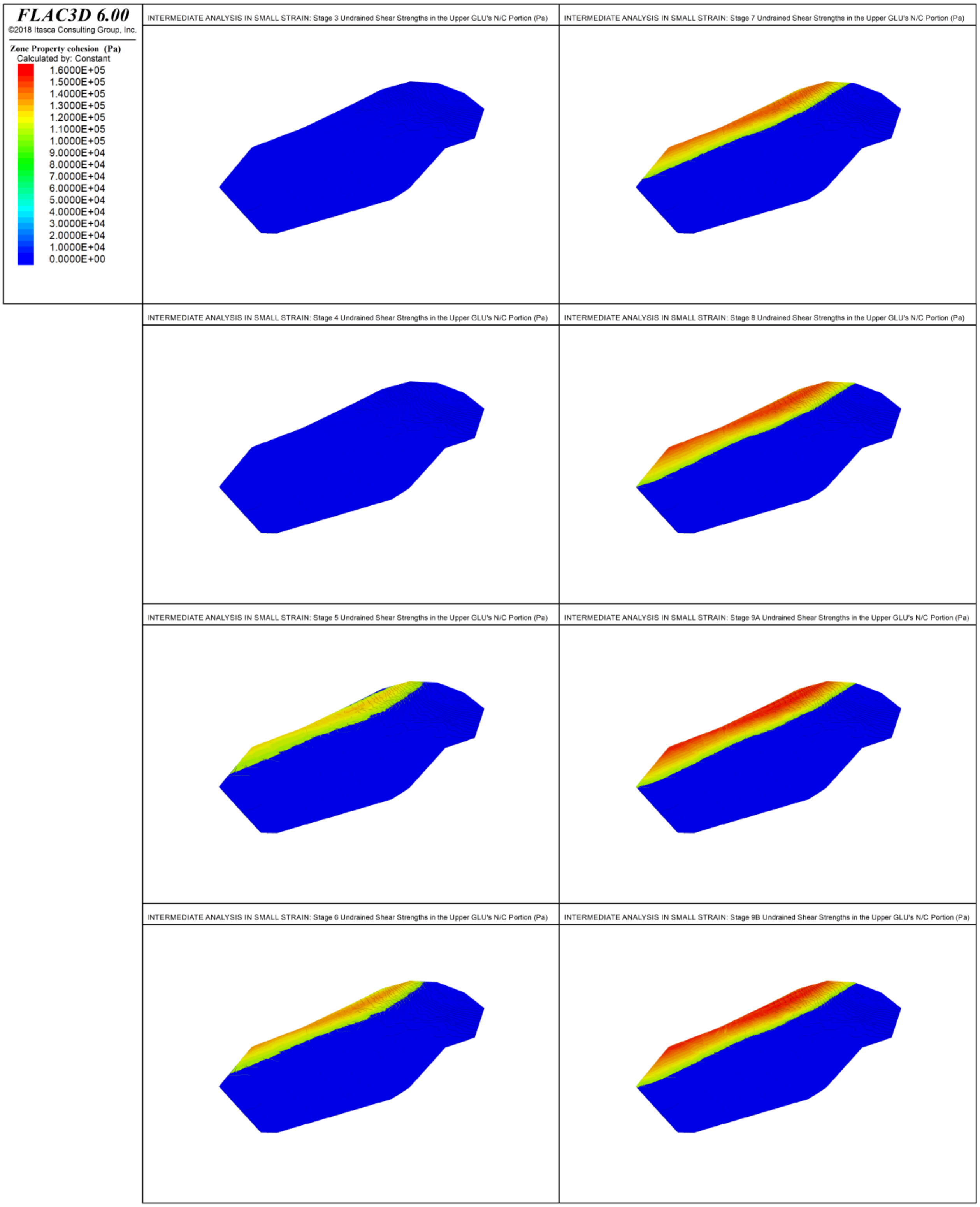

Figure 5.21 Undrained shear strengths in the normally consolidated portion of the Upper GLU predicted by the intermediate model in small strain.

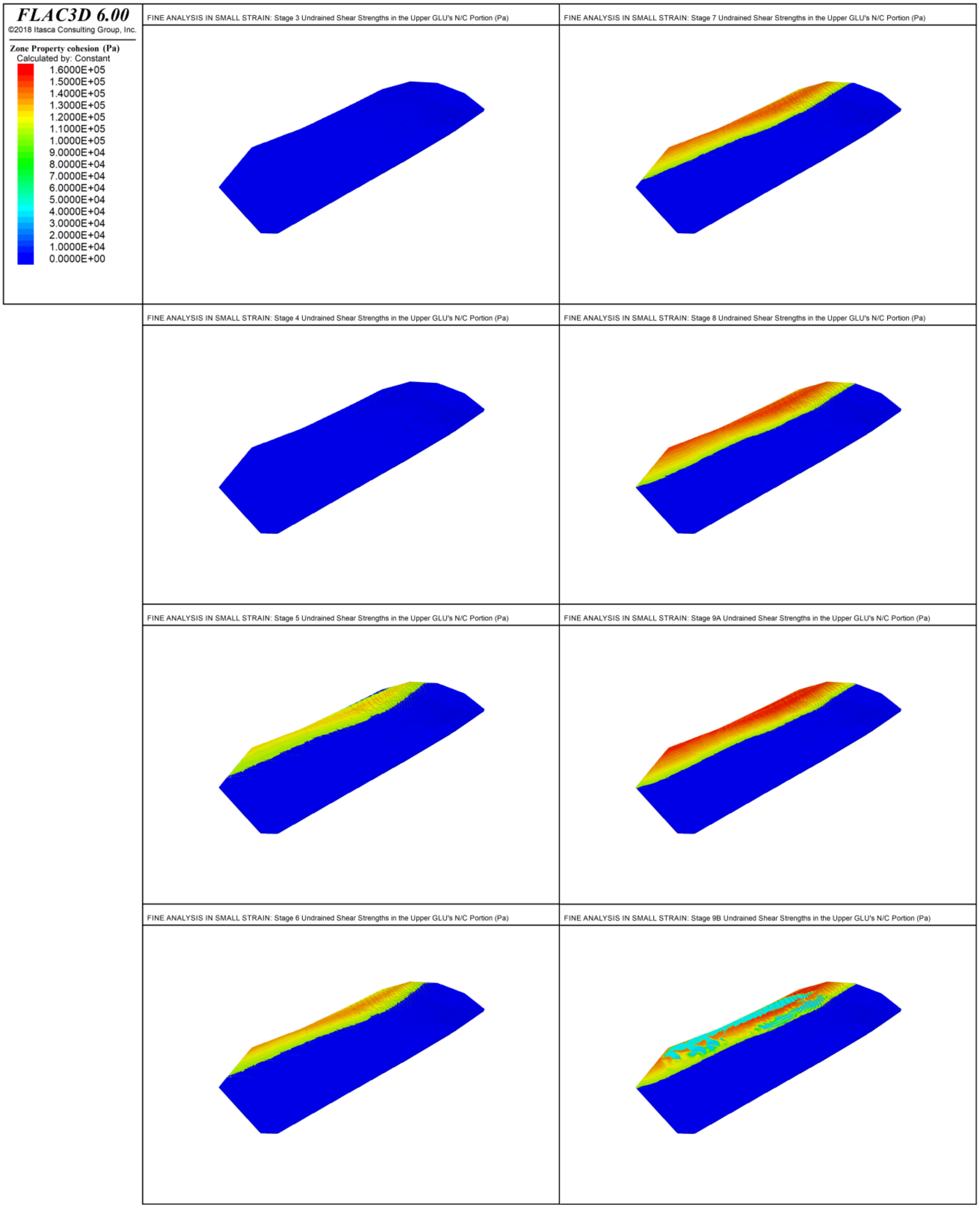

Figure 5.22 Undrained shear strengths in the normally consolidated portion of the Upper GLU predicted by the fine model in small strain.

Figure 5.20 plots the distributions of undrained shear strengths in the Upper GLU in construction stages 3 through 9B obtained using the coarse model. The figure shows that in construction stage 5, substantial portions of this unit transition to an undrained strength model; at that point in the simulation, the undrained shear resistance in its normally consolidated area varies from ~105kPa to ~130kPa, with an average value of 110kPa. In subsequent stages, undrained shear strengths are seen to rise in step with the increase in vertical overburden stresses (in Figure 5.8). In this model, weakening does not take place in stages 3 through 9A. In stage 9B, some weakening is seen to take place in the plastic yield zone (shown in Figure 4.17), but the average decrease in shear resistance of less than 1%, or <1.5kPa, is not visually detectable.

The evolution of shear strengths in the normally consolidated portion of the Upper GLU predicted by the coarse model in small strain are not materially different from those determined using large strain.

Figure 5.21 plots the distributions of undrained shear strengths in the Upper GLU in construction stages 3 through 9B obtained using the intermediate model. The figure shows that in construction stage 5, about a quarter of this unit by area transitions to an undrained strength model; at this point into the simulation, the undrained shear resistance in its normally consolidated area varies from ~105kPa to ~135kPa, with an average valueof ~110kPa. In subsequent stages, undrained shear strengths are seen to rise in step with the increase in vertical overburden stresses (in Figure 5.9). In this simulation, weakening processes begin in construction stage 9A, when plastic shear strains exceed 5% in a number of small areas under the core. In this stage, the loss of shear resistance due to strain-weakening in the plastic yield zones is minor at around 1% and is not visually detectable. In stage 9B, a further loss of shear resistance in the plastic yield zone is observed to an average value of about 3% and is seen on the plot as a number of barely detectable lighter patches (in Figure 5.21, bottom right).

There are significant differences in the way the evolution of shear strengths in the normally consolidated portion of the Upper GLU is predicted by the intermediate models under the small and large strain calculation schemes, especially in stage 9B. Recall that in this stage, the area of the plastic shear zone predicted in large strain is more than double of that predicted in small strain and that the maximum plastic shear strains are also greater in large strain. Consequently, even though the average drop in shear strength values across the surface of the plastic shear zone is comparable (3-4% in large strain vs. 3% in small strain), the overall loss of shear resistance to strain-weakening is much more significant in large strain.

Figure 5.22 plots the distributions of undrained shear strengths in the Upper GLU in construction stages 3 through 9B obtained using the fine model. The figure shows that in construction stage 5, about a quarter of this unit by area transitions to an undrained strength model; at that time, the undrained shear resistance in its normally consolidated area varies from ~105kPa to ~135kPa, with an average value of ~115kPa. In subsequent stages, undrained shear strengths rise in step with the increase in vertical overburden stresses (seen in Figure 5.10). In this simulation, the onset of strain-weakening takes place in construction stage 7 when the plastic yield zone emerges. In construction stages 7 and 8, the loss of shear resistance due to strain-weakening is negligible and cannot be detected on visual examination (Figure 5.22, right column, top two plots). In stage 9A, the drop in shear resistance due to strain-weakening in the plastic yield zones scattered in the region under the core reaches, on average, ~1%, or 1.5kPa. This decrease in shear strength is not visually detectable (Figure 5.22, right column, third plot down) because it is minor and takes place mostly in the soil layers located at the base and in the middle of the unit. In construction stage 9B, the plastic flow in the yield zone becomes uncontained, and strain-weakening processes continues until the soil in the plastic yield zone is weakened fully or near-fully. Figure 5.22 (bottom right) shows the Upper GLU at an advanced stage of collapse; in the figure, some of the soil layers located at the top of the Upper GLU are seen to have experienced full weakening (in light blue), and their shear resistance has decreased to its residual value of ~40kPa. However, the bulk of strain-weakening is taking place in soil layers located at the base and in the middle of this unit and is concealed in this view.

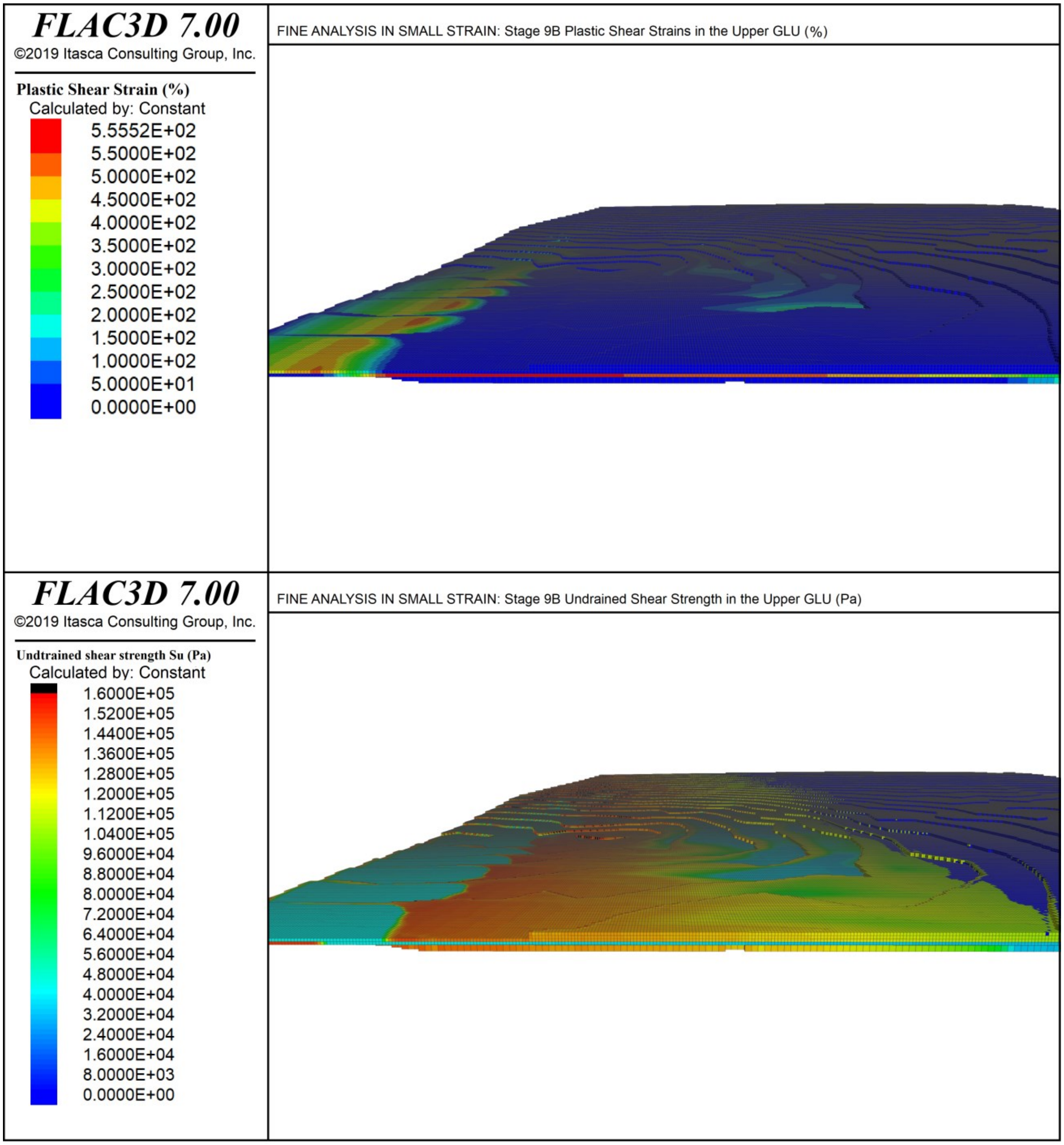

Figure 5.23 A cross-sectional view of the Upper GLU at an advanced point of collapse in construction stage 9B predicted by the fine model in small strain.

A better view of the soil layers that have sustained appreciable strain-weakening at this stage is seen in Figure 5.23 (bottom) showing the undrained shear strengths in of the Upper GLU in a cross-sectional view passing approximately through the center of the slide. In this figure, a single continuous soil band is seen at or close to the base of the unit (in light blue), where the undrained shear resistance has decreased to residual strength. The top plot of the figure showing the plastic shear strains in the unit in the same cross-sectional view demonstrates that the drop in shear resistance in the unit is related to its degree of plastic shear straining.

Figure 5.23 visualizes the shear band in the unit. From the figure, the shear band is seen to propagate through a thickness equal to a single zone, i.e. 12.5cm in the fine model. The soil in the shear band is seen to have accumulated plastic shear strains at a rate that is 1-2 orders of magnitude higher than the surrounding material belonging to the same unit. The zones in the shear band are also considerably more weakened that surrounding material, exhibiting residual strengths. In contrast, the soils outside the shear band have not strained to any significant degree and exhibit peak or near-peak undrained shear strengths.

The contrasting levels of straining and associated weakening in and outside the shear band, in conjunction with the observed thickness of the shear band, offer evidence to support the hypothesis of non-linear straining of the Upper GLU. These results match those observed under the large strain calculation scheme.

5.3. ONSET OF FAILURE

Pronounced scale effects have been identified in the simulations of Mount Polley, with some of them having already been reported in this chapter. Of those, the most consequential one is related to the different rate of accumulation of plastic shear strains in the Upper GLU and the associated rate of weakening in this material: in the fine model, a much higher rate of plastic shear strain accumulation is seen, resulting in an earlier emergence of a plastic yield zone and a greater extent of weakening from stage 7 on.

In the fine model, the loss of shear resistance to weakening is significant enough to trigger, in stage 9B, a collapse of the structure under undrained conditions. This response is markedly different from that of the coarse and intermediate models where the structure remains stable and a static equilibrium is reached. This effect is illustrated in Figure 5.24 showing the plots of the average force ratio during the mechanical calculation steps in construction stage 9B. The figure shows that in the coarse and intermediate models, the average force-ratio eventually reaches a value of 10^{-5}, indicating convergence and the attainment of static equilibrium. In the fine esh model, convergence is not attained and the model continues to deform indefinitely.

Stage 9B safety factors calculated for the coarse and intermediate models using the strength reduction method as described in §3.3.4.4 are 1.34 and 1.04, respectively. The safety factor of the fine model in stage 9B is assumed to equal unity due to observed collapse; in actuality, the safety factor (as defined in §3.3.4.3) likely varies throughout the collapse phase depending on the degree of weakening in the Upper GLU along with the degree of mobilization of shear resistance in the rest of the soil mass.

In the field, the collapse of the Mount Polley TSF embankment occurred within 2-4 weeks of the start of construction stage 9B. This means that the fine model correctly replicates the onset of failure.

The presence of the noted scale effects is an indication that the discretization levels of the coarse and intermediate models are not sufficient to minimize discretization errors. This means that the results produced by these two models do not adequately replicate field conditions. The failure of these two models to correctly replicate the onset of collapse in stage 9B confirms this conclusion.

The level of stage 9B stability predicted by the coarse, intermediate and fine models under the small strain calculation scheme are nearly identical to those obtained by the same models in large strain.

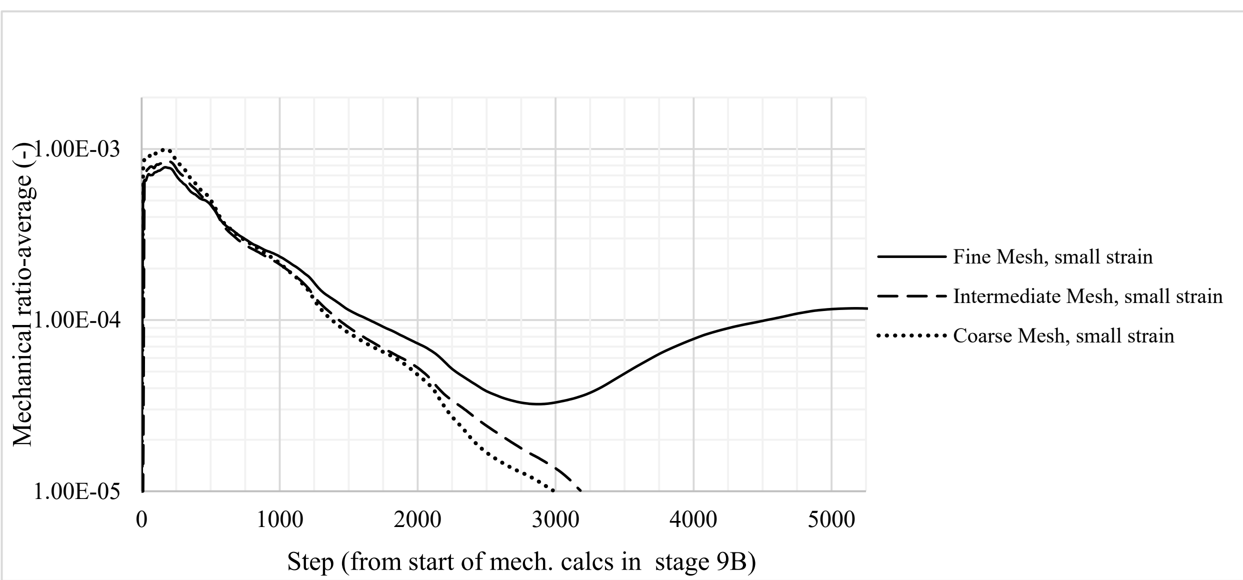

Figure 5.24 The plots of average force ratios vs. mechanical calculation steps in construction stage 9B.

5.4. EMBANKMENT DEFORMATIONS

5.4.1 EMBANKMENT SETTLEMENT

In small strain, settlement and other small deformation adjustments to added loads are predicted in each simulated construction stage and can be evaluated by tracking displacements. Since in small strain the mesh coordinates are not updated in response to strain and deformation increments, such deformations do not result in a downward shift of the surface that can be visualized.

The average incremental vertical displacements at the crest of embankment predicted by the coarse model in small strain were evaluated in stages 3 through 9B and are listed in Table 5.3. The settlements predicted in small strain are generally either equal to or slightly lower than those predicted in large strain (listed in Table 4.3 and visualized in Appendix 4B), especially in the core and shell regions. The difference between settlements predicted in small and large strains is shown in the table in brackets beside the settlement value.

Table 5.3 Embankment settlement in the area of the slide predicted by the coarse model in small strain.

	Approximate settlement of embankment surface due to the addition of material in the beach, crest and shell areas (m) (in brackets: difference between settlements predicted in small and large strain)		
	beach	crest	shell
Stage 3	0.13 (+0.01)	0.13	0.14 (+0.01)
Stage 4	0.05 (−0.06)	0.07 (−0.04)	0.13 (+0.01)
Stage 5	0.16 (−0.02)	0.18 (−0.01)	0.32
Stage 6	0.13 (−0.01)	0.16 (−0.04)	0.21 (−0.02)
Stage 7	0.12 (−0.02)	0.18 (−0.03)	0.17 (−0.01)
Stage 8	0.15 (−0.02)	0.18 (−0.02)	0.14 (−0.02)
Stage 9A	0.23 (+0.05)	0.21 (−0.02)	0.24 (−0.02)
Stage 9B	0.16 (+0.02)	0.19 (−0.04)	0.22 (−0.04)

As it has been the case with settlements predicted by the coarse model in large strain, the settlement values in Table 5.3 are used as a baseline for estimating the levels of deformations associated with failure processes seen in the simulations with a higher resolution.

5.4.2 LATERAL DISPLACEMENTS

5.4.2.1. CUMULATIVE SHEAR DISPLACEMENTS IN THE FOUNDATION

The accumulation of horizontal displacements in the Upper GLU was tracked in stages 3 through 9B and is illustrated in Appendix 5B, Figure 5A.1 to Figure 5A.3. Additionally, the maximum horizontal cumulative displacements predicted in each construction stage using the coarse, intermediate and fine models are listed in Table 5.4. The upstream-to-downstream direction of horizontal displacement was taken as sign-positive; the minor displacements noted in the direction normal to the dam cross-section were ignored.

The examination of horizontal displacements accumulated in the Upper GLU over the duration of embankment construction invites a number of observations; these are discussed further in this section.

(1) Horizontal displacements are largely in the upstream-to-downstream direction, i.e. consistent with the movement of the soil mass during collapse. The horizontal displacements in the direction normal to the dam centreline are smaller by 1-2 orders of magnitude and do not appear to offer any particular insight about the mechanical behaviour of the structure.

(2) In each simulated stage, horizontal displacements closely follow the footprint of the embankment, and the areas exhibiting the largest displacements are located under the core, where the loading extent is the greatest. This suggests that horizontal displacements in the Upper GLU are driven largely by embankment loading.

(3) With the exception of stage 9B (where collapse is predicted by the fine model but not by the two other models), the horizontal displacements predicted by the coarse, intermediate and fine models are nearly identical.

(4) There appears to be no notable accumulation of horizontal displacements in the direction of downstream that can be attributed to plastic yielding. In the intermediate model, the plastic

yield zone first emerges in construction stage 9A; yet no increase in deformation levels can be detected when the results of the coarse and intermediate models are compared. In the fine model, the plastic yield zone first emerges in construction stage 7; similarly, no increase in deformation levels in can be detected in this stage on comparing the results of the coarse and fine models.

Table 5.4 Cumulative maximum horizontal displacements in the Upper GLU (m).

Mesh	coarse	intermediate	fine
Stage 3	0.044	0.044	0.044
Stage 4	0.052	0.057	0.053
Stage 5	0.062	0.065	0.060
Stage 6	0.087	0.083	0.086
Stage 7	0.105	0.101	0.104
Stage 8	0.113	0.109	0.112
Stage 9A	0.137	0.134	0.137
Stage 9B	0.153	0.152	indefinite

Cumulative horizontal displacements throughout the entire structure in the downstream direction were also examined; some representative results are illustrated in Figure 5.25. The following can be noted from the figure:

(1) Movements in the foundation and embankment are concentrated in the zone above the Upper GLU; no significant lateral displacements are noted below the base of this unit.

(2) The lateral displacements in the foundation materials directly above the Upper GLU are almost exactly equal to those seen in the Upper GLU. This suggests that the soil mass is “riding” on top of the Upper GLU.

(3) In stage 7 and on, the slide begins to shape up: the soil mass experiencing significant lateral displacements corresponds to the soil mass that ultimately failed. In the cross-sectional view at the middle of the failure location, the upstream extent of slide passing through the upper till and core materials is clearly defined. Likewise, the extent of the slide on the downstream around the toe location can be identified by the presence of lateral displacements in the slide area and an absence of it further downstream.

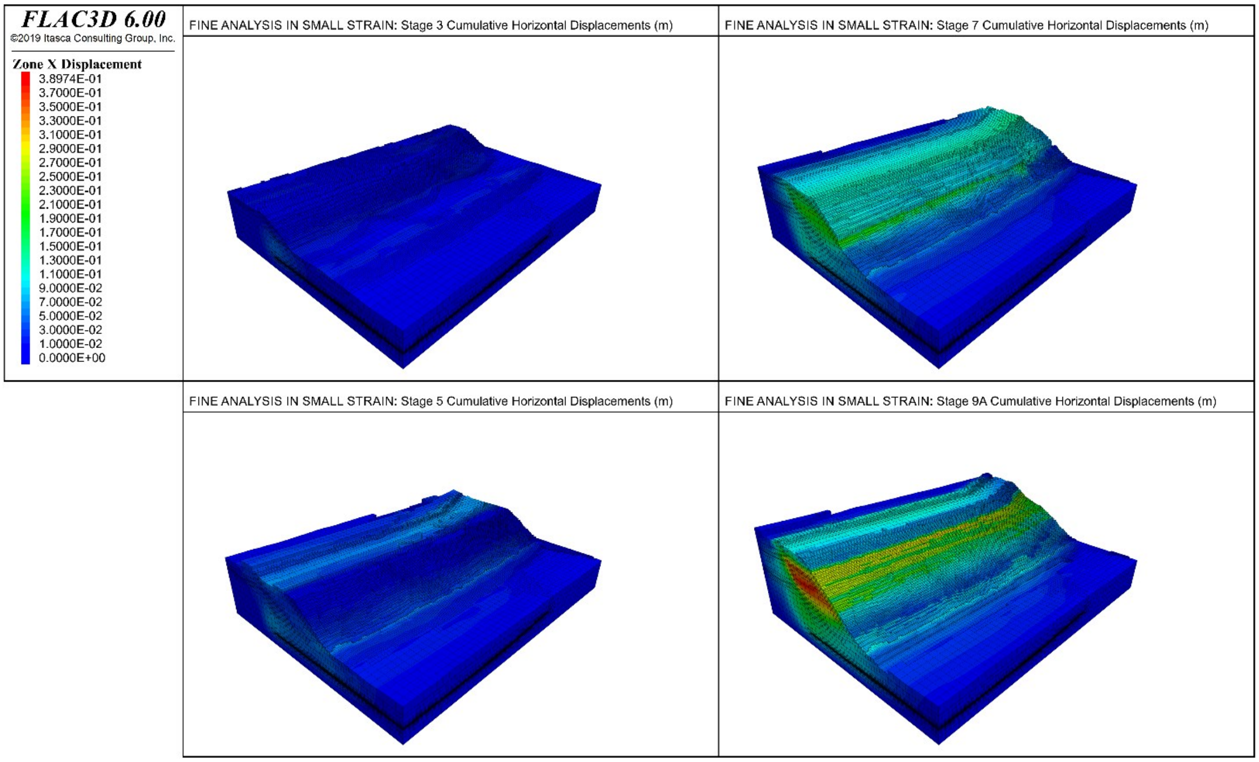

Figure 5.25 Lateral displacements accrued in the embankment and foundation materials, predicted by the fine model in small strain.

The lateral displacements predicted in small strain are very close to those predicted in large strain (discussed in §4.4.2) and invite the same conclusions.

5.4.2.2. PRE-FAILURE SURFACE DEFORMATIONS

The incremental surface deformations predicted by the fine model in stages 6 through 9A are seen in Figure 5.26. From the figure, the following observations are made:

(1) In construction stage 9A, horizontal displacements at the face of the dam range between 2 and 7cm, and vertical displacements range between 10 and 20cm. These movements take place mostly at near the top of the face; at the toe, the deformations are negligible.

(2) In the region of the toe excavation, some minor uplift in the order of 2cm is predicted in stage 9A. This deformation cannot be seen from the figure and was identified by closely examining the model results.

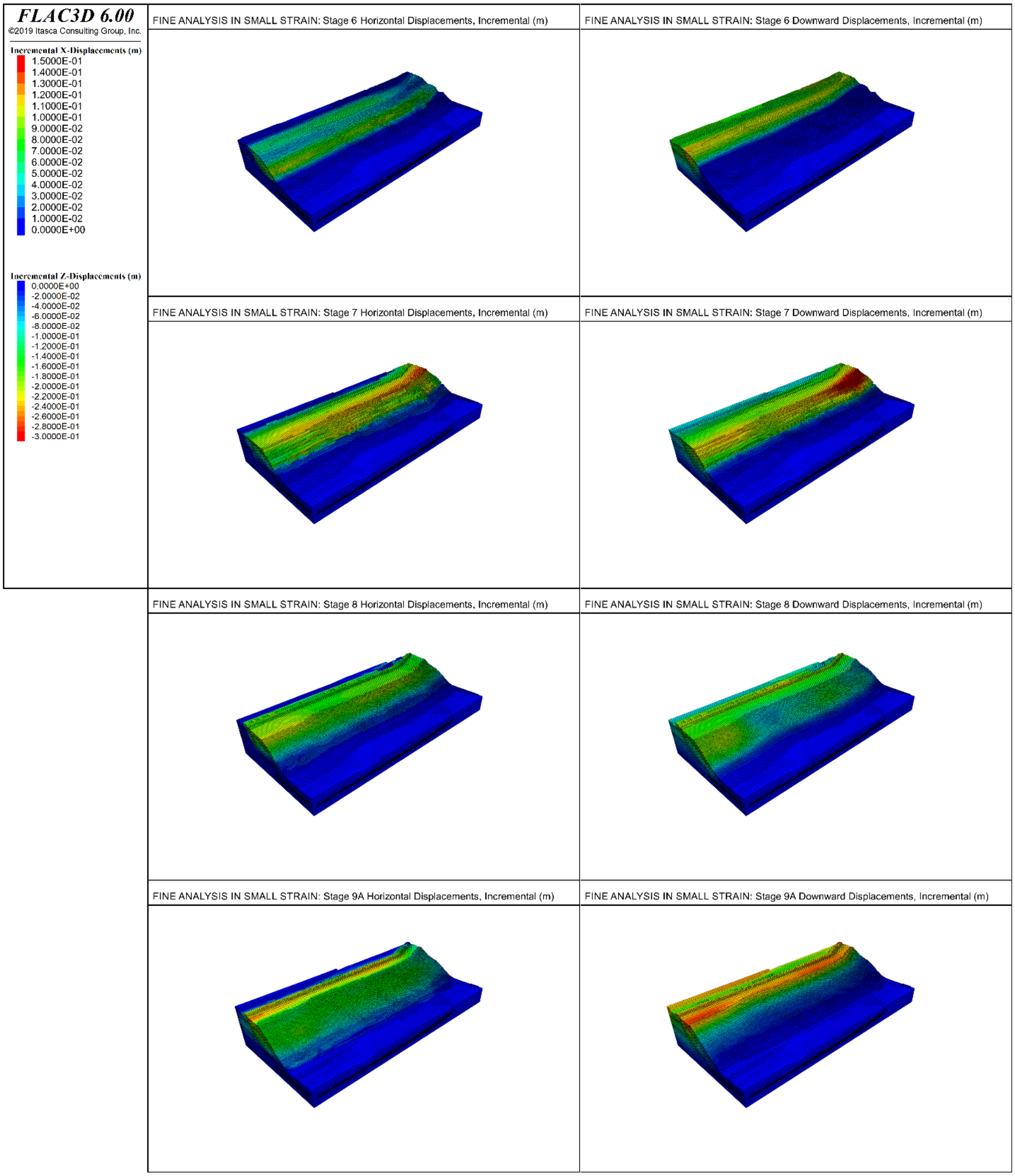

Figure 5.26 Incremental deformations of the embankment surface in construction stages 6 through 9A predicted by the fine model in small strain.

(3) The highest levels of deformation are observed at the crest in the core area where horizontal displacements reach 10-15cm and vertical displacements as high as 25cm are observed.

(4) The magnitude and location of incremental displacements in stage 9A are not materially different from those seen in stages 6 to 8. In each construction stage, the embankment surface settles by 10 to 30cm; in this context, the downward displacements in stage 9A do not stand out. Similarly, stage 9A incremental horizontal displacements at the face of the dam are very comparable to those seen in stages 6 through 8. Finally, the largest deformations are consistently observed at the crest and at the top of the face.

Incremental deformations incurred after the addition of stage 9A material would have been accrued between the fall of 2013 and the early summer of 2014. Their magnitude is very comparable to deformations seen in previous stages. This invites the conclusion that the levels of deformation predicted by the fine model in stage 9A are consistent with those observed in the field.

In stage 9B, the fine model does not attain a static equilibrium and deformations accrue indefinitely. Consequently, pre-failure incremental deformations are not evaluated this stage, since there is no clear way to distinguish pre-collapse deformations from deformations accrued after the initiation of collapse.

5.4.3 GEOMETRY OF THE FAILURE

The geometry of the failure at the Mount Polley was determined from field investigations of surface and subsurface, and is described in §4.4.3. The geometry of the failure predicted by the fine model in small strain, detailed in §5.4.3.1 to §5.4.3.4, will be compared against this description to evaluate the simulation's goodness of fit.

5.4.3.1. EXTENT AND LOCATION OF THE FAILURE

The predicted width and location of the slide base can be evaluated from the size and location of the plastic yield zone in stage 9B at an advanced point of collapse (8,400 mechanical calculation steps after the addition of stage 9B material) shown in Figure 5.27. In the figure, it can be seen that the plastic yield zone in the Upper GLU, with a width of ~220m, extends from Stn. 4+100 to Stn. 4+320.

Figure 5.27 also shows that in the middle of the plastic yield zone, in an area with a width of ~80m, the plastic shear straining and associated weakening processes are significantly more advanced than anywhere else in the plastic yield zone. In this area, coloured in hues of reds and 50% closer to the edges. In Figure 5.28 showing Upper GLU's cumulative horizontal displacements in the downstream direction at the same point in the simulation, the "red zone" is also identifiable

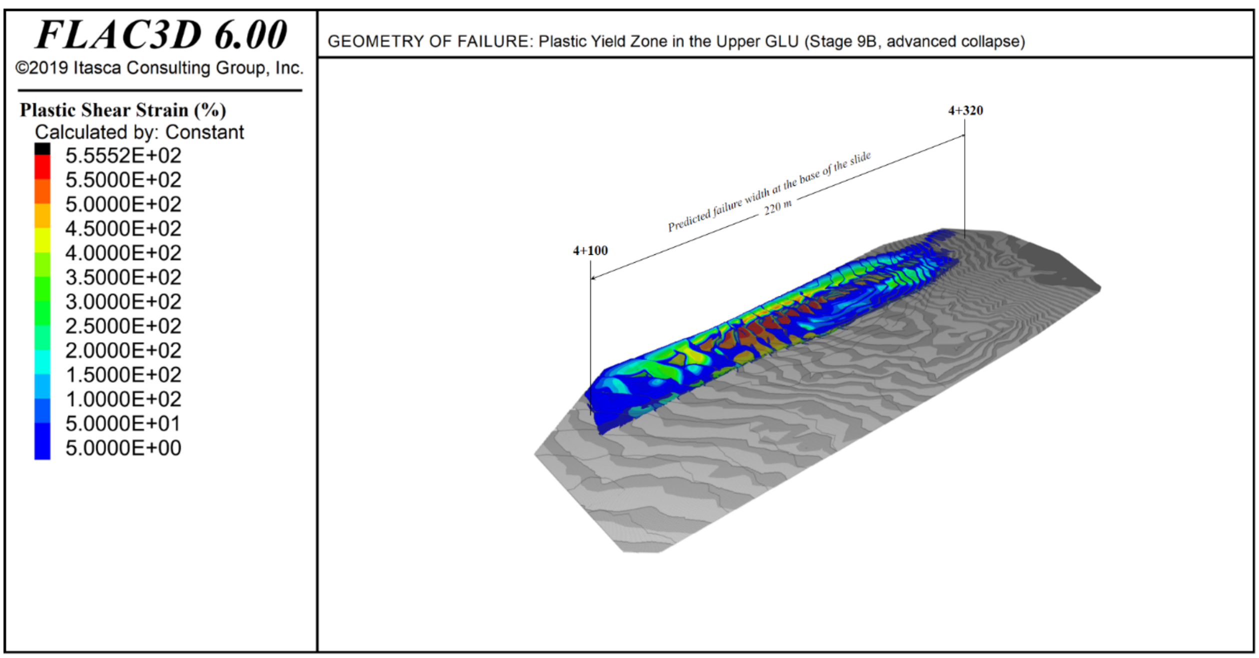

Figure 5.27 Plastic yield zone in the Upper GLU at an advanced point of collapse in stage 9B predicted by the fine model in small strain.

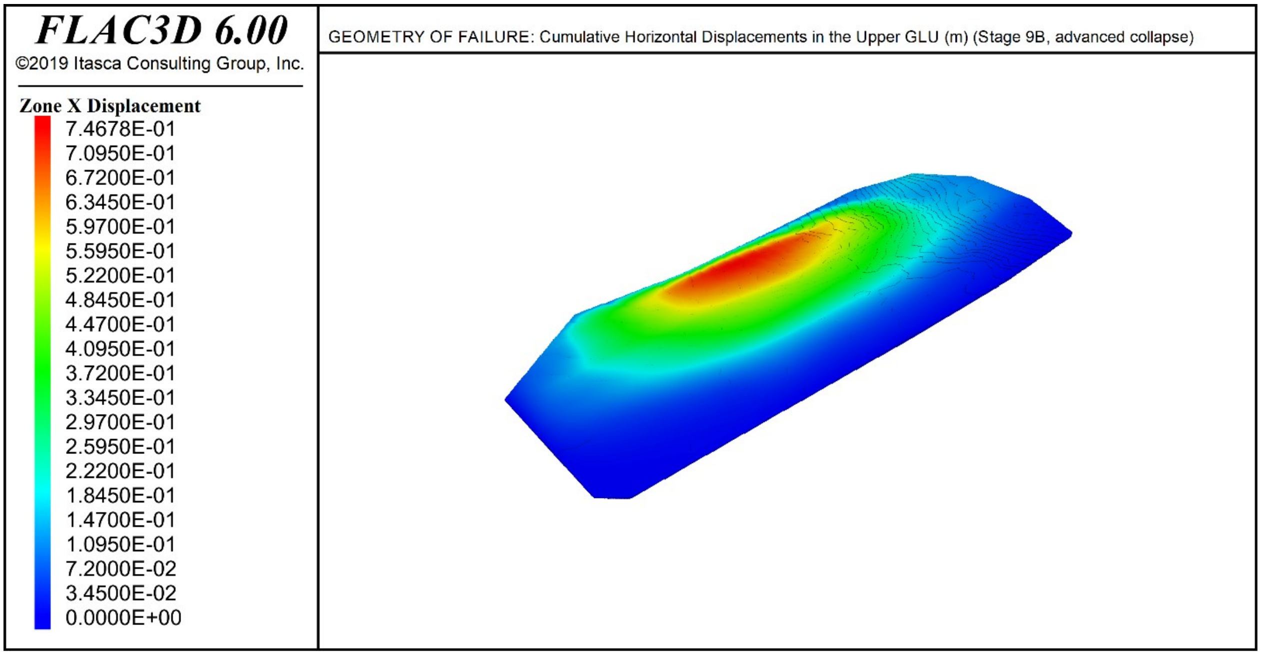

Figure 5.28 Cumulative horizontal displacements in the Upper GLU at an advanced point of collapse in stage 9B predicted by the fine model in small strain.

as the area experiencing substantially larger displacements than the neighbouring regions. Also in the figure the area with a width slightly lower than that of the plastic yield zone is seen to experience substantial shear displacements. The downstream edge of the displacing area is located ~90m away from the dam centreline, roughly at the location where the uplift was observed at ground surface.

The predicted extent and location of the slide in the embankment materials can be appreciated from Figure 5.29 showing incremental horizontal displacements at the same point of collapse. From the figure, the slide is seen to extend over a width of ~170m from Stn. 4+125 to 4+305. Also from the figure it is evident that that the "red zone" seen in Figure 5.27 is situated precisely below the predicted slide location in the embankment materials; this suggests that the movement in the embankment is caused by the large displacements in the "red zone."

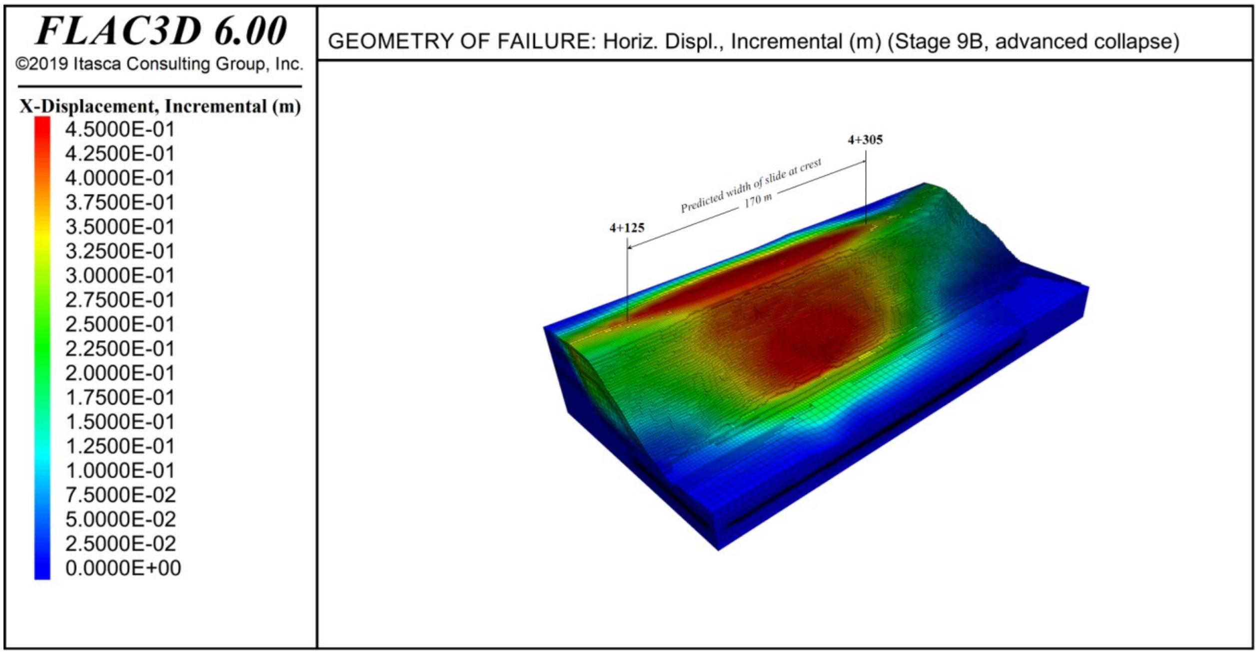

Figure 5.29 Incremental horizontal displacements in embankment at an advanced point of collapse in stage 9B predicted by the fine model in small strain.

A cross-sectional view of the embankment and foundation materials is seen in Figure 5.30 showing incremental horizontal displacements accrued 8400 mechanical calculation steps after the addition of stage 9B material. The figure illustrates the volume of the failing soil mass and the shape of the slip surface at the midpoint of the slide. On the upstream, the slip surface passes through the core and upper till materials to meet the Upper GLU at it upstream edge. In the Upper GLU, the slip surface becomes horizontal, with no significant displacements below it.

The predicted location and width of the base of slide agrees with field observations. The predicted location of slide centre is shifted along the dam centreline by about 20m in the south-east direction relative to the actual location. The predicted width of the slide at the crest and embankment level is much greater than that observed in the field.

Finally, the location and shape of the slip surface predicted by the fine model and pictured in Figure 5.30 is consistent with the location of cracks mapped by the field investigation team in the

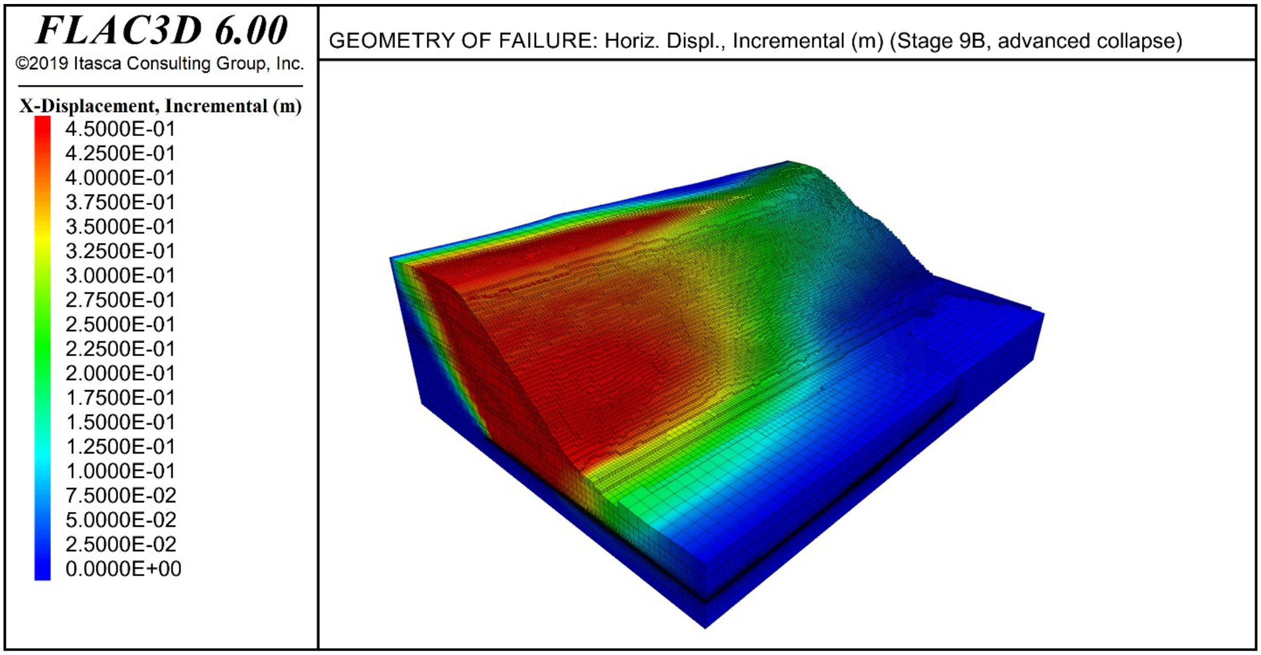

Figure 5.30 A cross-sectional view of the embankment and foundation in stage 9B showing incremental horizontal displacements predicted by the fine model in small strain.

exposed core and surficial tills (Figure 4.30, left) and with the evidence of large horizontal displacements in the Upper GLU but not below it.

Some differences can be noted in the extent and location of the failure predicted in the fine simulation under the small and large calculation schemes. The location of the slide center is better predicted in small strain than in large strain. However, the width of the slide at embankment and crest levels is over-predicted in small strain by nearly 70%, whereas in large strain, it matches field observations.

5.4.3.2. SLIDE CREST

In the advanced stages of collapse simulated by the fine model, a vertical drop is observed in the crest area. Figure 5.31 shows the incremental downward displacements in the embankment surface at the most advanced simulated point of collapse, 8400 mechanical calculation steps after the addition of stage 9B material. From the figure, a vertical drop at crest in the order of

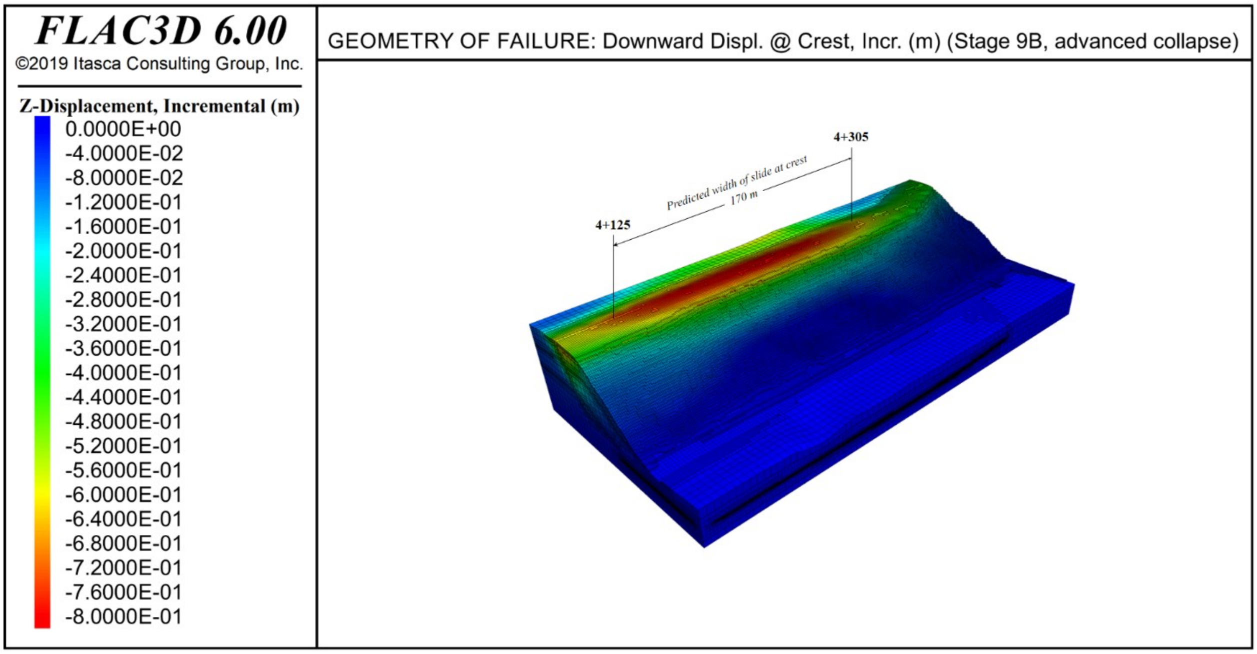

Figure 5.31 Incremental downward displacements in embankment at an advanced point of collapse in stage 9B predicted by the fine model in small strain.

0.8-1.0m can be seen at the exact location of unfolding slide (pictured in Figure 5.29). If downward displacements due to settlement, in the order of 0.25m, are taken into consideration, then ~0.6-0.8m of downward displacements seen at this point are attributable to failure processes.

The predicted downward displacement at crest level is consistent with the findings by the two investigating teams, who independently concluded that a crest drop took place and caused the dam to overtop.

5.4.3.3. SLIDE TOE

In the collapse stages simulated by the fine model, an uplift is noted at the embankment toe. Figure 5.32 shows the incremental upward displacements in the embankment surface at the most advanced simulated point of collapse. From the figure, the surface at the toe of the embankment directly in front of the unfolding slide is seen to uplift. At this point in the simulation, the upward displacements range from 10cm directly at the toe of the slope to 12cm in the middle and

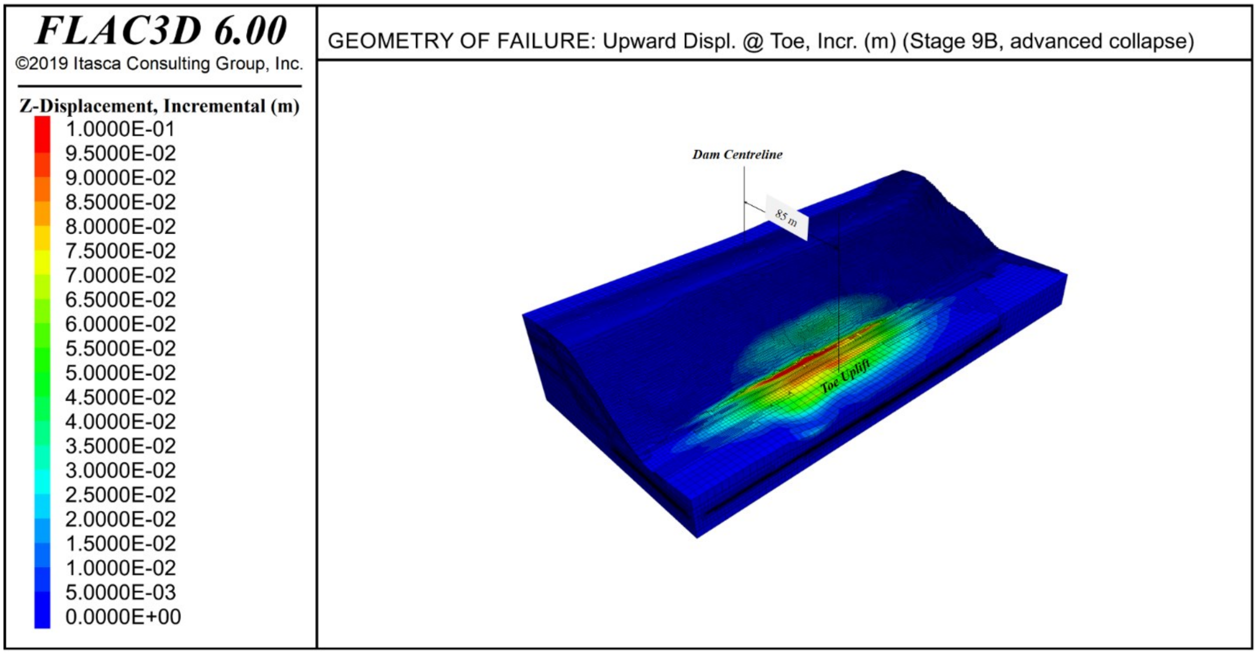

Figure 5.32 Incremental upward displacements at the embankment toe at an advanced point of collapse in stage 9B predicted by the fine model in small strain.

at the downstream edge of the 20m wide excavation, and the uplifted area spans a width of about 200m.

The location and span of the uplifted area at the embankment toe is consistent with the position and length of the "whaleback" features seen in Figure 4.30. The "whaleback" features are located at an estimated 85-95m downstream of the dam centreline, whereas the predicted location of uplift is about 80-85m downstream of the dam centreline.

5.4.3.4. SLIP SURFACE

The aspect of slip surface at the most advanced point of collapse that was simulated in small strain can be appreciated from Figure 5.33 plotting the zones exhibiting maximum shear straining rates in excess of $2*10^{-6}$ and rendering the rest of the domain as a semi-transparent wire mesh.

At this point of collapse, the slip surface is seen to have propagated widely in the Upper GLU, covering an area that generally corresponds to the actual location, shape and dimensions of the failure at foundation level shown in Figure 4.30. In the embankment, the slip surface has a width that is greater than the one seen at the base of the slide and has reached the domain boundary on one end. The upstream portion of the slip surface travels through the upper till and core materials but is not seen to extend into the shell area. The width of the slide on the embankment level is two to three times greater than that observed in the field. On the downstream, the slip surface is well-defined in the region of the slide toe corresponding to the location of uplift documented in situ.

The slip surface predicted in small strain is significantly wider than that predicted in large strain as well as that seen in the field. Overall, the geometry of the slide predicted in small strain has the main characteristics of the slip surface reconstructed from field observations, including the rotational-translational movement characterized by a drop at the crest, large shear displacements

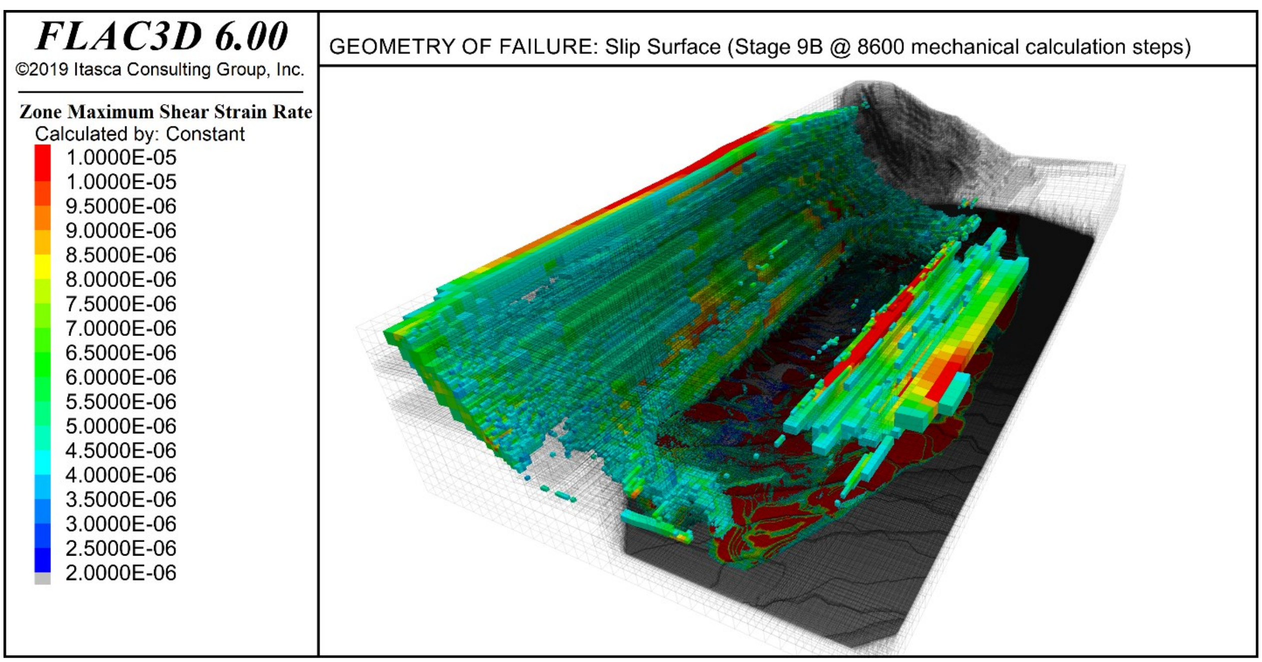

Figure 5.33 A view of the slip surface at the Mount Polley TSF, identified as the zones with high shear strain rates 8600 mechanical calculation steps after the addition of stage 9B material.

in the foundation and an uplift at the toe. The slide geometry is predicted considerably better in large strain than it is in small strain.

5.5. SUMMARY OF FINDINGS

The main findings made on the basis of the analyses conducted in small strain are listed below.

(1) *The fine simulation in small strain adequately models field conditions and can be used to evaluate the failure events.* The deformation analysis of Mount Polley exhibits significant scale effects. The results suggest that the coarse and intermediate analyses are in substantial error and do not adequately replicate field conditions.

(2) *In the simulation, the total and effective stresses in the embankment and foundation materials increase steadily over the duration of construction works.* The largest stress increases are observed under the core and, to a lesser extent, under the shell. By stage 9B, the pre-failure effective stresses in the Upper GLU near 1 MPa in the region under the core.

(3) *In the fine model, parts of the Upper GLU become normally consolidated around construction stage 5; prior to collapse, the normally consolidated portion of the unit continued expanding until it encompasses one quarter to one third of the unit by area.* The transition of this material to a state of normal consolidation marks the point of change in failure modes from drained to undrained, opening up the potential for strain-weakening.

(4) *In the fine model, a loss of shear resistance to strain-weakening takes place in portions of the Upper GLU starting in stage 7.* In stages 7 through 9A, the loss of shear strength is negligible. The strain-weakening processes become uncontained in stage 9B.

(5) *The Upper GLU strains non-linearly.* The fine simulation predicts the development of a shear band with the thickness of a single zone (i.e. 12.5cm). This zone strains more severely than the Upper GLU above or below it, weakening in the process. The soil outside the shear band does not accrue plastic shear strains to any appreciable degree and retains peak undrained strengths.

(6) *Pre-collapse levels of deformation predicted by the fine model are negligible.* Deformations associated with plastic yielding in the foundation were minor, as it would be expected based on field observations.

(7) *In stage 9B, collapse is generated in the fine model under undrained conditions.*

(8) *The predicted geometry of the failure matches some of the main characteristics of the slide documented in the field.* The predicted width at embankment levels is substantially greater than that seen in situ.

(9) *The model response is strongly mesh-dependent.* In the simulation of Mount Polley, models with a higher discretization level:

- Predict slightly greater overburden effective and total stresses in the Upper GLU. This in turn results in an earlier transition to a state of normal consolidation in portions of this stratum;
- Predict a higher rate of accummulation of shear plastic strain and an earlier onset of strain-weakening processes;
- Simulate the onset of failure at lower embankment loads (i.e. at an earlier construction stage); and
- Predict marginally greater shear displacements in the foundation under equivalent loading conditions (with the exception of stage 9B where, in the fine simulation, deformations accrue indefinitely).

The fine model produces adequate predictions under the small strain calculation scheme, triggering the onset of collapse at the correct point in the simulation and generally producing predictions that agree both with field observations and with the results obtained in large strain. The geometry of the failure appears to be the only prediction aspect not handled well in this mode.

CHAPTER SIX

DISCUSSION AND CONCLUSIONS

6.1. THE PROGRESSION OF FAILURE AT THE MOUNT POLLEY TSF

In this section, all findings accumulated over the course of this research undertaking are integrated to reconstruct the sequence of events that had led to the catastrophic collapse of embankment at the Mount Polley TSF. The section is organized to chronicle the course of this failure, beginning with the early stages and up to the collapse. This is accomplished by first reconstructing the full sequence of failure from the simulation data (in §6.1.1 to §6.1.4) and then interpreting it in terms of in-situ processes (in §6.1.5).

6.1.1 CHANGE OF SHEAR STRENGTH IN THE UPPER GLU FROM DRAINED TO UNDRAINED

The Upper GLU was identified by both IRP (2015) and KCB (2015) as having played a critical role in the failure of the Mount Polley TSF embankment. This material, shaped as an elongated pancake with a thickness varying from 2m at the centre to ~0m near the edges, was initially lightly overconsolidated, having been previously subjected to vertical consolidation pressures of in the range of 400-500kPa. Prior to the commencement of embankment construction works, this material, located approximately 10m below the surface, was subjected to vertical effective stresses of ~100kPa. The addition of embankment materials increased total stresses exerted on parts of this unit located directly under the dam shell and core portions, triggering consolidation processes that led to an increase in effective stresses.

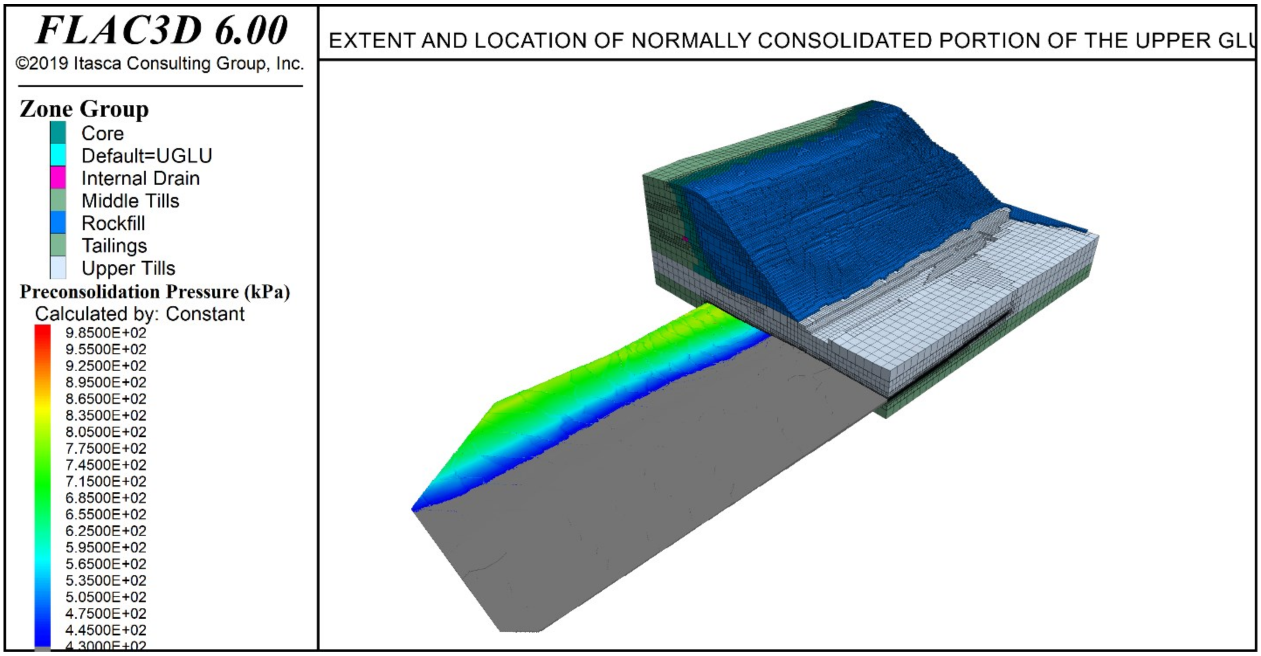

Figure 6.1 The size and position of the normally consolidated portion of the Upper GLU relative to the embankment before collapse.

Eventually, the preconsolidation pressures were exceeded in the portions of the Upper GLU located under the embankment, causing some of this material to become normally consolidated. This process took place gradually, with small portions of the Upper GLU transitioning as early as construction stage 4. By the time of failure, a quarter to a third of the Upper GLU by surface was normally consolidated, with vertical consolidation pressures as high as 1MPa. The pre-failure size and position of the normally consolidated portion of the Upper GLU relative to the embankment immediately prior to failure is seen in Figure 6.1. The figure shows that immediately before the collapse, the normally consolidated portion of the Upper GLU extended under the core and most of the shell. Under the toe of the slope and the region of excavation at the base of embankment, the unit remained overconsolidated.

The normally consolidated portions of the Upper GLU became contractive on shearing and thus susceptible to undrained failure. This change opened up the potential for the progressive failure of this strain-weakening material.

6.1.2 EMERGENCE OF PROGRESSIVE YIELD ZONE

The Upper GLU was a slightly sensitive, strain-weakening material capable of losing up to 50-70% of its undrained peak strength. The transition of portions of the Upper GLU to a state of normal consolidation made them susceptible not only to undrained failure, but also to a loss of strength to sensitivity. However, such potential would only be realized on sufficient disturbance. At Mount Polley, such disturbance in the Upper GLU was induced by loading-driven plastic deformations.

The Upper GLU's location relative to the embankment was particularly unfavourable, with its upstream portion located directly under the core where some of the largest increases in total and effective overburden stresses were noted. This was also the critical region where the rotation of the stress tensor is known to take place under a slope, leading to a repositioning of the plane of critical

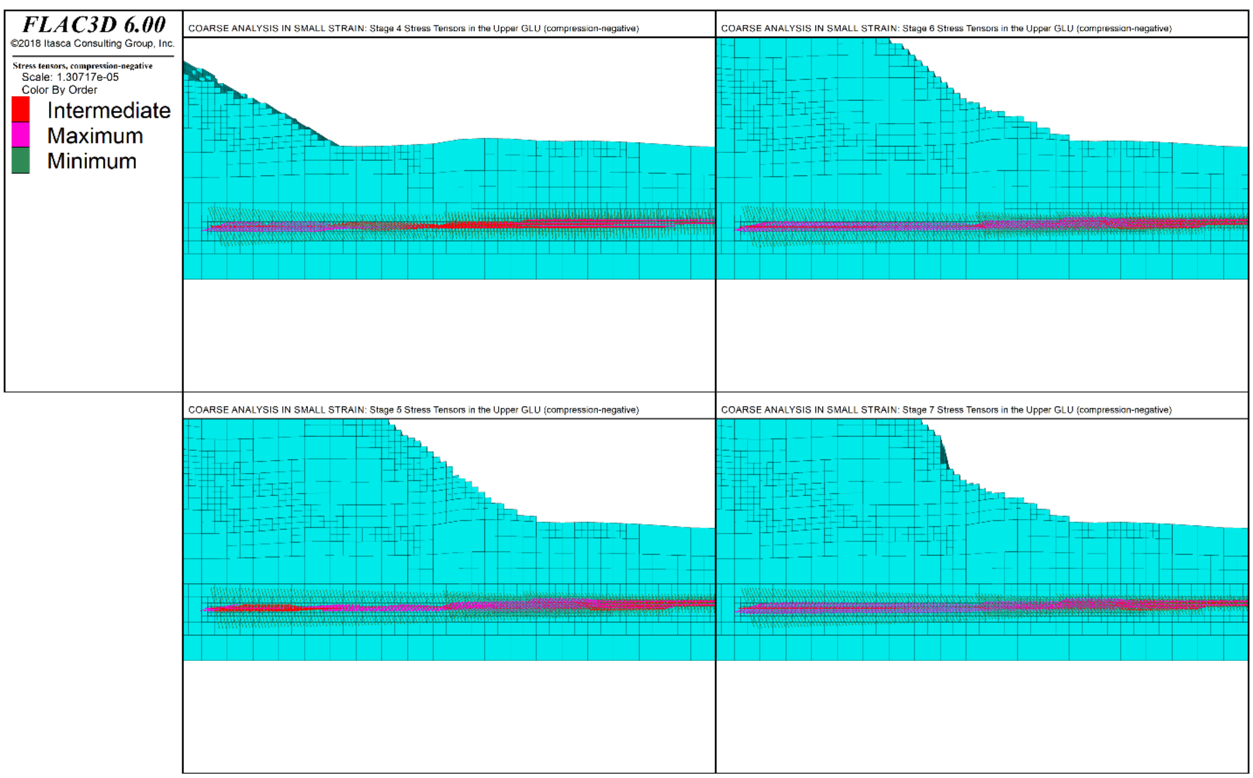

Figure 6.2 The orientation of the stress tensor in the Upper GLU during the early stages of construction prior to the emergence of yield zone.

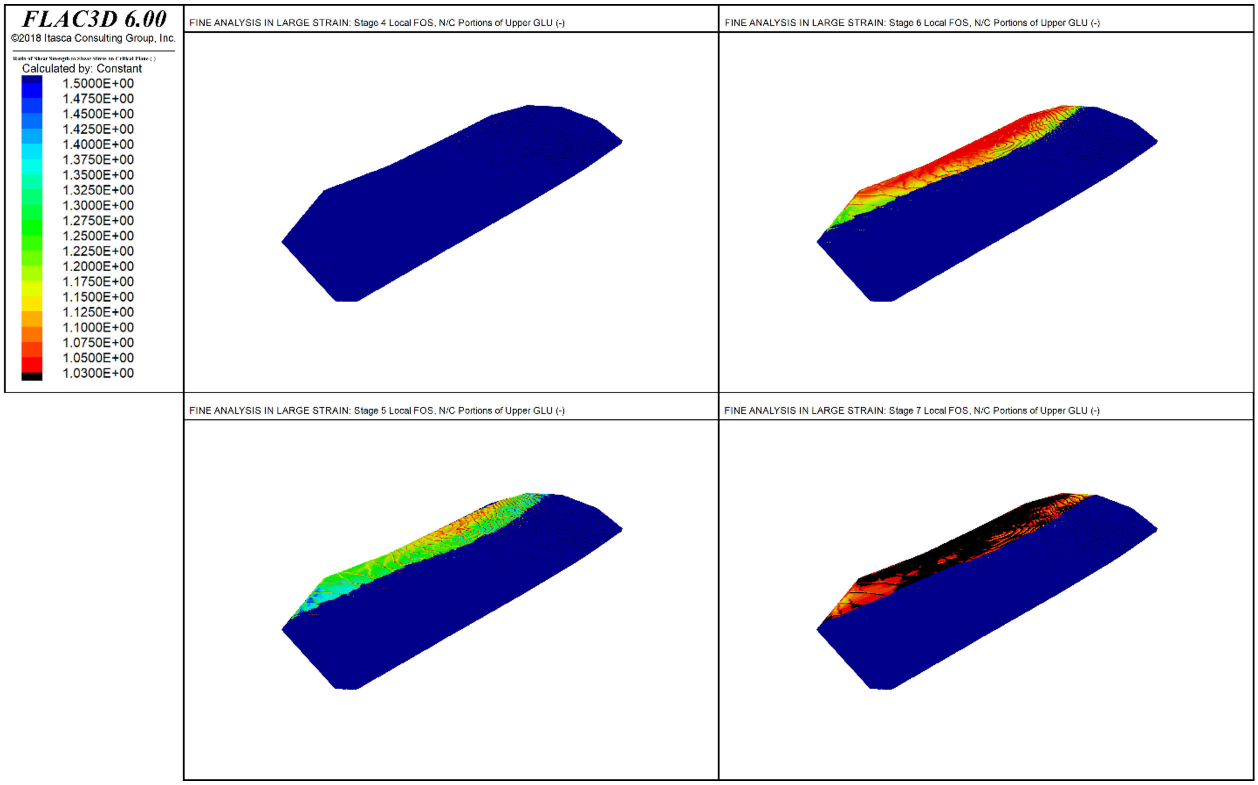

Figure 6.3 Ratio of shear strength to mobilized shear stress on critical plane in the normally consolidated portion of Upper GLU. In black: Upper GLU areas where the ratios are approaching unity.

stress closer to horizontal. With the addition of embankment materials, such gradual rotation of the stress tensor took place in the foundation at Mount Polley (illustrated in Figure 6.2). The gradual increase in shear stresses under new embankment loads combined with a drop in shear strength from drained to peak undrained in the normally consolidated portions of the Upper GLU eventually caused large sections of the unit to reach yield. By construction stage 6 or 7, a substantial fraction of the normally consolidated Upper GLU material exhibited local safety factors of unity, meaning that the mobilized shearing resistance was maximized (Figure 6.3, bottom right).

The confluence of these processes promoted a gradual accumulation of plastic shear strains in the normally consolidated portion of the Upper GLU. These strains were accruing principally in the horizontal plane in the upstream-to-downstream direction. The deformation analyses in Chapters Four and Five suggest that as early as 2011, some limited sections of the Upper GLU had accumulated sufficient levels of plastic strain to begin weakening, marking the beginning of a progressive failure in the foundation.

6.1.3 CONTAINED PROGRESSIVE FAILURE

The progressive failure of the foundation at the Mount Polley TSF initiated sometime during or after the completion of construction stage 7 in 2011. Until the summer of 2014, the failure processes were largely confined to the Upper GLU, with only minor deformation responses elsewhere in the soil mass.

In this period, four processes associated with or relevant to the unfolding of the progressive failure have been identified. In the plastic yield zone, a progressive reduction of shear resistance to strain-weakening in Upper GLU's plastic yield zone in response to new loading was ongoing. Associated with this weakening process was a compensatory transfer of stresses onto the neighbouring soils. The normally consolidated portion of the Upper GLU that was not a part of the plastic yield zone continued accumulating plastic shear strains, edging towards the threshold of strain-weakening; over time, a growing number of areas under the core reached this point and began strain-weakening as well, exacerbating the first two processes. Finally, closer to collapse, the Upper GLU material at the downstream edge of the normally consolidated zone that had newly transitioned to a state of normal consolidation experienced a drop in shear strength from drained to peak undrained and, at its operational stress levels would immediately reach yield and see a downward readjustment of stress states; this drop in shear resistance was another source of stress transfer onto the downstream area.

The processes outlined above associated with the progressive failure in the foundation were negligible until the placement of stage 9A loads in 2013, when they became more pronounced and had a measurable impact on the response in the soil mass. The predicted area of the plastic yield

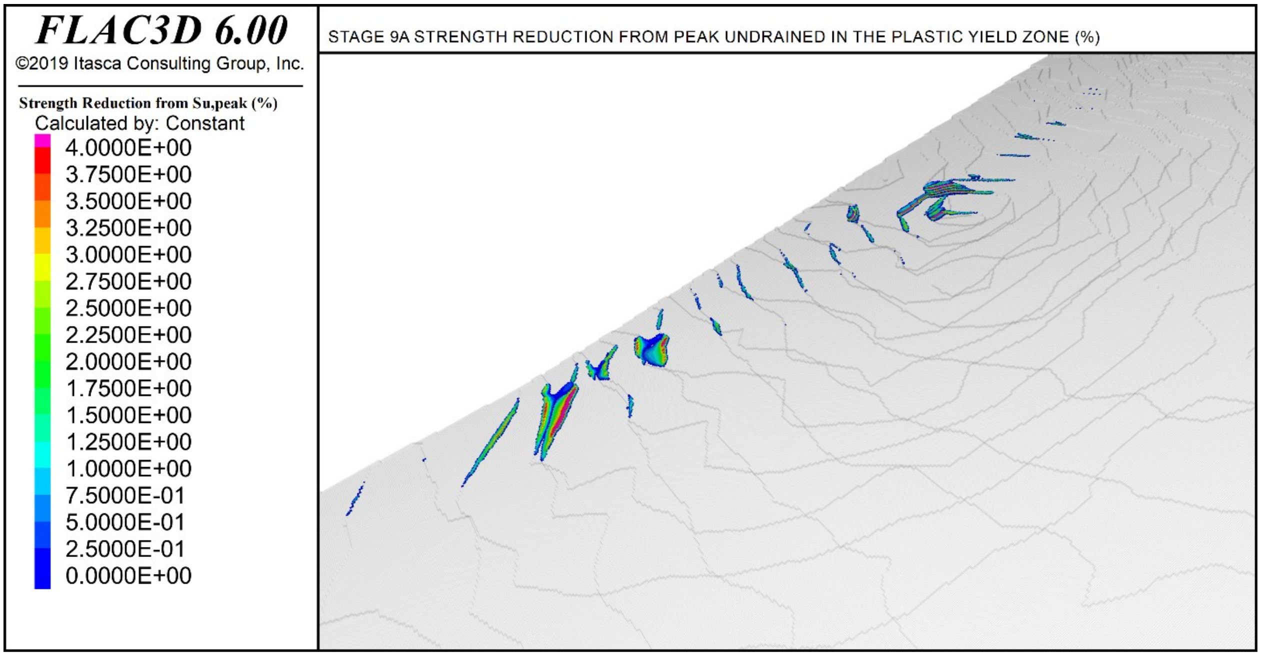

Figure 6.4 Predicted percent reduction of shear strength from the undrained peak value in the plastic yield zone of the Upper GLU in stage 9A.

zone and the extent of weakening was trivial in stages 7 and 8, as seen in Figure 4.19 (left column) and discussed in §4.2.2.2. The areal extent and degree of weakening after the completion of stage 9A works can be fully appreciated from Figure 6.4 which shows the plot of percent reduction in shearing resistance from peak undrained; the data in the figure indicate weakening of up to 8%, with an average of 1-1.5%. The impact of such strength reduction on the overall soil mass would have been largely immaterial. Likewise, the rate of accumulation of plastic shear strains in 2011-2013 (i.e. in stages 7 through 9A) was negligible, as evidenced by plots in Figure 4.16 and Figure 6.5. The latter shows the areas in the Upper GLU that have accumulated at least 0.3% of plastic shear strain. From these plots, the areal growth in time of the zone where plastic shear strains were accumulating can be appreciated; it is evident that by the time the soil had adjusted to stage 9A loads, the plastic shear strains in a substantial portion of the Upper GLU were close to the threshold of strain-weakening. Lastly, the coupled effect of a loss of shearing resistance in the material newly transitioning to a state of normal consolidation, and the associated stress transfer onto the

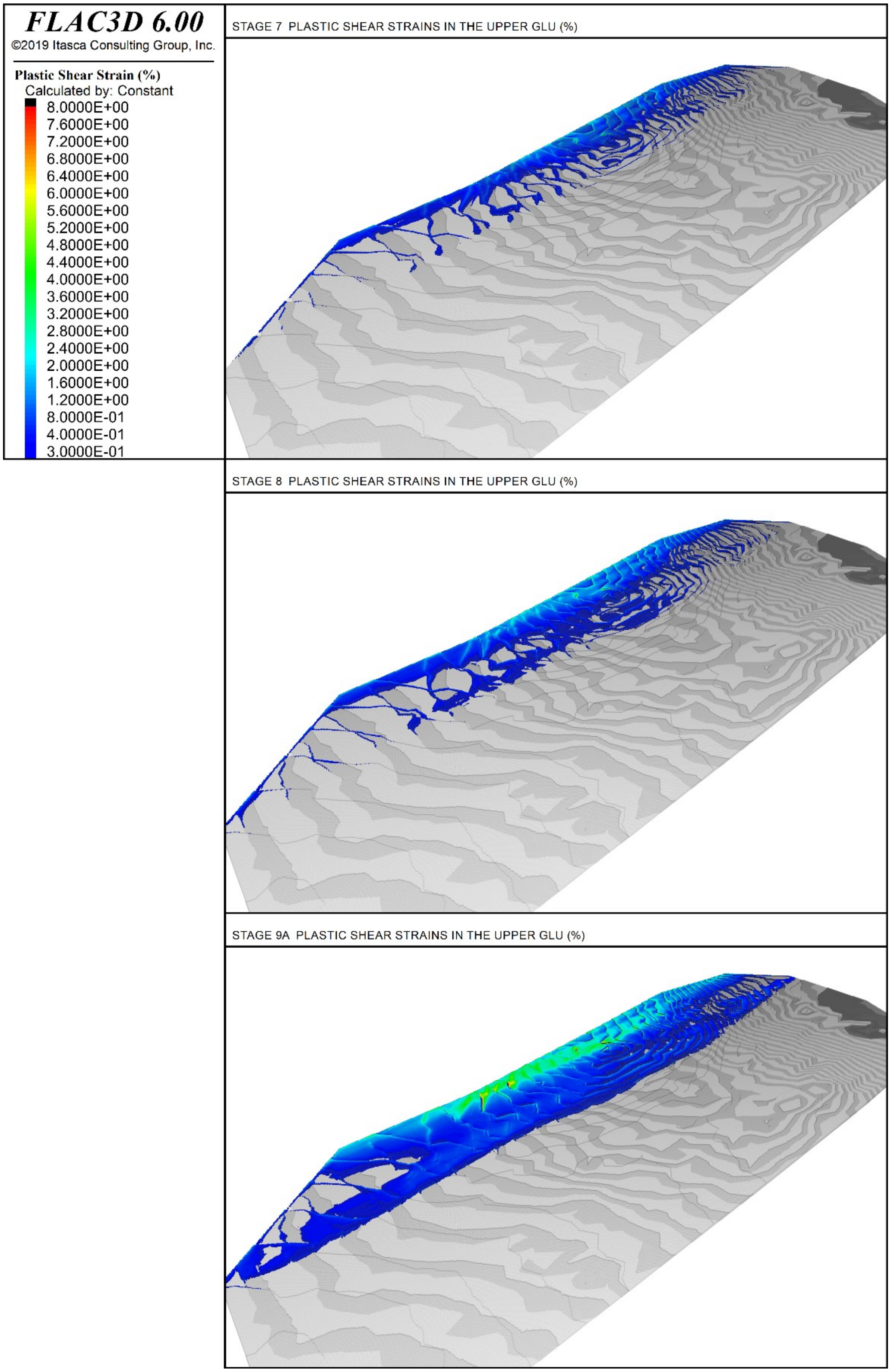

Figure 6.5 The evolution of plastic shear strains in the normally consolidated portion of the Upper GLU in stages 7 through 9A.

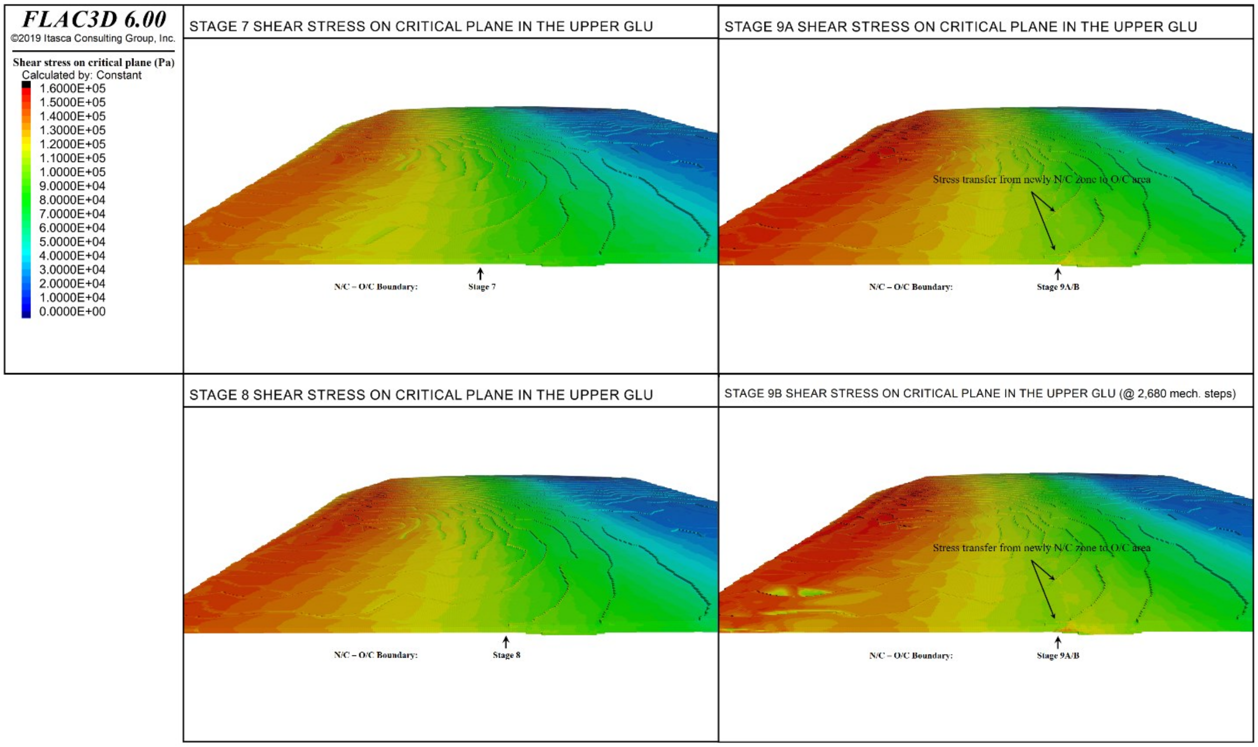

Figure 6.6 Predicted shear stresses along the critical plane in the Upper GLU.

downstream soils was not detected until stage 9A. Figure 4.7 showing the plots of shear stresses τ_{cr} and τ_{xz} illustrates the process of stress transfer from the normally consolidated area onto the overconsolidated area in stages 9A and 9B. This process was more pronounced at the base of the unit; this can be appreciated from Figure 6.6 (right column) and is consistent with the location where the shear band was known to propagate. The plots in the left column of the figure also show that this process was not taking place at an earlier stage.

The four processes related to the progressive failure in the foundation between construction 7 and 9A had a nearly imperceptible effect on the immediate stability of the structure. So why do they matter?

The reason why the progressive failure remained contained for three years after its initiation around 2011 was that there was a reserve of shear strength available in the soil mass around those Upper GLU areas that were seeing a drop in their shear resistance levels. Such reserve of not yet mobilized

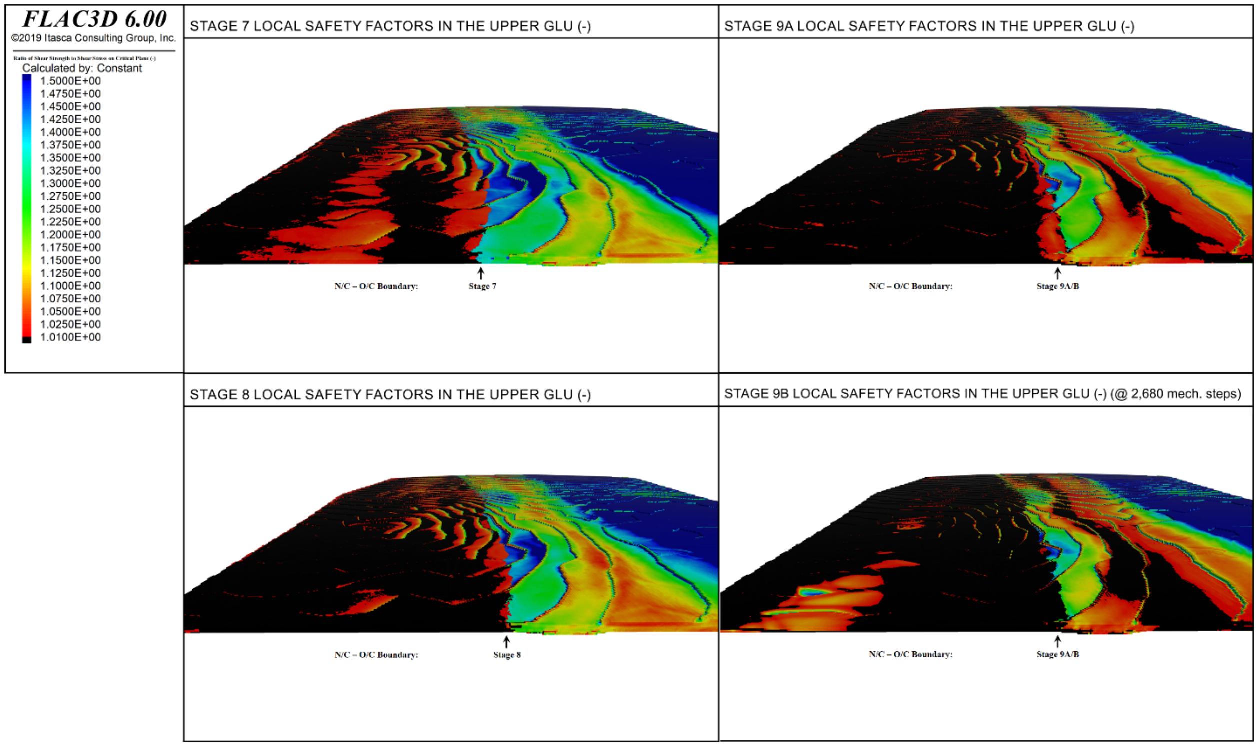

Figure 6.7 Local safety factors in the Upper GLU.

resistance meant that the surrounding soils could accommodate the ongoing stress transfers from the weakening areas. However, the processes described above tapped into this reserve, gradually depleting it.

The depletion of "unused shear strengths" in the Upper GLU can be visualized using the plots of local safety factors. In Figure 6.7, the local ratios of shear strength to mobilized shear stress are plotted in the normally consolidated and overconsolidated portions of the Upper GLU. The figure illustrates the gradual depletion of reserve strength in the overconsolidated portion of the Upper GLU immediately downstream of the leading edge of the normally consolidated area, seen as a drop in local safety factors from 1.2-1.5 in stage 7 to 1.0-1.2 after the adjustment to stage 9A loads. This depletion of not yet mobilized strengths is far more pronounced at the base of the unit where some of the overconsolidated material located immediately downstream of the emerging shear band is seen to reach local safety factors of unity in stage 9A.

In a parallel process, a substantial area of the normally consolidated portion of the Upper GLU eventually accrued sufficient plastic shear strains to bring it relatively close to the precipice of strain-weakening. This critical area is seen in Figure 6.5, bottom, in hues of green. At that point, a minor perturbation became sufficient to trigger strain-weakening processes over a large area.

Finally, the increase of shear strains and shear displacements in the Upper GLU placed the upper till above this stratum into some extension. The upper till was observed to be travelling on top of the Upper GLU in the area of the plastic yield zone but not upstream of it. By stage 9A, this unit was shown to extend, especially in the area of the "red zone," by ~0.1 m. This process is illustrated in Figure 6.8 showing the evolution of cumulative horizontal displacements in the foundation and embankment materials in a cross-sectional view through the middle of the slide. The figure focuses of two points, A and B, situated in the upper till; point A is located directly above the upstream edge of the Upper GLU and falls in the region of the unfolding slide, and point B is located

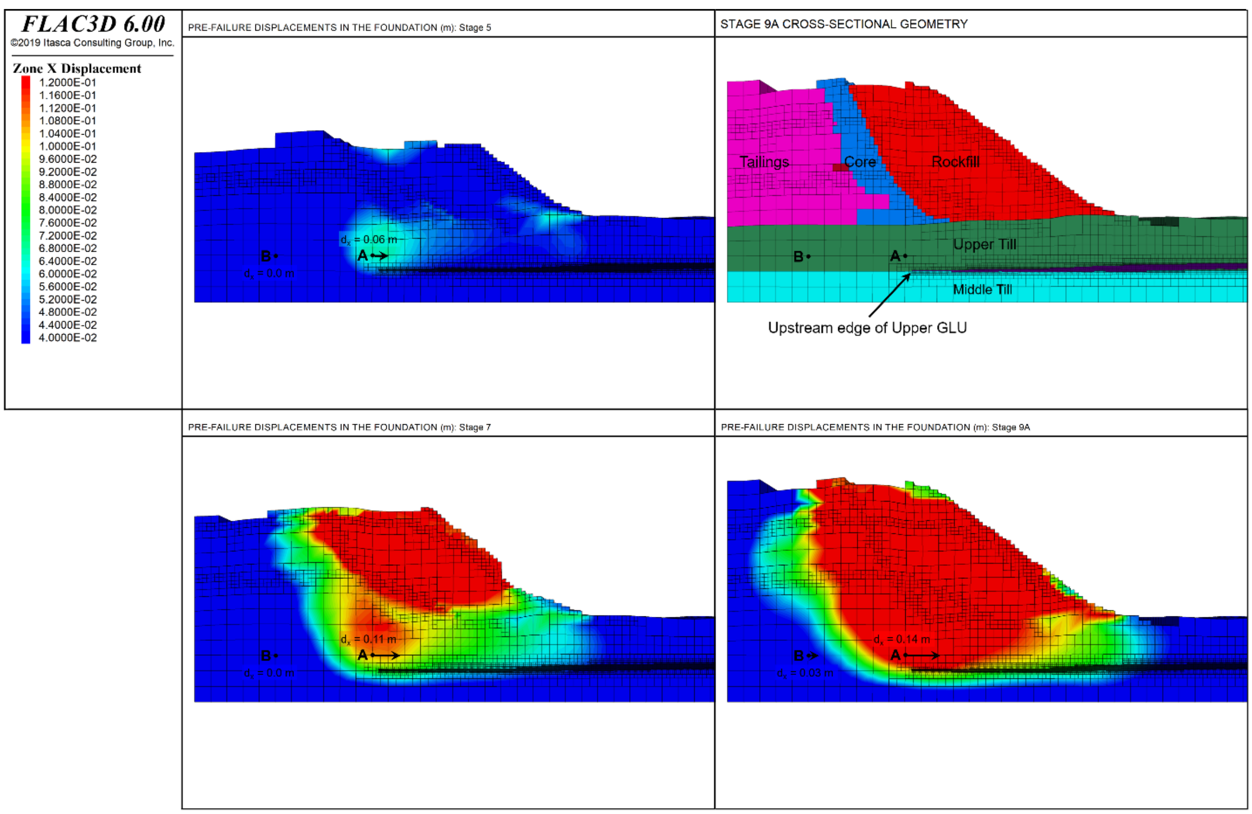

Figure 6.8 The evolution of cumulative horizontal displacements in the foundation and embankment materials, stages 5 to 9A.

immediately upstream of the unfolding slide. The figure shows that at point A, shear displacements in the downstream direction grew from ~6cm in stage 5 to ~14cm in stage 9A, while at point B, the shear displacements over the same period grew from 0 to 3cm. These data indicate that in order to accommodate the Upper GLU's growing shear displacements associated with accumulating shear strains around the plastic yield zone, the upper till strained in extension.

The materialization in stage 9A of a large zone that was close to the precipice of strain-weakening, combined with the depletion of shear strength reserves in the surrounding materials, as well as the growing extension strains in the upper till, created the pre-conditions for collapse. Therefore, while the progressive failure processes documented in this section did not have dramatic immediate consequences, they were essential to the unfolding of collapse.

6.1.3.1. CRITICAL AREA

The critical area in the Upper GLU can be visualized, with some difficulty, in Figure 6.5 (bottom plot). As it is the case with the plastic yield zone (and for the same reasons) the critical area tends to develop closer to the base of the Upper GLU stratum and is therefore partially concealed in this view by overlying soils.

A better view of this area is shown in Figure 6.9 (left) plotting in full colour the Upper GLU zones that have accumulated plastic shear strains in excess of 3.8%, with the rest of the stratum rendered

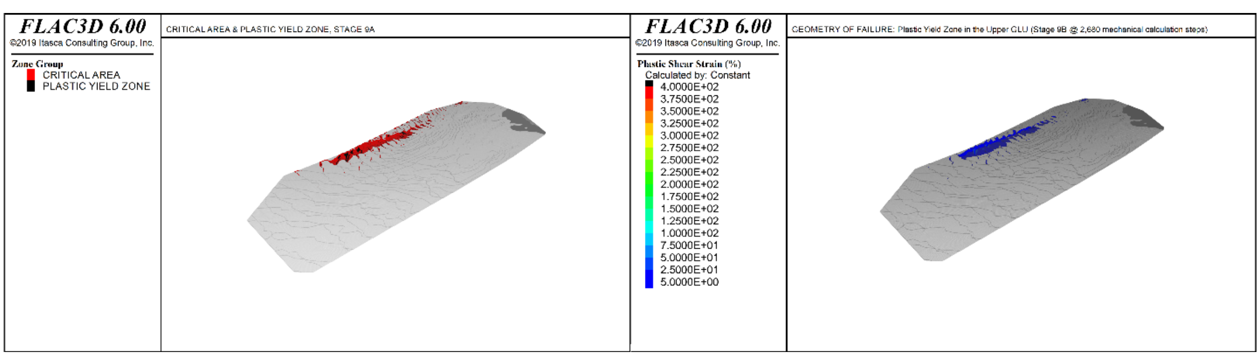

Figure 6.9 Left: areal distribution of the critical area after the completion of stage 9A. Right: the areal distribution of the plastic yield zone shortly prior to second phase of collapse.

with a wire mesh. From the figure, the critical area is seen to have developed around the plastic yield zone, extending over a width of ~200m. The significance of the shape of this zone (i.e. its spatial distribution) will be clarified in the next section.

6.1.4 COLLAPSE

On 4 August 2014, a section of embankment at the Mount Polley TSF with a length of about 100m experienced a sudden and catastrophic failure. The failure was brittle and with no observed precursors; in fact, a truck drove on the dam crest at the failure location within an hour of the collapse. In the preceding weeks, construction stage 9B had been underway, where the shell and core were built up from elevations of 966 mASL and 967.5mASL to final elevations at failure of ~970mASL. As the bulk of the embankment material at the failure location was added shortly prior to collapse, it is reasoned that the new material was supported under undrained conditions, i.e. no significant consolidation processes and associated gain in strength had taken place in the foundation as a result of new loads.

To reconstruct the unfolding of the collapse sequence, the simulated mechanical response of the soils involved in the failure was examined as a whole. On the basis of findings in §4.5 and §6.1.3, as well as upon the close examination of model states during collapse, a determination was made that it unfolded in two distinct phases. In phase one, an upsurge in the rate of loss of shear resistance to strain-weakening took place in the foundation. In phase two, multiple local failures in the upstream zone, followed by a sustained drop in shear resistance levels in those areas resulted in a global collapse.

These phases are distinct in that even though the progressive failure was advancing rapidly in the foundation from the start of stage 9B, an overall acceleration of the soil mass was not seen until the soil units on the upstream of the slide failed as well.

6.1.4.1. THE UPSURGE IN THE RATE OF LOSS OF SHEAR RESISTANCE TO STRAIN-WEAKENING

After the completion of stage 9A, a large portion of the Upper GLU came close to the onset of strain-weakening. As a result of the application of stage 9B loads and associated processes, this area soon began weakening en masse, surging the rate of loss of shear resistance in the foundation. In the simulation of the collapse phase, this process took place approximately between 0 and 2700-3000 mechanical calculation steps after the application of stage 9B loads and unfolded as follows.

Shortly after the start of construction stage 9B, the addition of new loads prompted, once again, a deformation response in the embankment and foundation materials. In the foundation, several processes related to progressive failure were activated in parallel.

- In the Upper GLU's plastic yield zone, weakening processes were triggered once more, causing a reduction of shear strength and an associated stress transfer onto the adjacent areas.
- The critical area in the Upper GLU that had emerged at the end of stage 9A responded to both the change in loading conditions and the stress transfer from the plastic yield zone by straining. As a consequence, the plastic shear strains in much of this area reached the threshold value of 5% very quickly, and weakening processes initiated in those parts as well. This process is visualized in Figure 6.9 placing the stage 9A "critical area" side-by-side with the plastic yield zone 2700 steps into the simulation of collapse and in Figure 6.10 (left column) showing the reduction of shear strengths in the foundation during phase one.
- The Upper GLU material located under the embankment but outside the plastic yield and critical zones responded to the increase in loading conditions and the stress transfer from the weakening areas by straining. Recall that this material had its "reserve shear strength" already largely depleted by stage 9A; therefore, plastic shear strains accumulated in it

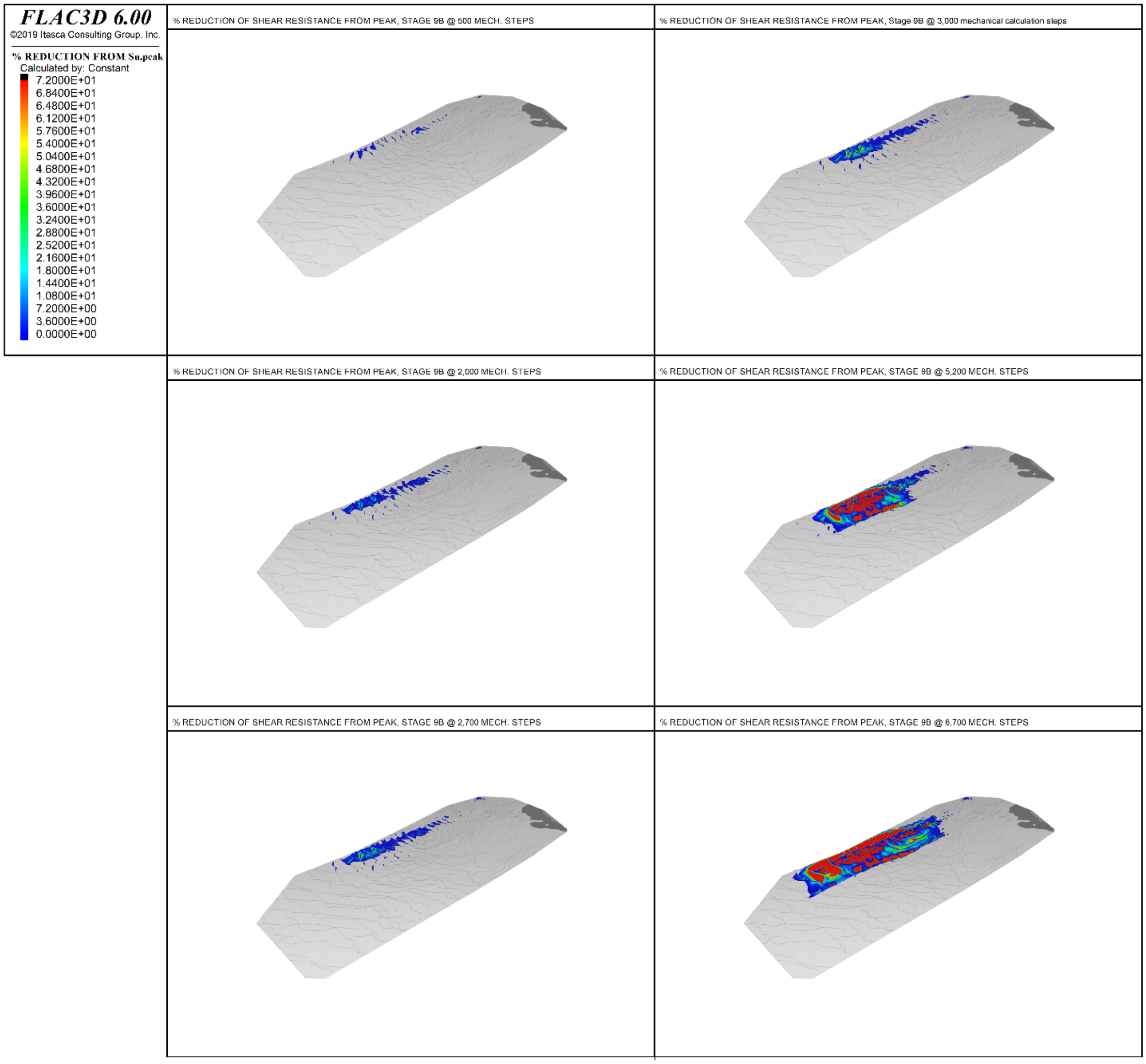

Figure 6.10 The reduction in shear resistance to strain-weakening in the plastic yield zone during collapse.

readily and rapidly. This broadened the area on the precipice of strain-weakening, conditioning a new portion of the unit for progressive failure (this process is clarified in §6.1.4.3).

The processes described here were observed in the simulation of collapse from the moment the load changes applied to the top of embankment propagated into the foundation (at this point in the simulation, this took ~1500 mechanical calculation steps from the placement of new loads) and until the endpoint of the simulation. These failure processes were inter-related and tended to fuel one another, creating a "feedback loop" of sorts, escalating as the simulation progressed. The loss of resistance in the weakening areas resulted in stress transfers, which in turn triggered straining in the surrounding areas, which in turn triggered more stress transfers and also allowed the already weakening areas to strain more readily, weakening more. At 3000 steps into the simulation of collapse, the aggregate rate of loss of shear resistance in the foundation became substantial, as it can be appreciated from Figure 6.10 by comparing the plots of percent shear strength reduction in the foundation at 3000 steps and at 5200 steps. The surge in the rate of loss of shearing resistance in the Upper GLU was one reason for the initiation of global collapse.

This section so far has been focused on the loss of shearing resistance in the foundation. Additionally, we shall examine (a) the shear deformations associated with this process and (b) the model convergence over this period.

At the end of stage 9A, cumulative shear displacements on the upstream edge of the Upper GLU were in the range of 10-12cm (Figure 4.42, top left). By the time the stage 9A critical area began weakening altogether, these displacements increased, but not significantly, reaching 14-18cm at the centre of the plastic yield zone (Figure 4.42, bottom left). After that, the rate of accumulation of plastic shear strains was seen to rise steeply, especially at the centre of the plastic yield zone. So, the shear displacements increased from 14-18cm at 2700 steps to >35cm at 5200 steps into the simulation of collapse. This process is visualized in Figure 6.11 and Figure 6.12.

The rapid accumulation of shear displacements was observed in step with the upsurge of weakening processes in the foundation; this is unsurprising as the two are related. However, these changes were precipitated by another process that materialized just before this upsurge: shortly before 2700 steps into the simulation, local failures began developing in the upper till material above the Upper GLU's upstream edge. At this point, the slip surface that was previously confined to the Upper GLU propagated into the upper till; this can be seen from Figure 4.39 (left column) showing the evolution of slip surface during phase one of collapse. In the next section, we will further explore the relationship between the local failures in the upper till and the upsurge in the rate of shearing and weakening in the Upper GLU. For now, it suffices to state that these interrelated processes triggered global collapse.

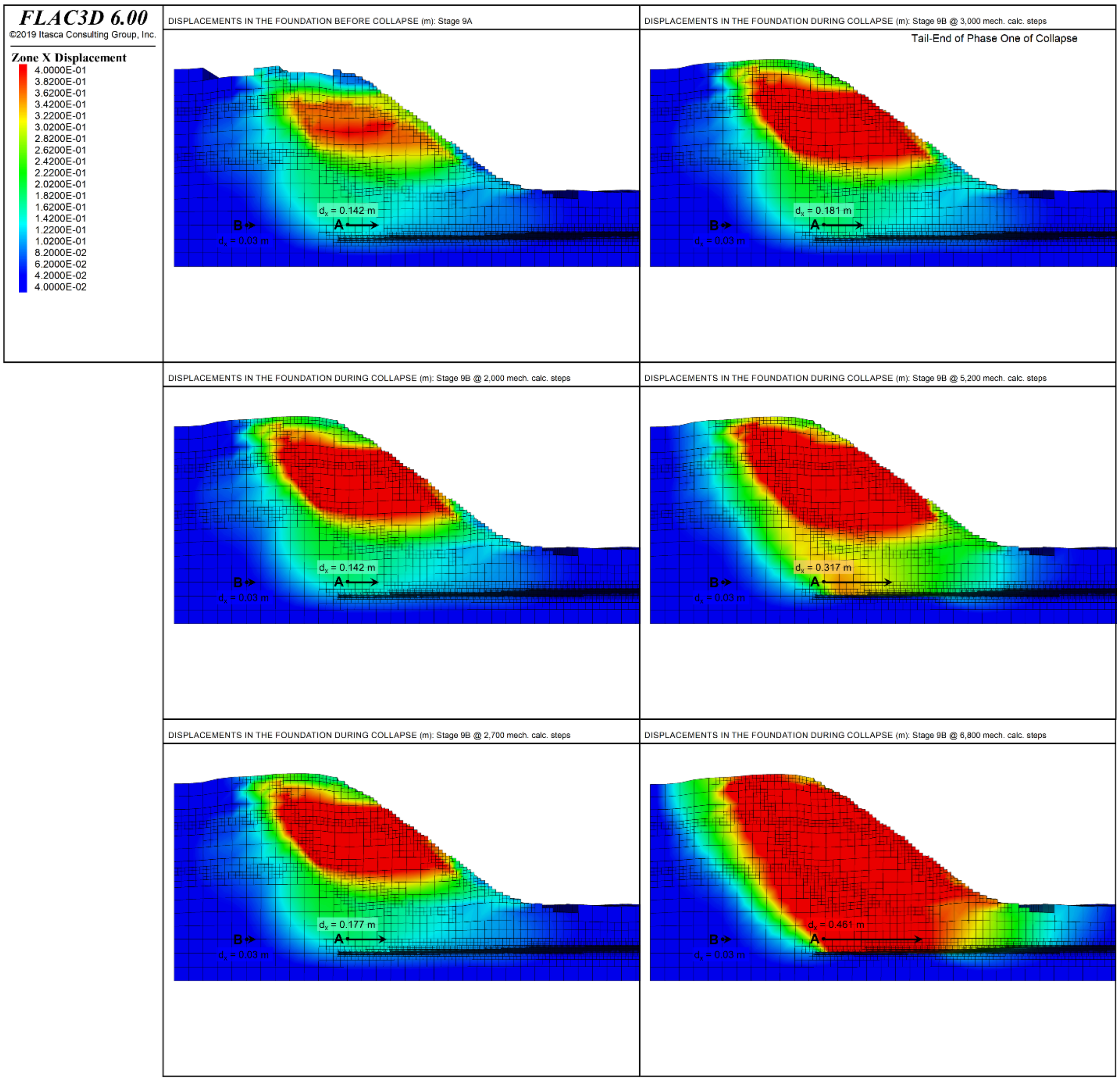

Figure 6.11 Evolution of shear displacements in the downstream direction during collapse. Point A: in the upper till material in the failure zone, the displacements increase from 14 to 18cm in phase one of collapse, and from 18 to 46cm in phase two. Point B: in the upper till material upstream of the slide, no shear displacements are observed.

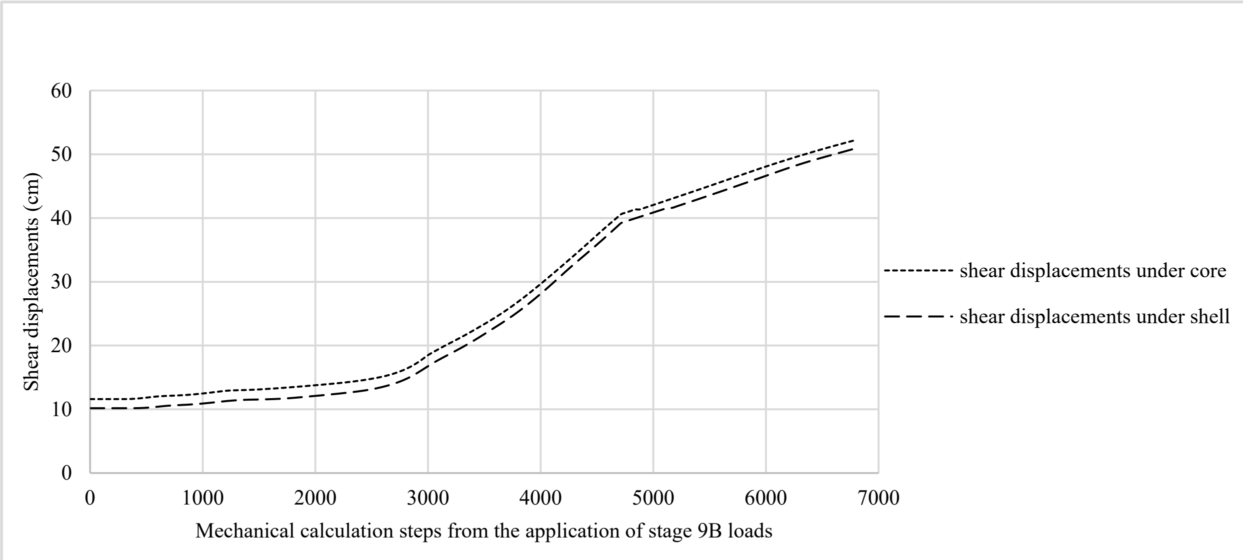

Figure 6.12 Plots of shear displacements in the downstream direction recorded during collapse in the upper till material located in the middle of the slide under core and shell regions.

Finally, the examination of model convergence over the duration of collapse offers clues about the overall behaviour of the soil mass. During phase one, the model appears to converge (as evidenced by a steady decrease of the average force ratios seen in Figure 4.24). This observation suggests that over this period, the increasing deformations of the overall structure were mobilizing sufficient amounts of shear resistance in the soil mass to counter the weakening processes in the Upper GLU. To determine whether this was in fact the case, the evolution of stress states in key areas over this period was examined. The simulation results indicate that the upper till and core materials above the Upper GLU's upstream edge, and the rockfill material located in the area of the future slip zone, have all experienced a steady increase in their mobilized shear resistance levels (see Figure 4.43 and Figure 4.45). This increase was pronounced in the core and upper till but modest in the rockfill. However, at or just before 2700 steps into the simulation of collapse, the mobilized shear stresses began decreasing in the area where local failures developed in the upper till.

The unfolding failure processes seen in phase one are complex and interrelated. They are summed up below for clarity.

- After the placement of stage 9B loads, the plastic yield zone in the foundation increased in size significantly, and the rate of loss of shearing resistance to weakening was seen to somewhat increase.
- Associated with the expansion of the plastic yield zone was a modest increase in shear displacements. At the centre of the plastic shear zone, the displacements increased to 14-18cm.
- Shortly after the expansion of the plastic yield zone and the associated increase in shear displacements, local failures developed in the upper till above the upstream edge of the Upper GLU at the centre of the plastic yield zone. In the zone of local failures, the levels of mobilized shear resistance began dropping.
- After the local failures had developed in the uppet till, the rate of loss of shear resistance to weakening was seen to rise steeply. An associated rapid accumulation of shear displacements was also noted. Figure 4.39 showing the development of the slip surface during collapse provides an indication that at 2700 calculation steps, the shear zone propagates from the Upper GLU into the upper till on the upstream zone precisely at the location where large shear displacements are observed shortly afterward.
- The global collapse began shortly afterward.
- In phase one, the model appeared to successfully approach convergence. The rate of loss of mobilized shear resistance to the unfolding failure processes appeared to be countered, for the time being, by the rate of mobilization of shear resistance elsewhere in the soil mass.

6.1.4.2. GLOBAL COLLAPSE

The application of stage 9B loads had the immediate effect of reigniting the process of progressive failure in the foundation. At first, this failure remained confined to the Upper GLU, with the rest of the soil mass adjusting, seemingly with success, to the new loading conditions. However, there came a point where the failure processes propagated into other soils and global collapse initiated. This period was characterised by a sustained drop in the mobilized shear resistance of most soil units in the shear zone, accompanied by an acceleration of the soil mass leading to collapse. In the simulation of the collapse phase, this process took place 2700-3000 mechanical calculation steps after the application of stage 9B loads; its unfolding is described below.

Recall from previous section that at the tail-end of phase one, local failures in the upper till on the upstream were noted, followed shortly after by a brisk accumulation of shear displacements in the foundation and rapid weakening (seen in Figure 6.11 and Figure 6.12 after 3000 mechanical calculation steps). To understand how these processes are interrelated, we must consider the events prior to them. The Upper GLU's plastic yield zone expanded considerably but was weakening rather slowly. The weakening material was also seeing increasing shear displacements in the downstream direction; and the materials above travelled along. The upper till, located immediately above the Upper GLU, would have been placed in extension under such circumstances. Eventually, this strong but relatively brittle material could not accommodate the increasing displacements and failed. In the simulation, this event took place at 14-18cm of shear displacements at the middle of the plastic yield zone, but these numbers are not critical – what came after is. The rapid accumulation of shear displacements seen in the foundation immediately after the local failure of the upper till is a direct consequence of the latter: the upper till, while intact and travelling on top of the plastic yield zone along with it, was also stabilizing it, preventing it from shearing excessively. Once the till "snapped," this stabilizing effect vanished, and the Upper GLU was free to deform and weaken. The moment when the local failures materialized in the upper till is probably the closest approximation of the start of the brittle failure in the simulation of Mount Polley.

After this point, the events in the simulation unfolded rapidly. The local failures propagated from the upper till into the core. This process can be appreciated from Figure 4.39, where the slip surface at 5200 steps into the simulation of collapse is seen to have propagated well into the core. As a consequence, the levels of mobilized shear resistance in the core began dropping, mirroring the process observed earlier in the upper tills. This process is visualized in Figure 4.43, where the evolution of stress states on the critical planes in two core zones close to the embankment base are plotted along with the soil's strength envelope. The data in the figure indicate that at 2700 or so steps into the simulation of collapse, the stress state along the critical plane stopped rising and began decreasing. This decrease was sustained until the end of the collapse simulation.

The model convergence in phase two (seen in Figure 4.24) shows an upward trend in the evolution of average force ratios, indicating that the overall soil mass began accelerating. This observation suggests that the aggregate rate of mobilization of shear resistance in the soil mass had now become lower than the overall rate of decrease in shear resistance in the failing portions of it.

The evidence presented in this section so far as well as in §6.1.4.1 invites the conclusion that after 2700-3000 mechanical calculation steps into the simulation of collapse, the Upper GLU, as well as the upper till and core materials located on the upstream edge of the slide all experienced a sustained decrease in the levels of mobilized shear resistance. The rockfill, on the other hand, manifested an entirely different mechanical response. From the start of the simulation in stage 3 and on, this material exhibited stress states plotting well below its strength envelope. The stress states were tracked in a number of rockfill elements thought to be in the area of the developing slip surface (see Figure 4.45; Appendix 4D, columns 21-30). These data indicate that during collapse, (a) the stress state on the critical plane increases steadily but modestly, and (b) the shear strength of this material is never mobilized to its full extent.

In sum, during phase two of collapse, three of the four major units involved in failure (i.e. the Upper GLU, the upper tills on the upstream, and the core) experienced sustained and considerable decreases in their levels of mobilized shear resistance, whereas the rockfill saw modest increases of the same. This corroborates the conclusion made on the basis of the convergence behaviour that at this point in the simulation, the aggregate rate of mobilization of shear resistance in the soil mass became insufficient to stabilize the structure.

6.1.4.3. AGGREGATE MECHANICAL RESPONSE IN THE SOIL MASS DURING THE COLLAPSE

The mobilization of shearing resistance observed over the duration of the collapse is conceptually illustrated in Figure 6.13, top left. The figure visualizes (qualitatively, not quantitatively) the change in the levels of mobilized shearing resistance in the Upper GLU, upper till, core and rockfill as deformation accumulates in response to loads added in stage 9B. The key insight to be learned from this graphic is that at some point after the start of construction, three of the four major materials involved in failure (i.e. the Upper GLU, the upper till and the core) saw their levels of mobilized shearing resistance drop continually, while the rockfill material experienced consistent but modest increases in its levels of shearing resistance. This resulted in an overall deficit of shearing resistance in the failing soil mass and led to the rapid collapse of the structure. Supplementing this graphic are the bottom two plots showing the accumulation of displacements in the simulation of the Mount Polley TSF at twelve representative locations shown in the top right plot. The acceleration of foundation materials in phase II of the collapse can be appreciated from the increase in the rate of accumulation of displacements in the Upper GLU and the upper till (Figure 6.13, bottom left, points A-E); the near-vertical drop in the upstream region of the slide and at the crest are seen to accelerate at the end of the simulation (Figure 6.13, bottom right, points F, G and H); and horizontal displacements and uplift in the toe region begin accumulating in the late stages of phase II (Figure 6.13, bottom plots, points L and K).

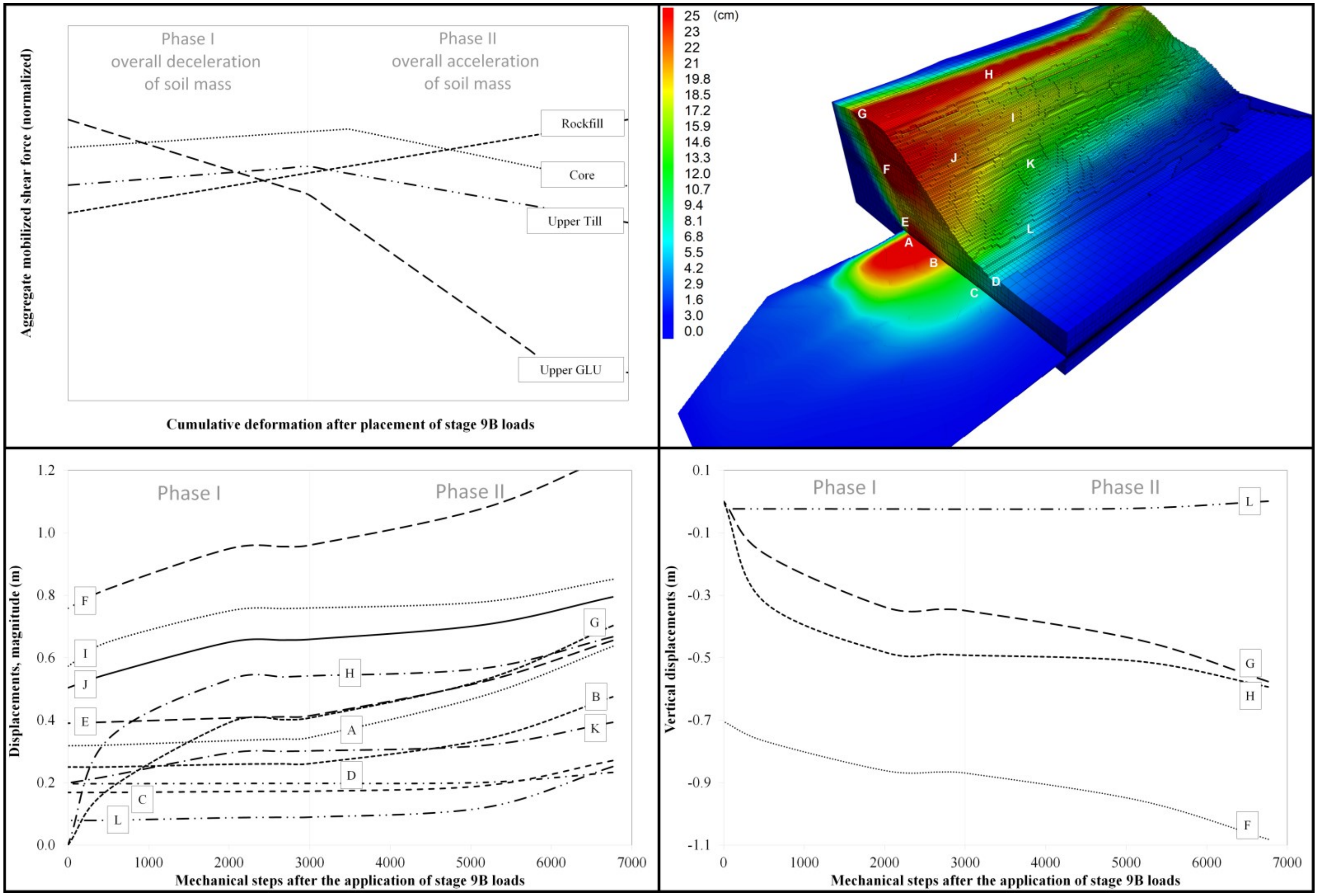

Figure 6.13 Top left: A conceptual model of mobilization of shear resistance in the soils involved in failure during collapse. Bottom left and right: displacements predicted by the fine model during collapse at 12 representative points in the slide zone. Top right: a plot (a) incremental horizontal displacements in the downstream direction at the end of simulation, and (b) of locations of 12 representative points in the slide zone whose displacements during collapse are captured in the bottom plots.

6.1.5 INTERPRETATION

The predicted mechanical and deformation behaviours observed in the fine model prior to and during the collapse phase invites the following conclusions regarding the unfolding of the failure in the field.

The onset of the collapse was precipitated by the emergence of the three material conditions in the foundation described in §6.1.3, i.e. the presence of a substantial area in the Upper GLU that was close to strain-weakening, the depletion of reserve shear strengths in the neighbouring soils and the growing extension strains in the upper till above the upstream edge of the Upper GLU. At this point, sometime after the completion of stage 9A works, the embankment became prone to collapse under certain trigger conditions.

The addition of stage 9B loads set off multiple interrelated progressive failure processes in the foundation, leading to a rapid expansion of the plastic yield zone and some further shear displacements in the foundation and materials above. This process placed the upper till unit in extension. Eventually, this strong but somewhat brittle material failed to accommodate the growing shear deformations and failed in extension and/or shear.

Prior to its failure, the upper till served to somewhat stabilize the Upper GLU, preventing it from accumulating excessive shear displacements. Once this unit "snapped," the Upper GLU began shearing rapidly and weakening in step. This caused the rate of loss of shearing resistance in the foundation to upsurge and exacerbated the local failures in the upper till, causing them to propagate broadly into the core.

The local failures in the till and core materials had the effect of decreasing the amount of shearing resistance that these materials could lend to the structure. Once the local failures began propagating on the upstream, the upper tills and core have experienced a sustained loss of shearing resistance.

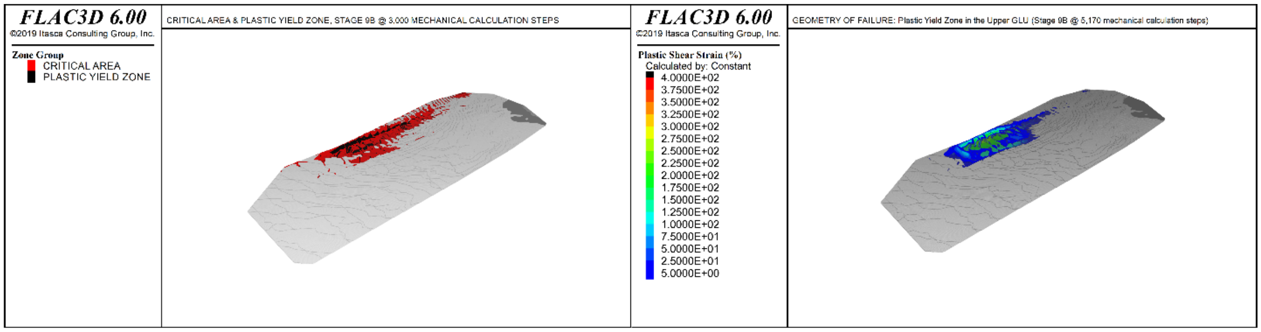

Figure 6.14 Left: The areal distribution of the critical area 3000 steps after the application of stage 9B loads. Right: The areal distribution of the plastic yield zone after the start of the second phase of collapse 5200 calculation steps into the simulation of stage 9B.

The findings about the manner in which the core and upper tills failed on the upstream of the slide made on the basis of the simulation results are consistent with field observations, including cracks in the exposed core at the base of embankment; microscopic shear planes in the samples obtained in this region; the expanded, debris-filled shear zone located in the core material in the washout zone; and large shear displacements in the foundation soils in the downstream direction.

The mechanical response of the rockfill was very different. At low confining stresses, this strong but uncompacted material was very ductile and required large deformations to mobilize its shear strength. At the levels of shear deformation in the Upper GLU that generated failures in the core and upper till materials on the upstream, the rockfill material did not deform enough to fully mobilize its otherwise substantial shear strength.

The expanding failures in the core and upper tills are the probable reason why the soil mass did not re-stabilize when the rockfill finally engaged fully if it did at all. The levels of vertical and horizontal displacements seen at crest level at the endpoint of the collapse simulation (illustrated in Figure 4.33 and Figure 4.37) are significant enough to ascertain that serious performance issues would have been encountered at that point, including excessive deformations of the core and possibly overtopping. This suggests that the significant shearing strength of the rockfill in the shell zone may have not been fully realized prior to the overtopping event.

6.1.5.1.THE CRITICAL AREA AS A PREDICTOR OF THE PLASTIC YIELD ZONE

In §6.1.3 and §6.1.4.1, an argument was presented that the so-called stage 9A "critical area" in the Upper GLU became a plastic yield zone shortly after the placement of stage 9B loads (this transition is illustrated in Figure 6.9). In the simulation of Mount Polley, this "critical area" was somewhat loosely defined as the zones with plastic shear stains between 3.8 and 5%. Such range was selected due to a couple of reasons. First, small variations of its lower bound do not seem produce radically different "critical areas." Second, the zones with plastic shear strains in excess of 3.8%, or even 3.5%, appear to approach in the model the threshold value of 5% rather quickly.

The approximate nature of the definition of such "critical area" does not diminish its value in terms of understanding the failure processes in the model of Mount Polley. Over the course of the collapse simulation, an observation was made that at any point, the current critical area is a reasonable predictor of where the plastic shear zone will propagate very shortly. For example, Figure 6.14 shows the "critical area" at 3000 steps into the simulation of the collapse plotted side-by-side with the plastic yield zone at 5200 steps; the correspondence between the two is rather good.

The pivotal role that the critical area formed in stage 9A played in the unfolding of the collapse is underscored by the deformation analysis introduced in §4.3.1 whereby the fine model using the least conservative strain-weakening curve produces a stable stage 9B embankment configuration. Recall that in the least conservative strain-weakening model, the onset of weakening takes place at plastic shear strains of 7.5% compared to 5% in the baseline model. Such a shift in the point of onset of weakening has the added effect of substantially contracting the stage 9A "critical area" and changing the stage 9B outcome as a result of it.

One can surmise that the size of the "critical area" is a function of the post-peak rate of weakening, i.e. the post-peak slope of the strain-weakening curve. It is reasonable to assume that a steeper curve would generate a higher rate of reduction in resistance over the same area and hence would reduce the size of the critical area that would be sufficient to destabilize the slope. However, this proposition was not investigated and remains speculative.

6.1.5.2. SENSITIVITY OF SIMULATED STAGE 9B RESPONSE TO LOADING

In the numerical simulation of the failure at Mount Polley, the collapse was triggered by the addition of stage 9B loads under undrained conditions combined with the excavation at the embankment toe.

In §4.3.3, an alternative scenario was evaluated where the excavation at the toe of embankment was eliminated in stages 9A and 9B; under these loading conditions, the collapse was also triggered in stage 9B in a manner similar to that observed in the baseline simulation.

Finally, in §5.1.1, an it was noted that in small strain that the total and effective stresses appear to be lower in small strain than they are in large strain. The reasons for this are fully explained in 6.6.1; for now, it suffices to state that by stage 9B, the total and effective overburden stresses are lower in small strain by about 25-30kPa; this difference is roughly equivalent to 40% of the stage 9B loads. This suggests that in stage 9B, the loading conditions predicted in small strain are

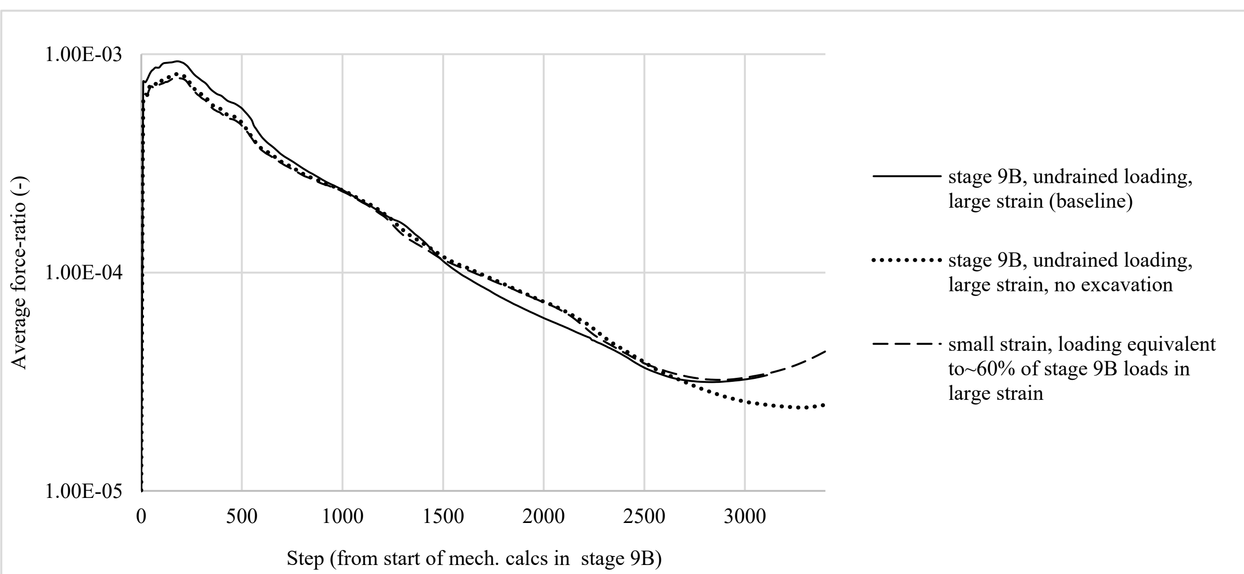

Figure 6.15 History charts of stage 9B average force ratios under three loading scenarios.

approximately equivalent to those that would be seen in large strain if only 60% of stage 9B loads were added. Despite that, the fine simulation in small strain predicts the onset of the collapse in a manner very similar to that seen in large strain. It appears that this difference in loading conditions does not have any discernible impact on the predicted outcome.

The history charts of stage 9B average force ratios obtained under the three loading scenarios described above are seen in Figure 6.15. The failure of models to attain a static equilibrium is seen in each of these scenarios, but the history curves are not entirely identical. For example, the scenario where the toe excavation is eliminated from the model shows that the onset of phase two of the collapse takes place a bit later into the simulation, and prior to it, the model attains a lower minimum average force ratio, suggesting that in this loading scenario, the soil mass had decelerated a bit more before failing. This finding supports our general understanding that the excavation at the toe of embankment in fact contributed in some way to the unfolding of the collapse, while demonstrating that its presence was not critical to its occurrence. Similarly, the response of the fine model run under the small strain calculation scheme is also consistent with expectation. At the start of stage 9B when the new loads are applied, the average force ratio is a bit lower than in the baseline simulation, as it would be expected with slightly lower added loads. However, at the start of phase two of the collapse (i.e. ~3000 calculation steps into its simulation), the responses of the two models appear to converge. This suggests that in this phase of the collapse, conditions other that loading govern the model response.

The findings presented in this section further substantiate the conclusions reached in §6.1.3 that the occurrence of the collapse event was predicated on the presence of specific conditions in the foundation (i.e. the materialization of a substantial area that was close to strain-weakening, and the depletion of reserve strengths around it) and that these conditions made the structure susceptible to collapse under a range of loading conditions.

6.2. NON-LINEAR STRAINING IN THE UPPER GLU

The proposition of non-linear straining in the Upper GLU is part of the hypothesis that shaped this research undertaking. This proposition was formulated in order to reconcile the apparent inconsistency arising from two preliminary findings, one being that the entire surface of the Upper GLU involved in the failure had to be fully weakened at collapse, and another suggesting that such level of weakening would require lateral displacements prior to the collapse of a magnitude not documented in the field.

The deformation analyses of Mount Polley introduced in Chapters Four and Five demonstrate a fairly consistent tendency for non-linear straining in the Upper GLU. Each simulation, irrespective of its resolution or calculation scheme, predicts non-uniform rates of plastic shear straining whereby a single layer of zones, commonly towards the base of the stratum, accrues plastic shear strains much faster than the soils above or below. The onset of weakening appears to accelerate these processes: once the most strained layer is seen to reach the threshold of strain-weakening, the rate of accumulation of plastic shear stains and displacements increases substantially. As a consequence, the formation of the shear band is best observed in the fine models where weakening processes are pronounced and is less conspicuous (but still detectable) in the intermediate and coarse ones.

The predicted non-linear straining of the Upper GLU is seen in Figure 6.16 which shows the plots of the plastic shear strains in this stratum in a cross-sectional view through the middle of the slide.

The top two plots were generated in the fine model where the Upper GLU thickness, varying from ~0m at the edges to ~2m in the middle, was modelled using 1 to 16 layers with a height of 12.5cm each. A single-zone shear band is distinctly seen in stage 9A emanating from the plastic yield zone under the core where the plastic shear strains in the order of 10-14% signal ongoing weakening. In the same plot, the Upper GLU zones above and below the shear band are less strained – in fact, their plastic shear strain levels are below the threshold of strain-weakening. In stage 9B, the shear band is seen to have accrued considerable levels of plastic shear strains and to have reached full weakening (seen in black), while the elements above and below exhibit plastic shear strains smaller in magnitude by one or two orders. The reduction of shear strength associated with weakening can be appreciated from Figure 6.17 which shows a cross-sectional view of shear strengths in the Upper GLU at an advanced point of the collapse. From the figure, the shear band in Figure 6.16 (top

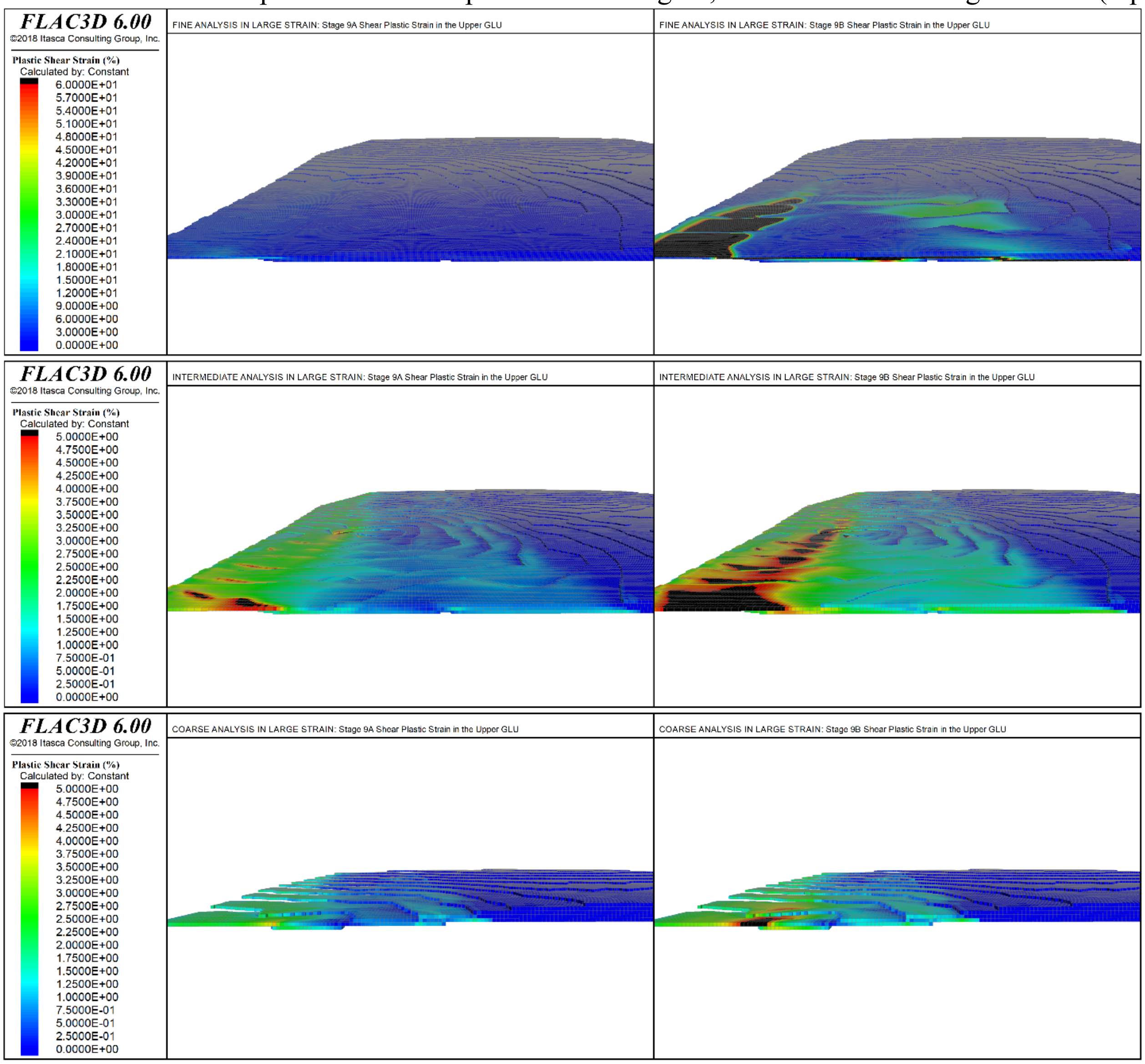

Figure 6.16 Cross-sectional view of plastic shear strains in the Upper GLU.

right) seen there is fully weakened (in black) and corresponds to the location of the lowest shear strengths (seen in light blue in Figure 6.17).

The two middle plots were generated in the intermediate model where the Upper GLU thickness was modelled using 1 to 8 layers with a height of 25cm each. The response is comparable to that seen in the fine model, with a couple of important differences. While the shear band can be distinguished in stage 9A, the plastic shear strains seen in it are not large, and the degree of weakening is negligible. The elements above and below the shear band show the same degree of shear straining as seen in the fine model in the equivalent areas. The lower degree of straining in the shear band combined with a doubled zone height produces shear displacements in the Upper GLU that are very close to those predicted by the fine model.

The two bottom plots were generated in the coarse model where the Upper GLU thickness was modelled using 1 to 4 layers with a height of 50cm each. In this model, the shear band is not as pronounced as either in the fine or the intermediate models but is still differentiated from the

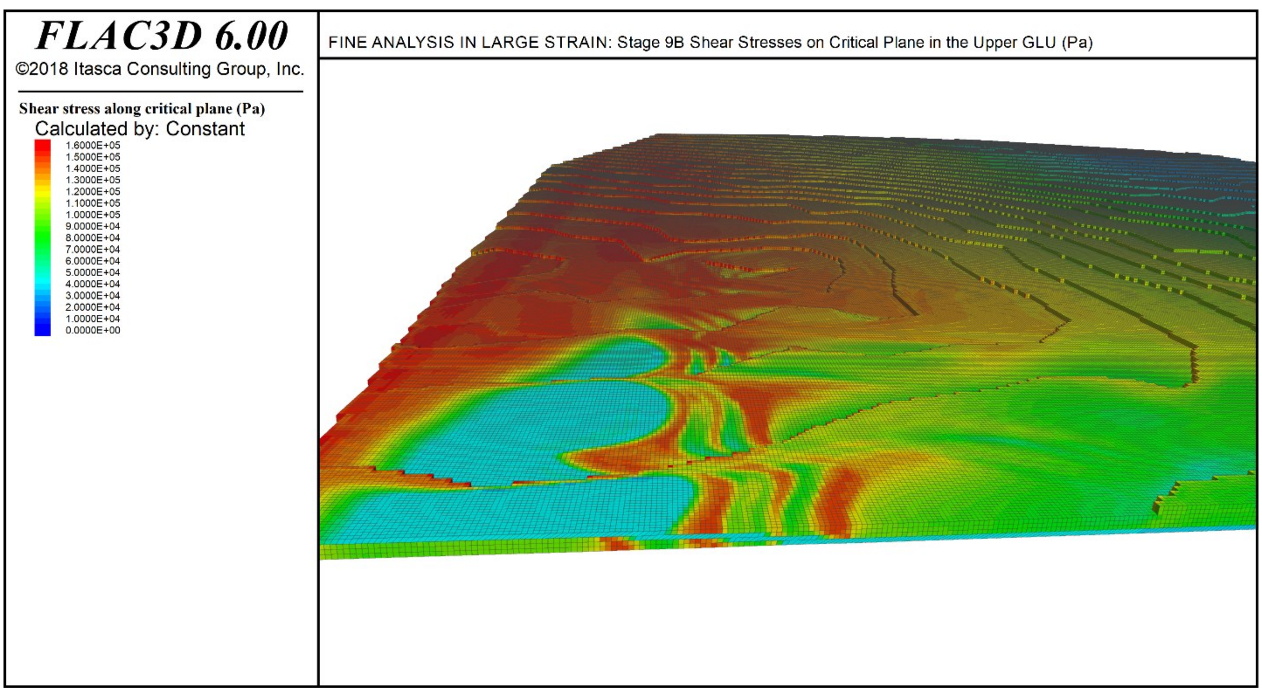

Figure 6.17 Cross-sectional view of shear strengths along the critical plane in the Upper GLU at an advanced point of collapse.

surrounding elements by its higher accumulation of plastic shear strains and, in stage 9B, some weakening (seen in black). The low levels of shear straining combined with a zone height of 50cm, produces shear displacements in the Upper GLU that are only 5 or 10mm lower than those predicted by the fine and intermediate models.

These findings invite the conclusion that the Upper GLU did not act as a uniform block but rather as a layered system composed of horizontal bands that strained more or less independently of one another. The results show that a single soil band tends to strain significantly more than others, and due to weakening eventually comes to control the mechanical stability of the whole structure.

6.2.1 SHEAR BAND THICKNESS

Due to the discrete nature of numerical analysis, the thickness of the shear band is defined in the models by the height of a zone, i.e. 50cm in the coarse analysis, 25cm in the intermediate analysis, and 12.5cm in the fine analysis. Such limitation is a consequence of the assumption inherent to finite volume analysis of constant strain rates across a single zone. Arguably, if models with yet finer resolutions would be evaluated, this pattern would endure. The root of this problem lies with the fact that constitutive models do not contain material parameters that include the dimension of length, so that the thickness of the shear band remains undefined (Sulem 2010; Vardoulakis and Sulem 1995, p.10). Therefore, while the deformation analysis helps demonstrate that the straining of the Upper GLU was non-uniform, such analysis cannot determine the true thickness of the shear band. Consequently, simulation results alone cannot be used to make definite determinations about the thickness of a shear zone.

In Chapters Four and Five, extensive evidence was introduced, demonstrating that the fine model adequately replicates field observations in that it correctly predicts the onset of the collapse, the geometry of the failure and also pre-failure deformations. In the same chapters, a determination was made that the coarse and intermediate models do not adequately replicate the events at Mount

Polley. In §4.3, the insufficient discretization level of the coarse and intermediate models was identified as the root cause of their failure to correctly replicate the collapse event. Therefore, it is reasonable to conclude that the shear band thickness is closer to 12.5cm than it is to 25 or 50cm. However, in §4.3.1 and §4.3.2, evidence was introduced that some discretization error is also present in the fine model and that the use of a yet finer mesh model in combination with a less conservative strain-weakening curve would also correctly replicate the failure events. Therefore, the good agreement between the predicted and observed outcomes does not constitute proof that the thickness of the shear band is modelled correctly. Consequently, in order to estimate the true thickness of the shear band, other evidence must be considered.

Aggregate evidence will be presented further in this section to demonstrate that the thickness of the shear band was probably between 1 and 3cm. Two arguments will be made to support this assertion. The first one is analytical based on the results of the analysis of upper and lower limit states introduced in §4.3.2, and the other is of geological nature.

The results of the upper and lower limit states analysis suggests that the true thickness of the shear band was much closer to zero than it was to 25 or 50cm. Recall that the analysis of upper limit state (that emulates a shear band with a thickness of 50cm) yields a safety factor of 1.34, whereas the analysis of the lower limit state (that assumes an infinitely thin shear band) predicts failure in stage 9A, inferring a stage 9B safety factor only marginally below unity. Such results indicate that the true thickness of the shear band that produced failure in stage 9B was a greater than zero but not by much. In other words, the shear band was very thin but it was not a pre-sheared plane.

The second piece of evidence pertains to the macro-structure of the Upper GLU. This deposit is a varved clay whose distinct layers are seen in Figure 6.18. In such materials, bands of clay are separated from one another by thin layers of coarser particles such as silt. These clays are formed by sedimentation in the still waters of glacial lakes, and seasonal variations of flow are thought to

Figure 6.18 A photograph of undisturbed Upper GLU material from outside the failure area by Thurber Engineering (reproduced with permission from the Government of British Columbia from IRP 2015, Figure 5.2.8).

account for such structured variation of particle size. It is tenable that this macro-structure controlled the shearing behaviour of this unit, with individual varves straining independently from one another and causing the Upper GLU to act as a layered system.

6.3. THREE-DIMENSIONAL STABILITY EFFECTS IN THE FAILURE AT MOUNT POLLEY

The question of three-dimensional slope stability effects in the failure at Mount Polley lays at the foundation this research undertaking. The substantial difference between the two- and three-dimensional safety factors calculated using limit equilibrium methods served as a clue that the failure of the embankment may have unfolded differently than inferred from the initial, two-dimensional analyses.

The two- and three-dimensional static analyses of the collapse invite very different conclusions regarding the ultimate strength of soils at failure. The former suggests that the slope failed when peak or near-peak undrained shear strengths were acting, on average, along the Upper GLU surface, whereas the latter indicates that the failure could only take place if the unit's shearing resistance was reduced to residual values. The difference in these results is largely owed to shear strengths along the sides of the slip surface that are not considered in two-dimensional analyses. In the case of Mount Polley, these sides pass through the rockfill and upper tills, two high-strength materials capable of mobilizing substantial amounts of shearing resistance.

Static analyses do not make use of stress-strain relationships to determine the extent of mobilized shearing resistance through the domain as a function of its current deformation levels; instead, they rely on the assumption that shear strengths are mobilized simultaneously across the entire slip surface. In a profile involving materials with contrasting deformation-strength behaviours, such assumption could be in considerable error.

The three-dimensional static analysis of Mount Polley was conducted under the premise that at failure, the full shear strength values were mobilized in all materials except the Upper GLU, whose shear resistance was reduced to residual. Such analysis assumes that peak strengths in the rockfill, core and upper tills, and residual strengths in the Upper GLU occur simultaneously at the same deformation levels. In the Upper GLU, with a shear band thickness of 1-3cm, the onset of weakening would have required just a few millimetres of shear deformation. Such deformation-strength behaviour is best described as "brittle." On the other hand, the rockfill, with its lack of compaction on placement and low in-situ confining stresses, exhibited a deformation-strength behaviour that can be qualified as "ductile." This material would have required considerable deformation levels to fully engage its shear strength. The upper till, described as "lightly overconsolidated" prior to the construction of the embankment, with a high fraction of silt, sand and gravel particles and sand-filled dessication cracks, and the core, similarly composed of low-plastic silts with sand and gravel, would have exhibited a deformation-strength behaviour that lay between these two extremes, i.e. less brittle than the Upper GLU yet less ductile than the rockfill. Therefore, the mobilization of shear resistance throughout the failing soil mass would have not been simultaneous as assumed by the static analyses.

The simulation results introduced in §4.5.2 demonstrate that in the collapse at Mount Polley, the mobilization of shear strengths was distinctly asynchronous. Under these conditions, the three-dimensional safety factor of the structure (as defined in §3.3.4.3) at any point after the initiation of the global collapse was probably either equal to or below unity, and would have varied throughout the course of this event. However, such a safety factor would have not resulted from a full weakening in the entire Upper GLU area involved in the failure, combined with full shear strength mobilization elsewhere, as it was suggested by the static analysis. Instead, the momentary safety factor at any point during the collapse would have been the result of a growing reduction of shear resistance in the Upper GLU combined with varying levels of shear strength mobilization in the other soils. In other words, the three-dimensional stability effects during the collapse at Mount Polley were realized in the form of varying levels of strength mobilization along the three-dimensional slip surface, where aggregate levels of shear resistance that would be sufficient to re-stabilize the soil mass were never simultaneously actuated.

The results of the deformation analysis of Mount Polley allow us to conclude that the particular combination of shear resistance levels throughout the soil mass that produced, in the three-dimensional limit equilibrium analysis of the failure, a safety factor of unity, did not actually occur in the actual slope at any single point in time. In this sense, the three-dimensional limit equilibrium analysis of Mount Polley is incorrect, and its successful prediction of failure is merely a result of assigning to the soils a certain combination of shear strengths – one of many possible, but not one that actually occurred – that produces a safety factor of unity.

6.3.1 SLIP SURFACE

The actual slip surface of the slide observed at the Mount Polley TSF failure site was composite, with (a) a broad base at the foundation level spanning a width of about 200m and characterized by large shear displacements in the downstream direction and an uplift at toe; and (b) a smaller section at the embankment level that was breached, with a width of only 50-100m. Such a complex slide configuration does not easily conform to geometric shapes that we traditionally use to describe slip surfaces for the purpose of limit equilibrium analysis. Additionally, the overtopping and washout events that followed this breach obscured the shape of the slip at the embankment level. As a result, the three-dimensional limit equilibrium analysis of the failure necessitated some guesswork regarding the shape of the slip surface.

In the three-dimensional limit equilibrium analysis of the failure at Mount Polley introduced in §2.4, a search for the slip surface with the lowest safety factor was conducted that included a broad range of ellipsoid shapes with varying ratios. The base of the slip surface was forced to pass through the Upper GLU. The resulting surface with the minimum safety factor resembles a large "bowl" with a broad base (seen in Figure 2.5 to Figure 2.7). The width and aspect ratio of this slip surface is reasonably close to that observed at the base of the slide but not at the embankment and crest levels. It could be said that the slip surface predicted by the limit equilibrium analysis is a rather poor match to that seen in the field.

In deformation analysis, the slip surface is not a modelling input. Instead, the shear surface develops naturally as a result of accruing deformations. The development and propagation of the slip surface in the numerical model of Mount Polley can be appreciated from Figure 4.39. Its shape appears to look like an inverted cleaved cone, radiating from a relatively small base in the "red zone" of the Upper GLU. This slip surface matches the width and aspect of the actual slide at embankment and crest levels. Additionally, the deformation analysis predicts a secondary slip zone at the Upper GLU level that does not appear to develop into a full failure surface. This slip zone, spanning an area with a width of 200m from Stn. 4+100 to Stn. 4+300 and incorporating a portion of the overconsolidated Upper GLU material under the embankment toe, matches the width of the slide at the foundation level that was documented in the field. The deformation analysis evidently predicts a slip surface that is much closer to actual.

The slip surface predicted by the limit equilibrium analysis appears to be wider and with a higher aspect ratio than either predicted numerically or observed in the field and incorporates a much larger area of the Upper GLU. As a consequence, this analysis over-emphasizes the effect of strain-weakening in this stratum in the stability calculations, producing, in theory, a less stable configuration with a lower safety factor. Had the limit equilibrium analysis been conducted using a slip surface shape closer to actual, with a much smaller area in the Upper GLU, a safety factor of unity would have not been achieved unless the shear resistance at failure of some other material other than the Upper GLU had also been adjusted downward. Such analysis would have provided good indication that some other material or materials involved in the failure were weaker than assumed from their strength envelopes. However, without the benefit of a deformation analysis, it would have been very difficult to determine the proper shape of the slip surface at the embankment level.

6.4. SCALE EFFECTS

In this section, some of the scale effects noted in the course of the simulation of the failure are revisited with the goal of determining the main reasons for the divergence of results as well as evaluating their implications.

6.4.1 STRESS DISTRIBUTIONS

Small differences in the stress distributions predicted by the coarse, intermediate and fine models (discussed in §4.1.1 and §5.1.1) were identified in each of the stages 3 through 9A, where the model was shown to be mechanically stable. The difference in the stress response can be appreciated from the data in Table 4.1 and Table 5.1 listing the maximum total and effective overburden stresses in the Upper GLU. Two reasons for this divergent response were identified: the discrete nature of finite volume modelling and the strategy adopted to create the subsurface geometry of this model.

In finite volume modelling, the model domain is discretized into finite zones. The stress states are evaluated at the centroids of these zones and assumed to be constant across them. Consider the Upper GLU, with a maximum thickness of 2m, discretized in the coarse, intermediate and mesh models into 4 X 0.5m, 8 X 0.25m, and 16 X 0.125m horizontal layers. Under these conditions, the finer mesh models invariably predict both higher maximum and lower minimum overburden stresses, even though the average stress values over the thickness of the unit are same or very close.

Furthermore, the geometry of the subsurface (such as the spatial distribution of the Upper GLU material) was generated with the use of surface meshes representing interfaces between soil units. The model domain was first discretized into uniform zones; then, these zones were binned into soil groups based on their centroids' location relative to the interface surfaces. Recall that the Upper GLU was shaped like a "pancake" with a thickness that varied from 2m in the middle to 0m at the edges (illustrated in Figure 3.2). In coarser models, particularly at the Upper GLU's edges, the zones' centroids would fall outside the spatial range specified by the surfaces representing the upper and lower bounds of this unit, creating a "jagged edge" appearance with occasional "holes" of missing material. In the finer mesh models, the smaller zones would fit better into the Upper GLU volume specified by these surfaces, and the unit had a more continuous appearance. As a consequence of this, some material located in the Upper GLU areas with some of the highest or lowest elevations was not represented in the coarse model as belonging to this unit.

The consequences of such divergent stress response can be significant, as the Upper GLU's transition to a normally consolidated state and the evolution of its undrained shear strength are both linked to the magnitude of effective overburden stresses. The models with a finer mesh resolutions do, in fact, predict an earlier emergence of a normally consolidated zone in the Upper GLU. So, the coarse model predicts that the Upper GLU preconsolidation pressures are first exceeded in stage 5, whereas the fine model indicates that a few zones in this unit transition to a state of normal consolidation as early as stage 3. However, the noted difference is immaterial because only a negligible amount of soil is involved.

6.4.2 DEFORMATIONS

Surface settlements and other small deformations predicted in response to new loading incurred in the absence of failure processes were remarkably close in the coarse, intermediate and fine models. Recall that in the coarse model, processes associated with progressive failure emerged in stage 9B and were largely immaterial. In the intermediate model, these processes initiated in stage 9A, and in the fine model, they were first noted in stage 7. A side-by-side comparison of the surface settlements and other deformations in each simulated construction stage up to but not including the construction stages where progressive failure processes were taking place reveals that these are near-identical in the coarse, intermediate and fine models. This result indicates that (a) this modelling aspect is not susceptible to scale effects and (b) the deformations in the coarse simulation can be used as a baseline to evaluate the magnitude of deformations associated with progressive failure.

The pre-failure cumulative shear deformations in the Upper GLU were very comparable in all three simulations, but some scale effects were noted. So, an increase in the model resolution resulted in a very slight increase of predicted shear displacements in the Upper GLU. Two conclusions can be drawn from this finding. First, a further minimization of discretization error (i.e. an increase of the model resolution) would result in the prediction of equal or slightly larger pre-failure shear deformations in this unit. Second, since the noted scale effects are very minor and, because the deformation-strength behaviour of the Upper GLU is well-calibrated, the predictions of any simulation irrespective of its resolution can be used to evaluate pre-failure shear displacements. Some implications of these findings are further discussed in §6.7.2.

6.5. SHAPE OF UPPER GLU'S STRAIN-WEAKENING CURVE

The goodness of fit of a deformation simulation of the failure at Mount Polley was evaluated using a number of indicators, the most important one being the correct replication of the onset of the collapse after the addition of stage 9B materials.

The coarse and intermediate simulations do not predict collapse, producing stable stage 9B configurations with respective safety factors of 1.34 and 1.04. Such predicted outcomes are proof that these two models do not adequately replicate field conditions. In §4.3, an argument is made that the failure by these two simulations to correctly replicate the embankment collapse in stage 9B is largely owed to discretization error, thought to be significant in the coarse model and modest in the intermediate one.

The fine model correctly predicts the onset of the embankment collapse after the addition of stage 9B material. Such result may be taken as confirmation that in this model, the discretization error has been sufficiently minimized and that it adequately replicates field conditions. However, in §4.3.2, an analytical argument is presented on the basis of the analysis of the lower limit state that the correct replication of the collapse in stage 9B in the fine simulation could be the result of some discretization error combined with the selection of an overly conservative strain-weakening curve. This argument is corroborated by evidence introduced in §6.2.1 that the actual thickness of the shear band in the Upper GLU was between 1 and 3cm rather than 12.5cm as indicated by the results of the fine model.

The combined findings of §4.3.2 and §6.2 invite the conclusion that the actual shape of the Upper GLU's strain-weakening curve is less conservative than that initially selected. A more accurate evaluation of the true shape of the strain-weakening curve would require a simulation with a yet more refined mesh; since such analysis is not computationally feasible at this point, the definition of the Upper GLU's strain-weakening behaviour will be left somewhat open-ended. It suffices to state here that the function that best describes the in-situ strain-weakening behaviour of the Upper GLU plots somewhere above the most conservative strain-weakening curve (seen in Figure 3.6 in red) and is probably bound on the upper end by the least conservative strain-weakening curve (seen in Figure 3.6 in black).

6.5.1 AN EVALUATION OF THE DIRECT SIMPLE SHEAR TEST IN THE CONTEXT OF THE MOUNT POLLEY CASE STUDY

In their 1966 paper, Bjerrum and Landva introduce the direct simple shear test as a means of evaluating the undrained shear strength behaviour of clayey soils at the base of a slide. The test is described to better replicate the in-situ conditions where relatively thin interstitial seams of clay under a slope are thought to strain in "simple shear." The authors are cautious in their interpretation of the testing results, stating that the testing procedure "offers some new possibilities" yet stressing the tentative nature of their findings and the many unanswered questions, including about the stress states during the shearing phase.

Ladd, in his 1991 Terzaghi Lecture, further endorses the use of this test to evaluate the behaviour of clays in the shear zone at the base of a slide. Ladd (1991) equivocates his endorsement by discussing some of the issues related to the selection of the time rate of shearing, the deviation from K_0 conditions and more, but recommends this test as the best of available methods to evaluate the strength behaviour of clayey soils in the horizontal portion of a failure surface under an embankment that it progressively built up. Ladd's (1991) concerns with the effects of the deviation from K_0 conditions on the undrained shear strengths are corroborated by Wrzesinski and Lechonowisz (2013) who show experimentally that the rotation of the stress tensor lowers the measured undrained shear strength values.

Finally, the direct simple shear test procedure has been modified from that described by Bjerrum and Landva (1966) and documented by the ASTM D6528 in that after straining the specimen to γ_s = 20%, the direction of shearing is reversed, sometimes multiple times, in order to determine the shear resistance and the resulting shape of the strain-weakening curve at large shear strains. Such modification of the procedure has unclear implications on the testing results.

The Mount Polley case study offers the rare opportunity to assess empirically the use of direct simple shear tests for the purpose of evaluating the strength behaviour of clays at the base of a slip surface. The Upper GLU's undrained strength model used to simulate the failure at Mount Polley was based entirely on, and calibrated against, the results from a series of direct simple shear tests conducted by KCB (2015).

The accurate replication of the failure, including pre-failure deformations and the geometry of the collapse, offers a strong argument that the modelling parameters used in the simulation, including the Upper GLU's undrained strength model, are reasonably accurate. This argument remains credible in the context of findings in §6.5 regarding the lower and upper bounds of the actual strain-weakening curve.

These findings invite the conclusion that direct simple shear tests are appropriate for the purpose of evaluating the undrained shear strength behaviour of slightly sensitive clayey soils at the base of a slip surface.

6.6. LARGE STRAIN VS. SMALL STRAIN

The simulation of the failure at Mount Polley was performed in both large strain and small strain. The observed model response was very comparable. Two major differences were identified in the model responses: one related to the distribution of stresses through the domain and another related to the predicted geometry of the slide. In this section, these differences of outcome are revisited with the purpose of determining whether the small strain calculation scheme is appropriate for modelling large strain problems such as the Mount Polley case study.

6.6.1 STRESS DISTRIBUTIONS

The distributions of stresses predicted by the simulation of Mount Polley under the small and large calculation schemes are somewhat different. The overburden total and effective stress values predicted in large strain are a bit greater than those evaluated in small strain. This discrepancy is illustrated in Table 6.1 listing the maximum total and effective overburden stresses after the attainment of a static equilibrium in each simulated stage. The data in the table shows that the maximum stress value in the Upper GLU is consistently greater in large strain than it is in small strain and the difference increases steadily with each subsequent stage.

6.6.1.1.STAGED CONSTRUCTION

The failure at the Mount Polley TSF was simulated in nine stages starting with the pre-construction ground surface, followed by the gradual addition of embankment material to reflect surveyed surface elevations after the completion of construction stages 3 through 9B.

Each stage was brought to solution, meaning that the model was allowed to deform in response to the newly added load until a new static equilibrium was established or until global collapse was diagnosed. Settlement was part of this accrued deformation. In large strain, settlement manifested itself as a downward shift of the mesh gridpoints, especially in the embankment and the foundation materials below it. The settled areas became denser due to a decrease in their volume. In small strain, the mesh gridpoints did not undergo a similar downward shift due to settlement but remained constant and the settlement is traceable only numerically through calculated strain and deformation values. The affected zones' densities and volumes also remained unchanged.

Table 6.1 Maximum total and effective overburden stresses in Upper GLU predicted in small and large strain.

Mesh	Maximum total overburden stresses at static equilibrium in Upper GLU (kPa)					
	coarse		intermediate		fine	
	small strain	large strain	small strain	large strain	small strain	large strain
Stage 3	497	504	563	570	600	602
Stage 4	520	531	593	595	623	627
Stage 5	727	746	804	816	833	850
Stage 6	815	830	878	891	918	930
Stage 7	903	920	963	981	1017	1036
Stage 8	956	973	1020	1037	1079	1095
Stage 9A	1031	1041	1100	1121	1150	1176
Stage 9B	1071	1066	1139	1161	varies	varies
Mesh	Maximum effective overburden stresses at static equilibrium in Upper GLU (kPa)					
	coarse		intermediate		fine	
	small strain	large strain	small strain	large strain	small strain	large strain
Stage 3	333	350	416	418	455	456
Stage 4	368	379	443	445	471	481
Stage 5	588	605	672	674	699	722
Stage 6	669	690	746	756	771	802
Stage 7	753	773	821	836	858	885
Stage 8	804	826	875	886	912	937
Stage 9A	862	883	917	924	978	995
Stage 9B	896	918	947	967	varies	varies

During the simulation of a subsequent stage, new embankment material was added to the corresponding construction stage's surveyed elevation. In small strain, the height of the added material amounted to the difference in surveyed embankment elevations. In large strain, the height of the added material amounted to the difference in surveyed embankment elevations, plus settlement accumulated in the preceding stage. This means that the load added in large strain was greater than in small strain.

This effect is demonstrated through the data presented in Table 6.2 listing the approximate embankment elevations in each stage along with estimated total added loads. It is evident from the table that, by stage 9B, the effect described above may result in added load differentials of about 30kPa, explaining the overburden stress differences of 25-30kPa in Upper GLU seen in Table 6.1.

Table 6.2 Approximate embankment elevations and estimated added total loads predicted in small and large strain modes.

	Maximum settled embankment elevations (mASL)			Estimated added total load (kPa)		
	small strain	large strain	difference	small strain	large strain	difference
Stage 3	944.6	944.4	0.2			
Stage 4	950.1	950.0	0.1	121.0	125.4	4.4
Stage 5	954.9	954.8	0.1	105.6	107.8	2.2
Stage 6	959.0	958.9	0.1	90.2	92.4	2.2
Stage 7	961.4	961.1	0.3	52.8	55.0	2.2
Stage 8	966.1	965.8	0.3	103.4	110.0	6.6
Stage 9A	968.0	968.0	0.0	41.8	48.4	6.6
Stage 9B	970.0	969.6*	0.4	44.0	44.0*	0.0
Cumulative			*1.5*			*24*

**estimated from the coarse simulation in large strain mode*

On first instinct, one may conclude that the large strain solution is more accurate since it accounts for material settlement. A closer examination of data reveals that this is not necessarily so. If the laboratory-tested soil unit weights (and associated dry densities) represent in-situ values measured after the embankment has settled (as it is the case with Mount Polley) then assigning such values to materials at placement would result in an overestimation of added loads when modelling in large strain. Instead, the modeller may consider a downward adjustment of dry density values from those measured in the laboratory to attain a "settled" dry density profile closer to actual.

Lastly, depending on when a ground survey is taken (i.e. immediately after the conclusion of a construction stage or sometime afterward when the ground has settled) it may or may not account for settling. However, this problem becomes more or less irrelevant when multiple stages are simulated sequentially, as errors in one stage are "compensated" in the next one.

Having determined that two otherwise identical models simulate different loading conditions under small and large strain calculation schemes when modelling multiple construction stages, it is of interest to consider the impact of this effect on the model responses. In theory, higher loading conditions in large strain should result in a less stable slope much in the same way that a heavier embankment would. In the example of the Mount Polley TSF simulation, this effect does not appear to have a particularly pronounced effect on the overall results. Specifically, the fine model correctly predicts the onset of global failure in stage 9B under both the large and small strain calculation schemes. This finding supports the conclusion reached in 6.1.5.2 that the model response in stage 9B is not particularly sensitive to the magnitude of the trigger.

6.6.2 GEOMETRY OF THE FAILURE

Significant differences were noted in the geometry of the failure predicted by the fine models under the large and small strain calculation schemes. The differences in the predicted geometry can be best evaluated by comparing the model states at the most advanced point of the simulation.

The small strain calculation scheme appears to significantly over-predict the width of the slide both at the base and embankment levels. In small strain, the predicted width of the slide at base at the most advanced point into the simulation is around 220m, about 80m greater than in large strain; this can be seen from either the plots of the plastic yield zones in Figure 6.19 or from the plots of horizontal cumulative displacements in the downstream direction in Figure 6.20. Similarly, the width of the slide at embankment level is greater in small strain at 170m compared to ~100m in large strain; this can be seen from Figure 6.22. The differences in the shape and dimensions of the developing slip surface predicted in large and small strains are visualized in Figure 6.21 showing the plots of zones with maximum shear strain rates in excess of $2*10^{-6}$ (-). The slip surface predicted in small strain appears considerably broader than the one predicted in large strain, propagating

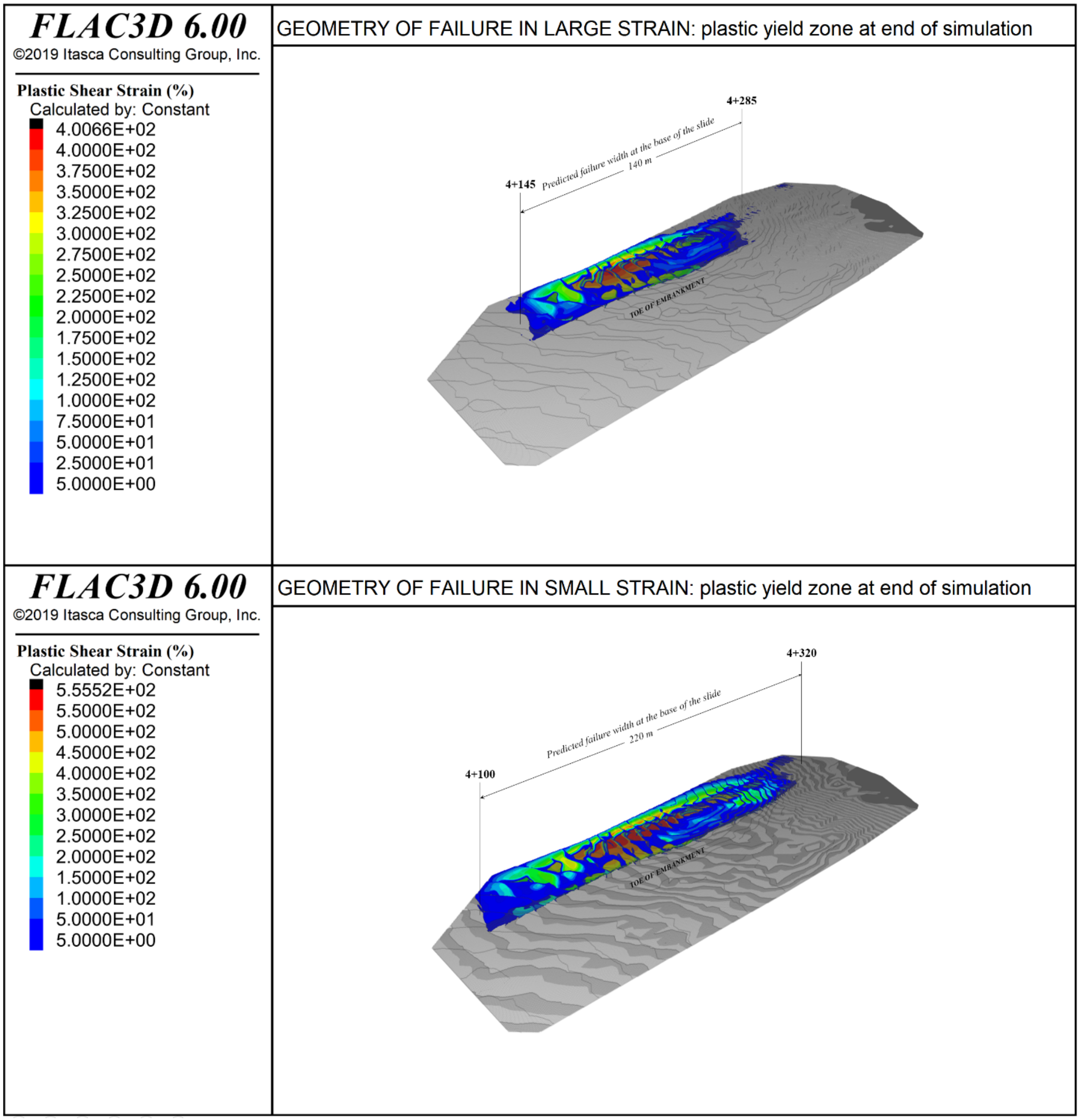

Figure 6.19 Plastic yield zone predicted in large and small strain at the endpoint of simulation.

widely through the core zone, reaching the domain boundary on the left. This surface does not curve into the rockfill material in the same way the one predicted in large strain does. At the base, the width of the conically-shaped slide (related to the area identified as “the red zone” in §4.4.3.1) is also much broader in small strain, at about 80m compared to 40-50m in large strain; this can

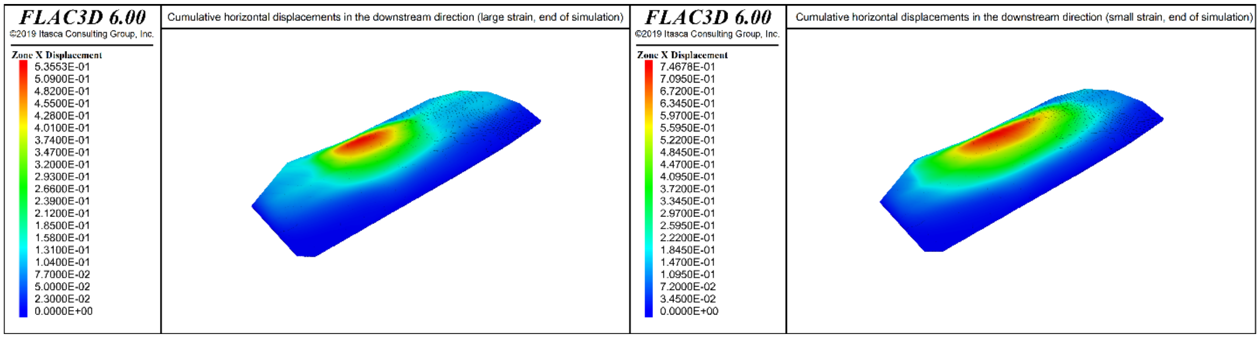

Figure 6.20 Cumulative displacements in the Upper GLU predicted in large and small strains at the endpoint of simulation.

be appreciated from Figure 6.20 where the "footprint" of the slide in the embankment is seen as the area in hues of rednor from Figure 6.21, where it is seen as the "funnel" at the base of the slip surface.

In §4.4.3, the conclusion has been reached that the geometry of the failure predicted by the fine model in large strain is remarkably close to that observed in the field. This simulation appears to replicate the composite nature of the slip surface, with a well-defined sliding mass at the embankment level, 40-50m wide at the base and ~100m wide at crest level; and a secondary slip surface at the foundation level with a width of ~200m, passing broadly through the Upper GLU, creating an uplift at the toe of the slide in the area where "whaleback" features were seen in the field. The fine model in small strain also predicts a composite slip surface with a broad base at the

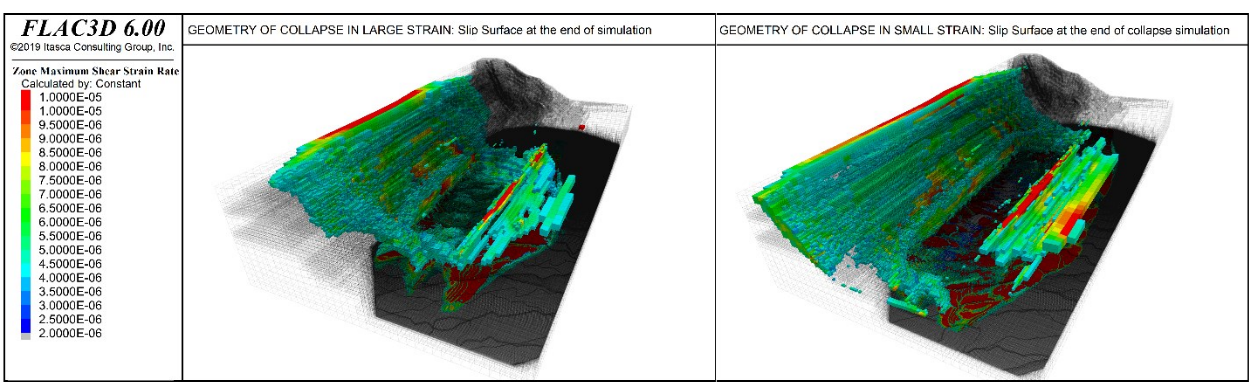

Figure 6.21 Slip surfaces predicted in large and small strain at the endpoint of simulation.

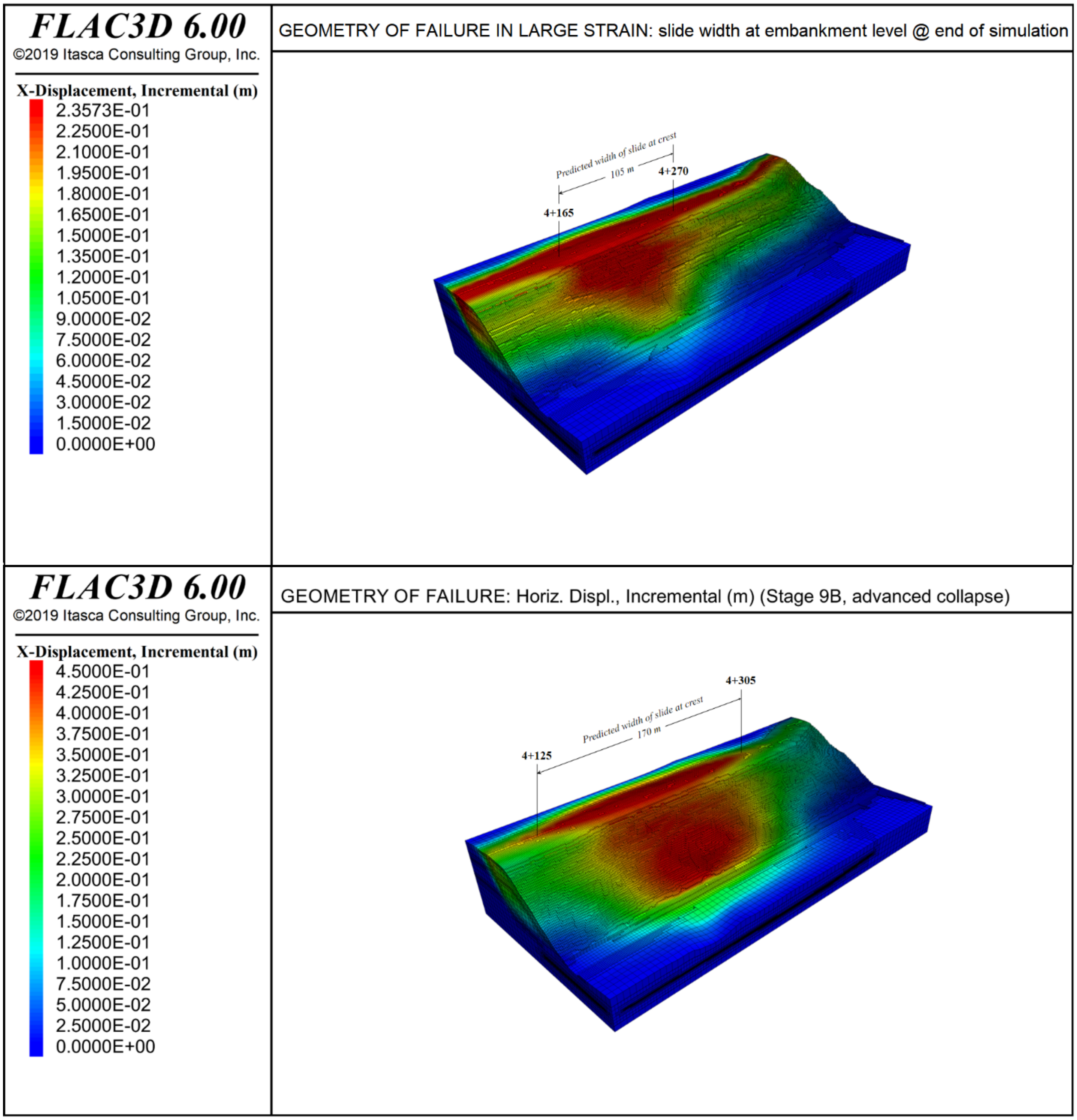

Figure 6.22 Incremental horizontal deformations in the embankment at the endpoint of simulation predicted in large and small strains.

Upper GLU level and a wide toe uplift area; and a well-defined slide at the embankment level. However, both the slip surface at the base of the slide and at the embankment level are much wider than observed in the field.

In all, the large strain mode appears to be better-suited for predicting the geometric features of a slip.

6.6.3 CONCLUSION

The predictions made by the coarse, intermediate and fine models under the large and small strain calculation schemes are generally very comparable to one another.

In particular, the fine simulation using the small strain calculation scheme produce, in stages 3 through 9, predictions that are nearly identical to those obtained in large strain regarding the onset of strain-weakening, evolution of strain-weakening, extent of embankment deformations before and during the collapse, the onset of collapse and more.

Two exceptions to the above were noted. First, as it has been discussed in §6.6.1, the total and effective overburden stresses predicted in large strain are slightly higher than those obtained in small strain, and the difference tends to increase as the staged simulation proceeds. However, this difference was shown to be immaterial to the predicted outcome. Second, the geometry of the failure predicted in small strain does not fit field observations nearly as well as that predicted in large strain.

The conclusion is reached that the small strain calculation scheme is generally adequate for problems involving large shear strains such as the Mount Polley case study.

6.6.3.1. MESH DISTORTION IN LARGE STRAIN

The concerns discussed in §3.3.2 regarding potential mesh distortion problems in large strain were found to be mostly unjustified. FLAC3D successfully simulated the behaviour of the model until an advanced stage of collapse, where plastic shear strains in the Upper GLU reached just under 400%, and has done so with only minor interventions to correct "bad geometry" issues discussed

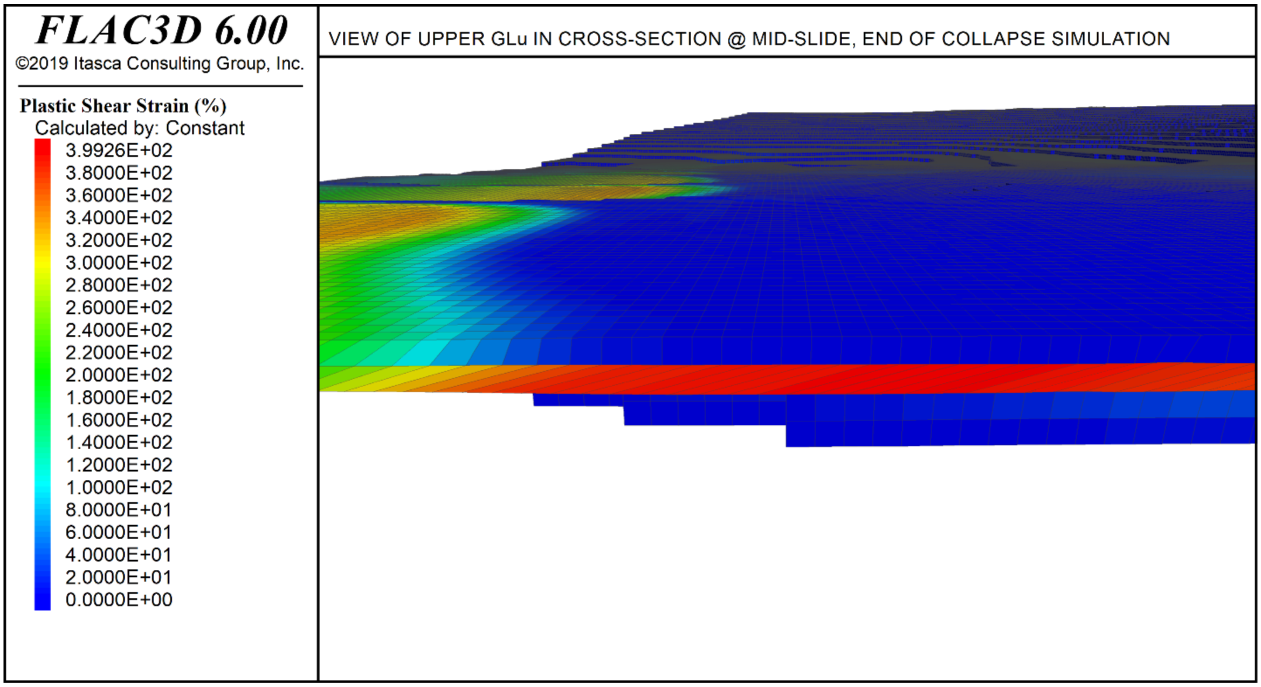

Figure 6.23 A cross-sectional view of Upper GLU at the endpoint of simulation in large strain showing shear plastic strains.

in Appendix 3E-IV. The vast majority of zones that experienced these issues were located at the face of embankment and not in the Upper GLU. Figure 6.23 below shows a close-up view of the Upper GLU's cross-section at the most advanced point of collapse that was simulated in large strain. The Upper GLU zones in the shear band seen in red exhibit shear strains upward of 398%.

6.7. OTHER

6.7.1 MECHANISM OF SHEAR STRENGTH REDUCTION IN THE UPPER GLU

The shear strength reduction in the Upper GLU has been identified from the beginning as the primary cause of the embankment collapse at the Mount Polley TSF. As a part of the hypothesis at the foundation of this thesis, a proposition was put forward that sensitivity was the mechanism responsible for such weakening. In this section, this proposition is revisited in the context of findings introduced in Chapter Four.

In the exploratory stages of this thesis (§1.3) two mechanisms of shear strength reduction in clayey soils have been identified: sensitivity discussed by Rosenqvist (1953) and by Skempton and Northey (1952) and post-peak reduction of shear strength to residual described by Skempton (1964; 1985). It has been established in §2.5 that there is a potential for both of these mechanisms to develop in a soil such as Upper GLU, but the latter was deemed improbable due to an absence of field evidence of a continuous pre-sheared surface.

A post-peak reduction of shear strength takes place in a soil as a result of two phenomena, (a) dilatancy and (b) the reorientation of platy clay minerals parallel to the direction of shearing (Skempton 1985). The former takes place in heavily overconsolidated soils and can be ruled out as having taken place in the normally consolidated portion of the Upper GLU during the collapse. The latter takes place in soils with a clay content equal to or in excess of 20-25%. The Upper GLU, with an average clay content of 60% (KCB 2015, p. 25), would be susceptible, in theory, to this mechanism of weakening.

In order to determine whether a post-peak reduction in shear strength could have taken place in the Upper GLU due to a reorientation of platy clay grains rather than due to sensitivity, we will examine the manner in which both of these mechanisms manifest themselves.

A reduction of shear resistance due to sensitivity takes place on remoulding or disturbance. In a foundation unit under the face of an embankment, such disturbance is thought to be induced by shear straining (Bjerrum and Landva 1966). The structural feature formed by this process is classified as a "shear discontinuity" (Morgenstern and Tchalenko 1967a) whereby a soil band with a non-zero thickness strains more or less in simple shear. On such straining, the relationship between shear strain and shear resistance takes the form of a strain-weakening curve such as the one seen in Figure 3.6.

On the other hand, a post-peak drop in shear resistance due to a reorientation of platy clay minerals takes place at large shear displacements, and it is the shear movement that causes the realignment of soil grains. A preferential orientation of platy mineral grains in the shear zone can be identified under a microscope (Skempton 1985; Skempton and Petley 1967; Morgenstern and Tchalenko 1967a,b) or seen with the naked eye as pre-sheared planes. The structural feature formed by this process is classified as a "displacement discontinuity" with a shear band thickness of zero (Morgenstern and Tchalenko 1967a, Figure 2). The mechanical behaviour of such discontinuity is analogous to that of a discrete joint in rock, whereby the moving soil mass slips about the base as an independent block. Finally, a post-peak reduction in shearing resistance is commonly observed in slow-moving or historic slides, where substantial shear displacements had already taken place, and the peak shear strength in the direction of shearing has been long exceeded.

In view that the failure at Mount Polley TSF had no observable precursors, we can surmise that, had the grain reorientation been the reason for the shear strength reduction in the Upper GLU, pre-sheared planes would have formed in this stratum prior to the embankment construction due to historic soil movement, and the addition of new loads would have merely reactivated an old slide. The presence of such historic slide would have manifested itself in two ways. First, pre-sheared planes would have been identifiable in the failure zone as well as outside it. Second, over the duration of embankment construction, there would have been no strain-weakening in the direction of shearing and residual shear resistance would have been acting along it from the start.

As discussed in §2.5, the post-failure field investigation team did not find any continuous pre-sheared planes in or outside the failure zone (IRP 2015, p. 38), despite being specifically instructed to keep an eye out for such features. In other words, there is a lack of physical evidence of grain realignment.

On the basis of the modelling results introduced in Chapters Four and Five, two additional analytical arguments will be presented here that a reduction of shear strength due to particle realignment was not a mechanism of weakening in the Upper GLU.

The first argument builds on the results of the analysis of the lower limit state introduced in §4.3.2 to demonstrate that had a pre-sheared plane been present in the Upper GLU with residual strengths acting along it, the structure would have failed at an earlier construction stage. Recall that this analysis explores the limiting case of instant full weakening at zero plastic shear deformations. In other words, it could be said that this type of analysis mimics the emergence of a pre-sheared plane more or less in step with the emergence of non-zero plastic shear strains in the normally consolidated portion of the Upper GLU, i.e. in stages 5 to 7. This analysis predicts premature failure in stage 9A, i.e. earlier than expected by about a year and at lower loading conditions. An argument can then be made that a model of Mount Polley that includes a pre-sheared plane in the Upper GLU from the get-go would predict an even earlier failure.

The second argument is made on the basis of the three-dimensional static analysis of Mount Polley introduced in §2.4 paired with conclusions reached in §6.1.4.3. The results of the static analysis show that, to bring the soil mass in the failure zone to a limiting equilibrium, the entire area of the Upper GLU involved in the failure would have to exhibit residual shear resistance. Arguably, that such condition describes a pre-sheared surface. An underlying assumption of a static analysis is that shear strengths are mobilized simultaneously across the entire slip surface. The results of deformation analysis in Chapter Four provide good indication that peak shear resistance was not mobilized simultaneously, with the rockfill not fully engaging until it accrued significant deformations, and with the upper till and core materials failing in extension by that point. Therefore, the combined findings from the two analyses invite the conclusion that, had there been a historic, continuous pre-sheared plane with residual strengths acting along it, the structure would have failed at an earlier construction stage.

Based on a lack of field evidence of pre-sheared planes and on the two analytical arguments presented above, the mechanism of shear strength reduction due to clay particle realignment can be ruled out with a reasonable level of confidence. Also on the basis the modelling results introduced in Chapters Four and Five in conjunction with field evidence and laboratory tests, the conclusion is reached that sensitivity was in fact the mechanism of shear strength reduction in the Upper GLU.

6.7.2 ON THE VALUE OF INSTRUMENTATION AT MOUNT POLLEY

The original investigators of the Mount Polley failure made note of the poor level of instrumentation and monitoring at the failure site (IRP 2015, p.13; KCB 2015, pp.10-11). Only several piezometers were installed in the area involved in the failure, with all of the tips in embankment materials, and those in place were infrequently read. There were no inclinometers at the failure location that could have potentially detected shear displacements in the foundation materials prior to the events on 4 August 2014.

In this section, we will explore the question whether having better instrumentation at the failure location would have made a difference. Specifically, it is of interest to evaluate whether inclinometers in the foundation would have offered some kind of advance warning of the impending collapse.

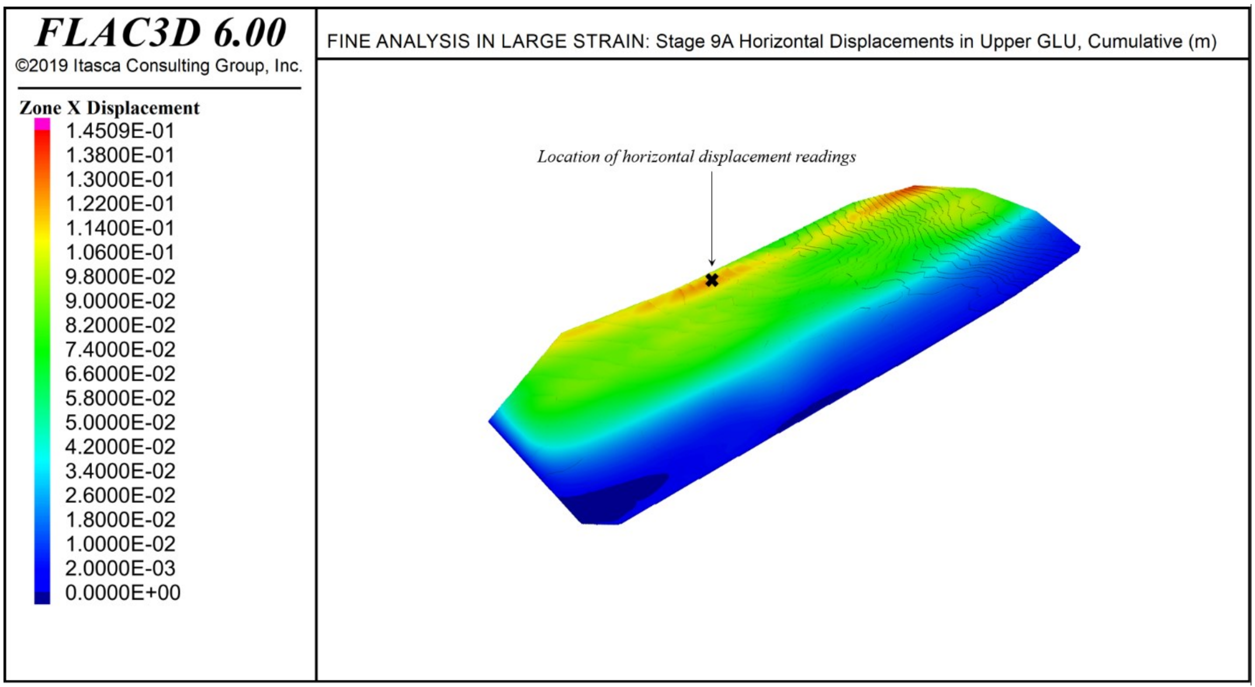

Figure 6.24 The location of simulated inclinometer readings shown in Figure 6.25 relative to the Upper GLU, and the cumulative displacements in this stratum after the completion of stage 9A.

To answer this question, the modelling results were processed to simulate inclinometer readings at a location roughly in the middle of the slide under the embankment crest. Figure 6.24 shows the location of the simulated inclinometer relative to the Upper GLU, and Figure 6.25 displays the plots of predicted cumulative horizontal displacements in the direction normal to the dam centreline after each of the construction stages 4 through 9A. The plots offer a clear indication of a shear zone that has developed at the base of the Upper GLU as early as stage 6 or 7. In this zone, displacements in the shear zone are unmistakable after the placement of stage 9A materials, almost a year prior to the collapse.

Nearly equal levels of shear deformation to those seen in the plots were predicted by all of the models irrespective of their resolution and shear band thickness (similar observations were made in §4.4.2.1); this indicates that predictions of shear deformations are not greatly affected by scale effects and that the actual shear displacements in the field were similar to those predicted. The

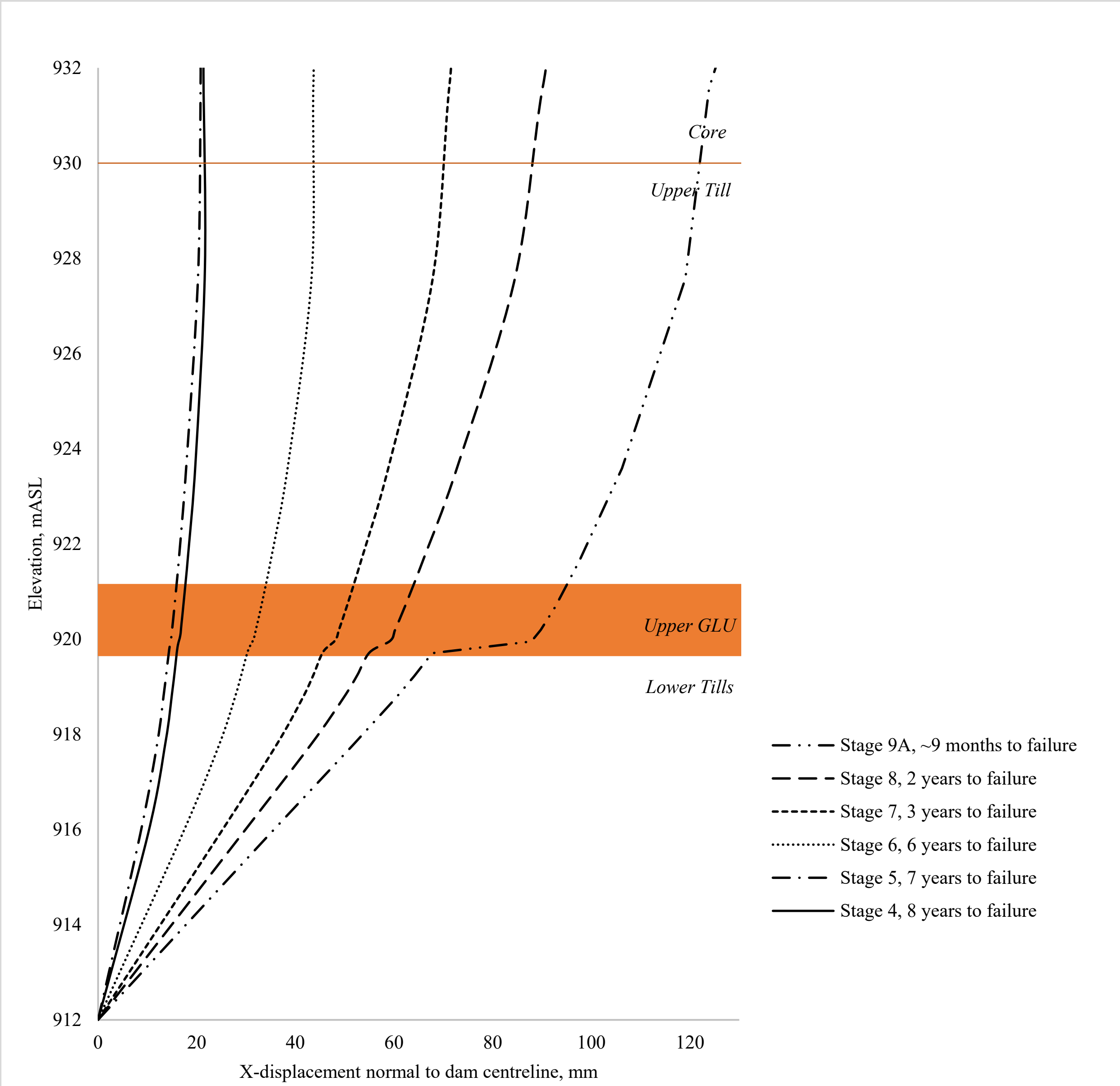

Figure 6.25 Cumulative displacements in the foundation materials at the middle of the slide under the dam crest.

development of a shear band at the base of a soil stratum, had it been detected by inclinometers, would have certainly raised concerns with the engineer of record well in advance of the collapse, opening up the possibility for mitigation measures.

The location of the simulated inclinometer was selected with the knowledge of the slide and represents a best case scenario for its placement. It is possible that the location of actual instrumentation, picked in advance by the operator, would be less fortuitous. Nonetheless, an inclinometer installed anywhere in the Upper GLU in the region of the crest would have produced similar readings; this can be appreciated from Figure 6.24 showing stage 9A cumulative horizontal displacements in the Upper GLU in the downstream direction, and from the plots included in Appendix 5C showing the evolution of cumulative horizontal displacements in the embankment. These plots indicate that between stages 3 and 9A, similar levels of shear displacements had developed in the Upper GLU everywhere under the crest and not only in the region of the future slide.

On the basis of these findings the conclusion is reached that the presence of inclinometers at or near the failure location under the crest would have offered a measure of advance warning.

This conclusion may seem somewhat counterintuitive. The collapse at Mount Polley was characterized as brittle and with no precursors that could have alerted to its nearing. The lack of apparent warning signs, such as excessive or unusual displacements at the dam surface, invited the hypothesis of non-uniform straining in the Upper GLU. On the scale of the whole structure that stood 40m tall and over 80m wide, a few cm of displacement at the face brought about by shear displacements in the Upper GLU would have been imperceptible; however, if seen on inclinometer plots as clearly originating at the base of a distinct stratum, they would have offered a measure of warning well in advance of the collapse.

6.7.3 REMARKS ON STAGE 9A STABILITY

A comment on the stability of embankment in stage 9A will be made here in the context of findings presented in §6.1.3 and §6.1.4. There is a broad conversation in the practice of engineering on what constitutes "instability," with definitions varying between fields of practice and as a function of their application (Sulem 2010). In this thesis until now, this topic has been largely circumvented in order to avoid unnecessary departures from the main subject.

Some of the limitations related to the definition of stability of a slope in terms of its safety factor as described in §3.3.4.3 have been broached in §3.3.4. In the case of Mount Polley, the biggest such limitation is probably related to the strain-weakening nature of the Upper GLU material.

In the context of the evidence presented in §6.1.3 and §6.1.4, it can be argued that the definition of stability by Lyapunov (1892) is better suited to the problem of collapse at Mount Polley. The author defines a mechanical system as stable if a small "disturbance of the initial conditions will not increase with time" (Lyapunov 1892; Sulem 2010). Conversely, the system can be thought of as unstable if minor perturbations will result in an escalating response of the system.

On the basis of this definition one can argue that the embankment at Mount Polley became unstable in stage 9A when the pre-conditions for collapse (i.e. the formation of a large area on the precipice of strain-weakening, combined with a depletion of reserve strengths in the surrounding materials and with the increased extension strains in the upper till) have materialized in the foundation and the embankment became susceptible to collapse on minor disturbance. Such disturbance was realized through a combination of added loads and toe excavation; however, as it has been shown in §6.1.5.2, the collapse response was not particularly sensitive to the type or magnitude of disturbance.

6.7.4 FUTURE RESEARCH

The deformation analysis of the progressive failure at Mount Polley was built on the foundation of an extensive database of knowledge regarding the properties of soils at the failure location that has been put together by the two original investigating teams. However, there were several areas where information was sparse. In the course of this research endeavour, a number of limitations of knowledge, both general and site-specific, have become evident. This section aims to list and briefly discuss the main such limitations and gaps of knowledge that have been identified.

6.7.4.1. DEFORMATION BEHAVIOUR OF ROCKFILL AT LOW CONFINING STRESSES

Perhaps one of the more significant findings made in the course of this study pertains to the distinctly asynchronous mechanical response in the soil mass during collapse. Such response is owed in large part to the deformation behaviour ascribed to the rockfill. This behaviour was surmised to have taken place at Mount Polley on the basis of the three-dimensional limit equilibrium analysis introduced in §2.4 as well as observations about the deformation-strength behaviour of rockfills reported by others (Leps 1970). The tentative nature of the constitutive model assigned to the rockfill in the model of Mount Polley, in particular the model of its deformation modulus described in §3.2.3.3, is predicated on a lack of data with regard to such behaviour. As a consequence, the conclusions reached using, among other things, this constitutive model should be interpreted cautiously and viewed qualitatively rather than quantitatively.

The analyses introduced in Chapters Two, Five and Six highlight the pivotal role that the rockfill played in the unfolding of collapse at Mount Polley. A sizeable fraction of the three-dimensional slip surface (visualized in Figure 4.40) would have necessarily passed through this material, meaning that its contribution to the aggregate mobilized shear resistance, or lack thereof, was substantive. The three-dimensional limit equilibrium analyses in Chapter Two demonstrate that the rockfill, with its considerable shear strength, had the potential to stabilize the structure even on full weakening of the normally consolidated portion of the Upper GLU; yet the deformation analysis indicate that this potential was not realized.

Relative to other materials at Mount Polley, the rockfill was tested minimally. Furthermore, its role in the failure was not rigorously evaluated until this study. Considering its key role in this failure demonstrated here, this material merits considerably more attention and testing budget than it has been allotted.

In light of the extensive use of rockfills as building materials in embankments, the practice of geotechnique would greatly benefit from an expanded body of knowledge about the mechanical and deformation behaviour of this class of materials. At Mount Polley, the considerable shear strength of the rockfill appears to have been under-utilized, with meaningful consequences. There is a strong economic case for the better understanding of the deformation-strength behaviour of such materials at low confining stresses and also of the impact of compaction on these.

6.7.4.2. TESTING OF NON-LINEAR STRAINING OF SOILS WITH LAYERED MACRO-STRUCTURE

The proposition of non-linear straining of the Upper GLU is at the foundation of this research undertaking and was shown to be correct by the deformation analysis reported in this thesis. The distinct layered macro-structure of this varved clay is thought to have contributed at least in some part to this behaviour.

Current testing methods for such soils are not particularly suited for assessing either the effects of macro-structure or non-linear response. The direct simple shear test, pivotal to the development of Upper GLU's constitutive model in the simulation of the failure at Mount Polley, employs soil specimen with dimensions of just few inches: ASTM D2568 setting out its standard specifies the minimum diameter of the sample at just 45mm and its height at 12mm. At such specimen height, its macro-structure would be largely eliminated, and non-linear straining tendencies would be rather difficult to identify.

Going into the future, consideration should be given to new and/or improved methods of testing that (a) would consider the effects of such macro-structure on the soil's mechanical response, and (b) would allow for the better observation of a non-linear response. Such tests may help shed light on the question of shear band thickness and contribute to our understanding of strength anisotropy.

6.7.4.3. SENSITIVITY VS. RESIDUAL STRENGTH

In the model of failure at Mount Polley, the onset of full weakening in parts of the Upper GLU was first observed in the second phase of collapse, after multiple local failures began developing in the upper till and core materials on the upstream of this unit. Therefore, the correct determination of the Upper GLU's residual strength is probably not critical to the problem of Mount Polley, as it would affect the unfolding of the failure in its final phase, but it would have no bearing on the onset of failure in the first place.

Nevertheless, the correct determination of floor values of shear strength is of general importance to geotechnical researchers. In order to effectively assess the performance of earth structures, we must clearly understand their limiting conditions, the lowest shear resistance value of soils being an important one.

Geotechnical literature does not appear to make a clear distinction between the floor values of shear strength resulting from remoulding due to sensitivity as opposed to a reduction in resistance due to particle realignment. For example, the field vane shear test has been traditionally used to evaluate sensitivity. The current ASTM standard for it specifies that the measurement of remoulded strength is taken after 5 to 10 revolutions of the vane shear while past standards have specified ranges of 5 to 25 rotations (ASTM 2573). Arguably, such testing procedure would result in the creation of a polished slip plane with preferentially aligned grains in a manner similar to that described by Morgenstern and Tchalenko (1967a), and would be more suited to evaluating residual strength due to the process of particle realignment described by Skempton (1964; 1985). A similar effect would be observed in direct shear tests that are also commonly used to evaluate residual strengths. On the other hand, the direct simple shear tests emulate the effects of remoulding, and resulting strength reduction to sensitivity, by placing the tested specimen in states of simple shear alternating from one side to another. Such manipulation fatigues the soil sample but is unlikely to create a preferential alignment of grains in the same manner as the vane shear or direct shear tests do.

The loss of strength due to these two phenomena is fundamentally different. Consider the loss of strength to sensitivity in quick clays: this effect is in no way brought about by a realignment of particles. The remoulding by hand of a slightly sensitive clay has a clear and immediate effect on its shear strength, but it is not owed to the creation of preferential slip planes brought about by such manipulation.

We must ask ourselves then, are the residual strengths brought about by sensitivity effects and by particle realignment one and the same? Do they converge? Or do we merely confound the two because they are close? It is conceivable that a soil weakening due to its sensitivity may, at large shear displacements, undergo the formation of preferential slip planes. However, géotechnique is an empirical science first and foremost, and there is a long road between something that is conceivable and something that has been shown to happen.

6.8. CONCLUSIONS

6.8.1 THE UNFOLDING OF FAILURE PRIOR TO THE COLLAPSE

The decrease in the Upper GLU's shear strength took place via two mechanisms.

First, the shear strength in the stratum was reduced from drained to undrained with its transition to a normally consolidated state. This transition took place gradually starting approximately in construction stage 5. By stage 9, the entire portion of the unit located under the embankment (one quarter to one third by area) had become normally consolidated.

Second, load-induced shear deformations in soils at or near yield conditions triggered strain-weakening in a growing portion of the Upper GLU, initiating progressive failure. The plastic yield zone first emerged during or after construction stage 7 completed in 2011 but propagated very slowly until stage 9A. The loss of shear resistance to weakening prior to the collapse was immaterial.

6.8.2 STRESS TRANSFER

With the emergence of the plastic yield zone in stage 7, an associated process of stress transfer from the weakening areas onto the neighbouring materials had initiated. Additionally, starting sometime in stage 8 or 9A (built respectively in 2012 and 2013), the portions of the Upper GLU that had newly transitioned to a state of normal consolidation at the downstream edge of this area would experience a drop in strength from drained to undrained, and, if the stresses were elevated, an associated drop in stress state. This process also triggered a stress transfer onto the downstream area.

This stress transfer processes were not particularly pronounced until stage 9A, when they became clearly discernible. One consequence of the stress transfer process was the depletion of reserve strengths in the normally consolidated portion of the Upper GLU and, by the completion of stage 9A, in its overconsolidated portion located under the embankment toe.

6.8.3 MATERIAL PRECONDITIONS FOR COLLAPSE

Three material conditions were identified to have emerged in the foundation at the failure location shortly prior to the collapse of the embankment. First, a large area in the Upper GLU came close to the point of onset of strain-weakening. Second, the reserve shear strengths in the surrounding soils became largely depleted by the ongoing stress transfer processes and growing embankment loads. Third, the upper till material above the upstream edge of the Upper GLU had been placed under some extension strain due to growing shear displacements in the Upper GLU but not upstream of it. The combination of these three conditions precipitated the embankment collapse during the ongoing construction of stage 9B on 04 August 2014.

6.8.4 THE MECHANICAL BEHAVIOUR OF SOILS DURING THE COLLAPSE

During the collapse, the soils in the failure zone exhibited a strongly asynchronous mechanic response to deformation. The unfolding of the collapse can be seen as having taken place in two distinct phases.

First, an acceleration of the progressive failure took place in the foundation in response to new embankment loads whereby the plastic yield zone rapidly expanded and the rate of loss of shear resistance increased substantially. In parallel with the unfolding progressive failure in the Upper GLU, other soil units saw their stress states increase in response to the change in loading conditions. In this phase of the collapse, the aggregate loss of shear strength in the Upper GLU was countered and possibly surpassed by the aggregate mobilization of shear strengths elsewhere in the soil mass in response to overall deformations.

After the rapid increase in the plastic yield zone and an associated shear displacements, local failures developed in the upper till above the upstream edge of the Upper GLU. This portion of soil is thought to have failed in extension and/or shear, unable to accommodate the increasing shear displacements in the Upper GLU below it. Local failures in the upper till resulted in a rapid decrease in its stress state, including the shear stresses along the critical plane. The local failures propagated shortly after into the core, to the same effect. Eventually, the combined loss of shear resistance in the Upper GLU, upper till and core on the upstream of failure overtook the rate of overall mobilization of shear strength, leading to the collapse.

Over the duration of the collapse, the rockfill in the critical zones exhibited modest increases in its mobilized shear resistance. However, its substantial shear strength was not fully realized before considerable displacements accumulated in the foundation and embankment and caused critical performance issues such as overtopping and/or excessive deformations in the core.

6.8.5 THE NONLINEAR STRAINING OF THE UPPER GLU

The hypothesis that in the failure at Mount Polley, the Upper GLU strained non-linearly was confirmed by deformation analysis. The simulations of the failure consistently predict that the Upper GLU acted not as a single block but as a layered system whereby a thin soil band located at or near the base of the stratum strained much more extensively than the soils above or below. Due to its rapid accumulation of shear strains, this shear band weakened more rapidly than the rest of the Upper GLU, thus controlling the mechanical stability of the whole structure.

The actual thickness of the shear band is thought to have ranged between 1 and 3cm.

6.8.6 COLLAPSE TRIGGER

The results of the deformation analysis in this thesis indicates that the stage 9B embankment response is not particularly sensitive to the nature of the trigger. The collapse of the slope was seen to be triggered under several loading scenarios.

6.8.7 THREE-DIMENSIONAL SLOPE STABILITY EFFECTS

During the collapse at Mount Polley, the mobilization of shear strengths was distinctly asynchronous. The three-dimensional stability effects during the collapse at Mount Polley were realized in the form of varying levels of strength mobilization along the three-dimensional slip surface, where aggregate levels of shear resistance that would be sufficient to re-stabilize the soil mass were never simultaneously actuated.

As a result of the distinctly asynchronous strength mobilization throughout the soil profile resulting from contrasting deformation-stress behaviours of soils forming the slope, the limit equilibrium analyses of this failure were in error.

6.8.8 THE MECHANISM OF SHEAR STRENGTH REDUCTION IN THE UPPER GLU

The results of the deformation analysis of the Mount Polley failure confirm that the strength reduction in the Upper GLU was owed to its sensitivity. The mechanism of shear strength reduction due to clay particle realignment at large shear displacements was ruled out.

6.8.9 THE SHAPE OF STRAIN-WEAKENING CURVE

The function that best describes the in-situ strain-weakening behaviour of the Upper GLU plots somewhere above the most conservative strain-weakening curve (seen in Figure 3.6 in red) and is probably bound on the upper end by the least conservative strain-weakening curve (seen in Figure 3.6 in black).

6.8.10 THE VALUE OF DIRECT SIMPLE SHEAR TEST

The direct simple shear test was shown to be appropriate for the purpose of evaluating the undrained shear strength behaviour of the Upper GLU in the failure at Mount Polley. This finding bolsters Ladd's (1991) endorsement of this test for the purpose of evaluating the in-situ behaviour of slightly sensitive clayey soils at the base of a slip surface.

6.8.11 SMALL STRAIN AND LARGE STRAIN CALCULATION SCHEMES

The outcomes of the simulation of the Mount Polley failure obtained in small strain are very close to those seen in large strain. Differences were noted in two areas:

- Slightly lower overburden stresses are predicted in small strain. This effect is owed to the settlement of the surface in large strain, combined with the simulation of staged loading.
- The geometry of the failure at Mount Polley predicted in large strain closely resembles that seen in the field. On the other hand, the geometry of the slip predicted in small strain is much wider than that observed in-situ.

The use small strain calculation scheme for large shear strain problems such as that of Mount Polley can be justified. A determination was also made that in modelling the problem of Mount Polley, the mesh distortion problems in FLAC3D under the large strain calculation scheme were minor and were managed with relative ease.

6.8.12 THE VALUE OF SLOPE INSTRUMENTATION

On examination of the simulation results, the conclusion was reached that inclinometers installed in the upstream portion of the Upper GLU would have offered a measure of advance warning about the impending collapse.

6.8.13 FUTURE RESEARCH

Some areas of interest for future research were identified:

- The deformation-strength behaviour of rockfills at low confining stresses and the effects of compaction on these.
- Testing methods to assess the non-linear straining of materials and the evaluation of effects that macro-structure may have on a soil's mechanical response.
- The investigation of floor values of shear strength as a result of (a) soil sensitivity and (b) grain realignment.

BIBLIOGRAPHY

Akhtar, K. (2011). *Three dimensional slope stability analyses for natural and manmade slopes*. PhD thesis, University of Illinois, Urbana, Illinois.

Akhtar, K. and T.D. Stark. *Importance of side resistance in 3D stability analysis*. ASCE, *In* Proceedings of GeoFrontiers 2017 Specialty Conference, Orlando, Florida.

E. E. Alonso, M. Tapias, and J. Gili (2012). *Scale effects in rockfill behaviour.* Géotechnique Letters **2**(*3*): 155-160.

Arellano, D. and T.D. Stark. *Importance of three dimensional slope stability analysis in practice*. *In* Proceedings of Slope Stability 2000 Specialty Conference, Denver, Colorado, 5-8 August 2000. ASCE, Geotechnical Special Technical Publication No. 101:18-32.

ASTM International (2018) ASTM D2573/D2573M: *Standard Method for Field Vane Shear Test in Saturated Fine-Grained Soils*. West Conshohocken, PA: American Society for Testing and Materials.

ASTM International (2017) D6528-17: *Standard Test Method for Consolidated Undrained Direct Simple Shear Testing of Fine Grain Soils*. West Conshohocken, PA: American Society for Testing and Materials.

Azam, S. and R. Chowdhuri. *Engineering properties of an expansive soil*. *In* Proceedings of the 18th Intl. Conference on Soil Mechanics and Geotechnical Engineering, Paris 2013, pp. 199-202.

Basaran, Salami. *Lagrangian and Eulerian Descriptions in Solid Mechanics and Their Numerical Solutions in hpk Framework*. Diss. University of Kansas. 2008. http://hdl.handle.net/1808/3946 accessed 04 February 2019.

Becker, E., Chan, C. K. & Seed, H. B. (1972). Strength and deformation characteristics of rockfill materials in plane strain and triaxial compression tests, Report No. TE-72.3. Department of Civil and Environmental Engineering, University of California, Berkeley.

Bishop, A.W. (1955). The use of the slip circle in the stability analysis of earth slopes. Géotechnique **5**(1): 7-17.

Bishop, A.W. (1957). *Contribution to discussion on "The Usk scheme for the water supply of Swansea."* G.A.R. Sheppard and L.B. Aylen. In Proceedings of Instn. Of Civil Engineers 7: 281.

Bishop, A.W. and R.N. Morgenstern (1960). *Stability coefficients for earth slopes*. Géotechnique **10**(*4*): 129-150.

Bjerrum, L. (1954). Geotechnical properties of Norwegian marine clays. Géotechnique, **4**(2): 49-69.

Bjerrum, L. (1967). Engineering geology of Norwegian normally-consolidated marine clays as related to settlements of buildings. Géotechnique **17**(2): 83-118.

Bjerrum, L.. P*roblems of soil mechanics and construction on soft clays and structurally unstable soils (collapsible, expansive and others).* In Proceedings of the 8th Intl. Conference on Soil Mechanics and Foundation Engineering, Moscow 1973, pp. 111–159.

Bjerrum, L. and B. Kjaersnsli (1957). *Analysis of the stability of some Norwegian natural clay slopes*. Géotechnique **7**(1): 1-16.

Bjerrum, L. and A. Landva (1966). *Direct simple-shear tests on a Norwegian quick clay*. Géotechnique, **16**(*1*): 1-20.

British Columbia. Ministry of Energy and Mines. Mining and Mineral Resource Division. *Investigation Report of the Chief Inspector of Mines: Mount Polley Mine Tailings Storage Facility Breach*. Ministry of Energy and Mines, November 30, 2015. 188 pages.

Boutrup, E., and C.W. Lovell (1980). *Search technique in slope stability analysis*. Engrg. Geol. **16**(*1*): 51-61.

Bowles, Joseph E. *Foundation Analysis and Design.* 4th Ed. New York: McGraw-Hill, 1988.

Burland, J.B. and M.C. Burbridge. *Settlement on foundations of sand and gravel.* In Proceedings of Instn. Civ. Engrs 1985, Part 1, pp. 1325-1381.

Cadling, L. and S. Odenstad (1950). *The vane borer. In* Proceedings of Royal Swedish Geotechnical Institute No. 2.

Capozio, N.U., J. M. Ouimet, M. M. Dupuis (1982). *Geotechnical problems related to the building of a tailings dam on sensitive varved clay*. Canadian Geotechnical Journal **19**(*4*): 472-482.

Cavounidis, S. (1987). On the ratio of factors of safety in slope stability analysis. Géotechnique, **37**(2): 207-210.

Cedergren, Harry R. *Seepage, Drainage, and Flow Nets.* 3rd Ed. New York: Wiley, 1989. ISBN-10: 0471611786.

Celestino, T. B., and Duncan, J.M. (1981). *Simplified search for non-circular slip surface*. *In* Proceedings of 10th Int. ConI. on Soil Mech. and Found. Engrg., A.A. Balkema, Rotterdam, The Netherlands **3**: 391-394.

Chambon, René (2002). *Small strain vs large strain formulation in computational mechanics*. Revue Française de Génie Civil, **6**(*6*): 1037-1049.

Chambon, R., D. Caillerie, and G. Viggiani (2004). *Loss of uniqueness and bifurcation vs instability: some remarks.* Revue Française de Génie Civil **8**(*5-6*): 517-553.

Chan, D., Professor, Civil and Environmental Engineering, *CIVE 664 class notes.* University of Alberta, 2016.

Chang, C. S., and Duncan, J. M. (1977). *Analysis of consolidation of earth and rocklill dams*. Geotech. Engrg. Rep. No. TE 77-3, U.S. Army Engr. Wtwy. Experiment Stn., Vicksburg, Miss.

Chaudhary, K., V. Domingos, G. Gitirana, M. Fredlund, H.-H. Lu. *Three-Dimensional Slope Stability: Geometry Effects*. *In* Proceedings of Tailings and Mine Waste 2016, Keystone, Colorado.

Chen, Wa-I-Fah. *Limit Analysis and Soil Plasticity*. Ft. Lauderdale, FL: J. Ross Pub, 2007. ISBN: 978-1-932159-73-8.

Chen, R.H. and Chameau, J.L. (1982). *Three-dimensional limit equilibrium analysis of slopes*. Géotechnique **32**(*1*): 31-40.

Ching, Jianye, Kok-Kwang Phoon (2013). *Multivariate distribution for undrained shear strengths under various test procedures*. Canadian Geotechnical Journal, 2013, 50(9): 907-923.

Clifton, A.W., D.G. Fredlund and O. Mickleborough (1986). *Highwall stability analysis under dragline loadings at a Saskatchewan coal mine*. *In* Proceedings of Intl. Symposium on Geotechnical Stability in Surface Mining, Calgary, AB: 341-353.

Clough, R.W. and Woodward, R.J. (1967). *Analysis of embankment stresses and deformations*. J. Soil Mech. and Found. Div., ASCE **93**(*4*): 529-549.

Conte, E., A. Donato and A. Troncone (2013). Progressive failure analysis of shallow foundations on soils with strain-softening behaviour. Computers and Geotechnics **54**: 117-124.

Conte, E., F. Silvestri and A. Troncone (2010). *Stability analysis of slopes in soils with strain-softening behaviour*. Computers and Geotechnics **37**: 710–722.

Dawson E. M., W. H. Roth, and A. Drescher (1999). *Slope stability analysis by strength reduction.* Géotechnique, **49**(*6*): 835-840.

Dey, R., B. Hawlader, R. Phillips and K. Soga (2015). *Large deformation finite-element modelling of progressive failure leading to spread in sensitive clay slopes.* Geotechnique **65**(*8*): 657-668.

Dolbow, J. and T. Belytchko (1998). *An introduction to programming meshless element free Galerkin method*. Archives of Computational Methods in Engineering **5***(3)*: 204-241.

G. T. Dounias, D. M. Potts, and P. R. Vaughan (1988). *Finite element analysis of progressive failure: two case studies.* Computers and Geotechnics **6**(*2*): 155–175.

Dow John O. A Unified Approach to the Finite Element Method and Error Analysis Procedures. Academic Press 2013, 564 pages, ISBN 0123995450.

Drucker, D., & Prager, W. (1952). *Soil Mechanics and Plastic Analysis or limit design*. Quarterly of Applied Mathematics, **10***(2)*: 157-165.

Duncan, J. M. (1996). *State of the art: limit equilibrium and finite-element analysis of slopes*. J. Geotech. Engn Div. Am. Soc. Civ. Engrs **122***(7)*: 577-596.

Duncan, J.M., and C.Y. Chang, (1970). *Nonlinear analysis of stress and strain in soils*. J. Soil Mech. and Found. Div., ASCE **96***(5)*:1629-1653.

Duncan, J.M. and P. Dunlop (1969). *Slopes in stiff fissures clays and shales.* J. Soil Mech. and Found. Div. ASCE **96***(2)*: 471-494.

Duncan, J.M., G. Lefevbre and P. Lade (1980). *The landslide at Tuve, near Göteborg, Sweden, on November 30, 1977*, report to National Research Council, National Academy of Sciences. National Academy Press, Washington, D.C..

Duncan, J.M. and S.G.Wright. *Soil strength and slope stability*. Hoboken NJ, John Wiley and Sons 2005. ISBN: 0-471-69163-1.

Eid, H. T. (2010). Two and three dimensional analyses of translational slides in soils with nonlinear failure envelopes. Canadian Geotech. J. **47**(4): 388-399.

Eid, H. T., Elleboudy, A. M., Elmarsafawi, H. G., and Salama, A. G. (2006). *Stability analysis and charts for slopes susceptible to translational failure*. Canadian Geotech. J., **43**(*12*): 1374-1388.

Eide, O. and L. Bjerrum (1955). *The slide at Bekkelaget*. Geotechnique **5***(1)*: 88-100.

Eisenstein, Z., and Simmons, J. V. *Three-dimensional analysis of Mica Dam*. In Proceedings Int. Symp. Criteria and Assumptions for Numer. Anal. of Dams. Quadrant, Swansea, U.K., 1975, pp. 1051-1070.

El-Ramly, H., N.R. Morgenstern and D.M. Cruden (2003). *Probabilistic stability analysis of a tailings dyke on presheared clay-shale*. Can. Geotech. J. **40**: 192-208.

El-Ramly, H., N.R. Morgenstern and D.M. Cruden (2002). *Probabilistic stability analysis for practice*. Can. Geotech. J. **39**: 665-683.

Fan K., Fredlund, D.G., and Wilson, G.W. (1986). *An interslice force function for limit equilibrium slope stability analysis.* Can. Geotech. J. **23**: 287-296.

Fellenius, B. (1955). *The landslide at Guntorp*. Géotechnique **5***(1)*: 120-128.

Fellenius, W. (1936). *Calculation of the stability of earth dams*. *In* Proceedings of the 2nd Intl. Congress on Large Dams, Washington, D.C. **4**: 445.

FLAC3D 6.0 Documentation. Itasca™ Consulting Group, Inc. Minneapolis MN, USA. 22 April 2018.

Fortin, Michel, and R Glowinski. Augmented Lagrangian Methods: Applications to the Numerical Solution of Boundary-value Problems. Amsterdam: North-Holland Pub. Co., 1983.

G. Frantziskonis, C.S. Desai (1987). *Constitutive model with strain softening.* International Journal of Solids and Structures **23***(6)*: 733-750.

Fredlund, Murray, Senior Director, SoilVision Systems Ltd. Personal interview 05 March 2019.

Fredlund, D.G. and J. Krahn (1977). *Comparison of slope stability methods of analysis.* Can. Geotech. J. **14**: 429-439.

Fredlund, M., H.-H. Lu, Z. Ivkovic, G. Gitirana. *Multi-Plane Slope Stability Analysis of Tailings Dams. In proceedings* Tailings and Mine Waste 2017, Banff, Alberta. University of Alberta Geotechnical Centre, 2017, pp. 514-523.

Galerkin, B.G. (1915) Series solution of some problems of elastic equilibrium of rods and plates. (in Russian). Vestn. Inzh. Tech. **19**: 897-908.

Gens, A., Hutchinson, J.N. and Cavounidis, S. (1988). *Three-dimensional analysis of slides in cohesive soils*. Géotechnique **38***(1)*: 1-23.

Gitirana, G. Jr., M.A. Santos and M.D. Fredlund. *Three-dimensional analysis of the Lodalen Landslide*. ASCE GeoCongress 2008, New Orleans, US, March 9-12.

Golder Associates. *Mount Polley Mine Tailings Storage Facility, Perimeter Embankment Breach; Update Report: Post-Event Environmental Impact Assessment Report.* Report No. 1411734-124-R-Rev0-10000. Submitted to Mount Polley Mining Corporation, 3 June 2016. 73 pages. Available from: http://www2.gov.bc.ca/assets/gov/environment/air-land-water/spills-and-environmental-emergencies/docs/mt-polley/p-o-r/2016-06-03_peeiar_summary_report_v2.pdf [Accessed 28 August 2017].

Golder, H.Q., and D.J. Palmer (1955). Investigation of a bank failure at Scrapsgate, Isle of Sheppey, Kent. Géotechnique **5**(1): 55-73.

Griffiths D. V. and P. A. Lane (1999). *Slope stability analysis by finite elements*. Géotechnique, **49**(*3*): 387-403.

Hall, E.B. and B.B. Henkel. *Triaxial testing using large scale high pressure equipment.* Special Technical Publication No. 361, ASTM Symposium September 1963.

Hammah, R.E., Yacoub, T.E., Corkum, B.C. and Curran, J.H. *The Shear Strength Reduction Method for the Generalized Hoek-Brown Criterion.* Alaska Rocks 2005, The 40th U.S. Symposium on Rock Mechanics (USRMS): Rock Mechanics for Energy, Mineral and Infrastructure Development in the Northern Regions, held in Anchorage, Alaska, June 25-29, 2005. American Rock Mechanics Association (ARMA), 2005.

Hashiguchi, K. (1993). Fundamental requirements and formulations of elastoplastic constitutive equations with tangential plasticity. International J. of Plasticity **9**(5): 525-549.

Henkel, D.W. (1956). The effect of overconsolidation on the behaviour of clays during shear. Géotechnique, **11**(4): 135-150.

Henkel, D.J. and A.W. Skempton (1955). A landslide at Jackfield, Shropshire, in a heavily over-consolidated clay. Géotechnique, **5**(2): 131-137.

Hill, R. (1962) *Acceleration waves in solids*. J. Mech. Phys. Solids **10**: 1-16.

Hobbs, Bruce E., and Alison Ord. *Structural Geology : The Mechanics of Deforming Metamorphic Rocks*. Elsevier, 2015. ISBN: 9780124079335.

Hodge, Robert A.L. and R. Allan Freeze (1977). *Groundwater flow systems and slope stability*. Canadian Geotechnical Journal **14**(*4*): 466-4776.

Hoek, E. (1983). *Strength of jointed rock masses*. Géotechnique **33***(3)*: 187-223.

Hoek, E., and Bray, J. 1977. *Rock slope engineering*. 1st Ed. The Institution of Mining and Metallurgy, London, United Kingdom. Accession No. 1977-039835.

Holtz, W.G. and Gibbs, H.J. (1956). *Triaxial tests on pervious gravelly soils.* J. of Soil Mech. and Found. Div. ASCE Vol. 82, No. SM1, Proc. Paper 867: 1-22.

Holtz, R. D, William D Kovacs, and Thomas C Sheahan. *An Introduction to Geotechnical Engineering*. 2nd ed. Upper Saddle River, NJ: Pearson, 2011. ISBN: 9780130317216.

Hovland, H.J. (1977). *Three-dimensional stability analysis method*. ASCE Journal of the Geotechnical Engineering Division **103**(*GT9*): 971-986.

Hungr, O. (1987). An extension of Bishop's simplified method of slope stability analysis to three-dimensions. Géotechnique, **37**(1): 113-117.

Hungr, Oldrich, F. M. Salgado, P. M. Byrne (1989). *Evaluation of a three-dimensional method of slope stability analysis*. Canadian Geotechnical Journal, **26***(4)*: 679-686.

Hutchinson, J.N. and Sarma (1985). Discussion of three-dimensional limit equilibrium analysis of slopes by R.N. Chen and J.L. Chameau. Géotechnique, **35**(2): 215-216.

Hutchinson, J.N. (1961). A landslide on a thin layer of quick clay at Furre, Central Norway. Géotechnique, **11**(2): 69-94.

Independent Expert Engineering Investigation and Review Panel (IRP). *Report on Mount Polley Tailings Storage Facility Breach*. Government of British Columbia, January 30, 2015. 147 pages.

Ireland, H.O. (1954). Stability analysis of the Congress Street open cut in Chicago. Géotechnique **4**(4): 163-168.

Jaeger, J.C. *The behaviour of closely jointed rock*. In Proceedings of 11th Symposium of Rock Mechanics, Berkeley 1970, 57-68.

Jaeger J.C. (1971). 11th Rankine Lecture: Friction of Rocks and Stability of Rock Slopes. Géotechnique, **21**(2): 97-134.

Janbu, N. *Application of Composite Slip Surface for Stability Analysis.* European Conference on Stability Analysis 1954, Stockholm, Sweden.

Janbu, N. (1973). *Slope stability computations*. *In* Embankment-Dam Engineering: Casagrande Volume, R.C. Hirschfeld and S.J. Pouros, Eds., Wiley, Hoboken, NJ, pp. 47-86.

Janbu, N., Bjerrum, L. and Kjaernsli, B. (1956). *Veiledning ved Løsning av Fundamenteringsoppgaver.* Publication 16, Norwegian Geotechnical Institute, Oslo.

Jefferies, M., R.N. Morgenstern, D. Van Zyl and J. Wates. *Report on NTSF Embankment Failure, Cadia Valley Operations for Ashurst Australia.* Report No. H356804-00000-22A-230-0001. April 17, 2019. https://www.newcrest.com/sites/default/files/2019-10/190430_NTSF%20Embankment%20Slump%20Report%20-%20Market%20Release.pdf.

Kézdi, Árpád. *Handbook of Soil Mechanics.* Amsterdam: Elsevier Scientific Publishing Co., 1974.

Kjaernsli, B. and N. Simons (1962). Stability investigations of the north bank of the Drammen River. Géotechnique **12**(2): 147-168.

Kjellman, W. (1955). *Do slip surfaces exist?* Géotechnique **5**(*1*): 18-22.

Kiernan, M. and J. Montgomery. *Numerical simulations of the Fourth Avenue landslide considering strain-softening. In* Proceedings of American Society of Civil Engineers' Geotechnical Earthquake Engg. And Soil Dynamics V, June 10-13 2018.

Klohn, Crippen and Berger (KCB). *Mount Polley tailings dam failure – Assessment of failure mechanism*. Report no. M09954A01.730. BC Ministry of Energy and Mines, 1 May 2015. 978 pages.

Kötter, F. (1903). *Die Bestimmung des Drucks angekrummten, eine Aufgabe aus der Lehre vom Erddruck*. Sitzungsberichte der Akademie der Wissenschaften, Berlin, 229–233.

Kulhawy F.H. and J.M. Duncan. (1972). *Stresses and movements in Oroville dam*. J. Soil Mech. and Found. Diy., ASCE, **98***(7)*: 653665.

Kulhawy, F.H., J.M. Duncan and H. Bolton Seed. *Finite element analyses of stresses and movements in embankments during construction. A report of an investigation.* Berkeley, California, US. University of California, 1969. Contract report S-69-8. Contract No. DACW39-68-C-0078 with U.S. Army Engineers Waterways Experiment Station, Corps of Engineers, Vicksburg MS.

Lacasse, S.M., C.C. Ladd and A.K. Barsvary (1977). *Undrained behaviour of embankments on new Liskeard clays.* Canadian Geotechnical Journal, 1977, **14**(*3*): 367-388.

Ladd, C. (1991). *The Twenty-Second Karl Terzaghi Lecture: Stability evaluation during staged construction*. Journal of Geotechnical Engineering, **117**(*4*): 540-615.

Ladd, C.C., and Fott, R. (1974). *New design procedure for stability of soft clay*. J. Geotech. Engrg. Div., **100**(*7*): 763–786.

Lam, L. and Fredlund, D.G (1993). A general limit equilibrium model for three-dimensional slope stability analysis. Can. Geotech. J., **30**(6): 905-919.

Li, G. C., and Desai, C. S. (1983). Stress and seepage analysis of earth dams. J. Geotech. Engrg., ASCE, **109***(7)*: 946-960.

Lee, K.L. and J.M. Duncan (1975). *Landslide of April 25, 1974, on the Mantaro River in Peru,* report of inspection submitted to the Committee on Natural Disasters, National Research Council, National Academy of Sciences, Washington, D.C.

Leps, T.M. (1970). *Review of shearing strength of rockfill*. *In* Proceedings of American Society of Civil Engineers, J. Soil Mechanics and Foundations Division Vol. **96**: 1159-1170.

Lobbestael, A.J. A. Athanasopoulos-Zekkos, and J. Colley (2013). Factor of Safety Reduction Factors for Accounting for Progressive Failure for Earthen Levees with Underlying Thin Layers of Sensitive Soils. Mathematical Problems in Engineering, Vol. 2013, Article ID 893602. https://doi.org/10.1155/2013/893602.

Lu, HaiHua, Software Developer, SoilVision Systems Ltd. Email communications 16 April 2019.

Lyapunov, A.M. *The general problem of stability of motion*, 1892, English translation, Taylor & Francis.

Marachi, N. D., Chan, C. K. & Seed, H. B. (1972). *Evaluation of properties of rockfill materials*. J. Soil Mech. Found. Div. 98, No. SM1: 95–114.

Marachi, N. D., Chan, C. K., Seed, H. B. & Duncan, J. M. (1969). *Strength and deformation characteristics of rockfills materials, Report No. TE-69-5.* Department of Civil Engineering/Geotechnical Engineering, University of California, Berkeley.

Marsal, R.J. (1973). *Mechanical properties of rockfill. Embankment Dam Engineering*, Casagrande Vol., 109-200. New York: Wiley. Accession Number: 00096416.

Marsal, J. Raul (1967). *Large scale testing of rockfill materials.* Journal of the Soil Mechanics and Foundations Division, ASCE **93**(*2*): 27-43.

Marsal, Raul J., Gomez, E.M., Nunez, A.K. Cuellar, R.B. and Ramos, R.M. *Research on the behaviour of granular materials and rockfill samples.* Comission federal de electricidad, Mexico 1965, 76 p.

Matsui, T. & San, K.-C. (1992). Finite element slope stability analysis by shear strength reduction technique. Soils Found., **32**(1): 59-70.

McAndless, P. and Taylor, C. *Surficial Geology of the Mount Polley Property: Summary of 2005 Exploration Work*. Imperial Metals Corporation, 2005.

Mitchell, J.K. R.B. Seed, and H.B. Seed (1990). *Kettleman Hills waste landfill slope failure. I: Liner-system properties*. ASCE J. Geotech. Engg., **116**(*4*): 647-668.

Morgenstern, N.R., and Price, V.E. (1965). *The analysis of the stability of general slip surfaces.* Géotechnique, **15**(*1*): 79–93.

Morgenstern N. R.and J.S. Tchalenko (1967a). *Microscopic Structures in Kaolin Subjected to Direct Shear*. Géotechnique, **17**(*4*): 309-328.

Morgenstern, N.R. and J.S. Tchalenko (1967b). *Micro-structural observations on shear zones from slips in natural clays*. In Proceedings of Geotechnical Conference 1967, Oslo Vol. 1: 147-152.

Nguyen, V.U. (1985). *Determination of critical slope failure surface*. J. Geotech. Engrg., ASCE, **111**(*2*): 238-250.

Obrzud, R.F. and A. Truty. *A hardening soil model – a practical guidebook.*Z_Soil.PC 100701 report, revised 2018. http://www.zsoil.com/zsoil_manual_2018/Rep-HS-model.pdf.

Peck, R.B. and Wm.C. Reed (1954). *Engineering properties of Chicago subsoils*. University of Illinois Engineering Experiment Station Bulletin No. 423.

Penman, A.D., J.B. Burland and J.A. Charles. *Observed and predicted deformations in a large embankment dam during construction*. In Proceedings Ins. Civ. Engrs., London, 1971, **49**: 1-21.

Penner, E. (1963). *Sensitivity in Leda clay*. Nature **197**(*4865*): 347-348.

Petterson, K.E. (1955). *The early history of circular sliding surfaces*. Geotechnique 5(4): 275-296.

Potts, D. M., Dounias, G. T. & Vaughan, P. R. (1990). *Finite element analysis of progressive failure of Carsington embankment*. Géotechnique, **40**(*1*): 79-101.

Potts, D.M., N. Kovacevic and P.R. Vaughan (1997). *Delayed collapse of cut slopes in stiff clay*. Géotechnique **47**(*5*): 953-982.

Quigley, E W., Duncan, J. M., Caronna, S., Moroux, P. J., and Chang, C. S. (1976). *Three dimensional finite element analyses of New Melones Dam*. Geotech. Engrg. Rep. No. TE-3, Univ. of California, Berkeley, Calif.

Quinn, Joseph, Bill Chin, Mark Pernito and Jody Scammell (2014). *Geotechnical assessment of Alameda Dam*. *In* proceedings of GeoRegina 2014.

Quinn P. 2009. Large Landslides in Sensitive Clay in Eastern Canada and the Associated Hazard and Risk to Linear Infrastructure. Doctoral thesis, Queen's University.

Reyes, A. and D. Parra (2014). *3D slope stability analysis by the using limit equilibrium method analysis of a mine waste dump*. *In* Proceedings of Tailings and Mine Waste, October 5-8, Keystone, CO: 127-139.

Robertson, P.K. (2009). Interpretation of cone penetration tests – a unified approach. Canadian Geotech. J., **46**(11):1337–1355.

Robertson, P.K., L. de Melo, D.J. Williams and G.W. Wilson. *Report of the expert panel on the technical causes of the failure of Feijão Dam I.* December 12, 2019. http://www.b1technicalinvestigation.com/ accessed December 2019.

Rocscience Inc. *CPT Data Interpretation Theory Manual*. 2016. https://www.rocscience.com/help/settle/pdf_files/theory/CPT_Theory_Manual.pdf accessed 2017-2019.

Rosengren, K.J. and Jaeger, J.C. (1968). *The mechanical properties of an interlocked low porosity aggregate*. Géotechnique, **18***(3)*: 317-328.

Rosenqvist, I.Th. (1953). *Sensitivity of Norwegian quick-clays*. Géotechnique **3**(*5*): 195-200.

Roscoe, K.H. and Burland, J.B. (1968). *On the generalized stress-strain behaviour of "wet" clay.* Engineering Plasticity, Cambridge Univ. Press: 535–609.

Roscoe, K.H., Schofield, A.N. and Thurairajah, A. (1963) *Yielding of clays in states wetter than critical*. Géotechnique, **13***(3)*: 211-240.

Russell, David, Chief Software Architect, Itasca™. Personal interview 05 July 2018.

Schantz, T, P.A. Vermeer and P.G. Bonnier. *The hardening soil model: formulation and verification.* In Proceedings of Beyond 2000 in Computational Geotechnics, 10 years of Plaxis © Balkema, Rotterdam, 1999 ISBN 90 5809 040 X.

Schweiger, H.F. (2008). *The Role of Advanced Constitutive Models in Geotechnical Engineering*. Geomechanics and Tunnelling, **1***(5)*: 336-344, Wiley Online Library.

Seco E Pinto, P. S., and Marahna das Nevas, E. *Hydraulic fracturing in zoned earth and rockfill dams*. In Proceedings 11th Int. Con. on Soil Mech. and Found. Engrg., A. A. Balkema, Rotterdam, The Netherlands, 1985, **4**: 2025 - 2030.

Seed, R.B., J.K. Mitchell and H.B. Seed (1990). *Kettleman Hills waste landfill slope failure. II: Stability analyses*. ASCE J. Geotech. Engg. **116**(*4*): 669-690.

Sevaldson, R.A. (1956). *The slide in Lodalen, October 6, 1954*. Géotechnique, **6**(*4*): 167-182.

Siegel, R.A., Kovacs, W.D. and Lovell, C.W. (1981). *Random surface generation in stability analysis*. J. Geotech. Engrg., ASCE **107**(*7*): 996-1002.

Silvestri, T. (1961). Experimental determination of the shearing strength of rockfill. Geotecnica, **8**: 186-191.

Skempton, A.W. (1945). *A slip in the west bank of the Eau Brink cut*. J. Instn. Civil Engineers, **24**(*7*): 267.

Skempton, A.W. (1964). Fourth Rankine Lecture: Long-Term Stability of Clay Slopes. Géotechnique, **14**(2): 77-102.

Skempton, A.W. (1985). Residual strength of clays in landslides, folded strata and the laboratory. Géotechnique, **35**(1): 3-18.

Skempton, A.W. and J.D. Brown (1961). *A landslide in boulder clay at Selset, Yorkshire*. Géotechnique, **11***(4)*: 280-293.

Skempton, A.W. and R.D. Northey (1952). *The sensitivity of clays*. Géotechnique, **3**(*1*): 30-54.

Skempton, A.W. and D.J. Petley. *The strength along structural discontinuities in stiff clays.* In Proceedings of Geotechnical Conference 1967, Oslo Vol. 2: 29-46.

Slaughter, William S. *The Linearized Theory of Elasticity.* Boston, MA: Birkhäuser Boston , 2002.

SNC Lavalin and the Mount Polley Mining Corporation (2014). *Mount Polley Progress Report*. Report No. 621717. Submitted to the Government of British Columbia. 73 pages. Available from: http://www2.gov.bc.ca/assets/gov/environment/air-land-water/spills-and-environmental-emergencies/docs/mt-polley/p-o-r/2014-09-15_mpmc_progress_report.pdf [Accessed 28 August 2017].

SoilVision Systems Ltd. Team. (2019). SVSlope Verification Manual. Accessed at https://soilvision.com/downloads/docs/pdf/manuals/SVSLOPE5_Verification_Manual.pdf.

SoilVision Systems Ltd. Team. (2018). SVFlux Verification Manual. Accessed at https://soilvision.com/downloads/docs/pdf/manuals/SVFLUX5GT_Verification_Manual.pdf.

Spencer, E. (1967). A method of analysis of the stability of embankments assuming parallel inter-slice forces. Géotechnique, **17**: 11-26.

Stark, T.D. and Eid, H.T. (1998). *Performance of three-dimensional slope stability methods in practice*. Journal of Geotechnical Engg. 316 Division, ASCE, **124**(*11*): 1049-1060.

Stark, T.D. and D.G. Ruffing. *Selecting minimum factors of safety for 3D slope stability analyses*. *In* Proceedings of GeoRisk 2017, Boulder, Colorado. ASCE, Geotechnical Special Publication No. 283: 259-266.

Stianson, Jason Robert. *A three-dimensional slope stability method based on finite element stress analysis and dynamic programming*. PhD Thesis, University of Alberta, 2008.

Sulem J. (2010). *Bifurcation theory and localization phenomena.* European Journal of Environmental and Civil Engineering, Ed. Lavoisier, **14**(*8-9*): 989-1009.

SVOffice 5 Help Manual. SoilVision Systems Ltd. Saskatoon SK, Canada. 03 December 2018.

Tanaka, T., and Nakano, R. *Finite element analysis of Miyama rockfill dam*. In Proceedings Con. Numer. Meth. in Geomech., ASCE, New York, 1976, pp. 650-661.

Tankiewicz, M. (2015). *Experimental investigation of strength anisotropy of a varved clay*. Procedia Earth and Planetary Science, **15**: 732-737.

Tavenas F., Flon P., Leroueil S. and Lebuis J. 1983. *Remolding energy and risk of slide retrogression in sensitive clays.* Proc. of the Symposium on Slopes on Soft Clays, Linköping, Sweden, SGI Report No. 17, 423-454.

Tavenas F. 1984. *Landslides in Canadian sensitive clays — a state-of the-art.* Proc. of the 4th Int. Symposium on Landslides, Toronto, Ont., 1, 141-153.

Terzaghi, K.(1944). *Ends and Means in Soil Mechanics*. Engineering Journal of Canada, **27**: 608.

Thakur, Vikas. *Strain Localization in sensitive soft clays.* PhD Thesis, Norwegian University of Science and Technology, Trondheim, Norway, 2007.

Toyota, H., A. Susami and S. Takada (2014). Anisotropy of Undrained Shear Strength Induced by K_0 Consolidation and Swelling in Cohesive Soils. Intl. J. Geomechanics, **14**(4): 1-17.

Troncone A., E. Conte, A. Donato (2016). *Three-dimensional Finite Element Analysis of the Senise Landslide*. Procedia Engineering, **158**: 212-217.

Troncone, A. (2005). Numerical analysis of a landslide in soils with strain-softening behaviour. Géotechnique, **55**(8): 585–596.

Vardoulakis, I. (1976). *Equilibrium theory of shear bands in plastic bodies*. Mechanics Research Communications, **3**(*3*): 209-214.

Vardoulakis, I. and J. Sulem. *Bifurcation analysis in geomechanics.* Chapman and Hall, Suffolk Great Britain 1995. ISBN: 0 7514 0214 1

Vermeer, P.A. (1978). *A double hardening model for sand*. Geotechnique **28***(4)*: 413–433.

Wang, Q. *Finite difference, finite volume, and finite element methods*. YouTube, 4 September 2017, https://www.youtube.com/watch?v=prql73vq9sk&t=483s.

Wrzesinski, G. and Z. Lechonowicz (2013). *Influence of the rotation of principal stress directions on undrained shear strength*. Annals of Warsaw University of Life Sciences – SGGW, Land Reclam., **45**(*2*): 183-192.

N. Yoshida, N. R. Morgenstern, and D. H. Chan (1990). *A failure criterion for stiff soils and rocks exhibiting softening*. Canadian Geotechnical Journal **27**(*2*): 195–202.

Yu, H., Salgado, R., Sloan, S., and Kim, J. (1998). *Limit Analysis versus Limit Equilibrium for Slope Stability*. J. Geotech. Geoenviron. Eng., **124**(*1*): 1-11.

Zhang, K., Cao, P. & Bao, R. (2013). *Progressive failure analysis of slope with strain-softening behaviour based on strength reduction method.* J. Zhejiang Univ. Sci. A **14**(*2)*: 101-109. https://doi.org/10.1631/jzus.A1200121

Zhang, L., M.D. Fredlund, D.G. Fredlund and H. Lu. *Comparison of 2-D and 3-D slope stability analyses for unsaturated soil slopes*. *In* Proceedings of GeoRegina 2014, Regina, SK.

Zienkiewicz, O.C., C. Humpheson and R.W. Lewis (1975). *Associated and non-associated visco-plasticity and plasticity in soil mechanics*. Géotechnique, **25***(4)*: 671-689.

Zienkiewicz, O. C and Robert L Taylor. *The finite element method*. 5th Oxford: Elsevier Butterworth-Heinemann, 2000, ISBN 0750650494.

Zienkiewicz, O. C, Robert L Taylor, and J. Z Zhu. *The Finite Element Method: Its Basis and Fundamentals.* 7th Ed. Oxford: Elsevier Butterworth-Heinemann, 2013. ISBN-13 978-1856176330

APPENDIX 1A: MODELLING PARAMETERS USED IN THE RE-EVALUATION OF HISTORIC CASE STUDIES

I) *The slide at Lodalen, October 6, 1954*

Table 1A.1 Parameters used in the three-dimensional model of the Lodalen slide.

Modelling parameter	Source and formulation
3D FOS calculation method(s)	Bishop simplified 3D; Morgenstern-Price 3D
Geometry	Sevaldson (1956) Figs. 3 (excl. slide area), 4
Undrained strength model	Custom, extrapolated from su map in Sevaldson (1956, Figure 17)
Drained strength model	$\tau = c' + \sigma_n' \tan 27.1°$, $c' = 5 \ldots 10$ (kPa)
Pore water pressures	From ground water table (Sevaldson 1956, Figure 19) with uniform gradient below it of 12kPa/m (Sevaldson 1956, Figs. 11 & 19)
Soil unit weight ϒbulk	19.1 kN/m3
Slide width	~50m
Slide width-to-depth (aspect) ratio	2.6 (2-3)

II) *The stable slopes at Bakklandet, Trodheim*

Table 1A.2 Parameters used in the three-dimensional model of the Bakklandet stable slope.

Modelling parameter	Source and formulation
3D FOS calculation method(s)	Bishop simplified 3D; Morgenstern-Price 3D
Geometry	From Bjerrum and Kjaernsli (1957), Figure 5
Undrained strength model	Depth-dependent, from Bjerrum and Kjaernsli (1957), Figure 6 a to c
Drained strength model	not used
Pore water pressures	not applicable
Soil unit weight ϒbulk	19.1 kN/m3
Slide width	not applicable
Slide width-to-depth (aspect) ratio	2-3

III) *The Drammen River bank failure, 1955*

Table 1A.3 Parameters used in the three-dimensional model of the failure of the Drammen River embankment.

Modelling parameter	Source and formulation
3D FOS calculation method(s)	Bishop simplified 3D; Morgenstern-Price 3D
Geometry	From Kjaernsli and Simons (1962), Figs. 2, 3 (bathymetry), 12, 13
Undrained strength model	not used
Drained strength model	Overconsolidated clay near river bank: $\tau = 4 + \sigma_n' \tan 32.5° \ (kPa)$ Normally consolidated clay away from bank: $\tau = \sigma_n' \tan 32.5°$
Pore water pressures	Groundwater table 2m below surface to river elevation of -1m; Hydrostatic distributions below groundwater table
Soil unit weight Υ_{bulk}	19.1 kN/m^3
Slide width	35-40m
Slide width-to-depth (aspect) ratio	3-4

IV) *The Scrapsgate embankment failures, 1953*

Table 1A.4 Parameters used in the three-dimensional model of the Scrapsgate embankment failure.

Modelling parameter	Source and formulation
3D FOS calculation method(s)	Bishop simplified 3D; Morgenstern-Price 3D
Geometry	Extruded from cross-section in Golder and Palmer (1955), Figure 32 Tensile crack modelled at shown location
Undrained strength model 1 (based on vane shear tests)	Embankment fill: 1000 lb/ft^2 Zone 2: depth-dependent, $s_u = 250 + 10z_{datum}$ $(\frac{lb}{ft^2})$ Zone 3: depth-dependent, $s_u = 250 + 10z_{datum}$ $(\frac{lb}{ft^2})$ Datum: 33 ft above London clay surface
Undrained strength model 2 (based on undrained triaxial tests)	Embankment fill: 1000 lb/ft^2 Zone 2: 330 lb/ft^2 Zone 3: 205 lb/ft^2
Pore water pressures	not applicable
Soil unit weight Υ_{bulk}	Embankment fill: 107.5 lb/ft^3 Zone 2: 97 lb/ft^3 Zone 3: 97 lb/ft^3
Slide width	200-250ft (70-80m)
Slide width-to-depth (aspect) ratio	5-6

V) *The Congress St., Chicago, embankment failure, 1952*

Table 1A.5 Parameters used in the three-dimensional model of the failure of the Congress Street embankment.

Modelling parameter	Source and formulation
3D FOS calculation method(s)	Bishop simplified 3D; Morgenstern-Price 3D
Geometry	Extruded from cross-section in Ireland (1954), Figure 1
Undrained strength model	Stiff gritty clay: $s_u = 1420$ $(\frac{lb}{ft^2})$ Medium gritty clay: $s_u = 827$ $(\frac{lb}{ft^2})$ Medium low gritty clay: $s_u = 1060$ $(\frac{lb}{ft^2})$ Sand fill: $\tau = \sigma_n' \tan 30°$
Drained strength model	not used
Pore water pressures	not applicable
Soil unit weight Υ_{bulk}	Stiff gritty clay: 132 lb/ft^3 Medium gritty clay: 128 lb/ft^3 Medium low gritty clay: 128 lb/ft^3 Sand fill: 110 lb/ft^3
Slide width	200 ft (60m)
Slide width-to-depth (aspect) ratio	4

VI) *The Jackfield slide, 1951-53*

Table 1A.6 Parameters used in the three-dimensional model of the Jackfield slide.

Modelling parameter	Source and formulation
3D FOS calculation method(s)	Morgenstern-Price 3D; Fredlund 3D
Geometry	From Henkel and Skempton (1955), Figure 69
Undrained strength model	2" slip zone: $s_u = 450\ (\frac{lb}{ft^2})$ Soil above slip: $s_u = 1600\ (\frac{lb}{ft^2})$
Drained strength model	2" slip zone: $\tau = \sigma_n' \tan 19°$ (from Skempton, 1964) above slip zone: $\tau = 220 + \sigma_n' \tan 25°$ (psf)(based on reasoning by Skempton, 1964, p.89)
Pore water pressures	Hydrostatic with a water table 2 ft below surface
Soil unit weight Υ_{bulk}	130 lb/ft^3
Slide width	400ft (120m)
Slide width-to-depth (aspect) ratio	22

VII) *The landslide at Selset, 1955-on*

Table 1A.7 Parameters used in the three-dimensional model of the Selset slide.

Modelling parameter	Source and formulation
3D FOS calculation method(s)	Morgenstern-Price 3D
Geometry	From Skempton and Brown, 1961, Figs. 1, 2 and 6
Undrained strength model	Not used
Drained strength model	Peak strength: $\tau = 180 + \sigma_n' \tan 32°$ (psf) Residual strength: $\tau = \sigma_n' \tan 30°$ Tensile crack modelled on the upstream at the location shown in Skempton and Brown 1961, Figs. 4 and 5
Pore water pressures	$r_u = 0.35$ (flow parallel to surface) $r_u = 0.45$ (horizontal flow)
Soil unit weight Υ_{bulk}	139 lb/ft^3
Slide width	~150ft (45 m)
Slide width-to-depth (aspect) ratio	~3

VIII) *Appendix 1A Figures*

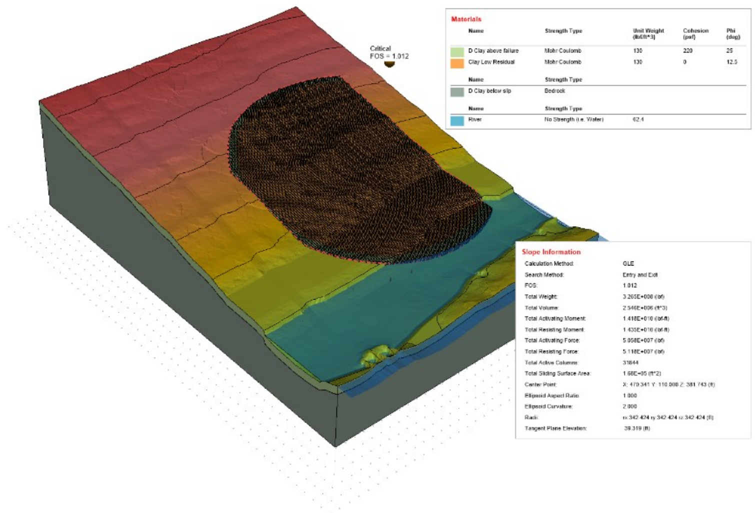

Figure 1A.1 A three-dimensional limit equilibrium analysis of the Jackfield slide. In this model, the limiting equilibrium is reached by lowering the residual angle of friction along the slide base to 12.5°.

APPENDIX 1B: INTERPRETATION OF THREE-DIMENSIONAL SLOPE STABILITY EFFECTS

Table 1B.1 2D and 3D safety factors for the case studies reviewed in Chapter One.

Case Study	2D analysis FOS	3D analysis FOS	$\frac{FOS_{3D}-FOS_{2D}}{FOS_{2D}}$	3D:2D Ratio	Aspect Ratio	Slope (x:z)	*Predicted 3D:2D Ratio	**Soil Profile	Surface shape
Lodalen	1.05	1.08-1.19	~8 (3-13)	1.08	2.6 (2-3)	2:1	1.16	uniform	uniform
Bakklandet A	0.74	1.03-1.05	~41 (39-42)	1.41	2.5	5:1	1.34	mixed	convex
Bakklandet B	0.67	1.08	61	1.61	2.5	5:1	1.34	mixed	concave
Drammen slide (B)	1.01	1.09	8	1.08	3.5 (3-4)	1.3:1	1.08	uniform	uniform
Drammen A	1.14	1.31-1.37	17 (15-20)	1.18	3.5	1.7:1	1.10	uniform	concave
Drammen C	1.26	1.79-1.89	46 (42-50)	1.46	3.5	2.6:1	1.18	uniform	convex, composite
Scrapsgate	1	1.22	22	1.22	5.5 (5-6)	2:1	1.08	mixed	uniform
Congress St.	1.04	1.2	15	1.15	4	1.5:1	1.09	mixed	uniform
Jackfield	1.07	1.39	33	1.30	22	6:1	1.03	mixed	uniform
Selset	0.99-1.14	1.23-1.43	24 (24-25)	1.23	3	2.5:1	1.5	uniform	concave

*Roughly estimated using the relationships reported by Akhtar and Stark (2017).
**A soil profile is labelled here "uniform" if the slip passes through a single soil type with a single strength behaviour.

APPENDIX 2A: RESULTS OF A TWO-DIMENSIONAL DEFORMATION ANALYSIS OF FAILURE AT THE MOUNT POLLEY TSF

I) *Model geometry*

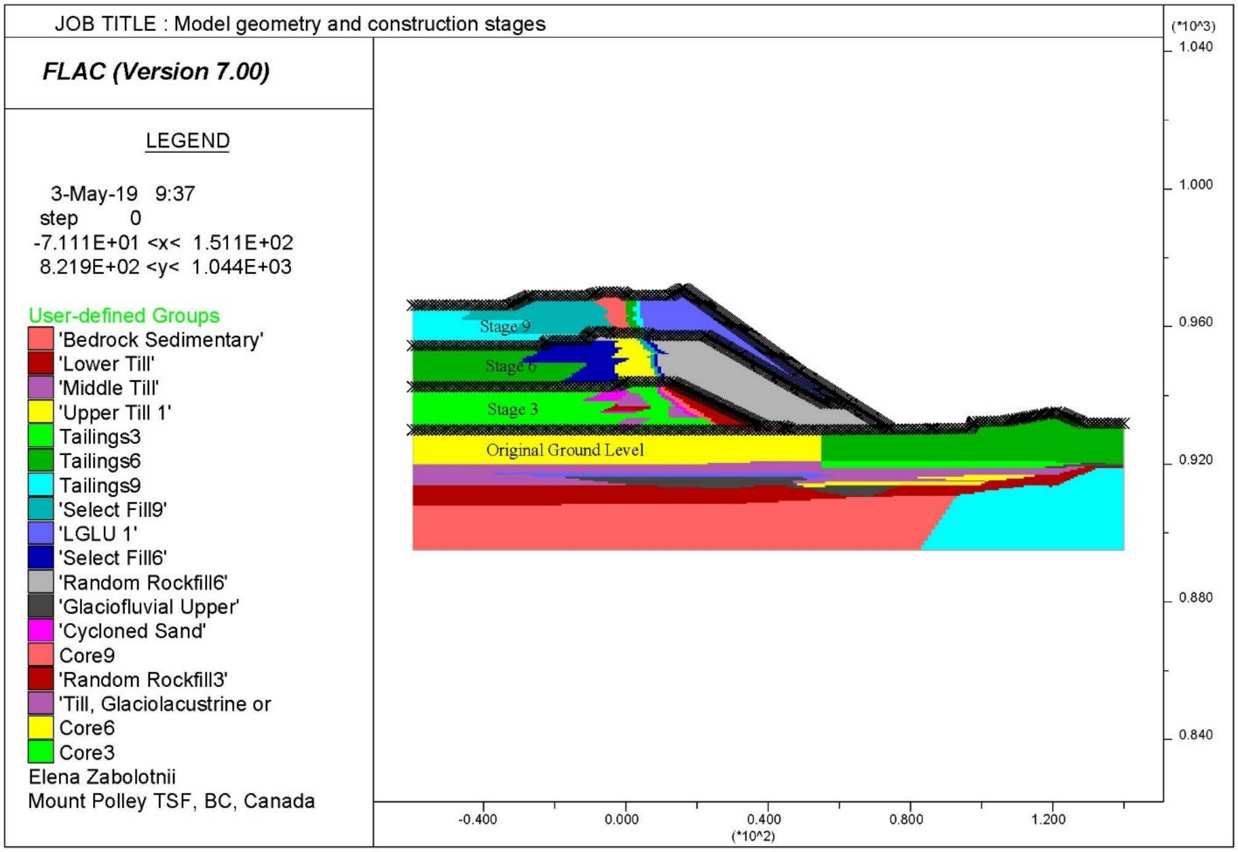

Figure 2A.1 Mount Polley TSF model used for deformation analysis, showing regions of construction stages 3, 6 and 9 as well as the original ground level.

II) *Stage 3 results*

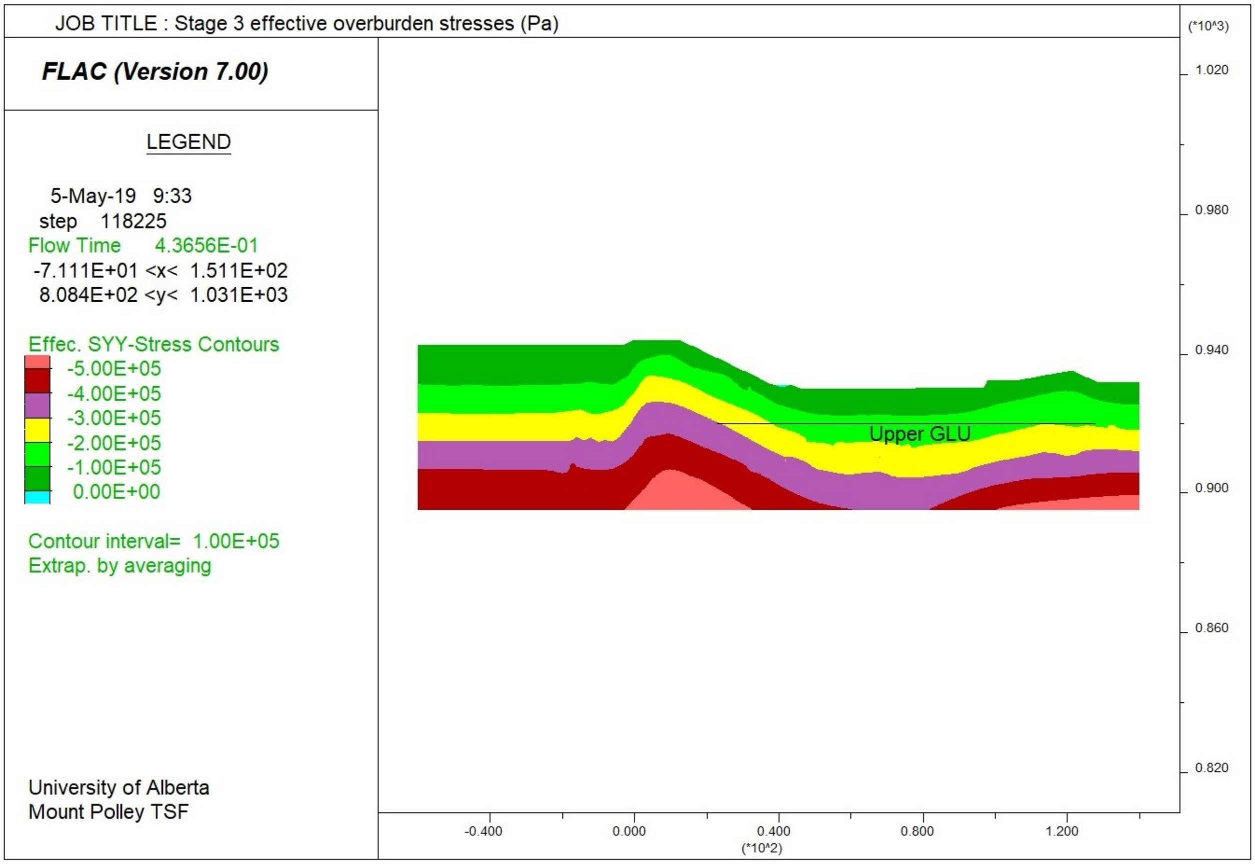

Figure 2A.2 Stage 3 overburden effective stresses in the embankment at static equilibrium under steady state pore pressure conditions.

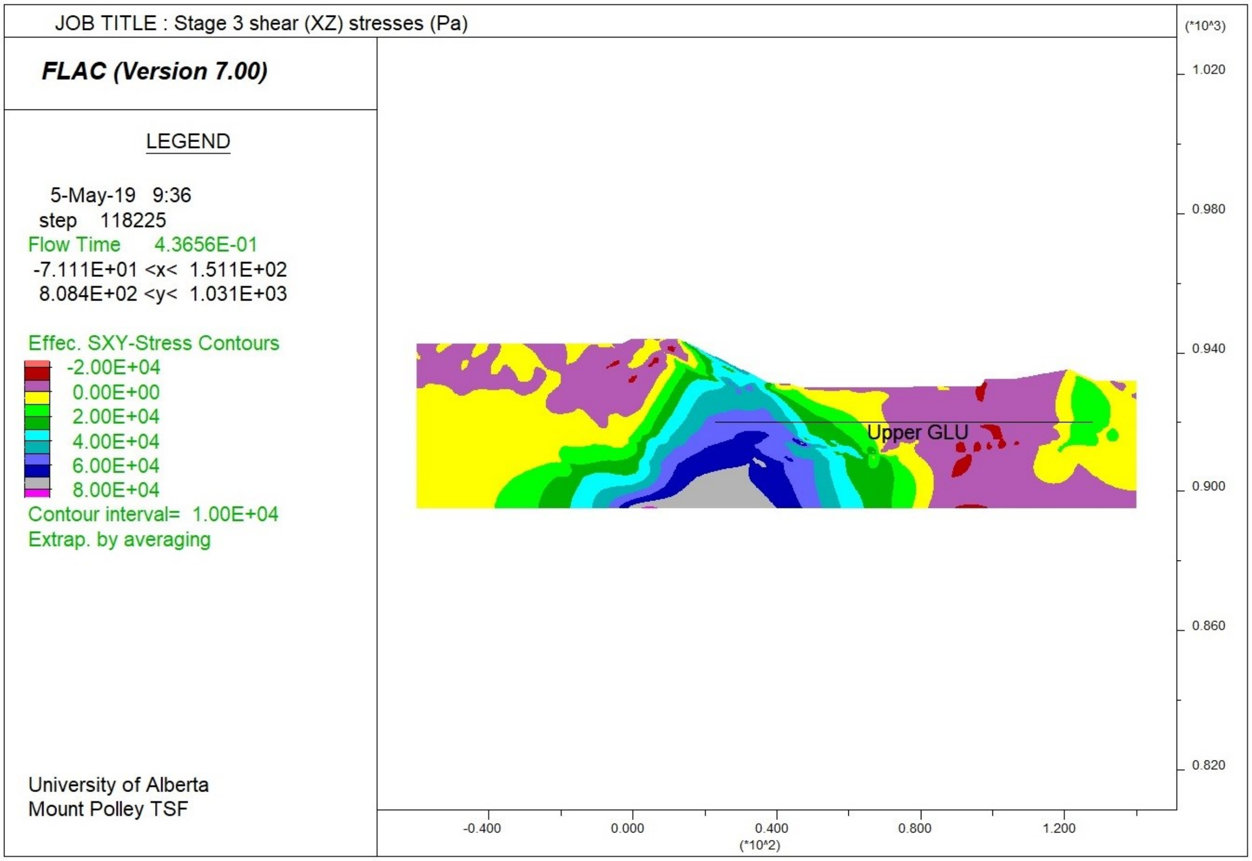

Figure 2A.3 Stage 3 XZ shear stresses in the embankment at static equilibrium under steady state pore pressure conditions.

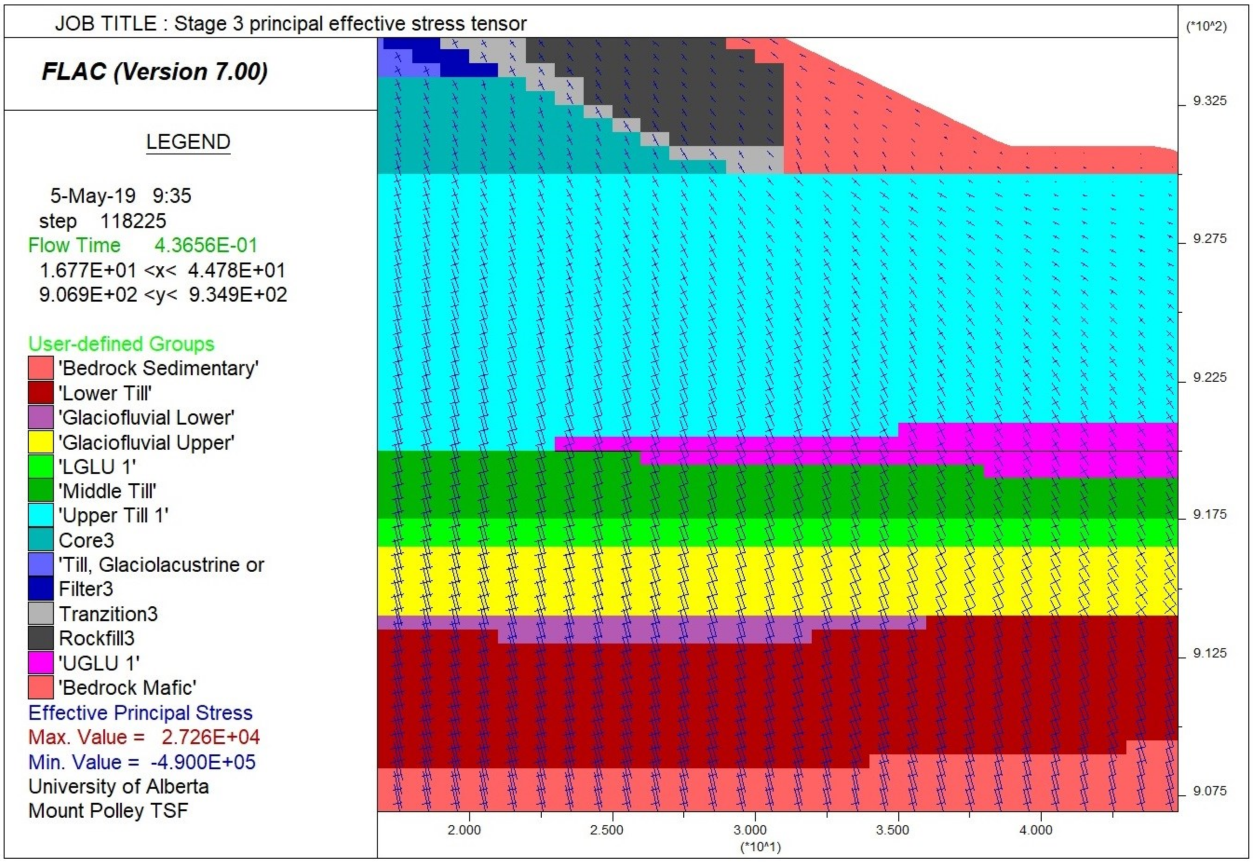

Figure 2A.4 Stage 3 principal effective stresses in the embankment at static equilibrium under steady state pore pressure conditions (shown as tensors).

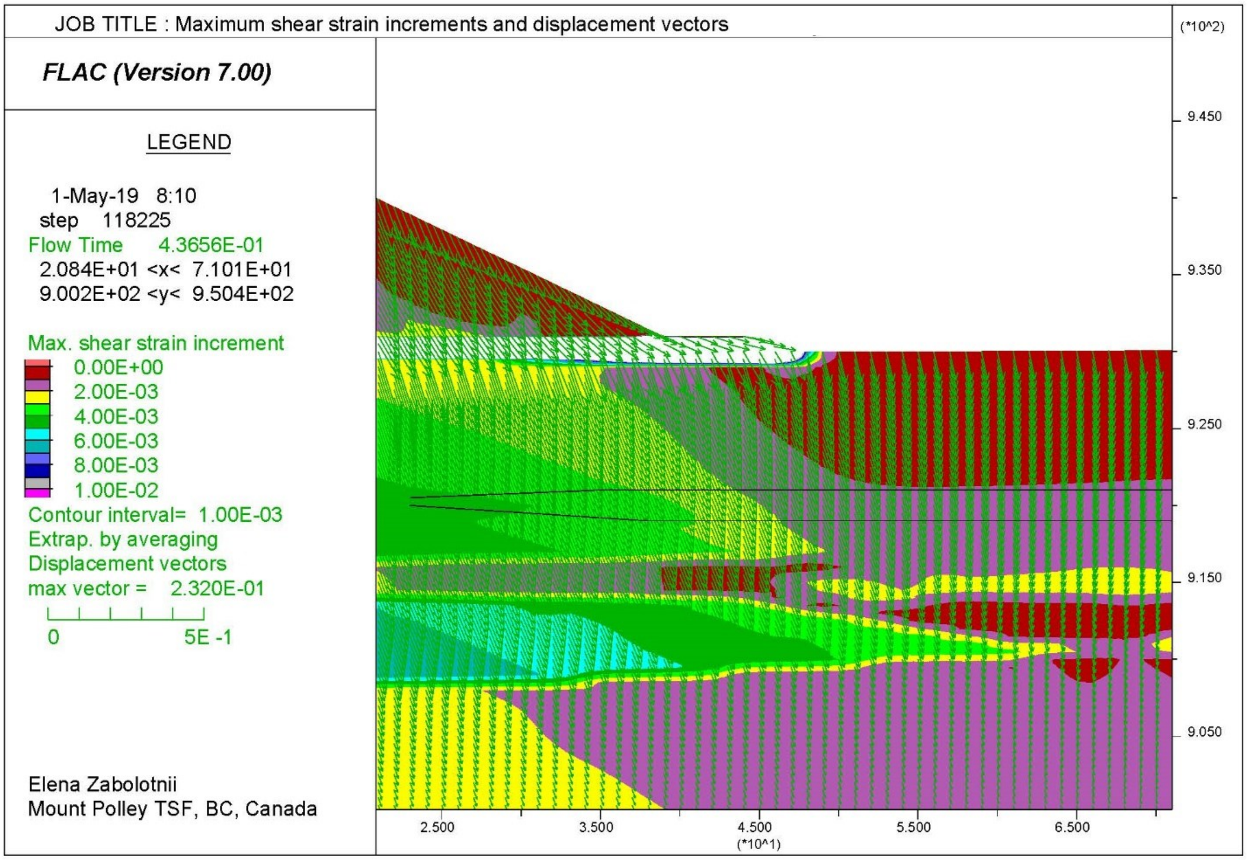

Figure 2A.5 Stage 3 shear strain increments (-) and displacement vectors around the normally consolidated portion of Upper GLU.

III) *Stage 6 results*

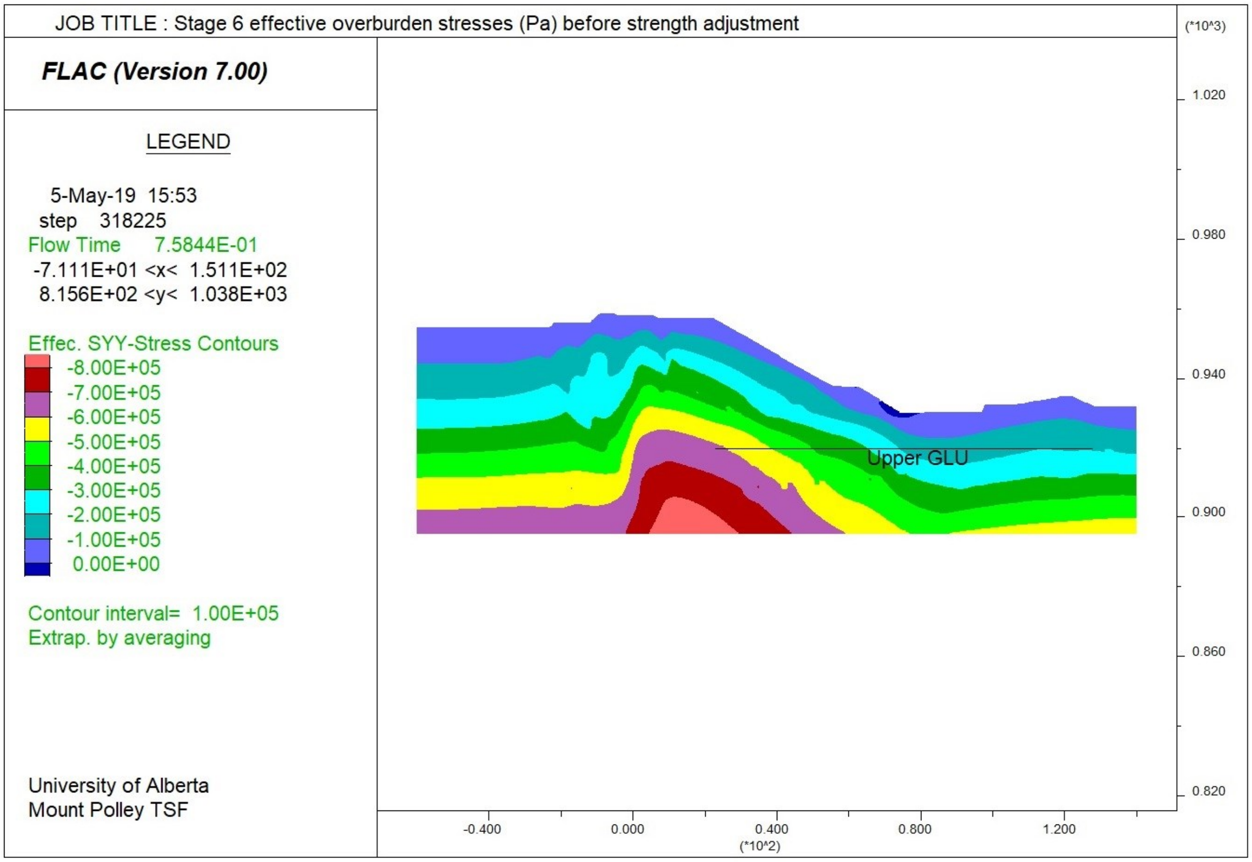

Figure 2A.6 Stage 6 overburden effective stresses in the embankment at static equilibrium under steady state pore pressure conditions (before the strength reduction in the Upper GLU to peak undrained values).

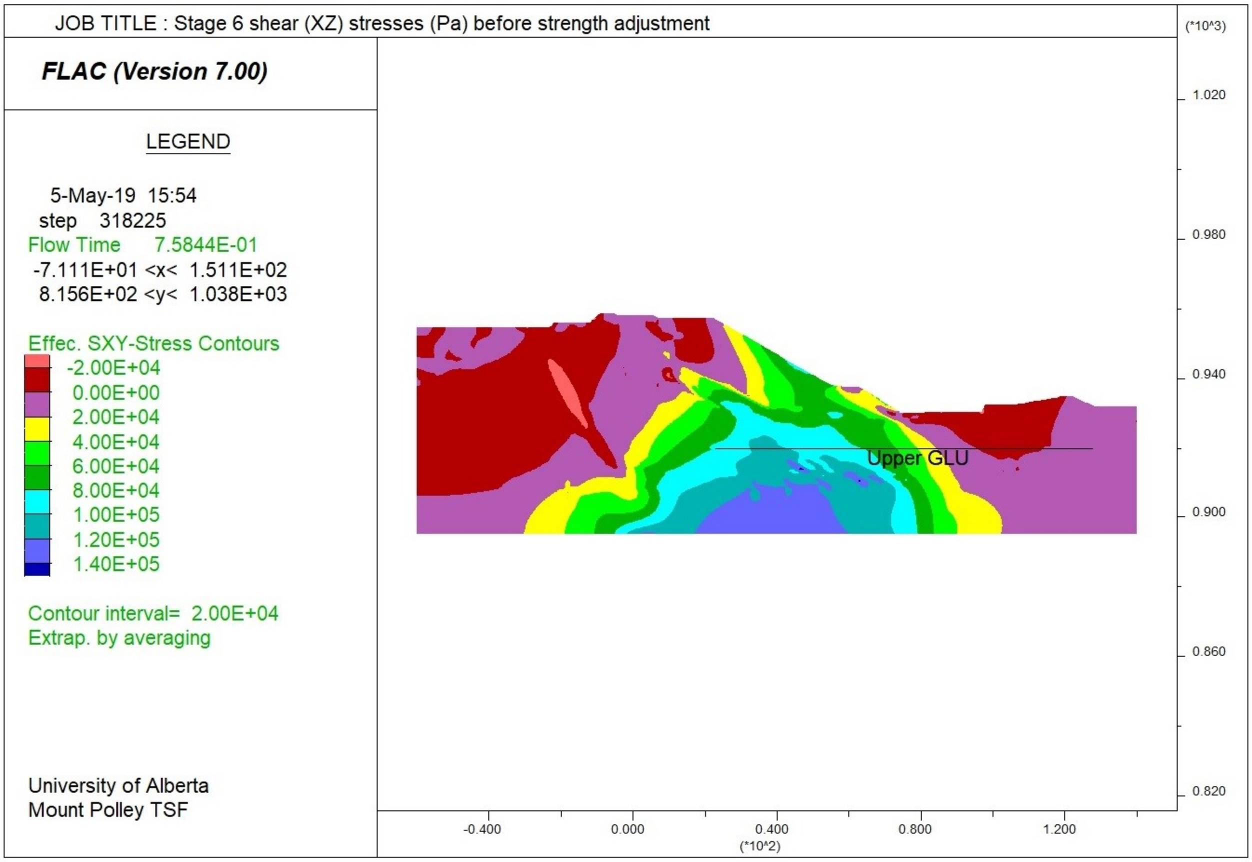

Figure 2A.7 Stage 6 XZ shear stresses in the embankment at static equilibrium under steady state pore pressure conditions (before the strength reduction in the Upper GLU to peak undrained values).

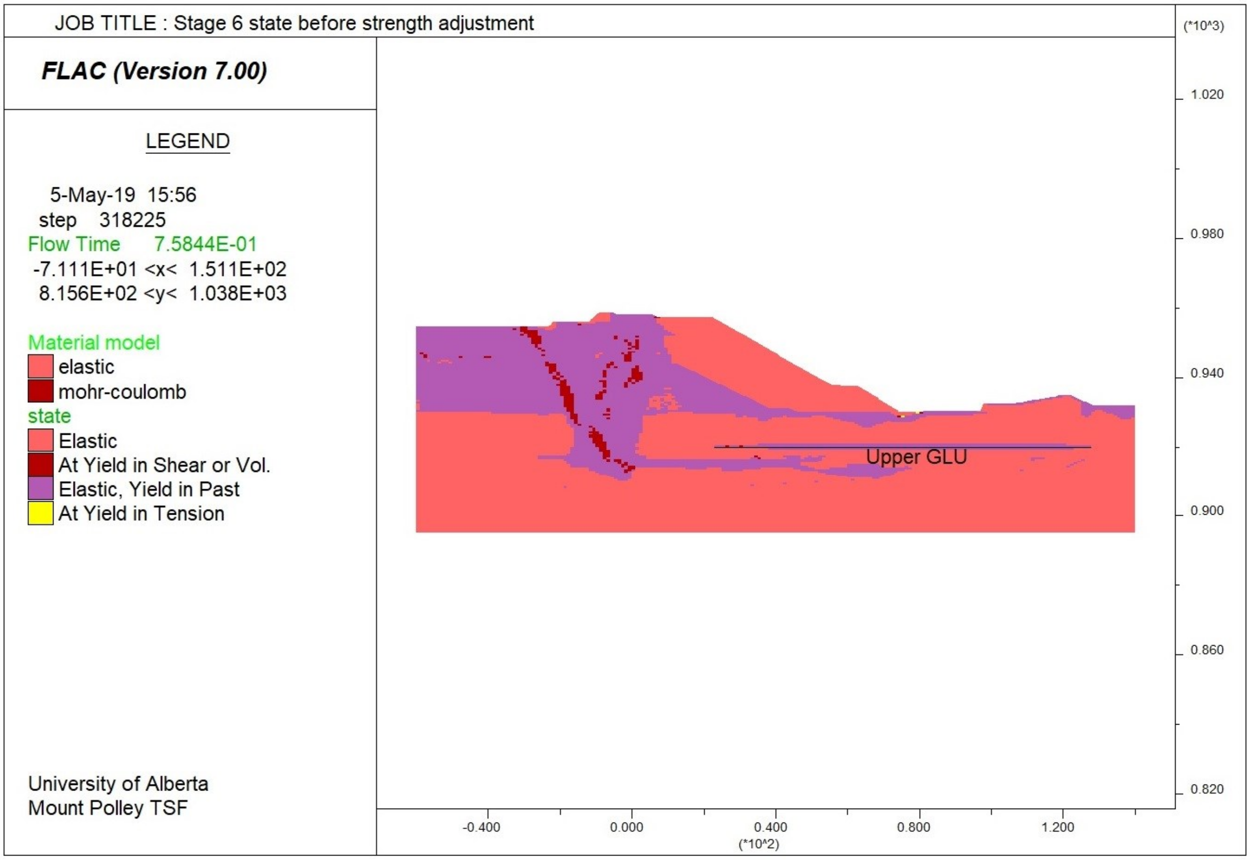

Figure 2A.8 Stage 6 state (before the strength reduction in the Upper GLU to peak undrained values).

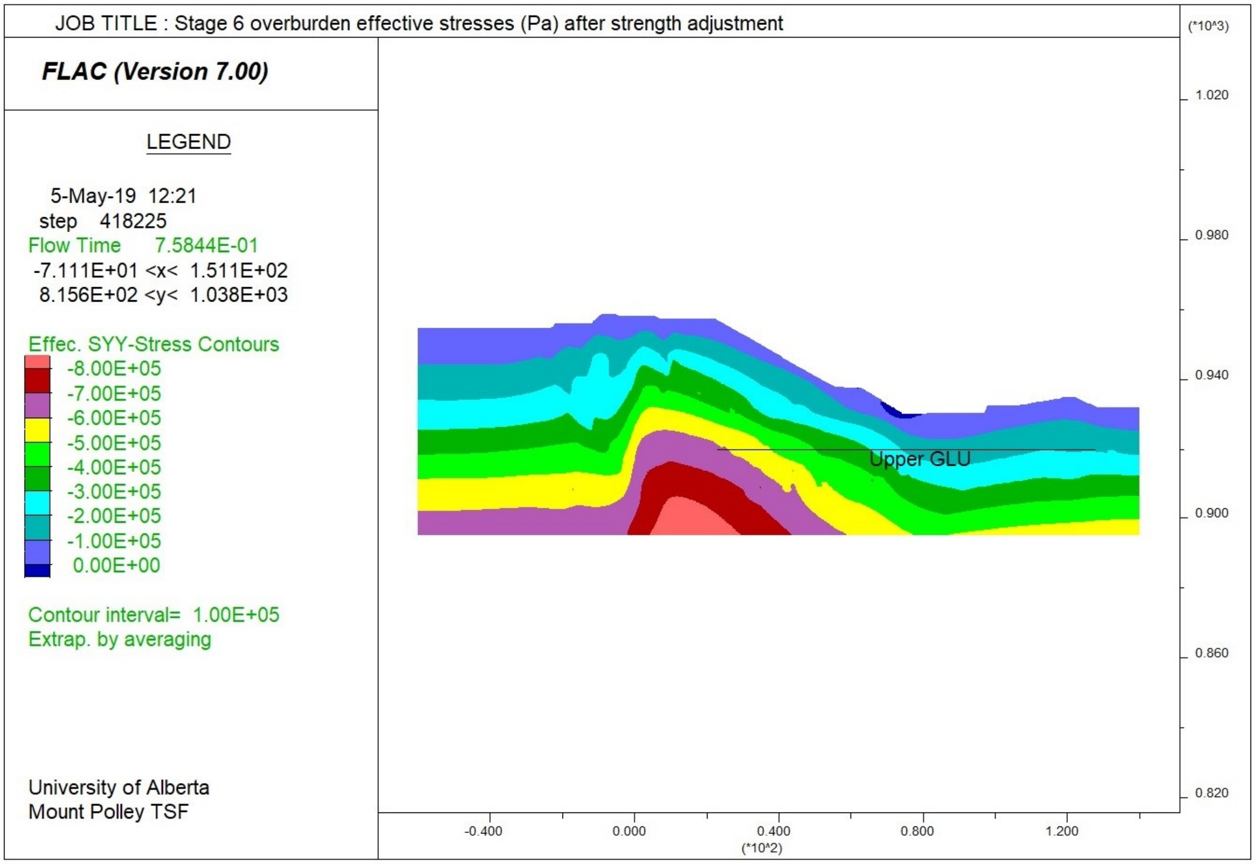

Figure 2A.9 Stage 6 overburden effective stresses in the embankment at static equilibrium under steady state pore pressure conditions (after the strength reduction in the Upper GLU to a peak undrained value of 115kPa).

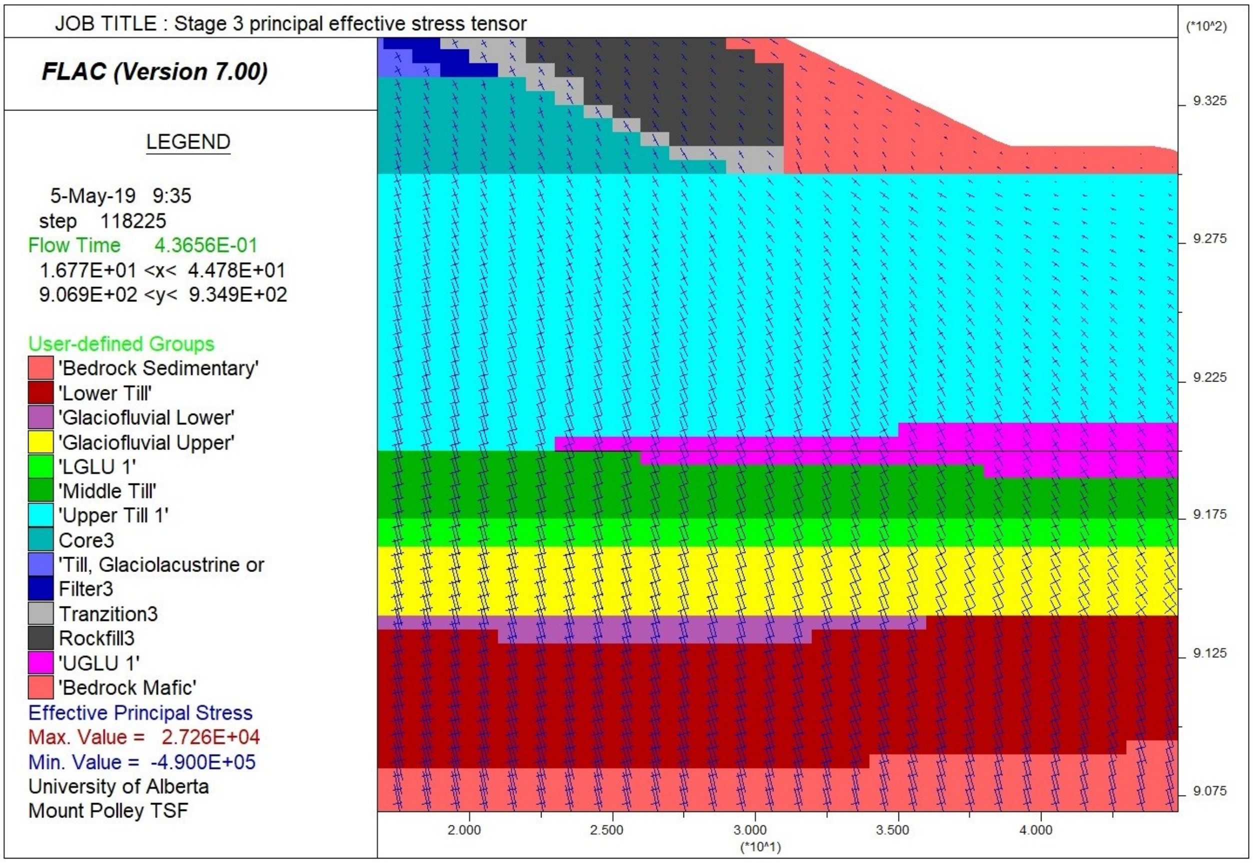

Figure 2A.10 Stage 6 principal effective stress tensors in the embankment (especially the normally consolidated portion of Upper GLU) at static equilibrium under steady state pore pressure conditions (after the strength reduction in the Upper GLU to a peak undrained value of 115kPa).

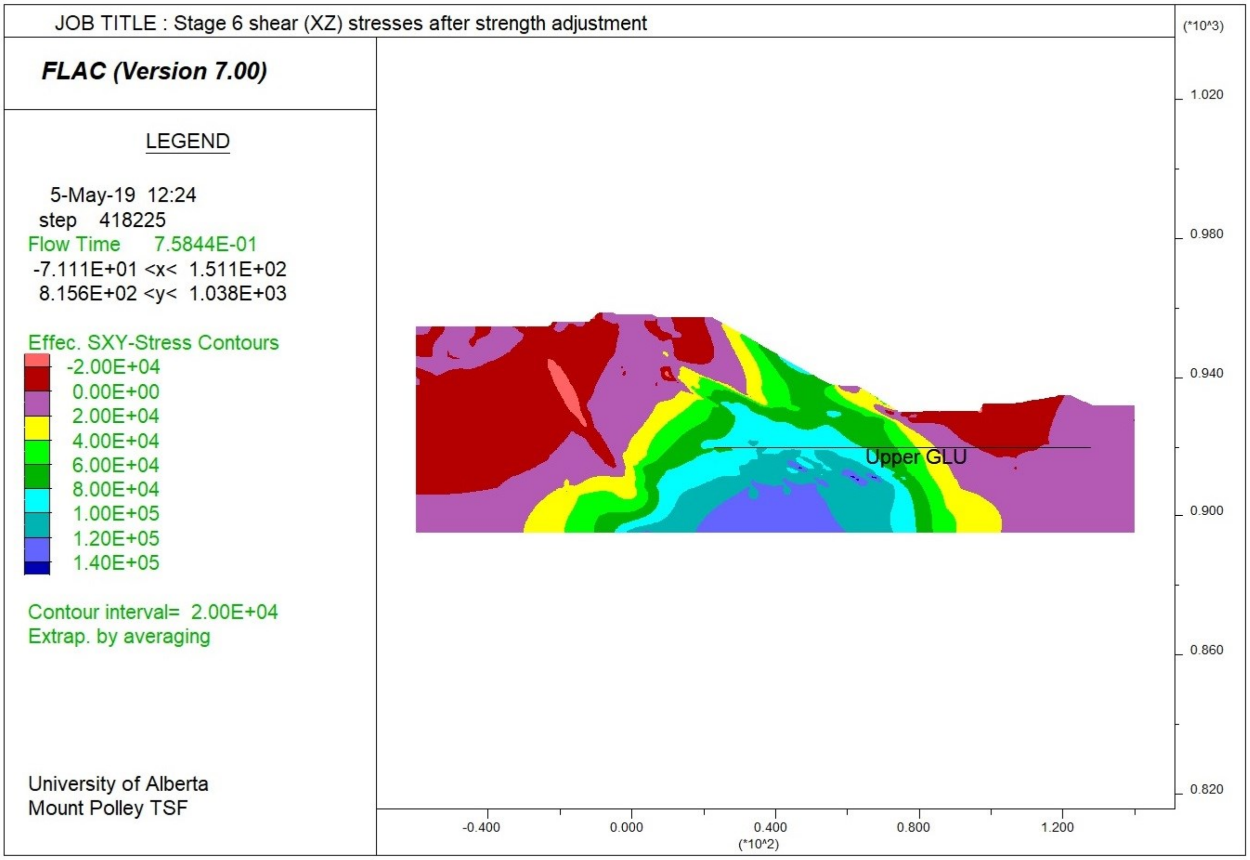

Figure 2A.11 Stage 6 XZ shear stresses in the embankment at static equilibrium under steady state pore pressure conditions (after the strength reduction in the Upper GLU to a peak undrained value of 115kPa).

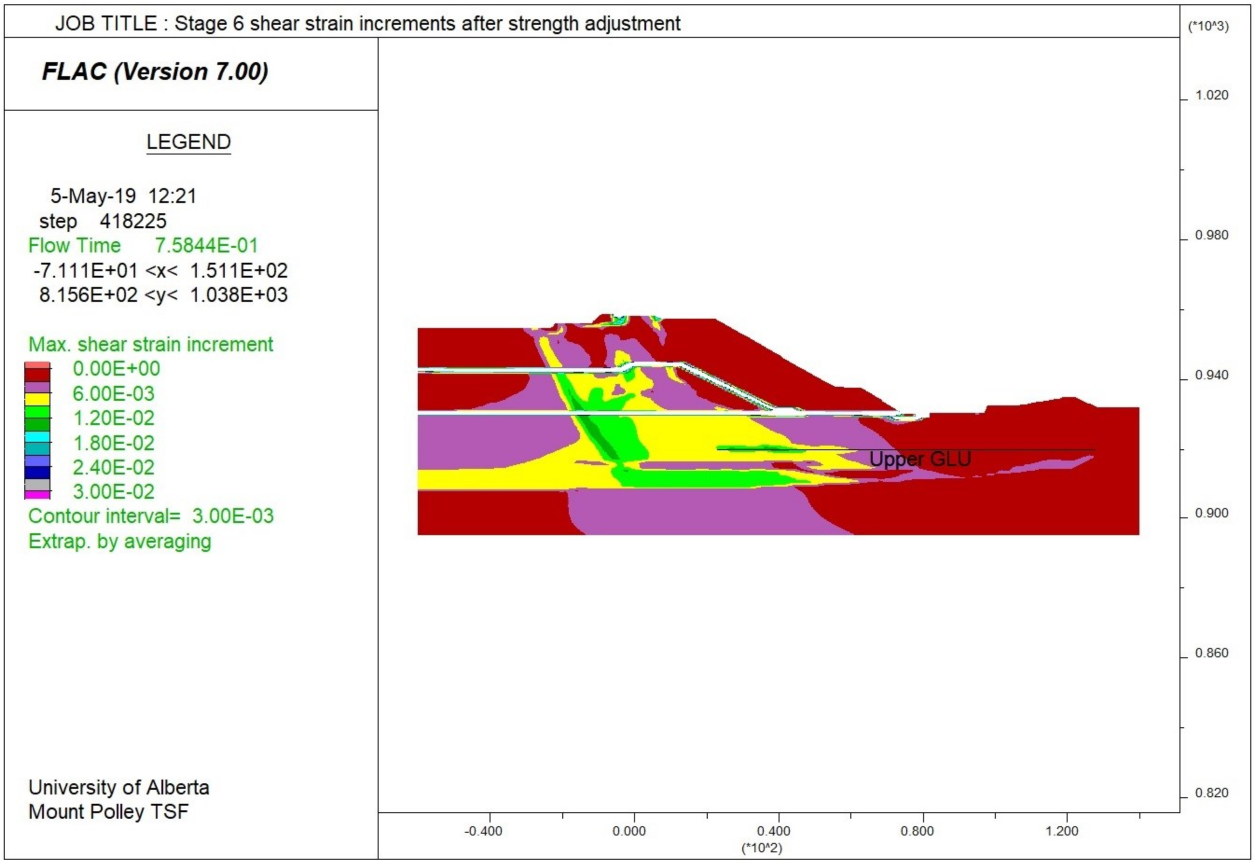

Figure 2A.12 Stage 6 shear strain increments (-)(after the strength reduction in the Upper GLU to a peak undrained value of 115kPa).

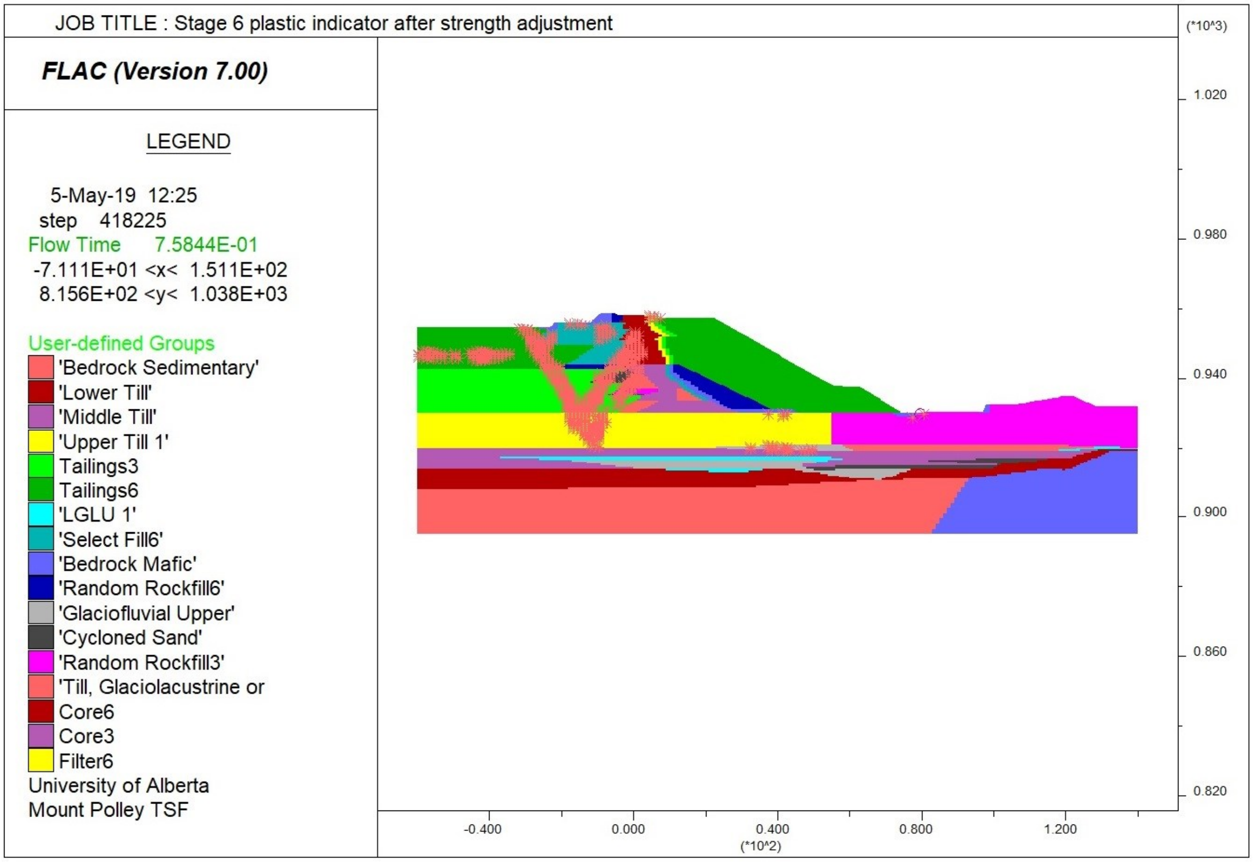

Figure 2A.13 Stage 6 plasticity indicator (after the strength reduction in the Upper GLU to a peak undrained value of 115kPa).

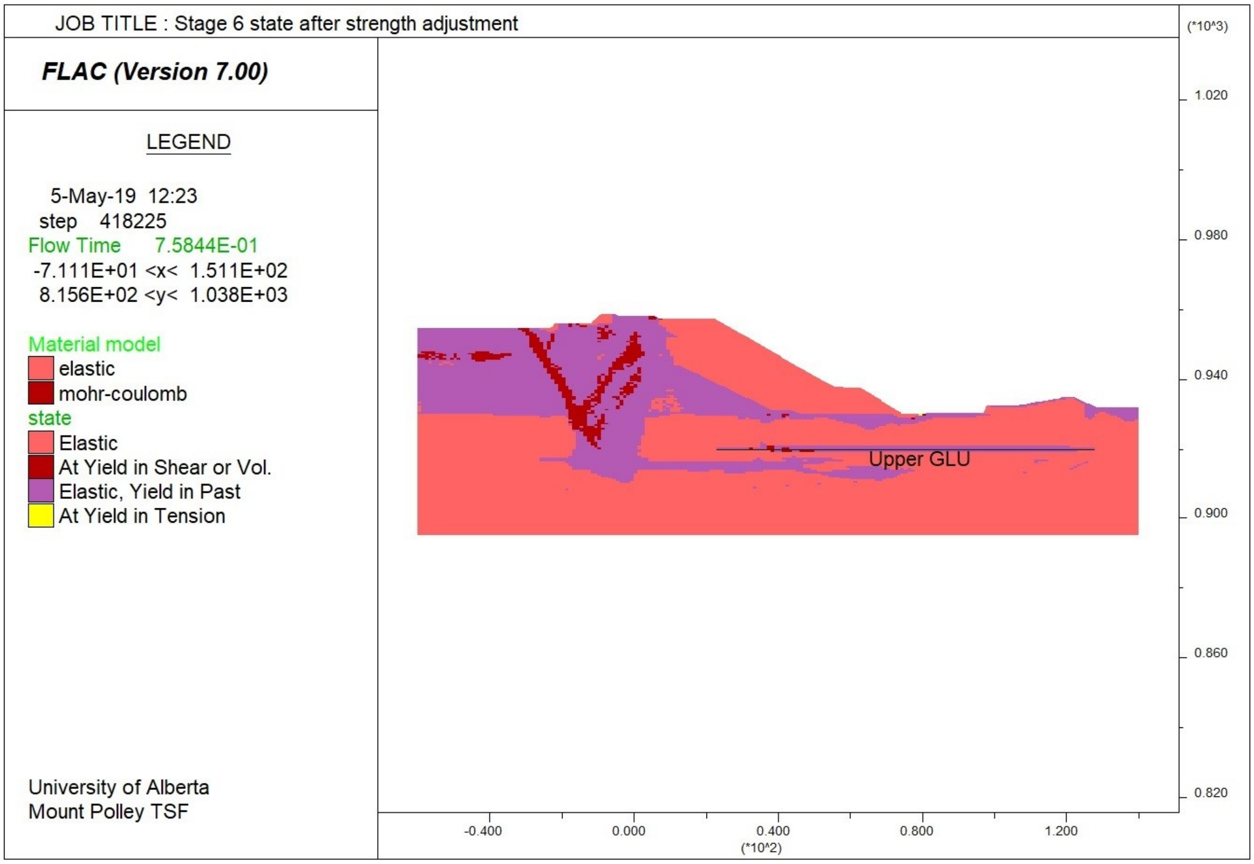

Figure 2A.14 Stage 6 state (after the strength reduction in the Upper GLU to a peak undrained value of 115kPa).

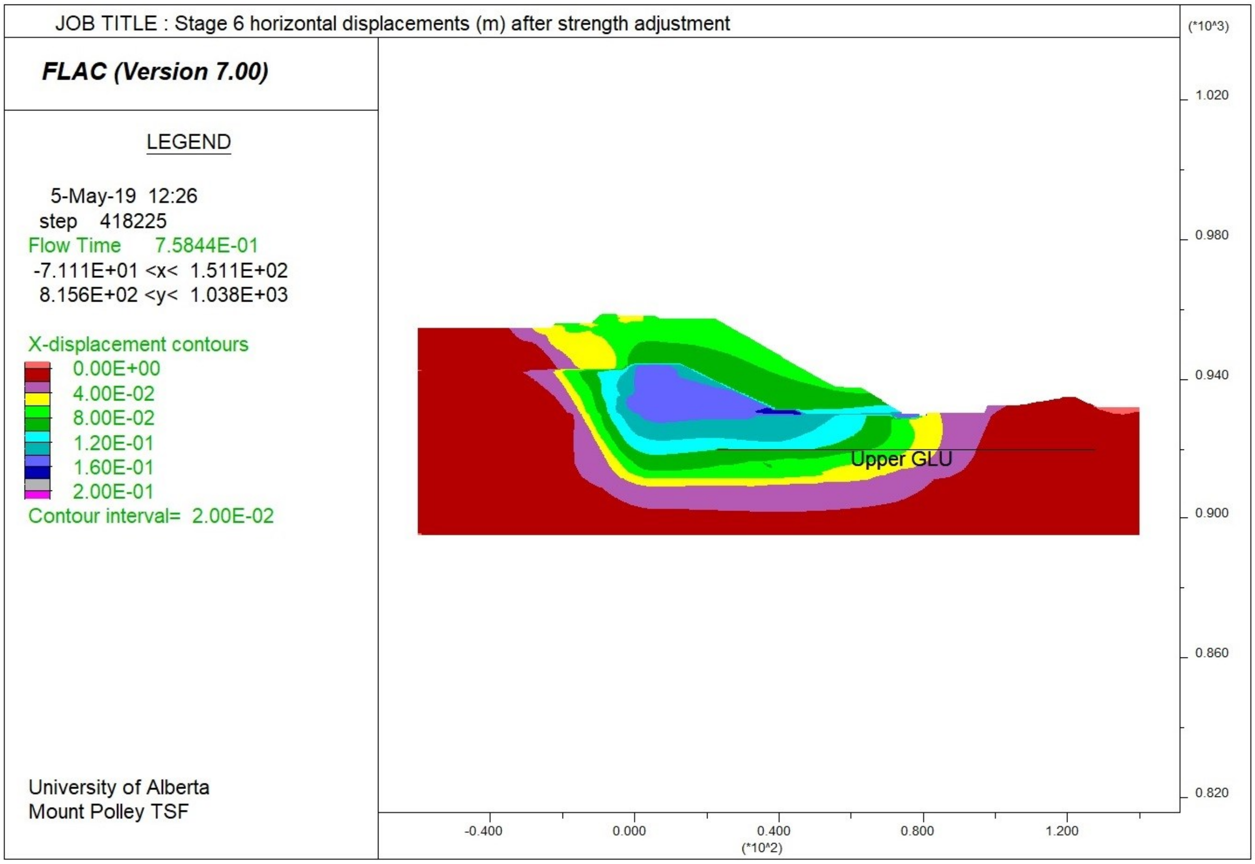

Figure 2A.15 Stage 6 horizontal displacements (after the strength reduction in the Upper GLU to a peak undrained value of 115kPa).

IV) *Stage 9 results*

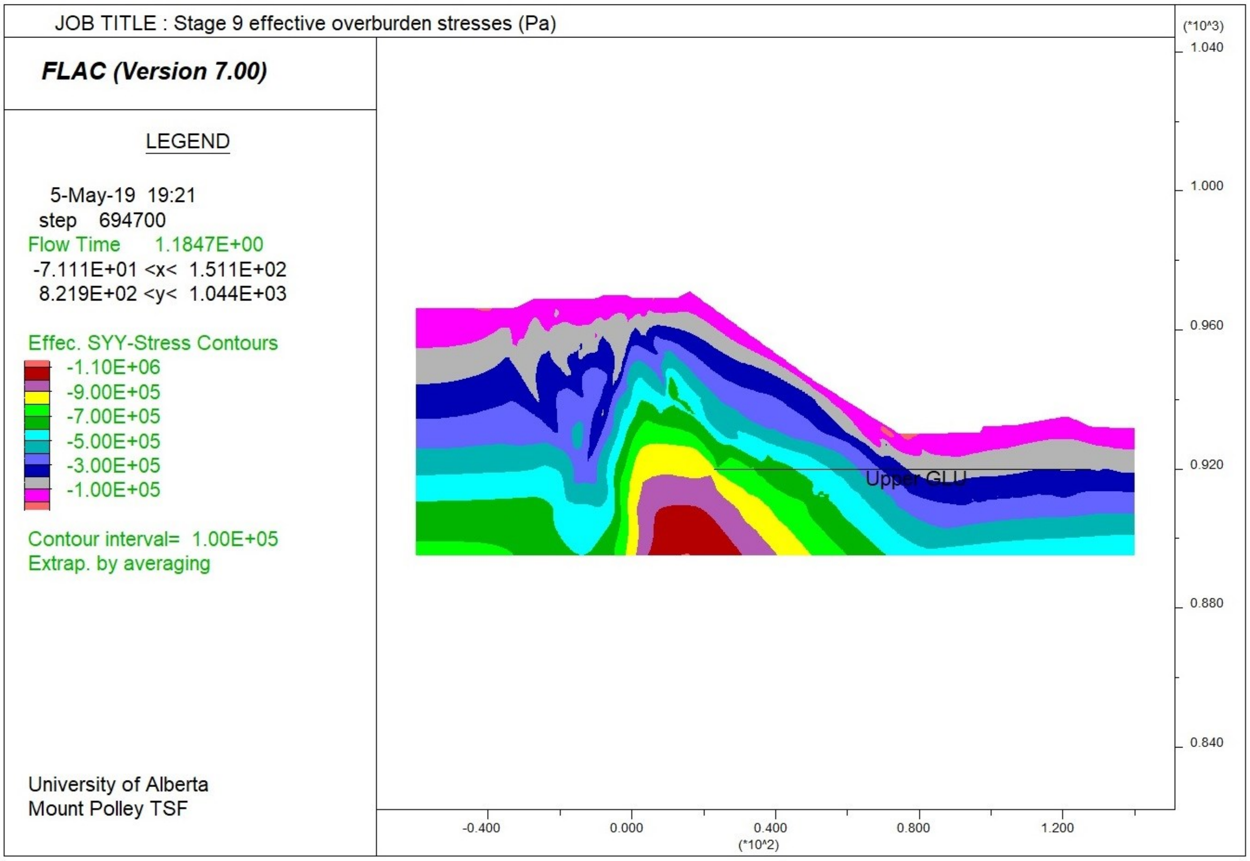

Figure 2A.16 Stage 9 overburden effective stresses in the embankment at static equilibrium under conditions of steady state pore pressures and peak undrained shear strengths in the Upper GLU's normally consolidated portion estimated based on the average overburden consolidation stresses.

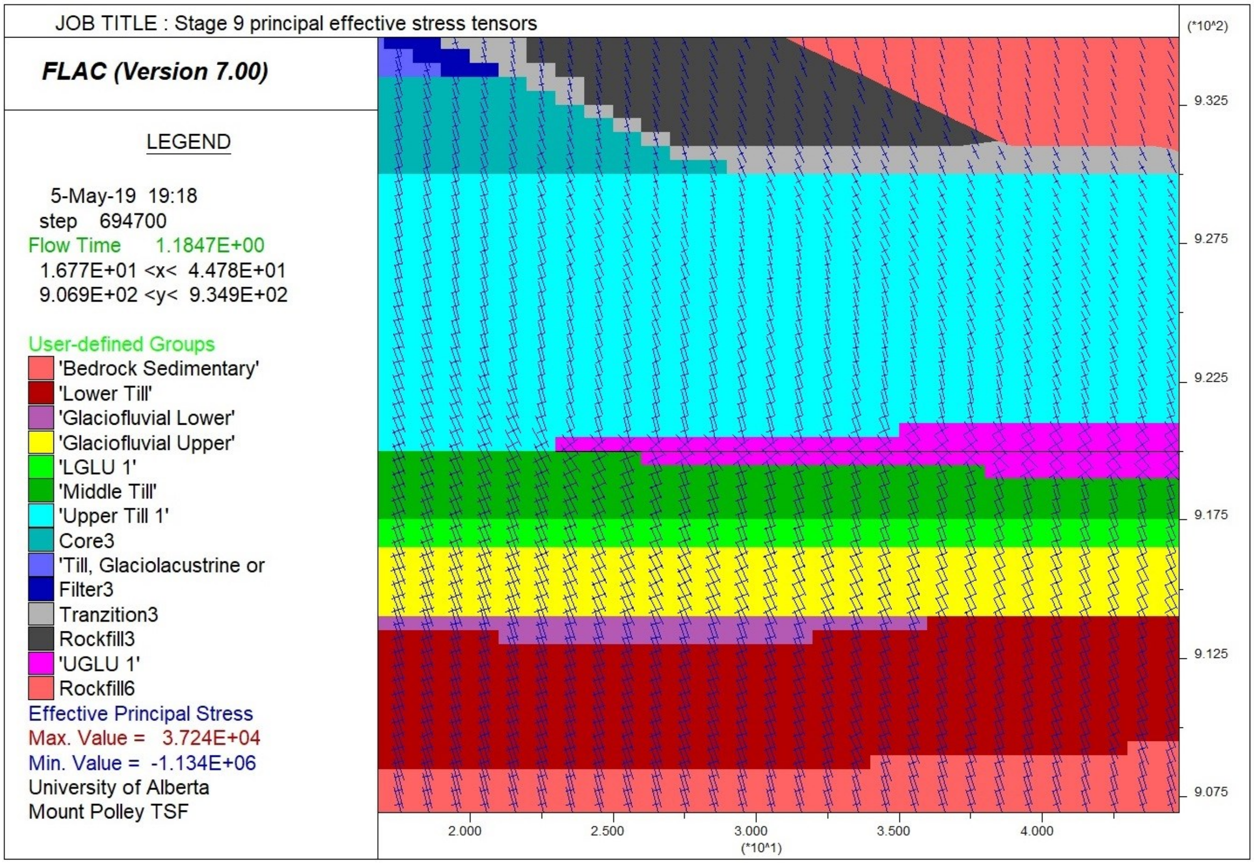

Figure 2A.17 Stage 9 effective stress tensors in the embankment (especially the normally consolidated portion of Upper GLU) at static equilibrium under conditions of steady state pore pressures and peak undrained shear strengths in the Upper GLU's normally consolidated portion estimated based on the average overburden consolidation stresses.

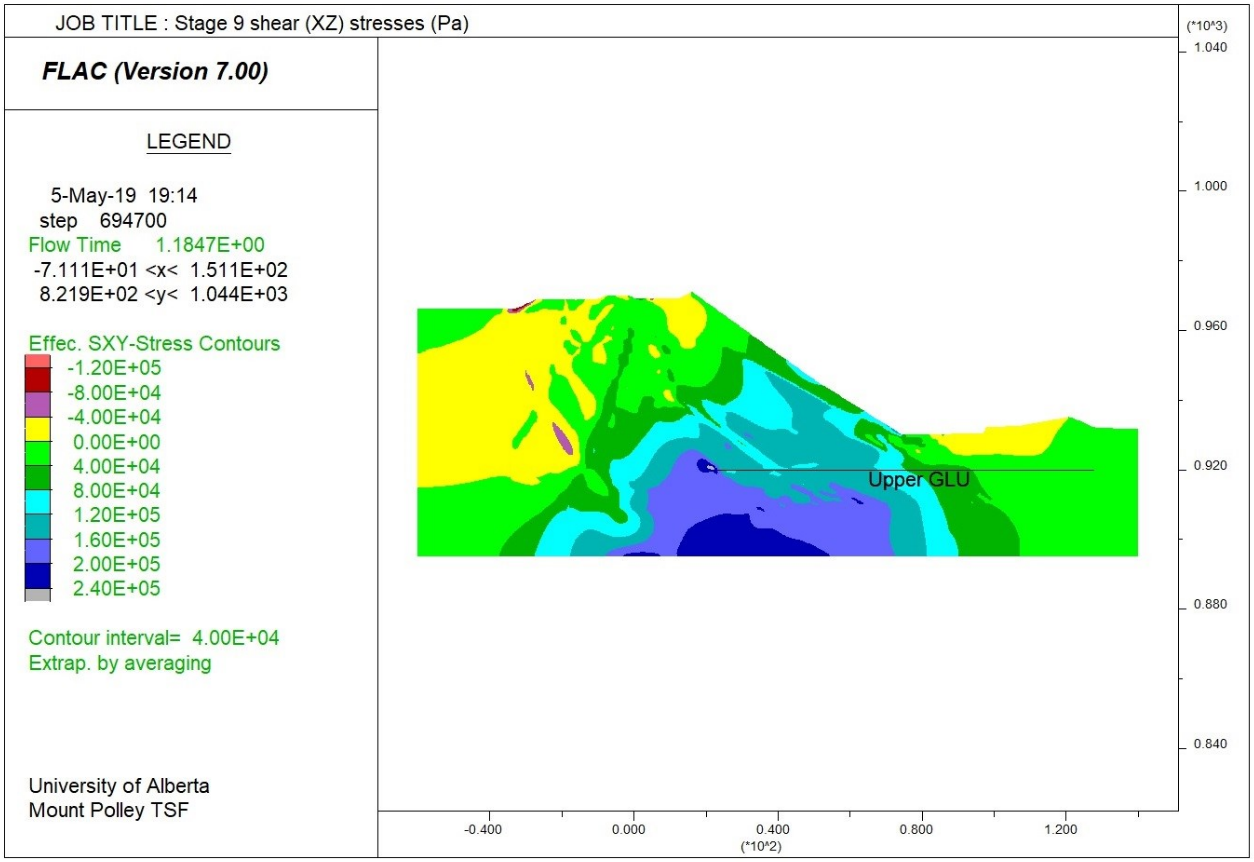

Figure 2A.18 Stage 9 shear (XZ) stresses in the embankment at static equilibrium under conditions of steady state pore pressures and peak undrained shear strengths in the Upper GLU's normally consolidated portion estimated based on the average overburden consolidation stresses.

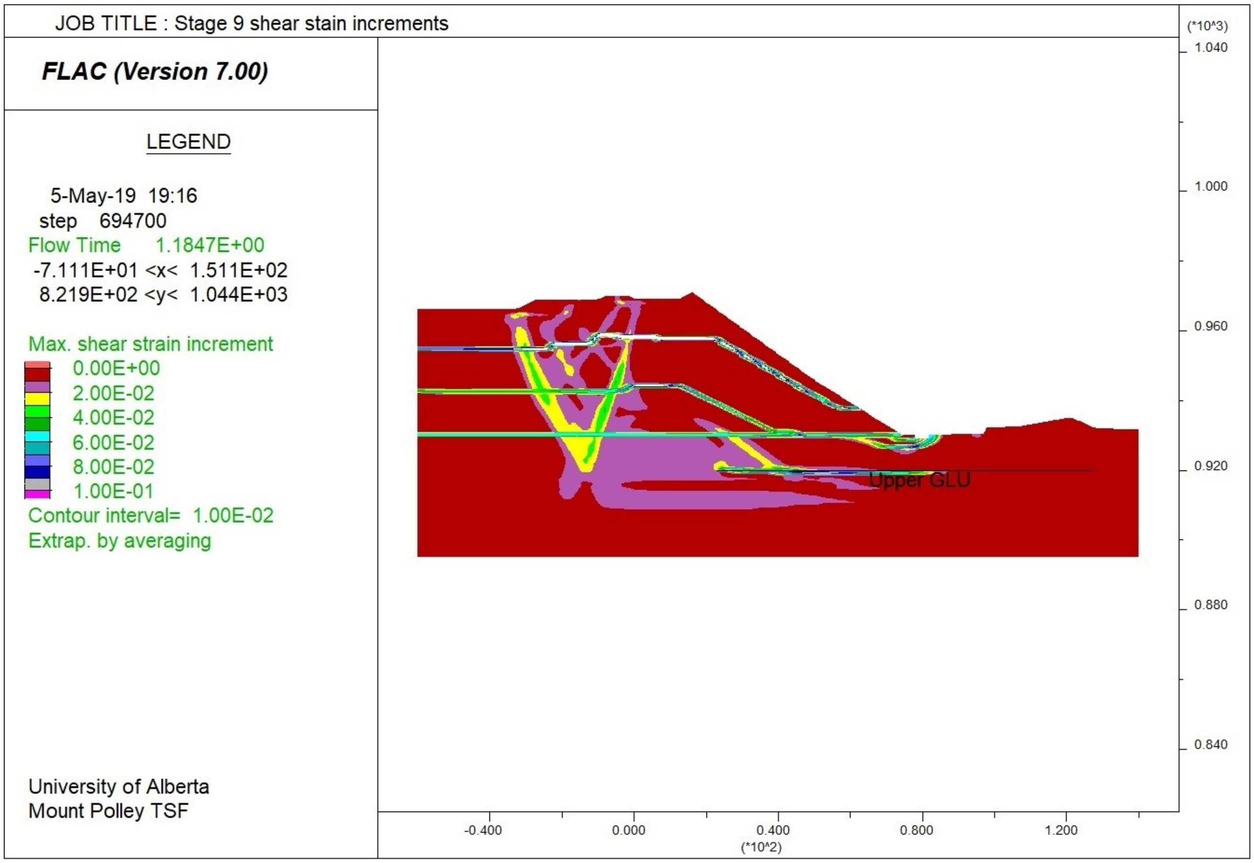

Figure 2A.19 Stage 9 shear strains in the embankment (especially the normally consolidated portion of Upper GLU) at static equilibrium under conditions of steady state pore pressures and peak undrained shear strengths in the Upper GLU's normally consolidated portion estimated based on the average overburden consolidation stresses.

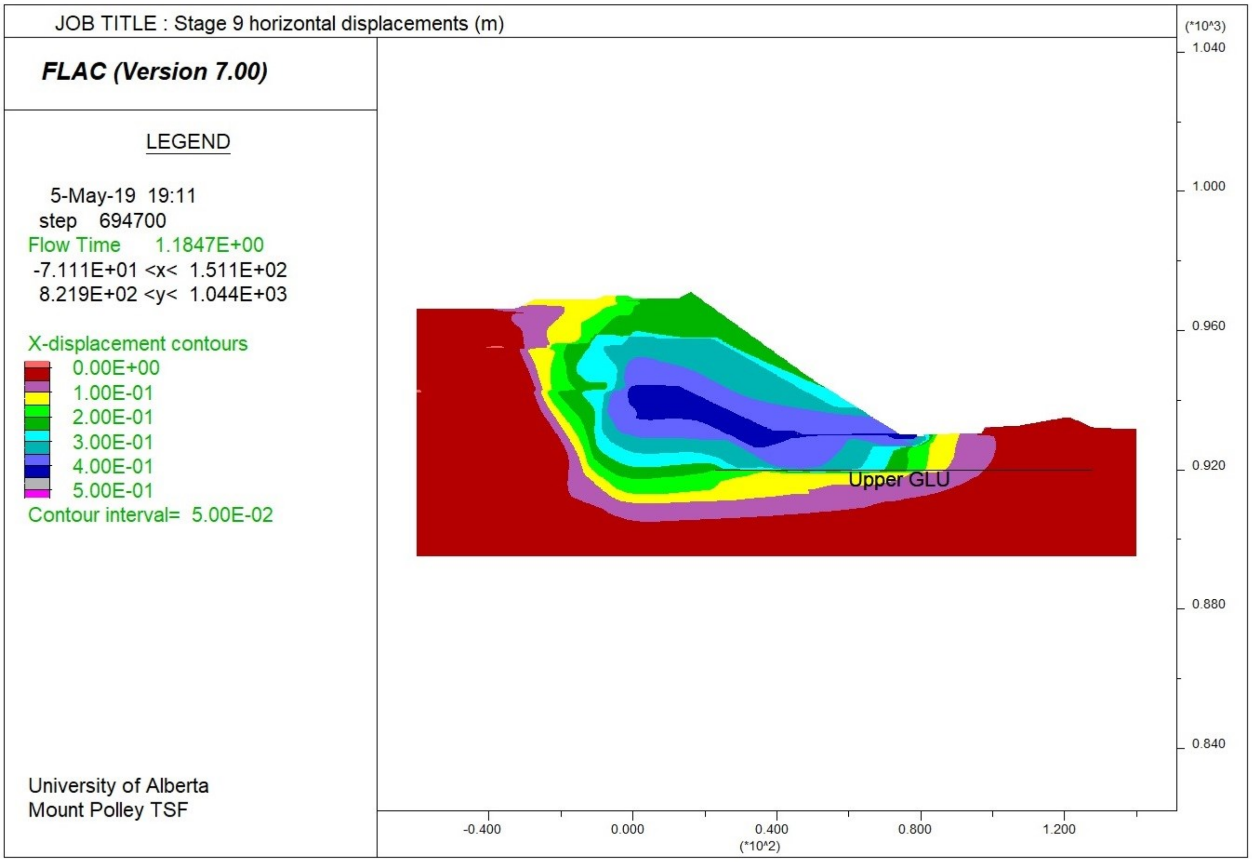

Figure 2A.20 Stage 9 horizontal displacements in the embankment at static equilibrium under conditions of steady state pore pressures and peak undrained shear strengths in the Upper GLU's normally consolidated portion estimated based on the average overburden consolidation stresses.

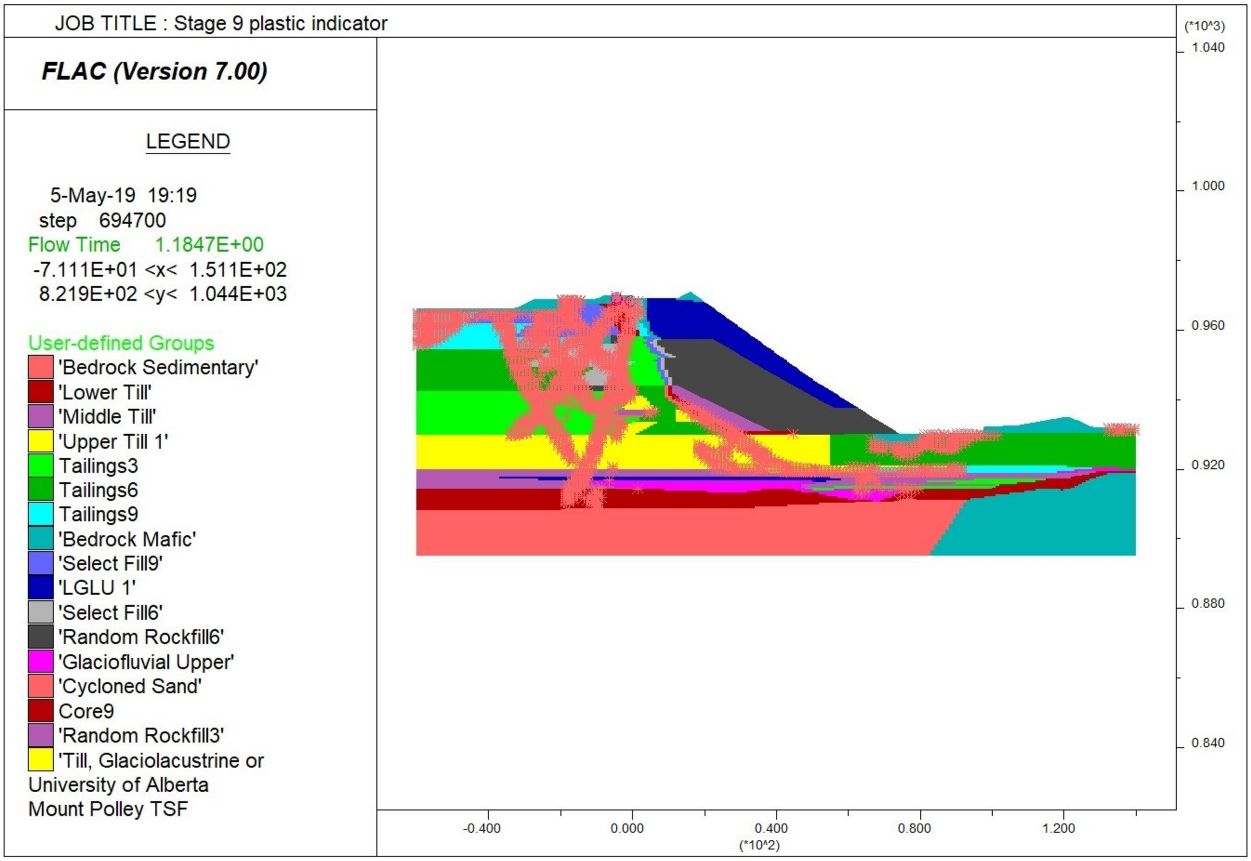

Figure 2A.21 Stage 9 plastic indicator at static equilibrium under conditions of steady state pore pressures and peak undrained shear strengths in the Upper GLU's normally consolidated portion estimated based on the average overburden consolidation stresses.

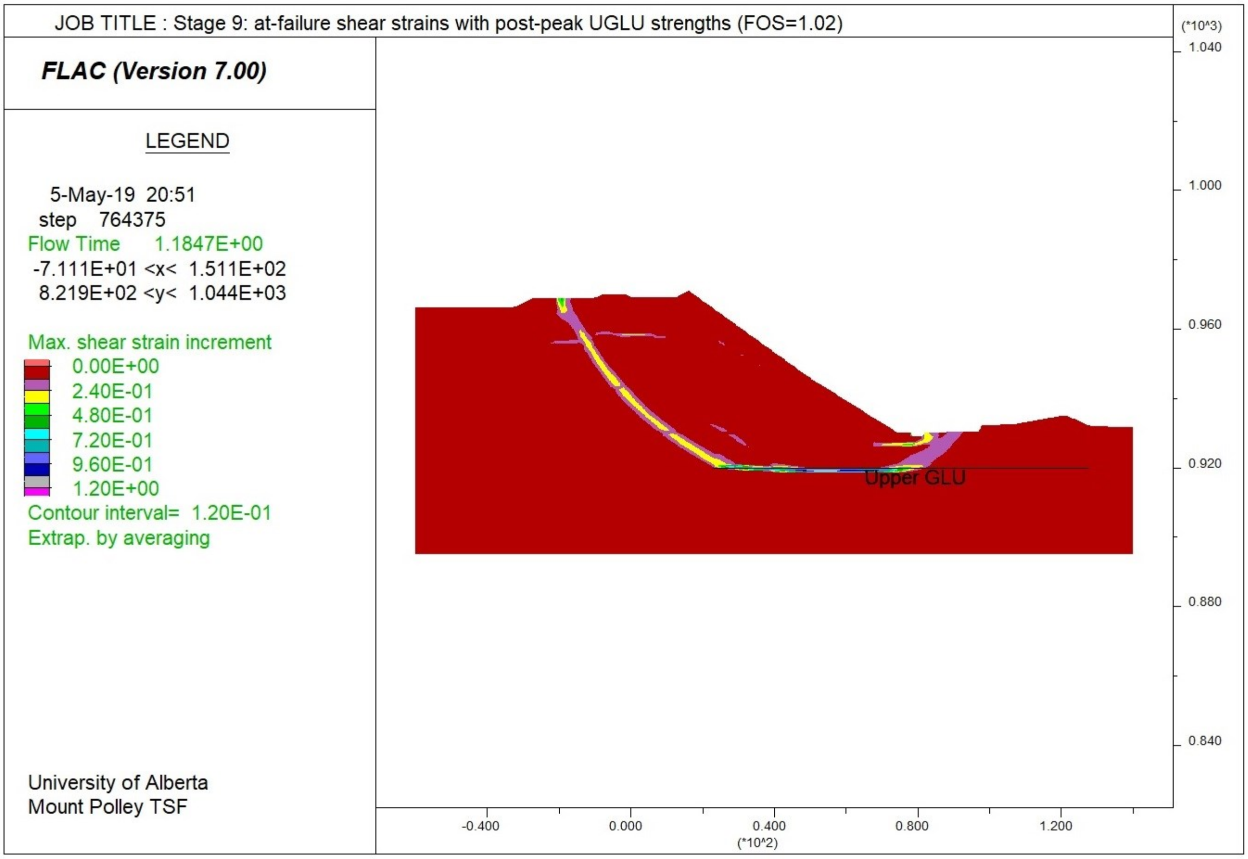

Figure 2A.22 Stage 9 shear strain increments at failure (failure was generated by assigning average post-peak strength values corresponding to 20% shear strains in the normally consolidated Upper GLU portions).

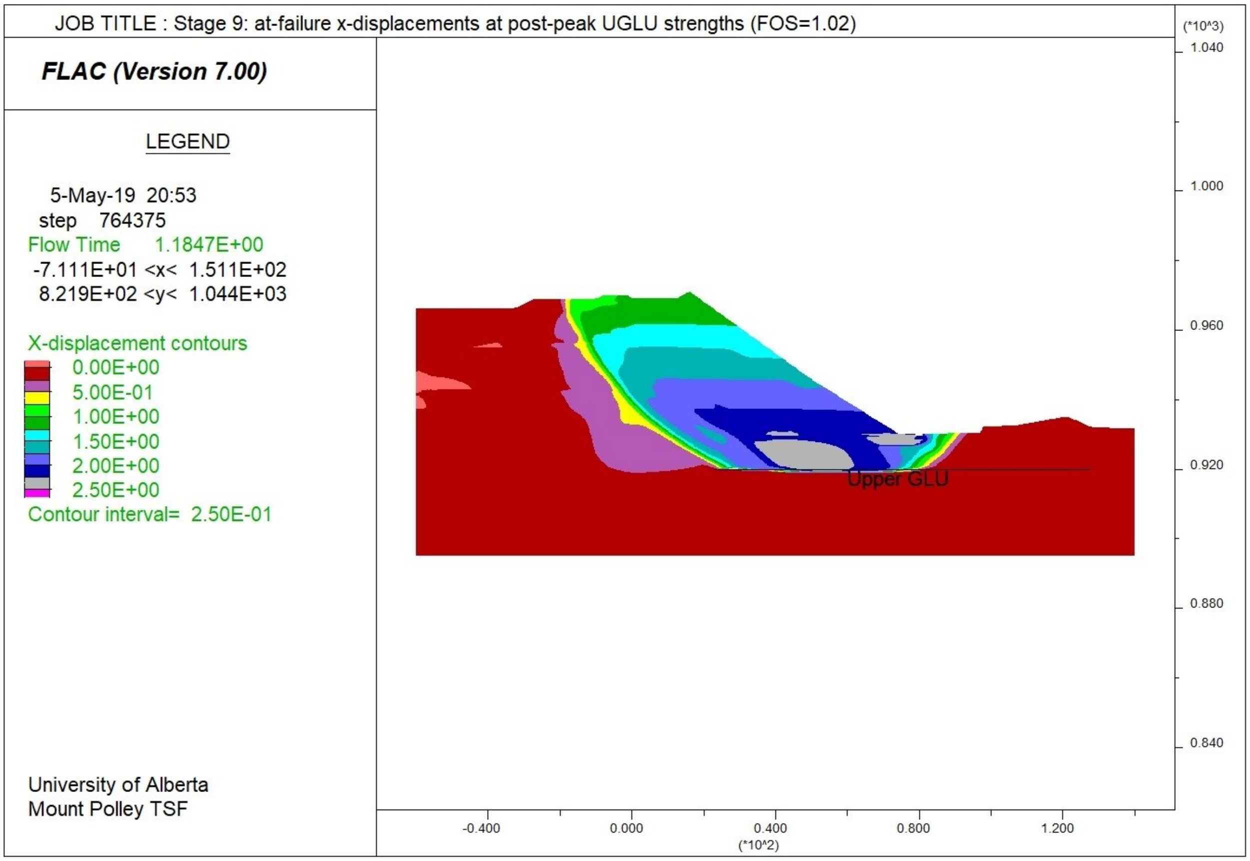

Figure 2A.23 Stage 9 horizontal displacements at failure (failure was generated by assigning average post-peak strength values corresponding to 20% shear strains in the normally consolidated Upper GLU portions).

APPENDIX 2B: MODELLING PARAMETERS FOR THE TWO- AND THREE-DIMENSIONAL LIMIT EQUILIBRIUM ANALYSES AND THE TWO-DIMENSIONAL NUMERICAL ANALYSIS

Table 2B.1 Material properties in the two-dimensional limit equilibrium analysis using the IRP (2015) model.

Material (as shown in Figure 3.4)	Property	Unit	Source		In model	
			KCB (2015)	IRP (2015)	Adapted value	Group
Core	Unit weight	kN/m^3	22.8	20.5	22.8	Core
	Void ratio	-	0.31	0.3	0.31	
	Strength model	-	Mohr-Coulomb	Mohr-Coulomb	Mohr-Coulomb	
	Friction angle	°	33	35	35	
	Cohesion	kPa	0	0	0	
	Hydraulic conductivity	m/s	$2*10^{-9}$ - $2*10^{-8}$	-	$1*10^{-9}$	
Tailings	Unit weight	kN/m^3	18.1	18.6	18.6	Tailings
	Void ratio	-	0.9 - 1.0	1.04	1.04	
	Strength model	-	Mohr-Coulomb	Mohr-Coulomb	Mohr-Coulomb	
	Friction angle	°	28 - 32	30	30	
	Cohesion	kPa	0	0	0	
	Hydraulic conductivity	m/s	$5*10^{-7}$ - $5*10^{-9}$	-	$3*10^{-9}$	
Upper Till Upstr./Downstream	Unit weight	kN/m^3	22.7	21.6	21.6	Upper Till
	Void ratio	-	0.41	-	0.41	
	Strength model	-	Mohr-Coulomb	Mohr-Coulomb	Mohr-Coulomb	
	Friction angle	°	33/35	35	35	
	Cohesion	kPa	0	0	0	
	Hydraulic conductivity	m/s	$2*10^{-9}/4*10^{-9}$	-	$4*10^{-9}$	
Transition	Unit weight	kN/m^3	20.6	-	20.6	Transition
	Void ratio	-	0.34	-	0.31	
	Friction angle	°	35	-	35	
	Strength model		Mohr-Coulomb	Mohr-Coulomb	Mohr-Coulomb	
	Cohesion	kPa	0	0	0	
	Hydraulic conductivity	m/s	$5*10^{-4}$	-	$5*10^{-4}$	
Filter	Unit weight	kN/m^3	19.8	-	19.8	Filter
	Void ratio	-	0.31		0.31	
	Strength model	-	Mohr-Coulomb	Mohr-Coulomb	Mohr-Coulomb	
	Friction angle	°	34	-	34	
	Cohesion	kPa	0	0	0	
	Hydraulic conductivity	m/s	$1*10^{-4}$	-	$1*10^{-4}$	
Fills: GT/CoarseBearing/Coarse	Unit weight	kN/m^3	22.7/19.9/18.6	18	18	Fill 1-3
	Void ratio	-	-/0.59/0.90	-	0.45/0.54/0.47	
	Strength model	-	Mohr-Coulomb	Mohr-Coulomb	Mohr-Coulomb	
	Friction angle	°	33/33/28	30	30	
	Cohesion	kPa	0	0	0	
	Hydraulic conductivity	m/s	$4*10^{-9}/1*10^{-3}/10^{-6}$	-	$4*10^{-9}/1*10^{-3}/10^{-6}$	
Cycloned Sand	Unit weight	kN/m^3	18.1	18	18	Cycloned Sand
	Void ratio	-	0.6	-	0.6	
	Strength model	-	Mohr-Coulomb	Mohr-Coulomb	Mohr-Coulomb	
	Friction angle	°	32	30	30	
	Cohesion	kPa	0	0	0	
	Hydraulic conductivity	m/s	$1*10^{-5}$	-	$2*10^{-5}$	
Upper GLU	Unit weight	kN/m^3	18.6	20	18.6	UGLU
	Void ratio	-	1.2	1.16	1.2	
	Strength model	-	$s_u=\sigma'_{cv}*\tan 7.6°+$ 47.5 kPa	s_u/σ'_{ov}	s_u/σ'_{ov}	
	Undrained ratio	-	-	0.18 - 0.27	0.18	
	Hydraulic conductivity	m/s	$1*10^{-8}$	-	$1*10^{-8}$	

Bedrock Mafic/Sedimentary	Unit weight	kN/m^3	23.0/17.9	-	-	Bedrock
	Void ratio	-	0.33	-	0.33	
	Strength model	-	Mohr-Coulomb	bedrock	bedrock	
	Hydraulic conductivity	m/s	$1*10^{-10}$	-	$1*10^{-9}$	
Glaciofluvial Upper/Lower	Unit weight	kN/m^3	20.5/21.7	-	-	Bedrock
	Void ratio	-	0.56/0.40	0.41	0.41	
	Strength model	-	Mohr-Coulomb	bedrock	bedrock	
	Hydraulic conductivity	m/s	$1*10^{-6}/1*10^{-7}$	-	$1*10^{-6}$	
Rockfill	Unit weight	kN/m^3	20.4	22.8	22.8	Rockfill
	Void ratio	-	0.33	-	0.33	
	Strength model	-	Mohr-Coulomb	shear-normal fn.	Marsal 1973 Sample 1	
	Friction angle	°	40	-	variable	
	Cohesion	kPa	0	-	variable	
	Hydraulic conductivity	m/s	$5*10^{-2}$	-	$5*10^{-4}$	

Table 2B.2 Material properties in the two-dimensional limit equilibrium analysis using the KCB (2015) model.

Material (as shown in Figure 3.4)	Property	Unit	Source		In model	
			KCB (2015)	IRP (2015)	Adapted value	Group
Core	Unit weight	kN/m^3	22.8	20.5	22.8	Core
	Void ratio	-	0.31	0.3	0.31	
	Strength model	-	Mohr-Coulomb	Mohr-Coulomb	Mohr-Coulomb	
	Friction angle	°	33	35	35	
	Cohesion	kPa	0	0	0	
	Hydraulic conductivity	m/s	$2*10^{-9}$ - $2*10^{-8}$	-	$1*10^{-9}$	
Tailings	Unit weight	kN/m^3	18.1	18.6	18.1	Tailings
	Void ratio	-	0.9 - 1.0	1.04	1.04	
	Strength model	-	Mohr-Coulomb	Mohr-Coulomb	Mohr-Coulomb	
	Friction angle	°	28 - 32	30	28	
	Cohesion	kPa	0	0	0	
	Hydraulic conductivity	m/s	$5*10^{-7}$ - $5*10^{-9}$	-	$3*10^{-9}$	
Upper Till Upstream/Downstream	Unit weight	kN/m^3	22.7	21	22.7	Upper Till
	Void ratio	-	0.41	-	0.41	
	Strength model	-	Mohr-Coulomb	Mohr-Coulomb	Mohr-Coulomb	
	Friction angle	°	33/35	35	35	
	Cohesion	kPa	0	0	0	
	Hydraulic conductivity	m/s	$2*10^{-9}/4*10^{-9}$	-	$4*10^{-9}$	
Transition	Unit weight	kN/m^3	20.6	-	20.6	Transition
	Void ratio	-	0.34	-	0.31	
	Friction angle	°	35	-	35	
	Strength model		Mohr-Coulomb	Mohr-Coulomb	Mohr-Coulomb	
	Cohesion	kPa	0	0	0	
	Hydraulic conductivity	m/s	$5*10^{-4}$	-	$5*10^{-4}$	
Filter	Unit weight	kN/m^3	19.8	-	19.8	Filter
	Void ratio	-	0.31		0.31	
	Strength model	-	Mohr-Coulomb	Mohr-Coulomb	Mohr-Coulomb	
	Friction angle	°	34	-	34	
	Cohesion	kPa	0	0	0	
	Hydraulic conductivity	m/s	$1*10^{-4}$	-	$1*10^{-4}$	
Fills: GT/CoarseBearing/Coarse	Unit weight	kN/m^3	22.7/19.9/18.6	18	22.7/20.7/18.6	Fill 1-3
	Void ratio	-	-/0.59/0.90	-	0.45/0.54/0.47	
	Strength model	-	Mohr-Coulomb	Mohr-Coulomb	Mohr-Coulomb	
	Friction angle	°	33/33/28	30	33/33/30	
	Cohesion	kPa	0	0	0	
	Hydraulic conductivity	m/s	$4*10^{-9}/1*10^{-3}/10^{-6}$	-	$4*10^{-9}/1*10^{-3}/10^{-6}$	
Cycloned Sand	Unit weight	kN/m^3	18.1	18	18.1	Cycloned Sand
	Void ratio	-	0.6	-	0.6	
	Strength model	-	Mohr-Coulomb	Mohr-Coulomb	Mohr-Coulomb	
	Friction angle	°	32	30	32	
	Cohesion	kPa	0	0	0	
	Hydraulic conductivity	m/s	$1*10^{-5}$	-	$2*10^{-5}$	
Upper GLU	Unit weight	kN/m^3	18.6	20	18.6	UGLU
	Void ratio	-	1.2	1.16	1.2	
	Strength model	-	$s_u=\sigma'_{cv}*47.5+47.5$ kPa	s_u/σ'_{ov}	$s_u=\sigma'_{cv}*47.5+47.5$ kPa	
	Undrained ratio	-	-	0.18 - 0.27	-	
	Hydraulic conductivity	m/s	$1*10^{-8}$	-	$1*10^{-8}$	

Bedrock Mafic/Sedimentary	Unit weight	kN/m^3	23.0/17.9	-	-	Bedrock
	Void ratio	-	0.33	-	0.33	
	Strength model	-	Mohr-Coulomb	bedrock	bedrock	
	Hydraulic conductivity	m/s	$1*10^{-10}$	-	$1*10^{-9}$	
Glaciofluvial Upper/Lower	Unit weight	kN/m^3	20.5/21.7	-	-	Bedrock
	Void ratio	-	0.56/0.40	0.41	0.41	
	Strength model	-	Mohr-Coulomb	bedrock	bedrock	
	Hydraulic conductivity	m/s	$1*10^{-6}/1*10^{-7}$	-	$1*10^{-6}$	
Rockfill	Unit weight	kN/m^3	20.4	22.8	20.4	Rockfill
	Void ratio	-	0.33	-	0.33	
	Strength model	-	Mohr-Coulomb	shear-normal fn.	Marsal 1973, Sample 1	
	Friction angle	°	40	-	variable	
	Cohesion	kPa	0	-	variable	
	Hydraulic conductivity	m/s	$5*10^{-2}$	-	$5*10^{-4}$	

Table 2B.3 Material properties in the two-dimensional numerical analysis using the KCB (2015) model.

Material (as shown in Figure 3.4)	Property	Unit	Source*		In model	
			KCB (2015)	IRP (2015)	Adapted value	Group
Upper Glacial Till Upstream (under embankment)	Dry density	kg/m^3	2023	1851	2023	Upper Till 1
	Porosity	-	0.29	-	0.29	
	Strength model	-	Mohr-Coulomb	Mohr-Coulomb	Mohr-Coulomb	
	Friction angle	°	33	35	33	
	Cohesion	kPa	0	0	0	
	Bulk modulus	Pa	-	-	$2.5*10^7$	
	Shear Modulus	Pa	-	-	$1.2*10^7$	
	Hydraulic conductivity k_h	m/s	$2*10^{-9}$	-	$2*10^{-9}$	
Upper Glacial Till Downstream	Dry density	kg/m^3	2023	1851	2023	Upper Till 2
	Porosity	-	0.29	-	0.29	
	Strength model	-	Mohr-Coulomb	Mohr-Coulomb	Mohr-Coulomb	
	Friction angle	°	35	35	35	
	Cohesion	kPa	0	0	0	
	Bulk modulus	Pa	-	-	$2.5*10^7$	
	Shear Modulus	Pa	-	-	$1.2*10^7$	
	Hydraulic conductivity k_h	m/s	$4*10^{-9}$	-	$4*10^{-9}$	
Upper GLU under embankment	Dry density	kg/m^3	1351	1502	1351	UGLU 1
	Porosity	-	0.55	0.54	0.55	
	Strength model, drained	-	Mohr-Coulomb	Mohr-Coulomb	Mohr-Coulomb	
	Friction angle φ'_{peak}	°	22	-	22	
	Friction angle φ'_{res}	°	12…14	-	-	
	Cohesion	kPa	0	-	0	
	Strength model, undrained	-	fn(σ'_{cv})	s_u/σ'_{ov}	fn(σ'_{cv})	
	$s_{u,peak}$	kPa	$0.134\sigma'_{cv}+47.5$	$0.27\sigma'_{ov}$	$0.134\sigma'_{cv}+47.5$	
	$s_{u@20\%strain}$	kPa	$0.11\sigma'_{cv}+36$		$0.11\sigma'_{cv}+36$	
	$s_{u@60\%strain}$	kPa	$0.03\sigma'_{cv}+22$	$0.09\sigma'_{ov}-0.14\sigma'_{ov}$	$0.03\sigma'_{cv}+22$	
	Bulk modulus	Pa	-	-	$2.5*10^7$	
	Shear Modulus	Pa	-	-	$1.2*10^7$	
	Hydraulic conductivity k_h	m/s	$5*10^{-9}$	-	$5*10^{-9}$	
Upper GLU downstream	Dry density	kg/m^3	1351	1502	1351	UGLU 2
	Porosity	-	0.55	0.54	0.55	
	Strength model, drained	-	Mohr-Coulomb	Mohr-Coulomb	Mohr-Coulomb	
	Friction angle φ'_{peak}	°	22	-	22	
	Cohesion	kPa	0	-	0	
	Bulk modulus	Pa	-	-	$2.5*10^7$	
	Shear Modulus	Pa	-	-	$1.2*10^7$	
	Hydraulic conductivity k_h	m/s	$1*10^{-8}$	-	$1*10^{-8}$	
Middle Glacial Till	Dry density	kg/m^3	1960	-	1960	MGT
	Porosity	-	0.33	-	0.33	
	Strength model	-	Mohr-Coulomb	Mohr-Coulomb	Mohr-Coulomb	
	Friction angle	°	32	-	32	
	Cohesion	kPa	0	0	0	
	Bulk modulus	Pa	-	-	$2.5*10^7$	
	Shear Modulus	Pa	-	-	$1.2*10^7$	
	Hydraulic conductivity k_h	m/s	$7*10^{-9}$	-	$1*10^{-10}$	
Lower Glaciolacustrine Unit	Dry density	kg/m^3	1610	1710	1610	LGLU 1, 2
	Porosity	-	0.43	0.38	0.43	
	Strength model	-	Mohr-Coulomb	Mohr-Coulomb	Mohr-Coulomb	
	Friction angle φ'_{peak}	°	28	-	28	
	Friction angle φ'_{res}	°	23	-	-	
	Cohesion	kPa	0	0	0	

	Bulk modulus	Pa	-	-	$2.5*10^7$	
	Shear Modulus	Pa	-	-	$1.2*10^7$	
	Hydraulic conductivity k_h	m/s	$2*10^{-8}$	-	$2*10^{-8}$	
Upper Glaciofluvial Unit	Dry density	kg/m^3	1731	-	1731	Glaciofluvial Upper
	Porosity	-	0.36	-	0.36	
	Strength model	-	Mohr-Coulomb	-	Mohr-Coulomb	
	Friction angle	°	30	-	30	
	Cohesion	kPa	0	-	0	
	Bulk modulus	Pa	$5.5*10^7$	-	$5.5*10^7$	
	Shear Modulus	Pa	$4.2*10^7$	-	$4.2*10^7$	
	Hydraulic conductivity k_h	m/s	$4*10^{-7}$	-	$4*10^{-7}$	
Lower Glaciofluvial Unit	Dry density	kg/m^3	1925	-	1925	Glaciofluvial Lower
	Porosity	-	0.29	-	0.29	
	Strength model	-	Mohr-Coulomb	-	Mohr-Coulomb	
	Friction angle	°	33	-	33	
	Cohesion	kPa	0	-	0	
	Bulk modulus	Pa	$5.5*10^7$	-	$2.5*10^7$	
	Shear Modulus	Pa	$4.2*10^7$	-	$1.2*10^7$	
	Hydraulic conductivity k_h	m/s	$4*10^{-7}$	-	$4*10^{-7}$	
Lower Glacial Till	Dry density	kg/m^3	2021	1827	2021	Lower Till
	Porosity	-	0.33	0.33	0.33	
	Strength model	-	Mohr-Coulomb	Mohr-Coulomb	Mohr-Coulomb	
	Friction angle	°	35	-	35	
	Cohesion	kPa	0	-	0	
	Bulk modulus	Pa	-	-	$2.3*10^7$	
	Shear Modulus	Pa	-	-	$1*10^7$	
	Hydraulic conductivity k_h	m/s	$1*10^{-9}$	-	$1*10^{-9}$	
Bedrock Sedimentary	Dry density	kg/m^3	1310	-	1310	Bedrock Sedimentary
	Porosity	-	0.51	-	0.51	
	Strength model	-	bedrock	bedrock	Elastic	
	Bulk modulus	Pa	-	-	$5.5*10^7$	
	Shear Modulus	Pa	-	-	$4.2*10^7$	
	Hydraulic conductivity k_h	m/s	$1*10^{-10}$	-	$1*10^{-10}$	
Bedrock Mafic	Dry density	kg/m^3	2138	-	2138	Bedrock Mafic
	Porosity	-	0.21	-	0.21	
	Strength model	-	bedrock	bedrock	Elastic	
	Bulk modulus	Pa	-	-	$5.5*10^7$	
	Shear Modulus	Pa	-	-	$4.2*10^7$	
	Hydraulic conductivity k_h	m/s	$1*10^{-10}$	-	$1*10^{-10}$	
Transition	Dry density	kg/m^3	2011	-	2011	Transition 3,6,9
	Porosity	-	0.25	-	0.25	
	Strength model	-	Mohr-Coulomb	-	Mohr-Coulomb	
	Friction angle	°	35	-	35	
	Cohesion	kPa	0	-	0	
	Bulk modulus	Pa	-	-	$5.5*10^7$	
	Shear Modulus	Pa	-	-	$4.2*10^7$	
	Hydraulic conductivity k_h	m/s	$5*10^{-4}$	-	$5*10^{-4}$	
Rockfill	Dry density	kg/m^3	2030	2243	2030	Rockfill 3,6,9
	Porosity	-	0.25	0.25	0.25	
	Strength model	-	Mohr-Coulomb	shear-normal	Mohr-Coulomb	
	Friction angle	°	40	variable	40	
	Cohesion	kPa	0	variable	0	
	Bulk modulus	Pa	-	-	$5.5*10^7$	
	Shear Modulus	Pa	-	-	$4.2*10^7$	

	Hydraulic conductivity k_h	m/s	$5*10^{-2}$	-	$5*10^{-2}$	
Filter	Dry density	kg/m^3	1863	-	1863	Filter 3,6,9
	Porosity	-	0.31	-	0.31	
	Strength model	-	Mohr-Coulomb	-	Mohr-Coulomb	
	Friction angle	°	34	-	34	
	Cohesion	kPa	0	-	0	
	Bulk modulus	Pa	-	-	$5.5*10^{7}$	
	Shear Modulus	Pa	-	-	$4.2*10^{7}$	
	Hydraulic conductivity k_h	m/s	$1*10^{-4}$	-	$1*10^{-4}$	
Core	Dry density	kg/m^3	2090	1860	2090	Core 3,6,9
	Porosity	-	0.24	0.23	0.24	
	Strength model	-	Mohr-Coulomb	Mohr-Coulomb	Mohr-Coulomb	
	Friction angle	°	33	35	33	
	Cohesion	kPa	0	-	0	
	Bulk modulus	Pa	-	-	$2.5*10^{7}$	
	Shear Modulus	Pa	-	-	$1.2*10^{7}$	
	Hydraulic conductivity k_h	m/s	$2*10^{-8}$	-	$2*10^{-8}$	
Fill	Dry density	kg/m^3	2074	-	2074	Till, Glaciolacustrine or Granular Fill
	Porosity	-	0.24	-	0.24	
	Strength model	-	Mohr-Coulomb	-	Mohr-Coulomb	
	Friction angle	°	33	-	33	
	Cohesion	kPa	0	-	0	
	Bulk modulus	Pa	-	-	$2.5*10^{7}$	
	Shear Modulus	Pa	-	-	$1.2*10^{7}$	
	Hydraulic conductivity k_h	m/s	$5*10^{-9}$	-	$5*10^{-9}$	
Cycloned sand	Dry density	kg/m^3	1470	-	1470	Cycloned Sand
	Porosity	-	0.375	-	0.375	
	Strength model	-	Mohr-Coulomb	-	Mohr-Coulomb	
	Friction angle	°	32	-	32	
	Cohesion	kPa	0	-	0	
	Bulk modulus	Pa	-	-	$2.5*10^{7}$	
	Shear Modulus	Pa	-	-	$1.2*10^{7}$	
	Hydraulic conductivity k_h	m/s	$2*10^{-5}$	-	$2*10^{-5}$	
Fill - Random Rockfill	Dry density	kg/m^3	1760	-	1760	Random Rockfill 3,6
	Porosity	-	0.35	-	0.35	
	Strength model	-	Mohr-Coulomb	-	Mohr-Coulomb	
	Friction angle	°	33	-	33	
	Cohesion	kPa	0	-	0	
	Bulk modulus	Pa	-	-	$5.5*10^{7}$	
	Shear Modulus	Pa	-	-	$4.2*10^{7}$	
	Hydraulic conductivity k_h	m/s	$1*10^{-3}$	-	$1*10^{-3}$	
Random Fill	Dry density	kg/m^3	1760	-	1760	Select Fill 6,9
	Porosity	-	0.35	-	0.35	
	Strength model	-	Mohr-Coulomb	-	Mohr-Coulomb	
	Friction angle	°	30	-	30	
	Cohesion	kPa	0	-	0	
	Bulk modulus	Pa	-	-	$2.5*10^{7}$	
	Shear Modulus	Pa	-	-	$1.2*10^{7}$	
	Hydraulic conductivity k_h	m/s	$1*10^{-5}$	-	$1*10^{-5}$	
Tailings, Coarse	Dry density	kg/m^3	1426	1326	1426	Tailings 3,6,9
	Porosity	-	0.47	0.5	0.47	
	Strength model	-	Mohr-Coulomb	-	Mohr-Coulomb	
	Friction angle	°	32	30	32	
	Cohesion	kPa	0	0	0	

	Bulk modulus	Pa	-	-	$2.5*10^{7}$	
	Shear Modulus	Pa	-	-	$1.2*10^{7}$	
	Hydraulic conductivity k_h	m/s	$1*10^{-5}$	-	$1*10^{-5}$	

APPENDIX 3A: THE ROCKFILL CONSTITUTIVE MODEL

I) *Evaluation of Hoek-Brown failure envelope for Samples 2, 3 and 4 from Marsal (1973)*

Evaluation of the Hoek-Brown Failure Envelope parameters for Samples 2, 3 and 4 from Marsal (1973)

adapted from Marsal (1973, p. 166)					
Sample 3		Sample 2		Sample 4	
σ_n' kPa	τ_f kPa	σ_n' kPa	τ_f kPa	σ_n' kPa	τ_f kPa
Triaxial Test 1					
196	0	196	0	196	0
275	294	262	245	268	270
490	510	441	425	466	467
785	589	687	491	736	540
1079	510	932	425	1006	467
1294	294	1111	245	1203	270
1373	0	1177	0	1275	0
Triaxial Test 2					
491	0	589	0	491	0
613	454	704	429	655	613
945	786	1018	743	1104	1062
1398	907	1447	858	1717	1226
1852	786	1876	743	2330	1062
2184	454	2190	429	2779	613
2305	0	2305	0	2943	0
Triaxial Test 3					
981	0	981	0	981	0
1031	381	1031	381	1039	444
1178	736	1178	736	1211	858
1412	1041	1412	1041	1484	1214
1717	1274	1717	1274	1839	1487
2072	1421	2072	1421	2253	1658
2453	1472	2453	1472	2698	1717
2833	1421	2833	1421	3142	1658
3188	1274	3188	1274	3556	1487
3493	1041	3493	1041	3912	1214
3727	736	3727	736	4184	858
3874	381	3874	381	4356	444
3924	0	3924	0	4415	0
Triaxial Test 4					
1668	0	1668	0	1668	0
1745	584	1745	584	1763	724
1970	1128	1970	1128	2042	1398
2329	1595	2329	1595	2487	1977
2796	1954	2796	1954	3066	2421
3340	2179	3340	2179	3740	2701
3924	2256	3924	2256	4464	2796
4508	2179	4508	2179	5187	2701
5052	1954	5052	1954	5861	2421
5519	1595	5519	1595	6441	1977
5878	1128	5878	1128	6885	1398
6103	584	6103	584	7164	724
6180	0	6180	0	7259	0
Triaxial Test 5					
2551	0	2551	0	2649	0
2659	825	2659	825	2776	965
2978	1594	2978	1594	3148	1864
3484	2254	3484	2254	3741	2636
4145	2761	4145	2761	4513	3228
4914	3080	4914	3080	5412	3601
5739	3188	5739	3188	6377	3728
6564	3080	6564	3080	7341	3601
7333	2761	7333	2761	8240	3228
7993	2254	7993	2254	9012	2636
8500	1594	8500	1594	9605	1864
8818	825	8818	825	9977	965
8927	0	8927	0	10104	0

Read from Graph
Calculated Value

Evaluation of the Hoek-Brown Failure Envelope parameters for Samples 2, 3 and 4 from Marsal (1973)

Strength envelope for Sample 1 adapted from Marsal (1973, p. 166)

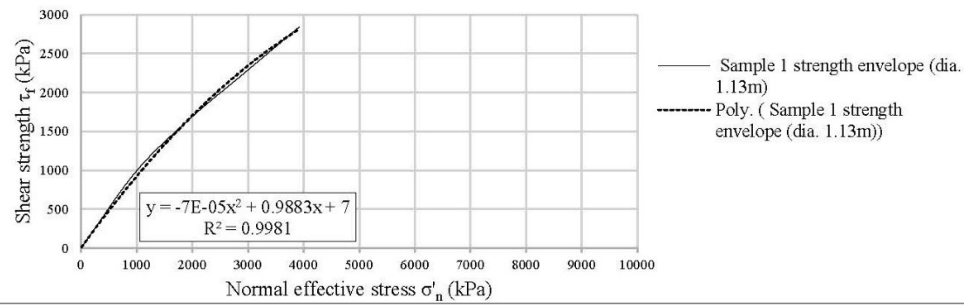

Triaxial test results and strength envelope for Sample 2 adapted from Marsal (1973, p. 166)

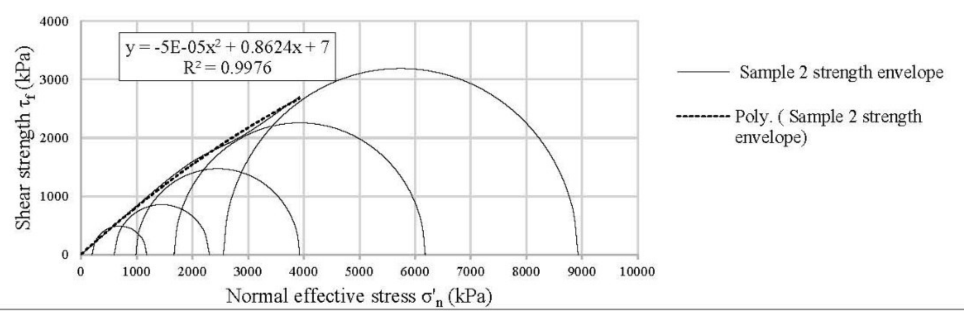

Triaxial test results and strength envelope for Sample 3 adapted from Marsal (1973, p. 166)

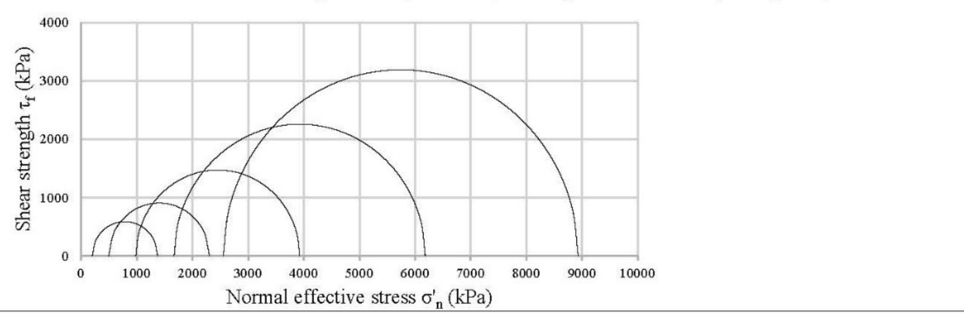

Triaxial test results and strength envelope for Sample 4 adapted from Marsal (1973, p. 166)

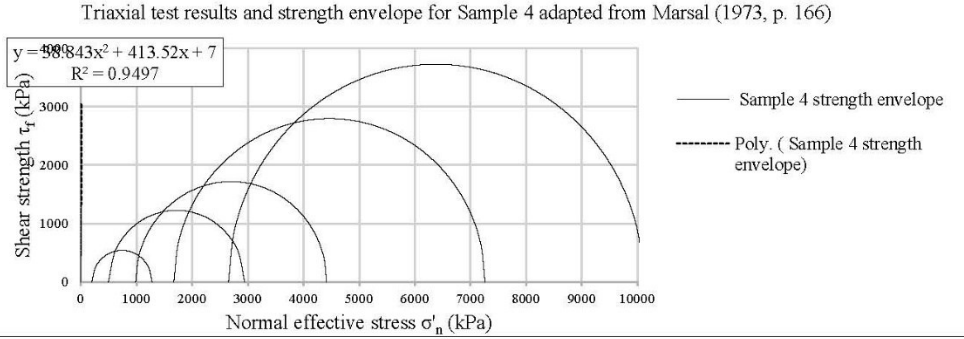

Evaluation of the Hoek-Brown Failure Envelope parameters for Samples 2, 3 and 4 from Marsal (1973)

Sample 2

σ'_3, kPa	σ'_1, kPa	y	xy	x^2	y^2
196	1177	962361	188815228	38494	926138694321
589	2305	2947231	1734739909	346450	8686167988534
981	3924	8661249	8496685269	962361	75017234240001
1668	6180	20363559	33960306944	2781223	414674525371972
2551	8927	40659752	103706764089	6505560	1653215453031380
x					
sum(x)		sum(y)	sum(xy)	sum(x^2)	sum(y^2)
5984		73594152	148087311439	10634089	2152519519326210

n	5
(sigci, kPa)^2	**-5965242**
mi	**0.0**
r^2	**0.970**

Conclusion: Hoek Brown envelope cannot be determined for this material (sigci=sqrt(negative))

Sample 3

σ'_3, kPa	σ'_1, kPa	y	xy	x^2	y^2
196	1373	1385800	271893929	38494	1920441196544
491	2943	6014756	2950237941	240590	36177292746914
981	4905	15397776	15105218256	962361	237091505746176
1668	7358	32373824	53989826352	2781223	1048064482972880
2453	10987	72841104	178642807781	6014756	5305826445050210
x		y	xy	x^2	y^2
sum(x)		sum(y)	sum(xy)	sum(x^2)	sum(y^2)
5788		128013260	250959984257	10037425	6629080167712730

n	5
(sigci, kPa)^2	########
mi	**0.0**
r^2	**0.944**

Conclusion: Hoek Brown envelope cannot be determined for this material (sigci=sqrt(negative))

Sample 4

σ'_3, kPa	σ'_1, kPa	y	xy	x^2	y^2
196	1275	1164457	228466426	38494	1355959662355
491	2943	6014756	2950237941	240590	36177292746914
981	4415	11788922	11564932727	962361	138978687816545
1668	7259	31267109	52144157496	2781223	977632098339117
2649	10104	55585971	147230562341	7015612	3089800212034740
x		y	xy	x^2	y^2
sum(x)		sum(y)	sum(xy)	sum(x^2)	sum(y^2)
5984		105821216	214118356931	11038281	4243944250599670

n	5
(sigci, kPa)^2	**-5841589**
mi	**0.0**
r^2	**0.985**

Conclusion: Hoek Brown envelope cannot be determined for this material (sigci=sqrt(negative))

Evaluation of the Hoek-Brown Failure Envelope parameters for Samples 2, 3 and 4 from Marsal (1973)

Verification of formulae using example in CIVE 697 Winter 2016 notes from Lecture 6-5/23								
σ'_3, kPa	σ'_1, kPa	y	xy	x^2	y^2	n	5	
0	38	1467	0	0	2151766	(sigci, kPa)	**37.4**	✓
5	72	4543	22714	25	20636668	mi	**15.5**	✓
8	81	5329	39968	56	28398241	r^2	**0.997**	✓
15	116	10120	151805	225	102421687			
20	134	13064	261290	400	170680899			
x								
sum(x)		sum(y)	sum(xy)	sum(x^2)	sum(y^2)			
48		34524	475777	706	324289261			

II) *Implementation*

Rockfill's constitutive model

Implementation of the rockfill constitutive model in the FLAC3D™ deformation analysis of the Mount Polley TSF failure

Flowchart

Assign a Mohr-Coulomb strength model to all rockfill zones roughly approximating the Sample 2 strength envelope for near-zero normal stresses. Assign a constant Young's modulus value to all zones.

```
fish define _dam_mc (a,b,c)
   loop foreach pnt zone.list
      if zone.group(pnt) = a
               ;zone.group(pnt) = a ;+ '_3'
               zone.model(pnt) = 'mohr-coulomb'
               zone.prop(pnt,'friction') = b
               zone.prop(pnt,'cohesion') = c
               zone.prop(pnt,'young') = 3e7
               zone.prop(pnt,'poisson') = 0.2
      else
      end_if
   end_loop
end
@_dam_mc('Rockfill', 44.1,7000)
```

↓

Establish an initial stress state in the rockfill

↓

1. Assign proper strength model to all rockfill zones:
Use Sample 2 envelope and zone's current stress state to determine equivalent cohesion and friction parameters.
2. Assign Young's modulus value zone based on its current minor principal effective stress; use a high lower cutoff value ($7*10^6$ as opposed to $3*10^6$).

See 'Rockfill_cmodel' FISH function on next page

↓

Step through a defined number of cycles while gradually adjusting the lower cutoff value of Young's modulus in the rockfill as well as by re-establishing the rockfill equivalent strength envelope parameters as a function of the changing stress state (done by running a modified 'Rockfill_cmodel' function as a subroutine*).

↓

Solve while running a 'Rockfill_cmodel' function as a subroutine*.

*NOTE that several subroutines are run in parallel with the solver, such as the 'UGLU_cmodel' and the 'Rockfill_cmodel' FISH functions

Implementation of the rockfill constitutive model in the FLAC3D™ deformation analysis of the Mount Polley TSF failure

The 'Rockfill_cmodel' FISH function

```
fish define _Rockfill_cmodel
   local _1
   local _2
   local _3
   local e_sig1
   local e_sig3
   local mc_rad
   local e_min
   local e_normal
   local tau
   local d_tau
   local e_friction
   local e_cohesion
   local invariant_1
      loop foreach pnt zone.list
         if zone.group(pnt) = 'Rockfill'
         if zone.model(pnt) = 'mohr-coulomb'
            _1 = math.abs(zone.stress.prin.x(pnt)+zone.pp(pnt))
            _2 = math.abs(zone.stress.prin.y(pnt)+zone.pp(pnt))
            _3 = math.abs(zone.stress.prin.z(pnt)+zone.pp(pnt))
                        e_sig1 = math.max(_1, _2, _3)
                         e_sig3 = math.min(_1, _2, _3)
                        mc_rad = math.abs((e_sig1 - e_sig3)/2.0)
                        e_min = e_sig3
                         e_normal = e_min + mc_rad*0.33    ; estimated normal effective stress on potential failure plane
                        tau   =  -0.00000004*e_normal^2 + 0.9697*e_normal + 7000 ; S3 curved envelope
                        d_tau = -0.00000008*e_normal + 0.9697                  ; tan (phi)
                        e_friction = math.atan(d_tau)*180./math.pi
                        e_cohesion = tau - d_tau*e_normal
            zone.prop(pnt,'friction') = e_friction
            zone.prop(pnt,'cohesion') = e_cohesion
; assign E = fn(e_sig3)
               if e_min < 70000
                     zone.prop(pnt,'young') = 1.05e7
               else
                     zone.prop(pnt,'young') = e_min*50.32+7e6 ; upper E bound not necessary for the anticipated range of in-situ stresses
               end_if
else
         end_if
         else
         end_if
      end_loop
end
```

APPENDIX 3B: UPPER GLU'S CONSTITUTIVE MODEL

Upper GLU's constitutive model

Implementation of UGLU's constitutive model in the FLAC3D™ deformation analysis of the Mount Polley TSF failure

Flowchart

Assign drained strength model to all UGLU zones

```
zone cmodel assign strain-softening…
range group 'UGLU'
zone property …
                density 1351 …
                young 2e7 …
                  poisson 0.4 …
                cohesion 0 …
                friction 22 …
range group 'UGLU'
```

Set preconsolidation pressure $\sigma'_p = 429\ kPa$ in each UGLU zone

```
fish define _initialize_sigp
   loop foreach pnt zone.list
      if zone.group(pnt) = 'UGLU'
         zone.extra(pnt) = 429
      else
      end_if
   end_loop
end
```

Define strain-weakening cohesion tables for $\sigma'_{cv} = 430 \ldots 2000\ kPa$

```
fish define _table_cohesion
local _coh_table
   loop local i (429, 2000)
   _coh_table = (string('c')+string(i))
   command
      table [_coh_table] delete
      table [_coh_table] add    (0.0,
[134*i+47466]) (0.04, [134*i+47466])   (0.1,
[122.1*i+37636])   (0.45, [28.9*i+ 21258])
   end_command
   end_loop
end
```

Solve sequentially Stages 0 through 9 to establish equilibrium for each stage while running a subroutine process ('*UGLU_cmodel*') that checks UGLU's current σ'_{ov} in each zone and, if greater than its current preconsolidation pressure σ'_p, updates the current consolidation pressure & switches its strength model to undrained. The undrained model is assigned to the zone as a function of its current preconsolidation pressure (rounded off to the nearest kPa) in the form of a strain-weakening cohesion table and a null friction table.

```
fish define _UGLU_cmodel
   local _sig_ov
   local _c_table
   loop foreach pnt zone.list
      if zone.group(pnt) = 'UGLU'
         _sig_ov = math.round(math.abs(zone.stress.effective.zz(pnt)/1000))
if zone.extra(pnt) < _sig_ov
               zone.extra(pnt) = _sig_ov
               _c_table = (string('c')+string(_sig_ov))
               zone.prop(pnt, 'table-cohesion') = _c_table
               zone.prop(pnt, 'table-friction') = 'fric_ss'          ; assign friction-weakening table with zero values
            else
            end_if
      else
      end_if
   end_loop
end
```

Upper GLU's constitutive model

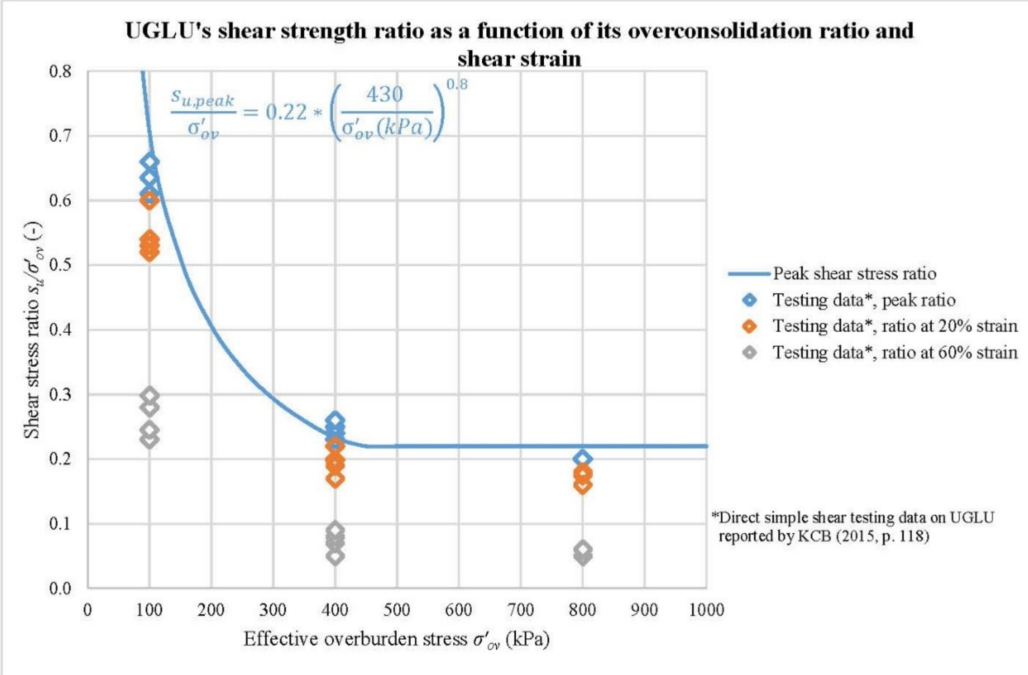

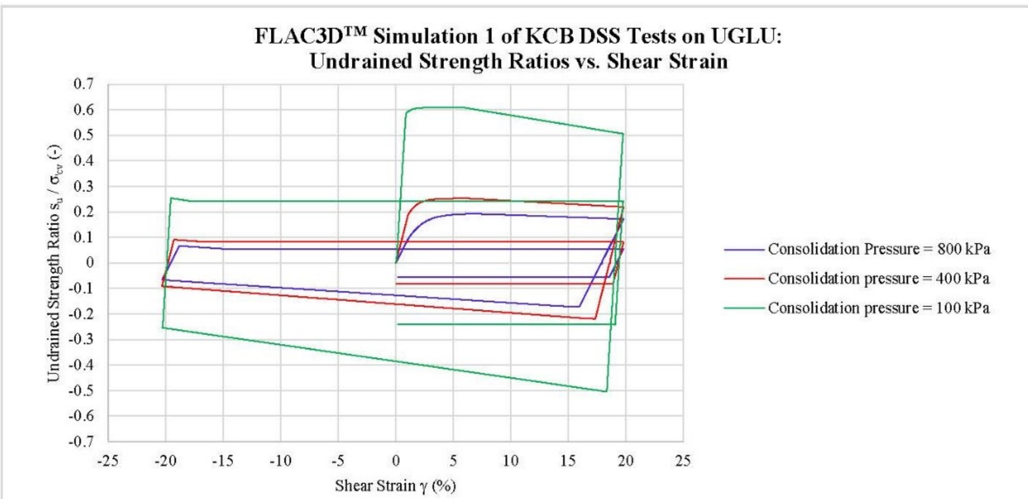

The strain-weakening model 1*:

$\gamma_s^p = 0 \ldots 5\%$ $\quad s_u = 134\sigma'_{cv} + 47kPa$

$\gamma_s^p = 20\%$ $\quad s_u = 122\sigma'_{cv} + 38kPa$

$\gamma_s^p = 60\%$ $\quad s_u = 29\sigma'_{cv} + 21kPa$

*Intermediate values between points are determined using linear interpolation

Upper GLU's constitutive model

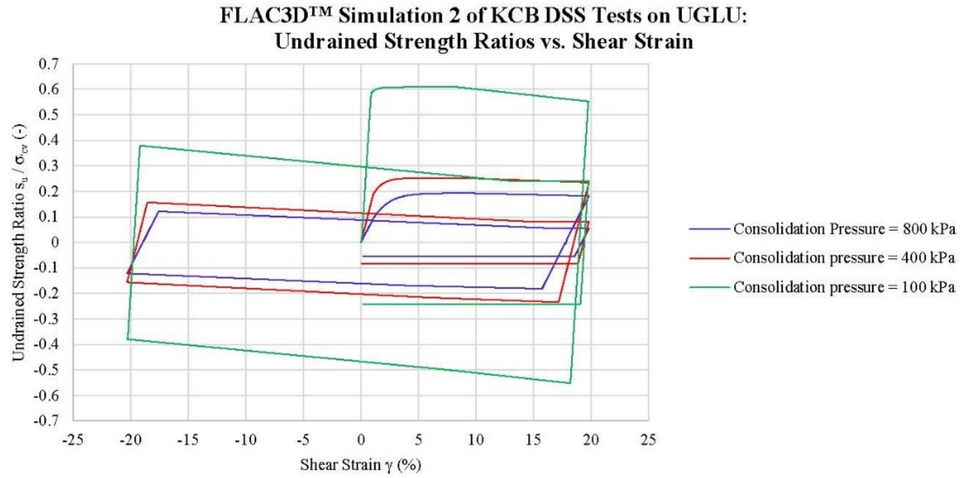

The strain-weakening model 2*:

$\gamma_s^p = 0 \ldots 7.5\%$ $\quad s_u = 134\sigma'_{cv} + 47kPa$

$\gamma_s^p = 30\%$ $\quad s_u = 122\sigma'_{cv} + 38kPa$

$\gamma_s^p = 90\%$ $\quad s_u = 29\sigma'_{cv} + 21kPa$

*Intermediate values between points are determined using linear interpolation

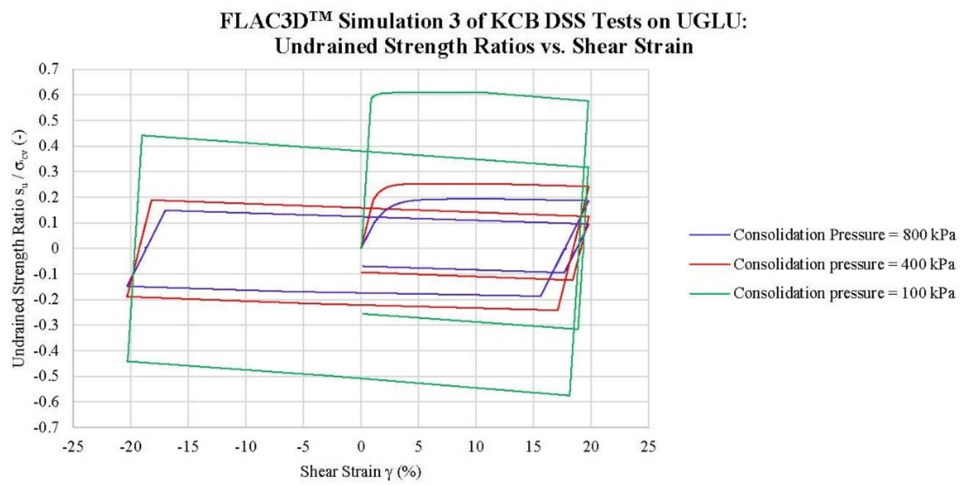

The strain-weakening model 3*:

$\gamma_s^p = 0 \ldots 10\%$ $\quad s_u = 134\sigma'_{cv} + 47kPa$

$\gamma_s^p = 40\%$ $\quad s_u = 122\sigma'_{cv} + 38kPa$

$\gamma_s^p = 120\%$ $\quad s_u = 29\sigma'_{cv} + 21kPa$

*Intermediate values between points are determined using linear interpolation

APPENDIX 3C: OTHER EMBANKMENT MATERIALS

Table 3C.1 Material properties for embankment materials involved in failure used for the three-dimensional deformation model.

Material (in Figure 3.1.1.2)	Property	Unit	Source*		In FLAC3D model	
			KCB (2015)	IRP (2015)	Adopted value	Group
Core	Dry density	kg/m^3	2084*	1850**	2090	Core
	Void ratio	-	0.31*	0.30**	0.31	
	Saturation	%	100	100**	100	
	Friction angle	°	33	35	33	
	Cohesion	kPa	0	0	0	
	Bulk modulus	Pa	-	-	$2.5*10^7…3.7*10^7$	
	Shear modulus	Pa	-	-	$1.2*10^7…1.1*10^8$	
	Hydraulic conductivity	m/s	$2*10^{-9}$ - $2*10^{-8}$	-	$4*10^{-9}$	
Rockfill	Dry density	kg/m^3	2025	2193	2025	Rockfill
	Void ratio	-	0.33	0.33	0.33	
	Saturation	%	20	-	0****	
	Friction angle	°	40	variable	variable***	
	Cohesion	kPa	0	0	variable***	
	Young's modulus	Pa	-	-	$50.32\sigma'_3+7e6$	
	Poisson ratio	Pa	-	-	0.35	
	Hydraulic conductivity	m/s	$5*10^{-4}$	-	$5*10^{-2}$	
Transition	Dry density	kg/m^3	2103*	-	2025	Rockfill
	Void ratio	-	0.34	-	0.33	
	Saturation	%	35	-	0****	
	Friction angle	°	35	-	variable***	
	Cohesion	kPa	0	0**	variable***	
	Young's modulus	Pa	-	-	$50.32\sigma'_3+7e6$	
	Poisson ratio	Pa	-	-	0.35	
	Hydraulic conductivity	m/s	$5*10^{-4}$	-	$5*10^{-2}$	
Filter	Dry density	kg/m^3	1862*	-	2025	Rockfill
	Void ratio	-	0.45	-	0.33	
	Saturation	%	50	-	0****	
	Friction angle	°	34	-	variable***	
	Cohesion	kPa	0	0**	variable***	
	Young's modulus	Pa	-	-	$50.32\sigma'_3+7e6$	
	Poisson ratio	Pa	-	-	0.35	
	Hydraulic conductivity	m/s	$1*10^{-4}$	-	$5*10^{-2}$	
Fills 1-3	Dry density	kg/m^3	1753*	-	1326	Tailings
	Void ratio	-	0.54	-	1.04	
	Saturation	%	100	-	100	
	Friction angle	°	30	-	32	
	Cohesion	kPa	0	-	0	
	Bulk modulus	Pa	-	-	$2.4*10^7…2.5*10^7$	
	Shear modulus	Pa	-	-	$1.2*10^7…2.3*10^8$	
	Hydraulic conductivity	m/s	$1*10^{-5}$	-	$5*10^{-7}$	

Material (in Figure 3.1.1.2)	Property	Unit	Source*		In FLAC3D model	
			KCB (2015)	IRP (2015)	Adopted value	Group
Cycloned Sand	Dry density	kg/m^3	1688*	-	1326	Tailings
	Void ratio	-	0.6	-	1.04	
	Saturation	%	100	-	100	
	Friction angle	°	32	-	32	
	Cohesion	kPa	0	-	0	
	Bulk modulus	Pa	-	-	$2.4*10^7…2.5*10^7$	
	Shear modulus	Pa	-	-	$1.2*10^7…2.3*10^8$	
	Hydraulic conductivity	m/s	$2*10^{-5}$	-	$5*10^{-7}$	
Tailings	Dry density	kg/m^3	1350 - 1421	1324**	1326	Tailings
	Void ratio	-	0.9 - 1.0	1.04**	1.04	
	Saturation	%	100	100**	100	
	Friction angle	°	28 - 32	30	32	
	Cohesion	kPa	0	0	0	
	Bulk modulus	Pa	-	-	$2.4*10^7…2.5*10^7$	
	Shear modulus	Pa	-	-	$1.2*10^7…2.3*10^8$	
	Hydraulic conductivity	m/s	$5*10^{-7}$ - $5*10^{-9}$	-	$5*10^{-7}$	
UGT	Dry density	kg/m^3	2023	1851	2023	Upper Till
	Void ratio	-	0.41	0.38-0.74	0.41	
	Saturation	%	100	100**	100	
	Friction angle	°	33-35	35	33-35	
	Cohesion	kPa	0	0	0	
	Bulk modulus	Pa	-	-	$2.4*10^7…2.5*10^7$	
	Shear modulus	Pa	-	-	$1.2*10^7…2.3*10^8$	
	Hydraulic conductivity	m/s	$2*10^{-9}$ - $4*10^{-9}$	-	$4*10^{-9}$	
Upper GLU	Dry density	kg/m^3	2023	1851	2023	Upper GLU
	Void ratio	-	1.2	0.78-1.43	1.2	
	Saturation	%	100	100**	100	
	Friction angle, peak	°	22	-	22	
	Cohesion	kPa	0	0	0	
	$s_{u,peak}$	kPa	$0.13σ'_{cv}+47$	$0.27σ'_{ov}$	$0.13σ'_{cv}+47$	
	$s_{u,residual}$	kPa	$0.03σ'_{cv}+22$	$0.13σ'_{ov}$	$0.03σ'_{cv}+22$	
	Bulk modulus	Pa	-	-	$2.5*10^7…4.1*10^7$	
	Shear modulus	Pa	-	-	$1.2*10^7…4.0*10^8$	
	Hydraulic conductivity	m/s	$5*10^{-9}$ - $1*10^{-8}$	-	$1*10^{-8}$	

Material (in Figure 3.1.1.2)	Property	Unit	Source*		In FLAC3D model	
			KCB (2015)	IRP (2015)	Adopted value	Group
All materials below upper till and Upper GLU	Dry density	kg/m^3	~2000	-	1960	Middle Till
	Void ratio	-	~0.5	-	0.5	
	Saturation	%	100	100	100	
	Friction angle	°	32	-	32	
	Cohesion	kPa	0	0	0	
	Bulk modulus	Pa	-	-	$2.5*10^7…3.3*10^7$	
	Shear modulus	Pa	-	-	$1.2*10^7…1.0*10^8$	
	Hydraulic conductivity	m/s	variable	-	variable	

*Calculated based on reported properties and geotechnical phase relationships.

**Estimated using reported data, geotechnical phase relationships and some assumptions.

***As per reported rockfill strength model, see Section 3.2.2.

****The rockfill was modelled as fully saturated to avoid errors in large strain mode; the unit's dry density was adjusted accordingly to produce effective loadings equivalent to dry rockfill. See Section 3.2.2.

APPENDIX 3D: EVALUATION OF PORE WATER PRESSURES

I) *Overview*

This appendix describes the method used to determine the pore water pressure distributions in the three-dimensional deformation model of the Mount Polley TSF failure.

Steady-state pore water pressure distributions were determined for construction stages 3 through 9. Hydrostatic pore water pressure conditions with a groundwater at surface were assumed for the pre-construction stage. The pore pressure distributions were established using the modelling strategy outlined below:

(1) As a first step, a two-dimensional seepage analysis was conducted on a typical cross-section of the Mount Polley TSF embankment at the failure location to determine pore water pressure distributions during construction stages 3, 6 and 9 (Section II). The calibrated results of the two-dimensional seepage analysis were used to establish the boundary conditions as well as to approximate the initial pore water pressure distributions in the three-dimensional seepage model.

(2) A three-dimensional steady state seepage analysis was conducted for construction stages 3 through 9, and verified against the two-dimensional analysis results (Section III). The resulting pore water pressure distributions were used in the deformation analysis of the Mount Polley TSF failure.

In addition to documenting the process of estimating the pore pressure distributions that was ultimately used in the analysis of the failure, this section also examines some of the more important considerations that affected the choice of modelling techniques (Section IV).

II) *Two-dimensional seepage analysis*

<u>Process</u>

The two-dimensional seepage analysis was conducted in SoilVision® Ver. 5.3.04 using the SVFlux module. The modelling and calibration process is described in the following sequential steps.

1. A steady-state seepage solution was found for construction stage 9, and verified against piezometer data recorded shortly prior to failure (KCB 2015, Table III-1), as well as against stage 9 steady-state seepage solutions reported by KCB (2015, Figure III-5) and IRP (2015, Figure H3).
2. Once the steady-state solution for stage 9 was judged to be adequate, steady-state seepage solutions for construction stages 3 and 6 were produced using the same material parameters while modifying accordingly the geometry and boundary conditions.
3. The steady-state solutions for construction stages 3, 6 and 9 (shown in Figure 3D.4) were used to approximate the boundary and initial conditions in the three-dimensional flow model:
    a. The shape of phreatic surface was used to produce three-dimensional surfaces. In FLAC3D, these surfaces were used to specify the initial groundwater table position with hydrostatic pore pressure distributions below. The shapes and positions of grounwater surfaces in construction stages 4, 5, 7 and 8 were obtained by interpolation combined with pond elevation data. Select surfaces are seen in Figure 3D.5.
    b. The steady-state pore pressure distributions on the upstream and downstream edges of the two-dimensional model were used to approximate the boundary conditions on the upstream and downstream face of the three-dimensional model. For stages 4, 5, 7 and 8, interpolation was used to approximate these distributions.
4. The pore water pressure distributions produced by this analysis were ultimately used as benchmarks to evaluate the quality of the three-dimensional solution for pore water pressure distributions.

<u>Geometry</u>

The typical cross-section of the Mount Polley TSF illustrated in Figure 3D.1 was used for the seepage analysis of construction stage 9. This same cross-section was modified based on data reported by both investigators (KCB 2015, Figure 2.6; IRP 2015, Figue H1) to represent stages 3 and 6.

<u>Boundary Conditions</u>

The following boundary conditions were applied in the two-dimensional seepage model:

1. Pond elevations of 941.5m, 954.0m and 966.83m were respectively applied to the top surface of tailings in construction stages 3, 6 and 9. These values correspond to reported pond elevations (IRP 2015, Drawing G1).
2. The internal drain installed on the upstream of the core at an elevation of 946.3m was simulated in the model as a constant total head boundary. In stage 9, the total head value was varied to calibrate the results; a total head value of 951.3m produced the best-matching results. In stage 6, the drain's total head value was varied between 946.3m (correcponding to zero pressure) and 951.3m (likely a high estimate) to explore the sensitivity of this parameter. The resulting pore pressure distributions varied by about 50kPa around the drain, but were similar elsewhere. Ultimately, a constant head value of 947m was selected for the internal drain.
3. The face of the dam and the downstream surface were assigned a "review boundary" condition, flagging potential seepage exit locations.
4. The downstream edge of the model was assigned hydrostatic pressure conditions with a water table at ground surface.

<u>Soil Properties</u>

Soil properties relevant to seepage analysis include saturated hydraulic conductivities, unsaturated hydraulic conductivity and volumetric water content behaviours, and porosities. Saturated horizontal hydraulic conductivities k_h and porosities n for the Mount Polley TSF soil profile were selected from values reported by the two investigators (KCB 2015; IRP 2015) and are shown in Figure 3D.1.

Model calibration

Stage 9 two-dimensional steady-state seepage results were verified against field piezometer data collected shortly prior to failure and compared to the seepage models proposed by KCB (2015, Figure III-5) and IRP (2015, Figure H3). The piezometer elevations are reported in Table 3D.1; the modelled values are reasonably close.

Table 3D.1 Stage 9 total heads in three piezometers near failure site.

Total head, m	G1 (G2-PE2-01) (coarse tailings, el. 947.8m ASL)**	G2 (G2-PE2-02) (core, el. 948.1mASL)**	G3 (G0-PE2-01) (tailings beach, el. 946.9mASL)**
Monitoring Data, May / July 2014*	952.9	951.4	956.4
2D Model (isotropic)	952.4	949.8	955.2
2D Model (anisotropic)	951.5	949.7	954.5
3D Model	953.3	950.1	954.8

*Reported by KCB (2015, Table III-1)
**Location of piezometers in plan view is shown in Figure 2.10 of Klohn Crippen Berger report (KCB 2015). Their elevations and relative positions in the dam cross-section are seen in Figure 3D.4.

Results

The resulting of the two-dimensional steady-state seepage analysis of the Mount Polley TSF cross-section at the failure location are illustrated in Figure 3D.4. Piezometric elevations in the Upper GLU (Figure 3D.4) are comparable to those obtained by the two investigators (KCB 2015; IRP 2015).

Table 3D.2 Piezometric elevations in the Upper GLU modelled by two-dimensional steady-state seepage analysis.

Location	Stage 3	Stage 6	Stage 9
Upstream	933.3 m	934.9 m	935.9 m
Under Rockfill	932.6 m	933.9 m	934.6 m
Downstream	931.2 m	931.2 m	931.2 m

III) *Three-dimensional flow calculations*

<u>Process</u>

The evaluation of steady-state pore pressure distributions in three dimensions was conducted FLAC3D using the software's uncoupled flow calculation mode. The modelling and calibration process is outlined below.

1. The model was configured for fluid flow using the isotropic fluid model.
2. Pore pressure distributions were separately evaluated for construction stage 3 through 9 as well as for pre-construction conditions.
    a. In the pre-construction stage, no flow calculations were conducted, and hydrostatic pore pressure distributions with a groundwater table at surface were assumed.
    b. For stages 3, 6, 9, initial and boundary conditions were estimated using the results from the two-dimensional steady state seepage analysis. For stages 4, 5, 7 and 8 interpolation was used to approximate the same.
3. Steady state pore pressures were compared against those in the two-dimensional analysis. In this comparison, the pore pressures (and resulting piezometric surface) in the Upper GLU were of special interest.

Soil properties

For this analysis, a simplified soil profile was used, where all dam materials upstream of the core were treated as having a permeability and porosity equal to that of tailings. The Upper and Lower Glaciofluvial units located below the Upper GLU were modelled as a single zone with appropriate permeability and porosity values. The model properties pertinent to flow calculations are shown in Figure 3D.6.

Boundary and initial conditions

Boundary conditions on the upstream and downstream faces: The boundary conditions for the three-dimensional model of flow at the Mount Polley TSF were formulated using the results of the two-dimensional steady-state seepage analysis. Pore pressure distributions on the upstream and downstream edges of the two-dimensional models were approximated by pressure gradients that were applied to the upstream and downstream faces of the three-dimensional model. As an example, for construction stage 9, the two-dimensional seepage model produces on the upstream edge of the model a pore pressure variation of 0kPa at the top of the tailings pond (with an elevation of 966.83 m) to ~380kPa at the elevation of 912m (corresponding to the base elevation of the three-dimensional model). The pore pressure at any elevation *z* of the upstream face is then described by the following function:

$$u \ = 380 + (z - 912) * (-6.931)\ (kPa) \tag{3D.1}$$

Boundary conditions at the tailings pond surface: In construction stages 3 through 9, the tailings pond surface was assigned constant pore pressure values respectively corresponding to total heads of 941.5m, 944.0m, 947.5m, 954.0m, 957.0m, 960.0m and 966.83 m.

Boundary conditions at the internal drain: The internal drain on the upstream side of the core, located about 7m upstream of the dam centreline with an elevation of 946.3 m, was modelled in construction stages 4 through 9 as a constant pressure area with pore pressures gradually increasing from 0 to 50 kPa.

Initial pore water pressure distributions: The initial conditions were approximated by the groundwater table surfaces developed as discussed in §3.2.4.

It is worth noting that the initial pore water pressures should have no bearing on the flow calculation results. The steady-state seepage is independent of transient states (such as the initial pore pressures) and is defined solely by the model's boundary conditions and hydrological properties. Theoretically, the same steady-state solution can be obtained in a model regardless of how the initial pore pressures are defined. However, transient states that better approximate steady-state pore pressure distributions will converge to steady state more rapidly.

Verification

The three-dimensional steady state pressure distributions were compared to the two-dimensional seepage solutions. Of special interest were the piezometric elevations in the Upper GLU, which appear to compare well in each of the modelled stages. Some deviation from the values in the two-dimensional analysis is attributable to a difference in the rendition of the Upper GLU surface, which in the three-dimensional model has an elevation varying from 918m to 922m and has a concave rather than flat appearance. Figure 3D.7 illustrates stage 3, 6 and 9 piezometric elevations in the Upper GLU at steady state.

Results

The steady-state pore pressure distributions used in the three-dimensional stability analysis of the Mount Polley TSF are shown in Figure 3D.8.

IV) *Modelling considerations and techniques*

Flow regime

Throughout the analysis presented in this thesis, drained conditions were assumed to have been reached after each construction phase, and no transient flow states and associated excess pore water pressures were considered.

In the assessment of the pore water pressure conditions, the Independent Review Panel (IRP 2015) concludes that at the time of failure, excess pore water pressures of up to 50kPa may have existed in the shear zone of the Upper GLU (IRP 2015, §6.3.2 & Appendix H). In their own investigation, Klohn Crippen Berger estimates that excess pore water pressures of about 97 to 158kPa may have persisted in the Upper GLU portions located directly under the dam (KCB 2015, Appendix VI).

The addition of embankment material in the core and upstream tailings zones between June 10 and August 1, 2014 (three days prior to failure) would have contributed to some of this excess pressure. In all, these excess pore pressures represent a relatively small portion of the load added to the ground and were not ultimately considered by the two investigators, who opted to assume fully drained conditions, reflected by steady-state pore pressure distributions, for the purpose of stability analysis.

The effect of ignoring the excess pore pressures by assuming fully drained conditions was evaluated using the above data. In stage 9, the portions of Upper GLU located under the dam crest would have experienced vertical effective stresses of about 850kPa under drained conditions, and of about 700-800kPa under the estimated partially drained conditions. By assuming fully drained conditions, the shear strength of the Upper GLU, nearing residual values at that stage, would have been overestimated by 1 to 4kPa, or 3 to 10%. Elsewhere in the Upper GLU, the overestimation of shear strength associated with the assumption of fully drained conditions was estimated to be much smaller due to significantly lower excess pore pressures.

As a consequence of the above findings, the use of fully drained conditions in the three-dimensional deformation analysis of the Mount Polley TSF failure is warranted for the most part. Drained conditions were simulated in FLAC3D through the use uncoupled flow calculations until a steady state was reached.

Table 3D.3 Change in embankment elevations and loading due to the summer of 2014 construction works.

Zone	Initial Elevation z_i (m)	Final Elevation z_f (m)	Change in Elev. Δz (m)	Change in load $\Delta\sigma$ (kPa)
Core	967.5	969.1	1.6	37
Shell	967	969	3	60
Upstream Tailings	965.8	967.6	1.8	32
Pond	966.4	966.83	0.43	4.2

Undrained conditions: A portion of embankment works was completed in the summer of 2014 immediately prior to failure, with materials being added to the shell, core and upstream tailings zone. The change in embankment elevations and loading, reported by IRP (2015, Figure HA.1-3) are listed in Table 3D.3 Change in embankment elevations and loading due to the summer of 2014 construction works. These works would have generated a change in total loading and would have increased the excess pore pressures in the Upper GLU. These undrained conditions were not fully modelled using transient pore pressure distributions, but were partially simulated in the normally consolidated portions of Upper GLU material by halting the processes of re-evaluation of pre-consolidation pressures and resulting re-calculations of its undrained shear strength when evaluating stage 9B stability. A similar approach was used for Stage 9A in the fine model where the new load was "added" under undrained conditions in order to rule out the possibility of the early onset of failure under the adapted constitutive model in the Upper GLU.

The effect of scaled permeabilities on the onset of convergence in FLAC3D flow calculations

The three-dimensional FLAC3D models of the Mount Polley TSF contain between $3*10^6$ and $1*10^7$ individual zones depending on the mesh size. In models this large, uncoupled flow calculations may take unfeasible amounts of time. The "fast flow" scheme available in this software cannot be applied in this circumstance due to the presence of a phreatic surface. To speed up the process, a modelling technique was used for uncoupled flow calculations consisting of assigning to all materials permeability values several orders of magnitude above those established experimentally while preserving the relative permeability ratios across the model.

Researchers have shown that the steady-state solution of the Laplace equation for groundwater flow is not governed by the absolute values of soils' hydraulic conductivities, but by their relative ratios (Cedergren 1989; Hodge and Freeze 1977). Varying the hydraulic conductivity values even by orders of magnitude should, in theory, produce the exact same flownet, so long as their relative contrasts are preserved across the model. This concept is demonstrated in Figure 3D.3.

It is worth noting that the variation of hydraulic conductivities in the manner described above does have an effect on seepage rates, and models using higher values predict higher flows. However, the effect of seepage, and resulting seepage forces, on mechanical stability is neglected in most stability analyses including the one of the Mount Polley TSF failure presented here.

Lastly, this approach is not recommended for transient flow states or for coupled flow and mechanical calculations.

Effect of anisotropic hydraulic conductivities on pore pressure distributions

A number of soils involved in failure at the Mount Polley TSF exhibit anisotropic permeability, with the ratio of horizontal to vertical hydraulic conductivities k_h/k_v ranging from 1 in uniform, homogeneous materials such as the rockfill to 10 in structured deposits such as the Upper GLU (KCB 2015, Tables 5.7, 5.8 and 6.2).

To explore the effect of this anisotropy on pore pressure distributions, two steady-state analyses of the stage 9 cross-section were conducted, one with using the isotropic hydraulic conductivity model and the other using reported k_h/k_v values. The results of this analysis are illustrated in Figure 3D.2. While the two solutions are evidently distinct, the main variations in pore pressure distributions appear to take place on the upstream, and the difference in the failure zone is not pronounced. In the Upper GLU, the anisotropic model predicts a piezometric surface only 0.2m higher than the one in the isotropic model. Additionally, the anisotropic model appears to be a poorer predictor of pressures observed in the piezometers installed in the dam materials (see Table 3D.1).

The results of this analysis suggest that the use of the isotropic hydraulic conductivity model is acceptable. These conclusions are supported by findings reported by the Independent Review Panel whose two-dimensional consolidation analysis shows that anisotropy has only a minor effect on consolidation times (EIIERP 2015, Figure H.A1-7).

In FLAC3D, it is possible to use either the isotropic or anisotropic models, but the computational requirements for the latter are more significant. Therefore, a decision was made to use the former in the modelling of the Mount Polley TSF failure. The results of the two-dimensional anisotropic analysis were consulted for verification.

V) *Appendix 3D Figures*

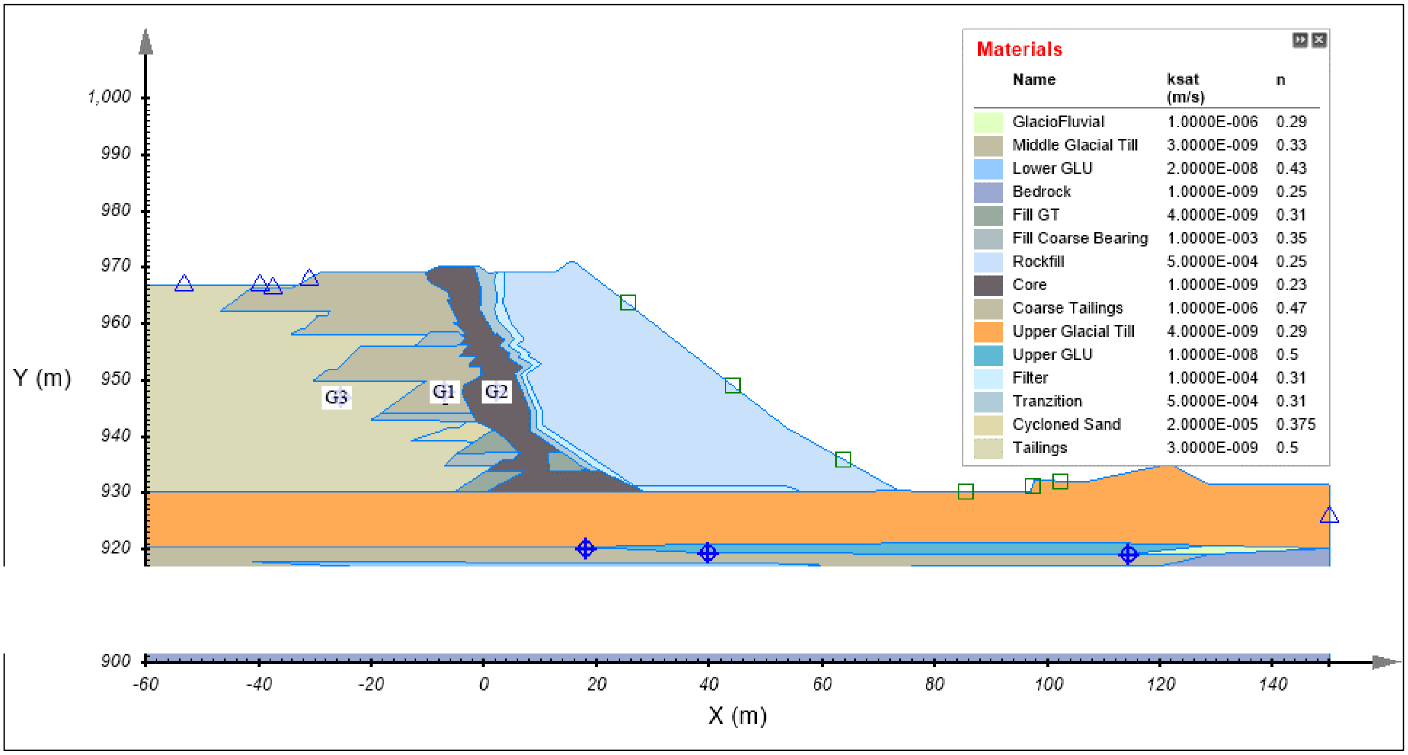

Figure 3D.1 Cross-sectional geometry and hydrological properties of the Mount Polley TSF.

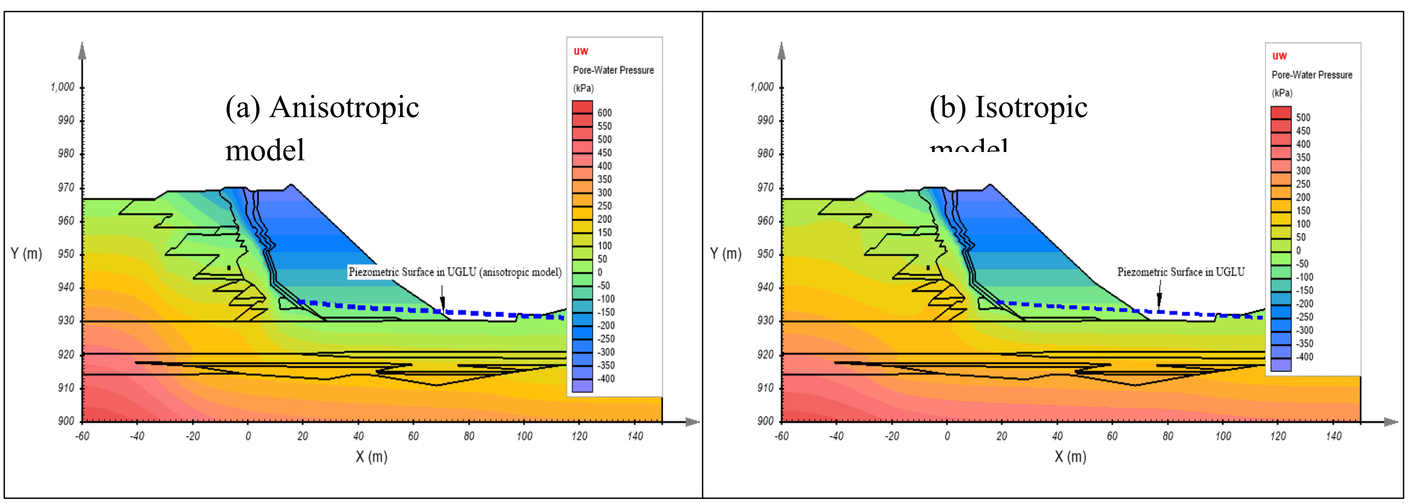

Figure 3D.2 Comparison of steady-state seepage solutions using (a) anisotropic and (b) isotropic hydraulic conductivity models.

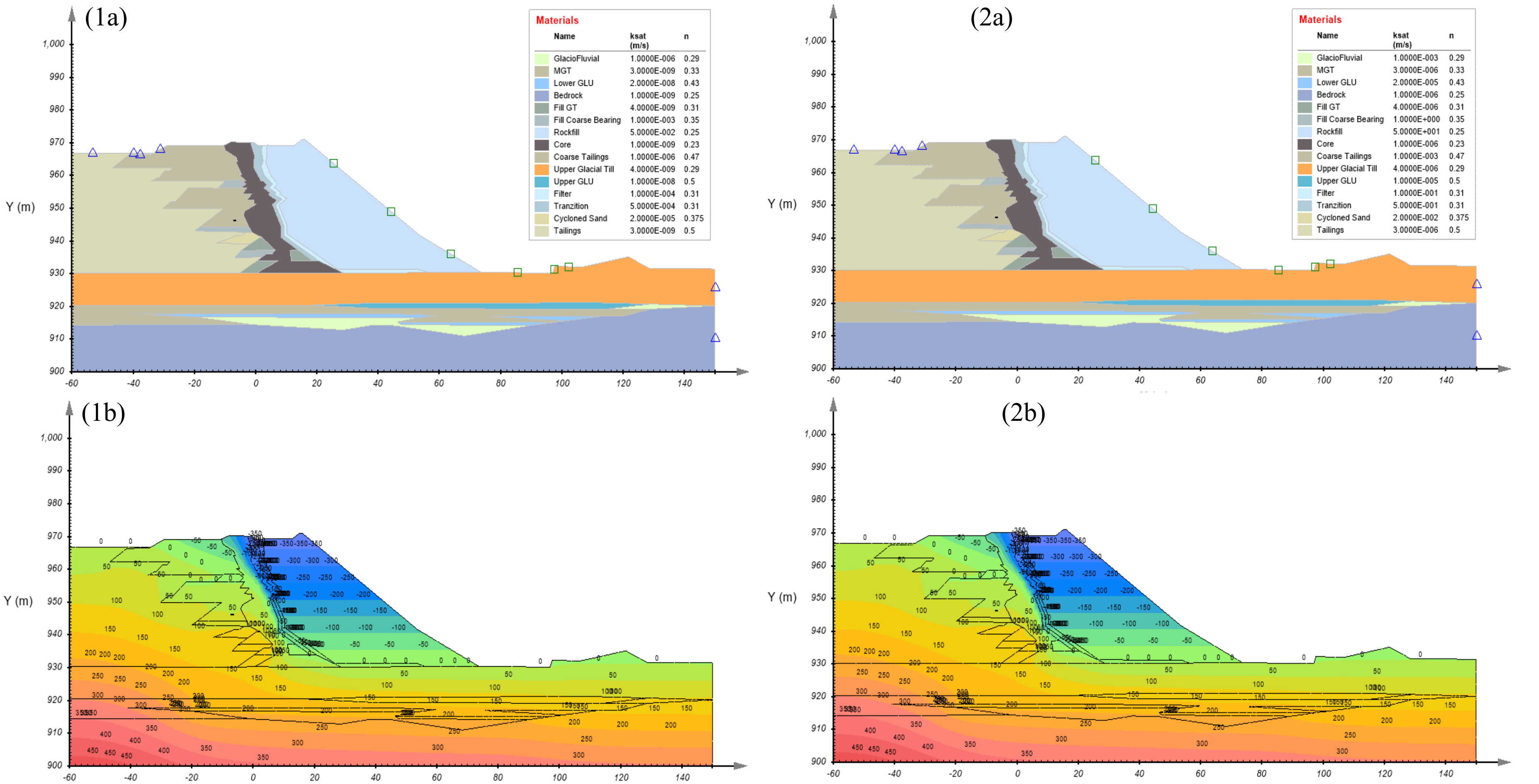

Figure 3D.3 Illustration of the concept of independence of the steady-state solution for groundwater flow of the magnitude of soil permeabilities. The model represented by the typical cross-section at the Mount Polley TSF failure using actual hydraulic conductivity values (seen in 1a) and the model of the same cross-section using hydraulic conductivities three orders higher than actual (2a) yield effectively identical steady-state pore pressure distributions (shown respectively in 1b and 2b).

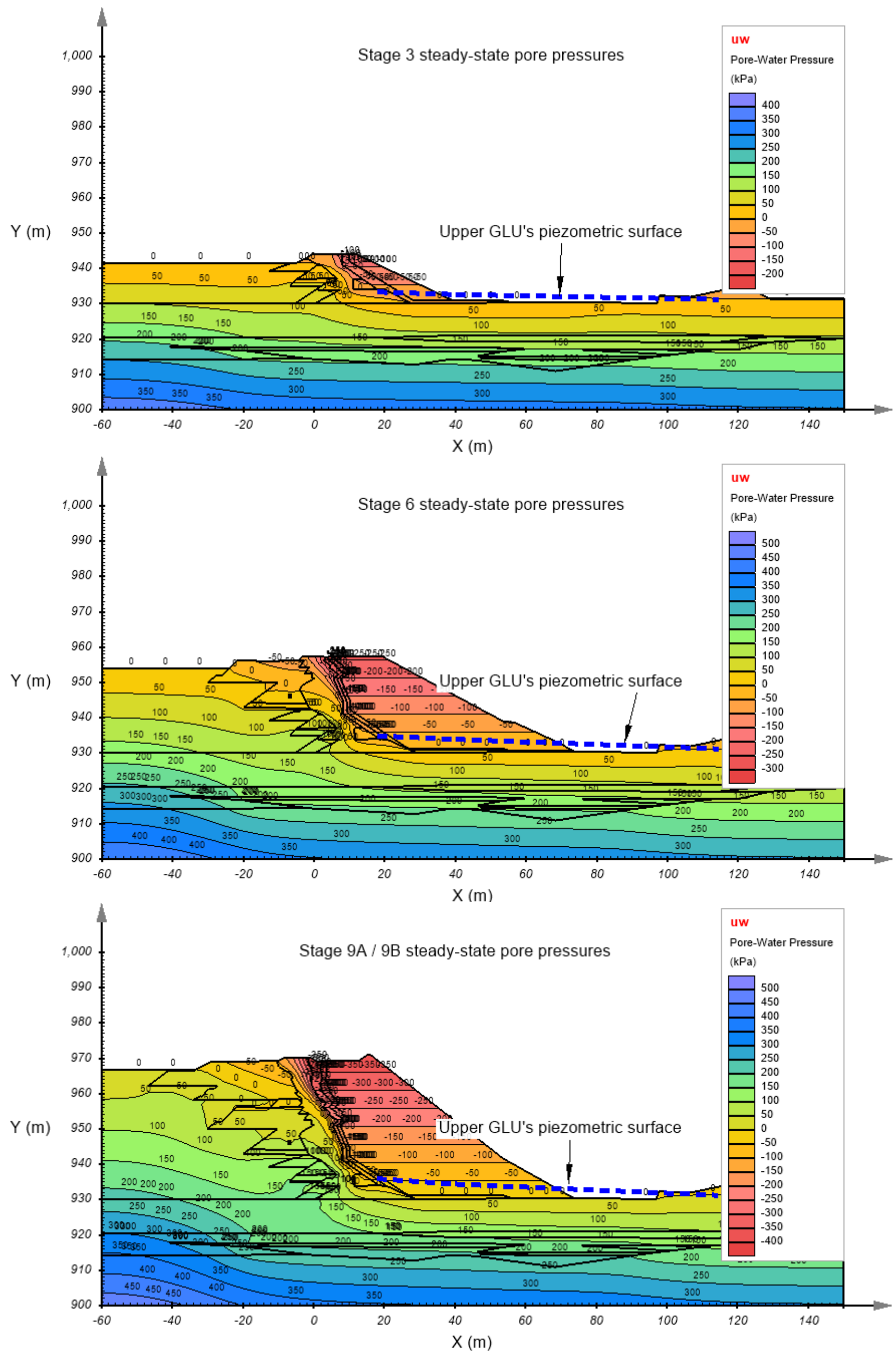

Figure 3D.4 Two-dimensional steady-state solutions for the pore pressure distributions at constructions stages 3, 6 and 9.

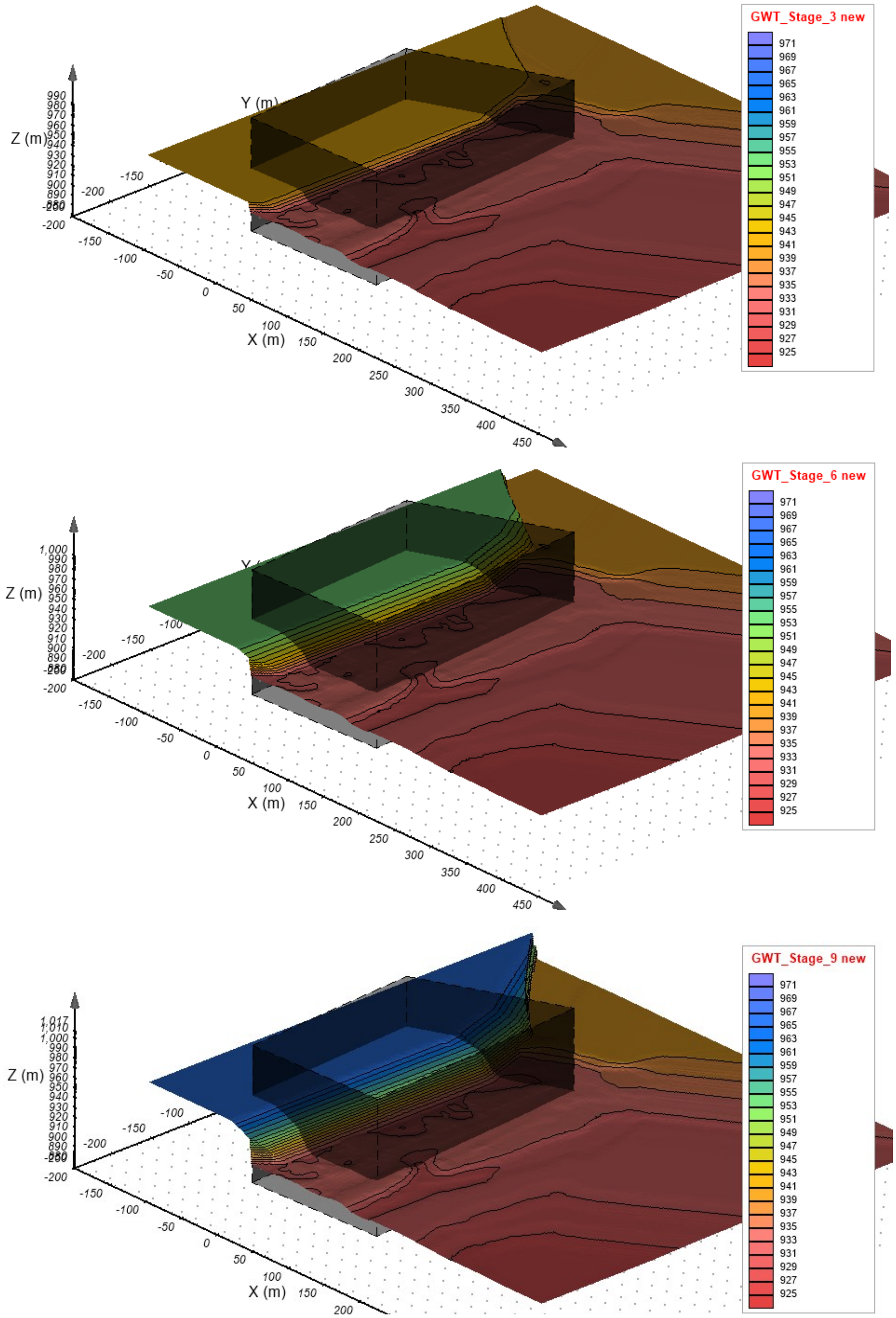

Figure 3D.5 These shapes of groundwater table in construction stages 3, 6 and 9 were used to approximate the initial pore water pressure distributions in the FLAC3D flow calculations.

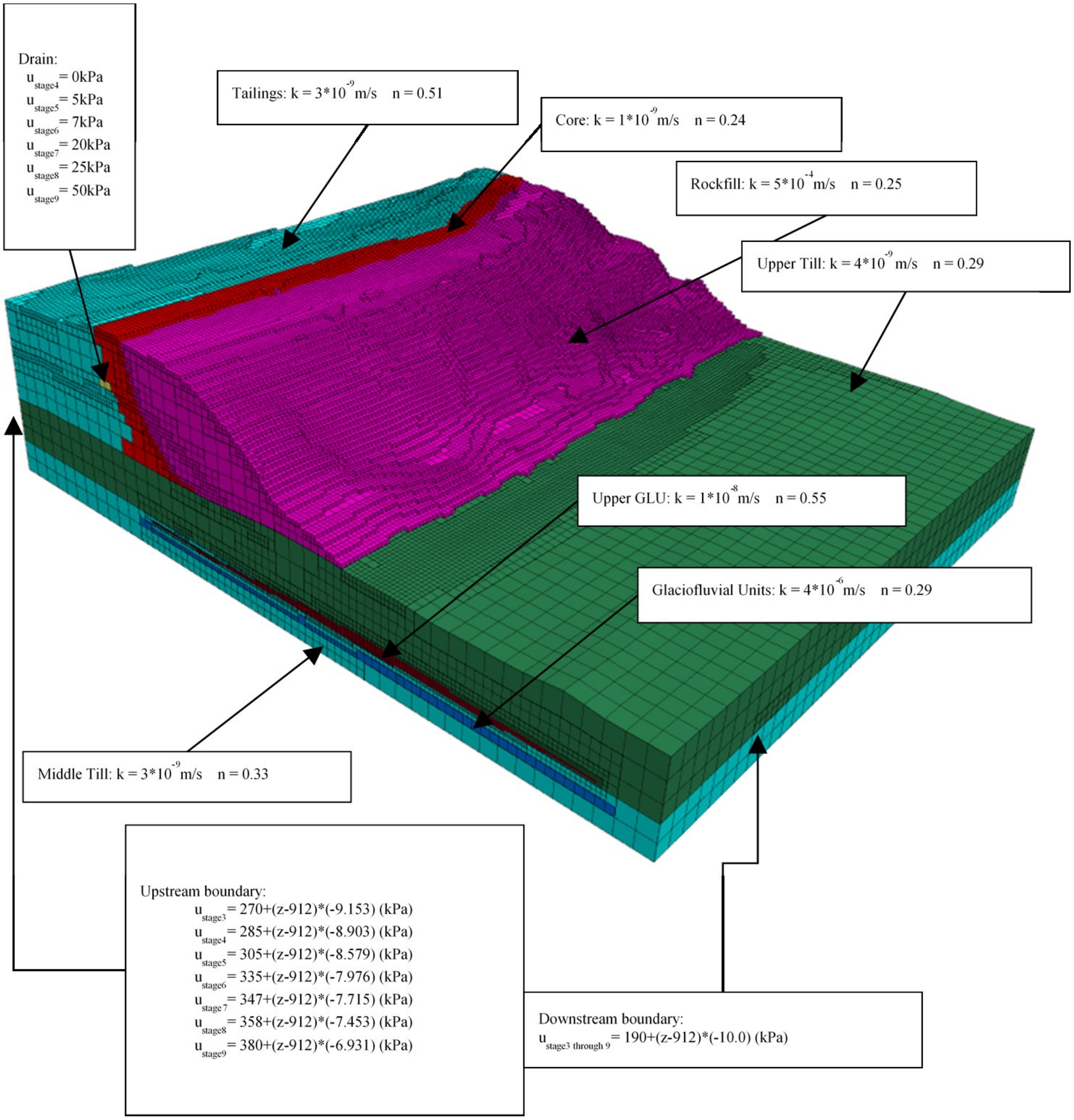

Figure 3D.6 Boundary conditions and hydrological soil properties used in the three-dimensional flow model (a cross-sectional view through the middle of the slide is seen here).

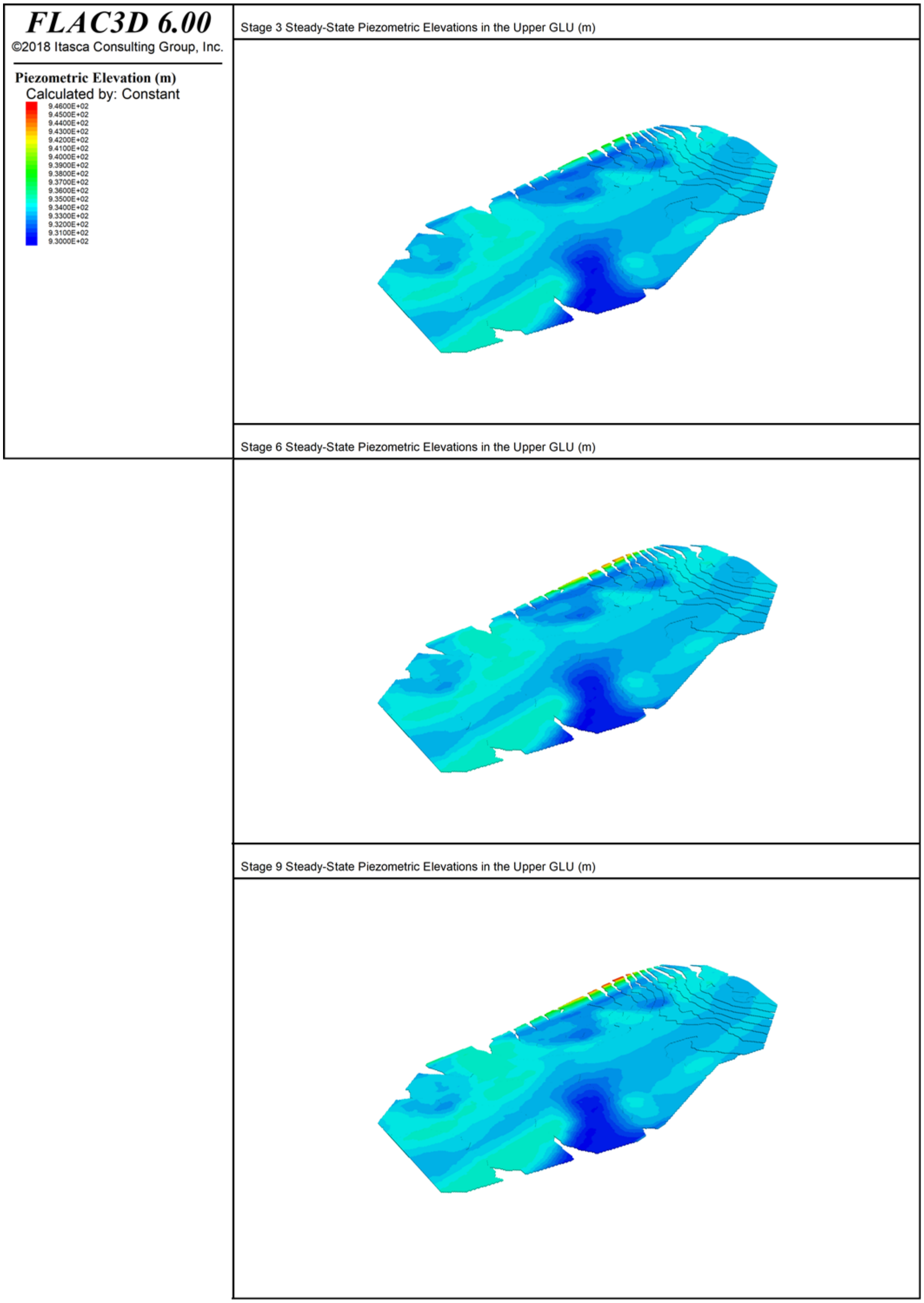

Figure 3D.7 Piezometric elevations in Upper GLU at steady state.

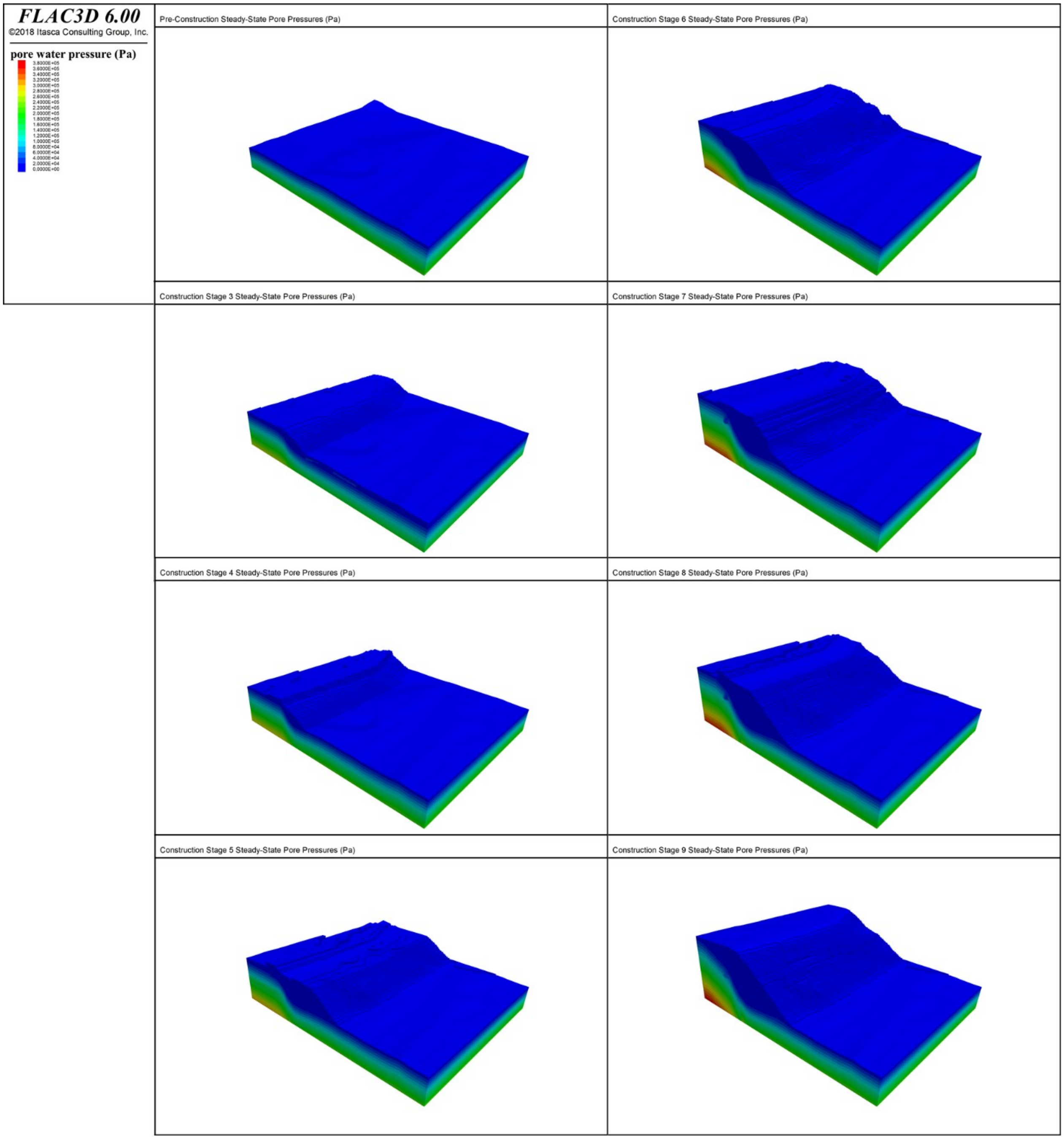

Figure 3D.8 Three-dimensional pore pressure distributions at steady state.

APPENDIX 3E: EVALUATION OF STRATEGIES TO MITIGATE GRID DISTORTION ERRORS IN LARGE STRAIN

I) *Problem formulation*

The Lagrangian formulation of the classical mechanics equations provides a means to track the trajectory of a system. The Lagrangian solution is commonly described as following the particles as they move in the system under the differentials of kinetic and potential energies. FLAC3D applies the Lagrangian calculation scheme to a system discretized into finite-volume zones whose vertices, termed "gridpoints," are tracked by computing their velocities, strains and new coordinates over each calculation timestep. The resulting relative motion of gridpoints may produce zone distortions that are meaningless from a perspective of physical processes – for example, a tetrahedral zone may compress to a point where its volume becomes negative. Distortions of this sort are termed in FLAC3D as "illegal geometry," and four separate tests are used to detect them: the zone's aspect ratio, its volume ratio, its orthogonality and planarity (Itasca 2018). When the software detects illegal geometry, calculations are ceased.

To date, there is no single solution that fully mitigates the issue of illegal geometry resulting from grid distortion. A number of strategies can be used separately or combined to prevent the formation of zones with such geometry. Each strategy has its drawbacks and must be evaluated in the context of the specific problem. A discussion of such strategies follows.

II) *Global remeshing*

The problem of grid distortion is commonly addressed by the strategy termed "global remeshing" or "global rezoning." This approach consists of re-discretizing the model domain to create a new, undistorted mesh within the spatial boundaries of the old, distorted system. The old solution is then mapped onto the new, undistorted mesh.

The process of remapping the solution from a distorted mesh onto an undistorted one is done by interpolating at each node the solutions from neighbouring nodes in the distorted mesh. This process introduces an error into the remapped solution (Russell 2018; Basaran 2008) due to the inaccuracy of interpolation. The magnitude of error in the new system depends on a number of factors such as the choice of interpolation method or methods, the spatial distribution and variation of material properties, the number and nature of transition zones, and the model's local resolution.

The error associated with remapping manifests itself during subsequent calculation cycles in a number of ways, including in the form of larger unbalanced forces at the mesh nodes. These unbalanced forces trigger additional deformation as the system adjusts to the new state. On the plots of average force ratios used in FLAC3D to evaluate whether equilibrium is attained, this error shows up as a new "peak" that is normally associated with a change in loading conditions.

The deformation incurred by the system due to its adjustment to the remapped solution presents an especially significant problem for models involving strain-weakening materials, as additional deformation in those may bring about a progressive loss of strength. Consider the case of the Mount Polley TSF. In this model, mesh distortion sufficient to trigger "illegal geometry" errors are generally brought about by plastic straining in Upper GLU zones where the peak undrained strength is exceeded. Remapping errors resulting in further deformation of Upper GLU zones that have either exceeded, or are about to exceed, the peak undrained shear strength may trigger in error a progressive growth of the plastic yield zones and an associated transfer of resistance to other areas of the model. This in turn may result in the prediction of a global failure that is unwarranted by the actual loading conditions. Repeated remeshing and remapping operations may be required over the course of a single modelling exercise, resulting in an accumulation of error. Since it is difficult to quantify at this point the impact of the remeshing error on the solution, the use of this strategy in strain-weakening systems is not defendable and was ruled out.

III) *Local remeshing*

"Local remeshing" is a modification of the global remeshing strategy described above consisting of re-discretizing only the severely distorted areas of a system rather than its entirety. This approach may result in a lower overall magnitude of remeshing error, but the associated problems persist. For example, the Mount Polley TSF model appears to be prone to severe distortion in the Upper GLU area but not elsewhere (the region of tailings, which tends to settle significantly over the course of modelling the construction stages, does not generally distort in a way that creates geometry errors). It would seem that the mesh distortion problems in this model can be mitigated by the local remeshing of the Upper GLU zone alone. However, even though the overall magnitude of remeshing error (and spike on the average force ratio plot) may decrease, the errors in individual zones of the remeshed area it is no different than with global remeshing. Consequently, the problems associated with global remeshing also apply here.

IV) *Localized small strain zones*

FLAC3D has a specialized *Fish* function, *zone.condition(pnt,i)*, to evaluate the geometric integrity of an individual zone using one or more of the four available tests (aspect ratio, volume ratio, orthogonality and planarity). Another *Fish* function, *gp.local.small(gpnt)*, enables the user to disable the coordinate update of an individual gridpoint, effectively applying the small strain mode at that node only. These two functions have been combined here to create a complex *Fish* function at is triggered at user-defined calculation intervals to run a check on of the model's geometric integrity and switch off the coordinate updates in zones where the "illegal geometry" error is about to be triggered.

The main concern with the application of this strategy is that, if enough zones are eventually switched to the small strain mode, the error associated with this mode may affect the large strain solution. Therefore, the application of this strategy was monitored by tracking the number and location of zones that have been "switched off" during each calculation cycle. Over the course of modelling the Mount Polley TSF, the large strain mode was disabled in an insignificant fraction of zones (as seen from Table 3E.1). Lastly, the effect of the error associated with the small strain mode was evaluated by comparing the small strain and large strain solutions, and the findings are discussed in Chapter 7.

Table 3E.1 Percentages and numbers of zones switched to small strain when running calculations in the large strain mode

Modelling Stage:	Percent (number) of zones switched to small strain mode at end of cycling:		
	Coarse model	Intermediate model	Fine model
stage 3	0 (0)	0 (0)	0 (0)
stage 4	0 (0)	0 (0)	0 (0)
stage 5	0 (0)	0 (0)	0 (0)
stage 6	0 (0)	0 (0)	0 (0)
stage 7	0.047 (404)	0.017 (559)	0.001(63)
stage 8	0.008 (66)	0.003 (102)	0.001(71)
stage 9A	0.008 (67)	0.003 (105)	0.001(82)
Stage 9B	0.055 (478)	0.005 (164)	not applicable (failure)

V) *Conceptual strategies*

Two strategies to mitigate "illegal geometry" errors are known in addition to the ones discussed, (a) zone repair and (b) mixed Lagrangian-Eulerian calculation schemes. Both of these strategies are conceptual at this point of research development, and have not yet been implemented as streamlined solutions. The first one is briefly examined here.

Zone repair

The three-dimensional model of the Mount Polley TSF was generated using block (i.e. cubic) zones that were more or less uniform and orthogonal. The choice of cubic zone shape was made in part to control the uniformity of Upper GLU zones whose edge size was of particular interest in the analysis. In addition to blocks, FLAC3D offers the ability to specify other zone shapes, such as degenerate bricks, pyramids, tetrahedral, wedges etc., termed "primitives."

The zone repair strategy exploits the fact that brick zones can be subdivided into several primitives. It is thought that a severely distorted brick zone can be repaired in this manner, and the old solution can then be remapped, with some processing, onto the new zones (Russell 2018). However, the variety of distortion patterns complicates the task of automating this strategy in order to make it feasible for large models such as the Mount Polley TSF containing in the order of $10^6 - 10^7$ zones.

APPENDIX 3F: INTERPRETATION OF CONE PENETRATION AND PRESSUREMETER TESTING RESULTS IN TERMS OF DEFORMATION MODULI

in failure area

RCPT12-114B	qt(bar)	fs(bar)	unit, est.	location, mASL	depth m	Qt	Fr	Ic	αE	E (Pa)
926.7	95	2.3	UGT	921.8-930.63	3.93	239.7	2.4	1.9	84.0	7.92E+08
928	25	0.4	UGT		2.63	93.1	1.6	2.1	99.5	2.43E+08
923	10	0.3	UGT		7.63	11.1	3.5	3.0	321.2	2.72E+08
921.5	65	5	UGLU	920.6-921.8	9.13	69.2	7.9	2.7	211.9	1.34E+09
921	50	3	UGLU		9.63	49.9	6.2	2.7	214.7	1.03E+09
918	65	2	MGT	below 920.6	12.63	49.5	3.2	2.5	165.1	1.03E+09
916.5	110	5	MGT		14.13	75.8	4.7	2.5	163.7	1.75E+09

outside failure

RCPT12-101	qt(bar)	fs(bar)	unit, est.	location, mASL	depth m	Qt	Fr	Ic	αE	E (Pa)
927	30	1.4	UGT	920.8-933.02	6.02	47.8	4.9	2.6	197.1	5.67E+08
926	180	6.5	UGT		7.02	254.4	3.6	2.1	99.4	1.77E+09
919	120	6	MGT	below UGT	14.02	83.6	5.1	2.5	164.6	1.93E+09
918	50	3	MGT		15.02	31.3	6.4	2.8	258.1	1.21E+09

outside failure

RCPT12-102	qt(bar)	fs(bar)	unit, est.	location, mASL	depth m	Qt	Fr	Ic	αE	E (Pa)
927	80	2.5	UGT	921-932.48	5.48	144.0	3.2	2.2	111.2	8.78E+08
925	50	1.5	UGT		7.48	64.8	3.1	2.4	146.6	7.11E+08
923	40	1.3	UGT		9.48	40.2	3.4	2.6	183.7	7.00E+08
920	210	11	MGT		12.48	166.3	5.3	2.3	134.0	2.78E+09

outside failure

RCPT12-103	qt(bar)	fs(bar)	unit, est.	location, mASL	depth m	Qt	Fr	Ic	αE	E (Pa)
927	100	4	UGT	921-930.58	3.58	277.3	4.0	2.1	101.8	1.01E+09
925	50	1.5	UGT		5.58	87.6	3.1	2.3	130.6	6.38E+08
923	80	4	UGT		7.58	103.5	5.1	2.4	152.8	1.20E+09

outside failure

RCPT12-104	qt(bar)	fs(bar)	unit, est.	location, mASL	depth m	Qt	Fr	Ic	αE	E (Pa)
927	60	2.5	UGT	920-931.74	4.74	124.6	4.2	2.3	132.5	7.82E+08
925	60	1.5	UGT		6.74	87.0	2.6	2.2	121.6	7.13E+08
923	50	1.5	UGT		8.74	55.2	3.1	2.4	156.4	7.55E+08
921	40	1	UGT		10.74	35.2	2.6	2.5	176.5	6.68E+08

outside failure

RCPT12-105	qt(bar)	fs(bar)	unit, est.	location, mASL	depth m	Qt	Fr	Ic	αE	E (Pa)
929	10	0.5	UGT	920-931.61	2.61	36.3	5.3	2.7	226.1	2.14E+08
927	100	3	UGT		4.61	214.9	3.0	2.0	95.9	9.50E+08
925	40	0.5	UGT		6.61	58.5	1.3	2.2	110.9	4.29E+08
923	40	0.4	UGT		8.61	44.5	1.0	2.2	116.9	4.48E+08
921	30	0.2	UGT		10.61	26.3	0.7	2.3	134.8	3.76E+08

ConeTec Job No. 14-02098 p.2

downstream of failure

RCPT12-106	qt(bar)	fs(bar)	unit, est.	location, mASL	depth m	Qt	Fr	Ic	αE	E (Pa)
927	30	2	UGT	920.5-928.65	1.65	179.5	6.8	2.4	146.8	4.35E+08
925	25	0.5	UGT		3.65	66.2	2.1	2.3	124.6	3.01E+08
923	20	0.2	UGT		5.65	33.1	1.1	2.3	134.8	2.52E+08
921	20	0.2	UGT		7.65	23.9	1.1	2.4	158.2	2.89E+08
919	175	8	UGLU	917.25-920.5	9.65	179.1	4.6	2.2	123.1	2.13E+09
918	90	5	UGLU		10.65	82.2	5.7	2.5	173.5	1.52E+09
916	100	3	MGT	below UGLU	12.65	76.8	3.1	2.3	137.5	1.34E+09

downstream of failure

RCPT12-107	qt(bar)	fs(bar)	unit, est.	location, mASL	depth m	Qt	Fr	Ic	αE	E (Pa)
927	40	1	UGT	919.5-928.41	1.41	281.4	2.5	1.9	81.3	3.22E+08
925	30	0.5	UGT		3.41	85.7	1.7	2.1	104.6	3.06E+08
923	30	1	UGT		5.41	53.2	3.5	2.5	165.7	4.77E+08
921	20	0.4	UGT		7.41	24.7	2.2	2.6	192.5	3.53E+08
919	90	4	UGLU	917.6-919.5	9.41	93.4	4.6	2.4	150.7	1.32E+09
918	40	3	UGLU		10.41	36.2	8.0	2.9	267.2	1.01E+09
916.5	20	1	MGT	916-917.6	11.91	14.5	5.8	3.0	338.3	5.85E+08
915.5	220	3	Glaciofluvial	915-916	12.91	168.1	1.4	1.8	74.2	1.61E+09

downstream of failure

RCPT12-108	qt(bar)	fs(bar)	unit, est.	location, mASL	depth m	Qt	Fr	Ic	αE	E (Pa)
927	15	0.1	UGT	920.5-928.26	1.26	116.8	0.7	1.8	66.1	9.73E+07
925	30	2	UGT		3.26	89.8	6.8	2.6	182.3	5.33E+08
923	40	1.5	UGT		5.26	73.8	3.9	2.4	152.9	5.93E+08
919.8	80	2.5	UGLU	917-920.5	8.46	92.3	3.2	2.3	130.4	1.02E+09
918	120	8	UGLU		10.26	114.7	6.8	2.5	168.2	1.98E+09

ConeTec Job No. 14-02098 p.3

downstream of failure

RCPT12-108B	qt(bar)	fs(bar)	unit, est.	location, mASL	depth m	Qt	Fr	Ic	αE	E (Pa)
927	20	1	UGT	920-928.44	1.44	136.6	5.1	2.3	139.6	2.75E+08
925	30	0.8	UGT		3.44	84.9	2.7	2.3	126.1	3.68E+08
921	20	0.5	UGT		7.44	24.6	2.7	2.7	208.0	3.81E+08
919	70	3.5	UGLU	917.5-920	9.44	71.9	5.2	2.5	174.1	1.18E+09
917.5	70	3.5	UGLU		10.94	61.7	5.2	2.6	184.2	1.24E+09

KCB CPT Job #12-02091

upstream of failure

RSCPT14-07	qt(bar)	fs(bar)	unit, est.	location, mASL	depth m	Qt	Fr	Ic	αE	E (Pa)
918	200	5	UGLU		13.58	145.0	2.5	2.1	100.8	1.99E+09
925	50	2	UGT		6.58	73.7	4.1	2.4	157.1	7.62E+08

References:

Rocscience Inc. CPT Data Interpretation Theory Manual. 2016.
https://www.rocscience.com/help/settle/pdf_files/theory/CPT_Theory_Manual.pdf accessed 2017-2019.

Robertson, PK (2009). Interpretation of cone penetration tests – a unified approach. Canadian Geotech. J., 46(11):1337–1355.

From IRP Appendix D3-D5, p.102 - Pressuremeter Data by In-Situ Engineering interpreted in terms of moduli (shear, young's)

Exclude following tests as not useable: MPM 04,07,08

Poor tests: MPM 03,09,10,12,13,16

Good tests:

Upper Till: MPM 01,02, 05,06,14,15,17,18

Lower Tills: MPM 11,12,16,03b

UGT			Shear Modulus kPa			Young's Modulus Pa				
MPM-01	9100	38400	133400	133400		2.73E+07	1.15E+08	4.00E+08	4.00E+08	0.00E+00
MPM-02	10600	43300	155300	155300		3.18E+07	1.30E+08	4.66E+08	4.66E+08	0.00E+00
MPM-05	5000	21000	43800			1.50E+07	6.30E+07	1.31E+08	0.00E+00	0.00E+00
MPM-06	13100	52400	52400	98300		3.93E+07	1.57E+08	1.57E+08	2.95E+08	0.00E+00
MPM-14	4300	33800	56700	72500		1.29E+07	1.01E+08	1.70E+08	2.18E+08	0.00E+00
MPM-15	6800	17900	50900	119200		2.04E+07	5.37E+07	1.53E+08	3.58E+08	0.00E+00
MPM-17	4100	16900	23000	31000		1.23E+07	5.07E+07	6.90E+07	9.30E+07	0.00E+00
MPM-18	1230	7930	10730	18030		3.69E+06	2.38E+07	3.22E+07	5.41E+07	0.00E+00
Lower Tills										
MPM-11	3400	34400	59500	50300	65900	1.02E+07	1.03E+08	1.79E+08	1.51E+08	1.98E+08
MPM-12	1300	5200	7200	16200		3.90E+06	1.56E+07	2.16E+07	4.86E+07	0.00E+00
MPM-16	700	4400	5100	12800		2.10E+06	1.32E+07	1.53E+07	3.84E+07	0.00E+00
MPM-03b	3800	41900	41900			1.14E+07	1.26E+08	1.26E+08	0.00E+00	0.00E+00

APPENDIX 4A: LARGE STRAIN RESULTS – ROTATION OF STRESS TENSOR AND SHEAR STRESSES

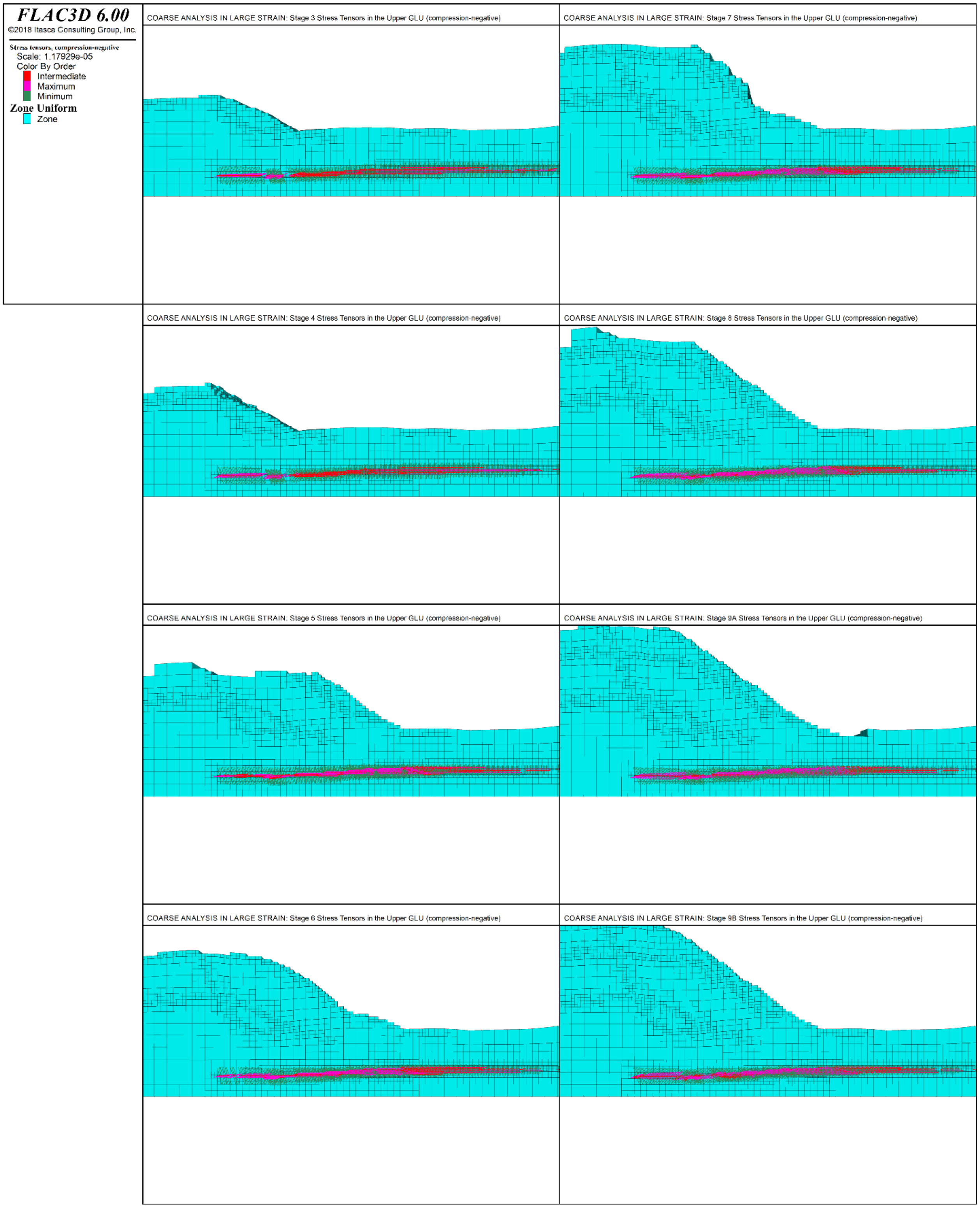

Figure 4A.1Orientation of stress tensor in Upper GLU in stages 3 through 9B predicted by the coarse model in large strain.

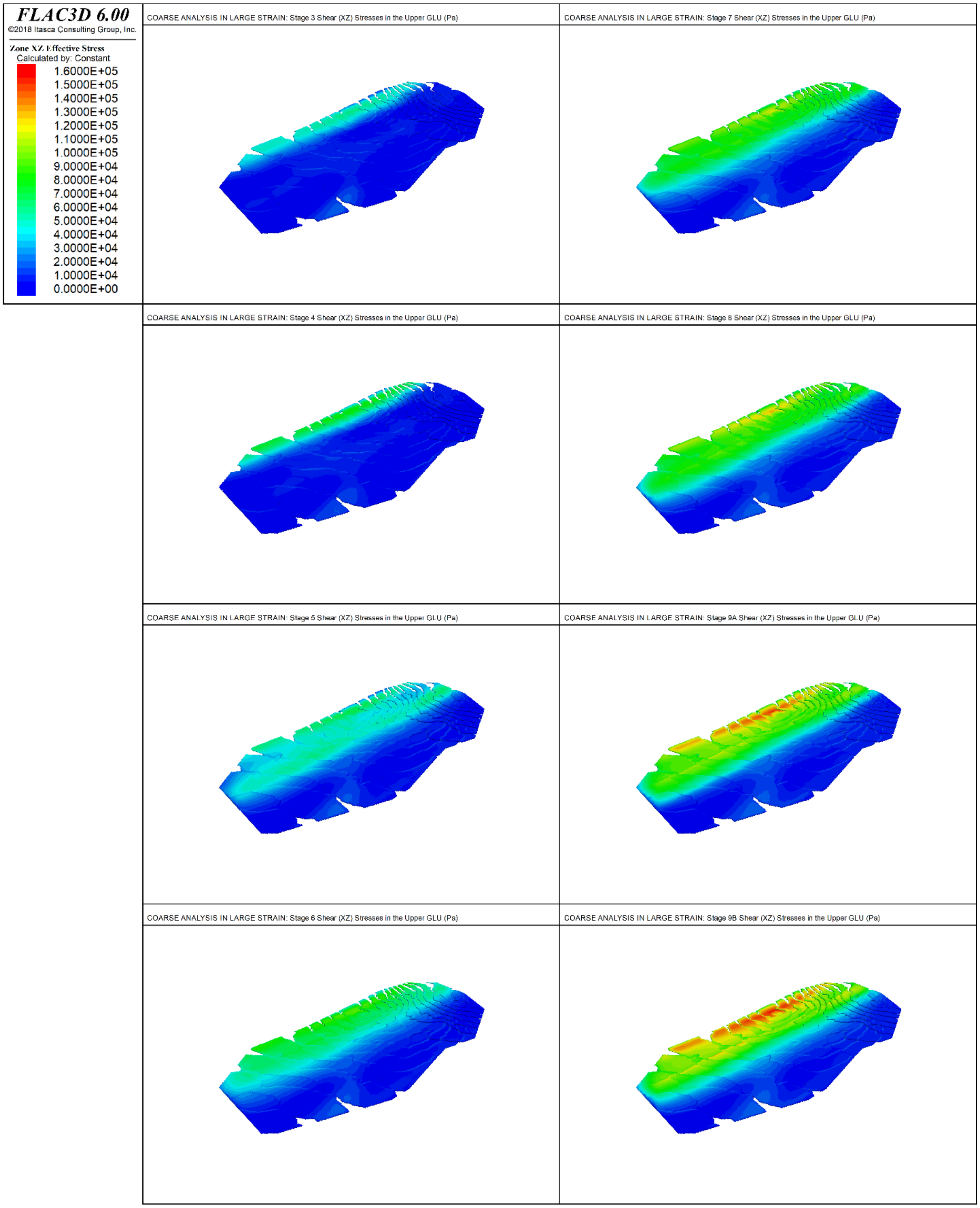

Figure 4A.2 The shear stresses in the horizontal (XZ) plane in the Upper GLU predicted by the coarse model in large strain.

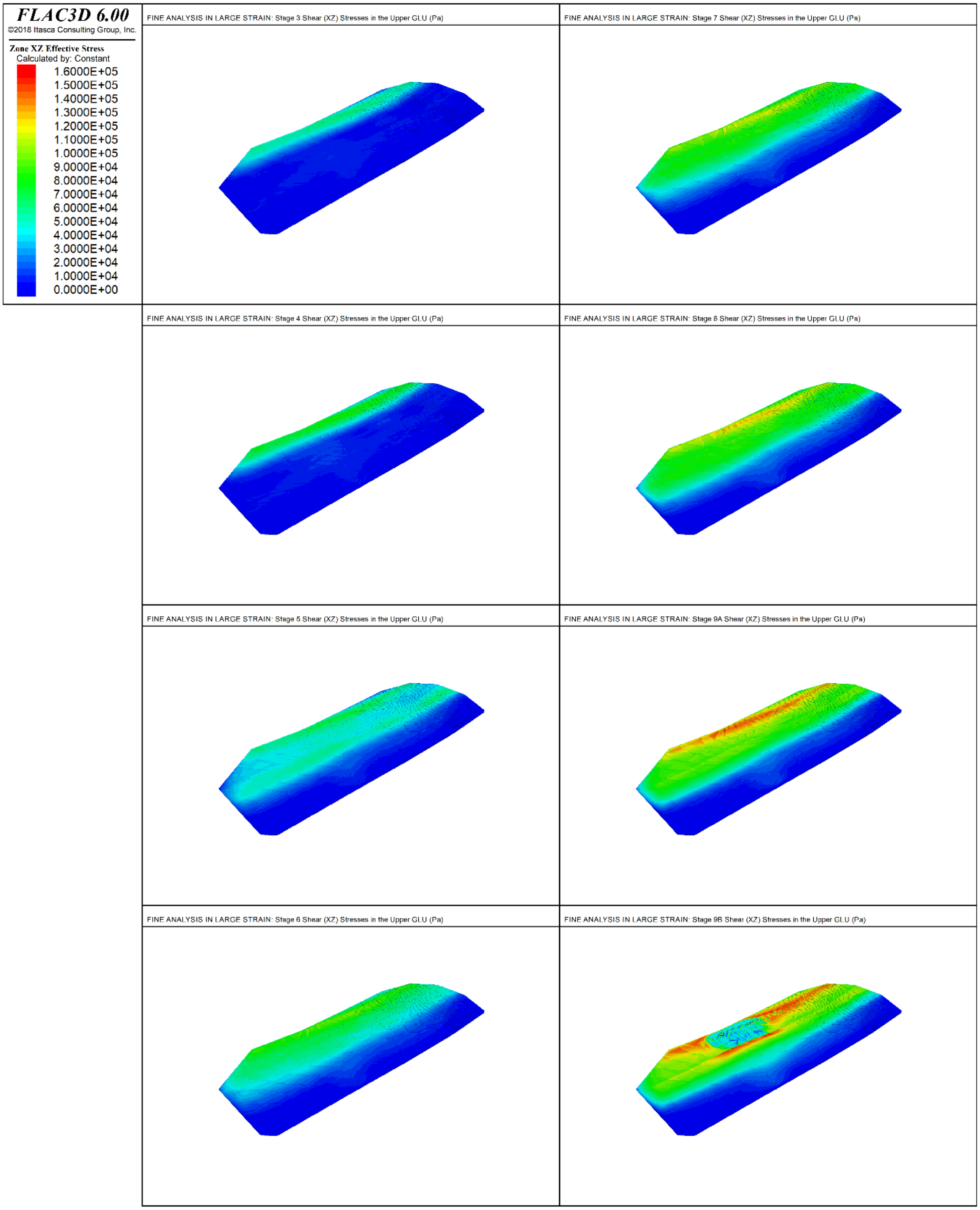

Figure 4A.3 The shear stresses in the horizontal (XZ) plane in the Upper GLU predicted by the fine model in large strain.

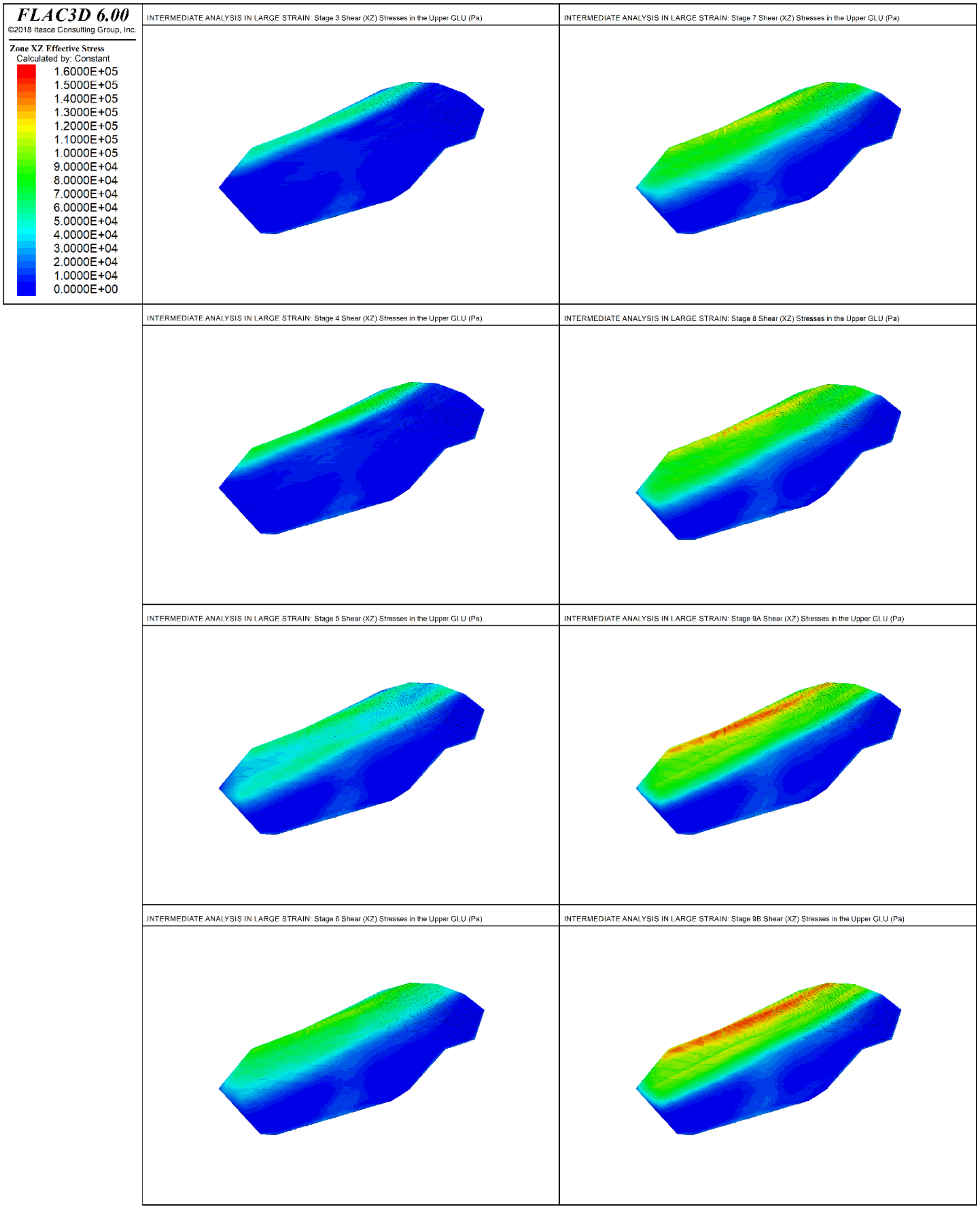

Figure 4A.4 The shear stresses in the horizontal (XZ) plane in the Upper GLU predicted by the intermediate model in large strain.

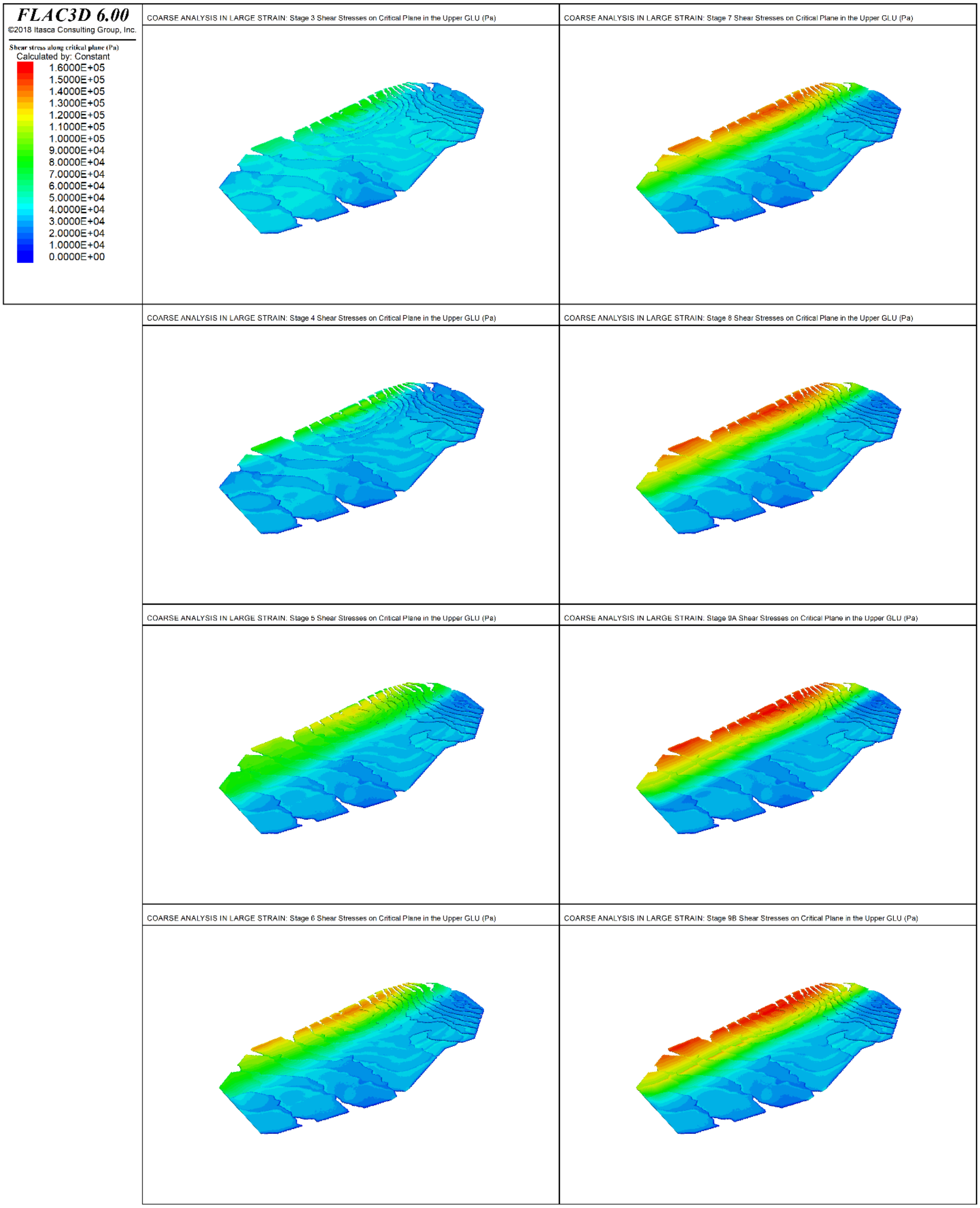

Figure 4A.5 The shear stresses in the critical plane in the Upper GLU predicted by the coarse model in large strain.

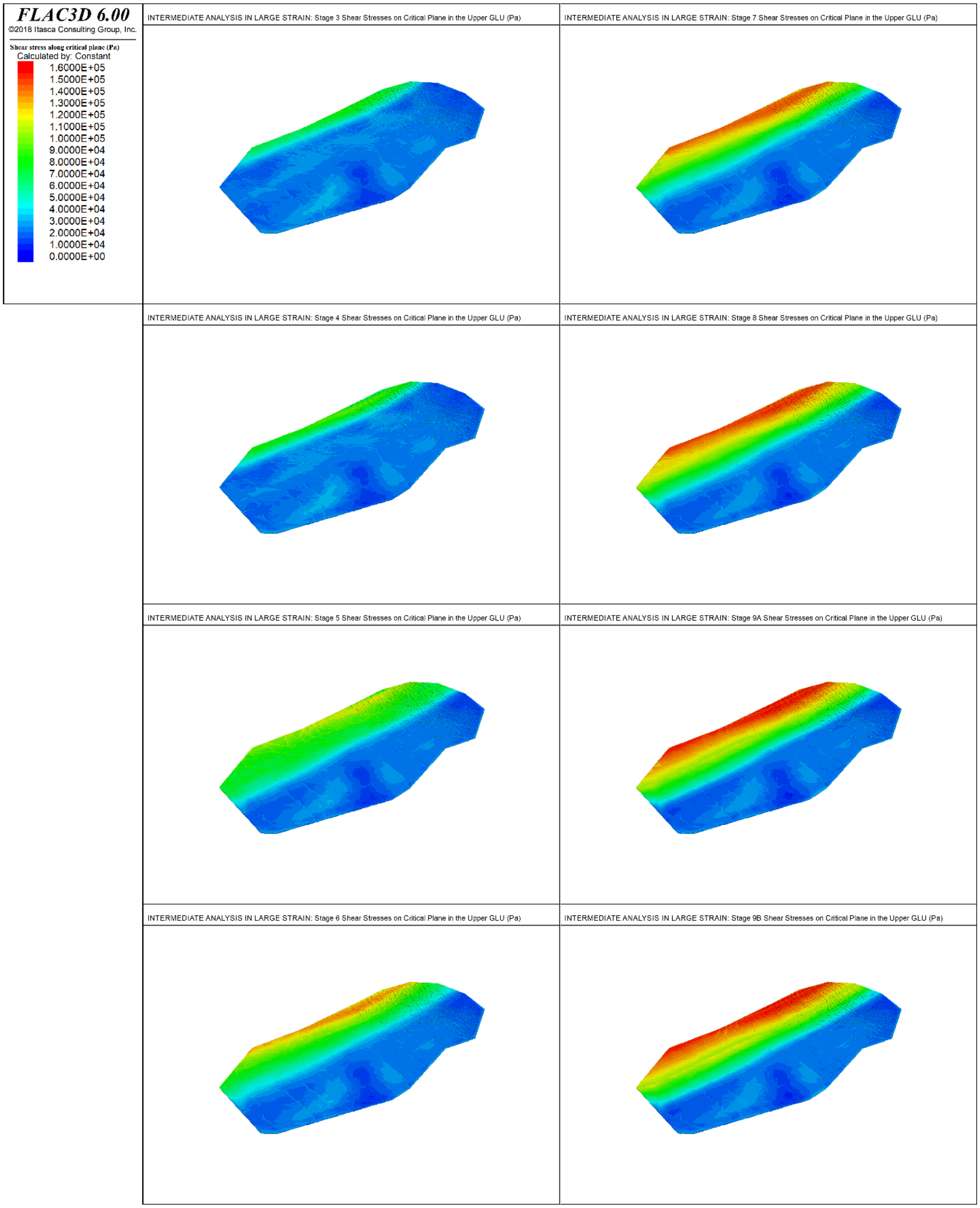

Figure 4A.6 The shear stresses in the critical plane in the Upper GLU predicted by the intermediate model in large strain.

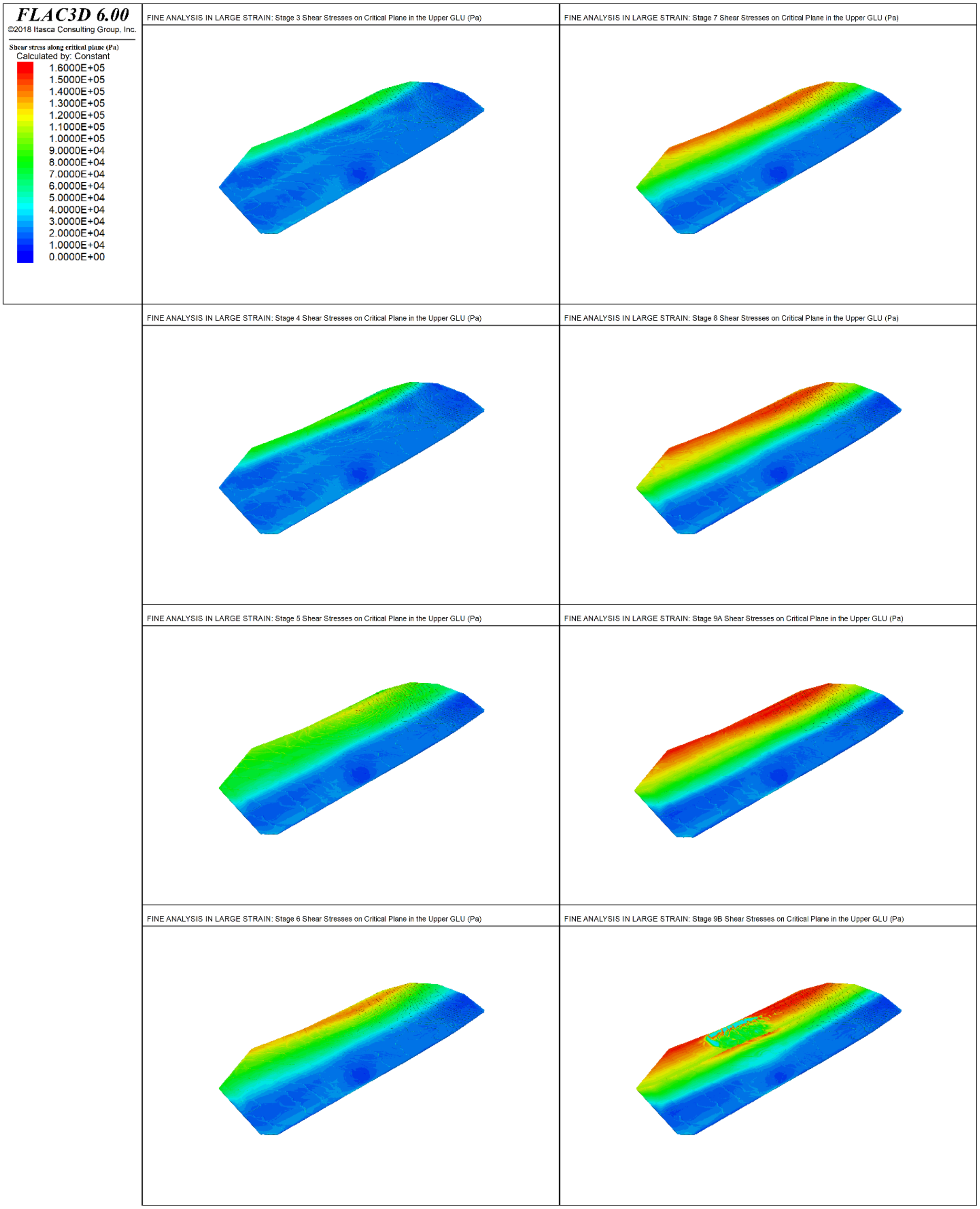

Figure 4A.7 The shear stresses in the critical plane in the Upper GLU predicted by the fine model in large strain.

APPENDIX 4B: LARGE STRAIN RESULTS – SETTLEMENT AT EMBANKMENT SURFACE

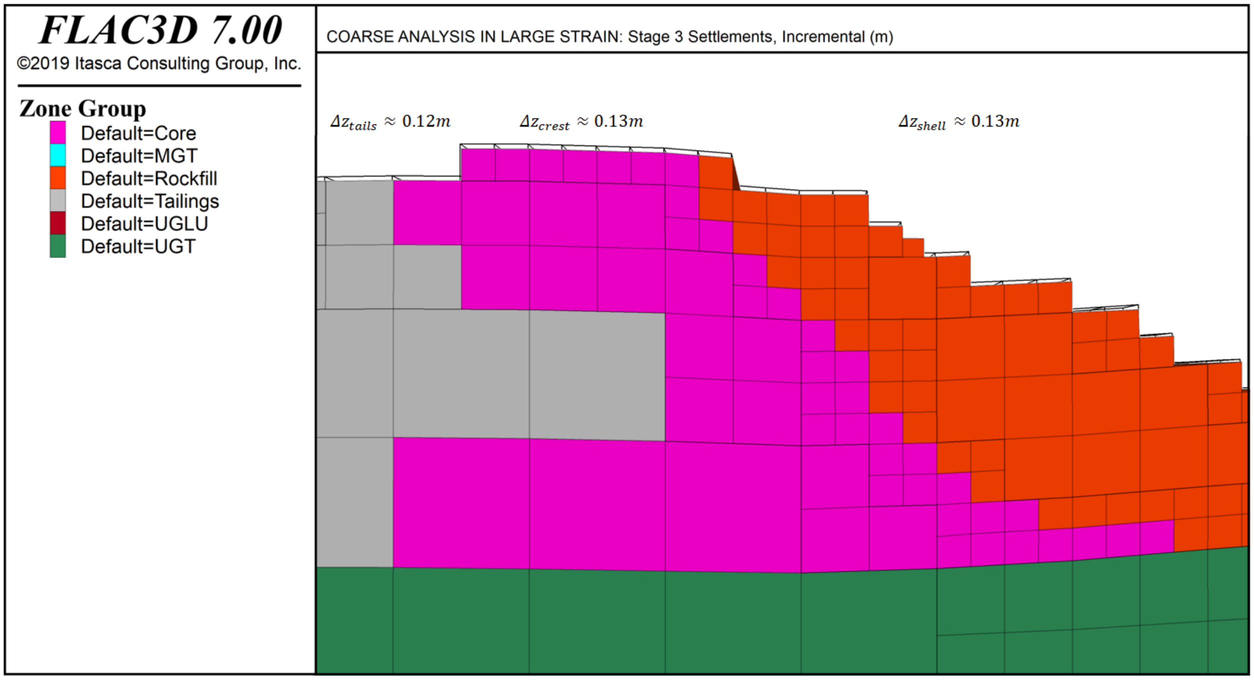

Figure 4B.1 Cross-sectional view of embankment settlement at the slide midpoint due to the addition of stage 1-3 material predicted by the coarse model in large strain. In black outline: embankment profile prior to settlement. In coloured fill: embankment profile after settlement.

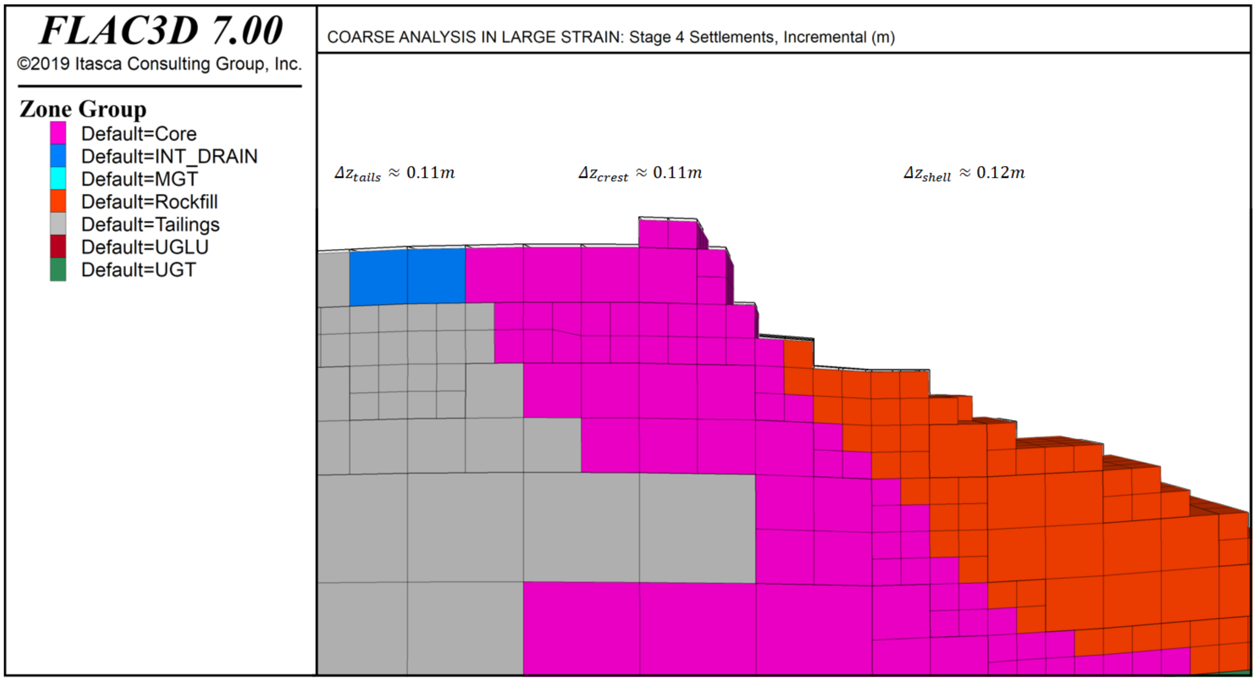

Figure 4B.2 Cross-sectional view of embankment settlement at the slide midpoint due to the addition of stage 4 material predicted by the coarse model in large strain. In black outline: embankment profile prior to settlement. In coloured fill: embankment profile after settlement.

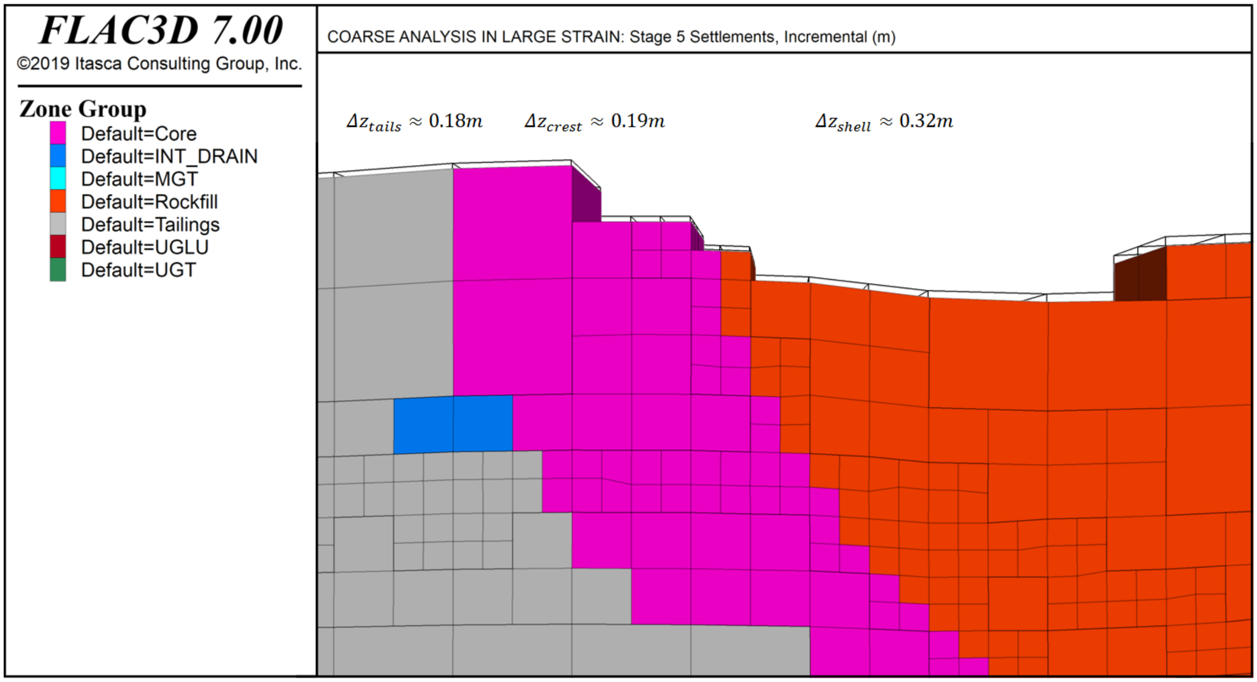

Figure 4B.3 Cross-sectional view of embankment settlement at the slide midpoint due to the addition of stage 5 material predicted by the coarse model in large strain. In black outline: embankment profile prior to settlement. In coloured fill: embankment profile after settlement.

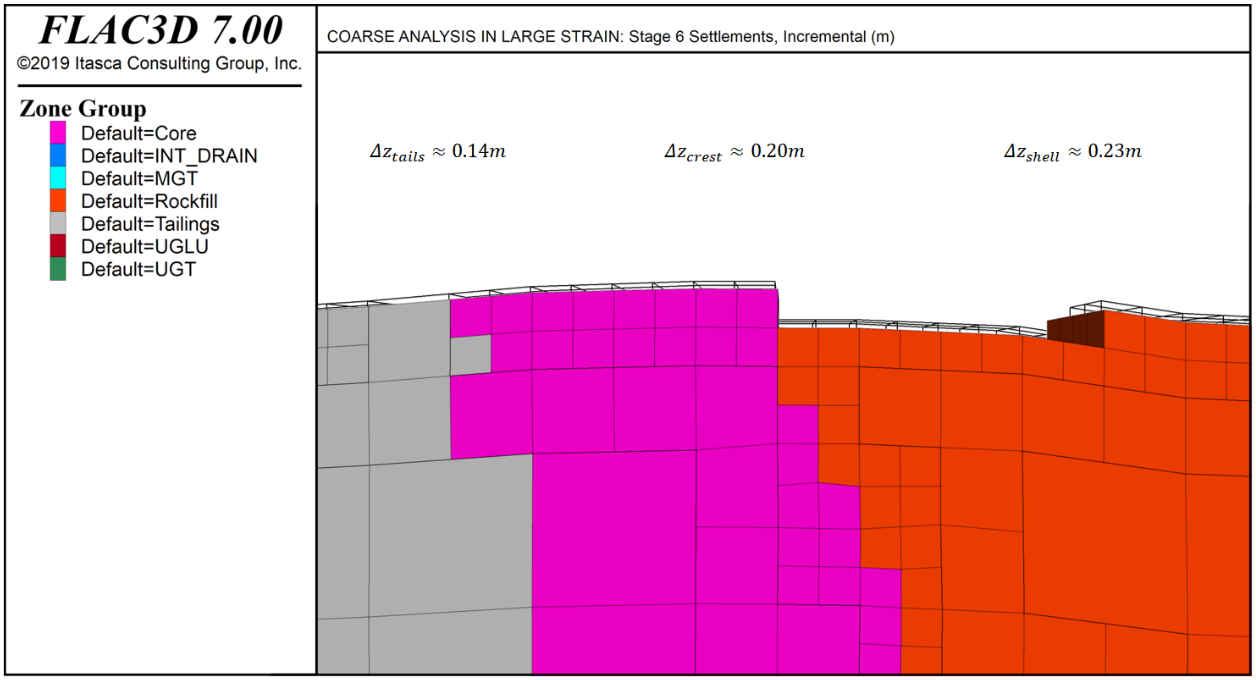

Figure 4B.4 Cross-sectional view of embankment settlement at the slide midpoint due to the addition of stage 6 material predicted by the coarse model in large strain. In black outline: embankment profile prior to settlement. In coloured fill: embankment profile after settlement.

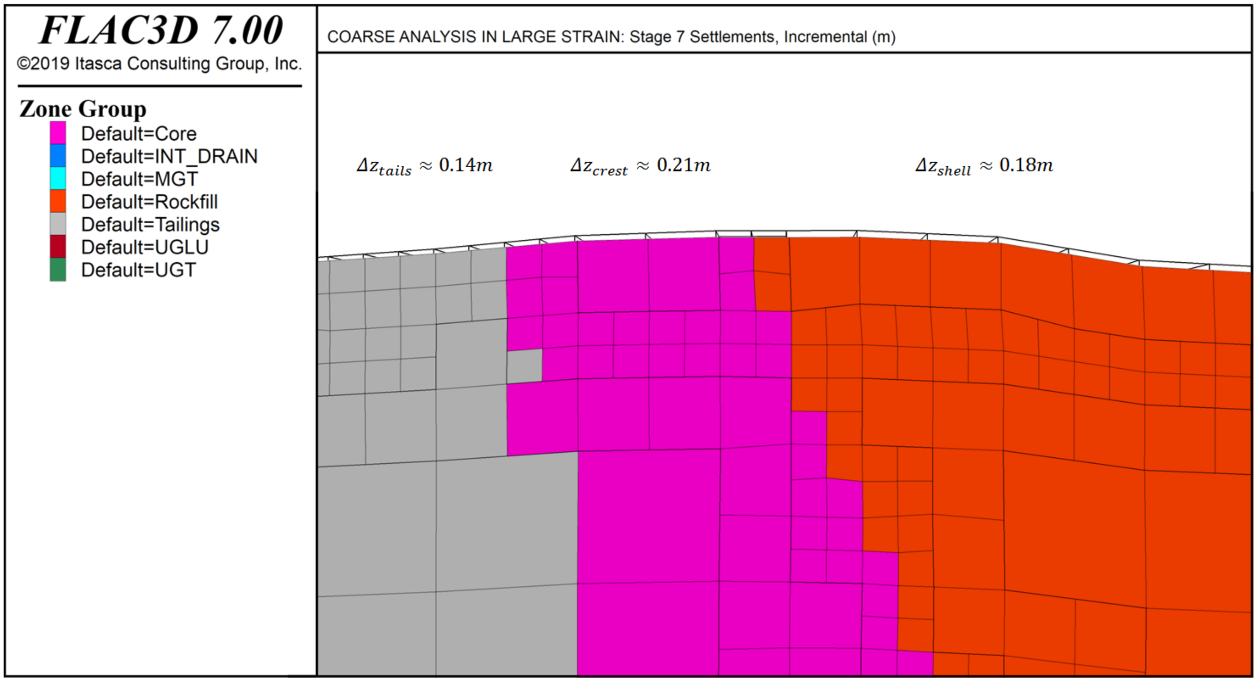

Figure 4B.5 Cross-sectional view of embankment settlement at the slide midpoint due to the addition of stage 7 material predicted by the coarse model in large strain. In black outline: embankment profile prior to settlement. In coloured fill: embankment profile after settlement.

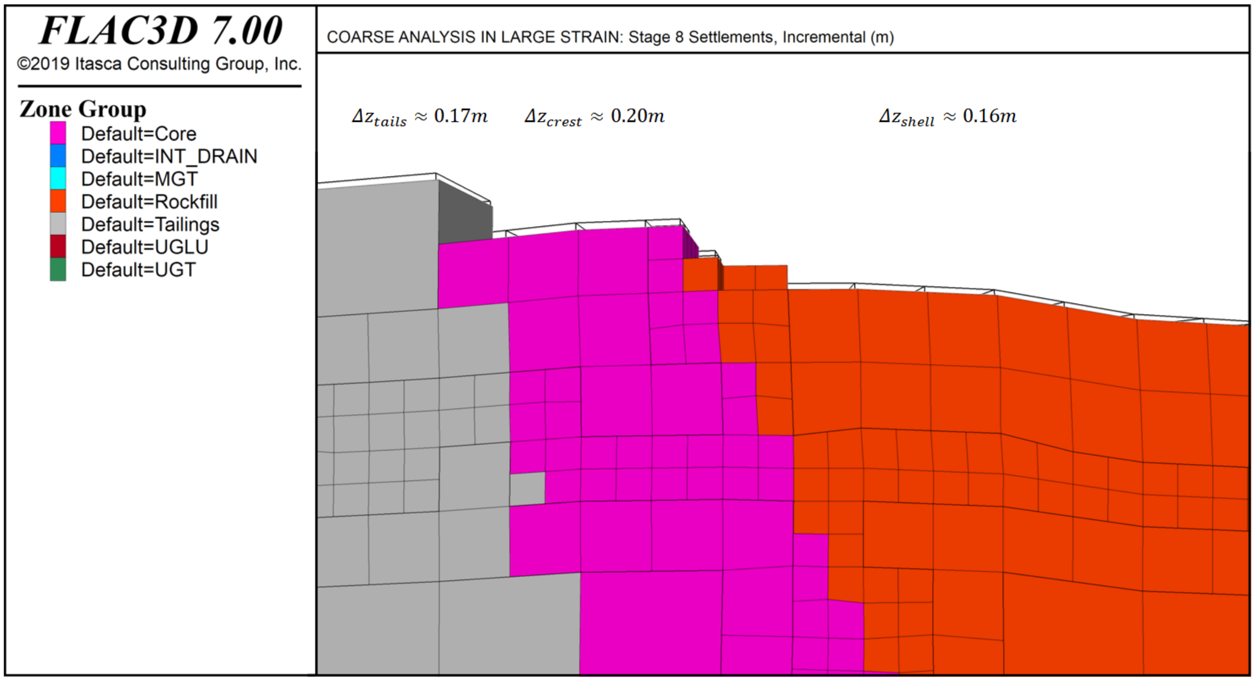

Figure 4B.6 Cross-sectional view of embankment settlement at the slide midpoint due to the addition of stage 8 material predicted by the coarse model in large strain. In black outline: embankment profile prior to settlement. In coloured fill: embankment profile after settlement.

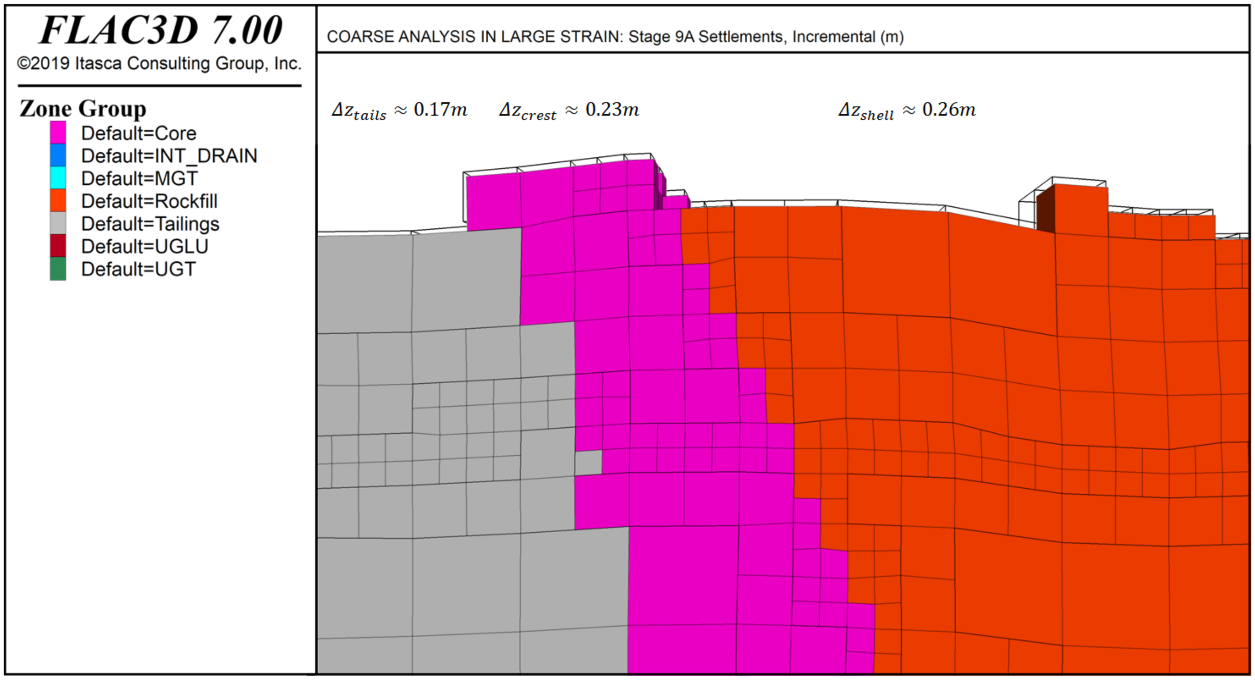

Figure 4B.7 Cross-sectional view of embankment settlement at the slide midpoint due to the addition of stage 9A material predicted by the coarse model in large strain. In black outline: embankment profile prior to settlement. In coloured fill: embankment profile after settlement.

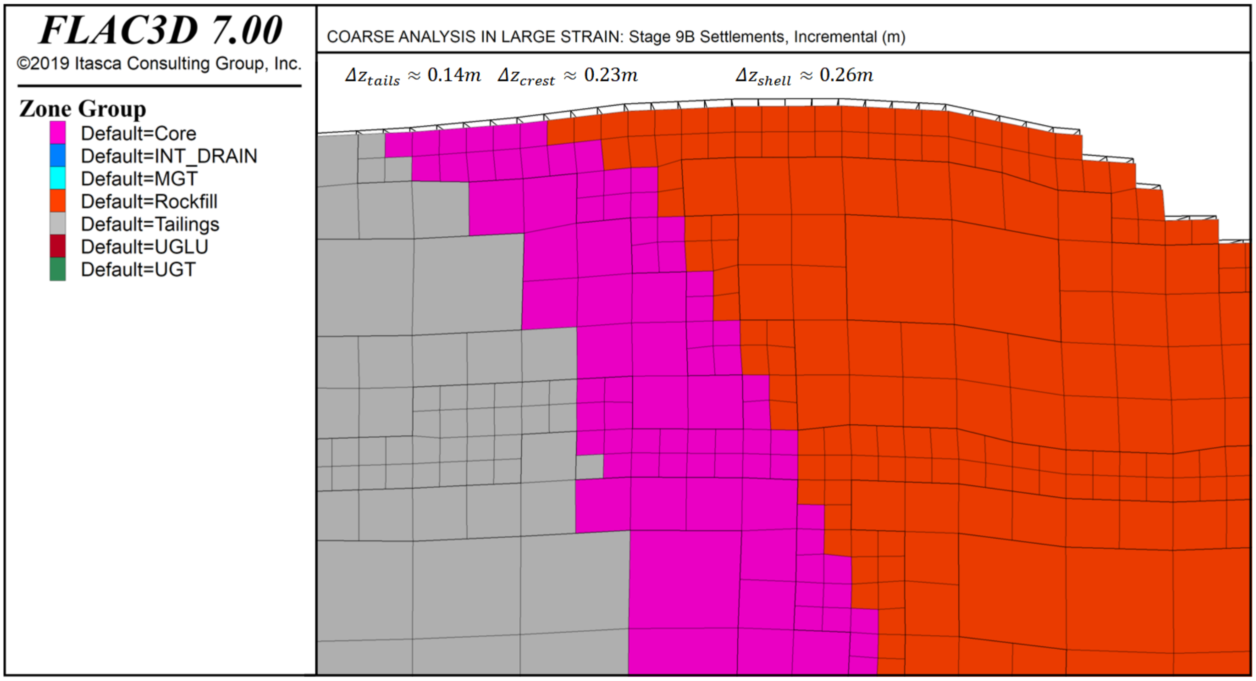

Figure 4B.8 Cross-sectional view of embankment settlement at the slide midpoint due to the addition of stage 9B material predicted by the coarse model in large strain. In black outline: embankment profile prior to settlement. In coloured fill: embankment profile after settlement.

APPENDIX 4C: LARGE STRAIN RESULTS – CUMULATIVE HORIZONTAL DISPLACEMENTS

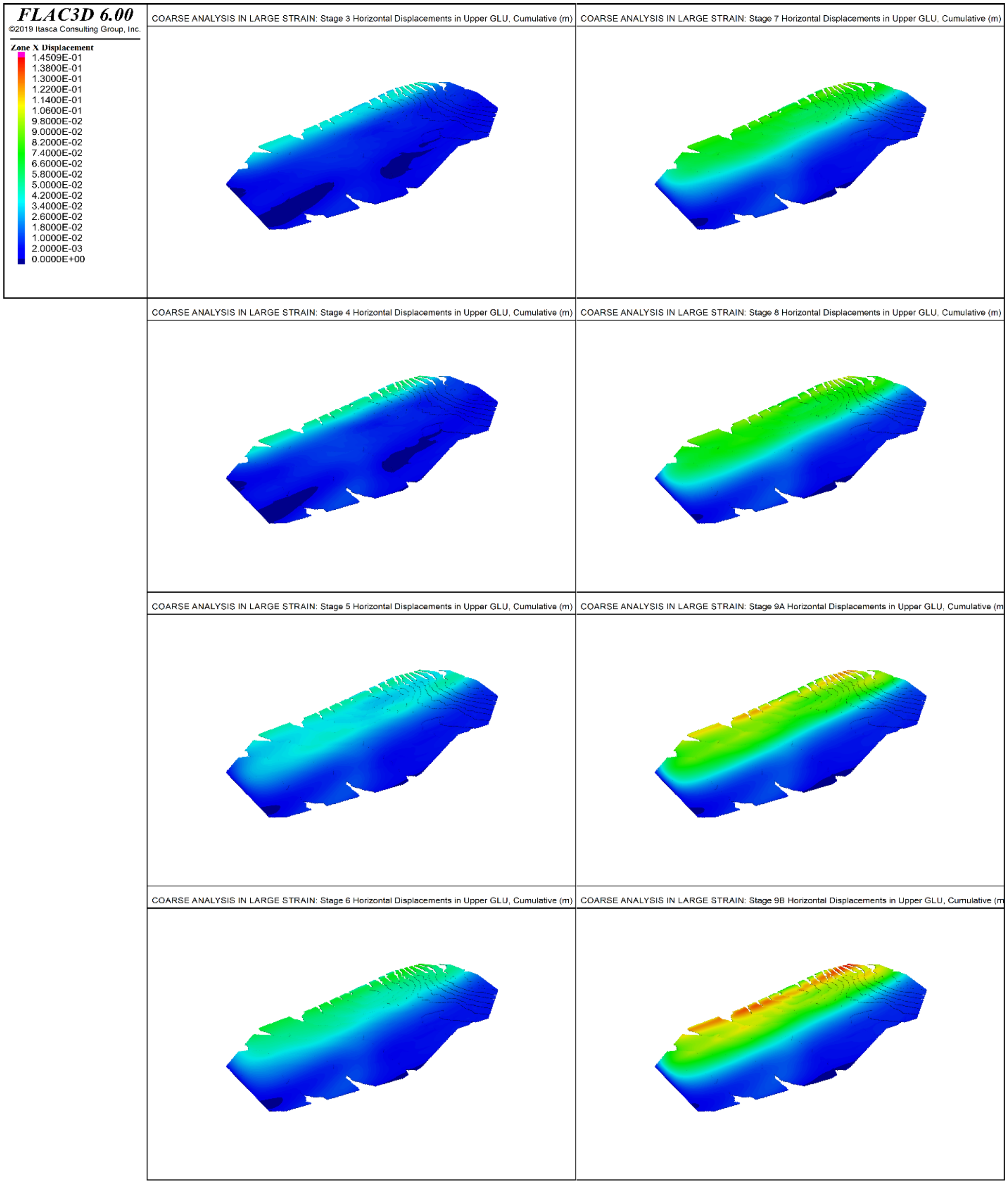

Figure 4C.1 Cumulative horizontal displacements in the Upper GLU predicted by the coarse model in large strain.

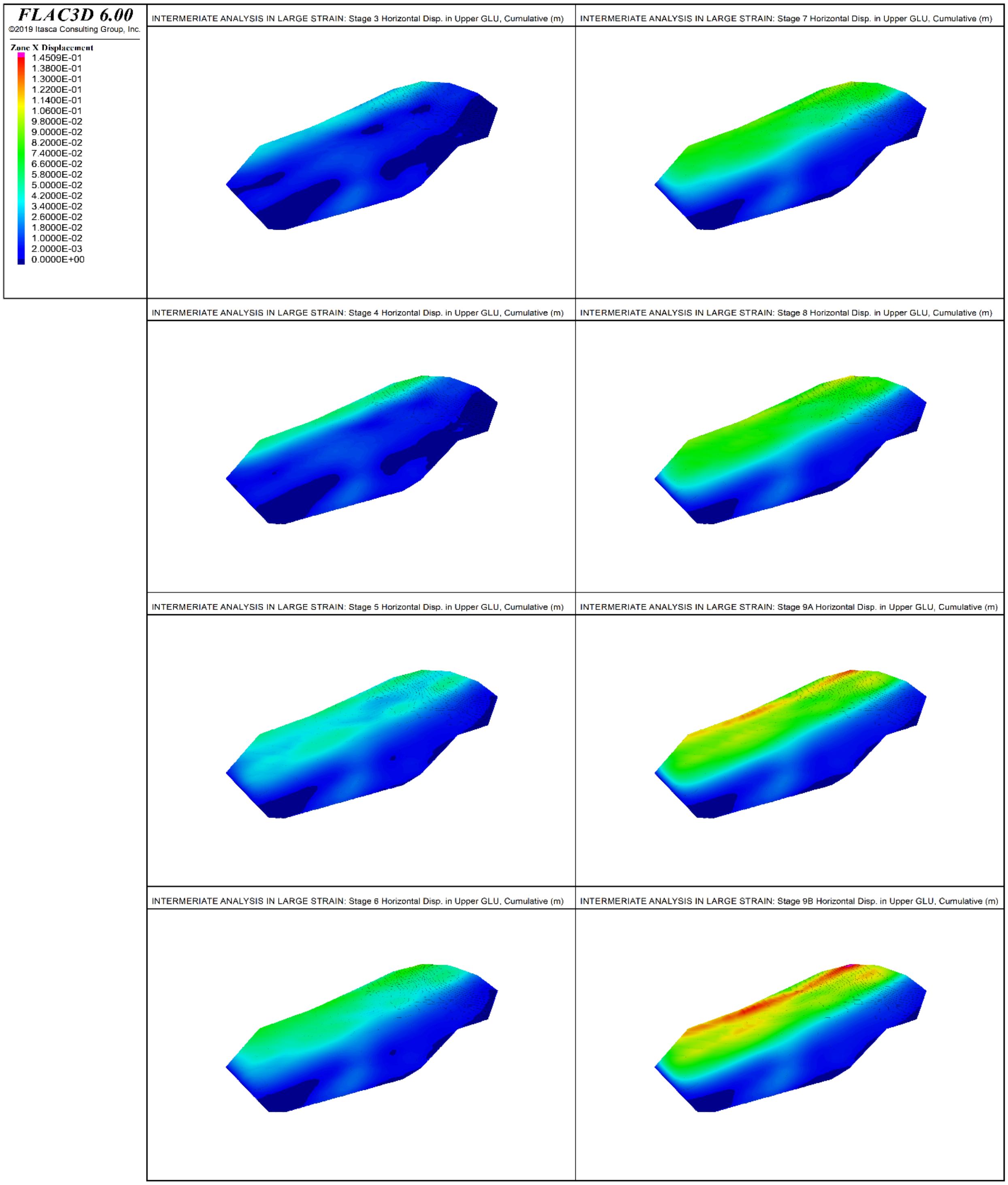

Figure 4C.2 Cumulative horizontal displacements in the Upper GLU predicted by the intermediate model in large strain.

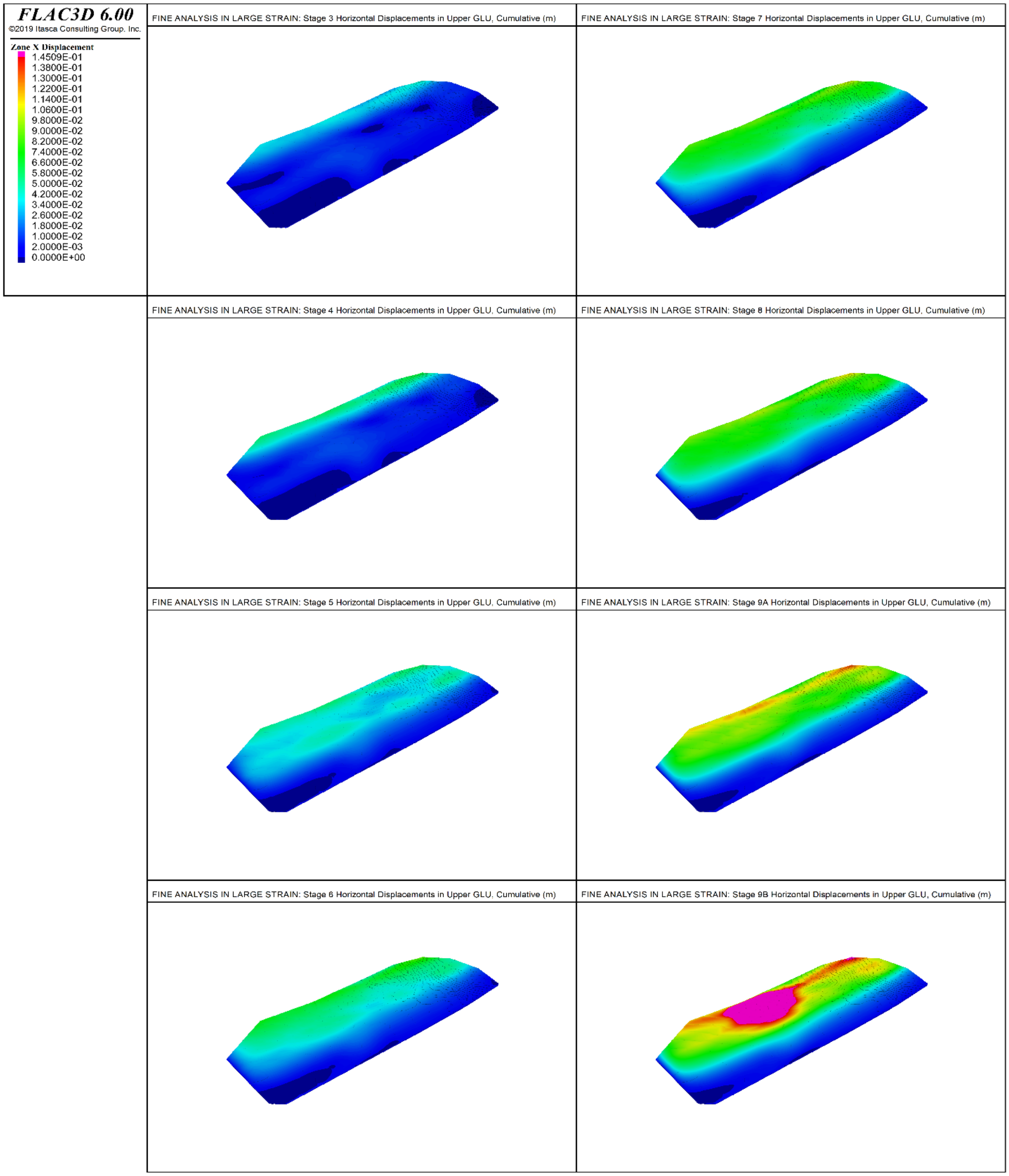

Figure 4C.3 Cumulative horizontal displacements in the Upper GLU predicted by the fine model in large strain.

APPENDIX 4D: STRESS STATES IN THE FAILURE ZONE

SEQUENCE	UGLU X-Displacement, cm			stresses on critical plane CORE (kPa) in upstream shear zone						stresses on critical plane UGT (kPa) upstream edge of UGLU, shear zone										stresses on critical plane (kPa) in Rockfill in critial areas									
	under	under	under	mid-failure		right of mid-slide		left of mid-slide		left of mid-slide		left of mid-slide		mid-failure		right of mid-slide		right of mid-slide		mid-height near CORE		base near toe, deep		mid-depth		shallow		near CORE, deep	
	CORE	SHELL	toe	sig'_n	tau	sig'_n	tau	sig'_n	tau	sig'_n	tau	sig'_n	tau	sig'_n	tau	sig'_n	tau	sig'_n	tau	sig'_n	tau	sig'_n	tau	sig'_n	tau	sig'_n	tau	sig'_n	tau
Stage 5 @equilibrium	4.7	4.1	4.8	148.3	89.1	147.4	89.0	168.1	94.2	215.9	148.2	230.7	155.4	206.3	140.5	226.7	153.7	150.5	97.1	77.8	65.7	72.0	62.4	52.6	30.2	79.6	50.7	60.8	51.9
Stage 6 @equilibrium	6.4	5.7	6.6	204.6	127.9	203.9	127.5	222.2	132.4	255.3	178.6	263.0	182.6	252.7	174.8	264.5	182.9	204.1	133.8	87.9	81.8	57.4	48.5	50.4	41.6	65.6	26.8	78.1	76.0
Stage 7 @equilibrium	8.0	7.1	8.0	205.9	133.6	207.5	134.7	254.8	161.0	286.4	199.9	291.9	203.8	291.0	200.7	289.5	202.2	237.2	160.7	113.2	100.6	67.7	68.5	74.8	67.5	69.2	30.1	102.9	90.5
Stage 8 @equilibrium	9.1	8.0	8.6	226.2	146.7	228.0	147.8	280.2	177.6	306.1	212.7	311.4	217.2	311.4	216.5	306.0	213.7	261.7	175.8	128.3	109.5	97.0	82.7	94.3	75.7	91.9	41.4	117.6	98.2
Stage 9A @equilibrium	11.6	10.2	10.5	265.0	171.8	266.8	173.0	316.6	201.3	334.6	215.5	345.3	223.7	351.5	227.9	336.5	218.0	308.9	200.1	137.7	122.1	100.3	88.6	101.2	85.0	96.4	46.2	129.4	112.6
	11.6	10.2	10.5	265.0	171.8	266.8	173.0	316.6	201.3	334.6	215.5	345.3	223.7	351.5	227.9	336.5	218.0	308.9	200.1	137.7	122.1	100.3	88.6	101.2	85.0	96.4	46.2	129.4	112.6
	11.6	10.2	10.5	265.0	171.8	266.8	173.0	316.6	201.3	334.6	215.5	345.3	223.7	351.5	227.9	336.6	218.0	308.9	200.1	137.7	122.1	100.3	88.6	101.2	85.0	96.4	46.2	129.4	112.7
	11.6	10.2	10.5	265.1	171.9	266.9	173.0	316.7	201.3	334.6	215.5	345.3	223.7	351.5	227.9	336.6	218.0	309.0	200.1	138.1	123.0	100.3	88.6	101.8	85.1	96.4	46.2	130.2	115.2
	11.6	10.2	10.5	267.4	173.4	269.2	174.5	318.8	202.5	335.2	215.7	345.4	223.7	352.1	228.2	336.8	218.1	310.3	201.0	138.7	124.7	100.5	88.6	102.8	85.4	96.4	46.2	131.2	115.6
	11.6	10.2	10.5	270.4	175.3	272.0	176.3	322.2	204.8	338.0	217.6	348.0	224.9	355.1	230.2	339.9	220.2	313.4	202.9	139.1	124.7	100.7	88.6	102.8	86.1	96.4	46.2	130.5	116.4
	11.6	10.2	10.5	273.4	177.3	275.1	178.3	325.9	207.7	340.5	219.3	350.8	226.9	358.1	232.1	342.6	221.9	316.8	205.2	139.1	125.4	100.8	88.9	102.7	86.4	96.5	46.3	131.3	117.2
	11.6	10.2	10.6	275.6	178.7	277.6	179.9	328.2	209.8	343.0	221.0	353.0	228.6	361.1	234.1	344.4	223.1	320.0	207.3	139.8	125.8	100.8	89.1	103.1	86.5	96.8	46.6	131.2	117.8
	11.6	10.2	10.6	277.1	179.6	279.0	180.9	329.5	210.9	343.8	221.4	353.9	229.2	362.5	235.0	344.9	223.4	321.5	208.3	139.5	126.4	100.7	89.3	103.4	86.9	96.8	46.6	131.7	118.6
Stage 9B #1, 500 steps	11.6	10.2	10.7	277.6	179.9	279.7	181.3	330.3	211.7	345.0	221.1	354.1	228.6	363.6	235.1	344.8	222.9	322.8	208.9	140.3	126.8	101.1	89.3	103.6	87.2	96.9	46.7	132.4	119.2
	11.7	10.2	10.7	279.3	180.7	281.4	182.1	331.7	211.9	346.3	220.6	354.8	227.3	364.5	235.3	345.6	222.5	324.3	209.2	140.5	127.3	101.2	89.8	103.9	87.6	97.1	46.9	132.8	119.6
	11.7	10.2	10.7	279.2	180.9	281.4	182.3	331.6	212.4	345.6	221.3	354.6	227.4	364.4	236.0	345.6	223.3	324.4	209.8	140.7	127.5	101.1	90.0	103.8	87.9	97.5	47.2	133.3	119.6
	11.8	10.2	10.7	277.6	179.9	280.0	181.4	330.9	212.1	345.7	221.7	354.7	227.9	364.2	236.0	346.0	223.9	323.9	209.5	141.0	127.5	101.1	90.1	104.0	88.0	97.5	47.2	133.7	119.8
	11.9	10.3	10.8	276.8	179.3	279.1	180.8	329.9	211.3	345.1	221.2	353.8	227.5	363.8	235.5	345.0	223.4	323.5	208.6	140.9	127.8	101.4	90.3	104.1	88.2	97.6	47.3	133.7	120.0
	12.0	10.4	10.8	276.0	178.8	278.5	180.4	328.9	211.0	344.5	220.9	353.3	227.1	363.1	235.3	344.5	223.1	322.8	208.6	141.0	128.1	101.4	90.6	104.2	88.4	97.8	47.5	133.9	120.4
	12.0	10.4	10.8	275.5	178.5	278.0	180.1	328.6	210.8	343.8	221.0	352.6	227.3	362.9	235.3	344.5	223.1	322.2	208.6	141.1	128.2	101.4	90.8	104.4	88.6	97.9	47.6	134.0	120.8
	12.1	10.5	10.8	274.8	178.0	277.3	179.6	328.4	210.6	343.7	220.9	352.4	227.5	362.7	235.2	344.5	223.1	321.9	208.3	141.5	128.3	101.6	91.1	104.5	88.9	98.2	47.9	134.5	120.9
	12.1	10.6	10.9	274.1	177.6	276.7	179.2	327.6	210.5	343.6	221.0	352.3	227.9	362.8	235.1	344.7	223.3	321.5	208.1	141.3	128.6	101.7	91.4	104.7	89.0	98.5	48.1	134.9	121.1
	12.1	10.6	10.9	273.2	177.0	275.8	178.6	326.8	210.6	343.5	221.0	352.0	227.9	362.8	235.2	344.7	223.3	321.0	208.0	141.6	128.7	101.7	91.5	104.8	89.1	98.6	48.2	135.6	121.1
	12.2	10.6	10.9	272.5	176.5	275.3	178.3	326.1	210.8	343.6	221.2	352.3	228.1	362.8	235.3	344.9	223.5	320.8	207.8	142.2	128.7	101.8	91.6	105.0	89.2	98.7	48.2	135.9	121.1
	12.2	10.7	10.9	272.2	176.4	275.0	178.2	325.5	210.8	343.8	221.4	352.6	228.3	363.0	235.3	345.3	223.7	320.6	207.7	142.3	129.0	101.9	91.6	105.3	89.2	98.7	48.3	136.6	121.4
	12.3	10.7	11.0	272.4	176.4	275.2	178.2	325.9	210.4	344.0	221.4	352.7	228.4	363.3	235.6	345.6	223.9	320.8	207.7	142.5	129.0	102.0	91.7	105.3	89.4	98.8	48.4	136.7	121.4
	12.3	10.8	11.1	271.9	176.1	274.8	177.9	325.9	210.5	343.8	221.3	352.5	228.2	363.3	235.6	345.6	223.9	320.8	207.8	142.4	129.2	102.1	91.9	105.4	89.5	99.0	48.5	136.9	121.5
	12.4	10.8	11.1	271.3	175.7	274.3	177.6	325.3	210.9	343.7	221.2	352.1	228.0	363.3	235.6	345.5	223.9	320.8	207.8	142.5	129.3	102.1	92.1	105.4	89.7	99.2	48.7	137.3	121.5
	12.5	10.9	11.2	271.4	175.8	274.6	177.9	324.5	210.4	343.6	221.1	352.1	228.0	363.1	235.5	345.6	223.9	320.6	207.7	142.7	129.3	102.1	92.2	105.3	89.7	99.2	48.7	137.4	121.6
	12.5	10.9	11.2	271.6	175.9	274.9	178.0	324.1	210.1	343.5	221.0	352.2	228.0	363.0	235.4	345.5	223.9	320.4	207.6	142.6	129.5	102.2	92.2	105.4	89.8	99.3	48.8	137.3	121.7
	12.6	11.0	11.3	271.6	175.7	274.8	177.9	324.3	209.6	343.0	220.6	351.8	227.7	362.9	235.4	345.2	223.7	320.5	207.5	142.6	129.5	102.2	92.3	105.4	89.9	99.3	48.8	137.3	121.8
	12.7	11.1	11.3	271.2	175.7	274.5	177.8	323.9	209.5	342.5	220.3	351.1	227.2	362.9	235.3	344.9	223.5	320.3	207.5	142.8	129.6	102.2	92.3	105.5	89.9	99.3	48.8	137.6	121.8
	12.8	11.2	11.3	270.8	175.5	274.1	177.6	323.3	209.6	342.2	220.0	350.5	226.8	362.7	235.2	345.0	223.6	320.1	207.4	142.9	129.6	102.2	92.4	105.5	90.0	99.4	48.9	137.5	121.9
	12.9	11.3	11.3	270.7	175.4	274.0	177.5	323.1	209.5	342.2	220.0	350.0	226.4	362.7	235.2	344.9	223.5	320.0	207.3	142.9	129.6	102.3	92.4	105.5	90.0	99.4	48.9	137.6	121.9
	12.9	11.3	11.3	270.6	175.3	273.9	177.5	323.1	209.5	342.1	220.0	349.5	226.1	362.8	235.3	345.0	223.6	319.9	207.3	142.9	129.7	102.2	92.5	105.6	90.1	99.4	48.9	137.7	121.9
	13.0	11.4	11.3	270.5	175.3	273.9	177.5	322.9	209.4	342.2	220.0	349.4	226.0	362.9	235.3	345.1	223.7	320.0	207.3	142.9	129.7	102.2	92.5	105.6	90.1	99.4	49.0	137.6	122.0
	13.0	11.4	11.3	270.3	175.2	273.8	177.4	322.6	209.2	342.2	220.0	349.1	225.8	363.0	235.4	345.1	223.7	319.9	207.3	143.0	129.8	102.2	92.6	105.6	90.1	99.5	49.0	137.7	122.1
	13.0	11.5	11.4	270.0	175.0	273.5	177.2	322.2	208.9	342.1	220.0	349.0	225.7	362.9	235.3	345.1	223.7	319.6	207.1	142.9	129.8	102.2	92.6	105.6	90.2	99.5	49.0	137.7	122.1
	13.0	11.5	11.4	269.7	174.7	273.2	177.1	321.7	208.6	342.0	219.9	348.8	225.6	362.7	235.2	344.9	223.6	319.3	206.9	143.0	129.8	102.3	92.6	105.6	90.2	99.5	49.0	137.9	122.0
	13.1	11.5	11.4	269.3	174.5	272.9	176.9	321.3	208.4	341.8	219.8	348.6	225.5	362.6	235.2	344.9	223.6	319.0	206.7	143.0	129.9	102.3	92.6	105.7	90.2	99.6	49.1	138.1	122.1
	13.1	11.5	11.4	269.1	174.4	272.7	176.7	321.0	208.1	341.6	219.6	348.4	225.3	362.6	235.2	344.9	223.6	318.9	206.6	143.1	129.9	102.3	92.7	105.8	90.2	99.6	49.1	138.2	122.1
	13.1	11.5	11.4	269.1	174.4	272.6	176.7	320.8	208.0	341.6	219.6	348.3	225.3	362.6	235.2	345.0	223.6	318.7	206.6	143.2	130.0	102.3	92.7	105.8	90.3	99.6	49.1	138.3	122.1
	13.2	11.6	11.4	269.1	174.4	272.7	176.7	320.8	208.0	341.6	219.6	348.3	225.3	362.7	235.2	345.0	223.7	318.7	206.5	143.2	130.0	102.3	92.8	105.8	90.4	99.7	49.2	138.5	122.1
	13.2	11.6	11.4	269.0	174.3	272.8	176.8	320.6	207.9	341.5	219.5	348.2	225.2	362.8	235.3	345.1	223.7	318.7	206.5	143.2	130.1	102.4	92.8	105.8	90.4	99.8	49.2	138.6	122.2
	13.3	11.6	11.4	269.0	174.3	272.8	176.8	320.2	207.6	341.4	219.4	347.9	225.0	362.8	235.3	345.0	223.7	318.6	206.4	143.3	130.1	102.4	92.8	105.8	90.4	99.8	49.3	138.7	122.3
	13.3	11.6	11.4	268.9	174.3	272.7	176.8	319.7	207.3	341.4	219.4	347.7	224.8	362.8	235.3	345.1	223.7	318.4	206.3	143.3	130.2	102.4	92.9	105.8	90.5	99.8	49.3	138.7	122.3
	13.4	11.7	11.4	268.9	174.3	272.8	176.8	319.5	207.2	341.2	219.3	347.4	224.6	362.8	235.3	345.1	223.7	318.3	206.3	143.3	130.2	102.4	92.9	105.9	90.5	99.8	49.3	138.8	122.4
	13.4	11.7	11.4	268.7	174.2	272.6	176.7	319.5	207.1	341.1	219.2	347.0	224.3	362.8	235.3	345.1	223.7	318.2	206.2	143.4	130.2	102.5	93.0	105.9	90.5	99.9	49.3	138.9	122.4
	13.5	11.8	11.5	268.5	174.0	272.3	176.5	319.3	207.0	340.9	219.0	346.7	224.1	362.8	235.3	345.1	223.7	318.1	206.2	143.5	130.2	102.5	93.0	105.9	90.6	99.9	49.3	139.0	122.4
	13.5	11.8	11.5	268.3	173.9	272.1	176.4	319.0	206.9	340.7	218.9	346.2	223.8	362.7	235.2	345.1	223.7	318.0	206.1	143.5	130.2	102.5	93.0	105.9	90.6	99.9	49.3	139.1	122.3
	13.6	11.9	11.5	268.2	173.8	272.0	176.3	318.9	206.8	340.5	218.7	345.7	223.4	362.6	235.2	345.0	223.7	317.9	206.0	143.5	130.2	102.5	93.0	105.9	90.6	99.9	49.3	139.0	122.3
	13.7	12.0	11.5	268.1	173.8	272.0	176.3	318.7	206.6	340.2	218.5	345.2	223.1	362.5	235.1	345.0	223.7	317.8	206.0	143.5	130.2	102.5	93.0	105.9	90.6	99.9	49.4	139.0	122.4
	13.7	12.0	11.5	268.1	173.8	272.0	176.3	318.6	206.5	340.0	218.4	344.8	222.8	362.5	235.1	345.0	223.7	317.8	206.0	143.5	130.2	102.5	93.0	105.9	90.6	99.9	49.4	139.0	122.4
	13.8	12.1	11.5	268.1	173.8	272.0	176.3	318.5	206.5	339.8	218.2	344.3	222.4	362.5	235.1	345.0	223.7	317.8	206.0	143.5	130.2	102.5	93.0	105.9	90.6	99.9	49.4	139.0	122.4
	13.8	12.2	11.5	268.0	173.7	272.0	176.3	318.3	206.4	339.6	218.0	343.8	222.1	362.6	235.1	345.0	223.7	317.8	205.9	143.5	130.3	102.5	93.0	105.9	90.6	99.9	49.4	139.0	122.4
	13.9	12.3	11.5	267.9	173.7	271.9	176.3	318.2	206.3	339.4	217.9	343.3	221.7	362.5	235.1	345.0	223.7	317.7	205.9	143.5	130.3	102.5	93.0	105.9	90.6	99.9	49.4	139.0	122.4
	14.0	12.3	11.5	267.9	173.7	271.9	176.2	318.0	206.1	339.1	217.7	342.8	221.3	362.5	235.1	344.9	223.7	317.6	205.9	143.5	130.3	102.5	93.1	105.9	90.6	99.9	49.4	139.0	122.4
	14.0	12.4	11.5	267.8	173.6	271.8	176.2	317.7	206.0	338.9	217.5	342.2	221.0	362.5	235.1	345.0	223.7	317.6	205.8	143.5	130.3	102.5	93.1	105.9	90.6	99.9	49.4	139.0	122.4
	14.1	12.5	11.5	267.7	173.5	271.7	176.2	317.5	205.9	338.6	217.4	341.7	220.6	362.5	235.1	345.0	223.7	317.5	205.8	143.5	130.3	102.5	93.1	105.9	90.6	99.9	49.4	139.0	122.4
Stage 9B seq.4	14.2	12.5	11.5	267.6	173.5	271.7	176.1	317.4	205.7	338.4	217.2	341.2	220.2	362.5	235.1	345.1	223.8	317.4	205.7	143.5	130.3	102.5	93.1	106.0	90.6	99.9	49.4	139.0	122.4
	14.3	12.6	11.5	267.5	173.4	271.6	176.1	317.2	205.6	338.2	217.0	340.6	219.8	362.5	235.1	345.1	223.8	317.4	205.7	143.5	130.3	102.5	93.1	106.0	90.7	99.9	49.4	139.1	122.4
	14.4	12.7	11.5	267.3	173.3	271.4	176.0	316.9	205.5	337.9	216.8	340.0	219.4	362.5	235.1	345.1	223.8	317.3	205.7	143.5	130.3	102.5	93.1	106.0	90.7	99.9	49.4	139.1	122.4
	14.5	12.8	11.5	267.2	173.2	271.3	175.9	316.6	205.3	337.6	216.6	339.4	218.9	362.4	235.1	345.1	223.9	317.2	205.6	143.5	130.3	102.5	93.1	106.0	90.7	100.0	49.4	139.1	122.4
	14.6	12.9	11.5	267.1	173.1	271.2	175.8	316.3	205.1	337.2	216.3	338.7	218.4	362.4	235.0	345.1	223.9	317.1	205.5	143.6	130.3	102.5	93.1	106.0	90.7	100.0	49.4	139.2	122.4
	14.7	13.0	11.5	267.0	173.1	271.2	175.8	316.1	204.9	336.9	216.0	337.9	217.9	362.3	235.0	345.1	223.9	317.0	205.5	143.6	130.3	102.5	93.1	106.0	90.7	100.0	49.4	139.2	122.4
	14.8	13.1	11.5	266.9	173.0	271.1	175.8	315.8	204.7	336.4	215.7	337.1	217.3	362.2	234.9	345.1	223.9	316.9	205.4	143.6	130.3	102.5	93.1	106.0	90.7	100.0	49.5	139.2	122.4
	14.9	13.3	11.5	266.8	173.0	271.1	175.7	315.5	204.5	336.0	215.4	336.3	216.7	362.2	234.9	345.1	223.9	316.9	205.4	143.6	130.3	102.5	93.1	106.0	90.7	100.0	49.5	139.2	122.4
	15.1	13.5	11.5	266.6	172.9	271.0	175.7	315.3	204.3	335.5	215.0	335.3	216.0	362.2	234.9	345.2	223.9	316.8	205.4	143.6	130.3	102.5	93.1	106.0	90.7	100.0	49.5	139.3	122.4
	15.2	13.6	11.5	266.5	172.8	270.8	175.6	314.9	204.1	334.9	214.6	334.1	215.1	362.1	234.8	345.1	223.9	316.7	205.3	143.6	130.4	102.5	93.2	106.0	90.7	100.0	49.5	139.3	122.4
	15.4	13.8	11.5	266.3	172.6	270.7	175.5	314.5	203.8	334.2	214.0	332.7	214.2	362.0	234.8	345.1	223.9	316.6	205.2	143.6	130.3	102.5	93.2	106.0	90.7	100.0	49.5	139.3	122.5
	15.7	14.1	11.5	266.1	172.5	270.5	175.4	314.0	203.5	333.4	213.4	331.2	213.1	361.9	234.6	345.0	223.8	316.4	205.1	143.6	130.3	102.6	93.2	106.0	90.7	100.0	49.5	139.3	122.4
	15.9	14.3	11.5	265.8	172.4	270.4	175.3	313.5	203.1	332.6	212.8	329.5	211.9	361.7	234.5	345.0	223.8	316.2	205.0	143.6	130.4	102.6	93.2	106.0	90.7	100.0	49.5	139.3	122.4
	16.2	14.6	11.5	265.6	172.2	270.2	175.2	312.9	202.7	331.6	212.0	327.7	210.6	361.5	234.4	344.9	223.7	316.1	204.9	143.6	130.4	102.6	93.2	106.0	90.7	100.0	49.5	139.3	122.4
	16.5	15.0	11.5	265.4	172.1	270.1	175.1	312.3	202.3	330.4	211.2	325.7	209.1	361.3	234.3	344.8	223.7	315.9	204.8	143.6	130.4	102.6	93.2	106.0	90.7	100.0	49.5	139.3	122.4
	16.9	15.3	11.5	265.1	171.9	269.9	175.0	311.6	201.9	329.2	210.2	323.5	207.6	361.2	234.1	344.7	223.7	315.8	204.7	143.6	130.4	102.6	93.2	106.0	90.7	100.0	49.5	139.3	122.5
	17.4	15.8	11.5	264.8	171.7	269.7	174.9	310.9	201.4	327.8	209.1	321.1	205.9	360.9	234.0	344.6	223.6	315.6	204.6	143.6	130.4	102.6	93.2	106.0	90.7	100.0	49.5	139.3	122.4
	17.9	16.2	11.5	264.5	171.5	269.4	174.7	310.1	200.8	326.2	207.9	318.6	204.2	360.6	233.7	344.5	223.5	315.4	204.5	143.6	130.4	102.6	93.2	106.0	90.7	100.0	49.5	139.3	122.5
	18.4	16.7	11.5	264.1	171.3	269.2	174.6	309.2	200.2	324.5	206.6	316.2	202.5	360.2	233.5	344.2	223.3	315.1	204.3	143.6	130.4	102.6	93.2	106.0	90.7	100.0	49.5	139.4	122.5
	18.9	17.1	11.5	263.7	171.0	268.8	174.4	308.2	199.5	322.7	205.2	313.9	201.0	359.7	233.1	343.9	223.1	314.7	204.1	143.6	130.4	102.6	93.2	106.0	90.7	100.0	49.5	139.4	122.5
	19.3	17.6	11.5	263.2	170.7	268.5	174.1	307.1	198.8	320.8	203.7	311.8	199.6	359.2	232.7	343.5	222.8	314.3	203.8	143.6	130.4	102.6	93.2	106.0	90.7	100.0	49.5	139.4	122.4
	19.7	18.0	11.5	262.7	170.4	268.0	173.9	306.1	198.0	319.0	202.3	310.0	198.5	358.5	232.2	342.9	222.4	313.9	203.5	143.6	130.4	102.6	93.2	106.0	90.7	100.0	49.5	139.4	122.4
	20.0	18.4	11.5	262.1	170.0	267.6	173.6	305.0	197.3	317.5	201.1	308.7	197.7	357.7	231.7	342.1	221.9	313.4	203.2	143.6	130.4	102.6	93.2	106.0	90.7	100.0	49.5	139.4	122.4
	20.4	18.7	11.5	261.5	169.7	267.1	173.2	304.0	196.6	316.0	199.9	307.5	197.0	356.8	231.1	341.1	221.2	312.9	202.9	143.6	130.4	102.6	93.2	106.0	90.7	100.0	49.5	139.5	122.4

	20.8	19.1	11.5	260.9	169.3	266.5	172.9	302.9	195.8	314.6	198.8	306.5	196.4	355.7	230.3	339.6	220.2	312.2	202.5	143.6	130.4	102.6	93.2	106.0	90.7	100.0	49.5	139.5	122.5
	21.2	19.5	11.5	260.3	168.9	265.9	172.5	301.9	195.1	313.3	197.7	305.6	195.8	354.4	229.5	337.7	219.0	311.5	202.0	143.6	130.4	102.6	93.2	106.0	90.7	100.0	49.5	139.5	122.5
	21.6	19.9	11.5	259.6	168.4	265.2	172.0	300.8	194.3	311.9	196.6	304.7	195.2	353.1	228.6	335.3	217.4	310.7	201.5	143.6	130.4	102.6	93.2	106.0	90.7	100.1	49.5	139.6	122.5
	22.0	20.3	11.5	258.9	168.0	264.5	171.6	299.8	193.6	310.6	195.5	303.4	194.4	351.6	227.7	332.3	215.5	309.8	200.9	143.6	130.4	102.6	93.2	106.0	90.7	100.1	49.5	139.6	122.5
	22.4	20.7	11.5	258.2	167.5	263.7	171.1	298.8	192.9	309.3	194.4	302.1	193.6	350.2	226.8	328.8	213.2	308.9	200.3	143.6	130.4	102.6	93.2	106.0	90.7	100.1	49.5	139.7	122.5
	22.8	21.2	11.5	257.4	167.0	262.9	170.6	297.8	192.2	308.0	193.4	300.7	192.8	348.6	225.8	324.8	210.7	307.8	199.7	143.6	130.4	102.6	93.2	106.0	90.7	100.1	49.5	139.8	122.5
	23.2	21.6	11.5	256.7	166.6	262.0	170.0	296.9	191.5	306.7	192.3	299.5	192.0	347.1	224.8	320.8	208.0	306.8	199.0	143.6	130.4	102.6	93.2	106.0	90.7	100.1	49.5	139.8	122.5
	23.6	22.1	11.5	255.9	166.1	261.1	169.5	295.9	190.8	305.5	191.3	298.2	191.2	345.7	223.9	316.6	205.3	305.7	198.3	143.6	130.4	102.6	93.2	106.0	90.7	100.1	49.5	139.9	122.5
	24.1	22.6	11.6	255.2	165.6	260.2	168.9	295.1	190.1	304.4	190.4	296.8	190.3	344.3	223.0	312.5	202.6	304.5	197.5	143.7	130.4	102.6	93.2	106.0	90.8	100.1	49.5	140.0	122.5
	24.5	23.0	11.6	254.6	165.3	259.3	168.3	294.3	189.5	303.4	189.5	295.4	189.4	343.1	222.2	308.3	199.8	303.4	196.8	143.7	130.4	102.6	93.2	106.0	90.8	100.1	49.5	140.1	122.5
	25.0	23.5	11.6	254.1	164.9	258.5	167.8	293.5	188.9	302.4	188.8	293.8	188.4	342.0	221.5	304.1	197.0	302.3	196.1	143.7	130.4	102.6	93.2	106.0	90.8	100.1	49.5	140.2	122.5
	25.5	23.9	11.6	253.6	164.6	257.7	167.3	292.9	188.4	301.5	188.0	292.4	187.5	341.1	220.9	300.0	194.2	301.2	195.4	143.7	130.4	102.6	93.2	106.0	90.8	100.1	49.5	140.3	122.5
	26.0	24.4	11.6	253.2	164.4	257.0	166.8	292.3	188.0	300.7	187.4	290.9	186.5	340.3	220.4	296.2	191.6	300.1	194.7	143.7	130.4	102.6	93.2	106.1	90.8	100.2	49.5	140.4	122.5
	26.5	24.9	11.6	252.9	164.2	256.3	166.4	291.8	187.5	299.9	186.8	289.6	185.7	339.5	219.9	292.8	189.3	299.2	194.0	143.7	130.4	102.6	93.2	106.1	90.8	100.2	49.5	140.6	122.5
	27.1	25.5	11.6	252.6	164.0	255.7	166.0	291.4	187.1	299.1	186.3	288.3	184.8	338.8	219.4	289.7	187.2	298.2	193.4	143.7	130.4	102.6	93.2	106.1	90.8	100.2	49.5	140.7	122.5
	27.6	26.0	11.6	252.4	163.8	255.1	165.6	290.9	186.8	298.4	185.8	286.9	184.0	338.1	218.9	286.8	185.2	297.3	192.8	143.7	130.4	102.6	93.2	106.1	90.8	100.2	49.5	140.8	122.4
	28.2	26.6	11.6	252.2	163.7	254.5	165.2	290.5	186.4	297.7	185.4	285.4	183.1	337.4	218.5	283.9	183.2	296.5	192.3	143.7	130.4	102.6	93.3	106.1	90.8	100.2	49.5	141.0	122.4
	28.8	27.2	11.6	251.9	163.6	253.9	164.8	290.0	186.0	297.1	184.9	283.9	182.1	336.7	218.0	281.1	181.3	295.6	191.7	143.7	130.4	102.6	93.3	106.1	90.8	100.3	49.5	141.1	122.4
	29.3	27.8	11.6	251.7	163.4	253.4	164.5	289.5	185.6	296.4	184.5	282.3	181.2	335.9	217.5	278.3	179.4	294.7	191.1	143.7	130.5	102.6	93.3	106.1	90.8	100.3	49.5	141.3	122.4
	29.9	28.4	11.6	251.5	163.3	252.8	164.1	289.0	185.2	295.7	184.1	280.8	180.2	335.2	217.0	275.7	177.6	293.7	190.5	143.7	130.5	102.6	93.3	106.1	90.8	100.3	49.5	141.4	122.4
	30.5	29.0	11.6	251.3	163.2	252.3	163.8	288.5	184.8	295.1	183.8	279.3	179.3	334.4	216.5	273.2	176.0	292.9	189.9	143.8	130.5	102.6	93.3	106.1	90.8	100.3	49.5	141.6	122.3
	31.2	29.7	11.6	251.2	163.1	251.8	163.5	287.9	184.3	294.5	183.4	277.8	178.4	333.7	216.0	271.0	174.6	292.0	189.3	143.8	130.5	102.6	93.3	106.1	90.8	100.4	49.5	141.8	122.3
	31.8	30.3	11.6	251.0	163.0	251.4	163.2	287.4	184.0	293.8	183.0	276.3	177.4	332.9	215.6	269.1	173.3	291.3	188.8	143.8	130.5	102.6	93.3	106.1	90.8	100.4	49.5	141.9	122.3
	32.4	31.0	11.7	250.9	162.9	251.0	162.9	287.0	183.6	293.2	182.6	274.8	176.5	332.2	215.1	267.3	172.1	290.6	188.3	143.8	130.5	102.6	93.3	106.1	90.8	100.4	49.5	142.1	122.3
	33.0	31.6	11.7	250.7	162.8	250.6	162.6	286.5	183.2	292.6	182.2	273.4	175.6	331.5	214.6	265.5	171.0	289.9	187.9	143.8	130.5	102.7	93.3	106.1	90.9	100.5	49.5	142.2	122.2
	33.7	32.3	11.7	250.5	162.7	250.2	162.3	286.0	182.8	291.9	181.8	271.9	174.6	330.8	214.1	263.7	169.9	289.2	187.4	143.9	130.5	102.7	93.4	106.2	90.9	100.5	49.5	142.4	122.2
	34.3	32.9	11.7	250.3	162.5	249.7	162.1	285.5	182.4	291.3	181.4	270.3	173.7	330.1	213.7	262.1	168.9	288.6	187.0	143.9	130.5	102.7	93.4	106.2	90.9	100.5	49.5	142.5	122.1
	34.9	33.5	11.7	250.2	162.4	249.3	161.8	284.9	182.0	290.8	181.0	268.8	172.7	329.5	213.3	260.6	168.0	288.0	186.6	143.9	130.6	102.7	93.4	106.2	90.9	100.6	49.5	142.6	122.1
	35.6	34.1	11.7	250.0	162.3	249.0	161.6	284.4	181.6	290.3	180.7	267.3	171.7	328.9	212.9	259.2	167.1	287.5	186.3	143.9	130.6	102.7	93.4	106.2	90.9	100.6	49.5	142.7	122.0
	36.2	34.8	11.7	249.9	162.2	248.6	161.3	284.0	181.2	289.9	180.4	265.8	170.8	328.4	212.6	257.9	166.3	286.9	185.9	143.9	130.6	102.7	93.4	106.2	90.9	100.6	49.5	142.9	121.9
	36.9	35.4	11.7	249.8	162.2	248.3	161.1	283.6	180.9	289.5	180.1	264.5	169.9	328.0	212.3	256.6	165.5	286.5	185.6	144.0	130.6	102.7	93.4	106.2	90.9	100.7	49.5	143.0	121.9
	37.5	36.0	11.8	249.7	162.1	248.1	161.0	283.2	180.6	289.2	179.9	263.2	169.1	327.5	212.0	255.4	164.8	286.0	185.3	144.0	130.6	102.7	93.5	106.2	91.0	100.7	49.5	143.1	121.8
	38.1	36.6	11.8	249.7	162.1	247.9	160.8	282.9	180.3	289.0	179.7	262.1	168.4	327.1	211.7	254.2	164.0	285.6	185.0	144.0	130.6	102.7	93.5	106.3	91.0	100.8	49.5	143.3	121.7
	38.8	37.3	11.8	249.6	162.1	247.6	160.7	282.5	180.0	288.8	179.5	261.1	167.8	326.6	211.4	252.9	163.3	285.2	184.7	144.1	130.7	102.7	93.5	106.3	91.0	100.8	49.5	143.4	121.6
	39.4	37.9	11.8	249.6	162.1	247.4	160.5	282.2	179.7	288.6	179.4	260.0	167.1	326.1	211.1	251.7	162.5	284.8	184.5	144.1	130.7	102.7	93.5	106.3	91.0	100.9	49.5	143.5	121.5
Stage 9B @ 5,170 steps	40.0	38.6	11.8	249.6	162.1	247.2	160.4	282.0	179.5	288.5	179.2	259.0	166.4	325.7	210.8	250.5	161.7	284.4	184.2	144.1	130.7	102.7	93.5	106.3	91.0	100.9	49.5	143.5	121.5
	40.6	39.2	11.8	249.6	162.1	247.0	160.3	281.7	179.3	288.4	179.1	258.0	165.8	325.2	210.5	249.4	161.0	284.0	184.0	144.1	130.7	102.7	93.6	106.3	91.0	101.0	49.5	143.6	121.4
	40.9	39.5	11.8	249.6	162.1	247.0	160.3	281.7	179.3	288.4	179.1	258.0	165.8	325.2	210.5	249.4	161.0	284.0	184.0	144.1	130.7	102.7	93.6	106.3	91.0	101.0	49.5	143.6	121.4
	41.1	39.7	11.8	249.6	162.1	247.0	160.2	281.6	179.2	288.4	179.1	257.6	165.5	325.1	210.4	248.9	160.7	283.9	183.9	144.1	130.7	102.7	93.6	106.3	91.0	101.0	49.5	143.7	121.4
	41.3	40.0	11.8	249.6	162.1	247.0	160.2	281.6	179.1	288.4	179.0	257.1	165.3	324.9	210.3	248.5	160.5	283.8	183.8	144.2	130.7	102.7	93.6	106.3	91.0	101.0	49.5	143.7	121.4
	41.3	40.2	11.8	249.7	162.1	246.9	160.2	281.5	179.0	288.4	179.0	256.7	165.0	324.8	210.2	248.1	160.2	283.7	183.7	144.2	130.7	102.8	93.6	106.3	91.1	101.0	49.5	143.7	121.3
	41.6	40.4	11.8	249.7	162.1	246.9	160.2	281.4	179.0	288.3	178.9	256.3	164.8	324.6	210.1	247.7	159.9	283.6	183.7	144.2	130.8	102.8	93.6	106.3	91.1	101.0	49.5	143.8	121.3
	41.8	40.7	11.8	249.7	162.2	246.9	160.1	281.3	178.9	288.3	178.9	255.9	164.5	324.5	210.0	247.3	159.7	283.5	183.6	144.2	130.8	102.8	93.6	106.3	91.1	101.1	49.5	143.8	121.3
	42.1	40.9	11.8	249.8	162.2	246.9	160.1	281.2	178.8	288.3	178.9	255.5	164.2	324.3	209.9	246.9	159.4	283.4	183.5	144.2	130.8	102.8	93.6	106.3	91.1	101.1	49.5	143.9	121.3
	42.3	41.1	11.8	249.8	162.2	246.9	160.1	281.2	178.8	288.3	178.8	255.1	164.0	324.2	209.8	246.5	159.2	283.3	183.5	144.2	130.8	102.8	93.6	106.4	91.1	101.1	49.5	143.9	121.2
	42.6	41.4	11.8	249.9	162.2	246.9	160.1	281.1	178.7	288.3	178.8	254.7	163.7	324.0	209.7	246.1	159.0	283.2	183.4	144.2	130.8	102.8	93.6	106.4	91.1	101.2	49.5	143.9	121.2
	42.8	41.6	11.9	249.9	162.3	246.9	160.1	281.0	178.6	288.2	178.8	254.3	163.4	323.9	209.6	245.8	158.7	283.2	183.4	144.2	130.8	102.8	93.6	106.4	91.1	101.2	49.5	144.0	121.2
	43.0	41.6	11.9	250.0	162.3	246.9	160.1	281.0	178.6	288.2	178.7	253.9	163.2	323.8	209.5	245.4	158.5	283.1	183.3	144.3	130.8	102.8	93.6	106.4	91.1	101.2	49.5	144.0	121.2
	43.3	41.8	11.9	250.0	162.4	246.9	160.1	280.9	178.5	288.2	178.7	253.5	162.9	323.6	209.5	245.0	158.2	283.0	183.3	144.3	130.8	102.8	93.7	106.4	91.1	101.2	49.5	144.0	121.2
	43.5	42.1	11.9	250.1	162.4	246.9	160.1	280.9	178.5	288.2	178.7	253.1	162.7	323.5	209.4	244.7	158.0	283.0	183.2	144.3	130.8	102.8	93.7	106.4	91.1	101.2	49.5	144.1	121.1
	43.8	42.3	11.9	250.2	162.5	246.9	160.1	280.9	178.4	288.1	178.6	252.7	162.4	323.4	209.3	244.3	157.8	282.9	183.2	144.3	130.9	102.8	93.7	106.4	91.1	101.3	49.5	144.1	121.1
	44.0	42.6	11.9	250.3	162.5	247.0	160.2	280.8	178.4	288.1	178.6	252.3	162.2	323.2	209.2	244.0	157.6	282.8	183.1	144.3	130.9	102.8	93.7	106.4	91.2	101.3	49.5	144.1	121.1
	44.3	42.8	11.9	250.4	162.6	247.0	160.2	280.8	178.3	288.0	178.5	251.9	161.9	323.1	209.1	243.6	157.3	282.8	183.1	144.3	130.9	102.8	93.7	106.4	91.2	101.3	49.5	144.2	121.1
	44.5	43.0	11.9	250.5	162.6	247.0	160.2	280.8	178.3	288.0	178.5	251.5	161.6	323.0	209.0	243.3	157.1	282.7	183.0	144.3	130.9	102.8	93.7	106.4	91.2	101.4	49.5	144.2	121.1
	44.8	43.3	11.9	250.5	162.7	247.0	160.2	280.7	178.2	287.9	178.4	251.1	161.4	322.8	208.9	243.0	156.9	282.6	183.0	144.4	130.9	102.8	93.7	106.4	91.2	101.4	49.5	144.2	121.1
	45.0	43.5	11.9	250.6	162.7	247.1	160.2	280.6	178.1	287.9	178.3	250.7	161.1	322.7	208.9	242.7	156.7	282.6	182.9	144.4	130.9	102.8	93.7	106.4	91.2	101.4	49.5	144.3	121.1
	45.3	43.8	11.9	250.7	162.8	247.1	160.2	280.5	178.1	287.9	178.3	250.3	160.8	322.6	208.8	242.4	156.5	282.5	182.9	144.4	130.9	102.8	93.7	106.4	91.2	101.4	49.5	144.3	121.1
	45.5	44.0	11.9	250.7	162.8	247.1	160.2	280.4	178.0	287.8	178.2	249.9	160.6	322.5	208.7	242.1	156.3	282.5	182.8	144.4	131.0	102.8	93.8	106.4	91.2	101.5	49.5	144.3	121.0
	45.8	44.3	11.9	250.8	162.8	247.1	160.2	280.3	177.9	287.7	178.2	249.5	160.4	322.3	208.6	241.8	156.2	282.4	182.8	144.4	131.0	102.8	93.8	106.4	91.2	101.5	49.5	144.3	121.0
	46.0	44.5	11.9	250.8	162.9	247.1	160.2	280.2	177.8	287.6	178.1	249.2	160.1	322.2	208.5	241.5	156.0	282.3	182.7	144.4	131.0	102.8	93.8	106.4	91.3	101.5	49.5	144.3	121.0
	46.3	44.8	11.9	250.9	162.9	247.1	160.2	280.1	177.7	287.6	178.1	248.8	159.9	322.0	208.4	241.2	155.7	282.2	182.7	144.5	131.0	102.8	93.8	106.5	91.3	101.5	49.5	144.3	121.0
	46.5	45.0	11.9	250.9	162.9	247.1	160.2	279.9	177.6	287.5	178.0	248.5	159.7	321.9	208.3	240.8	155.5	282.2	182.6	144.5	131.0	102.8	93.8	106.5	91.3	101.6	49.5	144.4	121.0
	46.8	45.3	11.9	250.9	162.9	247.1	160.2	279.8	177.5	287.4	178.0	248.1	159.4	321.7	208.2	240.5	155.3	282.1	182.5	144.5	131.1	102.8	93.8	106.5	91.3	101.6	49.5	144.4	121.0
	47.0	45.5	11.9	250.9	162.9	247.1	160.2	279.6	177.4	287.2	177.9	247.8	159.2	321.6	208.1	240.2	155.1	281.9	182.5	144.5	131.1	102.8	93.8	106.5	91.3	101.6	49.5	144.4	121.0
	47.3	45.8	12.0	250.9	162.9	247.0	160.1	279.5	177.3	287.1	177.8	247.4	159.0	321.4	208.0	239.8	154.9	281.8	182.4	144.6	131.1	102.8	93.9	106.5	91.3	101.7	49.5	144.4	121.0
	47.5	46.0	12.0	250.9	162.9	247.0	160.1	279.3	177.2	287.0	177.7	247.0	158.7	321.3	207.9	239.5	154.7	281.7	182.3	144.6	131.1	102.8	93.9	106.5	91.4	101.7	49.5	144.4	121.0
	47.8	46.3	12.0	250.9	162.9	246.9	160.1	279.1	177.1	286.8	177.6	246.7	158.5	321.1	207.8	239.2	154.5	281.6	182.2	144.6	131.1	102.8	93.9	106.5	91.4	101.7	49.6	144.4	121.0
	48.0	46.5	12.0	250.9	162.9	246.8	160.0	279.0	177.0	286.7	177.5	246.3	158.3	320.9	207.7	238.9	154.3	281.4	182.1	144.6	131.2	102.8	93.9	106.5	91.4	101.8	49.6	144.4	121.0
	48.2	46.8	12.0	250.9	162.9	246.8	160.0	278.8	176.9	286.6	177.5	246.0	158.1	320.8	207.6	238.6	154.1	281.3	182.1	144.7	131.2	102.8	93.9	106.5	91.4	101.8	49.6	144.4	121.0
	48.5	47.0	12.0	250.8	162.9	246.7	160.0	278.7	176.8	286.5	177.4	245.7	157.9	320.6	207.5	238.3	154.0	281.2	182.0	144.7	131.2	102.8	94.0	106.5	91.4	101.8	49.6	144.4	121.0
	48.7	47.3	12.0	250.8	162.8	246.7	159.9	278.5	176.7	286.3	177.4	245.3	157.6	320.4	207.4	238.1	153.8	281.1	181.9	144.7	131.2	102.8	94.0	106.6	91.5	101.8	49.6	144.4	121.1
	48.9	47.6	12.0	250.8	162.8	246.6	159.9	278.4	176.6	286.2	177.3	245.1	157.5	320.3	207.3	237.8	153.6	281.0	181.8	144.8	131.2	102.8	94.0	106.6	91.5	101.9	49.6	144.5	121.1
	49.2	47.8	12.0	250.8	162.8	246.6	159.9	278.3	176.5	286.2	177.3	244.8	157.3	320.1	207.2	237.5	153.5	280.9	181.8	144.8	131.2	102.9	94.0	106.6	91.5	101.9	49.6	144.4	121.1
	49.4	48.0	12.0	250.7	162.8	246.5	159.8	278.2	176.4	286.1	177.3	244.5	157.1	320.0	207.1	237.3	153.3	280.8	181.7	144.8	131.3	102.9	94.0	106.6	91.5	101.9	49.6	144.4	121.1
	49.6	48.3	12.0	250.7	162.8	246.5	159.8	278.0	176.4	286.1	177.3	244.3	157.0	319.9	207.0	237.1	153.2	280.7	181.6	144.9	131.3	102.9	94.1	106.6	91.5	102.0	49.6	144.4	121.1
	49.8	48.5	12.0	250.7	162.8	246.4	159.8	277.9	176.3	286.0	177.4	244.0	156.8	319.8	206.9	236.8	153.0	280.6	181.6	144.9	131.3	102.9	94.1	106.6	91.5	102.0	49.6	144.4	121.1
	50.1	48.7	12.1	250.7	162.8	246.4	159.7	277.8	176.2	286.0	177.4	243.8	156.7	319.6	206.8	236.6	152.9	280.5	181.5	144.9	131.3	102.9	94.1	106.6	91.6	102.0	49.6	144.4	121.1
	50.3	49.0	12.1	250.7	162.7	246.4	159.7	277.8	176.2	286.0	177.4	243.6	156.6	319.5	206.8	236.4	152.8	280.4	181.5	144.9	131.3	102.9	94.1	106.7	91.6	102.0	49.6	144.4	121.1
	50.5	49.2	12.1	250.6	162.7	246.3	159.7	277.7	176.1	286.0	177.5	243.4	156.4	319.5	206.7	236.2	152.7	280.3	181.4	145.0	131.3	102.9	94.1	106.7	91.6	102.1	49.6	144.4	121.1
	50.7	49.4	12.1	250.6	162.7	246.3	159.7	277.6	176.1	286.0	177.5	243.2	156.3	319.4	206.7	236.0	152.5	280.2	181.3	145.0	131.3	102.9	94.1	106.7	91.6	102.1	49.6	144.4	121.1
	50.9	49.6	12.1	250.6	162.7	246.3	159.7	277.5	176.0	286.1	177.6	243.0	156.1	319.3	206.6	235.7	152.4	280.1	181.3	145.0	131.3	102.9	94.2	106.7	91.6	102.1	49.6	144.4	121.1
	51.1	49.8	12.1	250.6	162.7	246.2	159.6	277.4	176.0	286.1	177.6	242.8	156.0	319.2	206.5	235.5	152.3	280.1	181.3	145.1	131.3	102.9	94.2	106.7	91.6	102.1	49.6	144.4	121.1
	51.3	50.0	12.1	250.6	162.7	246.2	159.6	277.3	175.9	286.1	177.7	242.6	155.9	319.1	206.5	235.3	152.2	280.0	181.2	145.1	131.4	102.9	94.2	106.7	91.7	102.2	49.6	144.4	121.1
	51.5	50.2	12.1	250.6	162.7	246.2	159.6	277.2	175.9	286.2	177.7	242.5	155.8	319.0	206.4	235.1	152.0	279.9	181.2	145.1	131.4	102.9	94.2	106.7	91.7	102.2	49.6	144.4	121.1
	51.7	50.4	12.1	250.6	162.7	246.2	159.6	277.2	175.9	286.2	177.8	242.3	155.7	319.0	206.4	234.9	151.9	279.8	181.1	145.2	131.4	102.9	94.2	106.7	91.7	102.2	49.6	144.4	121.1
	51.9	50.6	12.1	250.6	162.7	246.1	159.6	277.1	175.8	286.2	177.8	242.2	155.6	318.9	206.3	234.7	151.8	279.8	181.1	145.2	131.4	102.9	94.2	106.7	91.7	102.2	49.7	144.4	121.1
	52.1	50.8	12.1	250.6	162.7	246.1	159.6	277.0	175.8	286.3	177.9	242.1	155.6	318.8	206.3	234.4	151.6	279.7	181.0	145.2	131.4	102.9	94.3	106.7	91.7	102.3	49.7	144.4	121.1
Stage 9B @ 6,710 steps	52.3	51.0	12.1	250.6	162.7	246.1	159.6	277.0	175.8	286.3	177.9	241.9	155.5	318.7	206.2	234.2	151.5	279.7	181.0	145.3	131.4	102.9	94.3	106.7	91.8	102.3	49.7	144.4	121.1

APPENDIX 5A: SMALL STRAIN RESULTS – SMALL STRAIN SIMULATIONS

Figure 5A.1 Orientation of stress tensor in Upper GLU in stages 3 through 9B predicted by the coarse model in small strain.

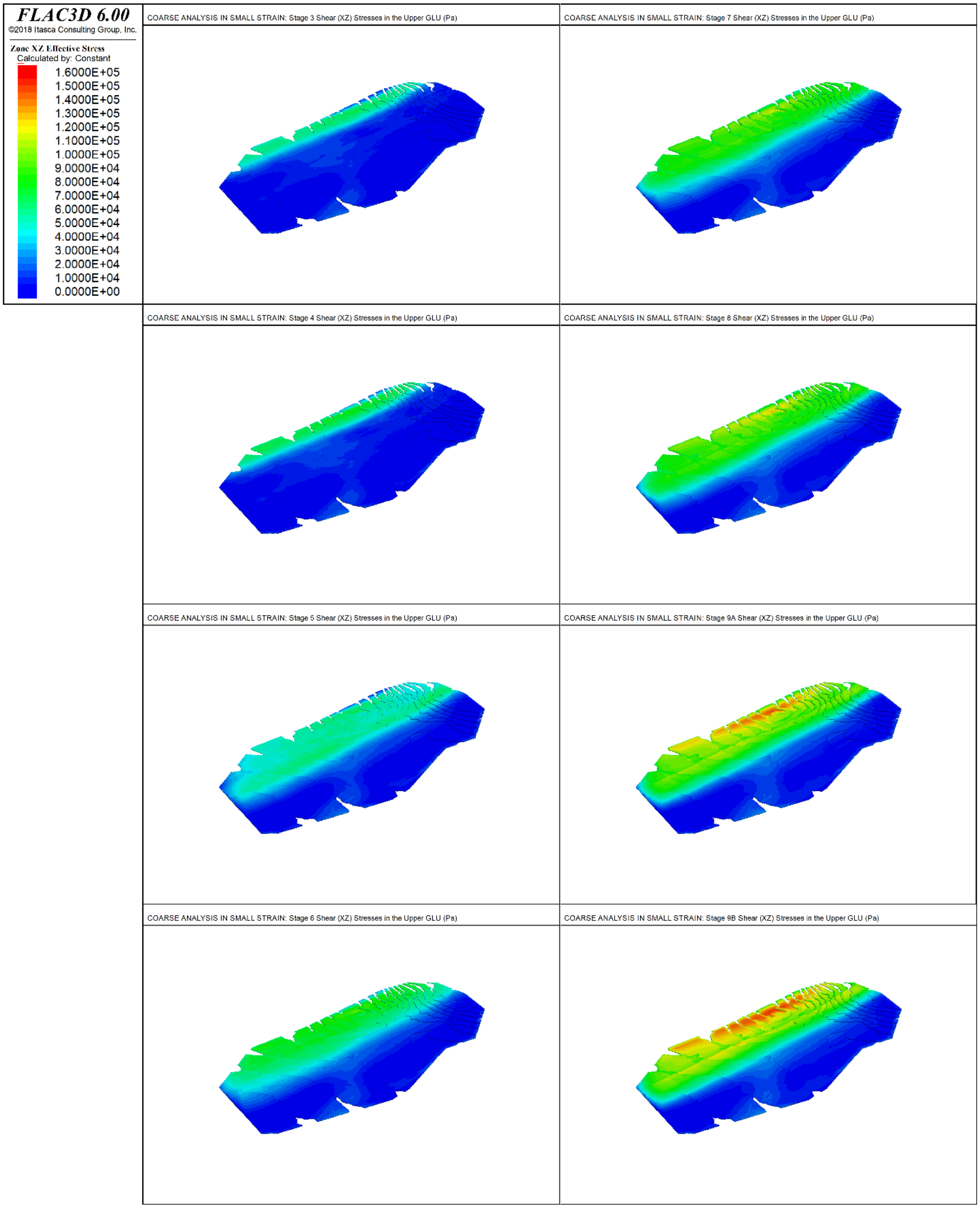

Figure 5A.2 The shear stresses in the horizontal (XZ) plane in the Upper GLU predicted by the coarse model in small strain.

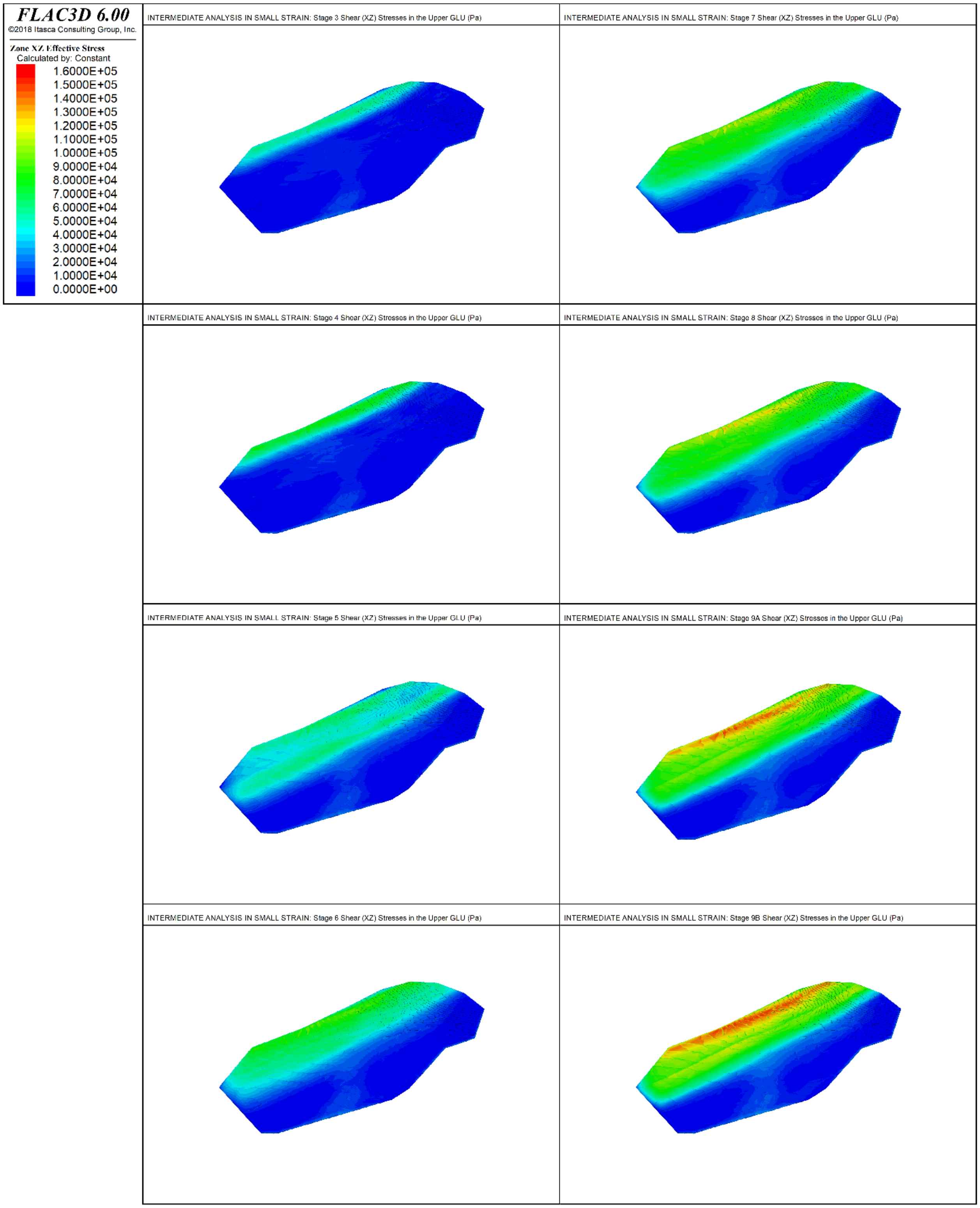

Figure 5A.3 The shear stresses in the horizontal (XZ) plane in the Upper GLU predicted by the intermediate model in small strain.

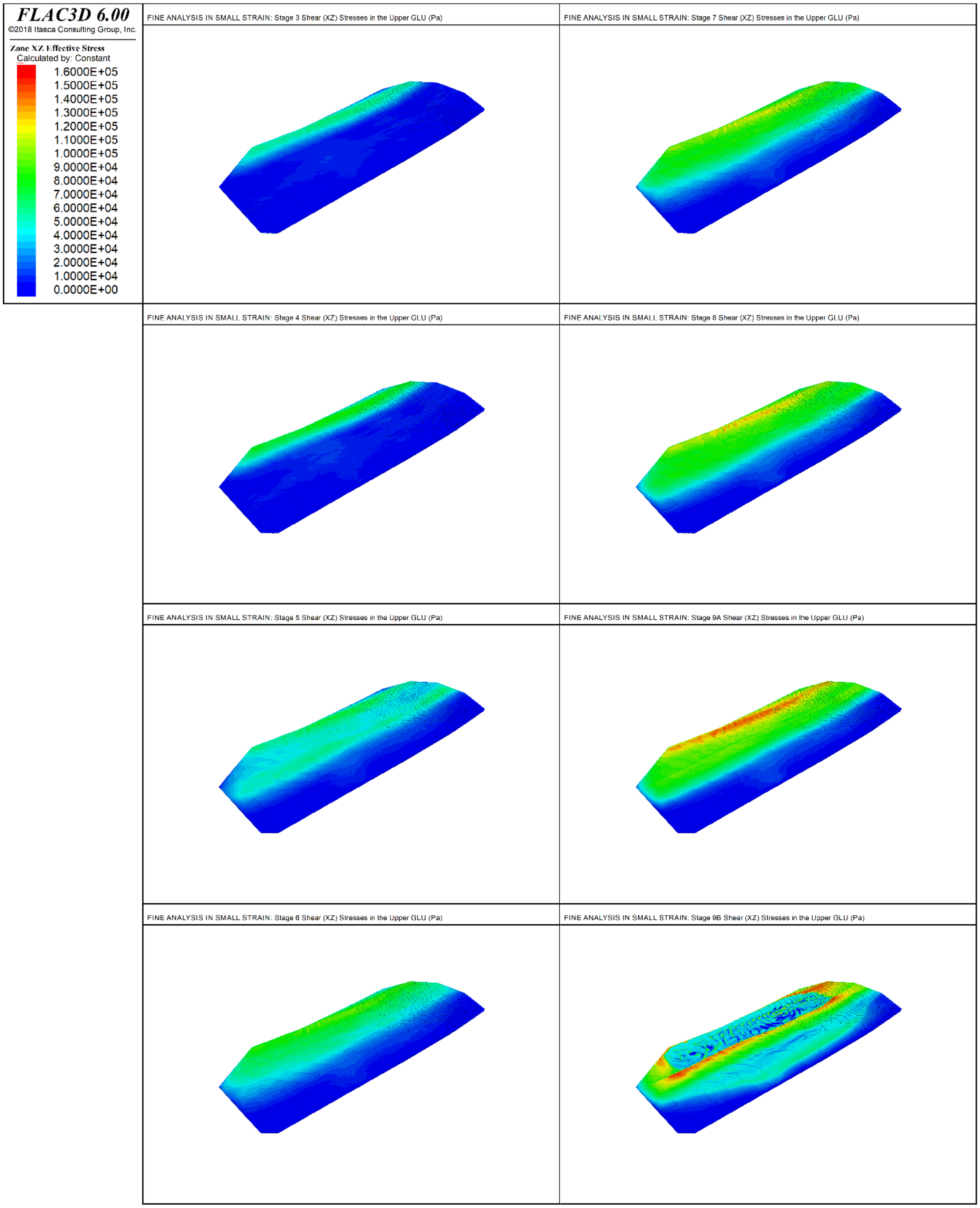

Figure 5A.4 The shear stresses in the horizontal (XZ) plane in the Upper GLU predicted by the fine model in small strain.

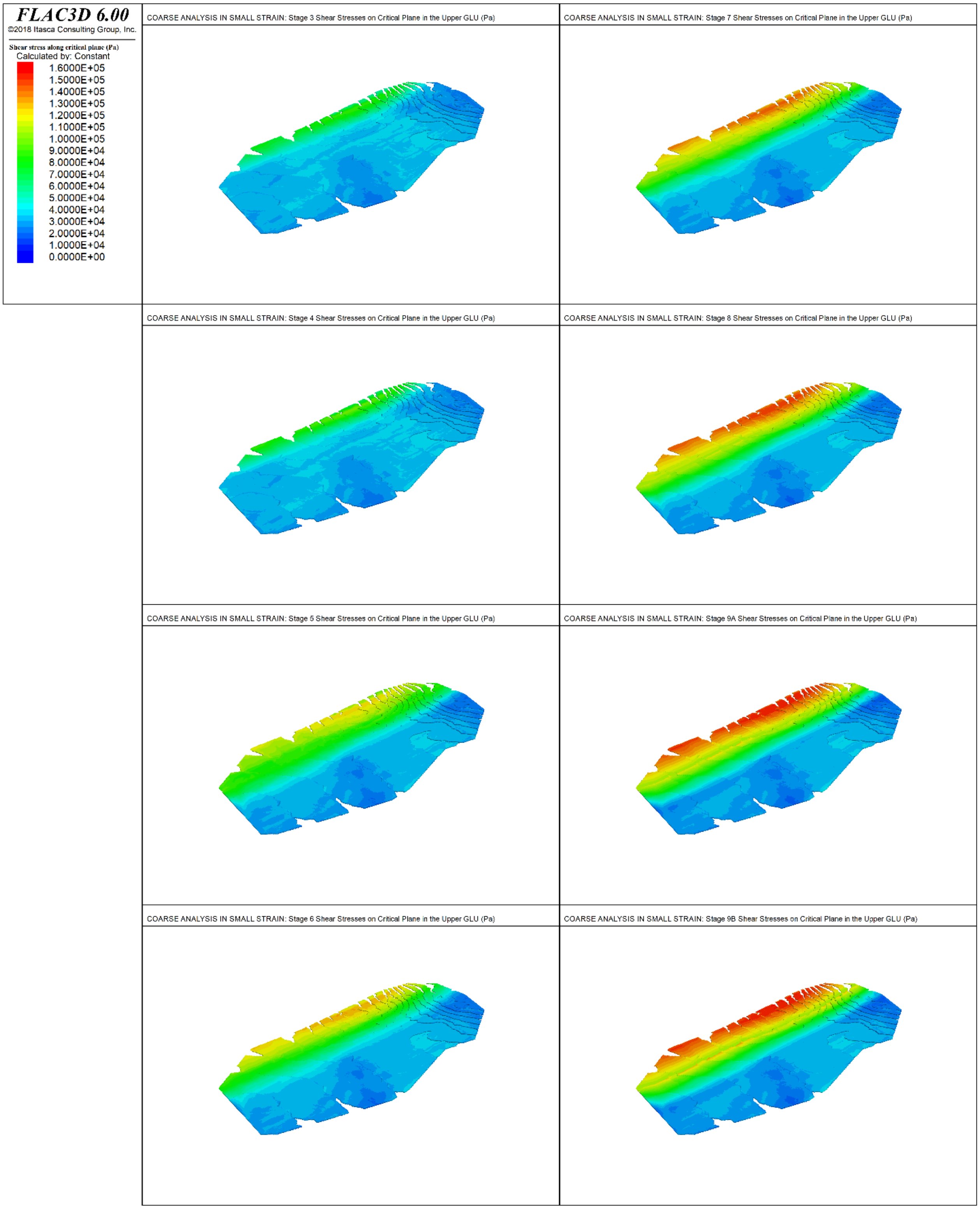

Figure 5A.5 The shear stresses in the critical plane in the Upper GLU predicted by the coarse model in small strain.

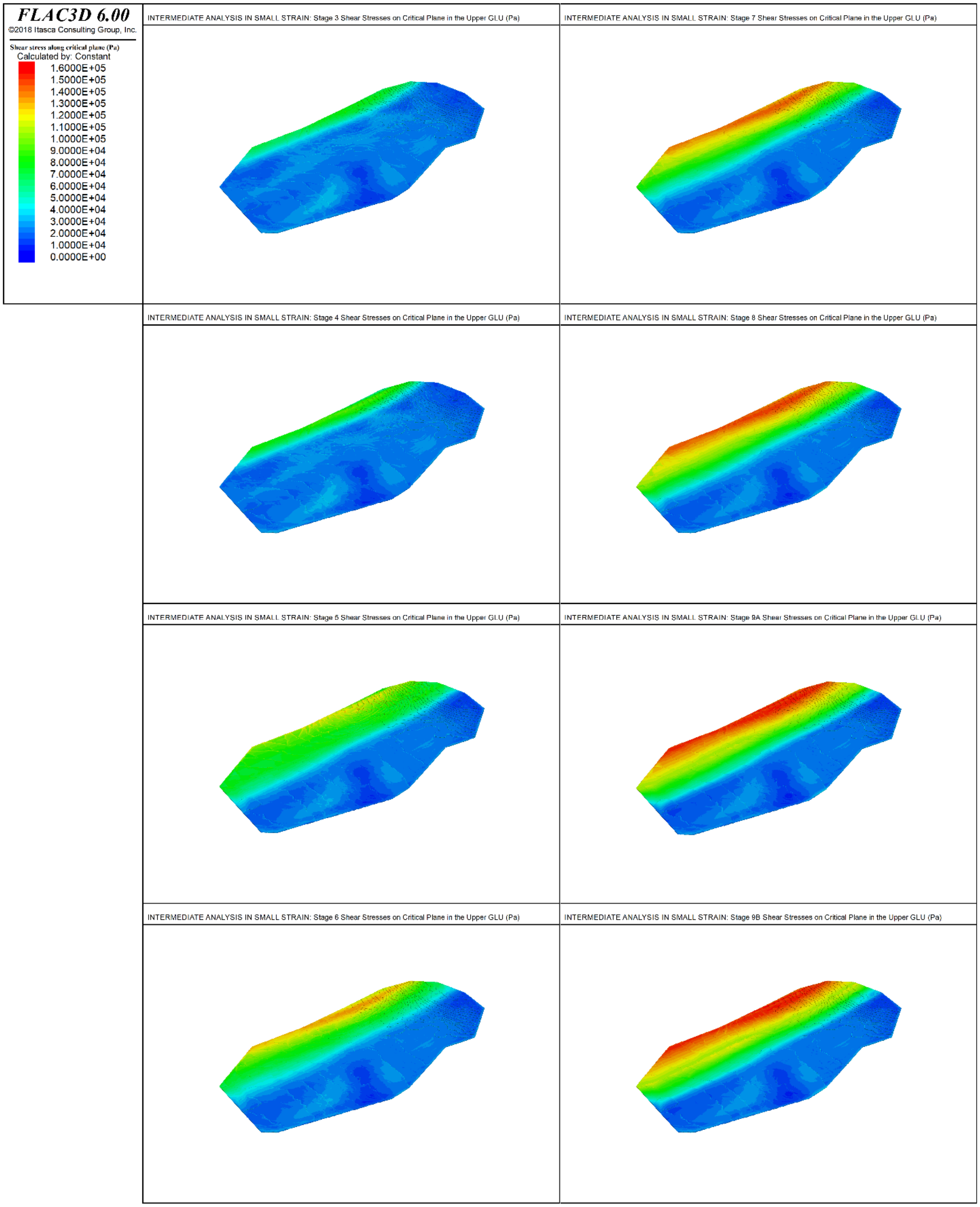

Figure 5A.6 The shear stresses in the critical plane in the Upper GLU predicted by the intermediate model in small strain.

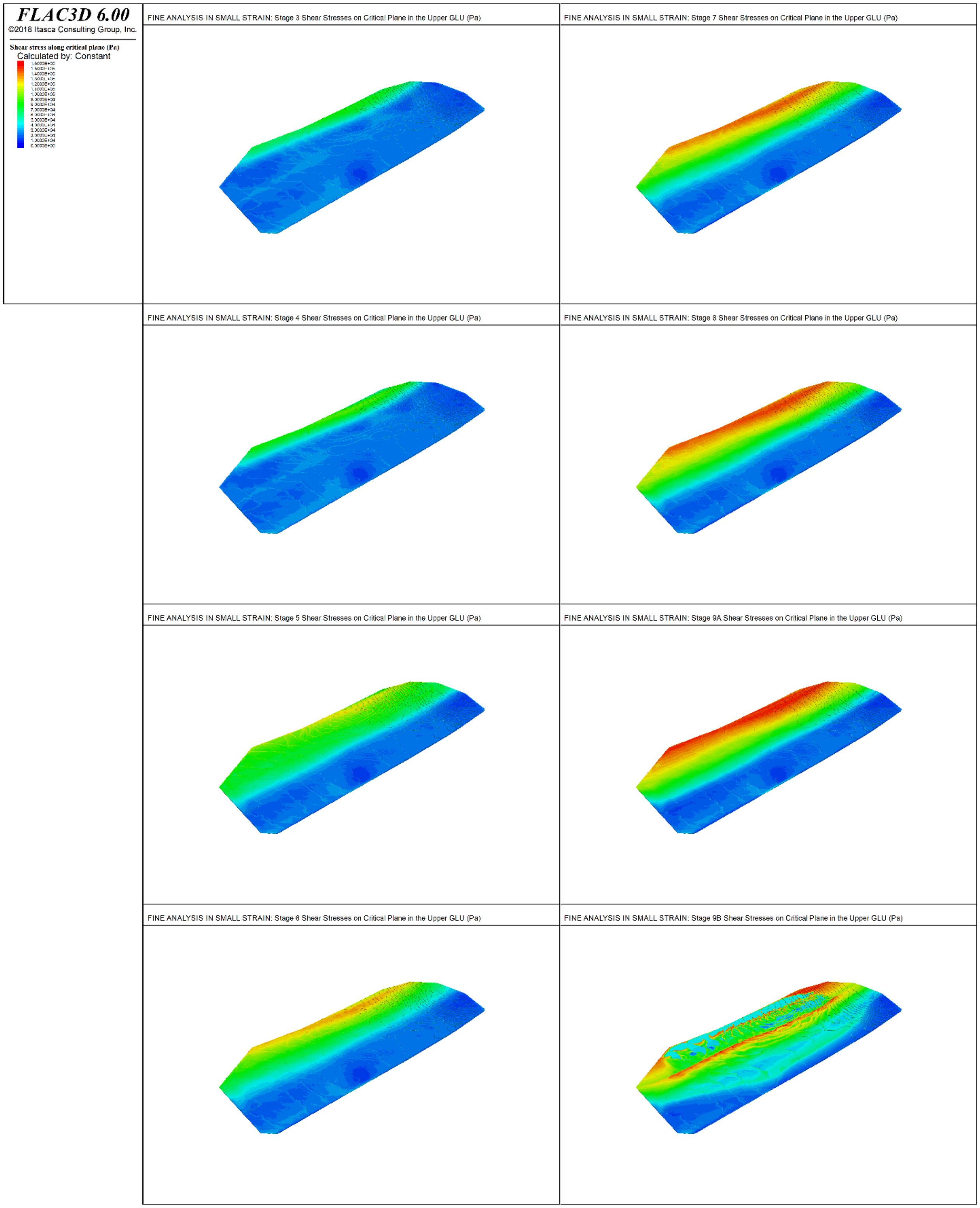

Figure 5A.7 The shear stresses in the critical plane in the Upper GLU predicted by the fine model in small strain.

APPENDIX 5B: SMALL STRAIN RESULTS – CUMULATIVE HORIZONTAL DISPLACEMENTS

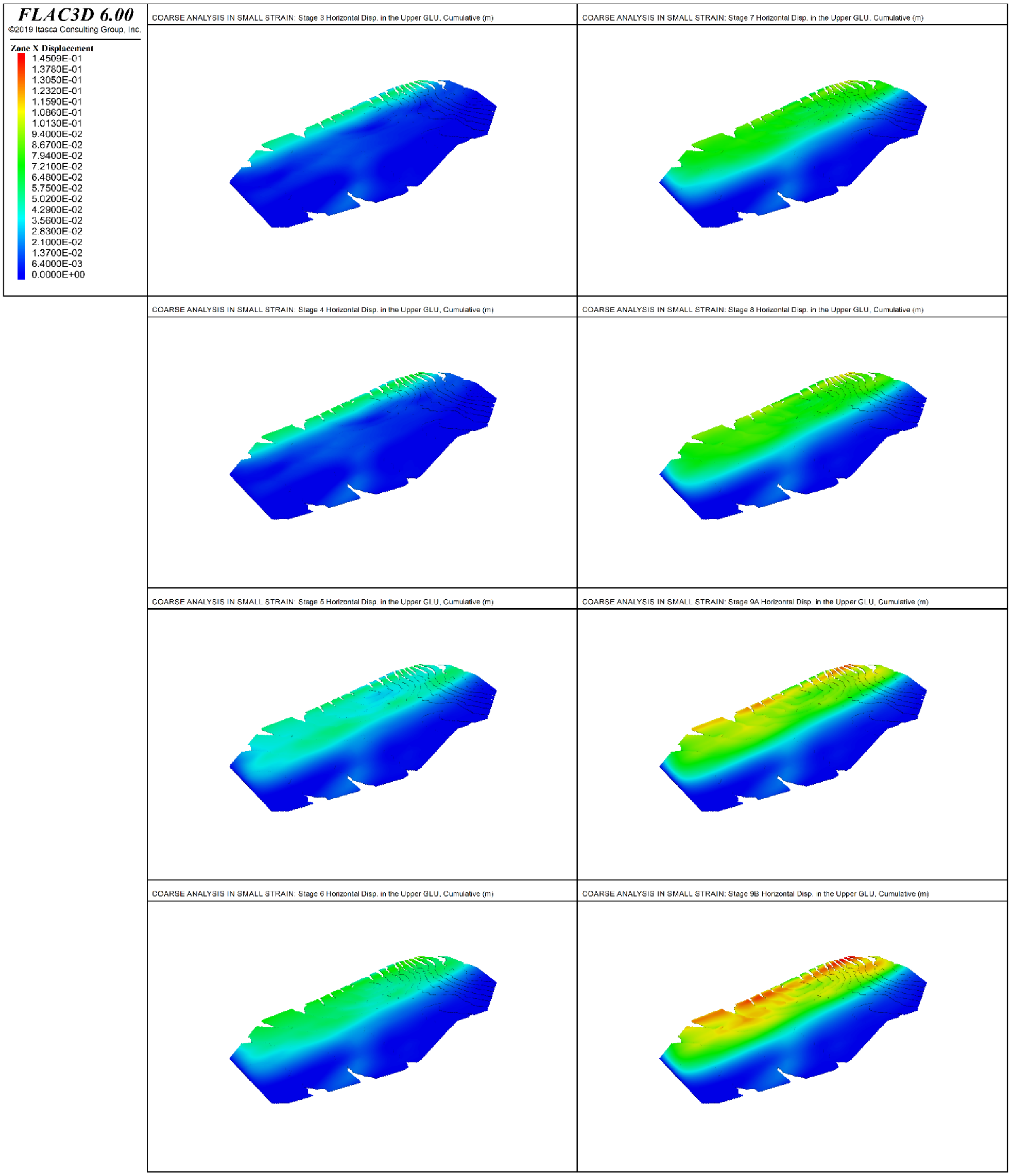

Figure 5B.1 Cumulative horizontal displacements in the Upper GLU predicted by the coarse model in small strain.

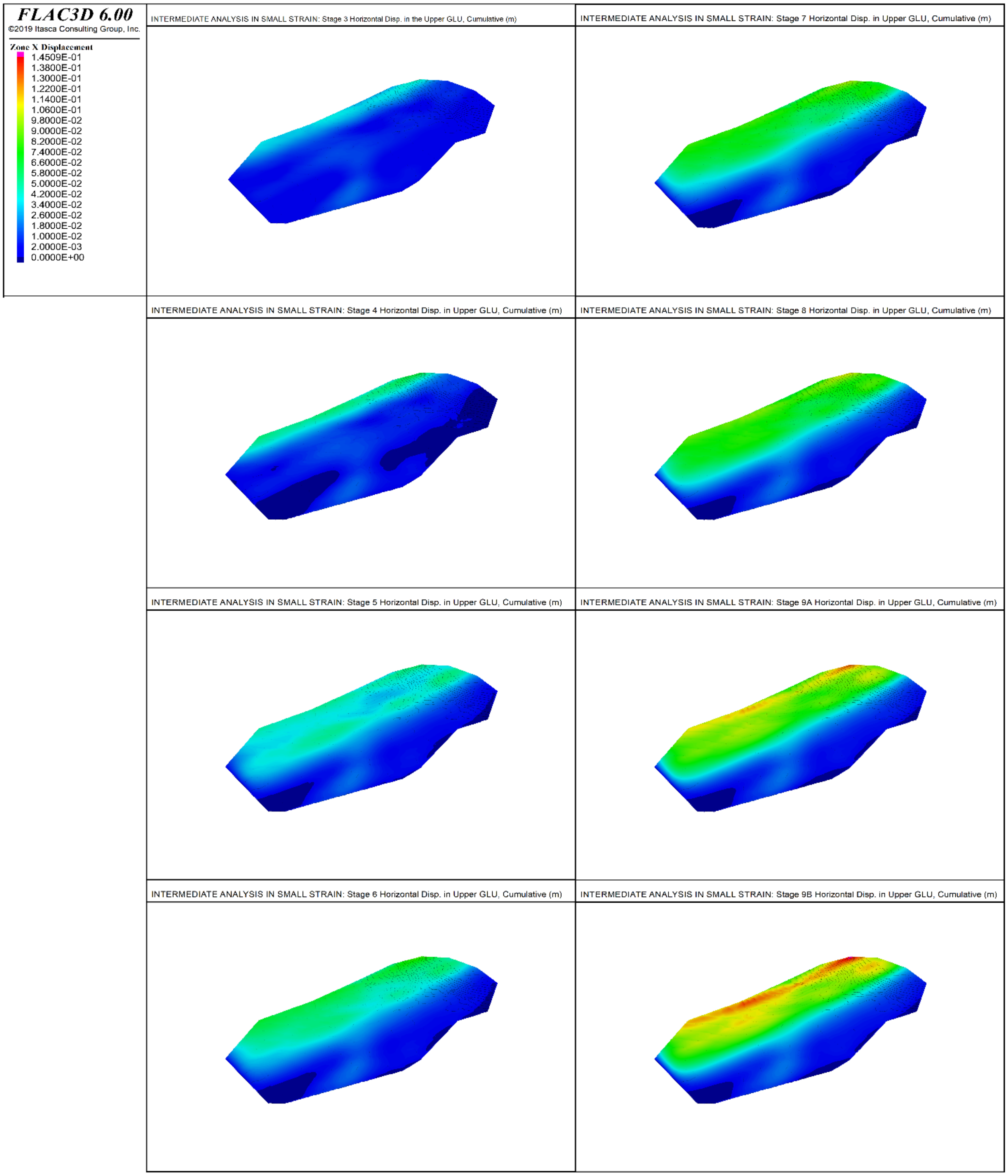

Figure 5B.2 Cumulative horizontal displacements in the Upper GLU predicted by the intermediate model in small strain.

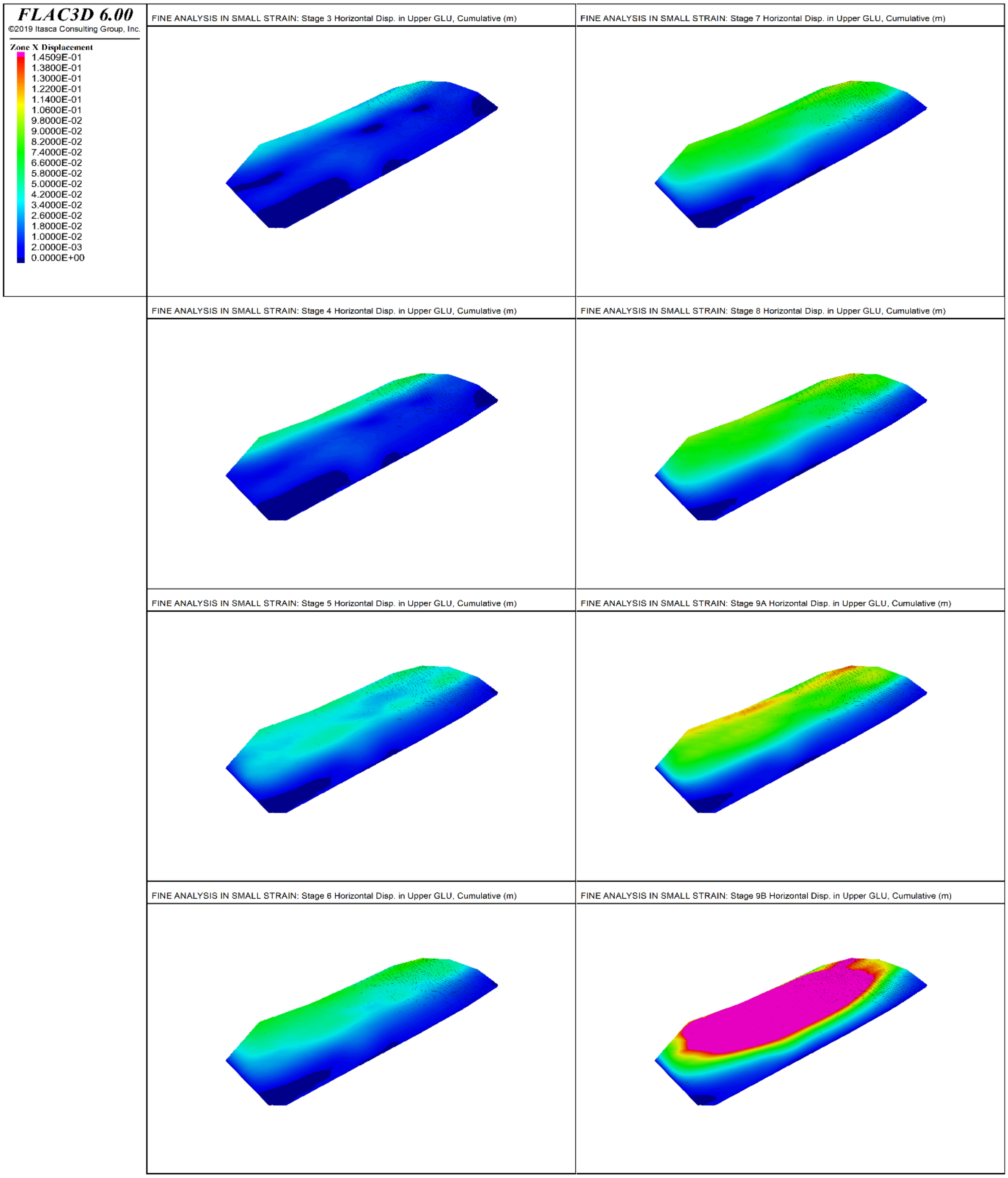

Figure 5B.3 Cumulative horizontal displacements in the Upper GLU predicted by the fine model in small strain.

APPENDIX 6A: REVIEW OF SLOPE ASSESSMENT METHODS

PREAMBLE: The text included in this appendix was originally intended to become the first chapter of this thesis. Ultimately, a decision was made, for the sake of brevity and relevance, to exclude this material from the main body of the manuscript. For reference and completeness, the full text of the original Chapter One is provided in this appendix without modifications.

REVIEW OF SLOPE ASSESSMENT METHODS

1.1. INTRODUCTION TO THE PROBLEM

The modern methods for evaluating slope performance emerged sometime at the start of 20th Century. In that period, numerous and substantial manmade embankments such as rockfill dams were built without an understanding on the part of the engineer of how safe they were (Leps 1970, p.1159). In 1936, at the Second Congress on Large Dams in Washington, D.C., Wolmar Fellenius submitted that slope stability assessments should be made an integral part of embankment construction practices. Fellenius' stated position attests for a then-growing awareness among practitioners of the issues of mechanical stability of manmade as well as natural slopes, and represents a suitable marker for the start of development of modern methods to assess slopes.

Fellenius and other geotechnical practitioners of the time took the view of slope instability problems as types of outright failure, or rupture. This simplified interpretation of failure processes in a slope greatly influenced the approaches for their assessment developed by geotechnical researchers in the next several decades. The slope assessment solution proposed by Fellenius (1936) and others, including Bishop (1955), Janbu (1954, 1956), Morgenstern and Price (1965) Spencer (1967), Fredlund and Krahn (1977) Hovland (1977) Hungr (1987), Lam and Fredlund (1993), focused on limiting conditions such as the ratio of ultimate strengths to working stresses, and sought to find such potential slip surface or surfaces where the said ratio was the lowest. This class of solutions is summarily known as "the limit equilibrium method" (in §1.2).The original method by Fellenius (in §1.2.1.1) made a substantial number of assumptions and simplifications that were necessary, at that state of research, to arrive at a working solution, yet were thought to introduce various errors into the result. Subsequent methods focused on improving on these in order to enhance the accuracy of solution. The main assumptions and simplifications that were eliminated and/or improved on include (a) fully satisfying the equations of equilibria, (b) representing the failure surface more realistically, (c) improving the estimation of internal stresses, and (d) including three-dimensional stability effects. In the end, the inability to determine the correct stress states acting along the slip surface emerged as the main limitation of this class of solutions, one that could not be fully overcome without stepping outside of limit equilibrium analysis.

One must recognize that the treatment of the slope stability problem as that of “rupture” was historically imposed by the state of research and technology. A more nuanced view of slope performance evolved over time, prompting practitioners to search for better solutions. Motivated by the need to overcome the constraints of limit equilibrium analysis, as well as by a more faceted understanding of slope performance issues, geotechnical researchers combined the principles of mechanics of deformable solids with emergent numerical techniques to create what is known today as “deformation analysis” (in §1.3). This type of analysis, ambitiously aiming to simulate the response of matter to loading and more, offers clear advantages over the limit equilibrium approach, although it has its own limitations (such as computational requirements, input data requirements, and more) and is not error-free. It is, however, the best tool we have got at present to assess slopes, and opportunities for its improvement are far from being exhausted.

1.2 LIMIT EQUILIBRIUM METHODS

1.2.1 TWO-DIMENSIONAL METHODS

1.2.1.1 THE ORDINARY METHOD BY FELLENIUS (1936)

Wolmar Fellenius presented the idea of determining dam stability by way of limit equilibrium calculations in the context of a discussion on suitable dam materials at the 1933 Congress on Large Dams in Stockholm, Sweden. His discourse appears to mark the birth of the notion of slope stability, and is a suitable starting point for a discussion on the evolution of methods for its determination. This approach for analyzing slope stability, which came to be known as “the ordinary method" or "the Swedish circle method," was published in English three years later (Fellenius 1936) and is a precursor to all limit equilibrium slope stability methods developed since.

The Ordinary Method seeks to satisfy the moment equilibrium in a slope with a cylindrical surface. Fellenius derives his solution in terms of the slope's maximum height as a function of the soil's strength and unit weight parameters, as well as geometry. Separate equations are developed for two strength models, "pure cohesion" and the "Coulomb equation" (the Mohr-Coulomb model).

Using the "pure cohesion" strength model and assuming a constant cohesion value k, two separate equations for the maximum height of the slope h are derived, one for a slip surface exiting through the toe of the slope (Eq. 1.1), and another for a slip surface exiting downstream of it (Eq. 1.2):

$$h = \frac{4k}{\gamma}\frac{1}{c} \qquad \text{Eq. 1.1}$$

$$h = \frac{k}{0.18\gamma} \qquad \text{Eq. 1.2}$$

where c is a factor of cohesion determined by trial depending on the slope inclination angle, and γ is a unit weight of the soil.

Using the "Coulomb equation," Fellenius proposes a solution where the slide cross-section is sub-divided into slices. The determination of the maximum height of the slope with the given geometry and strength parameters involves a combination of calculations and partial graphic solutions.

Fellenius also introduces the concept of safety factor (termed in his paper "degree of security" and denoted with s) by proposing that the slope height calculations can be carried out with corrected strength coefficients cohesion k/s and friction ϕ/s.

The Ordinary Method by Fellenius (1936) is a first attempt at a limit equilibrium solution for slope stability that greatly simplifies the problem in order to develop a working solution. The method considers the moment equilibrium of the failing mass, but not its force equilibrium. The interslice forces or the variations in undrained strength are ignored in the computations, and the shape of the slip surface in two dimensions is assumed to be circular. In the following three-four decades after the publication of this method, much of the research effort in the field of slope stability was focused on improving this solution by addressing its simplifications.

1.2.1.2 THE BISHOP (1955) METHOD

The Ordinary Method by Fellenius was designed to calculate the maximum allowable height of an embankment given its desired geometry and strength of materials. Bishop recognized that such formulation restricts the solution to a number of rather specific problems, and built on Fellenius' notion of "degree of security" to broaden its scope. In this 1955 paper, Bishop adapted the engineering concept of "safety factor" to the problem of slope stability by defining it as the factor by which the strength parameters must be reduced to bring the slope to a limiting equilibrium. Bishop's definition is still used today in its original form and is described in more detail in §4.3.4 (especially §4.3.4.3).

Recognizing that interslice forces impact stability calculations, Bishop (1955) expanded the method by Fellenius (1936) to account for such. Bishop formulated a theoretical framework for a method that would account for interslice forces acting at an arbitrary angle, but did not develop an applied procedure to carry out safety factor calculations; this method is known as "the complete Bishop method." Bishop offered a simplified method for the special case where the forces acting at the sides of a slice are strictly horizontal, and derived a solution for it:

$$F = \frac{\sum c'l + \tan\phi'(W\cos\alpha - ul)}{\sum W\sin\alpha} \qquad \text{Eq. 1.1}$$

where *F* is the safety factor of the slope, *c'* and ϕ' are the cohesion and friction of the soil, *W* is the weight of the slice, α is the angle of the slice base to the horizontal, *u* is the pore water pressure at the base of the slice and *l* is the length of the slice base. This solution provided for a higher accuracy of safety factor calculations, especially where effective stresses are used to evaluate shear strength, and pore water pressures are notable (Duncan and Wright 2005).

The simplified Bishop method was favourably compared to the Ordinary Method in numerous historic case studies of slope instability, including those of slides at Scrapsgate (Golder and Palmer 1955), Lodalen (Sevaldson 1956), and Drammen (Kjaernsli and Simons, 1962; Bjerrum and Kjaernsli, 1957), as well as in a comparative study of slope stability methods by Fredlund and Krahn (1976). Geotechnical researchers broadly agree that the simplified Bishop method produces safety factors that are considerably more realistic than the Ordinary Method. This suggests that the incorporation of the horizontal component of interslice forces into safety factor calculations eliminates a substantial source of error in the limit equilibrium method.

1.2.1.3 THE JANBU METHOD

Prior to Janbu's method (Janbu et al. 1956; Janbu 1954), all limit equilibrium solutions considered the shape of the slip surface to be circular in two dimensions. The deficiencies in the assumption of a circular slip surface were well recognized at the time. While documented case studies existed where failure occurred along a well-defined circular, or "spoon-shaped," slip surface (such as that at Lodalen investigated by Sevaldson 1956), they were outnumbered by case histories of non-circular slips. Since failure takes place along the weakest slip surface, the existence of non-circular slips provides compelling evidence that the assumption of a circular slip surface does not necessarily result in the prediction of the lowest safety factor, as cautioned by Bishop (1957). At the time of its initial formulation by Fellenius in 1936, the assumption of a circular slip surface was made to simplify computations; as calculation methods evolved over time, its usefulness was surpassed by the need for better predictions.

Janbu improves on previous limit equilibrium solutions by expanding them to include slip lines of arbitrary shapes. Janbu's simplified method assumes the interslice forces to be horizontal, and a function of slip line geometry and strength parameters:

$$P = \left[W - \frac{c'l}{F}\sin\alpha + \frac{ul\tan\phi'}{F}\sin\alpha\right]/m_\alpha \qquad \textit{Eq. 1.4}$$

where P is the normal force acting at the sides of a slice, F is the uncorrected safety factor, α is angle of base to horizontal, c' and ϕ' are soil strength parameters, u is the pore pressure at the base of the slice, l is the length of the slice base, and $m_\alpha>0.2$ is a parameter calculated for each slice as follows:

$$m_\alpha = \cos\alpha + \frac{\sin\alpha\tan\phi'}{F} \qquad \textit{Eq. 1.5}$$

The safety factor is then computed using Eq. 1.6 (adapted from Fredlund and Krahn 1977):

$$FOS = \frac{\sum(c'l\cos\alpha + (P - ul)\tan\phi'\cos\alpha)}{\sum P\sin\alpha + \sum kW \pm A - L\cos\omega} \qquad \textit{Eq. 1.6}$$

Like Bishop's simplified procedure, Janbu's method assumes interslice forces at the base of each slice to be horizontal; as a result, the condition of static force equilibrium along the slip surface is only satisfied in the vertical direction. Janbu (1973) attempted to rectify this shortcoming of the method by introducing a "generalized procedure of slices," also known as "the rigorous Janbu method;" however, the latter also does not fully satisfy the condition of static equilibrium (Duncan and Wright 2005). This suggests that the safety factors produced by this method are in some error. Morgenstern and Price (1965) and Fredlund and Krahn (1977) have determined empirically that the error is in the order of 2…8% when compared to limit equilibrium calculations considering the shear components of interslice forces (i.e. the Morgenstern-Price method).

1.2.1.4 THE MORGENSTERN-PRICE (1965) METHOD

In 1965, Morgenstern and Price published a limit equilibrium solution that aimed to fully satisfy the condition of static equilibrium along a slip surface of arbitrary shape. In considering the shear forces X acting along the side of a slice, a user-defined function f(x) is selected such that:

$$X = \lambda f(x) E \quad \textit{Eq. 1.7}$$

where E is the normal force acting at the side of the slice and λ is a constant evaluated in the iterative calculation of the safety factor. The normal and tangential forces acting in each slice are then input into the force equilibrium equations that are then solved for the safety factor and parameter λ using a numerical method outlined in the original paper, or other approaches such as the "best-fit regression" solution by Fredlund and Krahn (1977).

The effect on the safety factor of the assumption made in this method with regard to the distribution of internal forces has been evaluated by many. Morgenstern and Price (1965) concluded that the safety factor is not very sensitive to this assumption. Fredlund and Krahn (1977, p. 437) found that all safety factors are generally sensitive to the assumptions made with regard to side forces, but that the safety factors calculated using the Morgenstern-Price method are similar to those obtained using the Bishop and Spenser methods. In the same paper, they demonstrate that other limit equilibrium methods – including Bishop's, the Janbu rigorous, and Spenser's – can be seen as a subset of the Morgenstern-Price solution (Fredlund and Krahn 1977, p.435). Consequently, this method can be seen as the generalized limit equilibrium solution in two dimensions that is capable of considering a theoretically unlimited range of distributions of forces internal to the slide.

1.2.1.5 THE SPENCER (1967) METHOD

Spencer (1967) proposed an alternative method to fully satisfy the condition of static equilibrium along the slip surface by assuming that all interslice forces are parallel acting under an inclination

θ that is solved for as one of the unknowns. To satisfy the conditions of moment and force equilibria, Spencer derived two separate equations for these that yield distinct values for the safety factor. These equations are solved for a variety of θ values; a solution is found when the two safety factors converge (Fredlund and Krahn 1977). Although initially formulated for circular slip surfaces, the Spencer method was later expanded to include slip surfaces of arbitrary shapes.

It can be shown that the Spencer method is a special case of the Morgenstern-Price method where the arbitrary function *f(x)* correlating the ratio of shear and normal forces acting at the side of a slice at position x is constant:

$$\lambda f(x) = \lambda C = \frac{X}{E} \qquad \textit{Eq. 1.8}$$

$$\theta = \tan^{-1}\left[\frac{X}{E}\right] = \tan^{-1}(\lambda C) \qquad \textit{Eq. 1.9}$$

Spencer argued that this proposed simplification is immaterial to the results as it was demonstrated by Morgenstern and Price (1965) that the variation in the distribution of θ values is "quite small" (Spencer 1967, p.15).

Spencer's (1967) solution recognizes the effect that forces internal to the slide have on its stability, and attempts to address it by making assumptions about their magnitude and orientation, and incorporating these into safety factor calculations. As it is the case with the Morgenstern-Price method, some error is probably introduced into the solution by its assumption, rather than explicit determination, of internal forces.

At the time of its introduction, Spencer's (1967) method offered a much simpler way to compute safety factors than the more involved solution by Morgenstern and Price (1965) without a significant loss of accuracy. The relative simplicity of its implementation made this method appealing at a time when computational capabilities were limited.

1.2.1.6 PROBABILISTIC ANALYSIS OF SLOPE STABILITY

The high degree of uncertainty associated with the evaluation of soils' material parameters can be a substantial source of error in slope stability calculations. The slope stability evaluation methods discussed thus far do not offer a direct mechanism to account for the natural variability of soils' properties. To evaluate the impact of such error on the safety factor calculations, researchers commonly use sensitivity analysis that aims to determine how the variations (within the tested range) of a parameter's value influence the predicted outcome.

El-Ramli et al. (2002) propose an alternative approach to quantifying the effect of parameter uncertainty on the outcome. The method, named "probabilistic slope stability analysis," accounts for the variability of modelling parameters by expressing these as probability distributions based on observed sample variability. The outcome (i.e. the safety factor of the slope) is then also expressed as a probability function.

In this method, the modelled parameter xi is seen as consisting of two components, the trend of the mean t_i and the error of the mean ε_i:

$$x_i = t_i + \varepsilon_i \qquad \textit{Eq. 1.10}$$

The trend of the mean is determined using regression-to-the-mean techniques and can be a constant or a function (of location, for example). The error of the mean is evaluated as a function of scatter around the trend using statistical techniques. The slope analysis is then performed using the Monte-Carlo technique whereby multiple calculations of the safety factor are conducted where the values of parameters modelled as probability functions are determined individually for each slice in a random fashion using the assigned probability function. The resulting safety factor distribution allows quantifying the risk of failure (expressed as the probability that the safety factor is equal to or below unity) brought about by the variability of modelling parameters.

Albeit this method was coupled with a limit equilibrium analysis in a proof-of-concept study (El-Ramli et al. 2003), there is no reason – other than computational feasibility - why it cannot be combined with other slope stability evaluation methods, such as deformation analysis. The computation feasibility is not a minor issue in the way of implementing this method; in 2002, when it was published, this type of analysis was considered "uneconomic" by many even when used in conjunction with limit equilibrium methods (El-Ramli et al. 2002, p. 670). Today, a similar argument could be made about the application of this approach in deformation analysis, or even in three-dimensional limit equilibrium analysis.

1.2.2 THREE-DIMENSIONAL METHODS

At the inception of slope stability analysis, the reduction of stability problems to two dimensions was done out of necessity to make the solution feasible using available methods and technology. At the time, the reduction of stability problems to two dimensions was seen as acceptable because (a) discrepancies between prediction and field observation were generally ascribed to other characteristics of slope stability models, such as the shape of the slip surface or the assumptions about the inter-slice forces, and (b) the technology of the time did not allow for complex calculations required by three-dimensional models.

In time, a number of studies demonstrated that the differences in the safety factor values calculated by the various two-dimensional limit equilibrium methods are relatively minor (Duncan 1996; Fredlund and Krahn 1977). Additionally, a number of case studies became known where prediction by any of the existing two-dimensional limit equilibrium methods did not produce a reasonable fit, and three-dimensional effects were suspected (Quinn et al. 2014; Seed et al. 1990). Lastly, with the dramatic progress of computational technology in the second half of the 20th Century, three-dimensional slope stability analysis became "an idea whose time has come."

1.2.2.1 THE METHOD OF COLUMNS BY HOVLAND (1977)

The general approach taken to expand limit equilibrium methods to three dimensions involves the subdivision of the slide volume into vertical columns in a manner similar to the division of a two-dimensional cross-section of a slide into slices. The proposed solutions concentrate on, and are largely distinguished by, the assumptions regarding and derivation of inter-slice and inter-column forces.

Hovland (1977) proposes a three-dimensional stability analysis using the method of columns that is an expansion of the ordinary method of slices in that it ignores all forces acting on the sides of the elements. As it is the case with the Ordinary Method of Slices, Hovland's solution relies on the weight of the column alone to determine the normal force acting along the area of its base.

Hovland's solution is a first attempt at accounting for three-dimensional effects on slope stability and thus an effort to eliminate the error associated with the reduction of stability problems to two dimensions. However, in its derivation, he sacrifices any considerations of internal forces other than weight, with unclear effects on the outcome.

1.2.2.2 A THREE-DIMENSIONAL LIMIT EQUILIBRIUM METHOD BY CHEN AND CHAMEAU (1983)

Recognizing the effect of stresses internal to the slide on the safety factor, Chen and Chameau (1983) introduced a method for calculating a three-dimensional safety factor of a slope that included inter-slice and inter-column forces acting, respectively, along the direction of sliding on the column sides perpendicular to it, and normal to the direction of sliding on the column sides parallel to it. Adapting Spencer's (1967) approach in two dimensions, the method by Chen and Chameau (1983) makes the assumption that all inter-slice forces in the sliding mass are inclined at a constant angle θ. On the other hand, the inter-column shear forces are neglected entirely, with the inter-column forces assumed to be perpendicular to the surface of the column.

The authors tested their method in a series of parametric studies where a uniform soil profile with a Mohr-Coulomb strength model was assigned various strength parameters and slope angles; the ratios of the three- to two-dimensional factors of safety were plotted against the slides' length-to-height ratio. The authors found that for the most part, the ratios of the three- to two-dimensional factors of safety were found to be greater than unity (i.e. the three-dimensional factors of safety were greater than their two-dimensional equivalents). From the results of their parametric studies, the authors determined that for cohesionless soils in specific slide configurations, the three-dimensional safety factors can be lower than their two-dimensional equivalents.

1.2.2.3 AN EXTENSION OF BISHOP'S METHOD TO THREE DIMENSIONS BY HUNGR (1987)

To introduce three-dimensional stability effects and to account for forces internal to the sliding mass, Hungr (1987) proposed to extend the Bishop method to three dimensions. He based his solution on the following two assumptions:

(a) Vertical shear forces acting on longitudinal and lateral faces of the columns can be neglected in the equilibrium equations; and

(b) The vertical force equilibrium equation of each column and the summary moment equilibrium equation of the entire collection of columns are sufficient conditions to determine all unknown forces. Implicit in this assumption is that horizontal forces acting on lateral and longitudinal faces of the columns are ignored, as it is with the simplified Bishop method in two dimensions.

The original paper by Hungr (1987) reports, based on a parametric study, that his method produces higher safety factor values than earlier variants of three-dimensional limit equilibrium methods, and replicates safety factor values yielded by analytical solutions for wedge problems. In a follow-up study by Hungr et al. (1989), the method is verified against other three-dimensional limit equilibrium solutions and is found to be in good agreement with those in the case of rotational and translational slides, but tends to be conservative for non-rotational and asymmetric surfaces. The author also questions the validity of the conclusion by Chen and Chameau (1983) that the three-dimensional safety factors can be lower than their two-dimensional equivalents in the special case of cohesionless slopes and specific slide shapes by introducing his own analysis of the same and demonstrating that the ratios of three- to two-dimensional safety factors approach unity from the upper side as the slide aspect ratio approaches infinity. The comparison of analyses by Chen and Chameau (1983) and by Hungr (1987) is visualized in Figure 1.1 showing the results of the parametric studies by both authors. In the figure, the results published by Chen and Chameau (1983) where the three- to two-dimensional safety factor ratios are seen to drop below unity even at aspect ratios below one, are contrasted with Hungr's own results where this ratios never drop below unity although they are seen to reach this value in slides with higher aspect ratios. This finding by Hungr (1987) was largely confirmed by subsequent research by Gens et al. (1988), Arellano and Stark (2000) and others.

1.2.2.3 THREE-DIMENSIONAL ANALYSIS OF SLIDES IN COHESIVE SOILS BY GENS ET AL. (1988)

Gens et al. (1988) derived an analytical solution for the limit equilibrium safety factor along three-dimensional slip surfaces in rotational, cylindrically shaped slides with planar ends in soil profiles with uniform undrained strength c_u. The authors reasoned that a three-dimensional limit equilibrium safety factor F_3 is different from a two-dimensional one F_2 because of the added shearing resistance at the slide ends that is not considered in the latter:

$$F_3 = F_2\left(1 + \frac{2M_E}{lRL}\right) \quad \textit{Eq. 1.11}$$

where M_E is the first moment of area of each end plane about the slide's point of rotation, l is the length of the slip line passing through the cylindrical portion of slide, R is the slide radius and L is the length of the slide in the direction normal to its movement. The derivation of the three-dimensional safety factor for such slide was built on the Ordinary Method used to estimate F_2; the solution for the expression $\frac{2M_E}{lRL}$ is analytically derived in the paper in its general form. In evaluating it, Gens et al. (1988) considers three slide types: slope failure, toe failure and base failure. The solutions for the three-dimensional safety factor for these three cases are straight-forward but somewhat cumbersome and will not be replicated here.

In addition, Gens et al. (1988) evaluated three-dimensional limit equilibrium safety factors for cylindrical slides with curved ends, also passing through slopes with uniform strength c_u. As before, the solution is built from the Ordinary Method, and its derivation centers around calculating the contribution to the safety factor along the curved ends of the slide relative to its two-dimensional value. The authors do not provide an explicit mathematical expression for calculating these. Instead, their solution is presented in the form of charts plotting, among other things, the ratio of three- to two-dimensional safety factors F_3/F_2 against the aspect ratio of the slide L/H, where H is the height of the slope. Multiple charts are introduced for various curved shapes of the slide ends.

The method by Gens et al. (1988) is limited in its application to practical problems in that (a) it only considers slides in slopes with constant strength values throughout, and (b) it restricts the slide type to rotational along a very specific slip surface, thus excluding slides with arbitrary slip surfaces such as wedge slips, shallow slips and more. However, the value of this research paper is with the conclusions that it readily invites with regard to three-dimensional slope stability effects.

The formulation of the solution for the three-dimensional safety factor by Gens et al. (1988) offers a couple advantages over the other three-dimensional limit equilibrium solutions reviewed so far. First, it offers an analytical proof that three-dimensional safety factors are greater than their two-dimensional equivalents, with the two converging for infinitely wide slides. Second, it offers a convenient means to evaluating the difference between the two as a function of the slide aspect ratio and end shape. Gens et al. (1988) concluded that as a direct consequence of the first finding and upon reviewing a number of historic case studies of slides, two-dimensional back-analyses of slides are in error, overestimating soil strengths at failure by as much as 30%.

1.2.2.5 A GENERAL LIMIT EQUILIBRIUM MODEL FOR THREE-DIMENSIONAL SLOPE STABILITY ANALYSIS BY LAM AND FREDLUND, 1993

Lam and Fredlund (1993) introduced a generalized method calculating the three-dimensional limit equilibrium safety factors. The authors expanded the "best-fit regression" solution to the Morgenstern-Price method by Krahn and Fredlund (1977), adapting it to three dimensions. This method makes use of the Bishop's (1955) definition of the safety factor, but assumes an arbitrarily shaped slip surface with all soil movement taking place along a single plane. As it is the case with all other three-dimensional limit equilibrium methods, this solution involves subdividing the slide domain into columns, and the forces acting at their base are either calculated or assumed. With the internal distribution of stresses being undetermined in this solution, a total five of assumptions are made regarding the magnitude of shear forces acting at all sides of each column that are similar to that made by Morgenstern and Price (1965) in Eq. 1.7. For example, the following assumptions are made regarding the vertical and horizontal components of the inter-slice shear force:

$$X = \lambda_1 f_1(x) E \qquad \textit{Eq. 1.12}$$

$$H = \lambda_2 f_2(x) E \qquad \textit{Eq. 1.13}$$

where $\lambda_{1,2}$ are scaling factors determined as part of the safety factor calculations; $f_{1,2}(x)$ are functions that describe the variation of force ratios along the x-axis, and E is the normal inter-slice force. Two other relationships analogous to the ones above are formulated with regard to the vertical and horizontal components of the inter-column shear force as a function of the column's position along the y-axis. Finally, a fifth assumption is made regarding the component of the shear force acting at the column base in the direction normal to slipping:

$$T = \lambda_5 f_5(z) N \qquad \textit{Eq. 1.14}$$

where λ_5 is a scaling factor determined as part of the safety factor calculations; $f_5(z)$ is a function describing the variation of force ratio *T/N* along the x-axis, and *N* is the normal force acting on the base.

With multiple unknowns introduced into the equilibrium equations by the five assumptions described above, the problem of calculating the safety factor becomes indeterminate. In order to render it determinate, assumptions must be made with respect to at least some of the unknowns. Lam and Fredlund (1993) argue on the basis of studies by Fan et al. (1986) that a number of simplifying assumptions can be made with regard to the distribution of shear forces. For example, for simple and uniform geometries, all λi can be assumed to be zero – this would have the effect of reducing the solution to Bishop's method in three dimensions (in §1.2.2.3). For non-uniform geometries, only the vertical components of the inter-slice and inter-column forces were shown to have "values of significant magnitude," with all of other shear components reduced to zero.

Lam and Fredlund (1993) validated their method by comparing the outcomes against other solutions by Gens et al. (1988), Hungr et al. (1989, 1987) and others. The authors found that while the solution is not particularly sensitive to the form of inter-slice and inter-column functions f_i, they determined that either the half-sine function or a function obtained directly from stress analysis produce the most reasonable results.

1.3 DEFORMATION ANALYSIS

In geotechnical engineering, deformation analysis was developed as an alternative to traditional limit equilibrium methods to assess slope stability. The theoretical framework of deformation analysis is built on the principles of continuum mechanics, and its implementation was carried out using numerical methods. The technological progress around the turn of this century rendered this computationally demanding approach feasible and fuelled research efforts aimed at its implementation and verification in two dimensions, and, recently, in three.

Terminology

In geotechnical literature, the terms “numerical analysis” and “deformation analysis” appear to be used interchangeably. Strictly speaking, they are not the same. The first term refers to the technique of determining the behaviour of a complex system by subdividing it into simple components and evaluating them separately prior to assembling them back to model the overall response of the model (as discussed in §1.3.2); this approach is broadly used in the disciplines of engineering and mathematics and is applied to a vast range of problems. Deformation analysis, on the other hand, is a term that emerges from the field of mechanics of deformable solids where the stress distribution fields are considered to be a resultant of the state of current (and past) deformations. In geotechnical engineering, the principles of deformation analysis on one hand, and numerical analysis on the other, are inseparable from one another at this state of research and practice. Currently, every deformation analysis of a geotechnical problem involves numerical analysis (using the generalized finite element method, see §1.3.2), explaining the interchangeable use of these terms.

In this thesis, the term “deformation analysis” is used preferentially to emphasize the importance of deformation-stress responses in the problem under consideration.

1.3.1 ELEMENTS OF CONTINUUM MECHANICS

Continuum mechanics is a field of study that attempts to model the behaviour of matter by assuming that it can be described with continuous mathematical functions. Although continuum mechanics obviously errs in assuming that the world is continuous when abundant physical evidence of its discrete nature exists (including the particulate nature of matter but also, more relevantly, the granular structure of soils), this error is thought to be inconsequential because the scale of problems is usually larger than that of discrete elements by multiple orders of magnitude.

The principles of continuum mechanics have been successfully applied to soils and other solids in a branch of this discipline referred to as "the mechanics of deformable solids" that in turn was adapted by geotechnical engineers to evaluate the mechanical behaviour of structures such as slopes and embankments.

The principles of mechanics of deformable solids require that three basic conditions be met for a solution to be valid: (i) the stress equilibrium equations, (i) the stress-strain relations and (iii) the compatibility of strain and displacement (Chen 2007). However, adequately describing a domain with continuous mathematical functions to satisfy these conditions cannot be easily done and has not been accomplished but for a few simplest cases.

Instead, mathematicians and engineers have taken the approach of subdividing the continuous domain into simpler components whose behaviour can be easier described with mathematical relationships. This approach to obtaining a solution for the mechanical response of continuous matter (including but not limited to deformable solids) is commonly known as "numerical analysis."

1.3.2 NUMERICAL ANALYSIS

Numerical methods have been developed by mathematicians and engineers motivated by the need to find solutions to problems that cannot be adequately described by continuous mathematical models. The evolution of numerical methods applied to such problems can be traced at least to the end of 19th Century when a number of simplified formulations were independently published by researchers. Zienkiewicz and Taylor (2000, p. 3) classify these early solutions as falling into one of the three categories, "variational methods," "weighted residuals," and "finite differences." In time, these solutions crystallized into its modern formulation known as "the generalized finite element method." This method encompasses a variety of numerical techniques, the most common ones being “the finite element method,” “the finite difference method,” and “the finite volume method.”

1.3.2.1 REVIEW OF THE FINITE DIFFERENCE, FINITE ELEMENT AND FINITE VOLUME METHODS

The finite element method is expansively described by Zienkiewicz and Taylor (2000) and Zienkiewicz et al. (2013). In their books on the subject, the authors do not draw a hard line between the various numerical models (including the three listed). Instead, they treat all of these solutions as belonging to the “generalized finite element method” (Zienkiewicz and Taylor 2000, p. 82), differentiated only through their approach for approximating the continuous functions describing the “true” behaviour of interest within the modelled domain. Zienkiewicz and Taylor (2000, p. 2) appear to take the all-encompassing view of the finite element method that it is a procedure of solving continuum problems by discretizing them into simple components whose behaviours can be easily described using simple relationships. To find a solution, the behaviour of components is evaluated individually prior to assessing the aggregate response of the system.

However, a hard distinction appears to be drawn between these methods by modellers and developers of finite element, finite volume and finite difference engines. Wang (2017) explains the distinction as follows.

In the finite difference method, the modelled domain is subdivided into an ordered grid of nodes. The behaviour of interest, described by some continuous function within the domain, is then calculated at each of the nodes as exact values. In this method, the true shape of the function describing the investigated behaviour between the nodes is not known. Such approximation of the true function by its discrete values at arbitrarily selected nodes is a source of error in this numerical solution, especially where strongly non-linear behaviour is present and the density of the grid nodes is insufficient to capture this complexity (Wang 2017). Zienkiewicz and Taylor (2000, pp. 82-83) distinguishes this method by its approximation of "true behaviour" by discontinuous local shape functions, with the derivation of the approximation algorithm using the Taylor expansion; the authors note that the method is occasionally inaccurate and that the ease of its implementation and computational efficiency are the main reasons for using it.

In the final element method, the domain is discretized into elemental zones, and the continuous behaviour of interest is approximated within these by simple functions, most commonly by piecewise linear functions. This evidently introduces an error into the solution, albeit arguably its magnitude is lower than that in the finite difference method (Wang 2017).

Finally, in the finite volume approach, the modelled domain is discretized into zones (volumes), and the investigated behaviour is then approximated by the mean value of its function across individual zones. In this numerical scheme, this averaging of behaviour is a source of error as it tends to mask peaks (Wang 2017). Zienkiewicz and Taylor (2000, p.453) describes this method as an expansion of the point collocation method where subdomains are defined and their integrals are approximated as a constant.

In this thesis, the numerical modelling techniques will not be differentiated (unless specific differences are essential to the discussion) but will be, in accordance with the view taken by Zinekiewicz and Taylor (2000), referred to summarily as "the generalized finite element method," or, for simplicity, "the finite element method."

1.3.3 SLOPE STABILITY ANALYSIS BY FINITE ELEMENTS

In geotechnical engineering, the principles of mechanics of deformable solids (in §1.3.1) were combined with numerical analysis techniques (in §1.3.2) to develop a method for solving slope stability problems that, unlike the limit equilibrium solutions, made no assumptions regarding the forces and stresses internal to the slide but instead relied on stress-strain relationships and the compatibility of strains and deformations to determine them explicitly.

According to Duncan (1996), Clough and Woodward (1967) were the first geotechnical researchers to propose evaluating slope stability by means of finite element analysis, showcasing in the case study of a staged construction of an embankment dam the use of non-linear stress-strain relationships. Other researchers soon followed in their footsteps, exploring linear and non-linear elastic stress-strain relationships (Duncan and Dunlop 1969; Penman et al. 1971; Eisenstein and Simmons 1975); the hyperbolic model (Kulhawy and Duncan 1972; Quigley et al. 1976; Li and Desai 1983); the elasto-plastic and visco-elasto-plastic models (Tanaka and Nakano 1976; Chang and Duncan 1977; Seco e Pinto and Marahna Das Neves 1985); strain-softening behaviour (Troncone et al. 2016) and more. These studies demonstrated a number of advantages of deformation analysis over the limit equilibrium methods, some of which are listed below.

- In deformation analysis, stress states are calculated as a function of stress-strain relationships and with consideration for the compatibility of strains and deformations, rather than inferred based on various assumptions.
- Deformation analysis enables the modelling of stress path, and its results are stress-path dependent.
- Deformation analysis offers a means to assess the performance of structures with non-uniform stress-strain behaviours, including spatially variable stress-strain behaviours; as well as stress-dependent and stress-path dependent stress-strain behaviours.
- Deformation analysis offers a means for employing advanced constitutive models that allow modelling the strength of material as a function of stress path and/or deformations.
- The extent of deformations and excess pore pressures in response to loading are two additional aspects evaluated in deformation analysis in addition to the mechanical stability of the structure.

The advancements of deformation analysis can be categorized as follows:

- Formulation, testing and validation of stress-strain models. According to Duncan (1996), three basic stress-strain models are distinguished, linear and non-linear (or multilinear) elastic, hyperbolic, and elascoplastic; these are briefly described §1.3.3.1.
- Formulation, testing and validation of advanced soil strength models. With the expanded abilities of deformation analysis, soil strength models could now include complex considerations such a stress path, shear or volumetric strain, and plasticity. Some of the advanced constitutive models are briefly reviewed in §1.3.3.2.
- Three-dimensional analysis.
- Improvement of numerical methods.

Along with the many advantages of deformation analysis over limit equilibrium methods, there are a couple of shortcomings:

- Deformation analysis does not calculate safety factors, but merely predicts whether a structure is mechanically stable or not. To overcome this difficulty, a method for the calculation of safety factors by shear strength reduction was developed for this type of analysis (in §1.3.3.3 and §4.3.4.2). Additionally, hybrid methods for calculating safety factors in deformation analyses were proposed by Kulhawy (1969) and Stianson (2008) (in §1.4).
- The outcome of a deformation analysis (i.e. whether the structure is mechanically stable or not) is not immediately evident and must be assessed based on the model behaviour.
- In deformation analysis, the slip surface is not a modelling input. If the structure is mechanically unstable, a slip surface may develop naturally. This makes the evaluation of predicted slip surface rather challenging, especially in three dimensions.
- Finally, deformation analysis has its own sources of error. Some of them are associated with adapted numerical schemes were briefly discussed in §1.3.21. Additionally, as it is the case with limit equilibrium analysis (as discussed extensively in Chapter Two), the reduction of a deformation model to two dimensions is a significant source of error.

1.3.3.1 STRESS-STRAIN RELATIONSHIPS

Linear and non-linear elastic models

The linear elastic model is a stress-strain relationship developed with the assumption that the current state of stress at a point is proportional to its current strain. The constitutive model for infinitesimal deformation in a linear elastic soil is captured in the equation below:

$$\sigma_{ij} = C_{ijkl}\varepsilon_{kl} \qquad \textit{Eq. 1.15}$$

where σ_{ij} is the stress tensor, C_{ijkl} are the scalar components of the fourth order stiffness tensor C, and ε_{kl} is the strain tensor (Slaughter 2002, p.199). This model is the simplest of all stress-strain relationships that can be fully described by only two material properties, the soil's elastic modulus $E=\sigma/\varepsilon$ (also Young's modulus) and its Poisson ratio $\nu=\varepsilon_{lateral}/\varepsilon_{axial}$. Its simplicity is the biggest argument in favour of its use in deformation analysis, but it comes at the cost of introducing an error: the deformation-stress behaviour of soils is not well replicated by this model except at low stresses and small strains (Duncan 1996, p. 585).

The multilinear elastic models are modifications of the linear elastic model that are intended to improve the replication of actual deformation-stress behaviours observed in soils while preserving much of its simplicity. Piecewise linear functions can be used to emulate the observed tendency of the modulus to decrease as the stresses increase, and especially as the material approaches yield (Duncan 1996).

Hyperbolic model

The hyperbolic elastic model was introduced by Duncan and Chang (1970) as an improvement over the multilinear elastic model that was developed based on the response observed in drained triaxial compression tests of clays and sands. Rather than describing the stress-dependent changes in the modulus with piecewise linear functions, a continuous function was proposed in the following form:

$$\sigma_1 - \sigma_3 = \frac{\varepsilon}{a + b\varepsilon} \qquad \textit{Eq. 1.16}$$

where σ_1 and σ_3 are the major and minor principal stresses, ε is the strain, and a and b are curve-fitting parameters that can be interpreted as follows (Chan 2016).

$$a = \frac{1}{E_o} \qquad \textit{Eq. 1.17}$$

where E_0 is the initial slope of the ε vs. $(\sigma_1\text{-}\sigma_3)$ curve. To interpret parameter b, Eq. 1.16 is rearranged in the following form:

$$a + b\varepsilon = \frac{\varepsilon}{\sigma_1 - \sigma_3} \qquad \textit{Eq. 1.18}$$

This relationship can be visualized as a line by plotting ε vs. $\varepsilon/(\sigma_1\text{-}\sigma_3)$, with a slope equal to b and an intercept at a.

Elasto-plastic and visco-elasto-plastic models

All stress-strain models reviewed up to this point are based on Hooke's Law; in each of these models, the stress increment is related to and directly proportional to the strain increment through the incremental stiffness matrix C that may be stress-independent as it is with the linear elastic model, or stress-dependent as it is with the other two. These models all represent a one-to-one relationship between strain and stress, and are thus independent of the history of loading. Such models entirely ignore the plastic component of deformation that has been consistently shown to be present in soils (Duncan 1996).

The elasto-plastic and elasto-visco-plastic models aim to emulate the elastic as well as plastic deformation behaviours of a soil. In such models, the elastic and plastic components of strain are evaluated separately. The current state of stress is a function of, and proportional to the elastic strain component through the current incremental stiffness matrix *C*, and the latter is often a function of plastic strains that reflect the loading history. Most such models assume that plastic deformations take place after a certain level of stress is exceeded (Slaughter 2002, p. 194). Such models are dependent on the loading history and thus irreversible. They are developed from laboratory tests where, typically, the soils are cyclically loaded and unloaded to increasing stress levels; deformations in the loading stage are interpreted as a measure of total strain increments, and in the unloading stage as a measure of elastic strains. The "linear elastic perfectly plastic model" represents the simplest example of an elasto-plastic model where a perfectly elastic behaviour takes place up to a certain limiting stress and is followed by a perfectly plastic behaviour whereby further strains do not affect the stresses.

1.3.3.2 ADVANCED SOIL STRENGTH MODELS

The history of research of soil strengths reveals a consistent trend of discovering and establishing better relationships between the strength of soil (a response variable) and various properties and in-situ conditions thought to have an effect on it (independent variables). Static analyses such as limit equilibrium methods afford the practitioners the ability to consider (a) constant shear strength models; (b) depth-dependent or total-stress dependent shear strength models; (c) undrained strength ratios where the undrained shear strength is proportional to the overburden effective stresses; and (d) drained strengths where the shear strength of a soil is derived from two components, cohesion and friction generated by effective normal stresses acting on the shear plane. The limit equilibrium analyses were also adapted by practitioners to consider some rudimentary aspects of strength anisotropy (such as preferential slip planes) and contrasting deformation-stress behaviours (such as tensile cracks). The added sophistication of deformation analysis over static analysis such as limit equilibrium methods offers to the geotechnical engineers the ability to expand the shear strength functions to include considerations such as excess pore pressures, elastic and plastic strains, deformations, strength anisotropy and more. In response to this added capability, the geotechnical research community developed a number of advanced constitutive models that relate the mechanical response of soils to these parameters.

Lastly, in deformation analysis, deformation-stress models and shear strength models are two integral components of the constitutive model describing the mechanical response of a material; therefore, the distinction between the two sometimes becomes blurred: such examples include the linear elastic and elasto-plastic constitutive models discussed in previous section.

The basic classes of advanced constitutive models are briefly reviewed here.

Linearly-elastic and perfectly plastic model

The "linear elastic perfectly plastic model" represents the simplest example of an elasto-plastic model where a perfectly elastic behaviour takes place up to a certain limiting stress and is followed by a perfectly plastic behaviour whereby further strains do not affect the stresses. The strength behaviour of such material can be represented by failure criteria such as the Mohr-Coulomb envelope, the Drucker-Prager criterion (Drucker and Prager 1952), the Von Mises criterion and more (Schweiger 2008).

Cam-Clay and Modified Cam-Clay models

The original Cam-Clay model was introduced by Schofield (Roscoe and Burland 1968; Roscoe et al. 1963) to offer a more realistic way to simulate the mechanical behaviour of clays. This model predicts isotropic hardening in soils including at states below the strength envelope. Such modelled behaviour is aimed at replicating some aspects of hardening that has been long documented in soils, thought to be related to volumetric plastic strains associated with a decrease of void ratios and an increase of dry densities.

The original Cam-Clay model uses a logarithmic yield surface that has an undefined gradient along the x-axis. As a consequence, no strain-hardening is predicted in this model for purely isotropic stresses. To correct this deficiency, the logarithmic yield surface was later replaced by an elliptical-shaped one in the Modified Cam-Clay model (Roscoe and Burland 1968).

Other strain-hardening models

Vermeer's (1978) double-hardening model seeks to incorporate more sophisticated forms of strain-hardening into the constitutive models. Vermeer splits the strain tensor into its shear and volumetric components. The former contributes to friction-hardening, expanding the size and shape of the yield surface; and the latter contributes to isotropic hardening. Schanz et al. (1999) further propose an enhanced "hardening model" based on Vermeer's (1978) work. This enhanced model was successfully calibrated against tests on loose sand, and has been implemented in Plaxis©.

A class of isotropic hardening double surface plasticity models have been recently proposed to address some of the shortcomings in the Cam-Clay and similar models related to the prediction of plastic behaviours under conditions when the stress path remains within the elastic zone (for example, during unloading). This shortcoming was addressed by introducing a deviatoric yield surface in addition to the volumetric cap (Schweiger 2008).

Strain-weakening models

Strain-weakening is a soil property whereby on accumulation of plastic strains, the soil's yield stress decreases. Dilation and structural changes to the soil fabric are some of the processes thought to be responsible for the loss of strength in soils on straining.

A number of constitutive models have been proposed to replicate such mechanical behaviour. Frantziskonis and Desai (1987) propose to model the changes in the mechanical response to strain-weakening with the use of a damage variable in a tensor form. Adachi and Oka (1995) introduce an elasto-plastic constitutive model for soft rock that emulates strain-weakening with the use of a stress history tensor. Itasca (2018) propose simulating the strain-weakening behaviour by relating plastic shear strains and stress parameters through piecewise linear functions.

In geotechnical literature, the terms "strain-weakening" and "strain-softening" are used interchangeably. In this thesis, the term "strain-weakening" is used preferentially to emphasize the effect of this phenomenon on the strength behaviour.

1.3.3.3 THE SHEAR STRENGTH REDUCTION METHOD

Deformation analysis predicts the mechanical response of a model based on the assigned materials properties and domain geometry, but does not produce safety factors. If the domain is stable, a stable configuration can be attained where the mass reaches static equilibrium; if it is unstable, a static equilibrium cannot be attained and the soil mass continues deforming indefinitely. The modeller can infer from these results that a stable configuration has a safety factor above unity, and an unstable one equal to or below unity. However, such binary outcome is often unsatisfactory to practitioners that desire to evaluate the safety of a stable structure in more quantitative terms.

Matsui and San (1992) introduced an approach for calculating safety factors of stable structures in deformation analysis. The approach, titled "the shear strength reduction method," consists of reducing the strength parameters c' and ϕ' by a trial value of a safety factor $FOS_{trial}>1$ and then re-evaluating the stability of the model. The lowest trial value of a safety factor that results in the destabilization of the model is considered to be the actual safety factor of the structure.

The safety factors obtained using the shear strength reduction method are generally comparable to those calculated using limit equilibrium methods (Quinn et al. 2014; Duncan 1996; Matsui and San 1992). One of the criticisms leveled against this approach pertains to the dependency of the solution on a stress path that is imposed on the model by the reduction of strength parameters and may therefore be unnatural. The shear strength reduction method is further discussed in §4.3.4.2.

1.4 HYBRID APPROACHES

The limitations of traditional slope stability assessment methods, including limit equilibrium methods and deformation analysis, motivated some researchers to propose mixed solutions. Three such composite approaches to assessing slope stability are reviewed here. The first one by Akhtar and Stark (2017) seeks to address the failure by three-dimensional limit equilibrium methods to properly consider vertical sections of a slip surface. The second and third solutions by Kulhawy et al. (1969) and Stianson (2008) are hybrid methods for calculating safety factors that combine limit equilibrium technique with deformation analysis results, thus eliminating some sources of error in both of these approaches.

1.4.1 THE METHOD BY AKHTAR AND STARK (2017)

The three-dimensional limit equilibrium solutions discussed in §1.2 are not well-suited for stability problems where the slip surface includes vertical or near-vertical faces. Recall that the three-dimensional limit equilibrium methods rely on a range of stated assumptions about inter-slice and inter-column forces in order to determine the stress state along the inclined plane at the base of each column. As a consequence, resistance along fully vertical faces cannot be calculated at all and is generally ignored, and the estimations of resistance along near-vertical surfaces are highly susceptible to errors associated with the assumptions about the horizontal components of inter-slice and inter-column forces.

This means that three-dimensional limit equilibrium analyses of translational slides such as at Oceanside Manor (Stark and Eid 1998) and Jackfield (Skempton 1964; Skempton and Brown 1961) may be in significant error.

Akhtar and Stark (2017) propose a solution for this deficiency whereby the horizontal components of stresses along vertical and near-vertical slip faces are calculated using at-rest and active failure coefficients K_0 and K_a. The resulting horizontal stress estimations are combined with Mohr-

Coulomb strength criteria to evaluate resistance. The researchers report based on a parametric study that limit equilibrium calculations of three-dimensional factors of safety that incorporate side resistance calculations described above compare well to finite element and finite difference solutions; the best results were obtained when using horizontal stress estimates based on lateral earth pressure coefficients K_τ such that $K_0 > K_\tau > K_a$.

The method by Akhtar and Stark (2017) represents the latest modification of a series of solutions published by Stark and Eid (1998), Arellano and Stark (2000), Eid et al. (2006) and Eid (2010). All of these methods use the concept of lateral pressure coefficients to propose a variety of solutions for calculating horizontal stresses acting on vertical slip planes, and resulting frictional components of resistance.

1.4.2 THE KULHAWY ET AL. (1969) METHOD

A 1969 study of embankment stability during construction was conducted by Kulhawy, Duncan and Bolton Seed. As part of the recommended strategy to assess embankment performance, the researchers propose that calculations of safety factors are done in a manner consistent with limit equilibrium procedures that incorporate stresses determined by finite element method. Kulhawy et al. (1969) assert that safety factors calculated in this manner are nearly identical to those determined by the best limit equilibrium methods.

The method by Kulhawy et al. (1969) potentially offers a more accurate method to calculate safety factors because it addresses the error associated with the incorrect determination of stress states by limit equilibrium methods. The potential for such error arises from the limit equilibrium methods' various assumptions regarding forces internal to the slide. Additionally, this method offers an alternative way to calculate safety factors in deformation analysis that, unlike the shear strength reduction method (in §1.3.3.3) does not force a potentially unnatural stress path on the model.

The Kulhawy et al. (1969) method was initially used for two-dimensional analysis. It was later adapted to three dimensions in SoilVision®'s SV Office software (Lu 2019; SVOffice Manual 2018).

1.4.3 THE METHOD BY STIANSON (2008)

Stianson (2008) proposes a method for calculating safety factors that is similar to that by Kulhawy et al. (1969) in that the stress state is first determined by an independent stress-deformation analysis and then used as an input for a limit equilibrium analysis that uses traditional as well as advanced search techniques to determine the critical slip surface. The method by Stianson (2008) is formulated for three dimensions. Like the Kulhawy et al. (1969) method, this approach to calculating safety factors is an improvement over the limit equilibrium methods in that it makes no assumption about the stresses internal to the slide, and an alternative solution to the shear strength reduction method that does not impose a potentially unnatural stress path on the system.

1.5 SUMMARY

In this chapter, two main classes of methods and a number of hybrid solutions for evaluating slopes were reviewed.

The limit equilibrium methods treat the problem of slope instability as one of outright failure, or rupture, and examine the limiting conditions for such. These methods focus on evaluating the ratio of ultimate strengths to working stresses along the failure surface (i.e. the safety factor), as well as finding the potential failure surface with the lowest such ratio. The biggest source of errors in this class of solutions originate with its lack of consideration for the principles of mechanics of deformable solids, as well as with its rigid outlook on what constitutes failure.

As its name suggests, deformation analysis treats slope performance as a problem of deformation rather than one of rupture. Deformation analysis combines the principles of mechanics of deformable solids – namely, the satisfaction of (i) equations of equilibria, (ii) stress-strain relationships, and (iii) stress-displacement compatibility – with numerical techniques to attempt predicting the mechanical response of a model to loading. This method evaluates – rather than estimates – stresses, predicts deformation levels and determines, in a qualitative way, whether the model configuration is stable or not. To estimate the stability of the model configuration in a quantitative manner, methods for calculating safety factors were introduced by Kulhawy et al. (1969), Matsui and San (1992) and Stianson (2008).